UNIVERSITÉ DE LORRAINE | BIBLIOTHÈQUES UNIVERSITAIRES

AVERTISSEMENT
DROIT D'AUTEUR

Ce document est le fruit d'un long travail approuvé par le jury de soutenance et mis à disposition de l'ensemble de la communauté universitaire élargie.

Il est soumis à la propriété intellectuelle de l'auteur. Ceci implique une obligation de citation et de référencement lors de l'utilisation de ce document. Toute contrefaçon, plagiat ou reproduction illicite encourt une poursuite pénale.

Contact bibliothèque : ddoc-theses-contact@univ-lorraine.fr
(Cette adresse ne permet pas de contacter les auteurs)

Code de la Propriété Intellectuelle. articles L 122. 4
Code de la Propriété Intellectuelle. articles L 335.2- L 335.10

UNIVERSITÉ DE LORRAINE
34 COURS LÉOPOLD — CS 25233
54052 NANCY CEDEX
TÉL : 03 54 50 54 00
CONTACT@UNIV-LORRAINE.FR
WWW.UNIV-LORRAINE.FR

Thèse

Présentée et soutenue publiquement pour l'obtention du titre de
DOCTEUR DE l'UNIVERSITE DE LORRAINE

En Physique

par **Sandrine LOPES**

Thèse préparée à l'Institut Jean Lamour, UMR CNRS 7198,
Université de Lorraine, France

Sous la direction de **François MONTAIGNE et Matthieu DESJARDINS**

Optimisation de la distribution de champ magnétique le long d'un nanotube de carbone suspendu pour améliorer l'adressabilité de qubits de spin

Soutenue le 5 novembre 2025

Membres du jury :

Directeurs de thèse :	**François MONTAIGNE**	**Professeur,** **Institut Jean Lamour, Nancy**
	Matthieu DESJARDINS	**Docteur en sciences,** **Co-Fondateur de C12 QUANTUM ELECTRONICS**
Encadrants de thèse :	**Michel HEHN**	**Professeur,** **Institut Jean Lamour, Nancy**
	Daniel LACOUR	**Directeur de recherche,** **Institut Jean Lamour, Nancy**
Rapporteurs :	**Nora DEMPSEY** (Présidente)	**Directrice de Recherche,** **Institut Néel-CNRS, Grenoble**
	Romain MAURAND	**Directeur de recherche,** **CEA, Université Grenoble Alpes**
Examinateurs :	**Aurore FINCO**	**Chargée de Recherche,** **Laboratoire Charles Coulomb, Montpellier**
	Matthieu DELBECQ	**Maître de conférences,** **Sorbonne Université, Paris**

À Alexandre, ma famille et mes amis

Abstract

In this thesis, we investigate the use of an on-chip micromagnet to control the magnetic-field profile along a carbon nanotube for spin-qubit applications.The nanotube serves as a coherent conductor in which a single electron is confined in a gate-defined double quantum dot shaped by the electrostatic potential along the tube. Quantum information is encoded in the electron's spin state, which serves as the qubit. The quantum-dot circuit is embedded in a circuit quantum electrodynamics (QED) architecture that enables qubit manipulation, readout, and long-range coupling. Coupling of the spin qubit to photons in a microwave resonator is enabled through spin-charge hybridization engineered by controlling the field profile along the nanotube: the electron in the double well experiences different spin-quantization axes in the two dots. Here, magnetic-field control is implemented by integrating a micromagnet into the quantum-dot circuit. Optimal geometries for on-chip field gradients are identified through numerical simulations to maximize the magnetic-field difference between the two quantum dots. Thin-film magnetic characterization and local field sensing of the micromagnet - using NV-center magnetometry - are performed. The experimental data are matched with micromagnetic simulations to predict the magnetic field generated by the magnet at various external fields and positions, and hence to forecast spin-qubit performance. To further enhance spin-photon coupling, the spin-qubit architecture is integrated with a microwave circuit fabricated from niobium nitride (NbN), a high-kinetic-inductance, magnetic-field-resilient superconductor. The design and characterization of a high-impedance resonator are detailed. Finally, we demonstrate on-chip integration of the carbon-nanotube quantum-dot circuit, the micromagnet, and the NbN microwave circuitry.

Résumé

Dans cette thèse, nous étudions l'utilisation d'un micro-aimant intégré sur puce pour contrôler le profil de champ magnétique le long d'un nanotube de carbone, en vue d'applications de qubits de spin. Le nanotube sert de conducteur cohérent dans lequel un électron unique est confiné dans un double point quantique défini par des electrodes, en façonnant le potentiel électrostatique le long du tube. L'information quantique est encodée dans l'état de spin de l'électron, qui constitue le qubit. Le circuit de points quantiques est inséré dans une architecture d'électrodynamique quantique en circuit (cQED) permettant la manipulation, la lecture et le couplage longue distance de qubits. Le couplage du qubit de spin aux photons d'un résonateur micro-ondes est assuré par une hybridation spin-charge obtenue en contrôlant le profil de champ le long du nanotube: l'électron du double puits ressent des axes de quantification du spin différents dans les deux points. Ici, le contrôle du champ magnétique est mis en œuvre en intégrant un micro-aimant au circuit de points quantiques. Des géométries optimales de gradients de champ sur puce sont identifiées par simulations numériques afin de maximiser la différence de champ magnétique entre les deux points quantiques. Nous réalisons des caractérisations magnétiques de couches minces ainsi qu'une détection locale du champ produit par le micro-aimant, au moyen de magnétométrie à centres NV. Les données expérimentales sont confrontées à des simulations micromagnétiques pour prédire le champ magnetic généré par le micro-aimant sous différents champs magnétiques externes et à diverses positions, et ainsi estimer les performances du qubit de spin. Pour renforcer encore le couplage spin-photon, l'architecture de qubit de spin est intégrée à un circuit micro-ondes en nitrure de niobium (NbN), supraconducteur à forte inductance cinétique et résistant aux champs magnétiques. La conception et la caractérisation d'un résonateur à haute impédance sont détaillées. Enfin, nous démontrons l'intégration sur puce du circuit de double point quantique en nanotube de carbone, du micro-aimant et du circuit micro-ondes en NbN.

Résumé détaillé de la thèse

en français

Le spin électronique correspond au moment angulaire intrinsèque de l'électron et peut également être interprété comme un minuscule moment magnétique associé à l'électron. Il s'agit d'une notion fondamentale apparue dès les débuts de la mécanique quantique, il y a près d'un siècle, et qui joue depuis un rôle essentiel dans de nombreux domaines de recherche.

En physique de la matière condensée et en science des matériaux, le comportement des spins électroniques dans les cristaux est au cœur de la compréhension des propriétés des matériaux. Par exemple, l'interaction d'échange locale entre les spins non appariés de sites cristallins voisins peut conduire à l'alignement des spins dans une même direction, ce qui est à la base du ferromagnétisme.
Les propriétés ferromagnétiques des matériaux sont déterminantes dans de multiples domaines. Dans un matériau ferromagnétique, l'alignement des spins électroniques donne naissance à un moment magnétique macroscopique. Dans un aimant permanent, un ordre magnétique à longue portée est stabilisé en l'absence de champ externe. La contribution collective des différents moments magnétiques génère ainsi un champ magnétique robuste et durable. Ces aimants permanents sont au cœur de nombreux dispositifs électromagnétiques, où leur champ fixe interagit avec des courants électriques pour convertir l'énergie électrique en énergie mécanique (moteurs) ou l'inverse (générateurs), mais aussi dans des actionneurs, des capteurs de position ou de vitesse, et plus généralement partout où l'on a besoin d'une source de champ magnétique compacte et stable.
Le contrôle des configurations magnétiques au sein d'un matériau ferromagnétique a également permis le développement de phénomènes de transport dépendant du spin, tels que la magnétorésistance géante (Giant MagnetoResistance, GMR) et la magnétorésistance tunnel (Tunneling MagnetoResistance, TMR). Ces effets constituent le cœur de la spintronique, à l'origine de nombreuses applications basées sur des dispositifs à vanne de spin, utilisés par exemple dans les mémoires magnétiques à accès aléatoire (MRAM), les têtes de lecture de disques durs ou encore les capteurs de champs magnétiques.

Le spin électronique peut également être manipulé à l'échelle individuelle. Le contrôle cohérent et la lecture de spins uniques ont ouvert des perspectives en information quantique et en détection quantique. Les niveaux d'énergie discrets associés au spin peuvent en effet servir à encoder de l'information ou à sonder l'environnement local.

Cette thèse explore plusieurs des axes de recherche évoqués ci-dessus et a été réalisée en partenariat avec le laboratoire Nanomagnétisme et Spintronique de l'Institut Jean Lamour (Nancy) et la société C12 Quantum Electronics (Paris), qui développe des qubits de spin dans des boîtes quantiques hébergées dans un nanotube de carbone.

L'objectif de ce travail de thèse est de concevoir, caractériser et intégrer un aimant - développé grâce aux équipements et au savoir-faire du laboratoire nancéien - dans l'architecture de qubits de spin de C12, afin de façonner la distribution du champ magnétique le long d'un nanotube de carbone et, ce faisant, de contrôler l'orientation de spin d'un électron piégé dans des boîtes quan-

tiques situées dans ce nanotube.

Architecture hybride de qubit de spin : circuit de points quantiques inséré dans un circuit micro-onde

En 1998, Daniel Loss et David DiVincenzo ont proposé que le degré de liberté de spin d'un porteur de charge isolé, confiné dans un point quantique défini par des électrodes, puisse servir de système à deux niveaux pour encoder l'information quantique [1], ouvrant ainsi la voie à une implémentation physique de l'ordinateur quantique.

Les spins électroniques peuvent présenter des temps de cohérence longs, en raison de leur couplage relativement faible à l'environnement. Les qubits de spin définis dans des points quantiques offrent également une empreinte relativement compacte, en comparaison avec d'autres technologies concurrentes, telles que les qubits supraconducteurs ou les plateformes à atomes froids. Dans la perspective du calcul quantique à grande échelle, les architectures basées sur des circuits de points quantiques apparaissent donc particulièrement attractives.

Diverses implémentations de circuits de points quantiques ont ainsi été réalisées dans des hétérostructures semi-conductrices, par exemple à base d'arséniure de gallium (GaAs), ou dans des dispositifs à base de silicium, tels que les hétérostructures Si/SiGe ou les structures Si-MOS. C12 Quantum Electronics explore une voie complémentaire, dans laquelle les points quantiques sont hébergés dans des nanotubes de carbone. Ces nanotubes sont suspendus au-dessus d'électrodes qui façonnent le potentiel de confinement le long du tube, ce qui permet d'atténuer le bruit de charge associé à l'interaction avec le substrat. De plus, les nanotubes de carbone peuvent être fabriqués à partir de carbone ^{12}C isotopiquement pur, offrant ainsi un environnement pratiquement dépourvu de spins nucléaires, lesquels peuvent autrement limiter le temps de cohérence des qubits de spin électroniques.

La contrepartie d'un bon isolement vis-à-vis de l'environnement est que l'adressage et la manipulation des spins deviennent plus difficiles. Pourtant, pour l'implémentation physique d'un ordinateur quantique, il est indispensable de pouvoir réaliser des opérations de haute fidélité sur les qubits. En pratique, cela impose que les temps de cohérence du qubit, définis comme la durée pendant laquelle il préserve l'information quantique, soient très largement supérieurs aux temps d'opération et de mesure. La mise en œuvre d'opérations de contrôle et de lecture rapides du qubit est donc particulièrement cruciale.

Une approche efficace consiste à exploiter le couplage spin–orbite (SOC), qui permet de réaliser la résonance de spin par dipôle électrique (EDSR). Un SOC artificiel peut être créé en introduisant un gradient de champ magnétique à proximité du point quantique de façon à coupler les degrés de liberté de charge et de spin de l'électron. Les transitions de spin deviennent alors sensibles aux champs électriques, ce qui autorise un contrôle entièrement électrique de l'état de spin.

Au-delà du contrôle individuel des qubits, la mise à l'échelle vers des architectures quantiques de grande taille requiert une connectivité cohérente entre qubits distants [2], ainsi qu'une méthode de lecture à haute fidélité pour chacun d'eux. Une voie prometteuse repose sur l'électrodynamique quantique en circuit (cQED), dans laquelle les qubits de spin sont couplés aux photons d'un résonateur micro-onde. L'interaction dispersive spin–photon permet une lecture rapide et de haute fidélité de l'état de chaque qubit de spin [3], [4]. Au-delà de la mesure, l'interaction lumière–matière avec des résonateurs coplanaires peut également servir de médiateur d'un couplage cohérent entre spins éloignés, séparés par des distances allant du micron au millimètre [5].

L'architecture de qubit de spin développée par C12 Quantum Electronics s'inscrit dans cette approche d'électrodynamique quantique en circuit (cQED).

Dans les systèmes de points quantiques, le couplage aux photons micro-ondes est obtenu au moyen d'une architecture à **double point quantique**. Dans cette configuration, un électron (ou un trou) peut passer par effet tunnel entre les deux points, ce qui le délocalise entre les deux points et crée un dipôle électrique, capable de se coupler efficacement au champ électrique de la cavité.

Dans un tel dispositif à double point quantique, le couplage du degré de liberté de spin au champ électrique du résonateur est réalisé en hybridant les degrés de liberté de charge et de spin. Cela peut être obtenu via le couplage spin–orbite (SOC), soit intrinsèque au matériau hôte, soit artificiellement induit par l'application d'un champ magnétique antisymétrique par rapport au système à double point quantique, en analogie directe avec le contrôle électrique du spin dans les dispositifs à simple point quantique.

Dans le cas de qubits de spin hébergés dans des nanotubes de carbone, un couplage spin–orbite artificiel est nécessaire pour relier le spin à la charge du porteur. La transition de spin peut alors se coupler à la fois au champ électrique du résonateur et à un champ électrique de contrôle supplémentaire appliqué au dispositif pour le contrôle du qubit.

Pour obtenir des opérations de qubit de haute fidélité, incluant le contrôle électrique et la lecture via une cavité micro-onde, une stratégie consiste à augmenter le dipôle électrique associé à la transition de spin. On y parvient en renforçant l'hybridation spin–charge. Cependant, une hybridation plus importante accroît également la sensibilité du système au bruit de charge, ce qui peut réduire le temps de cohérence des qubits. Il est donc nécessaire de trouver un compromis entre adressabilité et cohérence du système.

Dans notre dispositif, trois énergies caractéristiques décrivent les propriétés du système :

- l'énergie de couplage tunnel t_c, qui décrit le système purement de charge. Elle caractérise la délocalisation de la charge entre les deux points quantiques;
- l'énergie de Zeeman ϵ_Z, qui décrit le système purement de spin. Le spin d'un électron est quantifié, ce qui signifie qu'il ne peut prendre que deux états. L'énergie de Zeeman correspond à l'écart en énergie entre ces deux états de spin, induit par l'application d'un champ magnétique symétrique B_s par rapport au double point quantique : $\epsilon_Z \propto B_s$;
- l'énergie d'hybridation spin–charge ϵ_{hyb}. Elle dépend d'un champ magnétique antisymétrique B_{as}, appliqué dans une direction non colinéaire à B_s et défini par rapport au système à double point quantique : $\epsilon_{\text{hyb}} \propto B_{as}$.

Le compromis entre adressabilité et cohérence que nous avons choisi, et qui est détaillé au Chapitre 1 de cette thèse, consiste à imposer la condition $t_c = \epsilon_Z = \epsilon_{\text{hyb}}$. L'énergie de tunnel t_c peut être contrôlée électriquement en ajustant les tensions de grille. Ce critère se traduit alors par une contrainte théorique sur la distribution du champ magnétique : le champ symétrique ressenti par les deux points doit être de même ordre de grandeur que le champ antisymétrique.

Cette contrainte théorique se transforme en une contrainte spatiale sur la distribution du champ magnétique. Dans nos dispositifs, les deux points quantiques sont séparés d'environ 500 nm. Il est donc nécessaire de générer un champ antisymétrique présentant des variations spatiales significatives sur des distances nanométriques, ce qui représente un défi expérimental.

Pour répondre à cette exigence, nous exploitons le champ magnétique généré par un micro-aimant intégré sur puce. En tenant compte de ces contraintes théoriques, ainsi que de la nécessité de rendre le design de l'aimant et le procédé de nanofabrication compatibles avec l'architecture de qubit de spin développée par C12, cette thèse présente la conception, la caractérisation et l'intégration d'un micro-aimant sur puce destiné à contrôler l'orientation du spin le long du nanotube de carbone.

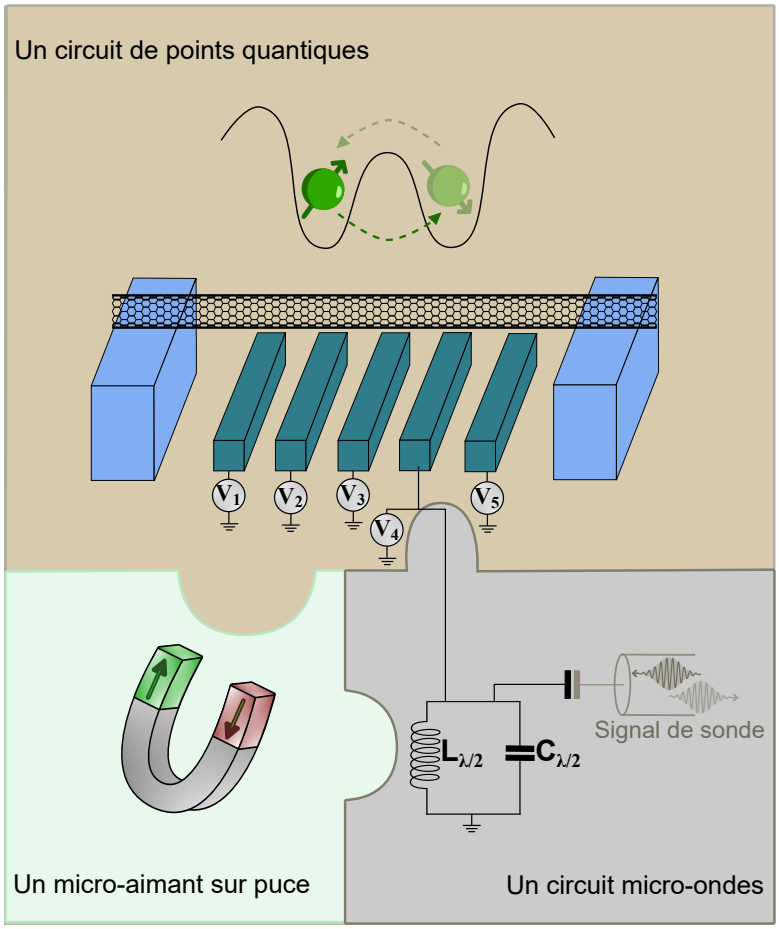

Une architecture modulaire de qubit de spin
L'architecture développée chez C12 repose sur trois éléments principaux : un circuit à boîtes quantiques hébergé dans un nanotube de carbone, un micro-aimant intégré sur puce permettant de façonner le spectre énergétique du qubit, et un circuit micro-ondes assurant la lecture du qubit et une connectivité longue distance.

Conception d'un micro-aimant intégré sur puce pour générer des gradients de champ magnétique et des asymétries de champ.

Le Chapitre 2 présente un premier micro-aimant intégré sur puce, conçu pour contrôler la distribution du champ magnétique le long du nanotube. Dans l'architecture proposée, l'une des électrodes utilisées pour définir le potentiel électrostatique est réalisée dans un matériau ferromagnétique et joue le rôle de micro-aimant sur puce. Bien que cette géométrie ne soit pas entièrement optimisée, elle s'intègre de manière naturelle à l'architecture développée par C12.

En nous appuyant sur des notions clés de nanomagnétisme, nous analysons d'abord la configuration magnétique attendue dans l'aimant. Nous présentons ensuite des caractérisations magnétiques, notamment des mesures SQUID-VSM (Dispositif à Interférence Quantique Supraconductrice - Magnétomètre à Echantillon Vibrant) qui permettent d'étudier l'évolution de l'aimantation sous champ magnétique externe et d'extraire différents paramètres magnétiques du film. Des mesures de MFM (Microscopie à Force Magnétique) sont également réalisées, elles révèlent les potentielles inhomogénéités de la configuration d'aimantation au sein du micromagnet.

Ces mesures et observations sont ensuite utilisées ou confrontées à des simulations micromagnétiques. A partir de ces simulations, le champ magnétique généré par le micro-aimant est calculé, ainsi que les propriétés de qubit de spin associées. Il apparaît que ce premier design n'atteint pas le régime cible : on trouve $B_{as}/B_s \leq 0.1$, et pour $t_c \approx \epsilon_Z$ la force de couplage spin–photon attendue

est $g < 0.06\,\frac{\Delta_g}{2}$, où $\frac{\Delta_g}{2}$ est la force de couplage attendue pour un système purement de charge.

Bien que le terme $\frac{\Delta_g}{2}$, déterminé par les fluctuations de tension de la cavité et par le profil du pseudo-potentiel photonique à travers le double point quantique, puisse être augmenté (par exemple en élaborant un pseudo-potentiel antisymétrique et en utilisant un résonateur de haute impédance), ces résultats motivent la conception d'un nouveau micro-aimant afin d'atteindre le régime idéal et d'augmenter g.

Dans la suite, nous poursuivons la conception d'un micro-aimant optimisé visant à maximiser la composante antisymétrique du champ magnétique entre les deux points quantiques, afin de renforcer l'hybridation spin–charge. Le Chapitre 3 de cette thèse est ainsi consacré à l'optimisation de la géométrie de l'aimant.

Des simulations numériques ont d'abord été développées pour explorer les configurations magnétiques permettant de maximiser les gradients et asymétries de champ générés sur puce. Dans un premier temps, nous négligeons les interactions entre moments magnétiques (échange et interactions dipolaires). Dans ce cadre simplifié, les simulations permettent de déterminer la configuration idéale des moments magnétiques pour maximiser une composante donnée du champ, ou son gradient, dans la direction souhaitée. Cela fournit la configuration magnétique « cible » que l'aimant devrait produire pour optimiser le champ généré.

Pour mettre en œuvre un tel aimant dans un dispositif réel, nous devons cependant utiliser un matériau magnétique dans lequel les interactions entre moments magnétiques ne peuvent plus être négligées. En tenant compte de ces interactions, ainsi que du fait que nous souhaitons utiliser un champ magnétique externe pour régler la composante symétrique du champ entre les deux points quantiques, il devient difficile d'obtenir une configuration proche de la configuration magnétique « cible » mise en évidence dans les simulations précédentes. C'est pourquoi nous avons adapté le cadre de simulation et recherchons désormais la géométrie d'aimant optimale permettant de maximiser l'asymétrie du champ magnétique entre les deux points quantiques, dans le régime d'aimants saturés où tous les moments sont alignés selon une direction donnée. Malgré la simplicité des principes sous-jacents, cette méthodologie fournit une recette pratique pour concevoir des asymétries de champ à l'aide d'aimants micro-structurés et conduit à la sélection d'une géométrie spécifique visant à maximiser la composante antisymétrique du champ produit.

Il demeure toutefois une question importante : quelle est la configuration magnétique effectivement réalisée lorsque l'aimant est constitué d'un matériau magnétique, au sein duquel les interactions entre moments jouent un rôle significatif ? Cette interrogation est particulièrement pertinente dans notre cas, où nous travaillons avec des couches minces de grande épaisseur (supérieure à 150 nm) : contrairement aux couches plus minces, qui présentent une aimantation essentiellement planaire, de telles épaisseurs peuvent conduire à des configurations magnétiques se développant dans le volume de la couche. Pour prendre en compte ces effets, nous présentons des simulations micromagnétiques préliminaires, réalisées à partir de paramètres magnétiques issus de la littérature pour différents matériaux. Pour certains matériaux, le régime cible $B_{as} \sim B_s$ peut être atteint.

Si ces simulations micro-magnétiques fournissent un premier aperçu des performances attendues du micro-aimant, les paramètres utilisés, tirés de la littérature, ne reflètent pas nécessairement de manière fidèle les propriétés des aimants effectivement fabriqués. C'est pourquoi, dans la suite de la thèse, nous nous concentrons sur la caractérisation expérimentale des couches minces et des micro-aimants, afin de déterminer précisément les propriétés magnétiques des films que nous réalisons.

Caractérisation et modélisation micromagnétiques d'un micro-aimant pour dispositifs sur puce

L'objectif des caractérisations présentées dans le Chapitre 4 est de décrire fidèlement les propriétés magnétiques de couches minces réalisées à partir de matériaux disponibles pour la fabrication. Nous concentrons notre étude sur trois matériaux magnétiques à base de cobalt : une couche mince de cobalt, un multicouche cobalt–tantale et un film cobalt–fer.

Nous commençons par des caractérisations de couches minces incluant des mesures de MFM, de diffraction des rayons X et de SQUID-VSM.

Les mesures de MFM renseignent sur les variations du champ magnétique généré par le film et sont ainsi directement liées à la présence de domaines magnétiques. Pour une couche mince présentant une aimantation uniforme dans le plan, le contraste MFM doit rester minimal. Ces observations fournissent un premier élément de comparaison entre les différents matériaux étudiés.

Nous poursuivons la caractérisation des matériaux magnétiques par des mesures de diffraction des rayons X. Les propriétés magnétiques de ces matériaux sont en effet étroitement liées à leur structure cristallographique, la contribution de l'anisotropie magnétocristalline dépendant directement de cette dernière. Ces mesures permettent ainsi d'identifier la structure cristalline propre à chaque matériau.

Enfin, des mesures de SQUID-VSM sont réalisées afin d'extraire, à partir de l'évolution de l'aimantation sous champ magnétique externe, les paramètres magnétiques clés de nos films. Un atout majeur de cette technique est qu'elle peut être mise en œuvre aussi bien à température ambiante qu'à basse température (4 K). Cette flexibilité est particulièrement importante dans notre contexte, le micro-aimant étant destiné à fonctionner à basse température car les qubits sont opérés à des températures cryogéniques.

À partir des différentes caractérisations de couches minces, nous extrayons les paramètres magnétiques nécessaires à la réalisation de simulations micromagnétiques à l'aide du logiciel Mumax[3]. Les simulations sont menées à la fois dans une géométrie de couche mince uniforme et dans la géométrie sélectionnée du micro-aimant.

Pour la géométrie de couche mince, la comparaison entre les simulations, les mesures MFM et les mesures SQUID-VSM montre un bon accord entre les observations expérimentales et les prédictions micromagnétiques.

Pour la géométrie de l'aimant, les simulations micromagnétiques peuvent être comparées qualitativement aux images MFM. Toutefois, notre objectif est d'accéder à une mesure locale du champ magnétique généré par le micro-aimant. Dans cette optique, nous proposons d'utiliser une microscopie à centre NV, qui constitue une plateforme de choix offrant à la fois la résolution spatiale et la sensibilité en champ magnétique nécessaires pour sonder le champ rayonné par l'aimant. Les mesures obtenues par spectroscopie d'un centre NV sont en bon accord avec les simulations micromagnétiques, ce qui permet de valider le cadre de simulation développé.

Nous proposons ensuite d'intégrer le micro-aimant dans notre architecture en l'enfouissant sous les électrodes utilisées pour façonner le potentiel le long du nanotube de carbone. Nous simulons alors la configuration magnétique et le champ généré par le micro-aimant le long du nanotube, pour différents champs externes, ce qui permet de formuler des prédictions fiables sur les performances du qubit. En particulier, pour un micro-aimant en cobalt–fer, nous montrons qu'il est possible d'atteindre $\alpha_{as}/\alpha_s \geq 0.5$. Pour $t_c \sim \epsilon_Z$, cela se traduit par un couplage spin–photon $g \sim 0.3$–$0.5, \frac{\Delta_g}{2}$, soit environ un ordre de grandeur supérieur à celui obtenu avec le premier design étudié.

Démonstration de l'intégration complète d'un aimant, d'un circuit micro-ondes avec un résonateur haute impédance et d'une architecture de points quantiques dans un nanotube de carbone

Une stratégie complémentaire pour augmenter la force de couplage spin–photon, en plus de l'augmentation du dipôle électrique du qubit de spin, consiste à accroître les fluctuations de tension de la cavité. Cela peut être obtenu en concevant un résonateur de haute impédance. Le nitrure de niobium (NbN) est, à cet égard, un matériau supraconducteur particulièrement attractif : sa forte inductance cinétique permet de réaliser des résonateurs de haute impédance qui présentent en outre une bonne robustesse aux champs magnétiques [6].

Le Chapitre 5 est consacré à la conception du circuit micro-onde. En nous appuyant sur des architectures déjà établies, nous utilisons des simulations électromagnétiques ainsi que des simulations au niveau circuit pour optimiser le fonctionnement de chaque élément et choisir de manière judicieuse leurs dimensions et propriétés. Nous présentons également une estimation expérimentale de l'inductance cinétique des couches minces de NbN, ainsi que la caractérisation de résonateurs réalisés dans ce matériau.

Le dispositif complet, associant un circuit à point quantiques dans un nanotube de carbone, un micro-aimant et une plateforme d'électrodynamique quantique en circuit (cQED) réalisée en NbN, est intégré à l'échelle de la puce, comme décrit au Chapitre 6. Différents procédés de nanofabrication visant à enfouir le micro-aimant dans le substrat, sous les électrodes, sont étudiés. Une méthode basée sur un procédé de planarisation chimico-mécanique est finalement retenue, et le procédé de nanofabrication conduisant à des dispositifs complets est présenté. La présence du micro-aimant ne perturbe pas de manière mesurable le contrôle électrostatique le long du nanotube, comme le confirment des mesures de transport dans des circuits à simple et double boîte quantique.

À partir d'un dispositif à simple boîte quantique, nous extrayons un couplage électron–photon $g_{\mathrm{QD}} \sim 2\pi \times 260\,\mathrm{MHz}$, en accord avec les paramètres du résonateur et du circuit. Cela se traduit par un couplage spin–photon atteignable de $g \sim 0{,}3 - 0{,}5$, $\frac{g_{\mathrm{QD}}}{2} \sim 2\pi \times (40\text{–}65)\,\mathrm{MHz}$. Cette valeur est du même ordre de grandeur que le couplage spin–photon rapporté pour deux qubits soumis à des oscillations iSWAP médiées par la cavité entre spins distants ($g \sim 2\pi \times 21\text{–}32\,\mathrm{MHz}$ dans [5]) et environ un ordre de grandeur plus élevée que le couplage rapporté pour des états quantiques dans des nanotubes de carbone couplés à des photons de cavité [7].
Une spectroscopie des états excités dans un circuit à boîtes quantiques, présentée au Chapitre 6, met en évidence l'effet du micro-aimant sur le spectre du point quantique. Ces résultats indiquent que le micro-aimant permet effectivement de façonner le profil du champ magnétique le long du nanotube de carbone.

Acknowledgements/Remerciements

I would like to start this acknowledgement section by thanking the members of my PhD jury: Nora Dempsey, Aurore Finco, Romain Maurand and Matthieu Delbecq. I am especially grateful to Nora Dempsey and Romain Maurand for acting as reviewers and for the time they spent carefully reading my manuscript.
I would also like to take this opportunity to thank the members of my PhD supervisory committee, Takis Kontos and Bertrand Kierren.

I was lucky enough to spend these PhD years between two teams and two places: the Spin team at the Institut Jean Lamour in Nancy and the start-up C12 Quantum Electronics in Paris.
This PhD format at the crossroads between industry and fundamental physics was set up thanks to Matthieu Desjardin, one of my PhD advisors, William Legrand, with whom I had the pleasure of working at the beginning of my PhD, and Stéphane Mangin, who was leading the Spin team in Nancy when I started.

These acknowledgements are organised in chronological order, starting with the teams in Nancy, with whom I worked during the first years of my PhD.



The Spin Team of the Institut Jean Lamour (Nancy)

First, I would like to thank my supervisors. I am very grateful to François Montaigne, my PhD advisor, for his guidance throughout my thesis. Thank you for your valuable advice on nanofabrication processes. Our discussions often helped me to take a step back from my work, and to organise my ideas and results more clearly.

I would also like to thank Michel Hehn and Daniel Lacour, who supervised me on a daily basis at the Institut Jean Lamour. Thank you for your availability and for your help. Thanks to your support and expertise, I was able to carry out the study of the magnetic properties of the magnets.

During these years, I was lucky to be part of such a lively team as the Spin team of the Institut Jean Lamour. I would like to thank both the permanent members and the students of the group. In particular, I am thinking of Valentin Desbuis, Jean-Loïs Bello, Maxime Vergès, Quentin Remy, Héloïse Damas, Anna Friedel, Eva Diaz, Yann Le Guen, Alberto Anadon, Junta Igarashi, Jude Compton-Stewart, Maryam Martirosyan, Jon Gorchon and Sebastien Petit-Watelot. Thank you for making lunch a friendly moment to relax. Thanks to you, I was able to discover and develop my skills in various card games !
I would like to express my special thanks to Jean-Loïs, who is now also part of the C12 team, whom I can always rely on and who greatly helped me with the organisation of my defence.

I would also like to thank all the members of the Institut Jean Lamour whom I met during my PhD and who contributed, directly or indirectly, to this work. I am especially grateful to the members of the technical competence centers. In particular, I would like to thank the members of the Minalor competence center: Laurent Badie, Demba Ba and Sébastien Geiskopf. Thank you for your great help and kindness in the clean room.

During the second part of my PhD, I had the chance to join the teams of C12 Quantum Electronics in Paris.



The Team of C12 Quantum Electronics (Paris)

First of all, I would like to thank my second PhD advisor, Matthieu Desjardins. Despite being co-founder and CTO of C12, and with your responsibilities constantly growing, you always followed my work while giving me a lot of freedom. I am very grateful for this.

I would also like to thank the different teams at C12. In particular, I would like to thank Quentin Schaeverbeke, from the theory team, for his valuable explanations on many topics throughout these years; Viktor Radovic, from the software team, for his help with the GDS files; Gulibusitan Abulizi, Jeanne Becdelievre and Elisa Passalacqua, from the nanofabrication team, for their nanofabrication advice and their support in the C12 cleanroom; Davide Stefani, Nikolai Struchkov

and Mohammadmehdi Torkzadeh, from the nanoassembly team, for the (sometimes quite challenging) nanotube assembly sessions; Alice Castan, Evan Telford and Romaric Le Goff, from the tube characterisation team, as well as the nanotube growth team, for providing the best possible nanotubes during my PhD; and finally the measurement team - Gulibusitan Abulizi, Michael Hynes, Louis Godet, Arthur Larrouy, Benoit Neukelmance and Felix Krauth - for their advice during the on-chip measurements. I am also grateful to the other PhD students working with C12, in particular Benjamin Hue, with whom I had many very enriching scientific discussions. Finally, I would like to thank the Business and Operations team at C12 for greatly simplifying many of my administrative tasks during the PhD.

This PhD thesis was also an opportunity for me to travel across France: in addition to Paris and Nancy, I also went to Dijon and Grenoble.

To carry out this project, I benefited from the help of Aurore Andrieux from the ICB Laboratory in Dijon. I would like to thank Aurore for agreeing to perform the chemical-mechanical planarisation on my samples. Thank you for your kindness : it made my visits to your lab in Dijon both very helpful and enjoyable.

I would also like to thank Frédéric Gustavo from the LaTEQS laboratory (PHELIQS) at CEA Grenoble for depositing NbN on my samples and for the very instructive visit of the lab.

Enfin, je souhaite terminer ces remerciements par quelques mots pour des personnes qui me sont chères.

Je souhaite remercier ma famille pour leur soutien sans faille pendant toutes ces années. En particulier, je veux remercier ma « famille de 5 » sur qui je peux toujours compter: mon père, ma mère, ma sœur et Alexandre.

Pour Alexandre, avec qui je partage mon quotidien : j'ai (enfin) fini, nous pouvons commencer ensemble un nouveau chapitre de nos vies !

J'ai également une pensée pour mon club d'amies de longue date, Claire, Ophélie, Athina et Aurélie, qui m'ont beaucoup soutenue. J'ai beaucoup de chance de vous avoir les filles.

Para algumas pessoas que me são muito queridas, gostaria também de acrescentar algumas palavras em português. Muito obrigada à minha Mamie, aos meus tios e tias, assim como aos meus primos e primas. Tenho muita sorte em ter uma família como vocês. O vosso apoio é verdadeiramente fundamental para mim.

"Tudo vale a pena quando a alma não é pequena."
Fernando Pessoa

Contents

Abstract i

Résumé iii

Résumé détaillé en français v

Acknowledgements xiii

Introduction 1

1 A hybrid architecture for spin qubit in quantum dots hosted in a carbon nanotube 7
1.1 Quantum dot circuit based on carbon nanotube . . . 7
1.1.1 Basics of electronic transport in quantum dots . . . 7
1.1.2 Quantum dots hosted in carbon nanotubes . . . 14
1.1.3 A double-quantum-dot based spin qubit in a CNT . . . 19
1.2 Hybrid CQED : a quantum-dot based device coupled to a cavity . . . 26
1.2.1 Quantum-dot based device coupled to a cavity in the literrature . . . 26
1.2.2 Microscopic description of the coupling mecanism . . . 26
1.2.3 Coulping of an interdot transtion in a DQD to a cavity electric field . . . 27
1.2.4 Properties of the hybrid light-matter system . . . 31
1.2.5 Dispersive readout of the qubit State via cavity measurement . . . 34
1.2.6 Towards a two-qubit gate mediated by a cavity . . . 36
1.2.7 Optimizing the coupling of the qubit with the microwave cavity . . . 37

2 A first design of magnet for artificial spin orbit coupling in a carbon nanotube spin qubit device 41
2.1 Introduction to magnetism in thin films . . . 41
2.1.1 Description of the magnetic energies . . . 41
2.1.2 Macrospin approximation for thin films: the Stoner Wolhfart model . . . 46
2.2 A central magnetic gate for artificial spin orbit coupling . . . 49
2.2.1 The macrospin model . . . 49
2.2.2 Thin film characterization : measuring the magnetization with a VSM magnetometer . . . 53
2.2.3 A qualitative measurement of the magnetization in the gate magnet with magnetic force microscopy . . . 58
2.2.4 Micromagnetic simulations . . . 63
2.2.5 Spatial distribution of the magnetic field along the carbon nanotube . . . 67

3 Optimized micro-magnet design for generating on-chip field gradients and asymmetries 71
3.1 Designing micro-magnets: bridging idealized models and practical constraints . . . 71
3.1.1 Ideal magnetization distributions for field and gradient optimization . . . 71

3.1.2 Realization with saturated magnets . . . 75
3.2 On-chip-micro-magnet compatible with a spin-qubit architecture . . . 79
3.2.1 Optimal geometry of a on-chip micromagnet . . . 79
3.2.2 Accurate modeling with micro-magnetic simulations . . . 85

4 Magnetic characterization of micro-Magnets for on-chip integration 89
4.1 Thin film characterization . . . 89
4.1.1 Material choice and remanent magnetic configuration of the thin films . . . 89
4.1.2 Crystallographic arrangement of the thin film . . . 92
4.1.3 SQUID-VSM measurements analysis . . . 96
4.1.4 Extracting micro-magnetic simulation parameters from the thin-film measurements . . . 101
4.2 Characterization of individual magnets . . . 106
4.2.1 Fabrication process of the micro-magnets . . . 106
4.2.2 Magnetic Force Microscopy: local qualitative mapping of the distribution of the magnetization . . . 110
4.2.3 NV center sensor: local quantitative mapping of the magnet's stray field . . . 112
4.2.4 Scanning NV-magnetometry . . . 117
4.2.5 Measurement and comparison with the micromagnetic model . . . 120
4.3 Modeling and predicting magnet performance for spin qubit integration . . . 126
4.3.1 Performance of the optimized magnet geometry . . . 126
4.3.2 Adapted magnet geometry for CNT spin qubit integration . . . 131

5 A high kinetic inductance and magnetic-field-resilient superconducting circuit for spin-qubit architecture 137
5.1 A superconducting circuit with high kinetic inductance superconducting material . 138
5.1.1 High kinetic inductance superconducting material . . . 138
5.1.2 Superconducting coplanar-waveguide resonators . . . 139
5.1.3 A microwave circuit with high kinetic superconducting material . . . 142
5.2 RF circuit design and validation via lumped and electromagnetic modeling . . . 146
5.2.1 Quite Universal Circuit Simulator (QUCS): modeling the circuit with lumped elements . . . 146
5.2.2 Modelling of the main resonator with DC-bias filtering . . . 147
5.2.3 Modeling of the main resonator with filtering of capacitively coupled DC gates 149
5.2.4 HFSS eigenmode simulations: electromagnetic modeling of the circuit . . . 153
5.2.5 Eigenmode simulation outcomes and analysis . . . 154
5.3 Characterization of NbN superconducting resonators . . . 158
5.3.1 Patterning of structures in the NbN Film . . . 158
5.3.2 Estimation of the kinetic inductance of the NbN film . . . 159
5.3.3 CPW resonator characterization . . . 162
5.3.4 Overview of the final microwave architecture . . . 166

6 Demonstrating the integration of a micro-magnet with a high impedance superconducting resonator in a carbon nanotube device 169
6.1 Co-integration of a micro-magnet and a superconducting coplanar waveguide resonator in a carbon nanotube device architecture . . . 169
6.1.1 How to integrate a micro-magnet on-chip ? - Fabrication process . . . 169
6.1.2 Overview of the additional fabrication process steps . . . 175
6.1.3 Integration of carbon nanotubes into the Chip . . . 178
6.1.4 Initial characterization after chip fabrication and carbon nanotube integration 181
6.2 Calibration of the electron-photon coupling . . . 186

6.2.1 Photon-number dependence of the differential conductance in the Coulomb blockade regime . . . 186
6.2.2 Dispersive shift of the resonator frequency induced by the quantum dot . . 193
6.2.3 Discussion on the cavity-quantum dot coupling . . . 196
6.3 Spectroscopic study of excited states under magnetic-field variation . . . 197
6.3.1 Protocol for magnetic-field spectroscopy of excited states in a carbon-nanotube quantum dot . . . 197
6.3.2 Excited-state spectroscopy in triangle I . . . 199
6.3.3 Excited-state spectroscopy in triangle II . . . 205

Conclusion and perspectives **211**

Appendix A : Micro-magnetic simulations **213**

Appendix B : Additional characterization of a NbN thin film **225**

Appendix C :Calibration of the RF setup for photon number estimation **229**

Appendix D : Etching rate calibration of Silicum and Cobalt-Iron **231**

References **233**

Introduction

In 1922, Otto Stern and Walther Gerlach carried out in Frankfurt a landmark experiment to test the "space quantization" predicted by the Bohr–Sommerfeld (old quantum) theory.

A few years earlier, this theory had introduced orbital quantization to account for why atoms absorb and emit light only at discrete wavelengths. In this framework, the magnitude of an atom's orbital angular momentum is quantized, $L = l\hbar$ with $l \geq 0$ an integer, and its projection along any chosen axis is likewise quantized, $L_z = m\hbar$ with $-l \leq m \leq l$ an integer. Thus, for a given orbital l, there are $2l+1$ allowed orientations. The magnetic moment associated with the angular momentum, $\boldsymbol{\mu}_L = -\frac{e}{2m_e}\mathbf{L}$ and its component $\mu_{L,z}$ are therefore quantized as well.

Their experiment rested on the following idea: a magnetic moment in a field feels a torque that tends to align it, and in a non-uniform field it experiences a net force that deflects its path. If magnetic moments could point in arbitrary directions, a beam of atoms would broaden continuously after passing through such a field. Conversely, observing discrete beam deflections would reveal quantized values of the projection of the atomic magnetic moment and, indirectly, the space quantization of orbital angular momentum.

The results, published in 1922 [8], were taken as crucial evidence for quantized angular-momentum orientation in atoms. After traversing the inhomogeneous magnetic field, the beam split into a discrete doublet, apparently signaling quantization of orbital angular momentum. To rationalize this, Stern and Gerlach used the silver atoms, for which $l = 1$. Although $2l + 1 = 3$ sublevels might be expected, hence contradicting the two observed, contemporary interpretations varied, and some arguments - including Stern's - emphasized two resolved components along the field axis instead of three.

The Stern–Gerlach result was reinterpreted only a few years later, when physicists-including Pauli (1927) and Dirac (1928)-developed and formalized the concept of electron spin, the electron's intrinsic angular momentum [9], [10], [11] . Within this framework, the splitting observed by Stern and Gerlach was understood as arising from the unpaired $5s$ electron of the silver atom. Summing orbital contributions over all electrons in the atom gives a total atomic orbital angular momentum $L = \sum_i l_i = 0$, while the total spin is $S = \frac{1}{2}$. The orbital magnetic moment of silver thus vanishes, leaving only the electron-spin magnetic moment with two possible projections - hence the observed doublet. The experiment is therefore recognized as a pivotal clue to the existence of electron spin.

Since then, the concept of electronic spin has woven through many active research fields.

In condensed matter and materials science, the behavior of electronic spins in crystals is central for understanding material properties. Exchange interactions can align or anti-align spin moments, producing ferro- and antiferromagnets [12],[13]. The resulting magnetic configurations govern spin-dependent transport phenomena (Giant MagnetoResistance [14] and Tunneling MagnetoResistance [15]). Spin–orbit coupling ties spins to crystal symmetry and orbital motion, yielding magnetic anisotropy [16], chiral textures such as skyrmions [17], [18], [19], [20], and topological insulators [21], [22]. Collective spin precessions (magnons) transport angular momentum

without charge flow, enabling low-power information processing [23].

At the level of single spins, coherent control and readout have opened perspectives in quantum information and quantum sensing. Discrete spin energy levels can encode information or probe the local environment. Here we offer a few illustrative examples and briefly highlight representative platforms.

For quantum sensing, a representative platform is point defects in crystals-most notably nitrogen-vacancy (NV) centers in diamond-which enable diverse modalities, including magnetometry [24], [25], [26], thermometry([27]) or strain/electric-field sensing [28]. In recent years, NV-center-based microscopes have transitioned from laboratory prototypes to commercial instruments, expanding access to nanoscale magnetometry and related measurements.

Beyond sensing, the spin coherence and optical addressability make NV centers natural building blocks for quantum information, with their spin manifold serving as a qubit ([29], [30]). NV centers thus stand as one promising spin-qubit platform - alongside others currently envisioned for scalable quantum devices. Notable alternatives include spin qubits in gate-defined quantum dots [1], [31], [32] - where electrostatic confinement quantizes the energy spectrum and two spin projections of a single level encode information - and donor-based systems [33], in which a substitutional impurity contributes an extra electron and both the electron and the donor nucleus provide spin degrees of freedom for qubit implementations.

This thesis explores several research areas introduced above and was carried out in partnership with the Nanomagnetism and Spintronics Laboratory at the Institut Jean Lamour (Nancy) and C12 Quantum Electronics (Paris), a company developing spin qubits in quantum dots hosted by carbon nanotubes.
The goal of this PhD work is to design, characterize, and integrate a magnet - developed using the facilities and know-how of the Nancy laboratory - into C12's spin-qubit architecture, in order to tailor the magnetic-field distribution along a carbon nanotube and thereby control the spin orientation of an electron trapped in quantum dots within the nanotube.
To frame the magnet's role and the desired magnetic field characteristics, we need to begin by presenting the essentials of the qubit architecture developed at C12.

What is a qubit and what does it take to build a quantum computer?

In classical computers, information is encoded in bits that take values 0 or 1. By contrast, quantum computers encode information in qubits - two-level systems that can be in the states $|0\rangle$, $|1\rangle$, or any superposition of the two:

$$|\psi\rangle = \cos\frac{\theta}{2}|0\rangle + e^{i\varphi}\sin\frac{\theta}{2}|1\rangle$$

By exploiting quantum superposition and entanglement, quantum algorithms are envisioned to solve certain problems in far fewer steps than their classical counterparts. This prospect has driven rapid advances in quantum computing and substantial investment aimed at identifying the most suitable qubit architectures [34].

In 2000, David DiVincenzo formulated five practical requirements for building a quantum computer [35]:

- **Scalable qubits**:
  The physical platform must support many, well-defined qubits.
- **Initialization**:
  It must be possible to prepare qubits reliably in a simple, known state.
- **Long coherence**:
  Errors in quantum system come from two sources. Bit-flip errors - as in classical systems

- arise from energy exchange with the environment and are characterized by the relaxation time T_1. Phase-flip errors are uniquely quantum, stemming from fluctuations in the $|0\rangle \leftrightarrow |1\rangle$ energy splitting and described by the pure-dephasing time T_φ. The coherence time T_2 encompasses both mechanism $\frac{1}{T_2} = \frac{1}{2T_1} + \frac{1}{T_\varphi}$.
These coherence times must greatly exceed gate times - for control operations - and measurement times - for readout.

- **Universal gating**:
The platform must implement a universal set of quantum gates, including high-fidelity single-qubit gates and at an entangling two-qubit gate.
- **Qubit-specific readout**:
The system needs the ability to measure individual qubits with high fidelity.

From Principles to Practice: Constructing a Spin-Qubit Platform that Fulfills DiVincenzo's Criteria

Daniel Loss and David DiVincenzo proposed in 1998 that the spin degree of freedom of a single charge carrier confined in a gate-defined semiconductor quantum dot could serve as a two-level system to encode quantum information [1].

Electron spins can exhibit long coherence times because their coupling to the environment is relatively weak compared with other degrees of freedom, such as electron charge.
Semiconductor spin qubits also offer a compact footprint compared with competing technologies such as superconducting (transmon-based) qubits or cold-atom platforms. From the perspective of large-scale quantum computation - and to satisfy the first DiVincenzo criterion (scalability) - semiconductor implementations therefore appear particularly attractive.

The first spin-qubit realizations used gate-defined quantum dots in gallium–arsenide (GaAs) heterostructures. However, magnetic-moment fluctuations from the nuclear spin bath in GaAs limited dephasing, leading to short coherence times, and coherence time of close to 10 ns were reported [36]. To overcome this, the community started to explore silicon-based devices. Because the dominant silicon isotope ^{28}Si has zero nuclear spin, magnetic fluctuations are strongly reduced - especially in isotopically enriched ^{28}Si resulting in significantly longer dephasing times. Coherence time $T_2 \sim 2$ s were reported for isotopically enriched silicon based device [37].
C12 Quantum Electronics pursues a complementary path in which quantum dots are hosted by carbon nanotubes. The nanotubes are suspended above electrostatic gates that shape the confinement potential along the tube, mitigating substrate charge noise. Moreover, nanotubes can be grown from isotopically purified ^{12}C providing a nuclear–spin-free environment for electron spin qubits.

The counterpart of being well-isolated from the environment is that addressing spins can be challenging.

One route is magnetic control, but purely magnetic driving typically yields slow gate times. To meet the spirit of DiVincenzo's third requirement - coherence times much longer than operation and measurement times - faster control is desirable. This is achieved electrically via spin–orbit coupling (SOC), which enables electric–dipole spin resonance (EDSR).
Artificial SOC can be engineered by introducing a magnetic-field gradient near the dot - typically with on-chip micromagnets - to couple charge and spin degree of freedom of the electron. Intrinsic SOC, requiring no external magnetic field, can be leveraged in the valence band of silicon-based quantum dots, motivating the growing interest in hole spin qubits.
Because stronger addressability usually increases environmental coupling and can shorten coherence, performance is best captured by gate fidelity - a dimensionless measure of how closely an

implemented gate matches the ideal target. Single qubit gate fidelities above 99.99% have been reported using EDSR enabled by a magnetic gradient for an electron spin qubit [38].

Beyond single-qubit control (initialization and one-qubit gates), scalable architectures require coherent connectivity between distinct qubits [2].
Heisenberg exchange coupling has enabled to demonstrate two-qubit gates - and even a six-qubit silicon processor [39] - but it is intrinsically short-ranged, linking nearest neighbours qubits.
One proposal for longer-range connectivity to longer-range connectivity is coherent electron shuttling, in which the electron - and its spin state - is physically and coherently transferred by tuning the quantum-dot electrostatic potentials [40], [41], [42].
A second route approach leverages circuit quantum electrodynamics (cQED), coupling spin qubits to photons of a microwave resonator. Through the light–matter interaction, coplanar-waveguide resonators can mediate interactions between distant spins over micron-to-millimetre distances. Beyond coupling, the dispersive spin–photon interaction also provides fast and high-fidelity readout of individual qubit state. This architecture therefore address DiVincenzo's fourth and fifth criteria.

The spin-qubit architecture pursued by C12 Quantum Electronics adopts this cQED-based strategy.

Coupling Spin Qubits to Microwave Photons with Engineered Magnetic-Field Profiles

cQED architectures are widely used with superconducting qubits to provide fast, high-fidelity readout and to couple distant qubits. They sit at the core of current proposition for superconducting-qubit quantum processors [43], [44], [45],[46].

In spin-qubit architectures, however, coupling the electronic spin to the cavity's electric field is less straightforward than in superconducting circuits, where the field directly couples to the transmon's electric dipole [47].
In quantum-dot systems, the first coupling to microwave photons was realized through the charge degree of freedom in a double-quantum-dot architecture [48]. There, an electron (or a hole) tunnels between two sites, forming an electric dipole that can couple to the cavity field.
In the double-quantum-dot setting, coupling the spin degree of freedom to the resonator's electric field is then engineered by hybridizing spin and charge degree of freedom. This is accomplished via spin–orbit coupling (SOC) - either intrinsic to the host material or induced artificially - in direct analogy with electrically driven spin control in single-dot devices. In this way, the spin transition can couple both to the resonator electric field and to an additional drive electric field sent to the device for qubit control.
Using on-chip micromagnets, strong coupling between an electron spin qubit and microwave-cavity photons has been demonstrated in silicon-based devices as well as coherent control of one qubit coupled to a cavity [3], [4]. Recently, iSWAP two-qubit gate has been achieved reported a two qubit gate fidelity estimated to 80% [5]. For hole-spin qubits, the strong-coupling regime has likewise been reached [49] and the coherent control of the qubit demonstrated [50].

When dealing with spin qubits hosted in carbon nanotubes, artificial spin-orbit coupling is needed to couple the spin to the charge of the charge carrier.
A proposed route for suspended nanotubes uses exchange interactions from ferromagnetic contact gates to set the spin orientation along the tube. With this approach, coherent control of quantum states coupled to a microwave cavity has been demonstrated [7].
In this thesis, we propose and implement the design, characterization, and integration of an on-chip micromagnet to control spin orientation along the carbon nanotube. Building on prior demonstrations in silicon-based devices, we pursue this second strategy to achieve higher control over the quantum-dot spectrum, since the qubit frequency can be set by the external magnetic field.

Thesis outline

This thesis is organized as follows.

In Chapter 1, we set out the theoretical background for quantum-dot circuits with carbon nanotubes as the host material. Within this framework we present the charge and spin-qubit implementations in this architecture. We then introduce circuit QED for carbon-nanotube spin qubits and derive the spin–photon coupling mechanism, identifying the magnetic-field requirements that maximize coupling while preserving coherence.

Chapter 2 presents a first on-chip magnet designed to control the magnetic-field distribution along the nanotube. Although not fully optimized, this geometry is readily integrable into C12's architecture. After introducing key notions of nanomagnetism, we analyze the expected magnetic configuration, report magnetic characterizations, and use them to predict the generated field and the corresponding spin-qubit properties.

In Chapter 3, we pursue an optimal magnet design that maximizes the antisymmetric field between the two dots to enhance spin–charge hybridization. We combine numerical modeling with preliminary micromagnetic simulations to identify the preferred geometry and material parameters for the on-chip gradient source.

Chapter 4 reports the magnetic characterization of the selected design. We combine thin-film measurements with local magnetic-field sensing-using NV-center spectroscopy-and compare the data to micromagnetic simulations. With the validated magnetic parameters, we simulate the magnetic configuration and field at various heights and external fields, enabling confident predictions of qubit performance.

Chapter 5 focuses on the microwave circuitry compatible with an on-chip magnet and, in particular, on operation under finite magnetic fields. To realize a fully integrated chip, we employ niobium nitride (NbN) - a high-impedance, field-resilient superconductor whose large kinetic inductance further enhances spin–photon coupling. Building on established architectures, we use electromagnetic and circuit-level simulations to analyze each circuit component and select dimensions and properties judiciously.

Finally, the last chapter presents the full integration of a micromagnet with a high-kinetic-inductance superconducting resonator in a carbon-nanotube device. We describe the nanofabrication process we developed to realize the complete device. We then present first characterizations of the complete chip, demonstrating successful integration.

Chapter 1

A hybrid architecture for spin qubit in quantum dots hosted in a carbon nanotube

1.1 Quantum dot circuit based on carbon nanotube

1.1.1 Basics of electronic transport in quantum dots

For gate-defined quantum dots, investigating electronic transport within the quantum dot circuit is essential for studying and probing the system's low-energy spectrum. In this section, we first introduce the fundamentals of electronic transport in a single quantum dot circuit. We then focus on transport through a double quantum dot circuit and explain how to identify the regions where tunneling between the two quantum dots occurs.

Quantum dots in the Coulomb Blockade regime

The most elementary electrostatically defined, quantum-dot-based electronic circuit consists of source and drain electrodes that are tunnel-coupled to the quantum dot. There is an additional gate called the plunger gate that allows to tune the electrochemical potential of the quantum dot.

To understand the transport properties of the circuit, it is essential to account for Coulomb interactions between charges in the quantum dot. In particular, when the Coulomb energy dominates over both the coupling to the source and drain - characterized by the tunneling rate Γ - and the thermal excitation energy $k_B T$, then Coulomb blockade effect governs the transport properties in the quantum dot. The quantum dot behaves as an almost isolated system. The strong confinement leads to localized electronic wavefunctions and the number of electrons in the dot remains an integer N. Each N-electron quantum dot has a well-defined ground state (the state with the lowest energy) and a set of excited states, labeled by an integer n. The plunger gate allows for tuning the energy levels in the quantum dot via capacitive coupling. Denoting $E_{\mathrm{N}}^{(\mathrm{n})}$ as the energy of the quantum state (N,n), for small variations in the plunger gate voltage around a specific value V_{pg}^0 the energy can be expressed as:

$$E_{\mathrm{N}}^{(\mathrm{n})}(V_{pg}) = E_{\mathrm{N}}^{(\mathrm{n})}(V_{pg}^0) - eN\alpha_{pg}\,\Delta V_{pg}$$

where e denotes the elementary charge, α_{pg} is the lever-arm of the plunger gate and $\Delta V_{pg} = V_{pg} - V_{pg}^0$ represents the deviation from the reference gate voltage.

At low temperatures, the electronic states in the source and drain are occupied up to their respective electrochemical potentials, μ_S and μ_D. Similarly, we can define the electrochemical potential of the quantum dot. For a quantum dot initially containing N-1 electrons in the state m, the electrochemical potential corresponds to the energy required to add an electron to the dot,

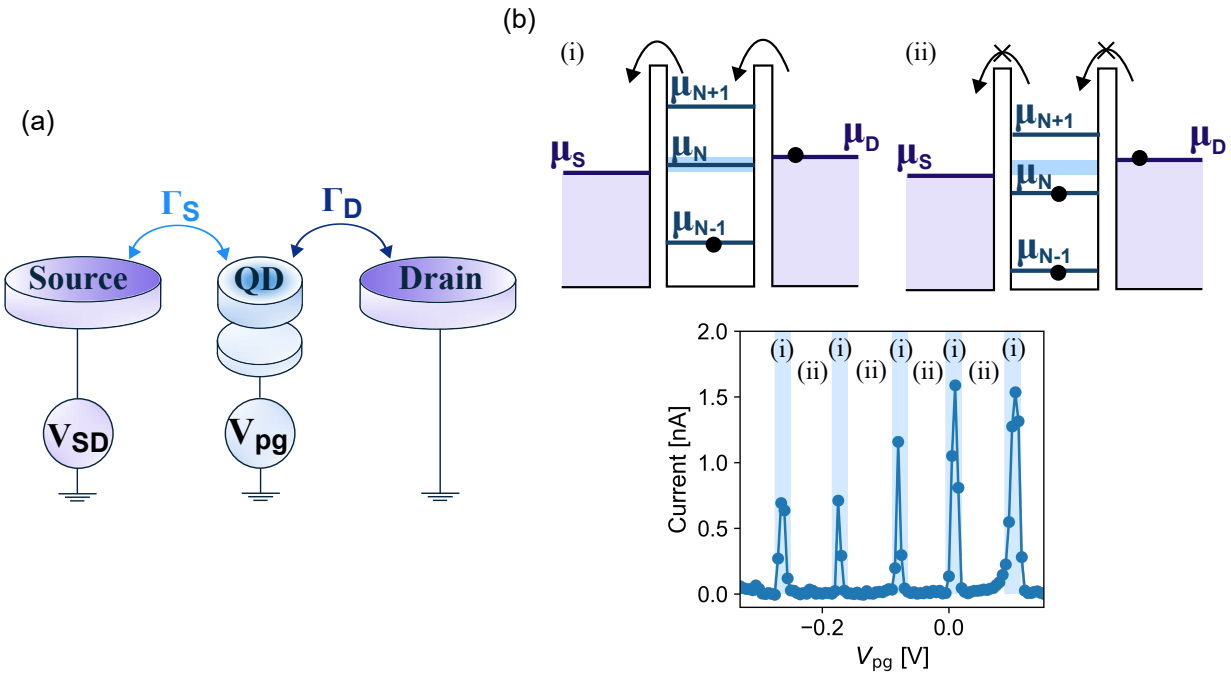

Figure 1.1: **Coulomb blockade in a single quantum dot**
(a) Schematic of a single quantum dot coupled to source and drain reservoirs. A source-drain bias V_{SD} is applied, and the dot's electrochemical potential is tuned by the plunger-gate voltage V_{pg}. $\Gamma_{\mathrm{S/D}}$ denote the tunneling rates between the quantum dot and the source/drain; these parameters set the width of the conductance peak in panel (b).
(b) Coulomb blockade in a single quantum dot. Current flows only when a dot electrochemical potential μ_N lies within the bias window, enabling single-charge carrier tunneling and producing a Coulomb peak in the measured current. When μ_N is outside the window, transport is blocked and no current is detected. The spacing between adjacent Coulomb peaks is proportional to the charging energy ΔE_c. The current measurement presented was performed on device 1 of chip C12-013-J.

placing it in state n :

$$\mu_{\mathrm{N}}^{(n,m)}(V_{pg}) = E_{\mathrm{N}}^{(n)}(V_{pg}) - E_{\mathrm{N-1}}^{(m)}(V_{pg}) \tag{1.1}$$

The plunger gate voltage enables control over the electrochemical potential of the quantum dot by shifting the energy of the state (N,m), leading to:

$$\mu_{\mathrm{N}}^{(n,m)}(V_{pg}) = \mu_{\mathrm{N}}^{(n,m)}(V_{pg}^{0}) - e\alpha_{pg}\,\Delta V_{pg} \tag{1.2}$$

By adjusting the voltage of plunger gate, one can control the elastic electron transport through the quantum dot circuit. When $\mu_S \approx \mu_{\mathrm{N}}^{(0)}(V_{pg}) \approx \mu_D$, the energy gained from removing an electron from the source is equal to the energy required to add an electron to the dot. Once the electron is inside the dot, the energy gained from removing it is balanced by the energy required to add an electron to the drain, allowing current to flow through the circuit. Current blockade occurs when the above conditions are not met. The electron transport can then be characterized through conductance measurements as represented Fig. 1.1.

Stability diagram of a single quantum dot circuit

To fully characterize the transport properties of the quantum dot, we can measure its charge stability diagram. This diagram is obtained by measuring the conductance while sweeping the plunger gate voltage for various source-drain voltages, resulting in the formation of the characteristic Coulomb blockade diamonds.

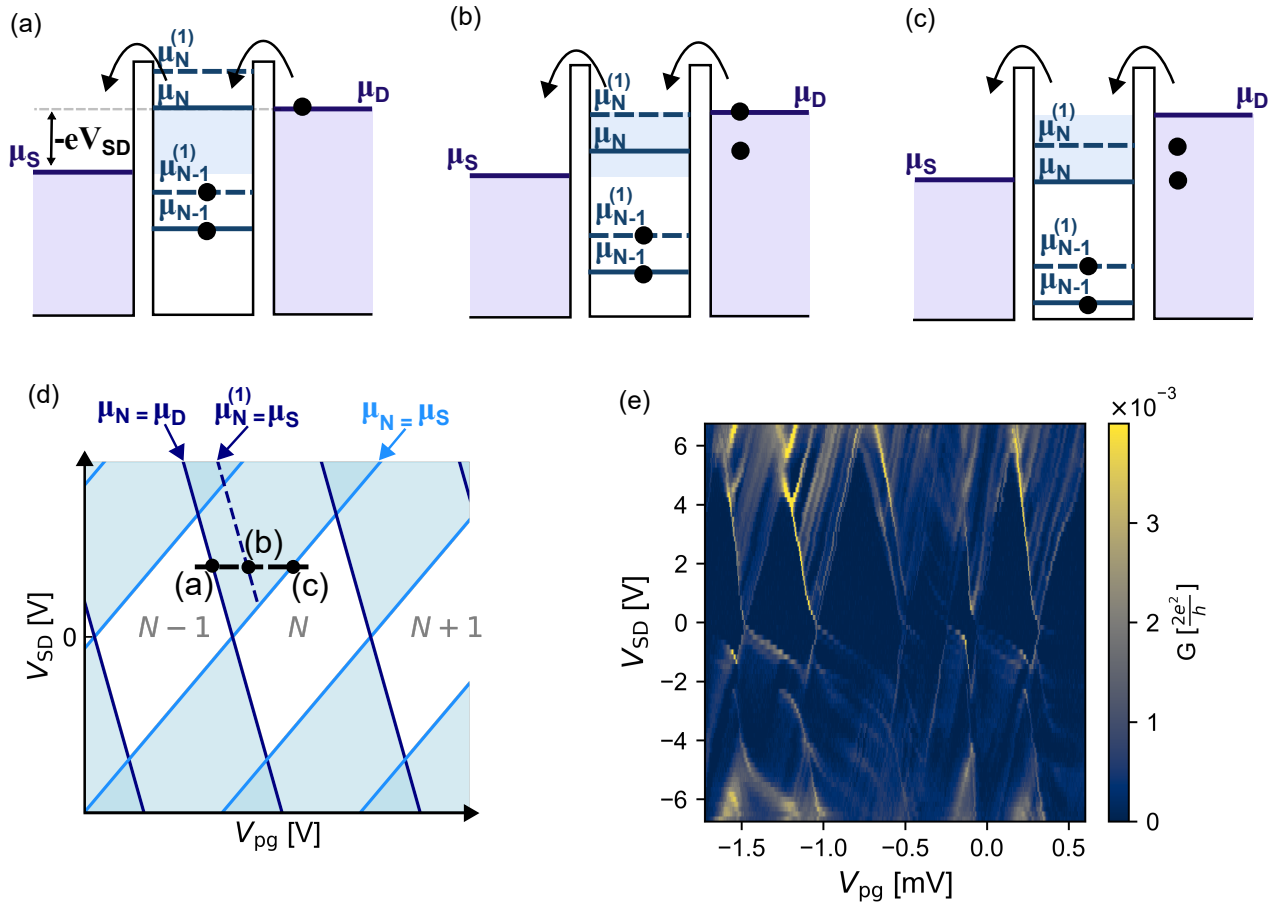

Figure 1.2: **Charge stability diagram of a single quantum dot**
(a-c) Schematic panels illustrating excited-state transport in a single quantum dot with electron charge carriers.
(d) Schematic charge-stability diagram. sThe Coulomb-blockaded region forms a diamond centered at $V_{SD} = 0V$. Outside the diamond, current flows in triangular regions at positive and negative bias. Additional lines parallel to the diamond edges indicate transport via excited states, as illustrated in panels (a-c).
(e) Measured charge-stability diagram for a single quantum dot formed in a carbon nanotube. The device (multi-walled or bundled carbon nanotube) exhibits similar features to those reported for carbon-nanotube quantum dots of the same type ([51], [52]). Measurement presented was performed on device 1 of chip C12-013-J

Applying a finite source-drain voltage $V_{SD} \geq 0$ opens a bias window $-eV_{SD} = \mu_D - \mu_S$ within which current can flow for a given number N of electrons in the quantum dot, provided that the following condition holds:

$$\mu_S \geq \mu_N^{(0)}(V_{pg}) \geq \mu_D \tag{1.3}$$

For a given bias window, there exists a finite range of plunger gate voltage allowing current to flow:

$$|V_{pg}| = \frac{V_{SD}}{\alpha_{pg}} \tag{1.4}$$

This relationship defines triangular regions in the charge stability diagram where current can flow, as represented Fig. 1.2. As the size of these triangles increases with increasing V_{SD}, the triangles corresponding to conductance resonances from the energy levels N and N+1 will eventually intersect. At the intersection point, where $\mu_N^{(0)}(V_{pg}) = \mu_S$ and $\mu_{N+1}^{(0)}(V_{pg}) = \mu_D$, we obtain :

$$eV_{SD} = \mu_{N+1}^{(0)}(V_{pg}) - \mu_N^{(0)}(V_{pg}) \approx \Delta E_c + \Delta_{orb} \approx \Delta E_c \tag{1.5}$$

where ΔE_c is the characteristic energy for charging the dot and Δ_{orb} is the single-particle level spacing - i.e. the energy separation between quantized levels in the dot due to confinement. We assume here single occupancy of each orbital. Here we supposed single occupation level. In typical quantum dots, the single-particle spacing is small compared to the charging energy. By measuring the bias voltage at the intersection point, we can determine the charging energy ΔE_c which serves as the characteristic energy scale for charging the quantum dot as represented Fig. 1.3.

Capacitance model

The stability diagram can also be described using a capacitance model. The interactions between electrons in the dot, as well as between the electrons and the gate electrodes, are represented by a capacitance matrix. The number of charges in the metallic island is determined by the electrostatic energy of the system:

$$Q_{\text{dot}} = -e\text{N} = C_\Sigma V_{\text{dot}} + \left(C_\text{D} V_\text{D} + C_\text{S} V_\text{S} + C_{\text{pg}} V_{\text{pg}}\right) \tag{1.6}$$

here $C_{\text{dot}} = C_\Sigma = -\sum_{i=\{\text{S,D,pg}\}} C_i > 0$, and we assume that when the voltages are set to zero, no charges reside on the gates or in the dot. The potential of the island can therefore be expressed as:

$$V_{\text{dot}} = \frac{Q_{\text{dot}}}{C_\Sigma} - \sum_{i=\{\text{S,D,pg}\}} \frac{C_i}{C_\Sigma} V_i \tag{1.7}$$

This equation shows how the potential of the quantum dot is influenced by both the charge on the dot and the applied voltages at the source, drain, and plunger gate, weighted by their respective capacitances.
The electrostatic energy required to add N electrons to the quantum dot is given by:

$$E_{elec}(\text{N}) = \int_0^{-e\text{N}} \text{d}Q\; V_{\text{dot}}(Q) = \frac{e^2\text{N}^2}{2C_\Sigma} + e\text{N} \sum_{i=\{\text{S,D,pg}\}} \frac{C_i}{C_\Sigma} V_i \tag{1.8}$$

With this model, the electrochemical potential of the quantum dot can be defined as:

$$\begin{aligned} \mu_\text{N}^{(0)} &= E_{elec}(\text{N}) - E_{elec}(\text{N}-1) + \epsilon_N^0 = \frac{e^2}{C_\Sigma}\left(\text{N} - \frac{1}{2}\right) + \epsilon_N^0 + e \sum_{i=\{\text{S,D,pg}\}} \frac{C_i}{C_\Sigma} V_i \\ \mu_\text{N}^{(0)} &= \Delta E_c \left(N - \frac{1}{2}\right) + \epsilon_N^0 + e\left(\alpha_\text{S} V_\text{S} + \alpha_\text{D} V_\text{D} + \alpha_{\text{pg}} V_{\text{pg}}\right) \end{aligned} \tag{1.9}$$

where the charging energy of the quantum dot is defined as $\Delta E_c = {}^{e^2}/_{C_\Sigma}$, ϵ_N^0 is the electrochemical potential of the single particle problem and the lever arm of gate i is defined as $\alpha_i = {}^{C_i}/_{C_\Sigma}$.
The four boundaries of the Coulomb blockade diamonds are defined by the following four linear equations:

$$\mu_\text{N}^{(0)} = \mu_\text{S},\; \mu_\text{N}^{(0)} = \mu_\text{D},\; \mu_{\text{N+1}}^{(0)} = \mu_\text{S} \text{ and } \mu_{\text{N+1}}^{(0)} = \mu_\text{D}$$

The slopes of these equations is related to the lever arms in the circuit. Therefore, by analyzing the Coulomb blockade diamonds, we can extract the slopes of the diamond boundaries and determine the lever arms of the circuit. In particular, the plunger-gate lever arm can be obtained from the diamond height and width (see Fig. 1.3). An alternative is to extract it directly using Eq. (1.4).

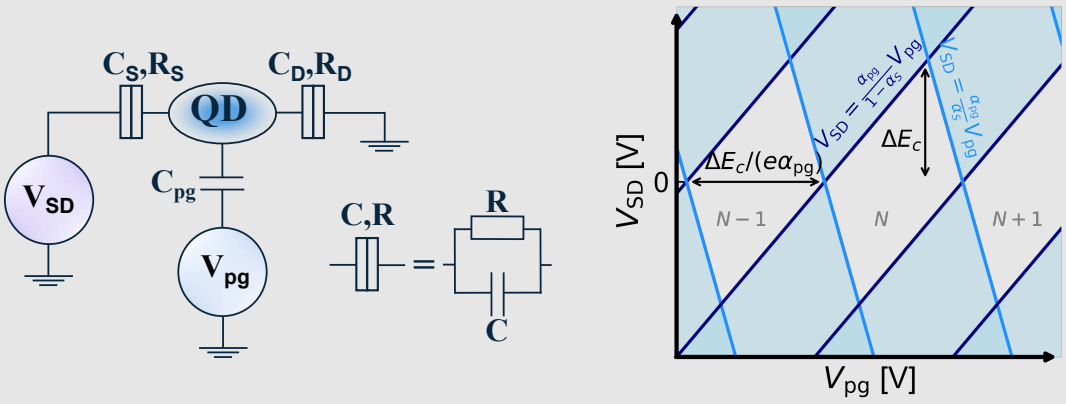

Figure 1.3: Quantum dot (with N charges) in the capacitance model, tunnel coupled to source/drain and capacitively to the gate. Tunnel barriers are treated as a resistor in parallel with a capacitor.
From the charge stability diagram, characteristic parameters of the quantum dot can be determined.

Electronic transport in a double-quantum-dot circuit

Single quantum dots can be mutually coupled by bringing the two dots closer together, i.e., by reducing their spatial separation. We consider the case of two quantum dots, labeled 0 and 1, connected in series. We are interested in the transport properties of the double quantum dot circuit. The coupling between the dots is described by both capacitive coupling and tunneling interactions. The charge stability diagram of coupled quantum dots is typically obtained by measuring the conductance while sweeping the charge on each dot. The energy levels of each quantum dot

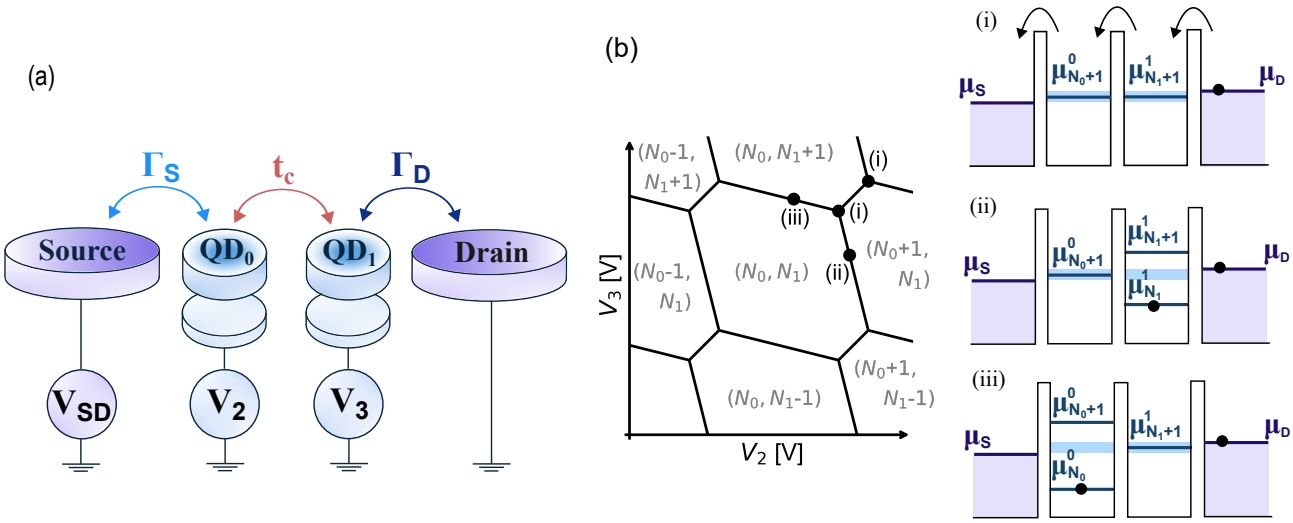

Figure 1.4: **Transport in a double quantum dot circuit**
(a) Schematic of a double quantum dot coupled to source and drain reservoirs. A source-drain bias V_{SD} is applied, and the dots' electrochemical potentials are tuned by the plunger-gate voltages V_2 and V_3. t_c corresponds to the tunnel coupling between the two dots.
(b) Charge-stability "honeycomb" pattern defined by the transport lines where conduction is allowed. Panels (i)-(iii) illustrate the corresponding transport regimes.

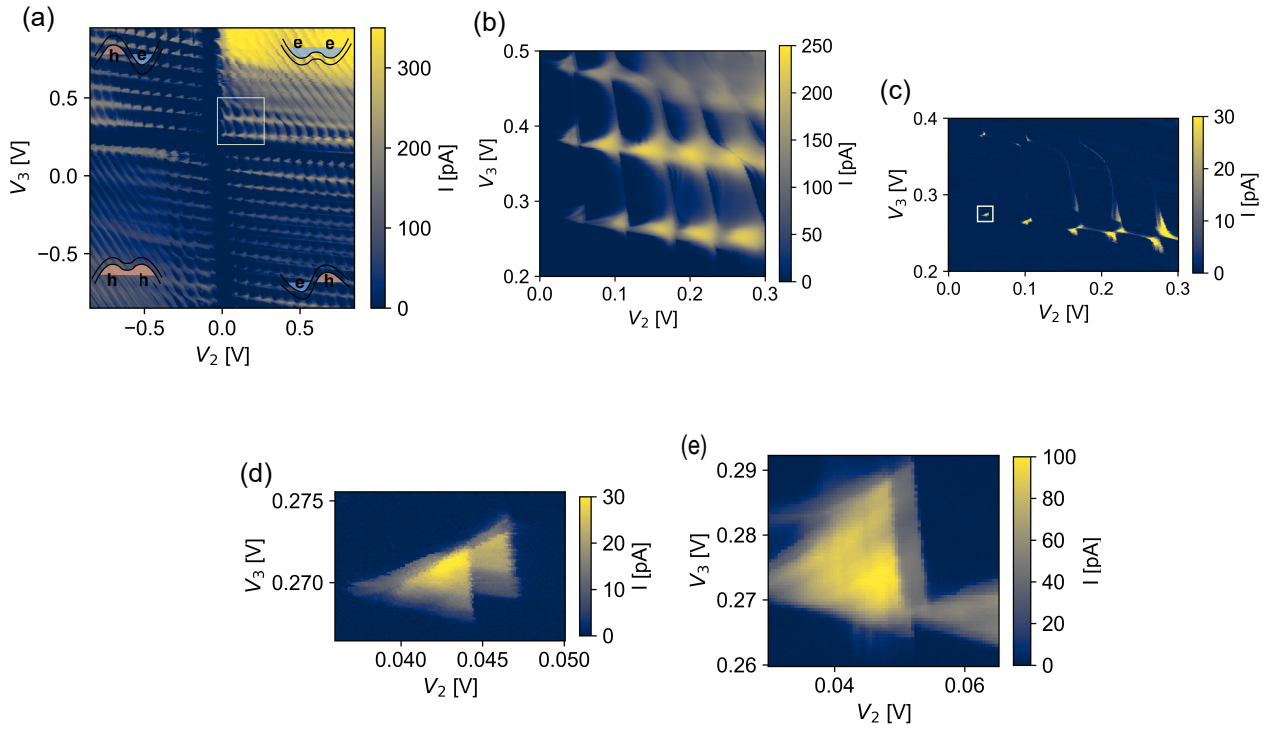

Figure 1.5: **Stability diagram of a double quantum dot circuit.**
Current measured through a double quantum dot system in a suspended semiconducting carbon nanotube, with the dots connected in series between source and drain contacts.
(a) Wide-range charge stability diagram acquired at a source-drain bias voltage of $V_{SD} = 5\,mV$. Four distinct regions can be identified, corresponding to different charge carrier configurations: two homopolar regions (electron-electron in the top right and hole-hole in the bottom left) and two heteropolar regions (an electron on one dot and a hole on the other) in the top left and bottom right quadrants. In the homopolar regions, for large plunger gate voltages, the two dots merge into a single quantum dot regime due to strong interdot coupling.
(b) Zoom into the electron-electron region, where the characteristic honeycomb pattern of the double quantum dot charge stability diagram is observed.
(c) Same region as (b), with a reduced source-drain bias of $V_{SD} = 1\,mV$, revealing bias triangles at the triple points. The white rectangle highlights a region that is further magnified in panel (d). As the interdot tunnel coupling is increased by increasing the voltage on plunger gate 2, current suppression between the triple points is lifted and the sharp corners of the bias triangles become rounded.
(d-e) Evolution of the bias triangles with source-drain bias voltage: (d) corresponds to $V_{SD} = 1\,mV$, and (e) to $V_{SD} = 5\,mV$.
These measurements were performed on device 1 of chip C12-013-J.

are tuned using separate plunger gates, while the voltages on the other gates in the system are kept constant. The resulting stability diagram typically presents hexagon-shaped regions, forming a honeycomb pattern. Within each hexagonal region, the state (N_0,N_1) is stable, where N_0 and N_1 denote the number of electrons in dots 0 and 1 respectively as represented Fig. 1.4.

The electrochemical potentials of dots 0 and 1 are denoted as $\mu^0_{N_0}(N_1)$ and $\mu^1_{N_1}(N_0)$, respectively. When there is no source-drain bias, electron transport through the double quantum dot occurs only at the triple point where:

$$\mu^0_{N_0}(N_1) \approx \mu^1_{N_1}(N_0) \approx \mu_S \approx \mu_D \tag{1.10}$$

Under a finite source-drain voltage ($V_{SD} \geq 0$), electron transport through the double quantum dot

occurs when:

$$\mu_S \leq \mu^0_{N_0}(N_1) \leq \mu^1_{N_1}(N_0) \leq \mu_D \tag{1.11}$$

This condition defines triangular regions at the triple point of the charge stability diagram, where electron transport through the double quantum dot circuit is allowed as displayed in Fig. 1.4.

A typical charge stability diagram of a double quantum dot circuit obtained during this PhD work is shown in Fig. 1.5. In the regime of weak interdot tunnel coupling, current flows only at the triple points, where well-defined bias triangles are observed (see Fig. 1.5(c-e)).

Capacitance model

Similarly to what was done in the case of a single quantum dot, we can describe the circuit with a capacitance model. The energy levels of the dots 0 and 1 are tuned using two plunger gates labeled 2 and 3. The electrochemical potentials of the dots are given by :

$$\begin{aligned}
\mu^{(0)}_{0,N_0}(N_1) &= \epsilon^0_{N_0} + \frac{e^2}{C_{\Sigma,0}}\left(N_0 - \frac{1}{2}\right) - e\left(\alpha_{0,2}V_2 + \alpha_{0,3}V_3\right) + \frac{e^2}{\tilde{C}_{0,1}}N_1 \\
\mu^{(0)}_{1,N_1}(N_0) &= \epsilon^0_{N_1} + \frac{e^2}{C_{\Sigma,1}}\left(N_1 - \frac{1}{2}\right) - e\left(\alpha_{1,2}V_2 + \alpha_{1,3}V_3\right) + \frac{e^2}{\tilde{C}_{0,1}}N_0
\end{aligned} \tag{1.12}$$

where

$$\begin{aligned}
C_{\Sigma,j} &= C_{jj}\left(1 - \frac{C_{10}C_{01}}{C_{00}C_{11}}\right) > 0, \\
\tilde{C}_{0,1} &= \frac{C_{00}C_{11} - C_{01}C_{10}}{-C_{01}} > 0, \\
\alpha_{0j} &= \frac{C_{01}C_{1j} - C_{11}C_{0j}}{C_{00}C_{11} - C_{01}C_{10}} > 0, \\
\alpha_{1j} &= \frac{C_{10}C_{0j} - C_{00}C_{1j}}{C_{00}C_{11} - C_{01}C_{10}} > 0
\end{aligned}$$

In the above equations $C_{i,j}$ correspond to the cross capacitance depicted in the schematic Fig.1.6.

A charge stability region in the stability diagram corresponds to a region associated with the same ground state (N_0, N_1). The charge in the double quantum dot remains stable as long as the electrochemical potentials of the source and drain, $\mu_S = \mu_D$, are not resonant with any of the electrochemical potentials within the double quantum dot. Boundaries of the charge stability region correspond to six equations :

$$\begin{aligned}
\mu_{S/D} &= \mu^{(0)}_{0,N_0+1}(N_1) \\
\mu_{S/D} &= \mu^{(0)}_{1,N_1+1}(N_0) \\
\mu_{S/D} &= \mu^{(0)}_{0,N_0}(N_1) \\
\mu_{S/D} &= \mu^{(0)}_{1,N_1}(N_1) \\
\mu^{(0)}_{0,N_0+1}(N_1 - 1) &= \mu^{(0)}_{1,N_1}(N_0) \\
\mu^{(0)}_{0,N_0}(N_1) &= \mu^{(0)}_{1,N_1+1}(N_0 - 1)
\end{aligned}$$

These conditions result in six linear equations that enclose the six boundary lines of the hexagonal area forming the honeycomb pattern (see Fig. 1.6). The slopes of these equations are function of the lever arms in the circuit.

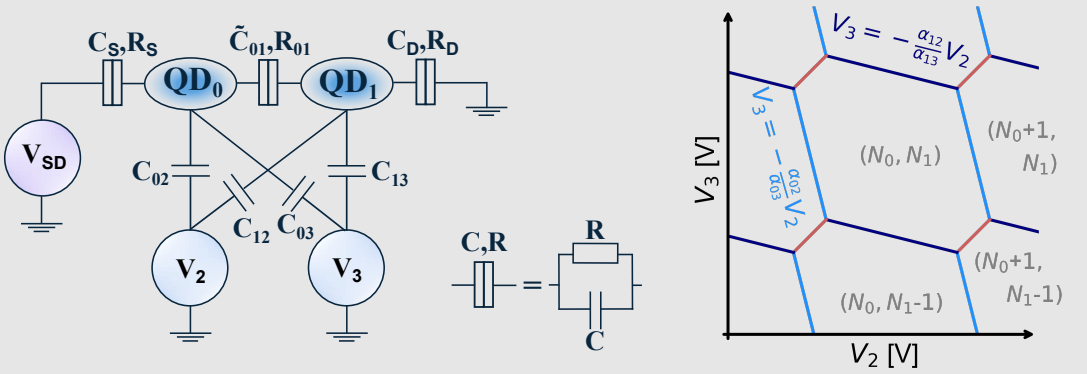

Figure 1.6: Double quantum dot in the capacitance model tunnel coupled to source/drain and capacitively to the gate. Tunnel coupling between the dots is modeled by a tunnel barrier. From this model one obtains the slopes of the charge-stability diagram lines.

.

1.1.2 Quantum dots hosted in carbon nanotubes

A quantum dot circuit with a carbon nanotube

Carbon nanotubes provide an attractive platform for quantum dot circuit experiments [53]. By suspending the nanotube above the plunger gates, interactions with the substrate can be minimized [54]. Using five plunger gates enables independent control over the electrochemical potential of each dot, the tunneling coupling between the dots - characterized by t_c - and the coupling to the source and drain, characterized by Γ_S and Γ_D. This full tunability allows precise control over the stability diagram of the double quantum dot [55].

To gain insight into the energy levels of each quantum dot, we will next discuss key properties related to the band structure of carbon nanotubes.

From Graphene band structure to CNT band struture

The carbon nanotube structure consists of one or more concentric cylinders of graphene, resulting in single-wall or multi-wall carbon nanotubes (SWCNT or MWCNT) as schematized in Fig.1.7. Since there are various ways to roll up a graphene sheet, numerous atomic structures of carbon nanotubes can exist. Each structure is described by its chiral vector **C**, which connects the lattice points that align when the graphene sheet is rolled. The electronic structure of a carbon nanotube retains many properties from graphene. However, due to the rolling of the graphene sheet, additional effects emerge on the band structure.

Graphene has a rhombic unit cell with a two-atom basis and a hexagonal Brillouin zone, see Fig. 1.7. The points K and K' represent the corners of the hexagon in k-space. The three K (or K') points are connected by reciprocal lattice vectors, so that, following Bloch's theorem, they correspond to equivalent electronic states. The resulting band structure is unusual: the valence band (denoted π) and the conduction band (denoted π^*) touch only at the Dirac points, K and K'. Close to the Fermi energy, the dispersion relation is linear, with a slope that determines the Fermi velocity. Writing $\mathbf{k} = \mathbf{K} + \kappa$ or $\mathbf{k} = \mathbf{K}' + \kappa$, the dispersion relation reads, for $|\kappa| \ll |\mathbf{K}|, |\mathbf{K}'|$:

$$E = \pm \hbar v_F |\kappa| \tag{1.13}$$

The positive sign applies to electrons and the negative sign to holes. The slope of the dispersion

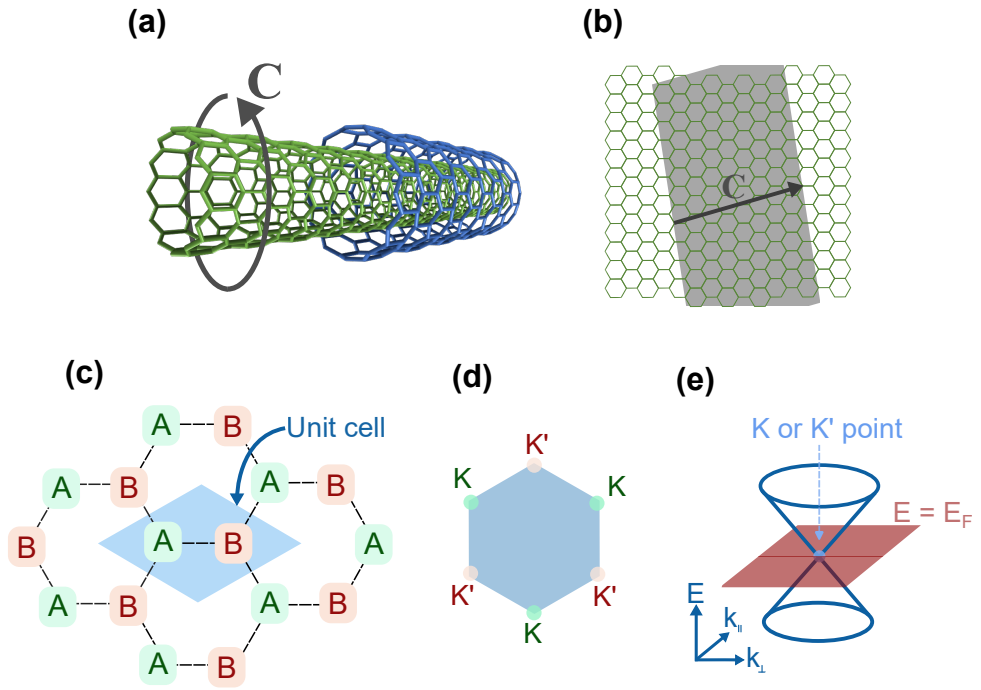

Figure 1.7: **From graphene to carbon-nanotube band structure**
(a)Schematic of a multi-wall carbon nanotube (MWCNT).
(b) A single-wall nanotube can be viewed as a rolled-up graphene strip. The chiral vector **C** pans the tube circumference.
(c) Graphene segment with the unit cell shaded (blue) and the A/B sublattices indicated.
(d) First Brillouin zone of graphene in reciprocal space, showing the six symmetry points, labeled K and K'.
(e) Energy dispersion of Graphene near a Dirac point, linear around the Fermi level.

relation determines the Fermi velocity. Undoped graphene is neither a true metal nor a semiconductor, but rather a semi-metal.

The zone-folding approximation allows us to derive the band structure of a carbon nanotube from that of graphene. We assume that rolling graphene into a nanotube does not fundamentally alter the band structure - neglecting curvature effect - except for the addition of a periodic boundary condition on the component of the wavevector transverse to the nanotube:

$$\mathbf{k}.\mathbf{C} = 2\pi p \quad \text{such that} \quad k_\perp = \frac{2p}{D} \tag{1.14}$$

where **C** is the chiral vector, p is an integer and D is the diameter of the nanotube.
The allowed values of the transverse component of the wavevector $k_\perp$ correspond to a set of lines in reciprocal space. The band structure of the nanotube depends on the position of the quantization line relative to the Dirac points K and K'. This is because the one-dimensional dispersion relation of the nanotube is a cut along a quantization line in the two-dimensional dispersion relation of graphene, given by:

$$E_{\text{CNT}}(k_\parallel) = E_{\text{Graphene}}\left(k_\parallel, k_\perp = \frac{2p}{D}\right) \tag{1.15}$$

As a result, carbon nanotubes can either be metallic or semiconducting as illustrated in Fig. 1.8. In a random collection of nanotubes with varying atomic structures, semiconducting nanotubes outnumber metallic ones by a 2:1 ratio.

Perturbations to the zone-folding approximation arise in carbon nanotubes, with one striking example stemming from the curvature of the nanotube. The curvature breaks the equivalence of

the three carbon-carbon bond directions, causing a slight displacement of the Dirac points from their original positions in reciprocal space. In metallic carbon nanotubes, this shift of the Dirac cones relative to the quantization lines introduces a small bandgap [53]. Likewise, uniaxial and torsional strain act as effective gauge fields that shift the Dirac cones with respect to the quantization lines, thereby opening (or tuning) a small gap [53]. These nanotubes are often referred to as narrow-bandgap nanotubes. As a result, purely metallic carbon nanotubes are relatively rare.

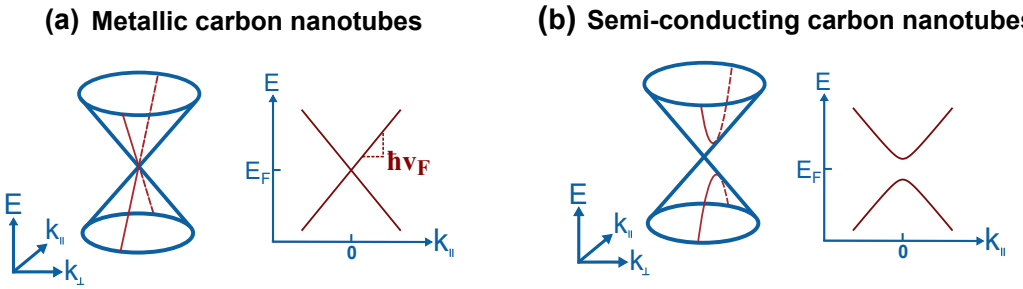

Figure 1.8: **Metallic vs. semiconducting carbon nanotubes**
For carbon nanotubes, in the zone-folding picture, circumferential boundary conditions quantize the graphene wavevector into parallel lines in the Brillouin zone. (a) If these lines passes through a Dirac point, the nanotube is metallic. (b) If the lines avoid the Dirac points, a gap opens and the tube is semiconducting.

Energy levels in quantum dot hosted in a carbon nanotube

Let's consider the case of carbon-nanotube with a bandgap. Longitudinal confinement is introduced with the plunger gates voltage. The dispersion relation close to the Fermi-energy reads:

$$E_0^{\pm} = \pm\sqrt{\left(E_G^0\right)^2/4 + E_{\text{conf}}^2} \quad \text{with} \quad E_{\text{conf}} = \hbar v_F \kappa_{\parallel} \tag{1.16}$$

$E_G^0 = 2\hbar v_F |\Delta\kappa_{\perp}|$ is the band gap set by transverse quantization, with $|\Delta\kappa_{\perp}|$ the mismatch between an allowed transverse wave-vector and the graphene Dirac point. In typical devices the transverse confinement is strong, so transport can be treated within a single subband. The longitudinal wavevector is quantized by the longitudinal confinement.

Each state in the system is four-fold degenerate, as it can be described by two quantum numbers: spin and valley. The valley quantum number refers to two Dirac points K and K'. These valleys can be thought of as two states with different circulation orientations around the nanotube. The degeneracy between the K and K' valleys can be lifted by applying a longitudinal magnetic field. We can define a valley-dependent magnetic moment, or orbital magnetic moment, such that the magnetic energy of a state is given by:

$$E_{\text{mag}} = \left(\mp g_{\text{orb}}\gamma + \frac{1}{2} g_s \sigma\right)\mu_B B_{\parallel} \tag{1.17}$$

Here, the sign $-$ applies for electrons, while the sign $+$ applies for holes. g_{orb} is the orbital g-factor, g_s is the spin g-factor and γ, σ are the valley and spin quantum number denoted by $\gamma = \{1, -1\}$ for $\{K, K'\}$ and $\sigma = \{1, -1\}$ for $\{\uparrow, \downarrow\}$.

For low energy electron ($\kappa_{\parallel} \sim 0$) the orbital g-factor is given by $g_{\text{orb}}^0 = \frac{\mu_{\text{orb}}^0}{\mu_B} = \frac{Dev_F}{4\mu_B} \approx 3.5\ D[\text{nm}]$, where D is the tube diameter [53].
We highlight that the effective orbital g-factor, g_{orb}, can be smaller than g_{orb}^0.
Confinement in a quantum dot can lower g_{orb}. The orbital magnetic moment μ_{orb} comes from motion of the electron around the circumference. For states such that $\kappa_{\parallel} \approx 0$, the electron velocity

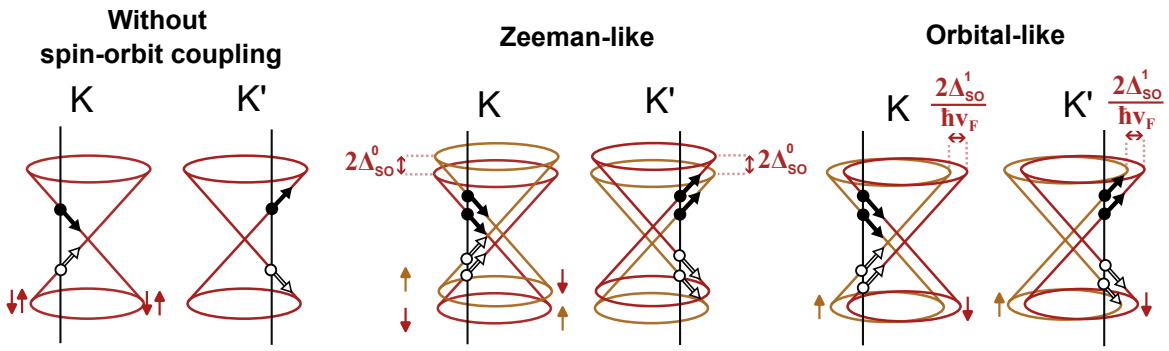

Figure 1.9: **Two spin-orbit coupling (SOC) mechanisms in carbon nanotubes**.
Zeeman-like SOC produces a spin-dependent *vertical* shift of the bands-an effective Zeeman splitting with opposite sign in the two valleys
Orbital-like SOC produces a spin-dependent *horizontal* shift of the band structure equivalent to a spin-dependent magnetic field coupling to the orbital magnetic moment.

points mostly around the tube and so μ_{orb} is maximal. Going to higher longitudinal momentum, a larger fraction of the velocity points along the tube. The confinement reduces the fraction of the Fermi velocity v_F directed around the nanotube, leading to a decrease in the orbital g-factor, i.e., $g_{orb} \leq g^0_{orb}$ [53].
In addition, renormalization of the orbital g-factor can arise from tunneling processes to the source and drain reservoirs [53], [56].

Spin orbit coupling and inter-valley scattering.

In carbon nanotubes, spin-orbit coupling arises due to symmetry breaking caused by the nanotube's curvature. Detailed calculations reveal two distinct contributions to the spin-orbit interaction [53]:

- **Zeeman-like contribution**: This corresponds to a vertical shift of the Dirac cones for the two spin orientations, with the shift being opposite for the two valley states. The strength of this coupling is characterized by Δ^0_{SO}.
- **Orbital-like contribution**: This results in a horizontal shift of the Dirac cones for the two spin orientations. This contribution can be understood as a spin-dependent magnetic flux coupling to the orbital moment, with a coupling strength characterized by Δ^1_{SO}.

These two contributions are schematically represented if Fig. 1.9.
Under the assumption that electron and hole shells do not mix, meaning that:

$$E^0_G \gg g_{orb}\mu_B\left|B_\parallel\right|, \left|\Delta^1_{SO}\right| \tag{1.18}$$

where E^0_G is the bandgap of the carbon nanotube and $\left|B_\parallel\right|$ is the amplitude of the magnetic field applied along the carbon-nanotube. The total spin-orbit coupling can then be expressed as [53]:

$$\Delta_{SO} = 2\left(\Delta^0_{SO} \mp \Delta^1_{SO}\frac{g_{orb}}{g^0_{orb}}\right) \tag{1.19}$$

The sign $-$ holds for electrons and the sign $+$ holds for holes.
In this expression, g^0_{orb} is orbital g-factor for an unconfined electron, while g_{orb} is the effective g-factor taking into account the effect of confinement in a quantum dot, as mentionned above.
The total spin-orbit coupling results in an energy splitting of the two spin states within a given valley at zero magnetic field. The strength of the spin-orbit coupling reported in the literature ranges from $\Delta_{SO} = 150\,\mu$eV [57] to $\Delta_{SO} = 3.4\,$meV [58].

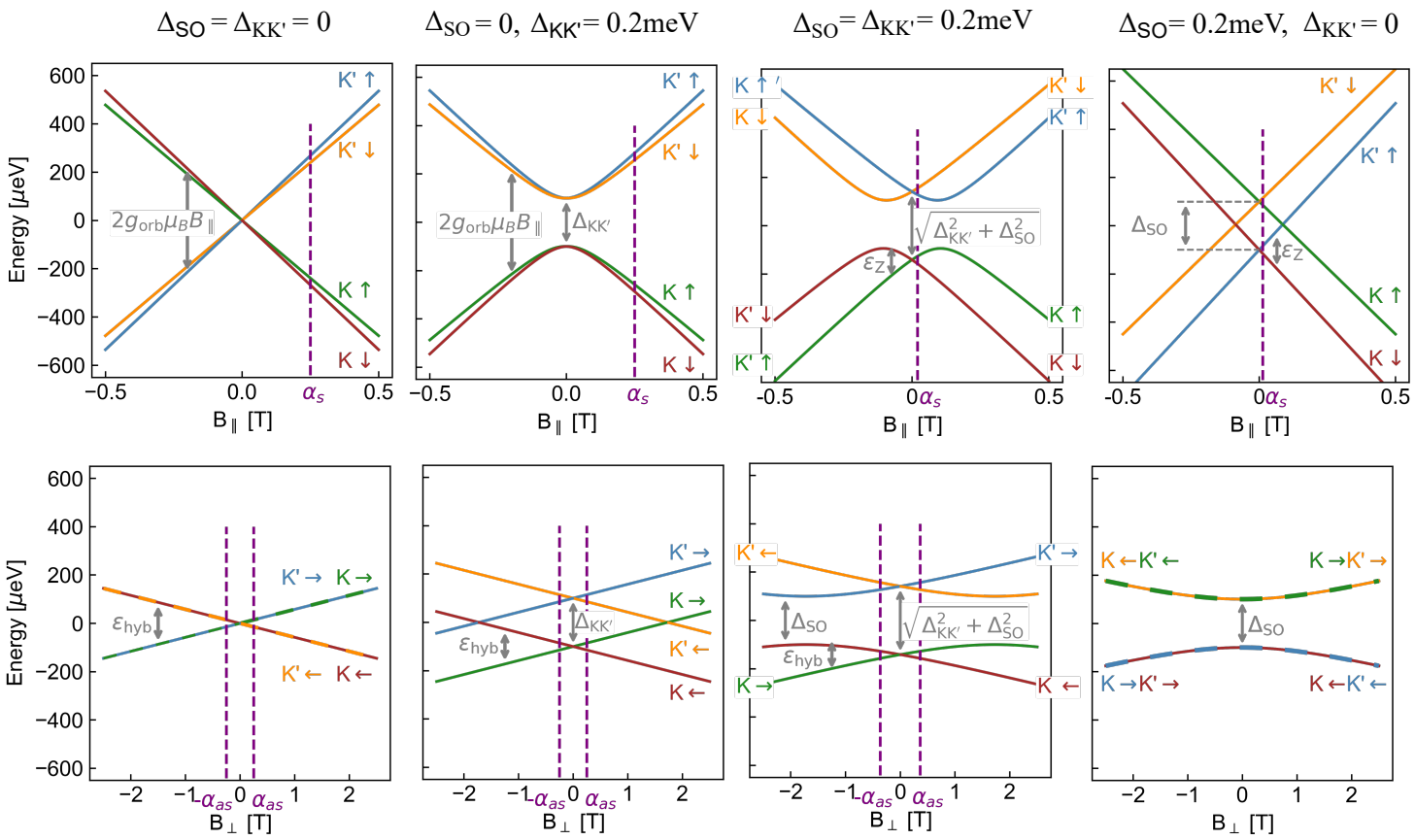

Figure 1.10: **Single-particle energy levels plotted as a function of magnetic field (parallel and perpendicular)**
A magnetic field parallel to the nanotube axis is denoted $B_\parallel$ while a field transverse to the tube is $B_\perp$. The panels show the evolution of the levels with $B_\parallel$ and $B_\perp$ for different strengths of spin-orbit coupling Δ_{SO} and intervalley scattering $\Delta_{KK'}$. The orbital g-factor was fixed to $g_{\text{orb}} = 3.5$ $D = 17.5$ with $D = 5$ nm and $g_s = 2$ is the spin g-factor.
The Zeeman splitting energy ϵ_Z and the spin-charge hybridization energy ϵ_{hyb} defined in Sec. 1.1.3, are shown.
The dashed purple lines indicate the symmetric and antisymmetric field values required for a spin qubit in a double-quantum-dot architecture to minimize decoherence from charge noise, as detailed in Sec. 1.1.3.

Inter-valley scattering was also experimentally observed in carbon-nanotubes between states in different valley with the same spin quantum number. $\Delta_{KK'}$ is the phenomenological parameter describing the strength of avoided level crossing between opposite valley states. The microscopic origin of this parameter is unknown but it is suspected that $\Delta_{KK'}$ can be significantly large in the presence of electrical disorder [59]. Experimentally, inter-valley scattering parameters can range from $\Delta_{KK'} = 25\,\mu$eV [60] to $\Delta_{KK'} = 700\,\mu$eV [57].

Energy spectrum of a quantum dot state in a carbon nanotube

Under the assumption that there is no mixing between holes and electrons, and taking into consideration all the previous points, the Hamiltonian of the system can be written as [53]:

$$\mathrm{H_{CNT}} = E_0^{\pm} + \left(\mp g_{\text{orb}}\hat{\gamma}_z\hat{\sigma}_0 + \frac{1}{2}g_s\hat{\gamma}_0\hat{\sigma}_z\right)\mu_B B_\parallel + \frac{1}{2}g_s\mu_B B_\perp\hat{\gamma}_0\hat{\sigma}_x + \frac{\Delta_{SO}}{2}\hat{\gamma}_z\hat{\sigma}_z + \frac{\Delta_{KK'}}{2}\hat{\gamma}_x\hat{\sigma}_0 \qquad (1.20)$$

In this expression, $E_0^{\pm} = \pm\sqrt{\left(E_G^0\right)^2/4 + E_{\text{conf}}^2}$ is the energy without magnetic field, spin orbit coupling and intervalley scattering. The sign $-$ (or $+$) holds for electrons (or holes). $\hat{\gamma}_i$, $\hat{\sigma}_i$ for $i \in \{0, x, y, z\}$ are the Pauli matrices operators acting in the valley subspace and the spin subspace respectively.

The different parameters presented in this section depends on the properties of the nanotube and vary from one nanotube to the other. Hence different devices can display different energy spectrum. Single-particle energy spectra for various carbon-nanotube properties are presented Fig.1.10.

1.1.3 A double-quantum-dot based spin qubit in a CNT

In a double quantum dot circuit, the charge stability diagram can be used to identify the operating regime of an interdot transition, which occurs when: $\mu^{(0)}_{0,\mathrm{N}_0}(\mathrm{N}_1) = \mu^{(0)}_{1,\mathrm{N}_1+1}(\mathrm{N}_0 - 1))$. This condition corresponds to a single charge transferring from one dot to the other. Such a system behaves as an artificial molecule and serves as the foundation for charge qubits and various spin qubit architectures.

Charge qubit properties

The dynamics of the double quantum dot (DQD) in this interdot regime circuit is governed by the Hamiltonian:

$$\mathrm{H}_{\mathrm{DQD}} = \frac{\epsilon}{2}\hat{\tau}_z + t_c\hat{\tau}_x \tag{1.21}$$

where $\hat{\tau}_i$ for $i \in \{0, x, y, z\}$ are the Pauli matrices operators in the basis $\{|R\rangle, |L\rangle\}$, ϵ is the energy detuning between the two dots, and t_c is the energy related to the interdot tunneling rate.
The eigenstates and eigenvalues of $\mathrm{H}_{\mathrm{DQD}}$ are:

$$\begin{gathered}\mathrm{H}_{\mathrm{DQD}}\ |\pm\rangle = \pm\sqrt{\left(\frac{\epsilon}{2}\right)^2 + t_c^2}\ |\pm\rangle = \pm\frac{\Omega}{2}\ |\pm\rangle \\ \text{with}\ \ |+\rangle = u|L\rangle + v|R\rangle\ \ \text{and}\ \ |-\rangle = v|L\rangle - u|R\rangle\end{gathered} \tag{1.22}$$

with the coefficients $u = \sqrt{\frac{1}{2} - \frac{1}{2}\frac{\epsilon}{\sqrt{\epsilon^2+4t_c^2}}}$ and $v = \sqrt{\frac{1}{2} + \frac{1}{2}\frac{\epsilon}{\sqrt{\epsilon^2+4t_c^2}}}$.
The eigenstates $|-\rangle$ and $|+\rangle$ interpreted as bonding and antibonding states, analogous to molecular orbitals in a diatomic system.

At large detuning $\epsilon \gg t_c$, the electron is localized in one of the dots, depending on the detuning sign :

- For $\epsilon > 0$, the electron is in the left dot $|-\rangle = |L\rangle$.
- For $\epsilon < 0$, the electron is in the right dot $|-\rangle = -|R\rangle$

Near resonance $\epsilon \sim 0$: The electron is fully delocalized across both dots, forming a molecular-like state.

The bonding and antibonding states of the double quantum dot system can serve as the basis for encoding quantum information, forming what is known as a **charge qubit**. The two-level system is defined by $|0\rangle = |-\rangle$ and $|1\rangle = |+\rangle$. The qubit frequency is given by :

$$\hbar\omega_\tau = \Omega = \sqrt{\epsilon^2 + 4t_c^2} \tag{1.23}$$

Despite successful implementations of charge qubits in various platforms, their coherence times remain relatively short. The limitation seems to arise from charge noise, which originates from random fluctuations of localized charge defects. These fluctuations induce variations in the surrounding electric field and appear as fluctuations of ϵ and t_c thereby perturbing the qubit properties.

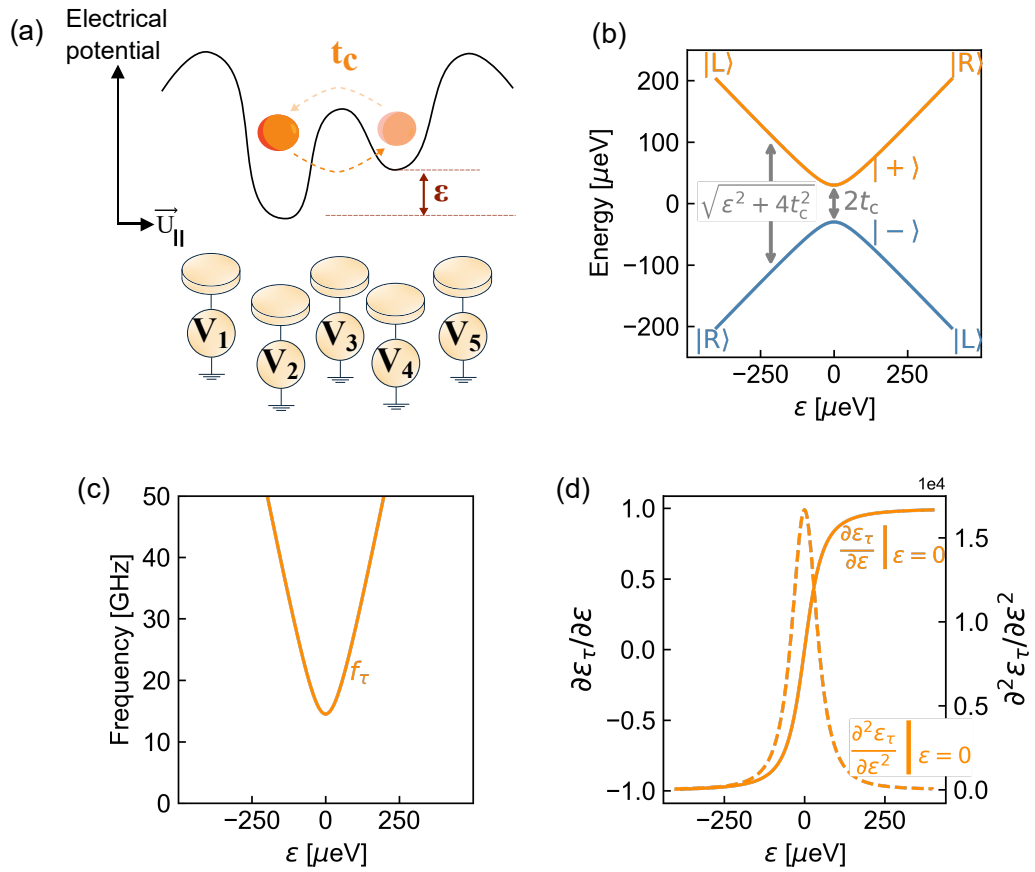

Figure 1.11: **Charge qubit in a double quantum dot**
(a) Schematic of the double-quantum-dot device. Five plunger gates control the electrostatic potential along the nanotube to define the two dots. The interdot tunnel coupling is t_c and the dot detuning is ϵ.
(b) Charge-qubit energy spectrum.
(c) Qubit frequency f_τ as a function of detuning.
(d) First (solid line) and second (dashed line) derivatives of the qubit energy $\Omega = \epsilon_\tau = hf_\tau$ with respect to ϵ as a function of ϵ
For the plots, the tunneling rate between the dots is set to $t_c/h = 7\,\text{GHz}$

One approach to mitigate the impact of charge noise is to operate the qubit at its charge sweet spot where the qubit energy is less sensitive the small variations in detuning. This occurs at $\epsilon = 0$, where :

$$\frac{\partial\Omega}{\partial\epsilon}\Big|_{\epsilon=0} = 0$$

However, even when operated at the charge sweet spot, coherence times for charge qubits remain limited, typically reaching only tens of nanoseconds ([61], [62], [63]) though recent experiments have extended coherence into the hundreds of nanoseconds regime ([64]).

Properties of double-quantum-dot based spin qubit

In comparison to the charge degree of freedom, the spin of a single carrier typically exhibits much larger coherence times and is not sensitive to charge noise. To achieve electrical control over the spin state, the goal is to hybridize both the charge and spin degrees of freedom. Ideally, this would enable the creation of an electrically tunable and addressable qubit with long coherence times.

At zero magnetic field, the spin states remain degenerate, and the Hamiltonian of the system

is given by:

$$H_{DQD} = \frac{\epsilon}{2}\hat{\tau}_z\hat{\sigma}_0 + t_c\hat{\tau}_x\hat{\sigma}_0 \tag{1.24}$$

where $\hat{\tau}_i, \hat{\sigma}_i$ for $i \in \{0, x, y, z\}$ are the Pauli matrices operators acting in the charge subspace $\{|R\rangle, |L\rangle\}$ and spin subspace $\{|\uparrow\rangle, |\downarrow\rangle\}$, respectively.

At finite magnetic field, the Zeeman splitting of the spin states must be considered.
We define $\vec{\mathbf{u}}_\parallel$ as the unit vector parallel to the double quantum dot axis and $\vec{\mathbf{u}}_\perp$ as the unit vector perpendicular to the quantum dot axis. The magnetic field can then be expressed as:

$$\vec{\mathbf{B}} = \vec{\mathbf{B}}_\parallel + \vec{\mathbf{B}}_\perp = B_\parallel\vec{\mathbf{u}}_\parallel + B_\perp\vec{\mathbf{u}}_\perp \tag{1.25}$$

The Hamiltonian describing the Zeeman interaction on each dot is:

$$H_Z = \frac{\hat{\tau}_0 + \hat{\tau}_z}{2}\left[\frac{1}{2}g_S\hat{\sigma}_z\alpha_\parallel^R + \frac{1}{2}g_S\hat{\sigma}_x\alpha_\perp^R\right] + \frac{\hat{\tau}_0 - \hat{\tau}_z}{2}\left[\frac{1}{2}g_S\hat{\sigma}_z\alpha_\parallel^L + \frac{1}{2}g_S\hat{\sigma}_x\alpha_\perp^L\right] \tag{1.26}$$

Here, $\alpha_i^d = \int \mathrm{d}x\, B_i(x)\phi_d^*(x)\phi_d^*(x)$ represents the magnetic field averaged over the wavefunction of the electron in dot $d \in \{L, R\}$, with ϕ_d being the wavefunction in dot d.
For each magnetic field component B_i, we define the symmetric and anti-symmetric parts over the two quantum dots as follows:

$$\alpha_i^s = \frac{\alpha_i^R + \alpha_i^L}{2} \text{ and } \alpha_i^{as} = \frac{\alpha_i^R - \alpha_i^L}{2} \tag{1.27}$$

The Zeeman interaction Hamiltonian can now be rewritten as:

$$H_Z = \frac{1}{2}g_s\alpha_\parallel^s\hat{\sigma}_z\hat{\tau}_0 + \frac{1}{2}g_s\alpha_\parallel^{as}\hat{\sigma}_z\hat{\tau}_z + \frac{1}{2}g_s\alpha_\perp^s\hat{\sigma}_x\hat{\tau}_0 + \frac{1}{2}g_s\alpha_\perp^{as}\hat{\sigma}_x\hat{\tau}_z \tag{1.28}$$

From the expression of the Hamiltonian, we see that the anti-symmetric parts of the magnetic field (α_i^{as}) introduces terms that couple the spin and charge degrees of freedom.

From this point onward, we will consider a symmetric longitudinal magnetic field and an anti-symmetric transverse magnetic field, such that $\alpha_\parallel^{as} = 0$ and $\alpha_\perp^s = 0$.
In this case, the Hamiltonian becomes:

$$H_Z = \frac{1}{2}g_S\alpha_s\hat{\sigma}_z\hat{\tau}_0 + \frac{1}{2}g_S\alpha_{as}\hat{\sigma}_x\hat{\tau}_z \tag{1.29}$$

where $\alpha_s = \alpha_\parallel^s$ and $\alpha_{as} = \alpha_\perp^{as}$.
The total Hamiltonian can then be written as:

$$\begin{aligned} H &= H_{DQD} + H_Z \\ H &= \frac{\epsilon}{2}\hat{\tau}_z\hat{\sigma}_0 + t_c\hat{\tau}_x\hat{\sigma}_0 + \frac{1}{2}g_S\alpha_s\hat{\sigma}_z\hat{\tau}_0 + \frac{1}{2}g_S\alpha_{as}\hat{\sigma}_x\hat{\tau}_z \end{aligned} \tag{1.30}$$

By diagonalizing the Hamiltonian, we obtain the eigenenergies of the system, which can be plotted as a function of the detuning for various ratios of α_s/α_{as}, see Fig. 1.12. We define the eigenbasis of the Hamiltonian as $\{|\tau\sigma\rangle\}$ with $\tau \in \{+, -\}$ and $\sigma \in \{\uparrow, \downarrow\}$.

In the absence of an anti-symmetric magnetic field (Fig. 1.12(a)), no anti-crossing is observed between the energy levels $|-,\uparrow\rangle$ and $|+,\downarrow\rangle$. The transition energy $|-,\downarrow\rangle \rightarrow |-,\uparrow\rangle$ remains constant with respect to detuning, indicating a lack of hybridization between the spin and charge degrees of freedom.This transition is purely spin-like, with energy $\epsilon_\sigma = \epsilon_Z = g_s\mu_B\alpha_s$ determined solely by the Zeeman splitting. In contrast, the transition $|-,\downarrow\rangle \rightarrow |+,\downarrow\rangle$ is purely charge-like, corresponding to a transition between bonding and anti-bonding charge states with energy $\epsilon_\tau = \Omega = \sqrt{\epsilon^2 + 4t_c^2}$.

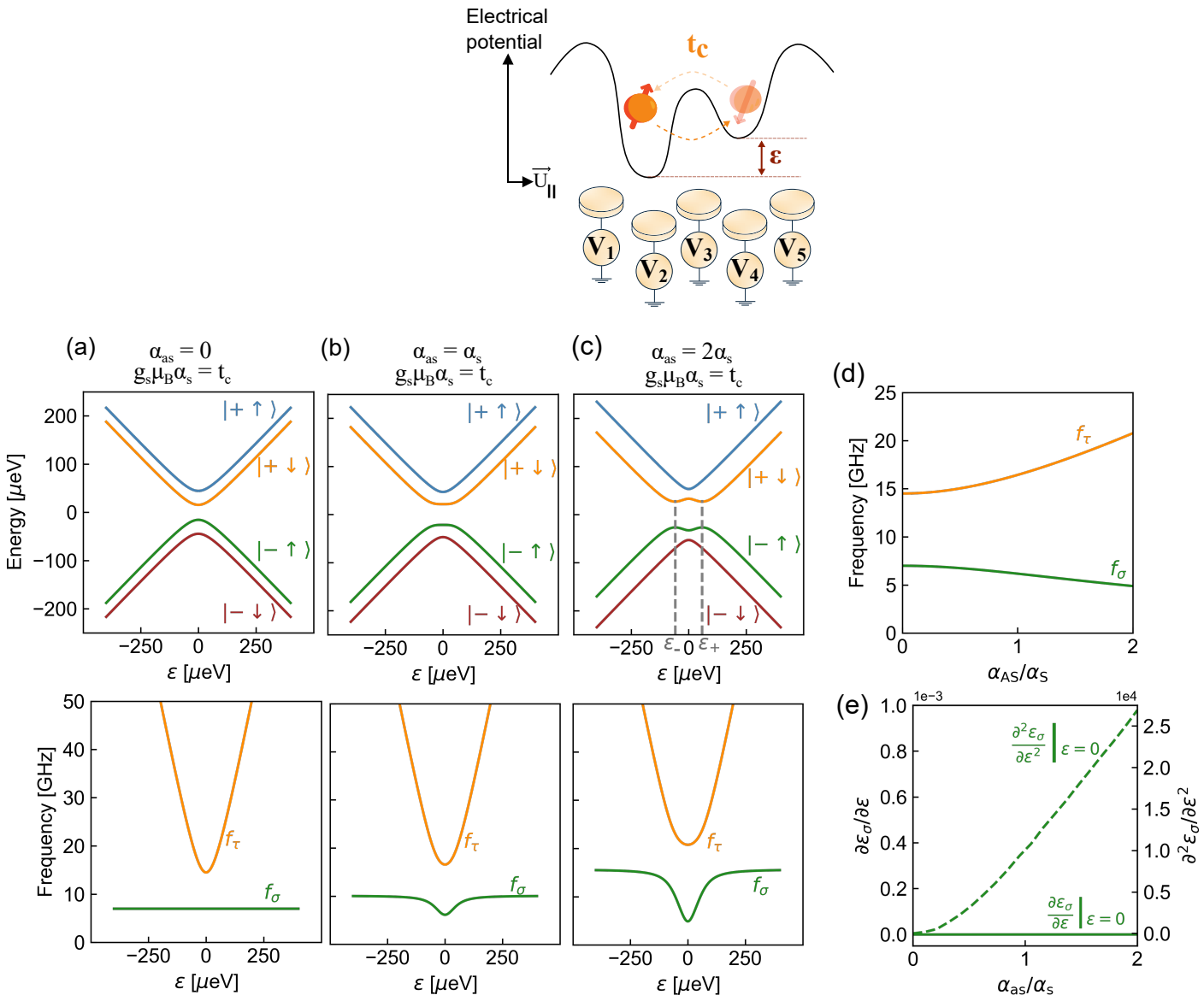

Figure 1.12: **Spin qubit in a double quantum dot**
A spin qubit is realized by applying a magnetic field to the double quantum dot.
(a-c) Energy spectra and transition frequencies of the charge-like (f_τ) and spin-like (f_σ) modes versus detuning various for different values of the antisymmetric field α_{as},
(d) Dependence of f_τ and f_σ on the magnetic field ratio α_{as}/α_s (antisymmetric vs symmetric).
(e) First and second derivatives at $\epsilon = 0$ of the spin-qubit energy $\epsilon_\sigma = hf_\sigma$ as functions of First and second derivatives of the spin qubit energy with respect to ϵ at $\epsilon = 0$ as a function of α_{as}/α_s.
For the plots, the tunneling rate between the two dots is set to $t_c/h = 7\,\text{GHz}$.

When an anti-symmetric magnetic field is introduced (Fig. 1.12(b-c)), hybridization between spin and charge states occurs, manifesting as anti-crossings between the levels $|-,\uparrow\rangle$ and $|+,\downarrow\rangle$. The energy of the spin like-transition $|-,\downarrow\rangle \rightarrow |-,\uparrow\rangle$ becomes detuning-dependent. The depth of the energy dip in the transition spectrum reflects the strength of the artificial spin-orbit coupling induced by the anti-symmetric magnetic field. We define the characteristic hybridization energy as $\epsilon_{\text{hyb}} = g_s\mu_B\alpha_{as}$. The two states $|-,\downarrow\rangle$ and $|-,\uparrow\rangle$ define the computational states of the spin qubit. As the transition $|-,\downarrow\rangle \rightarrow |-,\uparrow\rangle$ acquires an electric dipole moment due to the antisymmetric magnetic field, the spin qubit becomes electrically addressable, enabling control via an external electric field.

We now examine the **influence of the magnetic field on the susceptibility of the spin qubit to charge noise**.
At first order, the zero detuning point ($\epsilon = 0$) constitutes a sweet spot for the spin-like transition across all values of α_s/α_{as}, as the derivative of the spin transition energy with respect to detuning vanishes: $\frac{\partial \epsilon_\sigma}{\partial \epsilon}\Big|_{\epsilon=0} = 0$ (Fig. 1.12(e)). This implies a reduced sensitivity of the qubit transition frequency to small fluctuations in detuning, enhancing the qubit's resilience to charge noise.
However, at second order, the presence of an anti-symmetric magnetic field significantly affects the curvature of the energy levels due to the anti-crossing between the energy levels $|-,\uparrow\rangle$ and $|+,\downarrow\rangle$, which emerges as α_{as} increases. To minimize the susceptibility to charge noise in the spin-like transition, it is desirable to avoid such anti-crossings. This anti-crossings occur at detunning value $\epsilon = \epsilon_\pm$ given by :

$$\epsilon_\pm = \pm \frac{\sqrt{(\epsilon_Z^2 + \epsilon_{\text{hyb}}^2)^2 - 4t_c^2\epsilon_Z^2}}{\sqrt{(\epsilon_Z^2 + \epsilon_{\text{hyb}}^2)}} \tag{1.31}$$

This equation is valid only if $2t_c\epsilon_Z \geq (\epsilon_Z^2 + \epsilon_{\text{hyb}}^2)$, which also implies $2t_c \geq \epsilon_Z$. Hence, the regime favoring reduced sensitivity to charge noise corresponds to:

$$2t_c\epsilon_Z \geq \epsilon_Z^2 + \epsilon_{\text{hyb}}^2 \tag{1.32}$$

This condition establishes a trade-off between the tunnel coupling, the Zeeman energy, and the spin-charge hybridization energy to maximize the addressability of the spin qubit while minimizing its susceptibility to charge noise.

Properties of double-quantum-dot based spin qubit hosted in a carbon nanotube

To accurately predict the energy spectrum of a spin qubit hosted in a carbon nanotube, it is essential to incorporate the valley degree of freedom. The full system Hamiltonian can then be written as:

$$\begin{aligned} H &= H_{\text{DQD}} + H_{\text{spin,Z}} + H_{\text{valley}} \\ &= \frac{\epsilon}{2}\hat{\tau}_z\hat{\sigma}_0\hat{\gamma}_0 + t_c\hat{\tau}_x\hat{\sigma}_0\hat{\gamma}_0 \\ &\quad + \left[\frac{1}{2}g_S\hat{\sigma}_z\hat{\gamma}_0 - g_{\text{orb}}\hat{\sigma}_0\hat{\gamma}_z\right]\hat{\tau}_0\alpha_S + \frac{1}{2}g_S\alpha_{as}\hat{\sigma}_x\hat{\gamma}_0\hat{\tau}_z \\ &\quad + \frac{\Delta_{SO}}{2}\hat{\gamma}_z\hat{\sigma}_z\hat{\tau}_0 + \frac{\Delta_{KK'}}{2}\hat{\gamma}_x\hat{\sigma}_0\hat{\tau}_0 \end{aligned} \tag{1.33}$$

where $\hat{\gamma}_i$ (for $i \in \{0,x,y,z\}$) are the Pauli matrices operators acting in the valley subspace $\{|K\rangle, |K'\rangle\}$. In this formulation, we assume that the orbital g-factor, the spin-orbit interaction strength Δ_{SO} and and the intervalley coupling $\Delta_{KK'}$ are identical for both quantum dots. In the above Hamiltonian, we consider applying the symmetric field along the longitudinal direction of the nanotube, and the anti-symmetric field along the transverse direction.

The eigenenergies of this Hamiltonian can be computed numerically as a function of the detuning ϵ, for different values of the spin-orbit coupling strength and intervalley scattering as presented Fig.1.14. The eigenstates of the system are expressed in the basis $\{|\tau\sigma\gamma\rangle\}$ where $\tau \in \{-,+\}$ denotes the bonding/antibonding charge states, $\sigma \in \{\uparrow,\downarrow\}$ the spin states and $\gamma \in \{K,K'\}$ the valley state. The computational basis of the qubit is defined by the two lowest-energy eigenstates of the system.

In all simulations, the symmetric magnetic field was chosen such that the Zeeman splitting ϵ_Z satisfies $\epsilon_Z = t_c$ ensuring a balanced contribution of spin and charge, see Fig. 1.13(a-c) . Additionally, the antisymmetric magnetic field was tuned such that the hybridization energy ϵ_{hyb} equals the Zeeman energy, i.e. $\epsilon_{\text{hyb}} = \epsilon_Z$, see Fig. 1.13(d). This choice fulfills the trade-off previously

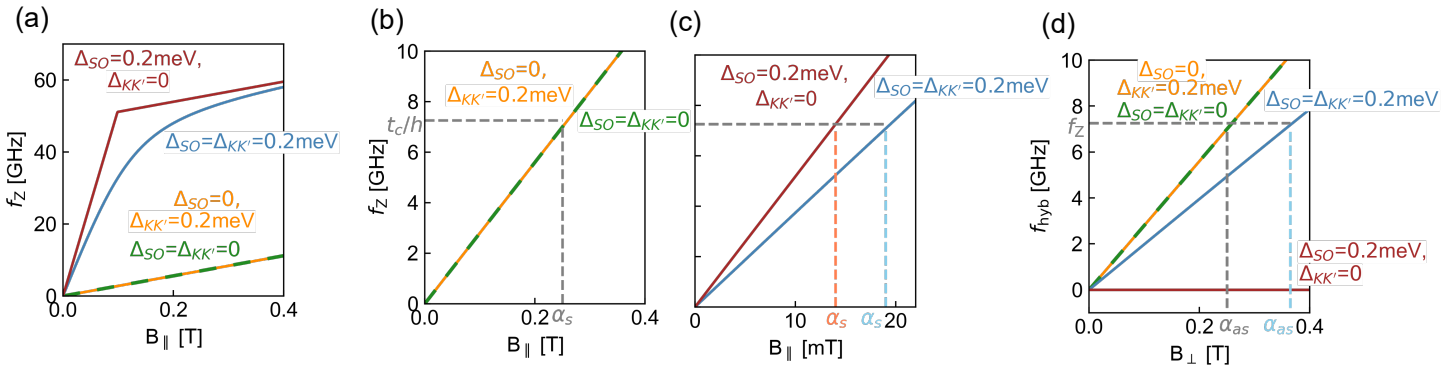

Figure 1.13: **Dependence of Zeeman splitting and spin-charge hybridization on magnetic field in a carbon nanotube**
Panels indicate the symmetric (α_s) and antisymmetric (α_{as}) magnetic field values required to satisfy $t_c = \epsilon_Z = \epsilon_{\text{hyb}}$ for various nanotube properties. The orbital g-factor was fixed to $g_{\text{orb}} = 3.5$ $D = 17.5$ with $D = 5\,\text{nm}$ and the spin g-factor is $g_s = 2$.
(a-c) Zeeman splitting frequency f_Z (such that $\epsilon_Z = hf_Z$) versus the magnetic field applied along the longitudinal direction of the nanotube $B_\parallel$.
(b) Zoom of (a) in the negligible-SOC regime, where $\epsilon_Z = g_s\mu_B\alpha_s$, with $g_s = 2$. Achieving $\epsilon_Z = t_c$ means requires a symmetric field of $\sim 200\,\text{mT}$ (dashed line)
(c) Zoom of (a) when SOC cannot be neglected, effectively increasing the g-factor of the Zeeman splitting. Meeting $\epsilon_Z = t_c$ then requires a smaller α_s.
(d) Spin-charge hybridization $\epsilon_{\text{hyb}} = hf_{\text{hyb}}$ versus magnetic field applied along the transverse direction of the carbon-nanotube. When SOC cannot be neglected, the value of the perpendicular magnetic field needed to satisfy the condition $t_c = \epsilon_Z = \epsilon_{\text{hyb}}$ increases. Dashed lines mark the required values.

identified between spin-charge hybridization and charge noise sensitivity, given by the condition: $2t_c\epsilon_Z = \epsilon_Z^2 + \epsilon_{\text{hyb}}^2$.

When $\Delta_{SO} = 0$ (Fig.1.14), the states $|\tau\sigma K\rangle$ and $|\tau\sigma K'\rangle$ are split in energy by $2g_{\text{orb}}\mu_B\alpha_s$. Applying a symmetric magnetic field parallel to the nanotube thus allows control over the energy splitting between valley states. Since typically $g_{\text{orb}} > g_s$ - for instance, for a nanotube of 5 nm diameter, one finds $g_{\text{orb}}^0 \sim 17.5$ - the energy separation between valley states is significantly larger than that of the spin-like and charge-like transitions between states $|\tau\sigma K\rangle$ (with $\tau \in +,-$ and $\sigma \in \uparrow,\downarrow$). As a result, introducing the valley degree of freedom does not affect our previous conclusions.

However, when $\Delta_{SO} \neq 0$ (Fig.1.14), in order to reach the regime $\epsilon_Z \sim t_c$ - with $t_c/h \sim 4-8\text{GHz}$ to obtain a qubit frequency in the range $f_\sigma \sim 4-8\text{GHz}$ - the qubit is defined by the two lowest-energy states (see Fig.1.14):

$$|0\rangle = |-\downarrow K\rangle \quad \text{and} \quad |1\rangle = |-\uparrow K'\rangle \tag{1.34}$$

with the Zeeman splitting given by:

$$\epsilon_Z = g_s\mu_B\alpha_s + \sqrt{\left(\frac{\Delta_{SO}}{2} + g_{\text{orb}}\mu_B\alpha_s\right)^2 + \left(\frac{\Delta_{KK'}}{2}\right)^2} - \sqrt{\left(\frac{\Delta_{SO}}{2} - g_{\text{orb}}\mu_B\alpha_s\right)^2 + \left(\frac{\Delta_{KK'}}{2}\right)^2} \tag{1.35}$$

In the limit where $g_{\text{orb}}\mu_B\alpha_s \ll \Delta_{SO}$, $\Delta_{KK'}$, this expression can be approximated as:

$$\epsilon_Z = g_s\mu_B\alpha_s + 2\frac{\Delta_{SO}g_{\text{orb}}\mu_B\alpha_s}{\sqrt{\Delta_{SO}^2 + \Delta_{KK'}^2}} \tag{1.36}$$

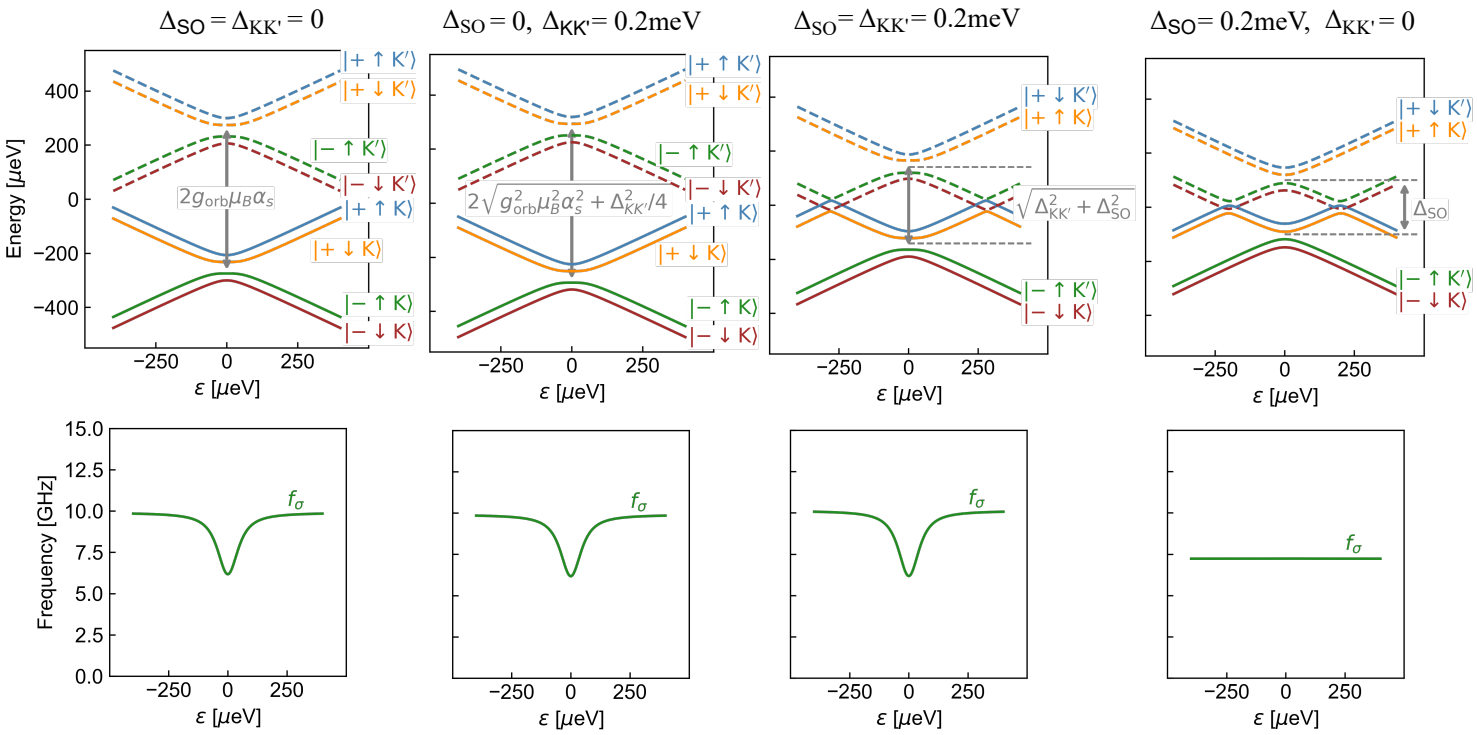

Figure 1.14: **Energy spectrum and detuning-dependent frequencies of a carbon-nanotube spin qubit**
Panels show the energy spectrum and the detuning dependence of the spin-qubit transition frequencies for different spin-orbit coupling and intervalley-scattering strengths. The orbital g-factor was fixed to $g_{\text{orb}} = 3.5$ $D = 17.5$ with $D = 5$ nm and the spin g-factor is $g_s = 2$. All plots use the optimal symmetric and antisymmetric field values determined in Fig. 1.13.

The Zeeman splitting as a function of the magnetic field longitudinal to the CNT - assumed to be symmetric ovec the two dots - is shown in Fig. 1.13(a-c).

The energy scale associated with spin-charge hybridization is given by:

$$\epsilon_{\text{hyb}} = \frac{1}{2}\left[\sqrt{\Delta_{SO}^2 + \left(\Delta_{KK'} + g_s\mu_B\alpha_{as}\right)^2} - \sqrt{\Delta_{SO}^2 + \left(\Delta_{KK'} - g_s\mu_B\alpha_{as}\right)^2}\right] \tag{1.37}$$

The spin-charge hybridization as a function of the transverse magnetic field - assumed antisymmetric between the two dots - is shown in Fig. 1.13(d).

Notably for $\boldsymbol{\Delta_{KK'} = 0}$, spin-charge hybridization cannot be induced by the antisymmetric field. This is because spin-orbit coupling in carbon nanotubes causes scattering between the states $|K\leftarrow\rangle$ and $|K'\rightarrow\rangle$ (or $|K\rightarrow\rangle$ and $|K'\leftarrow\rangle$) as one sweeps from positive to negative values of the transverse magnetic field $B_\perp$. This effect renders the creation of artificial spin-orbit coupling via the antisymmetric field inefficient.
However **when $\boldsymbol{\Delta_{KK'} \neq 0}$**, we have $\boldsymbol{\epsilon_{\text{hyb}} \neq 0}$, and in the limit where $g_s\mu_B\alpha_{as} \ll \Delta_{SO},\ \Delta_{KK'}$, the hybridization energy is approximately:

$$\epsilon_{\text{hyb}} = \frac{\Delta_{KK'}}{\sqrt{\Delta_{SO}^2 + \Delta_{KK'}^2}} g_S\mu_B\alpha_{as} \leq g_S\mu_B\alpha_{as} \tag{1.38}$$

This implies that a stronger antisymmetric field is required to achieve the same hybridization strength as in the $\Delta_{SO} = 0$ case.
In this scenario, one could consider applying the antisymmetric field along the longitudinal direction of the nanotube, and the symmetric field along the transverse direction.

1.2 Hybrid CQED : a quantum-dot based device coupled to a cavity

1.2.1 Quantum-dot based device coupled to a cavity in the literrature

1.2.2 Microscopic description of the coupling mecanism

When the cavity's electric field is assumed to be constant in the vicinity of the dipole, the light-matter interaction can be described with the electric-dipole approximation by:

$$\mathrm{H}_{e-ph} = \vec{\mathbf{d}}.\vec{\mathbf{E}} \tag{1.39}$$

where $\vec{\mathbf{E}}$ represents the uniform cavity electric field and d denotes the electrical dipole.

However, this approximation does not always hold in mesoscopic QED. The circuit itself can influence the cavity's electric field distribution. In particular, the high density of states in fermionic reservoirs can cause field screening effects, leading to inhomogeneities in the electric field.
In a mesoscopic QED circuit, the dipole is linked to tunneling events within the nanoconductor or between the nanoconductor and the fermionic reservoir. Within this framework, the interaction between the cavity and the electrons in the nano-conductor can be expressed as [65] :

$$\mathrm{H}_{e-ph} = -e\int \mathrm{d}^3 r \hat{\Psi}^\dagger(\vec{\mathbf{r}})\hat{\Psi}(\vec{\mathbf{r}})V_\perp(\vec{\mathbf{r}})\left(\hat{\mathbf{a}}^\dagger + \hat{\mathbf{a}}\right) \tag{1.40}$$

$V_\perp(\vec{\mathbf{r}})$ represents the photonic pseudo-potential, which contains strong inhomogeneities, and $\hat{\mathbf{a}}^\dagger$, $\hat{\mathbf{a}}$ are the photon creation and annihilation operators, respectively.
$\Psi(\vec{\mathbf{r}})^{(\dagger)}$ is the field operator associated with the annihilation (creation) of an electron in the nanoconductor. It can be expanded in terms of local states associated with the nano-circuit elements:

$$\hat{\Psi}^{(\dagger)}(\vec{\mathbf{r}}) = \sum_{i,o} \psi^{(*)}_{i,o}(\vec{\mathbf{r}})\hat{\mathbf{c}}^{(\dagger)}_{i,o} \tag{1.41}$$

Here, $\psi_{i,o}(\mathbf{r})$ denotes the single-particle orbital, and $\hat{c}^{(\dagger)}_{i,o}$ is the electron annihilation (creation) operator. The indices (i,o) label the circuit element i and its orbital o.

The orbitals encompass both confined states in the nano-conductor and states within the fermionic reservoir. This interaction Hamiltonian captures the full range of excitations in the mesoscopic circuit.

To identify the different coupling mechanisms, the Hamiltonian describing the interaction of the cavity with a quantum dot can be expressed as :

$$\begin{aligned}
&\mathrm{H}_{e-ph} = \hat{\mathbf{h}}_{\mathrm{int}}(\hat{\mathbf{a}}^\dagger + \hat{\mathbf{a}}) \\
&\hat{\mathbf{h}}_{\mathrm{int}} = \sum_n \hbar g_n \hat{\mathbf{c}}^\dagger_n \hat{\mathbf{c}}_n + \sum_{n'\neq n} \hbar\left(\gamma_{n',n}\hat{\mathbf{c}}^\dagger_{n'}\hat{\mathbf{c}}_n + hc\right)
\end{aligned} \tag{1.42}$$

with the coupling coefficients given by :

$$\begin{aligned}
g_n &= -e\int \mathrm{d}r^3 \left|\psi_n\right|^2(\vec{\mathbf{r}})V_\perp(\vec{\mathbf{r}}) \\
\gamma_{n',n} &= -e\int \mathrm{d}r^3 \psi^\dagger_{n'}(\vec{\mathbf{r}})\psi_n(\vec{\mathbf{r}})V_\perp(\vec{\mathbf{r}})
\end{aligned} \tag{1.43}$$

the label $n \equiv o,i$ denotes an orbital o of the circuit element i.

The first term of h_{int} corresponds to the modulation of the quantum dot orbitals by the AC field of the microwave cavity . It is proportional to the electron density of each orbital and the pseudo-potential. The second term describes the modulation of the tunneling event between different orbitals. This contribution depends on the overlap of wavefunctions of the two involved orbitals and the pseudo-potential. This last mechanism is generally weaker in mesoscopic-QED due to the spatial separation of the orbitals. Therefore, in the following, this mechanism will be neglected.

This description of the dynamics of the cavity's coupling with the nano-circuits relies on two key assumptions. First, the dynamics of plasmons in the cavity conductor and the fermionic reservoir, which are responsible for screening effects, occur on much faster timescales than the tunneling processes in the nano-circuit. Second, the nano-circuit does not contain closed loops, thereby neglecting coupling mechanisms that rely on magnetic flux.

1.2.3 Coulping of an interdot transtion in a DQD to a cavity electric field

The system under investigation is a double quantum dot (DQD) circuit in which an electron can tunnel between orbitals localized in the left and right quantum dots. The interaction between this circuit and the photons of a microwave cavity can be described by the electron-photon coupling Hamiltonian:

$$\mathrm{H}_{e-ph} = \hbar\left(g_L\hat{\mathbf{n}}_L + g_R\hat{\mathbf{n}}_R\right)\left(\hat{\mathbf{a}}^\dagger + \hat{\mathbf{a}}\right) \tag{1.44}$$

where $\hat{\mathbf{n}}_i = \hat{\mathbf{c}}_i^\dagger\hat{\mathbf{c}}_i$ denotes the number operator associated with orbital i.
The Hamiltonian can alternatively be written using the Pauli operators $\hat{\boldsymbol{\tau}}_i$ ($i \in \{0, z\}$) in the orbital basis $\{|R\rangle, |L\rangle\}$:

$$\mathrm{H}_{e-ph} = \frac{\hbar}{2}\left(\hat{\mathbf{a}}^\dagger + \hat{\mathbf{a}}\right)\left(\Sigma_g\hat{\boldsymbol{\tau}}_0 + \Delta_g\hat{\boldsymbol{\tau}}_z\right) \tag{1.45}$$

where we define $\Sigma_g = g_R + g_L$ and $\Delta_g = g_R - g_L$. The total Hamiltonian of the system thus consists of the DQD Hamiltonian, the spin and valley contributions, and the cavity interaction term:

$$\mathrm{H} = \mathrm{H}_{\text{DQD}} + \mathrm{H}_{\text{spin,Z}} + \mathrm{H}_{\text{valley}} + \mathrm{H}_{e-ph}$$

The term proportional to Σ_g in H_{e-ph} corresponds to a global shift in the resonator's equilibrium position. This can be absorbed using a polaronic shift $U_{ps} = e^{\frac{\Sigma_g}{2\omega_c}\tau_0(\hat{\mathbf{a}}-\hat{\mathbf{a}}^\dagger)}$, where $\omega_C/(2\pi)$ is the frequency of the microwave cavity. Applying this transformation yields a renormalized Hamiltonian:

$$\tilde{\mathrm{H}} = U_{ps}^\dagger \mathrm{H} U_{ps} \quad \text{with} \quad \tilde{\epsilon} = \epsilon - \frac{\Sigma_g\Delta_g}{\omega_c} \tag{1.46}$$

and the effective interaction term becomes:

$$\tilde{\mathrm{H}}_d = \frac{\hbar\Delta_g}{2}\hat{\boldsymbol{\tau}}_z\left(\hat{\mathbf{a}}^\dagger + \hat{\mathbf{a}}\right) \tag{1.47}$$

Apart from a constant energy shift, the other components of the Hamiltonian remain unaffected by this transformation. For notational convenience, the tilde will be omitted in what follows.

From this formalism, the DQD can be viewed as an electric dipole interacting with the resonator field :

$$\frac{\Delta_g}{2} = \frac{g_R - g_L}{2} = -\frac{e}{2}\int \mathrm{d}r^3 V_\perp(\vec{\mathbf{r}})\left(\left|\psi_R\right|^2(\vec{\mathbf{r}}) - \left|\psi_L\right|^2(\vec{\mathbf{r}})\right) \tag{1.48}$$

where $V_\perp$ is the photonic pseudo-potential and $\psi_{R,L}$ and are the electronic wavefunctions of the respective dots. The strength of the photonic pseudo-potential is mostly determined by V_{zpf}, the amplitude of the resonator's vacuum voltage fluctuations, as well as the spatial profile of the

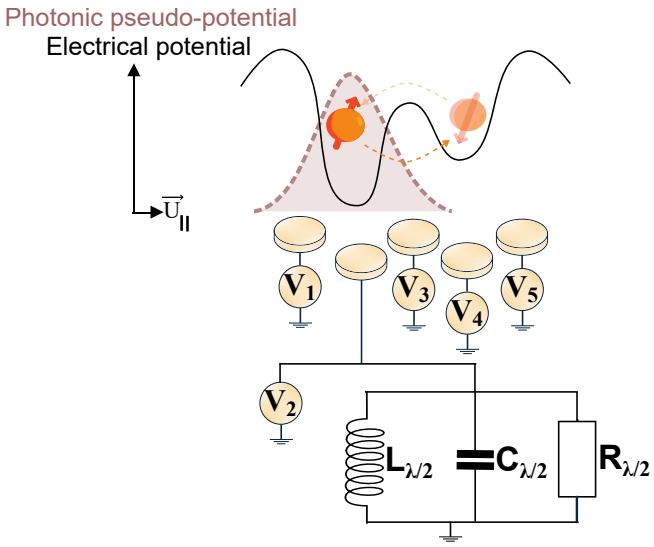

Figure 1.15: **Coupling a double quantum-dot spin qubit to a microwave resonato**
A microwave resonator, modeled as a parallel *RLC* circuit, is connected to a plunger gate that shapes the electrostatic potential along the carbon nanotube. This creates an asymmetric photonic pseudo-potential across the two dots, enhancing the coupling of the qubit to the cavity photons.

pseudo-potential itself. Notably, if the electric field distribution is symmetric such that $g_L \sim g_R$, then $\Delta_g \sim 0$ the double quantum dot does not couple effectively to the resonator. A practical strategy to enhance coupling is to connect only one of the plunger gates to the microwave resonator [66]. This configuration, depicted Fig. 1.15, results in a spatially asymmetric electric field that predominantly overlaps with one of the quantum dots, thereby creating a significant dipole moment.

Charge-photon coupling

We consider a charge qubit implemented in a double quantum dot (DQD), previously described, where the relevant eigenstates are the bonding $|-\rangle$ and antibonding $|+\rangle$ states. In this eigenbasis, the interaction between the qubit and the cavity photons is described by the Hamiltonian:

$$\mathrm{H}_{e-ph} = \sum_{\tau,\tau'} \hbar g_{\tau}^{\tau'} \left|\tau\right\rangle\!\left\langle\tau'\right| \left(\hat{\mathbf{a}}^{\dagger} + \hat{\mathbf{a}}\right) \tag{1.49}$$

where $\tau, \tau' \in \{-,+\}$ and $g_{\tau}^{\tau'} = \frac{\Delta_g}{2} \left\langle \tau \middle| \hat{\boldsymbol{\tau}}_z \middle| \tau' \right\rangle$ represents the coupling between the transition $\left|\tau'\right\rangle \rightarrow |\tau\rangle$ and the cavity field. Here, $\hat{\boldsymbol{\tau}}_z$ is the Pauli operator acting in the orbital basis $\{|R\rangle, |L\rangle\}$.

The charge-photon coupling strength associated with the transition between the bonding and antibonding states is characterized by the matrix element:

$$\begin{aligned} g_c = g_+^- &= \frac{\Delta_g}{2} \langle + | \hat{\boldsymbol{\tau}}_z | - \rangle \\ g_c &= -\frac{\Delta_g}{2} \frac{2t_c}{\sqrt{\epsilon^2 + 4t_c^2}} \end{aligned} \tag{1.50}$$

In the regime where $\epsilon \gg t_c$, the coupling strength g_c goes to zero. Physically, this corresponds to the electron being strongly localized in one of the two quantum dots, effectively suppressing the electric dipole associated with the bonding-antibonding transition and thereby decoupling the charge qubit from the cavity photons.
Conversely, the coupling strength $\left|g_c\right|$ reaches its maximum at zero detuning ($\epsilon = 0$), when the electron wavefunction is delocalized between the two dots, giving rise to a maximal electric dipole moment and, therefore, optimal coupling to the cavity field.

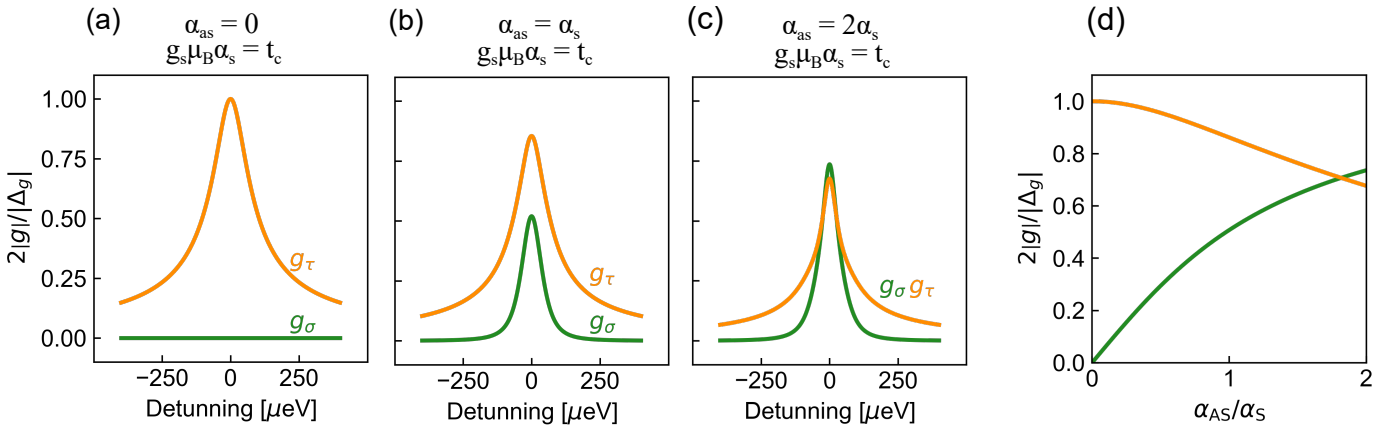

Figure 1.16: **Coupling strengths of spin-like and charge-like transitions in a double quantum dot for different magnetic-field configurations**
(a-c) Coupling strength versus detuning for the spin-like (green) and charge-like (orange) transitions as the antisymmetric magnetic field amplitude α_{as} is increased across the two dots. The symmetric component α_s is fixed such that $\epsilon_Z = g_s\mu_B\alpha_s = t_c$.
(d) Coupling strength of the spin-like (green) and charge-like (orange) transitions at zero detuning as a function of the ratio α_{as}/α_s, under the same condition $\epsilon_Z = g_s\mu_B\alpha_s = t_c$.

Spin-photon coupling

When an external magnetic field is applied, the eigenstates of the double quantum dot system are described by the set $\{|\tau\sigma\rangle\}$ where $\tau \in \{-,+\}$ and $\sigma \in \{\downarrow,\uparrow\}$. In this basis, the interaction Hamiltonian with the cavity photons can be written as:

$$\mathrm{H}_{e-ph} = \sum_{\tau\sigma,\tau'\sigma'} \hbar g_{\tau\sigma}^{\tau'\sigma'} \left|\tau\sigma\right\rangle\!\left\langle\tau'\sigma'\right| \left(\hat{\mathbf{a}}^\dagger + \hat{\mathbf{a}}\right) \tag{1.51}$$

where $g_{\tau\sigma}^{\tau'\sigma'} = \frac{\Delta_g}{2}\left\langle\tau\sigma\right|\hat{\boldsymbol{\tau}}_z\left|\tau'\sigma'\right\rangle$ characterize the coupling between the transition $\left|\tau'\sigma'\right\rangle \rightarrow |\tau\sigma\rangle$ and the cavity photon. $\hat{\boldsymbol{\tau}}_z$ is the Pauli operator acting on the subspace $\{|R\rangle, |L\rangle\}$.

The states $|-\downarrow\rangle$ and $|-\uparrow\rangle$ define the computational basis of the spin qubit. The corresponding **spin-photon coupling** is given by:

$$g_\sigma = g_{-\uparrow}^{-\downarrow} = \frac{\Delta_g}{2}\langle-\uparrow|\hat{\boldsymbol{\tau}}_z|-\downarrow\rangle \tag{1.52}$$

The charge-photon coupling corresponds to the transition between the bonding and antibonding orbital states (while conserving spin), such as $|-\downarrow\rangle \rightarrow |+\downarrow\rangle$:

$$g_\tau = g_{+\downarrow}^{-\downarrow} = \frac{\Delta_g}{2}\langle+\downarrow|\hat{\boldsymbol{\tau}}_z|-\downarrow\rangle \tag{1.53}$$

The values of these coupling constants can be determined numerically as a function of the detuning ϵ for different ratios of α_s/α_{as} as shown Fig. 1.16. The results quantitatively support the qualitative observations outlined earlier:

- **In the absence of an antisymmetric magnetic field** (see Fig. 1.16(a)), there is no spin-charge hybridization. Consequently, the spin-like transition $|-\downarrow\rangle \rightarrow |-\uparrow\rangle$ carries no electric dipole moment, resulting in a vanishing spin-photon coupling ($g_\sigma = 0$). However, the charge-like transition retains its dipolar character, and its coupling strength is given by $\left|g_\tau\right| = \left|g_c\right| = \frac{|\Delta_g|}{2}\frac{2t_c}{\sqrt{\epsilon^2+4t_c^2}}$.

- **As the antisymmetric field increases** (see Fig. 1.16(b-c)), spin-charge hybridization becomes significant, leading to a non-zero spin-photon coupling g_σ which increases with the strength of the antisymmetric field. Simultaneously, the charge-like transition shift toward spin-like character, and its associated charge-photon coupling g_τ decreases.

At zero detuning ($\epsilon = 0$), the coupling strengths of the spin-like and charge-like transitions can be determined analytically [67] :

$$|g_\sigma| = \frac{|\Delta_g|}{2}\sin(\varphi) \quad \text{and} \quad g_\tau = \frac{|\Delta_g|}{2}\cos(\varphi) \tag{1.54}$$

where φ is the average mixing angle, defined as $\varphi = \frac{\varphi_+ + \varphi_-}{2}$. The individual mixing angles $\varphi_\pm$ are given by: $\varphi_\pm = \arctan\left(\frac{\epsilon_{\text{hyb}}}{2t_c \pm \epsilon_Z}\right)$. The two coupling strengths at zero detuning as a function of α_s/α_{as} are plotted in Fig. 1.16(d).
In the limit where $\epsilon_{\text{hyb}} \gg 2t_c \pm \epsilon_Z$, the spin-like coupling $|g_\sigma|$ approaches its maximal value of $|\Delta_g|/2$, while the charge-like coupling g_τ tends to zero. This behavior highlights a transition in the nature of the spin-like transition: as the spin-charge hybridization increases, the transition acquires a predominantly electric dipole character, enhancing its coupling to cavity photons.

When **the valley degree of freedom in carbon nanotubes is taken into account**, the computational basis of the spin qubit is defined by (see Fig. 1.14):

$$\begin{aligned} |0\rangle &= |-\downarrow K\rangle \quad \text{and} \quad |1\rangle = |-\uparrow K\rangle \quad \text{if} \quad \Delta_{SO} = 0 \\ |0\rangle &= |-\downarrow K\rangle \quad \text{and} \quad |1\rangle = |-\uparrow K'\rangle \quad \text{if} \quad \Delta_{SO} \neq 0 \end{aligned} \tag{1.55}$$

The **spin-photon coupling** is given by:

$$g_\sigma = g_1^0 = \frac{\Delta_g}{2}\langle 1|\hat{\boldsymbol{\tau}}_z|0\rangle \tag{1.56}$$

The spin-photon coupling strength versus α_s/α_{as} - and the corresponding ratio $\epsilon_{\text{hyb}}/\epsilon_Z$ - is plotted in Fig. 1.17 considering various spin-orbit strengths and intervalley-scattering parameters.

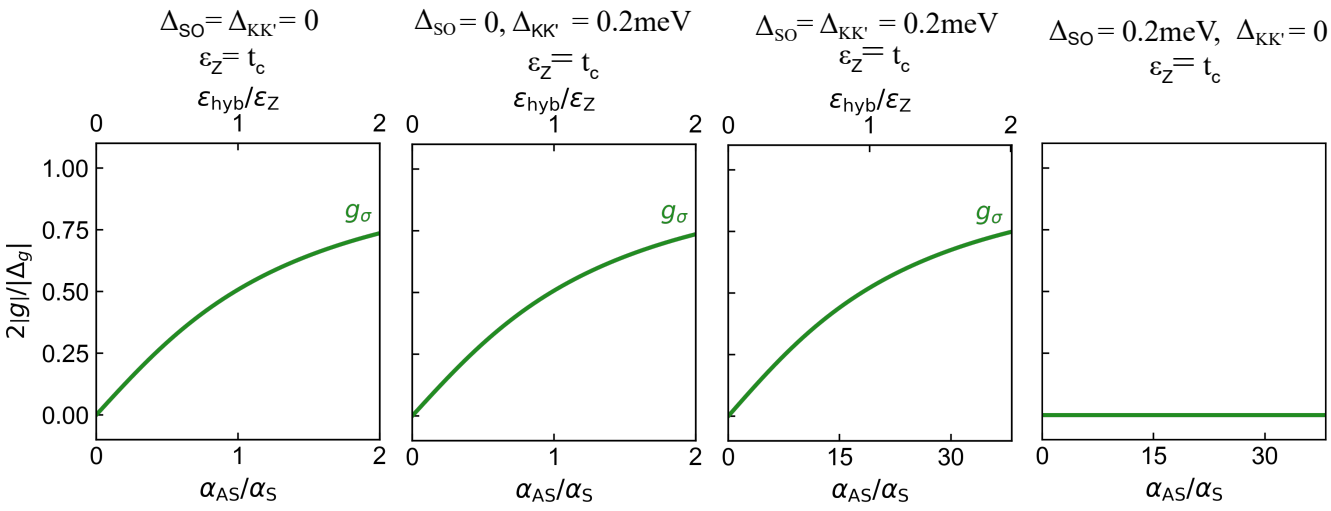

Figure 1.17: **Spin-photon coupling strengths for different carbon-nanotube properties**
Panels show the dependence of the spin-photon coupling strength on the ratio α_{as}/α_s for various spin-orbit couplings and intervalley-scattering strengths. With non-negligible SOC, achieving the same $\epsilon_{\text{hyb}}/\epsilon_Z$ (and thus comparable coupling) requires larger α_{as}/α_s.

In the absence of spin-orbit coupling ($\Delta_{SO} = 0$), the energy splitting between the valley states induced by the orbital magnetic moment and/or the intervalley scattering is typically large, as depicted Fig. 1.14. In this case, one can restrict the dynamics to a single valley, effectively neglecting the valley degree of freedom. Consequently, the analysis and conclusions made for a spin qubit without valley degree of freedom remain valid.

In the presence of spin-orbit interaction ($\Delta_{SO} \neq 0$), the characteristic energy scale associated with spin-charge hybridization, in the limit where $g_s\mu_B\alpha_{AS} \ll \Delta_{SO},\ \Delta_{KK'}$, is given by:

$$\epsilon_{\text{hyb}} = \frac{\Delta_{KK'}}{\sqrt{\Delta_{SO}^2 + \Delta_{KK'}^2}} g_s\mu_B\alpha_{AS} \leq g_s\mu_B\alpha_{AS}$$

This hybridization energy is always lower than in the case $\Delta_{SO} = 0$, where the hybridization is directly determined by the antisymmetric Zeeman energy. As a result, achieving the same degree of spin-charge hybridization - and therefore the same spin-photon coupling - requires applying a stronger antisymmetric field when spin-orbit coupling is present in the carbon nanotube (see Fig.1.17) .
Importantly, when $\Delta_{KK'} = 0$, the hybridization energy vanishes regardless of the applied antisymmetric field, and numerical simulations confirm that the spin-photon coupling is also zero in this regime.

Experimentally, inter-valley scattering is typically non-zero, with $\Delta_{KK'} \geq 60\,\mu\text{eV}$ [53]. Thus, although a stronger anti-symmetric field may be required - depending on the magnitude of spin-orbit coupling - spin-charge hybridization should remain achievable.

To improve control and reproducibility of nanotube properties - and in particularly to minimize spin-orbit coupling - systematic nanotube characterization is key . Spin-orbit coupling in carbon nanotubes depends on both the diameter and chirality [53], where chirality specifies how a graphene sheet is rolled to form a nanotube. Quantifying these parameters enables the selection of devices with target properties. At C12 Quantum Electronics, optical and electrical characterization methods are being developed for this purpose. Encapsulation is also promising: recent work on hBN-encapsulated carbon nanotubes [68] demonstrates clean four-fold degeneracy in shell filling, consistent with suppressed spin-orbit coupling and intervalley scattering.

1.2.4 Properties of the hybrid light-matter system

From this point onward, we consider only the two levels that form the computational basis of the qubit, denoting the ground state as $|g\rangle = |0\rangle$ and the excited state as $|e\rangle = |1\rangle$. The Pauli operators in the basis $\{|e\rangle, |g\rangle\}$ are represented by σ_i, with $i \in \{0, x, y, z\}$. The hybrid system composed of the qubit and a microwave cavity - schematized Fig.1.18 - is described by the **Rabi Hamiltonian**:

$$\begin{aligned} \text{H}_{\text{Rabi}} &= \hbar\omega_c \hat{\mathbf{a}}^\dagger \hat{\mathbf{a}} + \frac{\hbar\omega_q}{2}\hat{\boldsymbol{\sigma}}_z + \hbar g\left(\hat{\mathbf{a}} + \hat{\mathbf{a}}^\dagger\right)\hat{\boldsymbol{\sigma}}_x \\ &= \hbar\omega_c \hat{\mathbf{a}}^\dagger \hat{\mathbf{a}} + \frac{\hbar\omega_q}{2}\hat{\boldsymbol{\sigma}}_z + \hbar g\left(\hat{\mathbf{a}} + \hat{\mathbf{a}}^\dagger\right)\left(\hat{\boldsymbol{\sigma}}_+ + \hat{\boldsymbol{\sigma}}_-\right) \end{aligned} \tag{1.57}$$

Here, $\omega_c/(2\pi)$ denotes the cavity resonance frequency, $\omega_q/(2\pi)$ the qubit transition frequency, and g the qubit-photon coupling strength, whose value was analyzed in the previous section for both charge and spin qubits. The raising and lowering operators are defined as $\hat{\boldsymbol{\sigma}}_\pm = \frac{1}{2}(\hat{\boldsymbol{\sigma}}_x \pm i\hat{\boldsymbol{\sigma}}_y)$. This type of interaction is commonly referred to as transverse coupling, as it involves coupling along the $\hat{\boldsymbol{\sigma}}_x$ axis, which is perpendicular to the quantization axis $\hat{\boldsymbol{\sigma}}_z$.

In the Heisenberg picture, the time dependence of the operators is given by:

$$\begin{aligned} \hat{\mathbf{a}}(t) = \hat{\mathbf{a}} e^{-i\omega_c t} \text{ and } \hat{\mathbf{a}}^\dagger(t) = \hat{\mathbf{a}}^\dagger e^{i\omega_c t}, \\ \hat{\boldsymbol{\sigma}}_+(t) = \hat{\boldsymbol{\sigma}}_+ e^{i\omega_q t} \text{ and } \hat{\boldsymbol{\sigma}}_-(t) = \hat{\boldsymbol{\sigma}}_- e^{-i\omega_q t} \end{aligned} \tag{1.58}$$

Substituting these into the interaction term, the Rabi Hamiltonian becomes:

$$\begin{aligned} \mathrm{H}_{\text{Rabi}} &= \hbar\omega_c \hat{\mathbf{a}}^\dagger \hat{\mathbf{a}} + \frac{\hbar\omega_q}{2}\hat{\boldsymbol{\sigma}}_z + \hbar g\left(\hat{\mathbf{a}} e^{-i\omega_c t} + \hat{\mathbf{a}}^\dagger e^{i\omega_c t}\right)\left(\hat{\boldsymbol{\sigma}}_+ e^{i\omega_q t} + \hat{\boldsymbol{\sigma}}_- e^{-i\omega_q t}\right) \\ &= \hbar\omega_c \hat{\mathbf{a}}^\dagger \hat{\mathbf{a}} + \frac{\hbar\omega_q}{2}\hat{\boldsymbol{\sigma}}_z + \hbar g\left(\hat{\mathbf{a}}\hat{\boldsymbol{\sigma}}_+ e^{-i(\omega_c-\omega_q)t} + \hat{\mathbf{a}}\hat{\boldsymbol{\sigma}}_- e^{-i(\omega_c+\omega_q)t} + \hat{\mathbf{a}}^\dagger\hat{\boldsymbol{\sigma}}_+ e^{i(\omega_c+\omega_q)t} + \hat{\mathbf{a}}^\dagger\hat{\boldsymbol{\sigma}}_- e^{i(\omega_c-\omega_q)t}\right) \end{aligned} \tag{1.59}$$

Under the condition $g \ll \omega_c, \omega_q$ and assuming $|\omega_q - \omega_c| \ll \omega_q + \omega_c$, we can apply the rotating-wave approximation (RWA). Within this approximation, the fast-oscillating counter-rotating terms at frequencies $\omega_q + \omega_c$ are neglected, as they average out over the timescales of interest. The resulting Hamiltonian is:

$$\begin{aligned} \mathrm{H}_{\text{JC}} &= \hbar\omega_c \hat{\mathbf{a}}^\dagger \hat{\mathbf{a}} + \frac{\hbar\omega_q}{2}\hat{\boldsymbol{\sigma}}_z + \hbar g\left(\hat{\mathbf{a}}\hat{\boldsymbol{\sigma}}_+ e^{-i(\omega_c-\omega_q)t} + \hat{\mathbf{a}}^\dagger\hat{\boldsymbol{\sigma}}_- e^{i(\omega_c-\omega_q)t}\right) \\ &= \hbar\omega_c \hat{\mathbf{a}}^\dagger \hat{\mathbf{a}} + \frac{\hbar\omega_q}{2}\hat{\boldsymbol{\sigma}}_z + \hbar g\left(\hat{\mathbf{a}}\hat{\boldsymbol{\sigma}}_+ + \hat{\mathbf{a}}^\dagger\hat{\boldsymbol{\sigma}}_-\right) \end{aligned} \tag{1.60}$$

This simplified form is known as the **Jaynes-Cummings Hamiltonian**, which describes the coherent exchange of excitations between the two subsystems: the qubit and the cavity mode.

The Fock states $|n\rangle$, where n is an integer representing the photon number, are the eigenstates of the cavity Hamiltonian $\mathrm{H}_{\text{cav}} = \hbar\omega_c \hat{\mathbf{a}}^\dagger \hat{\mathbf{a}}$. In the absence of coupling between the two subsystems ($g = 0$), the bare states of the hybrid system are given by $|\sigma, n\rangle$, with $\sigma \in \{e, g\}$.
When the coupling is non-zero, the eigenstates of the hybrid system - referred to as dressed states - can be obtained from the bare states via a Bogoliubov-like unitary transformation:

$$U = e^{\Lambda(\hat{\mathbf{N}}_T)(\hat{\mathbf{a}}^\dagger\hat{\boldsymbol{\sigma}}_- - \hat{\mathbf{a}}\hat{\boldsymbol{\sigma}}_+)} \text{ where } \Lambda(\hat{\mathbf{N}}_T) = \frac{\arctan\left(2\lambda\sqrt{\hat{\mathbf{N}}_T}\right)}{2\sqrt{\hat{\mathbf{N}}_T}}$$

Here, $\hat{\mathbf{N}}_T = \hat{\mathbf{a}}^\dagger\hat{\mathbf{a}} + \hat{\boldsymbol{\sigma}}_+\hat{\boldsymbol{\sigma}}_-$ is the total excitation number operator, and $\lambda = g/\Delta$, where $\Delta = \omega_q - \omega_c$ is the detuning between the qubit and the cavity.
Applying this transformation to the Jaynes-Cummings Hamiltonian yields a diagonal form [47]:

$$\begin{aligned} \mathrm{H}_{\text{D}} &= U^\dagger \mathrm{H}_{\text{JC}} U \\ &= \hbar\omega_c \hat{\mathbf{a}}^\dagger \hat{\mathbf{a}} + \frac{\hbar\omega_q}{2}\hat{\boldsymbol{\sigma}}_z - \frac{\hbar\Delta}{2}\left(1 - \sqrt{1 + 4\lambda^2\hat{\mathbf{N}}_T}\right)\hat{\boldsymbol{\sigma}}_z \end{aligned} \tag{1.61}$$

The dressed eigenstates of the system take the form:

$$\begin{aligned} \left|\overline{g,n}\right\rangle &= \cos(\theta_n/2)\left|g,n\right\rangle - \sin(\theta_n/2)\left|e,n-1\right\rangle \\ \left|\overline{e,n-1}\right\rangle &= \sin(\theta_n/2)\left|g,n\right\rangle + \cos(\theta_n/2)\left|e,n-1\right\rangle \end{aligned} \tag{1.62}$$

with the mixing angle $\theta_n = \arctan\left(2g\sqrt{n}/\Delta\right)$.
The corresponding eigenenergies form doublets indexed by the total number of excitations n:

$$\begin{aligned} E_{\overline{g,n}} &= \hbar n\omega_c - \frac{\hbar}{2}\sqrt{\Delta^2 + 4g^2 n} \\ E_{\overline{e,n-1}} &= \hbar n\omega_c + \frac{\hbar}{2}\sqrt{\Delta^2 + 4g^2 n} \end{aligned} \tag{1.63}$$

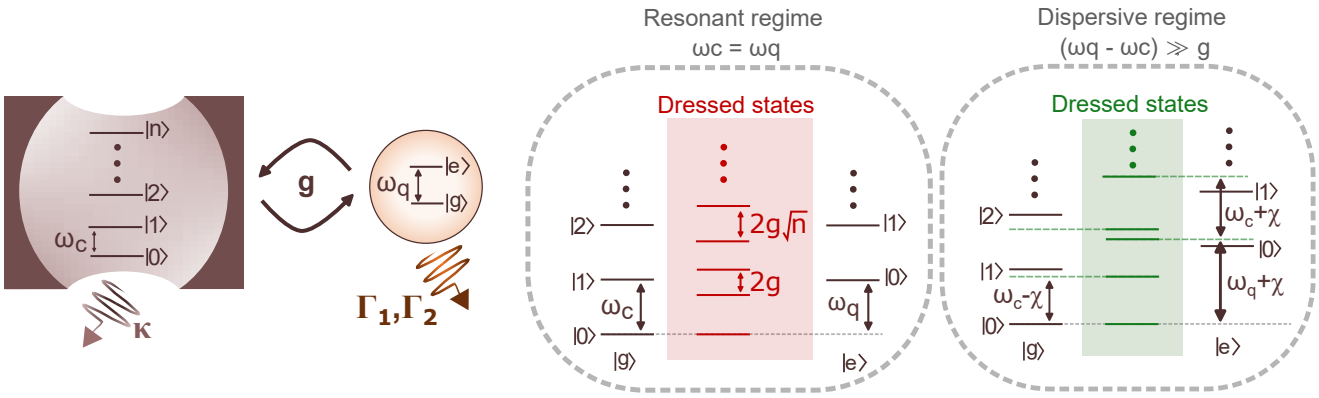

Figure 1.18: **Circuit quantum electrodynamics: coupling a two-level system to a microwave resonator**
A microwave resonator with decay rate κ is coupled to a two-level system at rate g. The two-level system has decoherence rate Γ_2. The energy spectrum is displayed for the resonant regime and the dispersive regime.

Resonant regime

At resonance, $\Delta = 0$, the eigenstates and eigenenergies of the Jaynes-Cummings Hamiltonian simplify to:

$$\begin{aligned} |\overline{g,n}\rangle &= \frac{1}{\sqrt{2}}|g,n\rangle - \frac{1}{\sqrt{2}}|e,n-1\rangle \quad \text{and} \quad E_{\overline{g,n}} = \hbar n\omega_c - \hbar g\sqrt{n} \\ |\overline{e,n-1}\rangle &= \frac{1}{\sqrt{2}}|g,n\rangle + \frac{1}{\sqrt{2}}|e,n-1\rangle \quad \text{and} \quad E_{\overline{e,n-1}} = \hbar n\omega_c + \hbar g\sqrt{n} \end{aligned} \tag{1.64}$$

The energy levels $E_{\overline{g,n}}$ and $E_{\overline{e,n-1}}$, presented Fig. 1.18, are split by $2g\sqrt{n}$-a feature known as the vacuum Rabi splitting. This spectrum has been observed experimentally across various qubit platforms ([69], [66], [49]), and provides direct evidence of the quantum nature of light-matter interaction.
However, at resonance, the dressed states represent maximally entangled qubit-resonator superpositions. In this regime, the qubit does not reside in a well-defined state, which makes it unsuitable for quantum information processing tasks.

Dispersive regime

In the dispersive regime, the qubit-resonator detuning is large compared to the coupling strength, i.e., $|\lambda| = |g/\Delta| \ll 1$. In this limit, the coherent exchange of excitations between the two systems becomes off-resonant and is effectively suppressed. Under these conditions, the diagonalized Hamiltonian from Eq. (1.61) reduces to [47]:

$$\begin{aligned} \mathrm{H}_{\mathrm{D}}^{\mathrm{disp}} &= \hbar\omega_c\hat{\mathbf{a}}^\dagger\hat{\mathbf{a}} + \frac{\hbar\omega_q}{2}\hat{\boldsymbol{\sigma}}_z + \hbar\frac{g^2}{\Delta}\hat{\boldsymbol{\sigma}}_z\hat{\mathbf{N}}_T \\ &= \hbar\omega_c\hat{\mathbf{a}}^\dagger\hat{\mathbf{a}} + \frac{\hbar\omega_q}{2}\hat{\boldsymbol{\sigma}}_z + \hbar\chi_{\mathrm{disp}}\left(\hat{\boldsymbol{\sigma}}_z\hat{\mathbf{a}}^\dagger\hat{\mathbf{a}} + \frac{1}{2}\left(\hat{\boldsymbol{\sigma}}_z + \hat{\boldsymbol{\sigma}}_0\right)\right) \\ &= \hbar\left(\omega_c + \chi_{\mathrm{disp}}\hat{\boldsymbol{\sigma}}_z\right)\hat{\mathbf{a}}^\dagger\hat{\mathbf{a}} + \frac{\hbar}{2}\left(\omega_q + \chi_{\mathrm{disp}}\right)\hat{\boldsymbol{\sigma}}_z \end{aligned} \tag{1.65}$$

Here, $\chi_{\mathrm{disp}} = g^2/\Delta$ denotes the dispersive frequency shift also referred to as the dispersive charge susceptibility. We have omitted the term $\frac{1}{2}\hbar\chi_{\mathrm{disp}}\hat{\boldsymbol{\sigma}}_0$, as it corresponds to a global energy offset and has no physical consequence. The energy spectrum obtain in this regime is represented Fig. 1.18.

The coupling between the two systems induces a shift in the qubit frequency, $\Delta\omega_q = \chi_{\text{disp}}/2$, known as the Lamb shift, and a shift in the cavity frequency, $\Delta\omega_c = \chi_{\text{disp}}\hat{\boldsymbol{\sigma}}_z$, which depends on the qubit state. As a result, measuring the cavity frequency provides direct information about the state of the qubit.
Since the dispersive Hamiltonian $\mathrm{H}_{\mathrm{D}}^{\text{disp}}$ commutes with the measured observable $\hat{\boldsymbol{\sigma}}z$, this readout protocol constitutes a quantum non-demolition (QND) measurement[1].
The dispersive regime is therefore well-suited for qubit state readout in quantum information processing.

1.2.5 Dispersive readout of the qubit State via cavity measurement

To enable readout of the cavity, the model must be extended to include one or more transmission lines capacitively coupled to the cavity. These lines allow photons to be exchanged between the cavity and the external environment. In this work, we consider a cavity coupled to a hanger-type transmission line, as represented Fig. 1.19, and denote by κ_c the photon loss rate into the line.

Master equations

In this formalism, the dynamics of the field operator $\hat{\mathbf{a}}$ are governed by the quantum Langevin equation:

$$\begin{aligned}\partial_t\hat{\mathbf{a}} &= \frac{i}{\hbar}\left[\mathrm{H}_{\mathrm{JC}},\hat{\mathbf{a}}\right] - \frac{\kappa}{2}\hat{\mathbf{a}} + \sqrt{\kappa_c}\hat{\mathbf{a}}_{\text{in}} \\ &= -i\omega_c\hat{\mathbf{a}} - ig\hat{\boldsymbol{\sigma}}_- - \frac{\kappa}{2}\hat{\mathbf{a}} + \sqrt{\kappa_c}\hat{\mathbf{a}}_{\text{in}}\end{aligned} \tag{1.66}$$

Here, the total cavity decay rate is given by $\kappa = \kappa_i + \kappa_c$, where κ_i accounts for internal losses of the resonator. The incoming ($\hat{\mathbf{a}}_{\text{in}}$) and outgoing ($\hat{\mathbf{a}}_{\text{out}}$) field mode operators are related by the input-output relations:

$$\hat{\mathbf{a}}_{\text{out}} + \hat{\mathbf{a}}_{\text{in}} = \frac{\sqrt{\kappa_c}}{2}\hat{\mathbf{a}} \tag{1.67}$$

The time evolution of the operator $\hat{\boldsymbol{\sigma}}_-$ is given by:

$$\begin{aligned}\partial_t\hat{\boldsymbol{\sigma}}_- &= \frac{i}{\hbar}\left[\mathrm{H}_{\mathrm{JC}},\hat{\boldsymbol{\sigma}}_-\right] - \Gamma_2\hat{\boldsymbol{\sigma}}_- \\ &= -i\omega_q\hat{\boldsymbol{\sigma}}_- + ig\hat{\boldsymbol{\sigma}}_z\hat{\mathbf{a}} - \Gamma_2\hat{\boldsymbol{\sigma}}_-\end{aligned} \tag{1.68}$$

Here, the last term describes the decoherence of the qubit with decay rate Γ_2.

For a large number of photons in the cavity, $\langle\hat{\mathbf{a}}^\dagger\hat{\mathbf{a}}\rangle > 10$, the field operator $\hat{\mathbf{a}}$ can be treated classically, allowing us to replace it with its expectation value: $\hat{\mathbf{a}} = \langle\hat{\mathbf{a}}\rangle$. Additionally, when the cavity is driven near resonance ($\omega \approx \omega_c$), we can apply the resonant approximation [65]:

$$\langle\hat{\mathbf{a}}\rangle = \bar{a}e^{-i\omega t} \tag{1.69}$$

Similarly, we can express the time-dependent expectation values of the incoming and outgoing field modes, as well as the lowering operator of the qubit:

$$\langle\hat{\mathbf{a}}_{\text{in}}\rangle = \bar{a}_{\text{in}}e^{-i\omega t},\ \langle\hat{\mathbf{a}}_{\text{out}}\rangle = \bar{a}_{\text{out}}e^{-i\omega t}\ \text{ and }\ \langle\hat{\boldsymbol{\sigma}}_-\rangle = \bar{\sigma}_-e^{-i\omega t} \tag{1.70}$$

Under these conditions, the time-independent qubit operator $\bar{\sigma}_-$ becomes:

$$\bar{\sigma}_- = \frac{ig\langle\hat{\boldsymbol{\sigma}}_z\rangle}{i(\omega_q-\omega)+\Gamma_2}\bar{a} \tag{1.71}$$

[1] Strictly speaking, the measurement is only approximately QND, as $\mathrm{HD}^{\text{disp}}$ is a perturbative approximation of the full Jaynes-Cummings Hamiltonian.

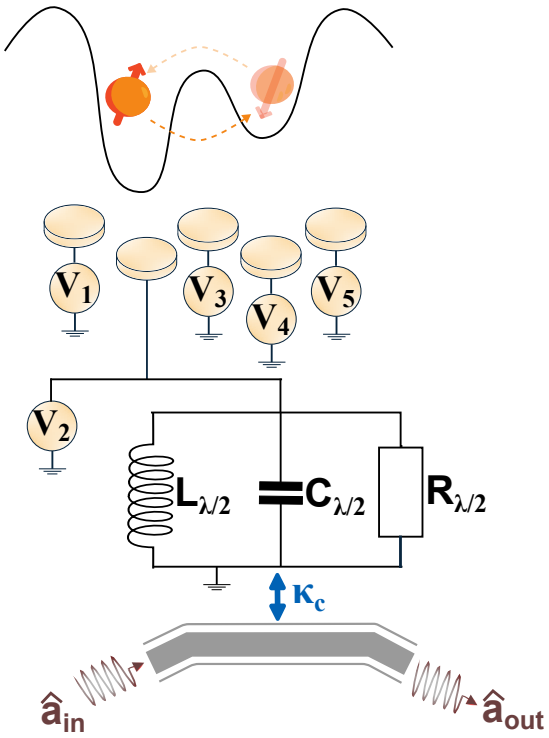

Figure 1.19: **Input-output formalism: dispersive readout of the qubit state**
A microwave resonator, modeled as a parallel *RLC* circuit, is capacitively coupled to a feedline to exchange photons with the external environment. Measuring the feedline transmission probes the resonator and the qubit dispersively coupled to it.

The frequency dependence of the field operator $\bar{a}$ is then given by:

$$\bar{a} = \frac{\sqrt{\kappa_c}\bar{a}_{\text{in}}}{-i(\omega-\omega_c)+\kappa/2-i\chi(\omega)\langle\hat{\sigma}_z\rangle} \tag{1.72}$$

where the charge susceptibility $\chi(\omega)$ of the nanocircuit comprising the qubit is expressed as:

$$\chi(\omega) = \frac{g^2}{(\omega-\omega_q)+i\Gamma_2} \tag{1.73}$$

Cavity read-out

In the context of a cavity coupled to a hanger-type transmission line, the scattering coefficient, denoted as S_{H} characterizes how an input signal is reflected by the cavity. This coefficient can be derived using the input-output relation of equation Eq. (1.67).

Without coupling to the qubit, the scattering coefficient is:

$$\begin{aligned} S_{\text{H}}(\omega) &= \frac{\bar{a}_{\text{out}}}{\bar{a}_{\text{in}}} = \frac{\sqrt{\kappa_c}/2\ \bar{a}-a_{\text{in}}}{a_{\text{in}}} \\ S_{\text{H}}(\omega) &= \frac{2i(\omega-\omega_c)-\kappa_i}{\kappa-2i(\omega-\omega_c)} \end{aligned} \tag{1.74}$$

Alternatively, it can be expressed in terms of amplitude $A(\omega)$ and phase $\phi(\omega)$:

$$S_{\text{H}} = A(\omega)e^{-i\phi(\omega)}$$

Near resonance ($|\omega-\omega_c| \ll \kappa/2$) the phase varies linearly with frequency:

$$\phi(\omega) = \phi(\omega_c) + \frac{2\kappa_c}{\kappa_i\kappa}(\omega-\omega_c) \tag{1.75}$$

When the cavity is coupled to a qubit, the scattering coefficient is modified and takes the form:

$$\begin{aligned} S'_{\mathrm{H}}(\omega) &= \frac{i\left[\omega - \left(\omega_c - \mathrm{Re}(\chi(\omega))\,\langle\hat{\boldsymbol{\sigma}}_z\rangle\right)\right] - \kappa_i/2 - \mathrm{Im}(\chi(\omega))\,\langle\hat{\boldsymbol{\sigma}}_z\rangle}{\kappa/2 + \mathrm{Im}(\chi(\omega))\,\langle\hat{\boldsymbol{\sigma}}_z\rangle - i\left[\omega - \left(\omega_c - \mathrm{Re}(\chi(\omega))\right)\right]} \\ &= \frac{2i\left[\omega - \omega'_c\right] - \kappa'_i}{\kappa' - 2i\left[\omega - \omega'_c\right]} \end{aligned} \tag{1.76}$$

The presence of the qubit leads to a shift in the cavity frequency given by:

$$\Delta\omega_c = \omega'_c - \omega_c = -\,\mathrm{Re}(\chi(\omega))\,\langle\hat{\boldsymbol{\sigma}}_z\rangle = \frac{g^2}{\left(\omega_q - \omega\right)^2 + \Gamma_2^2}\left(\omega_q - \omega\right)\langle\hat{\boldsymbol{\sigma}}_z\rangle \underset{\substack{\omega = \omega_c \\ \Gamma_2 \ll \omega_q - \omega_c}}{=} \frac{g^2}{\left(\omega_q - \omega_c\right)}\langle\hat{\boldsymbol{\sigma}}_z\rangle = \chi_{\mathrm{disp}}\,\langle\hat{\boldsymbol{\sigma}}_z\rangle$$

Thus, when the cavity is driven at its resonance frequency $\omega = \omega_c$ and the qubit decoherence is neglected ($\Gamma_2 \ll \omega_q - \omega_c$), we recover the frequency shift $\Delta\omega_c = \chi_{\mathrm{disp}}\,\langle\hat{\boldsymbol{\sigma}}_z\rangle$ previously obtained within the dispersive approximation.

By monitoring variations in the phase of the scattering coefficient, one can extract valuable information about the qubit state. Let us denote by $\phi'(\omega)$ the phase of the scattering coefficient S'_{H}, which includes the effects of the qubit-cavity interaction. In the limit where the cavity frequency shift satisfies $|\Delta\omega_c| \ll \omega_c,\ \kappa/2$, the phase can be approximated by:

$$\phi'(\omega_c) = \phi(\omega_c) - \frac{2\kappa_c}{\kappa_i\kappa}\Delta\omega_c \tag{1.77}$$

In the absence of external and thermal excitation, the qubit remains in its ground state, such that $\langle\hat{\boldsymbol{\sigma}}_z\rangle = -1$. Under these conditions, the measured phase shift $\Delta\phi = \phi'(\omega_c) - \phi(\omega_c)$ provides a direct probe of the qubit-cavity detuning $\Delta = \omega_q - \omega_c$ and is given by:

$$\Delta\phi = \frac{2\kappa_c}{\kappa_i\kappa}\frac{g^2}{\Delta^2 + \Gamma_2^2}\Delta \tag{1.78}$$

When the qubit is driven by an external excitation, the resulting phase shift $\Delta\phi$ enables measurement of the qubit state via the observable $\langle\hat{\boldsymbol{\sigma}}_z\rangle$, hereby providing a quantum-non-demolition readout mechanism in the dispersive regime.

Enhancing the coupling strength $|g|$ between a qubit and a cavity's photons significantly improves the readout process of the qubit state. A stronger coupling leads to more pronounced phase shifts in the cavity's scattering coefficient, corresponding to the qubit's ground and excited state. This increased distinction facilitates clearer differentiation between these states, thereby accelerating the readout process and enabling faster and more reliable measurements of the qubit state.

1.2.6 Towards a two-qubit gate mediated by a cavity

Coupling multiple qubits to a common cavity offers a viable approach for facilitating long-range interactions between them. In this context, we examine a system comprising two spatially separated qubits, each coupled to the same cavity mode. Due to their separation, direct qubit-qubit interactions are negligible, making the cavity the primary medium for their coupling. This setup is effectively described by the Tavis-Cummings model, an extension of the Jaynes-Cummings model to multiple qubits. The Hamiltonian for this system is:

$$\mathrm{H_{TC}} = \hbar\omega_c\hat{\mathbf{a}}^\dagger\hat{\mathbf{a}} + \sum_{i=1,2}\left[\frac{\omega_{q,i}}{2}\hat{\boldsymbol{\sigma}}_{z,i} + \hbar g_i\left(\hat{\mathbf{a}}\hat{\boldsymbol{\sigma}}_{+,i} + \hat{\mathbf{a}}^\dagger\hat{\boldsymbol{\sigma}}_{-,i}\right)\right] \tag{1.79}$$

Here $\omega_c/(2\pi)$represents the cavity resonance frequency, $\omega_{q,i}/(2\pi)$ denotes the transition frequency of qubit i and g_i the coupling strength between qubit i and the cavity photons. The operators $\hat{\boldsymbol{\sigma}}_{j,i}$ with $j \in \{0,x,y,z\}$ are the Pauli operators associated with qubit i and the operators $\hat{\boldsymbol{\sigma}}_{\pm,i}$ are defined by $\hat{\boldsymbol{\sigma}}_{\pm,i} = \frac{1}{2}\left(\hat{\boldsymbol{\sigma}}_{x,i} \pm i\hat{\boldsymbol{\sigma}}_{y,i}\right)$.

Similarly to the approach outlined in Section 1.2.4, when both qubits are operated in the dispersive regime - i.e., when their detunings from the cavity satisfy $\left|\Delta_{q,i}\right| = \left|\omega_{q,i} - \omega_c\right| \ll g_i$ - the Tavis-Cummings Hamiltonian can be approximated as:

$$\mathrm{H}_{\mathrm{TC}}^{\mathrm{disp}} = \hbar\left(\omega_c + \sum_{i=1,2} \chi_{\mathrm{disp},i}\hat{\boldsymbol{\sigma}}_{z,i}\right)\hat{\mathbf{a}}^\dagger\hat{\mathbf{a}} + \sum_{i=1,2}\frac{\hbar\omega_{q,i}}{2}\hat{\boldsymbol{\sigma}}_{z,i} + \hbar J\left(\hat{\boldsymbol{\sigma}}_{-,1}\hat{\boldsymbol{\sigma}}_{+,2} + \hat{\boldsymbol{\sigma}}_{-,2}\hat{\boldsymbol{\sigma}}_{+,1}\right) \tag{1.80}$$

with the effective qubit-qubit interaction strength given by:

$$J = \frac{g_1 g_2}{2}\left(\frac{1}{\omega_{q,1} - \omega_c} - \frac{1}{\omega_{q,2} - \omega_c}\right) \tag{1.81}$$

Here, $\chi_{\mathrm{disp},i} = \frac{g_i^2}{\omega_{q,1}-\omega_c}$ is the dispersive shift associated with qubit i.
The first term in the Hamiltonian allows for the dispersive readout of each qubit via the cavity, while the last term describes an effective exchange interaction of strength J.

When the two qubits are nearly resonant, such that $\left|\omega_{q,1} - \omega_{q,2}\right| \ll J$, an excitation can coherently transfer from one qubit to the other via virtual photon exchange. This mechanism enables the implementation of an iSWAP gate between distant qubits. Such interactions have been experimentally demonstrated in the context of spatially separated semiconductor qubits ([70], [5]), showing great potential for the realization of scalable quantum networks based on circuit QED architectures.
Importantly, the interaction strength J scales proportionally with the product $g_1 g_2$ of the individual qubit-cavity coupling strengths. Therefore, increasing the coupling strength of each qubit to the cavity enhances the effective qubit-qubit interaction rate. This allows for faster gate operations, ideally well within the qubits' coherence times, and is a crucial consideration for achieving high-fidelity two-qubit gates.

1.2.7 Optimizing the coupling of the qubit with the microwave cavity

Achieving qubit readout and two-qubit gate operations at timescales much shorter than the qubit coherence time is essential for scalable quantum information processing. As shown in the previous sections, optimizing both the fidelity of dispersive readout and the speed of cavity-mediated two-qubit gates relies on maximizing the qubit-cavity coupling strength $\left|g\right|$.
For spin qubits encoded in double quantum dots, this coupling strength is given by:

$$g = \frac{\Delta_g}{2}\langle 1|\hat{\boldsymbol{\tau}}_z|0\rangle \tag{1.82}$$

where $\{|1\rangle, |0\rangle\}$ denotes the computational basis of the qubit, and the operator $\hat{\boldsymbol{\tau}}_z$ acts in the orbital subspace of the double quantum dot defined by $\{|R\rangle, |L\rangle\}$.
Maximizing $\left|g\right|$ thus requires increasing both the dipolar coupling term Δ_g and the matrix element $\langle 1|\hat{\boldsymbol{\tau}}_z|0\rangle$ which quantifies the electric dipole of the qubit. Strategies to enhance either of these contributions are therefore central to improving the performance of spin qubits coupled to microwave cavities.

Optimizing the Electric Dipole of the Qubit

As discussed in Section 1.2.3, the strength of the electric dipole transition, characterized by the matrix element $\langle 1|\hat{\boldsymbol{\tau}}_z|0\rangle$, depends critically on the spatial distribution of the magnetic field. In order to maximize this term, one must enhance the spin-charge hybridization, which can be achieved by increasing the anti-symmetric component of the magnetic field across the double quantum dot.
However, as previously mentioned, stronger hybridization also increases the qubit's susceptibility to charge noise. Therefore, a trade-off must be established between improving the qubit's electromagnetic addressability and maintaining low sensitivity to charge fluctuations. This balance is characterized by the condition:

$$2t_c\epsilon_Z = \epsilon_Z^2 + (\epsilon_{\text{hyb}}^t)^2 \tag{1.83}$$

Where t_c is the interdot tunneling rate, ϵ_Z is the Zeeman splitting induced by the symmetric component of the magnetic field, and ϵ_{hyb} is the hybridization energy set by the anti-symmetric field. In the regime where $t_c \sim \epsilon_Z \sim \epsilon_{\text{hyb}}$, this condition is satisfied, and the coupling strength between the qubit and cavity photons simplifies to:

$$g \approx \frac{1}{2}\frac{\Delta_g}{2} \tag{1.84}$$

Importantly, in order to maximize the coupling strength while satisfying Eq. (1.83), the energy associated with the charge-like transition (characterized by $2t_c$) must be brought close to that of the spin-like transition (characterized by ϵ_Z), see Fig. 1.20. This ensures optimal spin-charge hybridization while maintaining control over decoherence induced by charge noise.

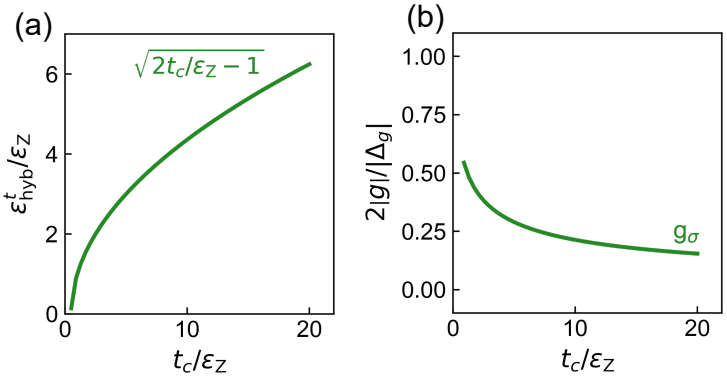

Figure 1.20: **Dependence of spin-charge hybridization and spin-photon coupling on interdot tunneling**
(a) Ratio $\epsilon_{\text{hyb}}/\epsilon_Z$ versus t_c/ϵ_Z as required by Eq. (1.83)
(b) Spin-photon coupling strength versus t_c/ϵ_Z with ϵ_{hyb} set to satisfy Eq. (1.83).

Optimizing the Dipolar Coupling Term

An effective strategy to enhance the qubit-cavity coupling strength is to increase the dipolar interaction term Δ_g. As previously discussed, this can be achieved by engineering the spatial profile of the cavity's electric field such that it overlaps asymmetrically with the double quantum dot. In addition to geometric optimization, one can also enhance the overall amplitude of the photonic pseudo-potential. Specifically, the coupling strength is directly related to the vacuum voltage fluctuations of the resonator, quantified by the zero-point fluctuation amplitude V_{zpf}.
For an $\lambda/2$ coplanar waveguide resonator, the voltage zero-point fluctuations are given by:

$$V_{\text{zpf}} = \sqrt{\frac{\hbar\omega_c^2 Z_0}{\pi}} \tag{1.85}$$

where Z_0 the characteristic impedance of the coplanar waveguide line.
From this expression, it is clear that increasing the characteristic impedance Z_c directly enhances V_{zpf}, and consequently the coupling strength $|g|$. Several approaches have been developed to realize high-impedance resonators, including the use of Josephson-junction arrays, compact lumped-element resonators, modified CPW geometries, and materials with high kinetic inductance such as NbTi, NbN, or granular aluminum (GrAl). These platforms offer promising avenues to significantly boost the coupling between microwave photons and semiconductor-based spin qubits.

Requirements for High-Fidelity Qubit Operations

It is important to emphasize that while maximizing the coupling strength between the qubit and the microwave cavity photons is crucial, it is not sufficient on its own to achieve high-fidelity readout of the qubit state or to enable high-fidelity gates between distant qubits.

When operating in the dispersive regime, where $\Delta = \omega_q - \omega_c \gg g$, achieving high-fidelity readout and coherent long-range interactions between qubits requires:

$$\text{Re}\{\chi(\omega)\} \approx \chi_{\text{disp}},\ J \gg \kappa,\ \Gamma_2 \tag{1.86}$$

These conditions ensure that the qubit-state-dependent cavity frequency shift can be resolved and that information can be exchanged reversibly between distant qubits before decoherence blurs their dynamics.
Therefore, in addition to increasing the coupling rate between the qubit and the cavity photons, it is equally essential to minimize sources of loss in the cavity - quantified by the cavity decay rate κ - and to preserve the qubit's coherence, characterized by its decoherence rate Γ_2.

It is worth noting that coupling the qubit to the cavity introduces an additional dissipation channel known as the Purcell effect. In the dispersive regime, the Purcell decay rate is given by [43]:

$$\Gamma_{\text{Purcell}} \approx \kappa\left(\frac{g}{\Delta}\right)^2 \tag{1.87}$$

This highlights an important trade-off: while increasing the coupling strength improves both the readout fidelity and the strength of cavity-mediated interactions, it simultaneously enhances the rate of qubit relaxation via the cavity. Therefore, especially in designs employing high-impedance resonators, it becomes crucial to minimize intrinsic microwave cavity losses to preserve qubit coherence.

In the remainder of this manuscript, we present our work aimed at enhancing the coupling between a spin qubit hosted in a carbon nanotube and a microwave cavity. This includes efforts to optimize the magnetic field distribution along the nanotube and to implement a high-impedance microwave resonator. All of these developments are pursued with the goal of satisfying the condition given in Equation 1.86.

Chapter 2

A first design of magnet for artificial spin orbit coupling in a carbon nanotube spin qubit device

While the symmetric magnetic field required to define a spin qubit can be applied using an external magnetic field, generating an anti-symmetric field along a double quantum dot typically requires a different approach. One effective strategy is to employ an on-chip micromagnet, whose stray field naturally contains both symmetric and anti-symmetric components. These components can be finely tuned through the external magnetic field.
In this chapter, we present a micromagnet geometry that, while not specifically optimized for maximizing the anti-symmetric field, offers a simple and practical integration into spin qubit architectures based on suspended carbon nanotubes.

2.1 Introduction to magnetism in thin films

2.1.1 Description of the magnetic energies

The stray field of a micromagnet is determined by its micromagnetic configuration, which arises from a balance between several competing interactions. In the following, we describe the various interactions that govern the behavior of magnetic moments in thin-film magnetic materials.

The exchange interaction

In magnetic materials, long-range magnetic order originates from short-range exchange interaction between spins. This interaction emerges when electron hopping between neighboring lattice sites of a crystal is considered in addition to the on-site Coulomb repulsion.

Taking into account Hund's coupling between different orbitals of the same lattice site, along with the Pauli exclusion principle, the hopping of electrons between neighboring sites becomes energetically favorable for either parallel or antiparallel spin configurations, depending on the material considered. These exchange processes reduce the overall Coulomb repulsion in the system, thereby lowering its total energy.

This behavior is captured by the exchange energy between two spins $\vec{\mathbf{S}}_i$ and $\vec{\mathbf{S}}_j$ in two neighboring sites:

$$E_{\text{ex}}^{i,j} = -J\vec{\mathbf{S}}_i\vec{\mathbf{S}}_j$$

where J is the exchange constant. This is a short-range interaction, typically limited to neighboring spins.
For $J > 0$, a parallel spin configuration lowers the energy, and the system tends to develop **ferromagnetic** order, as schematized Fig. 2.1.

The total exchange energy is obtained by summing over all neighboring spin pairs. In the continuum approximation-where the magnetization is treated as a continuous vector field, denoted $\vec{\mathbf{M}}$, rather than a collection of discrete spins-the exchange energy takes the form:

$$E_{\text{ex}} = \frac{A_{\text{ex}}}{M_s^2} \int_V \mathrm{d}V \left(\vec{\nabla} \cdot \vec{\mathbf{M}}\right)^2 \tag{2.1}$$

with A_{ex} is the exchange stiffness constant, M_s is the saturation magnetization, and the integral is taken over the volume V of the magnetic material. For $A_{\text{ex}} > 0$, spatial variations in magnetization are energetically favored, promoting uniform spin alignment and favoring ferromagnetic order.

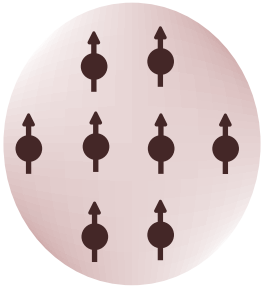

Figure 2.1: **Schematic of ferromagnetic order**
In a ferromagnet, exchange interactions favor parallel spin alignment, producing long-range magnetic order. Arrows denote spins on different lattice sites.

The Zeeman energy

The interaction between a magnetic moment $\vec{\mathbf{m}}$ and an external magnetic field $\vec{\mathbf{B}}_{\text{ext}}$ is described by the Zeeman energy :

$$E_{\text{Zeeman}} = -\vec{\mathbf{m}} \cdot \vec{\mathbf{B}}_{\text{ext}} \tag{2.2}$$

When considering a continuous magnetization $\vec{\mathbf{M}}(\vec{\mathbf{r}})$ rather than a collection of discrete magnetic moments, the Zeeman energy takes the form:

$$E_{\text{Zeeman}} = -\mu_0 \int_V \mathrm{d}^3 r \; \vec{\mathbf{M}}(\vec{\mathbf{r}}) \cdot \vec{\mathbf{H}}_{\text{ext}} \tag{2.3}$$

here μ_0 is the vacuum permeability.
Therefore, the Zeeman energy is minimized when the magnetization is uniform and aligned with the external magnetic field.

Under the **macrospin approximation** - meaning all magnetic moments are aligned in the same direction - the Zeeman energy simplifies to:

$$E_{\text{Zeeman}} = -\mu_0 M_S V H_{\text{ext}} \left[\cos(\theta)\cos(\alpha) + \sin(\theta)\sin(\alpha)\cos\left(\varphi - \beta\right)\right] \tag{2.4}$$

Here, θ and φ are the polar and azimuthal angles of the magnetization $\vec{\mathbf{M}}$, while α and β are the corresponding angles of the external magnetic field $\vec{\mathbf{H}}_{\text{ext}} = \vec{\mathbf{B}}_{\text{ext}}/\mu_0$, all defined in spherical coordinates as represented Fig. 2.2.

The demagnetizing field energy

A magnetic sample that has been initially magnetized by the application of an external magnetic field continues to produce a dipolar magnetic field $\vec{\mathbf{H}}_d$ both outside and inside the magnet. Inside the sample, this dipolar (or demagnetizing) field is oriented opposite to the magnetization direction, thereby acting to demagnetize the magnet. This self-demagnetizing effect strongly influences the behavior of magnetic materials. The energy associated with the demagnetizing field is given by:

$$E_{ms} = -\frac{1}{2}\mu_0 \int_V \mathrm{d}r^3 \; \vec{\mathbf{H}}_d(\vec{\mathbf{r}}) \cdot \vec{\mathbf{M}}(\vec{\mathbf{r}}) \tag{2.5}$$

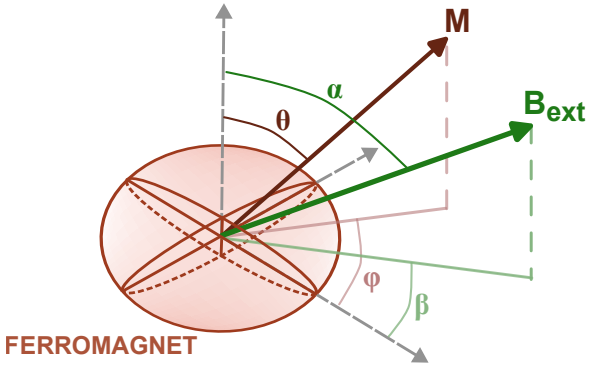

Figure 2.2: **Schematic of a ferromagnet under an external magnetic field $\vec{\mathbf{B}}_{\text{ext}}$.**
The ferromagnetic sample is approximated by an ellipsoid with magnetization $\vec{\mathbf{M}}$. The angles θ and φ denote, respectively, the polar and azimuthal angles of $\vec{\mathbf{M}}$, while α and β denote, respectively, the polar and azimuthal angles of $\vec{\mathbf{B}}_{\text{ext}} = \mu_0 \vec{\mathbf{H}}_{\text{ext}}$.

This expression closely resembles that of a magnetic moment in an external magnetic field, but includes a factor of $\frac{1}{2}$ to avoid double-counting the self-interaction. The demagnetizing field can be expressed as:

$$\vec{\mathbf{H}}_d(\vec{\mathbf{r}}) = -\overline{\overline{N}} \cdot \vec{\mathbf{M}}(\vec{\mathbf{r}}) \tag{2.6}$$

where $\overline{\overline{N}}$ is the demagnetizing tensor, which depends on the geometry of the sample.

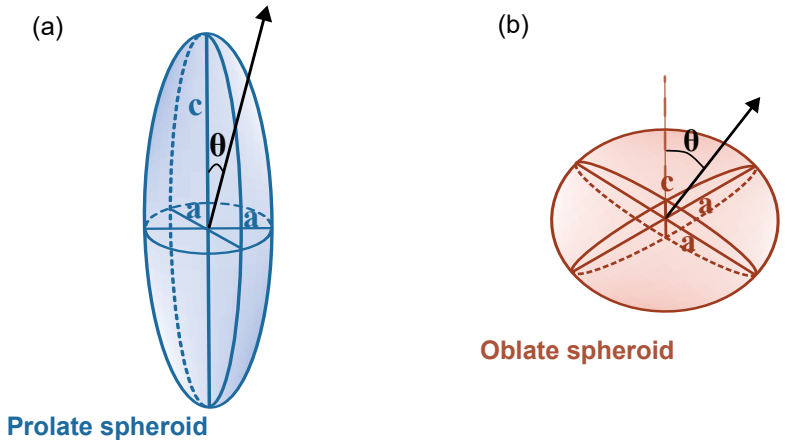

Figure 2.3: **Prolate and oblate spheroidal ferromagnets**
Schematic of a ferromagnet with magnetization $\vec{\mathbf{M}}$ represented as (a) a prolate spheroidal sample and (b) an oblate spheroidal sample.
The angle θ is measured between $\vec{\mathbf{M}}$ and the c-axis.

In the specific case of a **prolate spheroidal sample** - schematized Fig. 2.3 with semi-major axis c and equal semi-minor axes a - and under the assumption of uniform magnetization, the magneto-static energy can be simplified. If the magnetization has a constant magnitude M and is oriented at an angle θ with respect to the c-axis, the energy becomes:

$$\begin{aligned} E_{ms} &= \frac{1}{2}\mu_0 V\left[(M_S\cos(\theta))^2 N_c + (M_S\sin(\theta))^2 N_a\right] \\ &= \frac{1}{2}\mu_0 V M_S^2 N_c + \frac{1}{2}\mu_0 V (N_a - N_c) M_S^2 \sin^2(\theta) \\ &= \frac{1}{2}\mu_0 V M_S^2 N_c + K_{\text{demag}} V \sin^2(\theta) \end{aligned} \tag{2.7}$$

Here, N_c and N_a are the non-zero components of the demagnetizing tensor along the c- and a-axes respectively, satisfying the condition $2N_a + N_c = 1$. For a highly elongated ellipsoid (large aspect ratio $m = c/a$), the demagnetizing factors can be approximated as [71]:

$$N_c \approx \frac{\ln(2m) - 1}{m^2} \underset{m=a/c\gg 1}{\rightarrow} 0 \quad \text{and} \quad N_a \approx \frac{1 - N_c}{2} \underset{m=a/c\gg 1}{\rightarrow} \frac{1}{2} \tag{2.8}$$

For such large aspect ratios, the c-axis corresponds to the easy axis of magnetization: the magnetization is energetically favored along this direction and uniformly unfavorable in directions perpendicular to it. The demagnetizing field thus introduces a **shape-induced magnetic anisotropy**, with the corresponding shape anisotropy constant defined by:

$$K_{\text{demag}} = \frac{1}{2}\mu_0 (N_a - N_c) M_S^2 = \frac{1}{2}\mu_0 \Delta N M_S^2 \tag{2.9}$$

K_{demag} is expressed in is expressed in joules per cubic meter (J/m^3) and $\Delta N = N_a - N_c$. In the limit where the ellipsoid becomes spherical (c=a), the demagnetizing factors equalize, and the shape anisotropy vanishes.

A similar analysis applies when the sample is better approximated as an **oblate spheroid** - or a "flattened" ellipsoid represented Fig. 2.3 - where $a > c$. This analysis typically apply for thin films of magnetic material. Assuming uniform magnetization, the non-zero components of the demagnetizing tensor asymptotically approach [71]:

$$N_c \approx 1 - \frac{\pi}{4m} + \frac{1}{m^2} \underset{m=a/c\gg 1}{\rightarrow} 1 \text{ and } N_a = N_b \approx \frac{\pi}{4m} - \frac{1}{2m^2} \underset{m=a/c\gg 1}{\rightarrow} 0$$

In this case, the demagnetizing field energy becomes:

$$E_{ms} = \frac{1}{2}\mu_0 M_S^2 V \cos^2(\theta) \tag{2.10}$$

where θ is the angle between the magnetization and the c-axis, which is perpendicular to the plane of the spheroid. For magnetic thin film, this expression shows that the energy is minimized when the magnetization lies in the plane of the thin film : the demagnetizing field thus induces an in-plane shape anisotropy.

Electrostatic analogy

In the absence of any current density within the magnetic sample, Maxwell's equations yield:

$$\vec{\nabla} \times \vec{\mathbf{H}}_d = 0 \tag{2.11}$$

This implies that the dipolar magnetic field $\vec{\mathbf{H}}_d$ can be expressed as the gradient of a scalar potential V:

$$\vec{\mathbf{H}}_d = \vec{\nabla} V$$

Analogous to the treatment of electric fields derived from electric charge distributions, the dipolar magnetic field can be described in terms of magnetic pole densities, drawing a formal analogy to electric charges.

Magnetic poles arise at the surface of the sample where the magnetization vector $\vec{\mathbf{M}}$ has a component normal to the surface, see Fig. 2.4. The corresponding **surface magnetic pole density** is given by:

$$\rho_s = \vec{\mathbf{M}} \cdot \vec{\mathbf{n}} = M_s \cos(\theta) \tag{2.12}$$

Where M_s is the magnetization at saturation, $\vec{\mathbf{n}}$ is the unit vector normal to the magnetic sample surface, and θ is the angle between the magnetization and the surface normal.

In addition to surface poles, volume magnetic pole density can arise if the magnetization is non-uniform. Non-uniformity implies that the divergence of the magnetization is non-zero, indicating a net flux of magnetization through a given volume element. This flux must be accounted for by the presence of free magnetic poles within the volume. The volume magnetic pole density is therefore defined as:

$$\rho_V = -\vec{\nabla} \cdot \vec{\mathbf{M}} \tag{2.13}$$

In the special case of a uniformly magnetized sample - where $\rho_V = 0$ - minimizing the demagnetizing energy corresponds to minimizing the surface magnetic pole density. In a magnetic thin film, this condition is satisfied when the magnetization lies entirely in the plane of the film. In this configuration, $\vec{\mathbf{M}} \cdot \vec{\mathbf{n}} = 0$, and the surface pole density ρ_s vanishes. This recovers the earlier result: the energetically favorable magnetization configuration for a thin film lies in-plane.

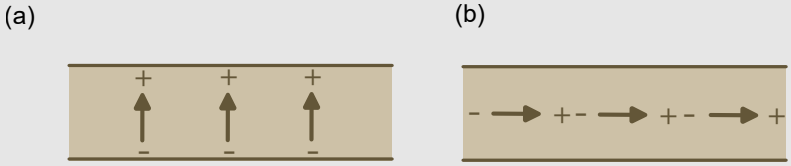

Figure 2.4: **Thin film magnetization orientations**
Schematic of a thin film with magnetization out of the plane (a) and in the plane (b). The surface magnetic pole density in case (a) is increased compared to case (b) making it energetically unfavorable.

Magnetic anisotropy of thin films

Crystal anisotropy

Crystal anisotropy can be understood as an intrinsic force in a crystalline material that tends to align the magnetization along specific crystallographic directions. This effect primarily originates from the coupling between the spin and the orbital motion of electrons within the crystal lattice. When an external magnetic field attempts to reorient the electron spins, the associated orbital motion also tends to rotate. However, because the orbital motion is strongly coupled to the crystal lattice, this reorientation can be energetically resisted. The resulting energy cost gives rise to magnetic anisotropy, and its strength is characterized by magnetocrystalline anisotropy constants.

In cubic crystals, the magnetocrystalline energy depends on the orientation of the magnetization $\vec{\mathbf{M}}$ with respect to the crystal axes. Let α_1, α_2 and α_3 be the direction cosines of the magnetization vector with the principal crystallographic axes. The magnetocrystalline anisotropy energy can then be expressed as:

$$E_{Kc} = \left[K_1\left(\alpha_1^2\alpha_2^2 + \alpha_1^2\alpha_3^2 + \alpha_2^2\alpha_3^2\right) + K_2\left(\alpha_1^2\alpha_2^2\alpha_3^2\right)\right]V \tag{2.14}$$

where K_1 and K_2 are the first- and second-order magnetocrystalline anisotropy constants, and V is the volume of the crystal.

In hexagonal systems, the anisotropy is typically uniaxial, with the hexagonal c-axis serving as the easy axis of magnetization. In this case, the anisotropy energy depends solely on the angle θ between the magnetization vector and the c-axis, and is given by:

$$E_{Kc} = \left[K_1 \sin^2(\theta) + K_2 \sin^4(\theta)\right]V \tag{2.15}$$

Although it is well established that magnetocrystalline anisotropy originates from spin-orbit coupling, the precise mechanisms remain complex. In most cases, it is not possible to compute the anisotropy constants accurately from first principles.

Surface or interface anisotropy

Surface or interface contributions to magnetocrystalline anisotropy is particularly significant in multilayer systems, especially when the thickness of the magnetic layers approaches the nanometer scale. These contributions arise due to symmetry breaking at the film interfaces, which alters the local electronic environment and leads to anisotropic magnetic behavior. In such cases, the axis perpendicular to the film plane becomes the easy axis of magnetization.

The energy associated with interface anisotropy can be expressed as:

$$E_{Ks} = \left(\frac{K_s^1}{t} + \frac{K_s^2}{t}\right) \sin^2(\theta) V \tag{2.16}$$

where K_s^1 and K_s^2 are the surface (or interface) anisotropy constants corresponding to the two interfaces of the magnetic film, t is the film thickness, and θ is the angle between the magnetization and the easy axis of magnetization normal to the film plane.

This expression highlights the fact that surface anisotropy becomes more dominant as the film thickness decreases, thereby playing a crucial role in stabilizing perpendicular magnetic anisotropy (PMA) in very thin films.

Magneto-elastic anisotropy

In addition to interface-induced anisotropy, magneto-elastic anisotropy can arise in multilayered thin films, particularly when the thickness of the layers approaches atomic dimensions. This form of anisotropy originates from strain caused by lattice mismatch between the different layers of the heterostructure, which alters the equilibrium direction of magnetization.

When the layer thickness t is smaller than a critical value t_c, the strain is uniformly distributed throughout the volume of the layer. In this regime, the lattice parameter assumes an intermediate value between the lattice constants of the adjacent materials. The associated volume magneto-elastic energy is given by:

$$E_{me} = K_{V,me} \sin^2(\theta) V \tag{2.17}$$

where $K_{V,me}$ is the volume magneto-elastic constant, V is the volume of the magnetic layer, and θ is the angle between the magnetization and the axis normal to the sample plane.

For layers with $t > t_c$, the system tends to relax the strain energy by introducing misfit dislocations at the interfaces. As a result, both layers retain their original lattice parameters, and the strain becomes localized at the interface. In this regime, the magneto-elastic anisotropy transitions to a surface effect, and the corresponding energy becomes:

$$E_{me} = \frac{1}{t} K_{S,me} \sin^2(\theta) V \tag{2.18}$$

where $K_{S,me}$ is the surface magneto-elastic constant.As before, θ is the angle between the magnetization and the axis perpendicular to the film plane.

2.1.2 Macrospin approximation for thin films: the Stoner Wolhfart model

In the macrospin model, all magnetic moments are assumed to be aligned in the same direction and rotate coherently as a single, collective magnetic moment-referred to as a macrospin. As a result, exchange interactions between individual spins are neglected, and the system is treated as a uniformly magnetized single domain.

The total magnetic energy

By considering the various magnetic energy contributions described above, the total magnetic energy of a thin magnetic film with uniaxial magnetocrystalline anisotropy perpendicular to the film plane and in the absence of an external magnetic field can be written as:

$$\begin{aligned} E_{\text{tot}} &= \left[K_1 + K_{V,me} + \frac{K_s^1 + K_s^2 + K_{S,me}}{t}\right] V \sin^2(\theta) + K_2 V \sin^4(\theta) + \frac{1}{2}\mu_0 M_S^2 V \cos^2(\theta) \\ &= \left[K_1 + K_{V,me} + \frac{K_s^1 + K_s^2 + K_{S,me}}{t} - \frac{1}{2}\mu_0 M_S^2\right] V \sin^2(\theta) + K_2 V \sin^4(\theta) + \frac{1}{2}\mu_0 M_S^2 V \\ &= K_{\text{eff}} V \sin^2(\theta) + C \end{aligned} \tag{2.19}$$

In the final expression, C is a constant and K_{eff} denotes the effective anisotropy constant, defined as the net contribution of all anisotropies (volume, surface/interface, and demagnetizing), and the approximation neglects constant terms and higher-order anisotropy contributions.
When an external magnetic field is applied, the Zeeman energy competes with the effective anisotropy energy. The total energy of the system is then given by:

$$E_{\text{tot}} = \left[K_{\text{eff}} \sin^2(\theta) - \mu_0 M_S H_{\text{ext}}\big(\cos(\theta)\cos(\alpha) + \sin(\theta)\sin(\alpha)\cos\big(\varphi - \beta\big)\big)\right] V \tag{2.20}$$

Here, θ and φ define the orientation of the magnetization in spherical coordinates, while α and β describe the direction of the external magnetic field. This expression governs the equilibrium states of the magnetization under the influence of both anisotropy and applied fields.

The Stoner-Wolhfart Model

The magnetic configuration of the system corresponds to the orientation of the magnetization that minimizes the total magnetic energy for a given magnitude and direction of the external magnetic field.

Starting from the energy expression in Eq. (2.20), we note that the total energy is minimized when the azimuthal angle of the magnetization equals that of the external field, i.e., $\varphi = \beta$. Substituting this condition simplifies the energy expression to:

$$E_{\text{tot}} = \left[K_{\text{eff}} \sin^2(\theta) - \mu_0 M_S H_{\text{ext}} \cos(\theta - \alpha)\right] V \tag{2.21}$$

This expression forms the basis of the Stoner-Wohlfarth model, which describes the coherent rotation of a single-domain ferromagnet under the influence of an external magnetic field.
The sign of K_{eff} determines the direction of the easy axis of magnetization:

- If $K_{eff} > 0$, the easy axis is perpendicular to the film plane.
- If $K_{eff} < 0$, the easy axis lies in the plane of the film.

In the following, θ denotes the angle between the magnetization and the easy axis, while α represents the angle between the external magnetic field and the easy axis of the sample. The equilibrium magnetic configuration corresponds to the orientation of the magnetization that minimizes the total energy. This is found by solving the conditions:

$$\frac{\partial E_{\text{tot}}}{\partial \theta} = 0 \quad \text{and} \quad \frac{\partial^2 E_{\text{tot}}}{\partial \theta^2} > 0$$

Analytical solutions to this model can be obtained in two particular cases:

- When the external magnetic field is applied along the easy axis of magnetization: $\alpha = 0°$,
- When the external magnetic field is applied transverse to the easy axis: $\alpha = 90°$.

In the first case, where the external magnetic field is applied along the easy axis of magnetization and swept from positive to negative values, the magnetization in the plane of the thin film

exhibits hysteresis. As the field is reversed, the magnetization follows a non-linear path, resulting in a hysteresis loop, see Fig.2.5(a). The coercive field H_c is defined as the field required to reduce the magnetization to zero.

In the second case, where the external field is applied transverse to the easy axis, the magnetization out of the plane of the thin film exhibits a linear response, see Fig.2.5(b). In this configuration, the component of the magnetization along the field direction vanishes when the external field is zero. The field required to fully align the magnetization along the field direction is called the anisotropy field, given by:

$$H_K = \frac{2K_{eff}}{\mu_0 M_s} \tag{2.22}$$

Notably, in the special case where the only source of anisotropy is the demagnetizing field, the anisotropy field simplifies to: $H_K = M_s$.

The Stoner-Wohlfarth asteroid maps the critical field required to reverse the magnetization as a function of the angle α between the external magnetic field and the easy axis of magnetization. The critical field for magnetization reversal is given analytically by:

$$H_{\text{crit}} = \frac{2K_{eff}}{\mu_0 M_s} \frac{1}{\sin^{2/3}(\alpha) + \cos^{2/3}(\alpha)} \tag{2.23}$$

This result defines the boundary of the so-called astroid curve in the space of applied field components. In this simple model, when the field is applied along the easy axis ($\alpha = 0$), the coercive field equals both the anisotropy and critical fields: $H_c = H_K = H_{\text{crit}} = \frac{2K_{eff}}{\mu_0 M_s}$.
However, in real materials, the coercive field H_c is typically lower than the theoretical anisotropy field. This discrepancy arises due to imperfections in the sample, such as defects and inhomogeneities, which facilitate the nucleation and propagation of magnetic domains-leading to magnetization reversal at lower applied fields.

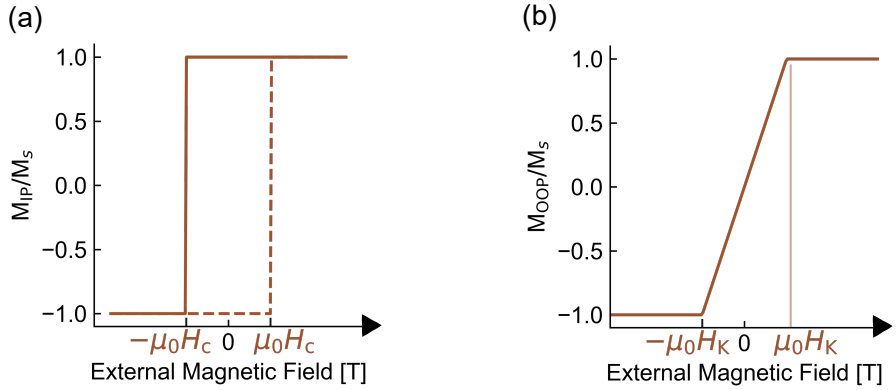

Figure 2.5: **Stoner-Wohlfarth $M(B)$ loops for a thin film**
(a) In-plane magnetization M_{IP} with the applied magnetic field swept along the film plane (longitudinal).
(b) Out-of-plane magnetization M_{OOP} with the magnetic field swept perpendicular to the film (transverse).

Finally, it is important to note that the model described above neglects thermal effects. At finite temperatures, thermal activation can significantly influence magnetization dynamics by enabling thermally assisted switching over energy barriers.

2.2 A central magnetic gate for artificial spin orbit coupling

To generate the required anti-symmetric magnetic field, we propose using the central gate not only to control the electrostatic potential along the carbon nanotube but also as a micromagnet. A schematic of the design is proposed as represented Fig.2.6 .This dual functionality is achieved by fabricating the gate from a ferromagnetic material, allowing it to produce a stray magnetic field while maintaining its electrostatic role.
In this section, we discuss the predicted micromagnetic configuration of the ferromagnetic gate, present the experimental characterization of its magnetic properties, and evaluate the expected stray magnetic field it produces-particularly its symmetric and anti-symmetric components relevant for spin qubit operation.

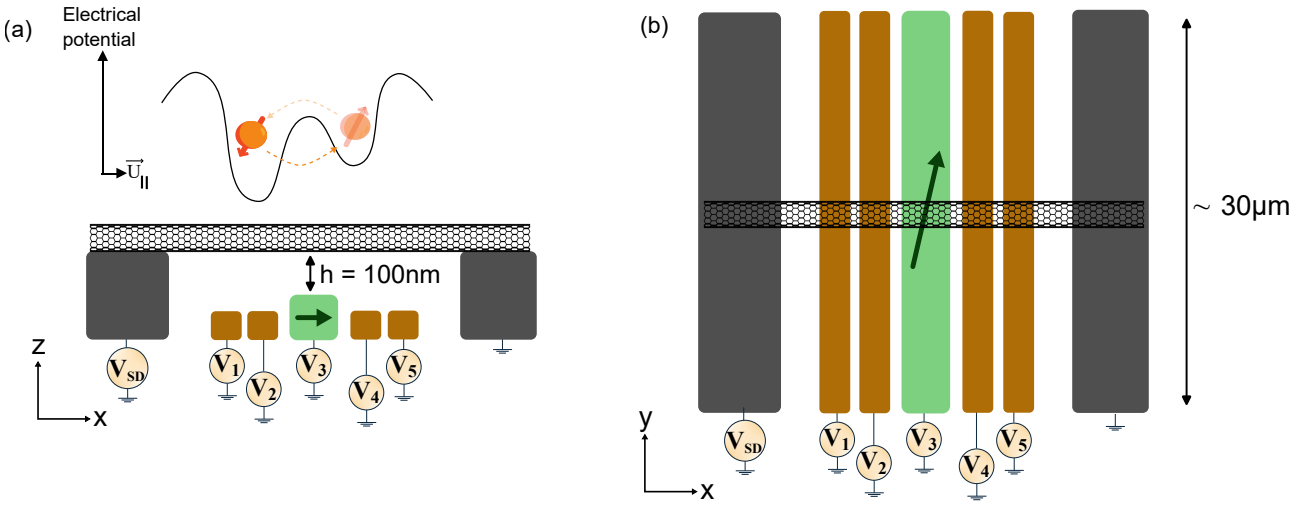

Figure 2.6: **A central magnetic gate in a carbon-nanotube double quantum dot architecture** (a) Side-view and (b) top-view schematics of the spin-qubit device. A suspended carbon nanotube bridges source and drain electrodes. Five plunger gates shape the electrostatic potential to form a double quantum dot. One plunger gate (shown in green) is fabricated from a magnetic material, acting as an on-chip micro-magnet that generates a magnetic field along the nanotube.

2.2.1 The macrospin model

We adopt the macrospin approximation in this analysis, assuming that the magnetization within the magnetic gate is uniform and undergoes coherent rotation as a single magnetic moment.

Given the gate's thickness ($t = 120\,\text{nm}$), both interface anisotropy and magneto-elastic anisotropy are neglected. Additionally, crystal anisotropy effects are not considered in this model. Under these assumptions, the magnetic configuration of the gate is determined solely by the competition between the demagnetizing energy (shape anisotropy) and the Zeeman energy arising from the external magnetic field.

Shape-induced anisotropy

The gate is expected to have a width of 200 nm and a length of 30 µm. Given its elongated geometry, the gate can be reasonably approximated as a prolate spheroid, a case discussed in the previous section. This geometry gives rise to a shape-induced magnetic anisotropy due to the demagnetizing field. The associated magnetostatic energy is expressed as:

$$E_{ms} = K_{\text{demag}} V \sin^2(\theta) \quad \text{with} \quad K_{\text{demag}} = \frac{1}{4}\mu_0 M_s^2 \tag{2.24}$$

Here θ enotes the angle between the magnetization vector and the long axis of the magnet. This expression captures the tendency of the magnetization to align along the elongated direction, reducing the surface magnetic pole density, and minimizing the demagnetizing energy.

Zeeman energy

In the absence of an external magnetic field, the stray field produced by the magnetic gate in the vicinity of the double quantum dot is negligible. This is because the magnetization within the gate is assumed to be uniform, leading to a zero volume magnetic pole density. Moreover, the surface magnetic poles are confined to the edges of the magnet, which are located several micrometers away from the double quantum dot. As a result, the magnetic field in the quantum dot region vanishes.

Consequently, in this device geometry, the external magnetic field serves two essential purposes:

- To **reorient the magnetization of the magnetic gate**, thereby generating surface magnetic poles that produce an anti-symmetric stray field in the region near the double quantum dot,
- To provide the **symmetric magnetic field component that defines the Zeeman splitting** in the spin qubit energy spectrum.

To fulfill both roles, the external magnetic field is applied along the longitudinal axis of the carbon nanotube, which corresponds to the transverse direction relative to the magnetic gate. The Zeeman energy is then given by:

$$E_Z = -\mu_0 M_s V H_{x,\text{ext}} \sin(\theta)\cos(\varphi) \tag{2.25}$$

Here θ denotes the polar angle of the magnetization $\vec{\mathbf{M}}$, measured with respect to the long axis of the magnetic gate, and φ is the azimuthal angle of $\vec{\mathbf{M}}$ around that axis. This expression captures the energy associated with aligning the magnetization with the external magnetic field applied along the x-axis (i.e., along the nanotube axis).

Magnetic configuration at equilibrium

The equilibrium magnetic configuration is obtained by minimizing the total magnetic energy, which consists of the sum of the demagnetizing field energy and the Zeeman energy. From the expression of the total energy, it is evident that the energy is minimized when the azimuthal angle $\varphi = 0$. Under this condition, the equilibrium configuration is determined by solving:

$$\left.\frac{\partial E_{\text{tot}}}{\partial \theta}\right|_{\varphi=0} = 0 \quad \text{and} \quad \left.\frac{\partial^2 E_{\text{tot}}}{\partial \theta^2}\right|_{\varphi=0} > 0 \quad \text{with} \quad E_{\text{tot}} = E_{ms} + E_Z$$

Solving these equations allows the definition of a critical magnetic field: $B^{\text{sat}}_{\text{x,ext}} = \frac{1}{2}\mu_0 M_s$.
Two regimes can then be identified based on the amplitude of the applied external field $B_{\text{x,ext}}$.

- For $\left|B_{x,\text{ext}}\right| \leq B^{\text{sat}}_{\text{x,ext}}$, the energy minimum occurs for:

$$\sin(\theta) = \frac{2B_{\text{x,ext}}}{\mu_0 M_s} \tag{2.26}$$

  In this regime, the component of the magnetization along the x-axis - i.e. aligned with the direction of the external magnetic field and given by $M_x = M_s \sin(\theta)$ - exhibits a linear dependence on the field amplitude.
- For $\left|B_{x,\text{ext}}\right| \geq B^{\text{sat}}_{\text{x,ext}}$, the energy minimum corresponds to:

$$\cos(\theta) = 0 \tag{2.27}$$

  indicating that the magnetization is fully aligned along the external field direction (the x-axis). In this case, the magnet is saturated.

Figure 2.8(a) plots M_x as a function of the external field amplitude $B_{x,\text{ext}}$.

Magnetic stray field of the magnet

Under the macrospin approximation, the magnetic field $\vec{\mathbf{B}}$ produced by the magnet at a point $\vec{\mathbf{r}}$ in space (outside the magnet region) can be derived by obtained by summing (integrating) the dipole field from all magnetic moments that make up the magnet. The resulting dipolar magnetic field is given by:

$$\vec{\mathbf{B}}(\vec{\mathbf{r}}, M_s) = \frac{\mu_0}{4\pi}\int_V \mathrm{d}^3 r' \frac{3\left(\vec{\mathbf{M}}\left(\vec{\mathbf{r}'}\right)\cdot\vec{\mathbf{u}}\right)\vec{\mathbf{u}} - \vec{\mathbf{M}}\left(\vec{\mathbf{r}'}\right)}{R^3} = \frac{\mu_0}{4\pi} M_s \int_V \mathrm{d}^3 r' \left[\frac{3\left(\vec{\boldsymbol{\mu}}\left(\vec{\mathbf{r}'}\right)\cdot\vec{\mathbf{R}}\right)\vec{\mathbf{R}}}{R^5} - \frac{\vec{\boldsymbol{\mu}}\left(\vec{\mathbf{r}'}\right)}{R^3}\right] = \mu_0 M_s \vec{\mathbf{Q}}(\vec{\mathbf{r}}) \tag{2.28}$$

Here :

- V is the volume of the magnet
- $\vec{\mathbf{M}}\left(\vec{\mathbf{r}'}\right) = M_s\vec{\boldsymbol{\mu}}\left(\vec{\mathbf{r}'}\right)$ is the magnetization at source point $\vec{\mathbf{r}'} = \left(x', y', z'\right)$, with M_s the saturation magnetization
- $\vec{\boldsymbol{\mu}}(\vec{\mathbf{r}'}) = \begin{pmatrix}\sin(\theta)\\ \cos(\theta)\\ 0\end{pmatrix}$ is the unit vector defining the orientation of the magnetization. Under the macro-spin approximation, all the source points have the same orientation of the magnetization.
- $\vec{\mathbf{R}} = \vec{\mathbf{r}} - \vec{\mathbf{r}'} = R\,\vec{\mathbf{u}}$, where $\vec{\mathbf{u}}$ is the unit vector pointing from the dipole to the observation point, and $R = \left|\vec{\mathbf{R}}\right|$ is the distance to that point.

The function $\vec{\mathbf{Q}}(\vec{\mathbf{r}})$ is a dimensionless vector field that encapsulates the spatial dependence of the dipolar field - how it varies with distance, orientation, and magnet geometry. It is independent of the saturation magnetization of the magnet and isolates the geometric contribution to the stray field distribution.
Figure 2.7 displays the magnetic field generated by the magnet within the macrospin approximation, for magnetization oriented along and transverse to the magnet's long axis.

Along the carbon nanotube - corresponding to the plane $y = 0$ - the component of the stray magnetic field produced by the magnet in the longitudinal direction (along x) is given by:

$$\begin{aligned}
B_x(M_s, x, y=0, z) &= \frac{\mu_0}{4\pi} M_s \iiint_V \mathrm{d}x'\mathrm{d}y'\mathrm{d}z' \left[\frac{3\left[\sin(\theta)(x-x') - y'\cos(\theta)\right](x-x')}{R^5} - \frac{\sin(\theta)}{R^3}\right] \\
&= \frac{\mu_0}{4\pi} M_s \left[\iiint_V \mathrm{d}x'\mathrm{d}y'\mathrm{d}z' \left[\frac{3\sin(\theta)(x-x')^2}{R^5} - \frac{\sin(\theta)}{R^3}\right] - \iiint_V \mathrm{d}x'\mathrm{d}y'\mathrm{d}z' \frac{3y'(x-x')\cos(\theta)}{R^5}\right] \\
&= \sin(\theta)\ \frac{\mu_0}{4\pi} M_s \iiint_V \mathrm{d}x'\mathrm{d}y'\mathrm{d}z' \left[\frac{3(x-x')^2}{R^5} - \frac{1}{R^3}\right] \\
&= \sin(\theta)\ B_x^{\text{xsat}}(x, y=0, z, M_s)
\end{aligned} \tag{2.29}$$

with :

$$\int_{-z_\text{m}/2}^{z_\text{m}/2}\int_{-y_\text{m}/2}^{y_\text{m}/2}\int_{-x_\text{m}/2}^{x_\text{m}/2} \mathrm{d}x'\mathrm{d}y'\mathrm{d}z' \frac{3y'(x-x')\cos(\theta)}{R^5} = 0$$

where z_m is the thickness of the magnet, y_m is the length of the magnet and x_m is the width of the magnet.
The transverse direction (along z) is similarly given by:

$$\begin{aligned}
B_z(M_s, x, y=0, z) &= \frac{\mu_0}{4\pi} M_s \iiint_V \mathrm{d}x'\mathrm{d}y'\mathrm{d}z' \frac{3\left[\sin(\theta)(x-x') - y'\cos(\theta)\right](z-z')}{R^5} \\
&= \sin(\theta)\ B_z^{\text{xsat}}(x, y=0, z, M_s)
\end{aligned} \tag{2.30}$$

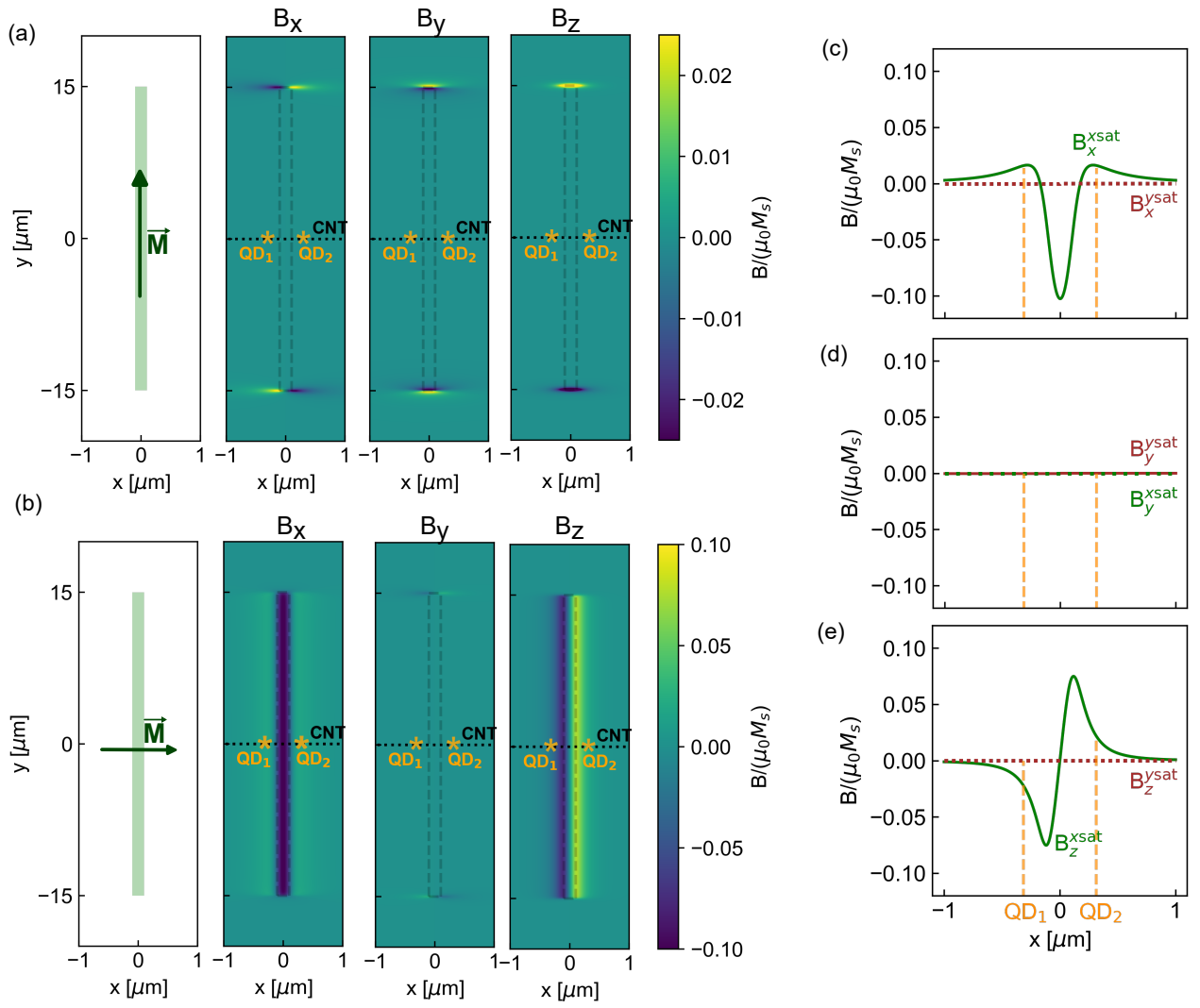

Figure 2.7: **Magnetic field from the micromagnet computed with a macrospin model**
(a) Magnet schematic with uniform magnetization $\vec{\mathbf{M}}$ aligned with the elongated direction of the magnet; the resulting field components (B_x, B_y, B_z) are computed at $h = 100\,\text{nm}$ above the top surface of the magnet (see Fig. 2.6).
(b) Same as (a) with a magnetization transverse to the elongated direction of the magnet.
(c-e) Comparison of B_x, B_y and B_z along the carbon nanotube (dashed lines in (a-b)) for the two magnetization orientations: longitudinal (red, as in (a)) and transverse (green, as in (b)).
Magnetic-field calculations were performed in Python with Magpylib.

In the equations Eq. (2.29) and Eq. (2.30), $B_x^{\text{xsat}}(M_s, x, y = 0, z)$ and $B_z^{\text{xsat}}(M_s, x, y = 0, z)$ represent the stray magnetic field components when the magnet is saturated in the x-direction, i.e., aligned with the external magnetic field.

Depending on the strength of the applied external magnetic field, the magnetic field expressions can be simplified:

- For $\left|B_{x,\text{ext}}\right| \leq \frac{1}{2}\mu_0 M_s$ (below saturation):

$$B_i(M_s, x, y = 0, z) = 2B_{\text{x,ext}} Q_i^{\text{xsat}}(x, y = 0, z) \tag{2.31}$$

where $i \in \{x, z\}$, and $Q_i^{\text{sat}x}$ is the normalized magnetic field component in the direction i corresponding to saturation of the magnet in the x-direction.

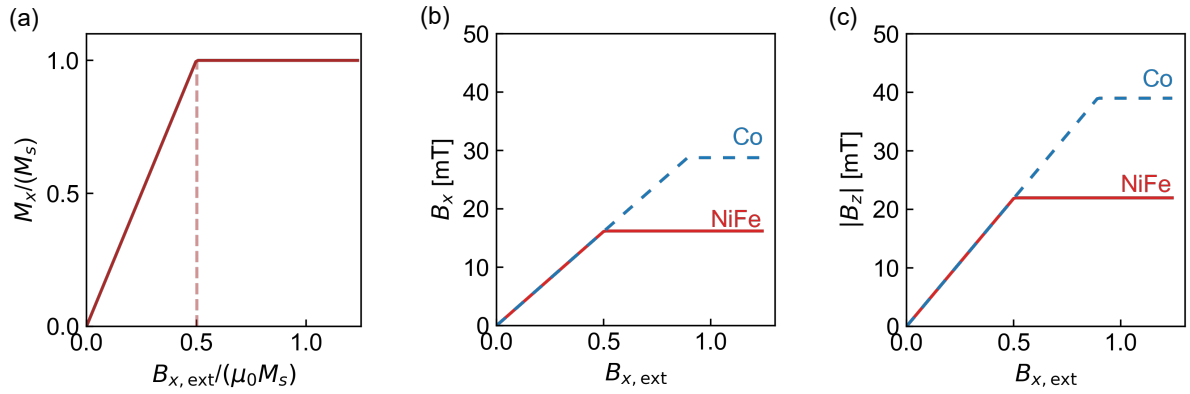

Figure 2.8: **Dependence of magnetization and stray field on the external field $B_{x,\text{ext}}$ under the macro-spin approximation**
(a) Evolution of the x-component of the magnet magnetization M_x, as a function of $B_{x,\text{ext}}$ under the macrospin approximation.
(b-c) Predicted evolution with $B_{x,\text{ext}}$ (macrospin model) of the magnetic field components B_x and B_y generated by the micromagnet at the quantum-dot positions indicated in Fig. 2.7, for two magnetic materials with different saturation magnetizations: $M_s(\text{NiFe}) = 800 \times 10^3\,\text{A m}^{-1}$ and $M_s(\text{Co} = 1420 \times 10^3\,\text{A m}^{-1})$. A the dots positions, B_x is symmetric over the two dots ($B_x(\text{QD}_1) = B_x(\text{QD}_1)$) while B_z is anti-symmetric over the two dots($|B_z(\text{QD}_1)| = |B_z(\text{QD}_1)|$) (see Fig.2.7).

- For $\left|B_{x,\text{ext}}\right| \geq \frac{1}{2}\mu_0 M_s$ (at or beyond saturation):

$$B_i(M_s, x, y = 0, z) = B_i^{x\text{sat}}(M_s, x, y = 0, z) \tag{2.32}$$

In Fig. 2.8, the magnetic field at the dot locations along the nanotube - calculated within the macro-spin approximation - is plotted versus$B_{\text{x,ext}}$ for two distinct magnetic materials. Notably, below saturation, the amplitude of the stray magnetic field is independent of the saturation magnetization M_s.
Therefore, increasing M_s by selecting a ferromagnetic material with a higher saturation magnetization does not enhance the stray field unless the magnet is fully saturated.

To enable nanofabrication of the magnetic gate, a lift-off process will be employed. This fabrication method requires the deposition of the magnetic material to be performed via electron-beam (e-beam) evaporation, rather than sputtering, in order to ensure well-defined patterning.
For practical reasons that will be detailed later, the external magnetic field applied during operation is unlikely to exceed 500 mT. As a result, using a material with a very high saturation magnetization (M_s) is unnecessary. Therefore, the magnetic gate is fabricated from $Ni_{80}Fe_{20}$ (permalloy), which has a typical saturation magnetization of $M_s \sim 800 \times 10^3\,\text{A m}^{-1}$.

2.2.2 Thin film characterization : measuring the magnetization with a VSM magnetometer

VSM measurement principle

The measurement of magnetization in a **Vibrating Sample Magnetometer** (VSM) setup relies on detecting changes in magnetic flux through a pick-up coil caused by the motion of a magnetized sample, see Fig. 2.9. As the sample oscillates near the coil, the resulting oscillatory magnetic field induces an alternating voltage according to Faraday's law:

$$V_{\text{emf}} = -\frac{\mathrm{d}\phi}{\mathrm{d}t} \tag{2.33}$$

Here, ϕ represents the magnetic flux through the coil, expressed as:

$$\phi(t) = \int_{\text{coil area}} \left(\vec{\mathbf{B}}_{\text{ext}} + \vec{\mathbf{B}}_m(\vec{\mathbf{r}}(t))\right) \cdot \vec{\mathbf{n}} \, \mathrm{d}A \tag{2.34}$$

In this expression, $\vec{\mathbf{B}}_{\text{ext}}$ is a static external magnetic field, $\vec{\mathbf{B}}_m \propto \vec{\mathbf{M}}$ is the field generated by the sample, $\mathbf{r}(\vec{\mathbf{t}})$ is the time-dependent position of the vibrating sample, and $\vec{\mathbf{n}}$ is a unit vector normal to the coil surface. Because only the sample vibrates, the induced AC signal originates solely from its time-varying field. Static background fields remain constant and therefore do not contribute to the detected signal. The measured signal is influenced by several key factors:

- the strength of the component of the magnetic moment perpendicular to the coil area, $M_\perp$,
- the spatial profile of the magnetic field around the sample
- the geometry and configuration of the pick-up coil,
- the amplitude and frequency of the sample's vibration.

In practice, the AC magnetic flux can be approximated as [72]:

$$\phi_{AC}(t) = GM_\perp \sin(\omega t) \tag{2.35}$$

where $M_\perp$ is the component of the sample's magnetization perpendicular to the pickup coil area, and G is a geometry-dependent calibration constant. This factor primarily depends on the coil configuration, the amplitude of the sample's vibration, and the distance between the sample and the pickup coils.
The induced voltage V_{emf} is then detected - typically using a lock-in amplifier synchronized to the vibration frequency - providing a direct and quantitative measure of the sample's magnetization along a specific direction. By sweeping the applied external magnetic field, one can obtain the magnetization curve as a function of field strength.

The VSM method offers the advantages of relatively fast data acquisition (on the order of a few minutes) and high sensitivity, typically down to approximately $\sim 1 \times 10^{-8}\,\mathrm{A\,m^2}$.

However, in our case, conventional VSM measurements were only feasible at room temperature. Since the magnet is intended to operate at cryogenic temperatures ($T \sim 10\,\mathrm{mK}$), it is preferable to employ a characterization technique capable of performing measurements across both room temperature and low-temperature regimes. For this reason, **SQUID-VSM measurements** were carried out at room temperature and at 4 K.

VSM-SQUID measurement principle

The SQUID (Superconducting Quantum Interference Device) functions as an extremely sensitive flux detector, coupled to the VSM pick-up coils. It consists of a superconducting loop interrupted by two Josephson junctions. When a bias current is applied, the supercurrent through the junctions depends periodically on the magnetic flux ϕ threading the SQUID loop:

$$I_c(\phi) = 2I_c^0 \cos\left(\frac{\pi\phi}{\phi_0}\right) \tag{2.36}$$

where $\phi_0 = h/e$ is the magnetic flux quantum. This periodic behavior leads to an oscillating voltage across the SQUID when operated in the resistive regime under a bias current:

$$V_{\text{SQUID}} = \Delta V \cos\left(\frac{\pi\phi}{\phi_0}\right) \tag{2.37}$$

Due to the non-linear and periodic nature of the SQUID's voltage-flux response, direct measurements can be ambiguous. To overcome this limitation, a **flux-locked loop** (FLL) is employed. The FLL actively cancels the magnetic flux induced by the sample in the SQUID loop by applying an

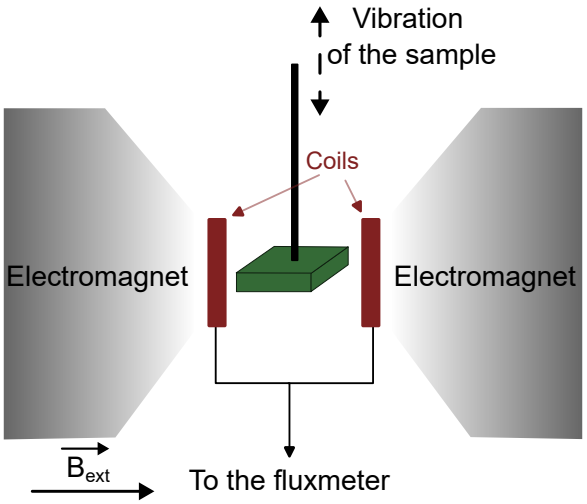

Figure 2.9: **Fundamental operating principle of a Vibrating Sample Magnetometer (VSM)**
In the schematic, the in-plane magnetization of the sample (shown in green)-i.e., the component of the sample's magnetization perpendicular to the pickup-coil area - is detected. The out-of-plane magnetization component can be measured by rotating the sample by 90°.

equal and opposite flux via a feedback coil. This ensures that the SQUID remains locked at its most sensitive operating point-where the voltage-flux relationship is linear. Any variation in magnetic flux detected by the SQUID is instantaneously counteracted by a precisely calibrated feedback current, thereby maintaining linear operation and enabling unambiguous, high-resolution measurements.
The feedback current - or equivalently, the voltage across a known resistor in the feedback path - is then measured. This current is directly proportional to the magnetic flux induced by the vibrating sample, and thus to the component of its magnetic moment perpendicular to the pickup coil area:

$$I_{\text{fb}} \propto \phi_{AC} \propto M_{\perp} \tag{2.38}$$

In the SQUID-VSM configuration, the sample is sinusoidally vibrated, generating a time-dependent magnetic flux that is detected by the pickup coils and transferred to the SQUID loop. This changing flux is then canceled in real-time by a matching feedback current, resulting in an AC feedback signal. The frequency of this signal matches that of the mechanical vibration, and its amplitude is directly proportional to the magnetic moment of the sample $M_{\perp}$.

In addition to enabling magnetic measurements at cryogenic temperature, the SQUID provides very low sensitivity, capable of detecting magnetic moments as low as $\sim 1 \times 10^{-10}\,\text{A}\,\text{m}^2$. While this level of sensitivity exceeds the requirements of the present work, it ensures robust measurements even for weakly magnetized samples.

VSM-SQUID measurement on a thin film of Permalloy (NiFe)

In this section, we describe the SQUID-VSM measurements performed on a thin film of Permalloy. The film consists of a 5 nm titanium layer, serving as an adhesion layer, followed by a Permalloy layer ($Ni_{80}Fe_{20}$) of thickness 112.5 ± 2.5nm and capped with a 5 nm platinum layer to prevent oxidation.
Magnetization measurements were performed both in-plane and out-of-plane by rotating the sample orientation with respect to the VSM pickup coils, while sweeping an external magnetic field, see Fig. 2.10. This was achieved by applying the magnetic field either parallel to the film surface for in-plane measurements, or perpendicular to the surface for out-of-plane measurements.
The measurement yields the total magnetic moment M_V of the total volume of the sample. To extract the volumetric magnetization M, this value is normalized by the total volume of the magnetic layer, $M = M_V / V$.

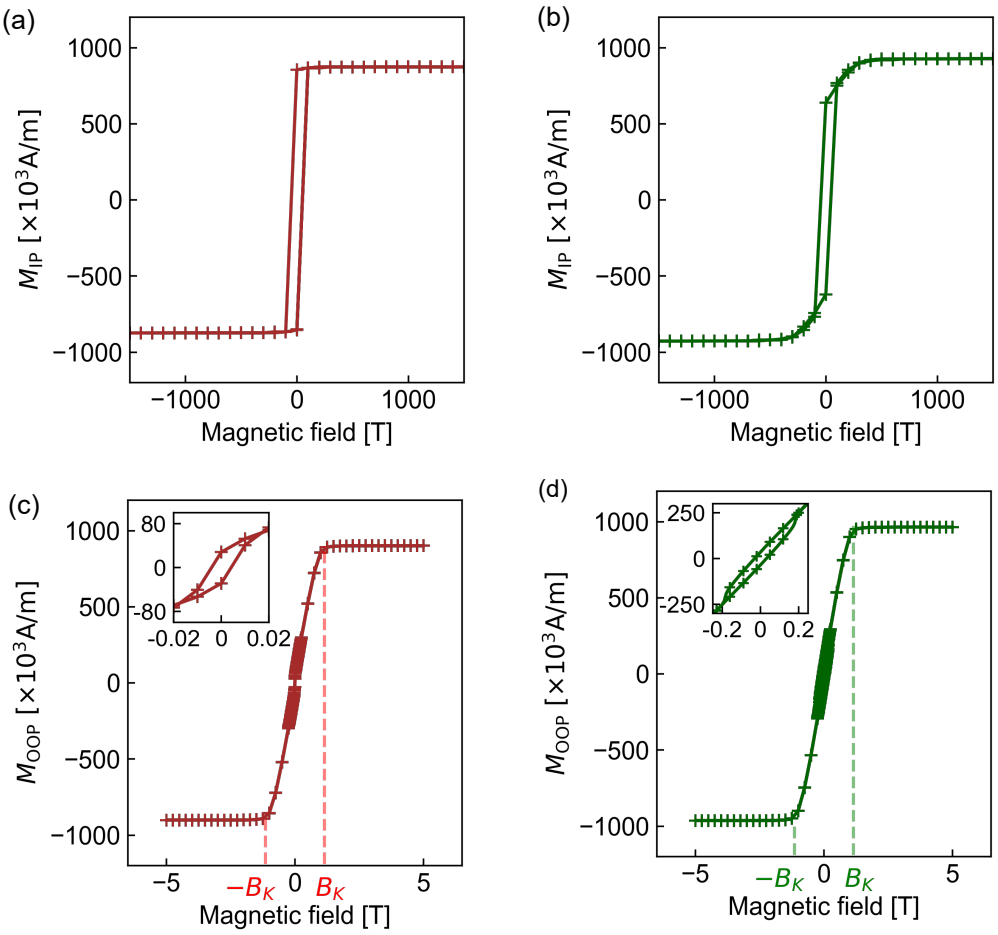

Figure 2.10: **SQUID-VSM measurements on a Permalloy (NiFe) thin film**
(a-b) In-plane magnetization M_{IP} with an external field applied in the film plane (see Fig. 2.9). Panel (a): room temperature ($T \approx 300\,K$), panel (b): low temperature ($T = 4\,K$)
(c-d) Out-of-plane magnetization M_{OOP} while applying an external magnetic field out of the plane of the thin film .with the field applied perpendicular to the film. Panel (c): room temperature ($T \approx 300\,K$), panel (d): low temperature ($T = 4\,K$).
Panel (c), a hysteretic feature - suggestive of a sudden reversal of the magnetization - appears. This may indicate a finite out-of-plane component of the magnetization but could also arise from a slight sample tilt in the setup.

Room Temperature Magnetization Measurements

At room temperature, the in-plane magnetization as a function of the applied magnetic field exhibits a clear hysteresis loop. A sharp reversal of the in-plane component occurs as the magnetic field is swept (either decreasing or increasing), resembling the behavior of a macrospin governed by the Stoner-Wohlfarth model, with an easy axis aligned within the plane of the thin film.
For the out-of-plane component, several magnetic configuration can be identified, depending on the strength of the applied magnetic field. At high magnetic fields, the Zeeman energy dominates, and the magnetization is saturated in the out-of-plane direction. As the field is reduced, the magnetization initially decreases linearly. This behavior indicates a gradual reorientation of the magnetization toward the in-plane direction, consistent with coherent rotation of a macrospin under an external field applied perpendicular to its easy axis - as predicted by the Stoner-Wohlfarth model.

In the literature, **perpendicular magnetic anisotropy** (PMA) at room temperature has been re-

ported in Permalloy thin films, associated with perpendicular anisotropy constants ranging from $K_\perp = (5.0 \pm 1.4)\,\mathrm{kJ\,m^{-3}}$ [73] to $K_\perp = 30\,\mathrm{kJ\,m^{-3}}$ [74].
The magnitude of the perpendicular magnetic anisotropy can be estimated in our sample by considering the effective anisotropy field, defined as:

$$\begin{aligned} H_K &= \frac{2K_{\mathrm{eff}}}{\mu_0 M_s} = M_s - \frac{2K_\perp}{\mu_0 M_s} \\ B_K &= \mu_0 M_s - \frac{2K_\perp}{M_s} \end{aligned} \tag{2.39}$$

From the in-plane and out-of-plane $M(B)$ curves, we extract the following parameters at room temperature:

$$M_s^{300K} = (900 \pm 20) \times 10^3 \mathrm{A\,m^{-1}} \quad \text{and} \quad B_K^{300K} \approx 1.1\,\mathrm{T} \tag{2.40}$$

We report B_K as the field at which the magnetization reaches 99% of M_s, see Fig.2.10. Note that the value of M_s depends on the thickness of the magnetic layer, which introduces some uncertainty in the estimate. Using these values, the perpendicular anisotropy constant is estimated to lie within the range:

$$K_\perp^{300K} = 2.5\,\mathrm{kJ\,m^{-3}} \text{ to } 25\,\mathrm{kJ\,m^{-3}} \tag{2.41}$$

Low Temperature Magnetization Measurements

At 4K, the behavior of the in-plane magnetization as a function of an applied in-plane magnetic field shows notable differences compared to room temperature. At high magnetic fields (($B \geq B_{\mathrm{sat}}$)), the magnetization is saturated along the direction of the external field. A hysteresis feature is also observed, indicating a sharp inversion of the magnetization direction at the coercive field $B = B_c$.
Unlike the behavior at room temperature, the saturation field B_{sat} and the coercive field B_c do not coincide. In the intermediate field range, $B_{\mathrm{sat}} \leq B \leq B_{\mathrm{c}}$, the magnetization decreases approximately linearly. This behavior suggests the emergence of an out-of-plane magnetization component, which reduces the system's perpendicular anisotropy energy.
This characteristic shape of the in-plane $M(B)$ curve is similar to that observed in [73] at room temperature for thicker Permalloy films. In their study, stripe domains were observed in films with thicknesses exceeding $t \geq 355\,\mathrm{nm}$. These domains represent a magnetic configuration that is predominantly in-plane, but includes an out-of-plane component that oscillates between positive and negative values to reduce the demagnetizing field energy.
From the out-of-plane magnetization curve, we can once again estimate the perpendicular magnetic anisotropy. The saturation magnetization and the effective anisotropy field are extracted as:

$$M_s^{4K} = (940 \pm 20) \times 10^3 \mathrm{A\,m^{-1}} \quad \text{and} \quad B_K^{4K} \approx 1.15\,\mathrm{T} \tag{2.42}$$

The perpendicular magnetic anisotropy energy is found to lie within the range:

$$K_\perp^{4K} = 13\,\mathrm{kJ\,m^{-3}} \text{ to } 40\,\mathrm{kJ\,m^{-3}} \tag{2.43}$$

The SQUID-VSM measurements were performed on thin Permalloy films. As such, shape anisotropy effects arising from the actual geometry of the gate magnet are not accounted for in these measurements. In the following section, we describe magnetic force microscopy measurements performed directly on the gate magnet to investigate the presence of inhomogeneities in the magnetization. Specifically, we aim to determine whether the magnetization is uniform and confined to the plane of the magnet, aligned along its longitudinal axis.

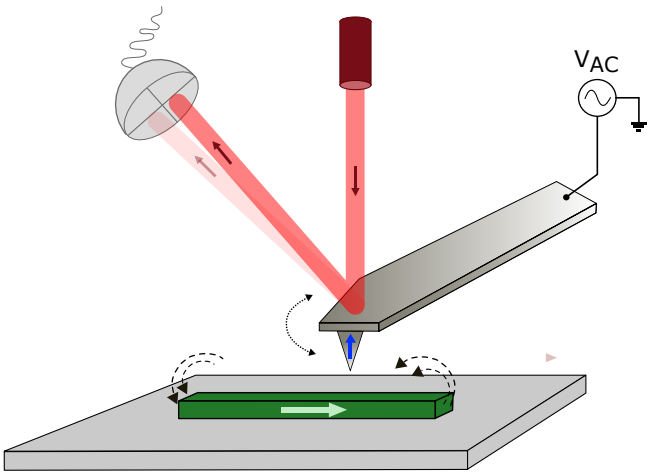

Figure 2.11: **Fundamental operating principle of a Magnetic Force Microscope (MFM)**

2.2.3 A qualitative measurement of the magnetization in the gate magnet with magnetic force microscopy

Magnetic force microscopy (MFM) enables localized measurements of the magnetization distribution along the gate magnet. This technique is particularly useful for verifying our earlier assumption that the magnetization within the magnetic gate is uniform and aligned along its longitudinal axis due to shape anisotropy.

MFM measurement principle

MFM operates by detecting the interaction between a magnetized tip - modeled as a magnetic moment - mounted on a flexible cantilever, and the stray magnetic field produced by the sample. The MFM setup is schematized Fig. 2.11. The resulting force acting on the magnetic tip is expressed as:

$$\vec{\mathbf{F}}_{\text{mag}} = \vec{\nabla}\left(\vec{\mathbf{m}}_{\text{tip}} \cdot \vec{\mathbf{H}}_d\right) \tag{2.44}$$

where $\vec{\mathbf{m}}_{\text{tip}}$ represents the magnetic moment of the tip, and $\vec{\mathbf{H}}_d$ denotes the stray field of the magnetized sample. In the absence of current density (i.e., $\vec{\nabla} \times \vec{\mathbf{H}}_d = 0$), this expression simplifies to:

$$\vec{\mathbf{F}}_{\text{mag}} = \left(\vec{\mathbf{m}}_{\text{tip}} \cdot \vec{\nabla}\right)\vec{\mathbf{H}}_d \tag{2.45}$$

The magnetic force microscope consists of several key components. As previously mentioned, the system includes a magnetic tip, typically fabricated from silicon or silicon nitride and coated with a magnetic alloy-such as cobalt (Co), iron (Fe), or nickel (Ni)-combined with another material like chromium (Cr) or platinum (Pt). The magnetic properties of the tip, including its saturation magnetization and coercive field, depend on the specific composition of this coating and the thickness. Structurally, the tip has a pyramidal shape with an apex radius of curvature on the order of tens of nanometers (approximately 50 nm).

An optical detection setup is used to detect the deflection of the cantilever - on which is mounted the magnetic tip. A laser beam is reflected off the back side of the cantilever, and the reflected beam is detected by a pair of photodiodes, see Fig.2.11. For our measurement, the MFM measurements were conducted in the so-called tapping mode. The cantilever is driven into oscillation and the photodiode signals allow extraction of the amplitude, phase, and frequency of its vibrations.

The MFM setup used in this study also includes a mechanism for applying an in-plane magnetic field. This is achieved using a rotatable permanent magnet. By adjusting the magnet's orientation, the direction and magnitude of the magnetic flux density near the sample can be finely controlled.

In tapping mode, the frequency shift of the cantilever - subjected to forced oscillations - is measured as the magnetic tip interacts with the sample.
The cantilever's motion can be modeled as a damped harmonic oscillator. In equilibrium, it oscillates at its natural frequency $\omega_0/(2\pi)$ around a mean position. The magnetic tip mounted on the cantilever oscillates similarly, and its position can be written as $Z(t) = Z_{eq} + z(t)$, where Z_{eq} is the equilibrium position and $z(t)$ the time-dependent displacement.
The dynamics of the system follow Newton's second law and are governed by [75]:

$$m\frac{\mathrm{d}^2 Z}{\mathrm{d}t^2} + \gamma\frac{\mathrm{d}Z}{\mathrm{d}t} + kZ(t) = F_{\mathrm{osc}}(t) + F_s(Z(t)) \tag{2.46}$$

Here, m is the effective mass of the cantilever, $\gamma = \frac{m\omega_0}{Q}$ the damping coefficient (with Q being the quality factor), and $k = m\omega_0^2$ the spring constant. The total force acting on the system includes the external driving force $F_{\mathrm{osc}}(t) = F_{\mathrm{osc}}^0 \cos(\omega t)$ and and the tip-sample interaction force $F_s(Z(t))$ which can be expanded to first order as:

$$F_s(Z(t)) = \sum_i F_i(Z_{eq}) \pm z(t)\sum_i \frac{\partial F_i}{\partial Z} \tag{2.47}$$

where F_i represents various attractive or repulsive interaction forces between the tip and the sample (hence the $\pm$ sign). At equilibrium, Eq. (2.46) simplifies to:

$$kZ_{eq} = \sum_i F_i(Z_{eq}) \tag{2.48}$$

Subtracting the equilibrium part yields the dynamic equation:

$$m\frac{\mathrm{d}^2 z}{\mathrm{d}t^2} + \gamma\frac{\mathrm{d}z}{\mathrm{d}t} + kz(t) = F_{\mathrm{osc}}(t) \pm z(t)\sum_i \frac{\partial F_i}{\partial z} \tag{2.49}$$

This indicates that the tip-sample interaction effectively modifies the spring constant of the cantilever, yielding an effective spring constant:

$$k_{\mathrm{eff}} = k \mp \sum_i \frac{\partial F_i}{\partial z} \tag{2.50}$$

As a result, the resonance frequency of the cantilever shifts to:

$$\omega_{\mathrm{eff}} = \sqrt{\frac{k_{\mathrm{eff}}}{m}} = \frac{1}{\sqrt{m}}\sqrt{k \mp \sum_i \frac{\partial F_i}{\partial z}} \approx \omega_0 \mp \frac{\omega_0}{2k}\sum_i \frac{\partial F_i}{\partial z} \tag{2.51}$$

where we have assumed $\sum_i \frac{\partial F_i}{\partial Z} \ll k$.
In the frequency domain, the oscillations of the tip are described by:

$$\begin{aligned} z(\omega) &= \frac{F_0}{k_{\mathrm{eff}} - m\omega^2 + i\gamma\omega} \\ z(\omega) &= A(\omega)e^{i\phi(\omega)t} \end{aligned} \tag{2.52}$$

with the amplitude and phase given by:

$$\begin{aligned} A(\omega) &= \frac{F_0}{\sqrt{\left(k_{\mathrm{eff}} - m\omega^2\right)^2 + \left(\gamma\omega\right)^2}} \\ \phi(\omega) &= \arctan\left(\frac{\gamma\omega}{m\omega^2 - k_{\mathrm{eff}}}\right) \end{aligned} \tag{2.53}$$

In the limit $\sum_i \frac{\partial F_i}{\partial Z} \ll k$, the changes in amplitude and phase due to tip-sample interaction are [76], [77] :

$$\begin{aligned} \Delta A &= \frac{\partial A}{\partial \omega}\Big|_{\omega=\omega_c}(\omega_0 - \omega_{\text{eff}}) = \frac{\partial A}{\partial \omega}\Big|_{\omega=\omega_c}\frac{\omega_0}{2k}\sum_i \frac{\partial F_i}{\partial z} \\ \Delta\phi &= \frac{\pi}{2} - \arctan\left(\frac{k}{Q\left(\mp\sum_i \mp\frac{\partial F_i}{\partial Z}\right)}\right) \approx \frac{Q}{k}\sum_i \frac{\partial F_i}{\partial z} \end{aligned} \tag{2.54}$$

Here, the drive frequency ω_c is chosen close to the cantilever's resonance frequency ω_0 ($|\omega_c - \omega_0| \ll \omega_0$) to maximize sensitivity. In particular, for optimal amplitude contrast, the drive frequency is selected near the inflection point of the amplitude curve, where the derivative $\frac{\partial A}{\partial \omega}\Big|_{\omega=\omega_c}$ is maximized.

The amplitude and phase shifts in the cantilever oscillations, as measured by the microscope, result from the combined effect of all interactions between the tip and the sample surface. Therefore, to isolate the magnetic contribution, it is essential to minimize or eliminate the influence of non-magnetic forces-most notably, Van der Waals interactions. This is achieved using a two-pass measurement technique known as **lift mode**.

In the first pass, the tip scans the surface in a closed-loop configuration to record the topography of the sample. This corresponds to a standard **Atomic Force Microscopy**(AFM) measurement, during which Van der Waals interactions dominate. In this mode, the frequency of oscillation is maintained constant by adjusting the tip-sample distance through a feedback loop involving a piezoelectric actuator connected to the cantilever.This ensures accurate mapping of the surface profile.

In the second pass, the recorded topography is used to follow the surface at a constant height h_{lift}. A feedback mechanism ensures that the tip maintains this fixed lift height, effectively compensating for surface morphology. As a result, the contribution of short-range forces like Van der Waals interactions remains constant and can be neglected. Under these conditions, variations in the frequency, amplitude, and phase of the cantilever oscillations are directly attributed to long-range magnetic forces, described by equation Eq. (2.45).

By performing a two-dimensional scan of the sample surface, an MFM image can be reconstructed. This image does not provide a direct measurement of the internal magnetization of the sample, but rather reflects the spatial variation of the magnetic stray field above the surface. Specifically, the measured signal is related to the second spatial derivative of the stray field produced by the magnetized sample:

$$\begin{aligned} F_{z,\text{mag}} &= m_{\text{tip},x}\frac{\partial H_d^x}{\partial z} + m_{\text{tip},y}\frac{\partial H_d^y}{\partial z} + m_{\text{tip},z}\frac{\partial H_d^z}{\partial z} \\ \frac{\partial F_{z,\text{mag}}}{\partial z} &= m_{\text{tip},x}\frac{\partial^2 H_d^x}{\partial z^2} + m_{\text{tip},y}\frac{\partial^2 H_d^y}{\partial z^2} + m_{\text{tip},z}\frac{\partial^2 H_d^z}{\partial z^2} \end{aligned} \tag{2.55}$$

Here $F_{z,\text{mag}}$ denotes the component of the magnetic force that is normal to the cantilever, which is the component that contributes to the observed shift in resonance frequency.

Usually, the tip's magnetic moment is initialized along z using an external magnet, so that $m_{\text{tip},x} = m_{\text{tip},y} = 0$.

Using the electrostatic analogy previously discussed, it follows that the **MFM signal is sensitive to inhomogeneities in the magnetization of the sample**. These inhomogeneities give rise to non-zero surface magnetic pole density and non-zero volume magnetic pole density (associated with divergence of magnetization within the bulk). As a result, MFM imaging is particularly effective in revealing magnetic domain patterns, stray fields emanating from the edges of the magnet, and other localized variations in the magnetic structure.

Characterization of the gate magnet

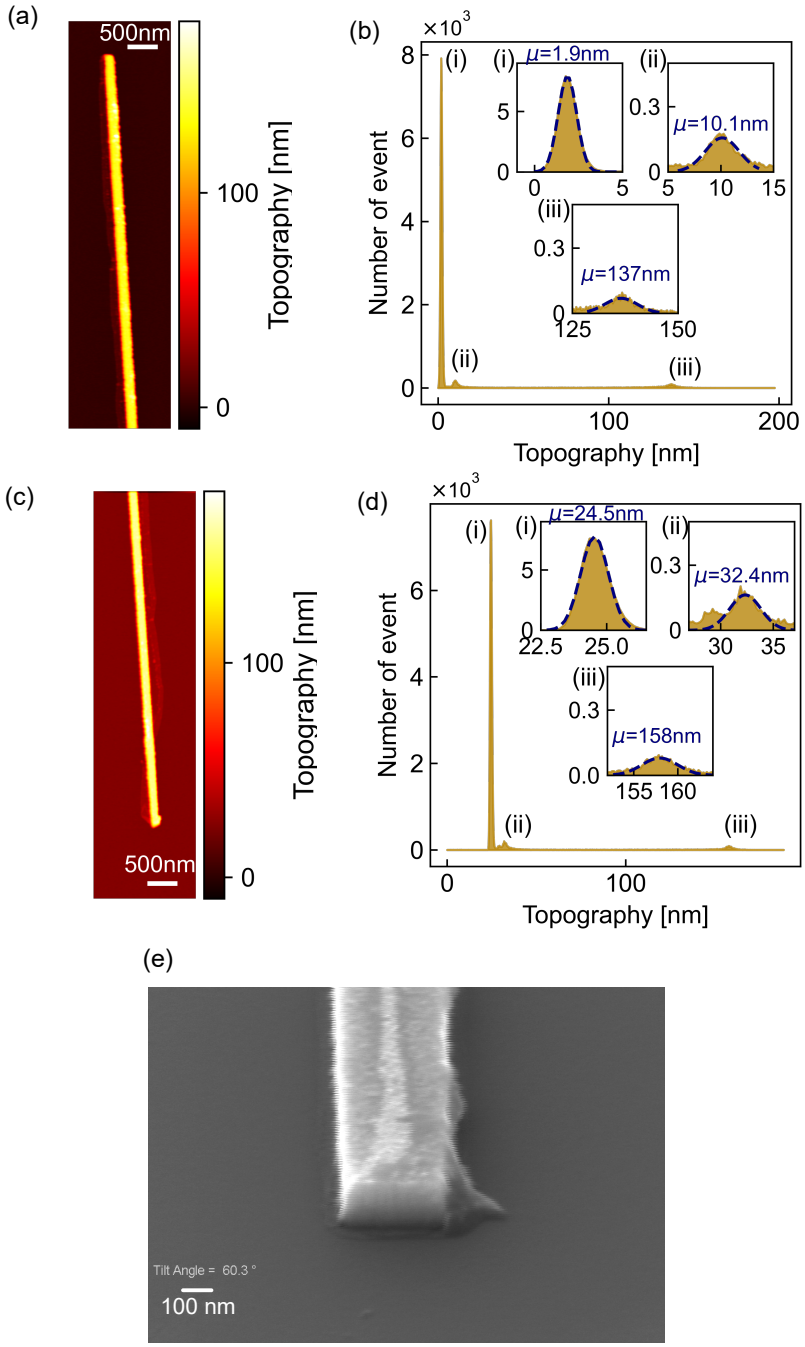

Figure 2.12: **Characterization of the central magnetic gate after nanofabrication**
(a) AFM scan on one edge of the gate.
(b) Topography analysis used to extract the gate thickness: the height histogram is fitted with Gaussian peaks. The gate height is estimated from peak (iii) after subtracting the thickness given by peak (ii), attributed to resist remaining beneath the magnetic gate, yielding a magnetic-layer thickness of ≈ 127 nm. Peak (i) corresponds to the substrate and reflects an AFM offset. Note that the development process was later optimized to remove resist residue.
(c-d) Same analysis as in (a-b) for the opposite edge of the gate.
(e) SEM image of the magnetic gate taken at a 60° tilt, where both the magnetic gate and residual resist are visible.

Nanofabrication of the gate magnet and topography characterization

The nanofabrication of the magnet consists of two main steps. First, the substrate (composed of Si/SiO_2) is coated with a resist. A bi-layer resist stack composed of PMMA/MA (a copolymer of methyl methacrylate and methacrylic acid) and PMMA (Poly(methyl methacrylate)) is used to obtain an undercut in the resist profile, which facilitates the lift-off process. An **electron beam lithography (EBL) step** is then carried out using a 20 keV acceleration voltage. This step defines the magnet pattern in the resist. A key parameter is to optimize the electron beam dose, which corresponds to the current density during EBL. Adjusting this dose enables us to achieve well-defined gates with the desired dimensions. After development, the exposed resist is dissolved in a solvent, revealing the desired pattern.

Next, a Permalloy ($Ni_{80}Fe_{20}$) film is deposited via evaporation, along with a titanium adhesion layer and a platinum capping layer. The final step is **the lift-off process**, in which the remaining resist - which was not dissolved during the development step - is removed in a solvent bath. This leaves only the magnetic gate on the surface of the substrate.

Scanning Electron Microscopy (SEM) and Atomic Force Microscopy (AFM) are used to characterize the topography of the magnet after the nanofabrication process. The results are presented Fig. 2.12.

MFM on the Magnetic Gate

The MFM measurements presented in Fig. 2.13 were performed at room temperature.

Within the gate magnet, the MFM signal exhibits no significant contrast variation. Such a variation would indicate a divergence in the magnetization within the bulk, implying a non-uniform magnetization-however, this does not appear to be the case. In contrast, a clear MFM signal is observed at the edges of the magnet. This contrast arises from the surface magnetic pole density at the boundaries of the magnet and corresponds to the stray magnetic field emanating from these edges.

Interestingly, a noticeable difference in MFM signal is observed between regions above the substrate and those above the magnet surface. This discrepancy is likely due to non-magnetic interactions, such as capacitive coupling between the tip and the sample. Capacitive forces can occur when either the tip or the sample exhibits dielectric properties, resulting in smooth contrast patterns unrelated to the magnetic domain structure. Additionally, electrostatic forces-arising from charge accumulation on the tip or sample, work function differences, or insufficient grounding-could also influence the MFM signal. These long-range interactions can mimic magnetic signatures and lead to misleading contrast in the acquired images.

Therefore, at room temperature, the macro-spin hypothesis discussed in Section 2.2.1 appears to remain valid, despite the presence of a small perpendicular magnetic anisotropy identified in the thin film measurements presented in Section 2.2.2. This observation is consistent with the dominant influence of **shape-induced anisotropy**, which can be quantified by the shape anisotropy constant introduced Eq. (2.9):

$$\begin{gathered} K_{\text{demag}} = \frac{1}{4}\mu_0 M_s^2 \\ K_s^{300K} = 243\,\text{kJ m}^{-3} \text{ to } 265\,\text{kJ m}^{-3} \quad \text{and} \quad K_s^{4K} = 276\,\text{kJ m}^{-3} \text{ to } 301\,\text{kJ m}^{-3} \end{gathered} \tag{2.56}$$

This shape anisotropy constant is approximately one order of magnitude greater than the perpendicular magnetic anisotropy constant. This supports the MFM observations: to minimize its total magnetic energy, the system favors in-plane magnetization aligned along the long axis of the gate magnet, as dictated by the geometry-induced anisotropy.

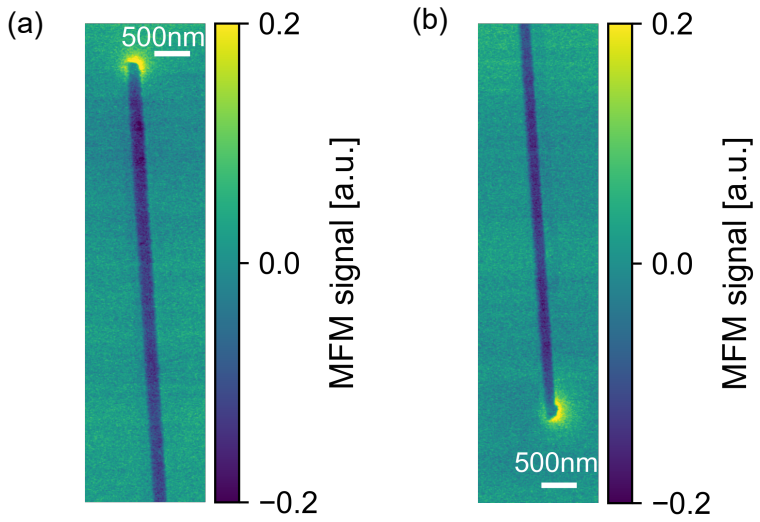

Figure 2.13: **MFM image of the magnet**
(a) and (b) are the MFM scans corresponding, respectively, to the AFM scans in Fig. 2.12(a) and (c). Before imaging, an external field was applied along the magnet's long axis and then reduced to zero. Magnetic contrast is visible at the magnet edges.

2.2.4 Micromagnetic simulations

To accurately model the equilibrium magnetization state and its evolution under an externally magnetic field, we employ micromagnetic simulations using the software MuMax3 [78]. These simulations incorporate material-specific parameters extracted from experimental characterizations described earlier.

Mumax3: a software for micro-magnetic simulations

Mumax3 is a high-performance GPU-accelerated software for micromagnetic simulations, widely used to model the magnetization dynamics in nanoscale and microscale magnetic materials. The software numerically solves the Landau-Lifshitz-Gilbert (LLG) equation, which governs the time-dependent behavior of the magnetization, using finite-element methods on a discretized three-dimensional mesh.
To set up a simulation in MuMax3, the user defines the system geometry, relevant material parameters (such as saturation magnetization, exchange stiffness, and magnetic anisotropy), the initial magnetization distribution, and any external magnetic fields. MuMax3 then integrates the LLG equation over time, tracking how the magnetization evolves and ultimately stabilizes into an energetically favorable state.

In our study, MuMax3 is used to compute steady-state (equilibrium) magnetic configurations. This is achieved by solving the LLG equation:

$$\frac{\partial \vec{\mathbf{M}}}{\partial t} = -\frac{\gamma_0}{1+\alpha^2}\left(\vec{\mathbf{M}} \times \vec{\mathbf{H}}_{\text{eff}} + \frac{\alpha}{M_s}\vec{\mathbf{M}} \times \left(\vec{\mathbf{M}} \times \vec{\mathbf{H}}_{\text{eff}}\right)\right) \tag{2.57}$$

where:

- $\vec{\mathbf{M}}$ the normalized magnetization vector and M_s the saturation magnetization,
- $\gamma_0 = \frac{g\mu_B}{\hbar}$ is the (absolute) gyromagnetic ratio, with μ_B the Bohr magneton and $g \approx 2$ the Landé g-factor,
- α is the Gilbert damping constant, responsible for energy dissipation and relaxation to equilibrium,
- $\vec{\mathbf{H}}_{\text{eff}}$ is the effective magnetic field acting on each computational cell.

The effective field $\vec{\mathbf{H}}_{\text{eff}}$ accounts for all the energetic contributions affecting the magnetization, namely:

$$\vec{\mathbf{H}}_{\text{eff}} = \vec{\mathbf{H}}_{\text{ex}} + \vec{\mathbf{H}}_d + \vec{\mathbf{H}}_{\text{ani}} + \vec{\mathbf{H}}_{\text{Zeeman}} \tag{2.58}$$

Here:

- $\vec{\mathbf{H}}_{\text{ex}} = \frac{2A}{\mu_0 M_s}\nabla^2\vec{\mathbf{m}}$ is the exchange field, where A is the exchange stiffness constant;
- $\vec{\mathbf{H}}_d$ is the demagnetizing field, arising from magnetostatic interactions;
- $\vec{\mathbf{H}}_{\text{ani}}$ is the anisotropy field, which aligns magnetization along preferred directions due to magnetocrystalline anisotropy or other sources of anistropy. It can be uniaxial, cubic, or user-defined;
- $\vec{\mathbf{H}}_{\text{Zeeman}}$ represents the external (applied) magnetic field.

In Mumax3, convergence toward the equilibrium state is typically determined by monitoring the torque acting on the magnetization. This torque is given by:

$$\vec{\boldsymbol{\tau}} = -\gamma\vec{\mathbf{M}} \times \vec{\mathbf{H}}_{\text{eff}} \quad \text{with} \quad \gamma = \mu_0 \frac{\gamma_0}{1+\alpha^2} \tag{2.59}$$

The torque quantifies how much the magnetization vector is forced to rotate. As the simulation progresses, MuMax3 monitors this torque. When its maximum value across the simulation grid drops below a specified threshold, indicating that the magnetization is no longer significantly changing, the simulation is considered to have converged.

Thanks to its GPU-based architecture, MuMax3 offers substantial computational efficiency, enabling rapid and large-scale micromagnetic simulations. This makes it particularly powerful for studying complex magnetic configurations such as domain structures, skyrmions, spin waves, and other dynamic phenomena in magnetic nanostructures.

Micromagnetic Simulations of the Gate Magnet

To accurately determine the magnetic configuration within the gate magnet under varying external magnetic fields, we perform micromagnetic simulations using the MuMax3 software. These simulations incorporate the magnetic properties extracted from prior experimental characterizations.

The gate geometry is defined with a width of 200 nm and a thickness of 110 nm. To model a long magnetic rectangle, periodic boundary conditions are applied along its longitudinal direction. Hence, the magnetization distribution at the rectangular ends (i.e., the short edges of the rectangle) is not considered here, as it does not influence the magnetic field along the carbon nanotube. The discretized 3D grid used for the simulation has a mesh size of 4 nm × 4 nm × 4 nm.

The material parameters used in the simulations are summarized in the table below:

Table 2.1: Magnetic parameters of NiFe at room temperature and 4 K.

	Room temperature	4 K
Exchange stiffness	$13 \times 10^{-12}\,\text{J m}^{-1}$	$13 \times 10^{-12}\,\text{J m}^{-1}$
Saturation magnetization	$920 \times 10^{3}\,\text{A m}^{-1}$	$980 \times 10^{3}\,\text{A m}^{-1}$
Uniaxial anisotropy constant	$30 \times 10^{3}\,\text{J m}^{-3}$	$40 \times 10^{3}\,\text{J m}^{-3}$

The saturation magnetization is taken from the SQUID-VSM measurements. The exchange stiffness is chosen in agreement with values reported in the literature [79], [80].

To account for perpendicular magnetic anisotropy, we include a uniaxial anisotropy term in the simulations. The anisotropy constant is defined by the perpendicular anisotropy constant $K_\perp$ determined earlier (see Section 2.2.2), and the easy axis is set perpendicular to the film plane. MuMax^3 is used to compute the micromagnetic equilibrium configuration of the system for various external magnetic field strengths, see Fig. 2.14. Once the magnetization distribution is obtained, the magnetic stray field is calculated using a Python code, which evaluates the dipolar field

contribution from each discretized unit cell within the MuMax3 grid. These results are presented Fig 2.15.

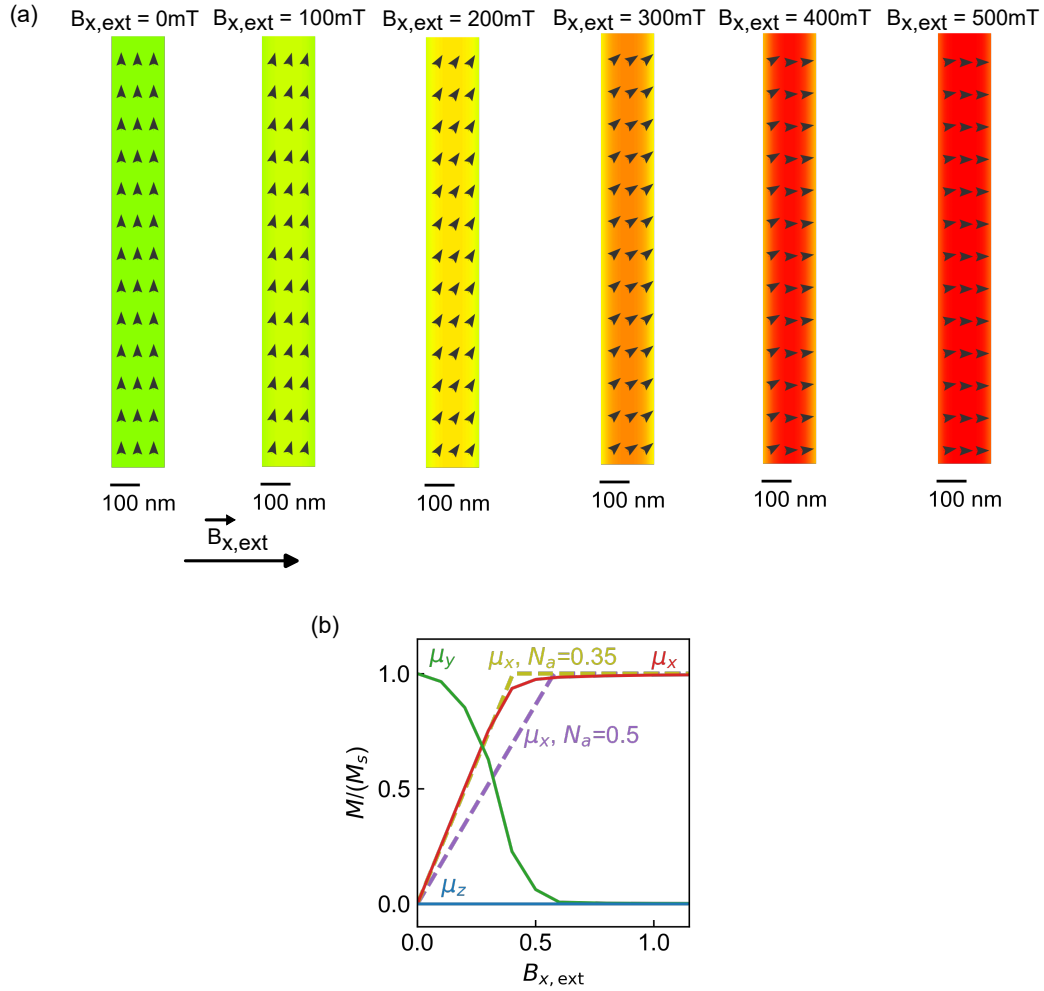

Figure 2.14: **Micromagnetic simulations of the central magnetic gate**
(a) Simulated magnetization textures in the gate for different external fields $B_{x,\text{ext}}$ applied transverse to the gate's long axis.
(b) Evolution of the normalized mean magnetization components μ_x, μ_y and μ_z versus $B_{x,\text{ext}}$ obtained from the micro-magnetic simulations. The μ_x curve is compared to macrospin predictions for a prolate spheroid ($N_a = 0.5$) and for a rectangular prism ($N_a = 0.35$).
The micromagnetic simulation results shown use room-temperature parameters (see Table 2.1).

In agreement with the MFM measurements, the simulations - presented Fig. 2.14(a) - show that at room temperature and in the absence of an external magnetic field, the magnetization lies in the plane of the thin film, aligned along the longitudinal axis of the gate magnet. Under an external magnetic field, the magnetization exhibits a coherent rotation, behaving as a single magnetic moment. This observation qualitatively supports the macrospin approximation.

However, a quantitative comparison between the macrospin model and micromagnetic simulations - whether based on the magnetization response to the external magnetic field (Fig. 2.14(b)) or the resulting stray field (Fig. 2.15(b)) - reveals deviations. This discrepancy arises because the gate magnet cannot be adequately modeled as a prolate spheroid. To improve the accuracy of the model, we instead consider the demagnetizing factors for a rectangular prism, as described in [81].

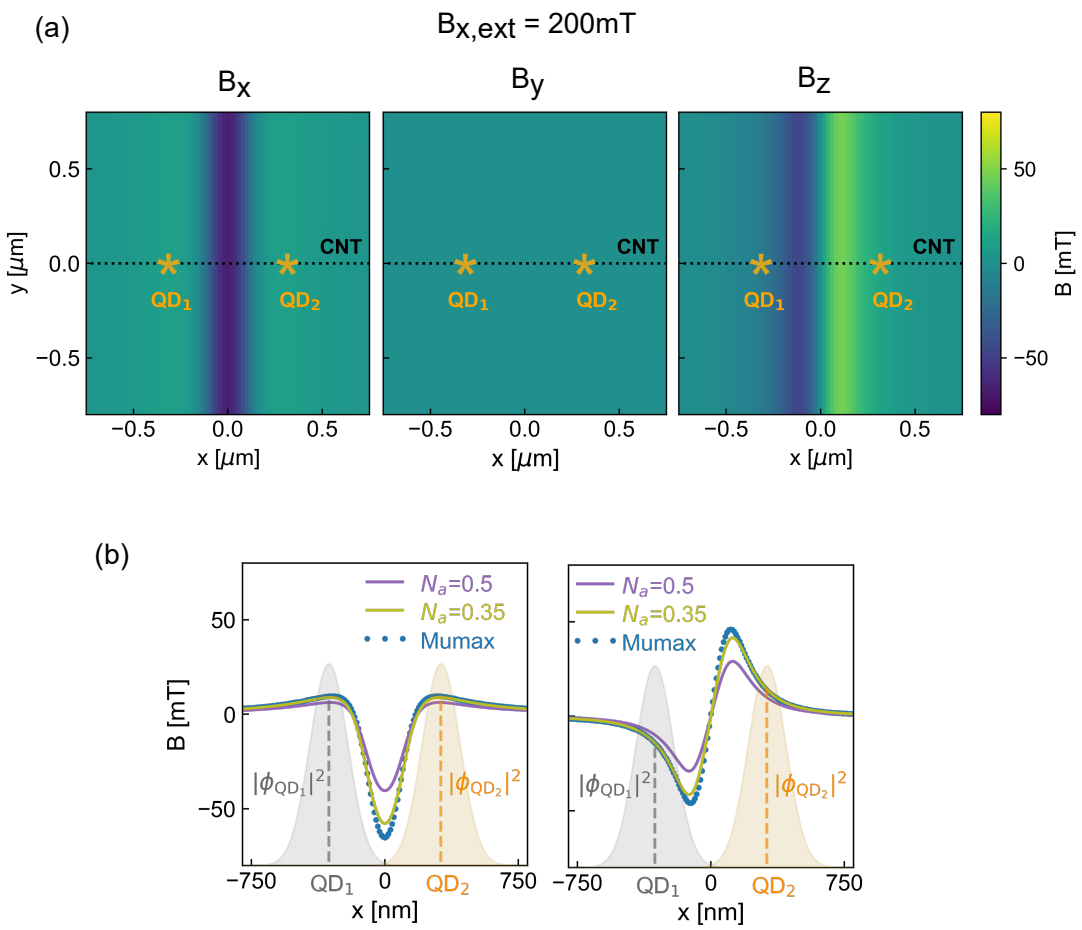

Figure 2.15: **Magnetic field from the magnet computed via micromagnetic simulations**
(a) Two-dimensional maps of the field components B_x, B_y and B_z computed from micro-magnetic simulations at $B_{x,\text{ext}} = 200\,\text{mT}$, evaluated at $h = 100\,\text{nm}$ above the magnet top surface (see Fig. 2.6). The CNT is indicated by the dashed black line; quantum-dot positions are marked by orange stars. (b) Line profiles of B_x and B_z along the CNT extracted from (a). These are compared to macrospin predictions for a prolate spheroid ($N_a = 0.5$) and a rectangular prism ($N_a = 0.35$). The finite dot size is included by weighting with a Gaussian electron probability density $\left|\phi_{\text{QD}}\right|^2$.
Results from the micromagnetic simulations were obtained using room-temperature parameters (Table 2.1).

For our gate geometry, modeled as a rectangular prism, the demagnetizing factors are:

$$\begin{aligned} &N_a = 0.35 \;\; N_b = 0.65 \;\; N_c = 0 \\ &\text{and} \;\; N_a + N_b + N_c = 1 \end{aligned} \tag{2.60}$$

The corresponding demagnetizing energy can be expressed as:

$$\begin{aligned} E_{ms} &= \frac{1}{2}\mu_0 V\Big[(M_S\cos(\theta))^2 N_c + \big(M_S\sin(\theta)\cos(\varphi)\big)^2 N_a + \big(M_S\sin(\theta)\sin(\varphi)\big)^2 N_b\Big] \\ &= \frac{1}{2}\mu_0 V M_S^2 N_c + \frac{1}{2}\mu_0 V\big[N_a\cos^2(\varphi) + N_b\sin^2(\varphi) - N_c\big]M_S^2\sin^2(\theta) \end{aligned} \tag{2.61}$$

where θ and φ are the polar and azimuthal angles of the magnetization vector $\vec{\mathbf{M}}$.
The magnetic configuration at equilibrium is found by minimizing the total magnetic energy, defined as the sum of the demagnetizing energy and the Zeeman energy. In the absence of an external magnetic field, since $N_a\cos^2(\varphi) + N_b\sin^2(\varphi) - N_c \geq 0$ (for $\varphi \in [0, 2\pi]$), the energy is minimized

when the **magnetization lies in the plane of the permalloy film**, aligned with the **longitudinal axis** of the gate magnet.
When an external magnetic field is applied, the Zeeman energy is given by Equation Eq. (2.25). Minimizing the total energy with respect to φ yields $\varphi = 0$. The total energy then simplifies to:

$$E_{tot} = \frac{1}{2}\mu_0 V M_S^2 N_c + \frac{1}{2}\mu_0 V [N_a - N_c] M_S^2 \sin^2(\theta) - \mu_0 M_s V H_{x,\text{ext}} \sin(\theta) \tag{2.62}$$

The macrospin model therefore remains valid if the demagnetizing factors are properly adjusted. The behavior of the system can be characterized in two regimes:

- For $\left|B_{x,\text{ext}}\right| \leq B_{\text{x,ext}}^{\text{sat}} = (N_a - N_c)\mu_0 M_s$, the minimum energy configuration corresponds to:

$$\sin(\theta) = \frac{2B_{\text{x,ext}}}{(N_a - N_c)\mu_0 M_s} \tag{2.63}$$

  In this regime, the component of the magnetization aligned with the external field, given by $M_x = M_S \sin(\theta)$, exhibits a linear dependence on the applied field. Consequently, the stray magnetic field produced by the gate magnet is:

$$B_i(M_s, x, y = 0, z) = \frac{1}{N_a - N_c} B_{\text{x,ext}} Q_i^{x\text{sat}}(x, y = 0, z) \tag{2.64}$$

  where $i \in \{x, z\}$, and $Q_i^{x,\text{sat}}$ is the normalized stray field component in the direction i, corresponding to full saturation of the magnetization along the x-axis (i.e., the direction of the external magnetic field). The explicit form of $Q_i^{x,\text{sat}}$ is provided in Eq. (2.28).

- For $\left|B_{x,\text{ext}}\right| \geq B_{\text{x,ext}}^{\text{sat}} = (N_a - N_c)\mu_0 M_s$, the energy minimum is reached when:

$$\cos(\theta) = 0 \tag{2.65}$$

  indicating that the magnetization is fully aligned with the external field. The stray field in this saturated state is thus given by:

$$B_i(M_s, x, y = 0, z) = B_i^{x\text{sat}}(M_s, x, y = 0, z) \tag{2.66}$$

Comparing the micromagnetic simulation results with the corrected macrospin model at room temperature shows good agreement. Using the low-temperature parameters, we find that the macrospin model continues to apply: the strong shape anisotropy ensures a uniform magnetization along the long axis of the magnet, and the magnetization rotates coherently under the influence of the external magnetic field.

2.2.5 Spatial distribution of the magnetic field along the carbon nanotube

The previous results allow us to predict the spatial distribution of the stray magnetic field along the carbon nanotube for a given external field strength. This, in turn, enables us to quantitatively assess how efficient is the electric dipole of the qubit by the symmetric and antisymmetric components of the magnetic field produced by the gate magnet.
The magnetic gate is positioned symmetrically between the two plunger gates. As a result, we assume that the two quantum dots are also symmetrically located with respect to the gate magnet. Under this symmetry, the symmetric component of the magnetic field experienced by the two dots is defined by the longitudinal field along the carbon nanotube axis. This contribution is expressed as:

$$\alpha_s = \int \mathrm{d}x \left|\phi_R(x)\right|^2 \left[B_{x,\text{magnet}}(x) + B_{x,\text{ext}}(x)\right] = \int \mathrm{d}x \left|\phi_L(x)\right|^2 \left[B_{x,\text{magnet}}(x) + B_{x,\text{ext}}(x)\right] \tag{2.67}$$

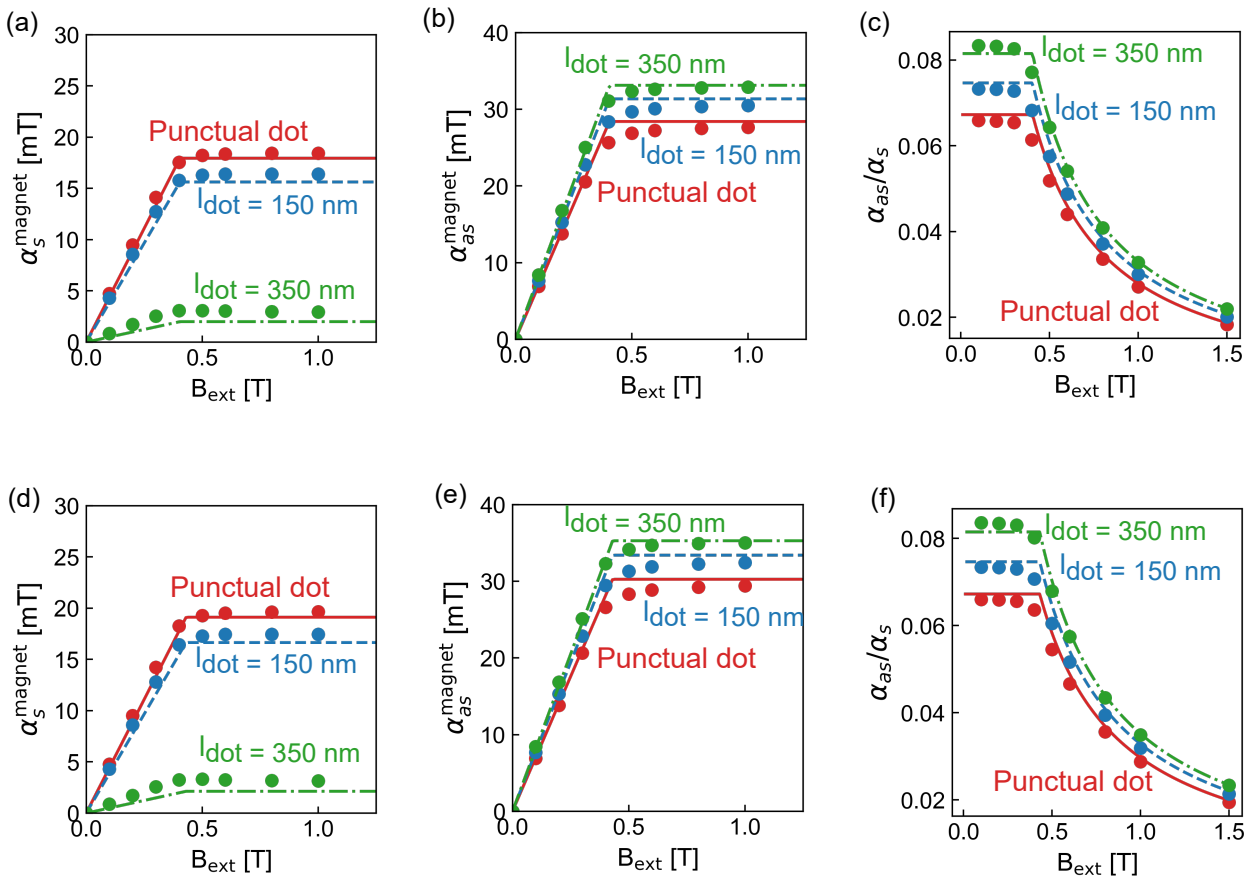

Figure 2.16: **Capability of the micro-magnet to induce spin-charge hydration**
(a) Symmetric field component α_s^{magnet} produced by the micro-magnet versus external field $B_{x,\text{ext}}$ for various dot sizes l_{dot}.
(b) Antisymmetric field component α_s^{magnet} versus $B_{x,\text{ext}}$ for the same dot sizes l_{dot}.
(c) Ratio α_s/α_{as} versus $B_{x,\text{ext}}$, where α_s is the total symmetric component defined in 2.67. Curves for multiple dot sizes l_{dot} are shown.
(d-f) Same as (a-c) using low-temperature micromagnetic parameters. Panels (a-c) use room-temperature parameters (see Table 2.1).
In all six panels, dotted curves show micromagnetic-simulation results, while solid curves show the results of the macrospin predictions for a rectangular prism.

where $|\phi_d(x)|^2$ denotes the probability density of the electron in quantum dot $d \in \{R, L\}$.
The antisymmetric component of the magnetic field between the two dots is generated solely by the gate magnet and is defined as:

$$\alpha_{as} = \left| \int \mathrm{d}x \, |\phi_R(x)|^2 \, B_{z,\text{magnet}}(x) \right| = \left| \int \mathrm{d}x \, |\phi_L(x)|^2 \, B_{z,\text{magnet}}(x) \right| \tag{2.68}$$

The probability density $|\phi_d|^2$ in each dot is modeled as a Gaussian function, and by varying its standard deviation σ, we account for the spatial extension of the quantum dot. The full width at half maximum (FWHM) of the Gaussian is given by $l_{\text{dot}} = \sigma/2.355$, σ being the standard deviation of the Gaussian. Consequently, the values of α_s and α_{as} can be evaluated for different dot sizes, allowing us to quantify the magnetic field profile experienced by each dot , see Fig. 2.16.

As previously discussed, the external magnetic field is unlikely to exceed 500 mT. Consequently, the magnetic gate remains unsaturated, and the ratio α_{as}/α_s remains approximately constant. This can be understood by noting that, below saturation, the magnetic field generated by the mag-

net exhibits a linear dependence on the external magnetic field:

$$\frac{\alpha_{as}}{\alpha_s} = \frac{\left| \int \mathrm{d}x \left|\phi_d(x)\right|^2 Q_z^{x\mathrm{sat}}(x, y=0, z) \right|}{N_a - N_c + \int \mathrm{d}x \left|\phi_d(x)\right|^2 Q_x^{x\mathrm{sat}}(x, y=0, z)} \tag{2.69}$$

The value of this ratio depends on the overlap between the normalized stray field components $Q_i^{x\mathrm{sat}}(x, y=0, z)$, for $i \in \{x, z\}$, and the electron probability density $\left|\phi_d(x)\right|^2$ in dot d. Electrostatic tuning of the values of α_s and α_{as} - and thus of the energy spectrum of the qubit - can be achieved by controlling and modifying the shape and spatial extension of the electron's probability distribution within each quantum dot.

In the best-case scenario, the performance of this gate magnet is intrinsically limited. Specifically, the ratio between the antisymmetric and symmetric components of the magnetic field, α_{as}/α_s typically remains below 0.1 (see Fig.2.16), which limits the achievable electric dipole moment of the qubit. As a result, the coupling strength g between the spin transition and the cavity photons is bounded by:

$$g = \frac{\Delta_g}{2} \langle 1|\hat{\boldsymbol{\tau}}_z|0\rangle < 0.06 \, \frac{\Delta_g}{2} \tag{2.70}$$

Here, $\{|1\rangle, |0\rangle\}$ denotes the computational basis of the qubit, and $\hat{\boldsymbol{\tau}_z}$ is the Pauli operator acting on the orbital subspace spanned by the localized states $\{|R\rangle, |L\rangle\}$ of the double quantum dot.
To estimate the matrix element $\langle 1|\hat{\boldsymbol{\tau}}_z|0\rangle$, we assume that the interdot tunnel coupling t_c is approximately equal to the Zeeman splitting $t_c \sim \epsilon_Z = g_s \mu_B \alpha_S \sim 5.5\,\mathrm{eV}$, with $g_s = 2$ representing the electron Landé g-factor. Furthermore, this estimate is made under the assumption that spin-orbit coupling Δ_{SO} is negligible compared to the inter-valley scattering $\Delta_{KK'}$. As discussed in the previous chapter, if Δ_{SO} is not negligible, the effective dipole matrix element-and thus the spin-photon coupling strength - would be further reduced.

Preliminary measurements performed by the teams of C12 Quantum Electronic aimed at realizing a spin qubit using this central magnetic gate geometry did not show promising results. Therefore, the focus of the subsequent work is **to explore optimized magnet geometries and magnetic materials**. The goal is to **enhance the magnetic dipole coupling, g, of the spin transition**, thus improving the qubit performance.

Chapter 3

Optimized micro-magnet design for generating on-chip field gradients and asymmetries

In the literature, patterned magnets have been widely used to generate antisymmetric magnetic fields in order to electrically drive spin transitions, thereby enabling the creation of an effective magnetic dipole associated with the spin degree of freedom [82], [83], [84]. Most previous efforts have focused on optimizing the geometry of these magnets-typically adopting a split-pair configuration of aligned and elongated bars-placed in close proximity to the quantum dot electrodes. This strategy, combined with maximizing the magnet thickness, has enabled the realization of strongly inhomogeneous magnetic field profiles at the nanoscale. Field gradient values approaching $1\,\mathrm{mT}\cdot\mathrm{nm}^{-1}$ have been achieved between quantum dots separated by 60-120nm. These gradients translate into an antisymmetric component of the magnetic field reaching approximately 30 mT [85] or 40 mT [86] along a direction transverse to the double-quantum-dot axis.

Alternative magnet geometries beyond the conventional split-pair bar design have also been proposed and demonstrated in other contexts [87], [88].

However, optimal designs for these magnetic elements remain to be identified, particularly when the non-uniformity of the internal magnetization is taken into account. In this chapter, we present numerical simulations aimed at designing micro-magnets to maximize the antisymmetric magnetic field component. These numerical approaches are complemented by micromagnetic simulations that incorporate the effects of magnetization non-uniformity and domain formation induced by the demagnetizing field energy. This chapter is based on work that was published in the scientific article [89].

3.1 Designing micro-magnets: bridging idealized models and practical constraints

3.1.1 Ideal magnetization distributions for field and gradient optimization

As a preliminary step, we use numerical simulations to identify ideal magnetization distribution that maximize a specific magnetic field component or its spatial gradient. While these ideal field distributions are not achievable in devices, they serve as theoretical benchmarks to inform the design of practical micro-magnets optimized for on-chip integration.

Numerical simulation framework

The quantity optimized in the simulations, denoted Q, typically corresponds to a single com-

ponent of the magnetic flux density $\vec{\mathbf{B}}(\vec{\mathbf{r}})$ or one of its spatial derivatives. Each simulation focuses on maximizing Q n the vicinity of a target point, taken to be $\vec{\mathbf{r}} = \vec{\mathbf{0}}$.

No constraints are imposed on the magnetization direction. The magnet is modeled as a thin film centered around $\vec{\mathbf{r}} = \vec{\mathbf{0}}$ with a circular exclusion zone of radius R around the evaluation point where no magnetic moment is allowed. The simulation volume is discretized into a 3D grid, and at each point, the direction of the elementary magnetic moment $\vec{\mathbf{m}}(\vec{\mathbf{r}}) = M_s \mathrm{d}r^3 \ \vec{\boldsymbol{\mu}}(\vec{\mathbf{r}})$ is chosen to maximize Q. Here, $\mathrm{d}r^3$ is the volume element, M_s the saturation magnetization, and $\vec{\mu}$ the local magnetization unit vector.

Since Q is a linear functional (e.g., a single field component or derivative rather than a nonlinear combination), the problem remains linear. This allows the optimal magnetization distribution and the resulting maximum value of Q to be reconstructed by linearly summing the contributions of all elementary dipoles.

In these simulations, we focus on optimizing either the magnetic field component $Q = B_x$ or one of the spatial derivatives: $Q = \frac{\partial B_x}{\partial x}$, $Q = \frac{\partial B_y}{\partial x}$ and $Q = \frac{\partial B_z}{\partial x}$. The resulting optimal magnetization distributions $\vec{\boldsymbol{\mu}}$ are evaluated in the $z = 0$ and presented Fig.3.1. Each distribution exhibits a distinct polar pattern around the evaluation point $\vec{\mathbf{r}} = \vec{\mathbf{0}}$ which reflects the characteristic symmetry and spatial structure of the corresponding dipolar field.

Magnetic field and gradients generated from an elementray dipole

We now analyze the contribution to the quantity Q of a single magnetic moment $\vec{\mathbf{m}}$ located at position $\vec{\mathbf{r}}_\mathbf{j}$. The distance from the dipole to the origin is denoted r_j and the unit vector pointing from the dipole to the origin is $e_j = \frac{\vec{\mathbf{r}}_j}{r_j}$. After selecting a Cartesian coordinate system (x, y, z), the elementary contribution to a magnetic field component or its gradients with respect to the x-direction are given by:

$$\mathrm{d}\vec{\mathbf{B}}_j \cdot \vec{\mathbf{u}}_x = \frac{\mu_0 \mathrm{d}m}{4\pi r_j^3}\left[3(\vec{\mathbf{e}}_j \cdot \vec{\mathbf{u}}_x)(\vec{\mathbf{e}}_j \cdot \vec{\boldsymbol{\mu}}_j) - \vec{\boldsymbol{\mu}}_j \cdot \vec{\mathbf{u}}_x\right] \tag{3.1}$$

$$\mathrm{d}\frac{\partial \vec{\mathbf{B}}_j \cdot \vec{\mathbf{u}}_x}{\partial x} = \frac{\mu_0 \mathrm{d}m}{4\pi}\frac{\partial r_j^{-3}}{\partial x}[3(\vec{\mathbf{e}}_j \cdot \vec{\mathbf{u}}_x)(\vec{\mathbf{e}}_j \cdot \vec{\boldsymbol{\mu}}_j) - \vec{\boldsymbol{\mu}}_j \cdot \vec{\mathbf{u}}_x] + \frac{\mu_0 \mathrm{d}m}{4\pi r_{ji}^3}\left[3\frac{\partial}{\partial x}(\vec{\mathbf{e}}_j \cdot \vec{\mathbf{u}}_x)(\vec{\mathbf{e}}_j \cdot \vec{\boldsymbol{\mu}}_j)\right] \tag{3.2}$$

$$\mathrm{d}\frac{\partial \vec{\mathbf{B}}_j \cdot \vec{\mathbf{u}}_y}{\partial x} = \frac{\mu_0 \mathrm{d}m}{4\pi}\frac{\partial r_j^{-3}}{\partial x}\left[3(\vec{\mathbf{e}}_j \cdot \vec{\mathbf{u}}_y)(\vec{\mathbf{e}}_j \cdot \vec{\boldsymbol{\mu}}_j) - \vec{\boldsymbol{\mu}}_j \cdot \vec{\mathbf{u}}_y\right] + \frac{\mu_0 \mathrm{d}m}{4\pi r_{ji}^3}\left[3\frac{\partial}{\partial x}(\vec{\mathbf{e}}_{ji} \cdot \vec{\mathbf{u}}_y)(\vec{\mathbf{e}}_j \cdot \vec{\boldsymbol{\mu}}_j)\right] \tag{3.3}$$

$$\mathrm{d}\frac{\partial \vec{\mathbf{B}}_j \cdot \vec{\mathbf{u}}_z}{\partial x} = \frac{\mu_0 \mathrm{d}m}{4\pi}\frac{\partial r_j^{-3}}{\partial x}\left[3(\vec{\mathbf{e}}_j \cdot \vec{\mathbf{u}}_z)(\vec{\mathbf{e}}_j \cdot \vec{\boldsymbol{\mu}}_j) - \vec{\boldsymbol{\mu}}_j \cdot \vec{\mathbf{u}}_z\right] + \frac{\mu_0 \mathrm{d}m}{4\pi r_{ji}^3}\left[3\frac{\partial}{\partial x}(\vec{\mathbf{e}}_j \cdot \vec{\mathbf{u}}_z)(\vec{\mathbf{e}}_j \cdot \vec{\boldsymbol{\mu}}_j)\right] \tag{3.4}$$

Here, $\mathrm{d}\vec{\mathbf{B}}_j$ denotes the magnetic field at the origin due to an elementary magnetic moment $\mathrm{d}m$ at $\vec{\mathbf{r}}_j$.

Assuming the magnet lies in a thin film at $z = 0$, we introduce the polar angle θ defined as the angle between $\vec{\mathbf{u}}_x$ and $\vec{\mathbf{ej}}$ in the xy-plane. The orientation of the dipole moment $\vec{\mathbf{m}}_j$ is described by two angles: the out-of-plane (polar) angle ψ and and the in-plane (azimuthal) angle ϕ. In terms

of these variables, the expressions above become:

$$\mathrm{d}\vec{\mathbf{B}}_j \cdot \vec{\mathbf{u}}_\mathbf{x} = \frac{\mu_0 \mathrm{d}m}{4\pi r_j^3}\left[3\cos(\theta)\cos(\phi-\theta)\sin(\psi) - \cos(\phi)\sin(\psi)\right] \tag{3.5}$$

$$\mathrm{d}\frac{\partial \vec{\mathbf{B}}_j \cdot \vec{\mathbf{u}}_x}{\partial x} = -\frac{3\mu_0 \mathrm{d}m}{4\pi r_j^4}\left[\cos(\phi-3\theta)\sin(\psi) + \cos^2(\theta)\cos(\phi-\theta)\sin(\psi)\right] \tag{3.6}$$

$$\mathrm{d}\frac{\partial \vec{\mathbf{B}}_j \cdot \vec{\mathbf{u}}_y}{\partial x} = -\frac{3\mu_0 \mathrm{d}m}{4\pi r_j^4}\left[-\sin(\phi-3\theta)\sin(\psi) + \cos(\theta)\sin(\theta)\cos(\phi-\theta)\sin(\psi)\right] \tag{3.7}$$

$$\mathrm{d}\frac{\partial \vec{\mathbf{B}}_j \cdot \vec{\mathbf{u}}_z}{\partial x} = \frac{3\mu_0 \mathrm{d}m}{4\pi r_j^4}\cos(\theta)\cos(\psi) \tag{3.8}$$

To maximize the transverse gradient $\frac{\partial \vec{\mathbf{B}}_z}{\partial x}$,the optimal dipole orientation is out of plane ($\psi = 0$ or $\psi = \pi$). The sign of $\cos(\theta)$ then determines whether the dipole should point upwards or downwards, see Fig.3.1(d).

Conversely, to maximize B_x, $\frac{\partial \vec{\mathbf{B}}_x}{\partial x}$ and $\frac{\partial \vec{\mathbf{B}}_y}{\partial x}$, the dipole should lie in the plane ($\psi = \frac{\pi}{2}$, see Fig.3.1(a-c)), since any out-of-plane component reduces all terms proportionally. To determine the optimal azimuthal orientation ϕ of the in-plane dipole, we solve:

$$\frac{\partial \mathrm{d}Q}{\partial \phi}\Big|_{\psi=\frac{\pi}{2}} = 0 \text{ with } \mathrm{d}Q = \mathrm{d}\vec{\mathbf{B}}_j \cdot \vec{\mathbf{u}}_x,\ \mathrm{d}\frac{\partial \vec{\mathbf{B}}_j \cdot \vec{\mathbf{u}}_x}{\partial x} \text{ or } \mathrm{d}\frac{\partial \vec{\mathbf{B}}_j \cdot \vec{\mathbf{u}}_y}{\partial x} \tag{3.9}$$

This leads to the following expressions for the optimal dipole angle ϕ :

$$\phi = \arctan\frac{3\sin(2\theta)}{3\cos(2\theta)+1} \tag{3.10}$$

$$\phi = \arctan\frac{-5\sin(3\theta)-\sin(\theta)}{-5\cos(3\theta)-3\cos(\theta)} \tag{3.11}$$

$$\phi = \arctan\frac{5\cos(3\theta)-\cos(\theta)}{-5\sin(3\theta)-\sin(\theta)} \tag{3.12}$$

The function arctan implies that the quadrant of the angle is chosen by the signs of the numerator and denominator. The signs of the numerator and denominator determine the signs of the dipole components m_y and m_x respectively.

From Equations Eq. (3.5) and Eq. (3.10), we recover the well-known result that the field along a dipole's axis is positive only within a cone of half-angle $\arccos(1/\sqrt{3}) \approx 54.7\,\mathrm{deg}$, see Fig.3.1(h). This can be seen directly in Equation Eq. (3.5) by setting $\phi = 0$, where the sign of the field depends on the angle θ. It also manifests in the change of sign in the denominator of Eq. (3.10) as for $\cos(\theta) \geq 1/\sqrt{3}$, $m_x \geq 0$.

Additionally, the angular dependence of the optimal dipole orientation reveals the structure of the optimal magnetization distribution. When maximizing B_x the optimal in-plane dipole orientation completes two full rotations as one loops once around the origin (see see Fig.3.1(h-k)), a consequence of the π-periodicity of Eq. (3.10). In contrast, when optimizing the field gradients, the dipole orientation rotates three times around the origin (see see Fig.3.1(i-j) and (l-m)). This behavior arises from the equations Eq. (3.11) and Eq. (3.12), even though these expressions are formally 2π-periodic.

Magnetic field and gradients of the ideal magnetization distribition

The preceding analysis reveals the ideal internal magnetization distributions that a nanomagnet should emulate in order to maximize the stray magnetic field or its spatial gradients. These idealized configurations provide valuable benchmarks for determining the upper performance limits of practical micro-magnets.

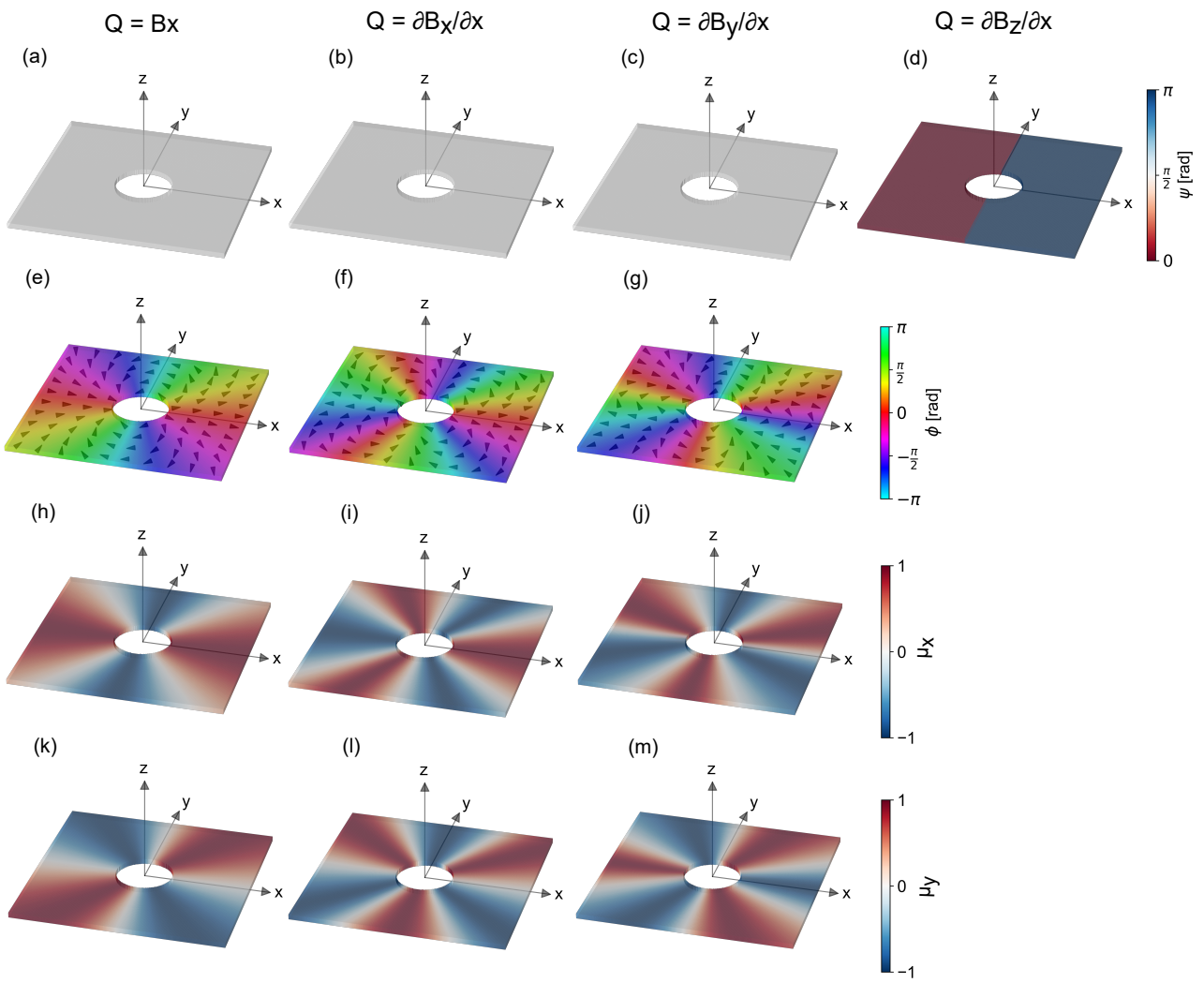

Figure 3.1: **Ideal magnetization distributions for optimizing a selected field quantity Q (either a field component or one of its spatial derivatives)**
(a,e,h,k) Optimal distributions for $Q = B_x$.
(b,f,i,l) Optimal distributions for $Q = \frac{\partial B_x}{\partial x}$
(c,g,j,m) Optimal distributions for $Q = \frac{\partial B_y}{\partial x}$
(d) Optimal distributions for $Q = \frac{\partial B_z}{\partial x}$
Each elementary magnetic moment $\vec{\mathbf{m}}_j$ is parameterized by two angles: the out-of-plane (polar) angle ψ and the in-plane (azimuthal) angle ϕ.
Panels (a-d) show the polar angle, (e-g) show the azimutal angle, (h-j) show the normalized magnetization component μ_x and (k-m) show the normalized magnetization component μ_y.

For each quantity being optimized, the value Q can be computed by summing the contributions from all elementary magnetic moments $\vec{\mathbf{m}}_j$ of the simulation space within the simulation domain. This cumulative value defines a fundamental upper bound on the field or gradient that a thin magnetic film can produce.

In addition to the shape of the micro-magnet, one of the most critical factors affecting the achievable field strength is the minimal distance between the magnet and the quantum dot. This constraint is modeled by introducing a exclusion zone - the circular region of radius R centered at the evaluation point - within which no magnetic material is permitted. This exclusion zone accounts for practical limitations such as chip layout constraints and nanofabrication tolerances, which prevent the magnet from being placed arbitrarily close to the quantum dot.

To provide quantitative insight, consider a large simulation domain - typically $x \sim 30t$ and $y \sim 30t$, where t is the thickness of the magnetic film. The optimized values of Q depend on the exclusion radius R, and can be expressed as

$$\begin{aligned} Q &= \vec{\mathbf{B}}_j\left(\vec{\mathbf{r}} = \vec{\mathbf{0}}\right) \cdot \vec{\mathbf{u}}_x \approx \frac{0.77}{R} \mu_0 M_s t \\ Q &= \left.\frac{\partial \vec{\mathbf{B}}_j(\vec{\mathbf{r}}) \cdot \vec{\mathbf{u}}_x}{\partial x}\right|_{\vec{\mathbf{r}}=\vec{\mathbf{0}}} \approx \frac{0.98}{R^2} \mu_0 M_s t \\ Q &= \left.\frac{\partial \vec{\mathbf{B}}_j(\vec{\mathbf{r}}) \cdot \vec{\mathbf{u}}_y}{\partial x}\right|_{\vec{\mathbf{r}}=\vec{\mathbf{0}}} \approx \frac{0.92}{R^2} \mu_0 M_s t \\ Q &= \left.\frac{\partial \vec{\mathbf{B}}_j(\vec{\mathbf{r}}) \cdot \vec{\mathbf{u}}_z}{\partial x}\right|_{\vec{\mathbf{r}}=\vec{\mathbf{0}}} \approx \frac{0.48}{R^2} \mu_0 M_s t \end{aligned} \tag{3.13}$$

The expressions Eq. (3.13) show that achieving large field components or gradients requires the magnetic material to extend as close as possible to the quantum dot, within fabrication constraints.
For example, considering a cobalt micro-magnet with saturation magnetization $M_s = 1400 \times 10^3\,\mathrm{A\,m^{-1}}$, thickness 200 nm and exclusion radius $R = 200\,\mathrm{nm}$, the corresponding optimized values of Q are:

$$\begin{aligned} Q &= \vec{\mathbf{B}}_j\left(\vec{\mathbf{r}} = \vec{\mathbf{0}}\right) \cdot \vec{\mathbf{u}}_x \approx 1.4\,\mathrm{T} \\ Q &= \left.\frac{\partial \vec{\mathbf{B}}_j(\vec{\mathbf{r}}) \cdot \vec{\mathbf{u}}_x}{\partial x}\right|_{\vec{\mathbf{r}}=\vec{\mathbf{0}}} \approx 8.6\,\mathrm{mT \cdot nm^{-1}} \\ Q &= \left.\frac{\partial \vec{\mathbf{B}}_j(\vec{\mathbf{r}}) \cdot \vec{\mathbf{u}}_y}{\partial x}\right|_{\vec{\mathbf{r}}=\vec{\mathbf{0}}} \approx 8.1\,\mathrm{mT \cdot nm^{-1}} \\ Q &= \left.\frac{\partial \vec{\mathbf{B}}_j(\vec{\mathbf{r}}) \cdot \vec{\mathbf{u}}_z}{\partial x}\right|_{\vec{\mathbf{r}}=\vec{\mathbf{0}}} \approx 4.2\,\mathrm{mT \cdot nm^{-1}} \end{aligned} \tag{3.14}$$

While this analysis assumes a planar (thin-film) geometry, full three-dimensional optimal magnetization distributions can be obtained by rotating the 2D solution around the x-axis in the case of optimizing the field or its longitudinal gradient.
Finally, these idealized distributions offer qualitative insight into the shapes and layouts that real micro-magnets should approximate. For more complex quantities Q, which may not be linear and thus not decomposable into dipole contributions, a similar strategy is possible but would require nonlinear optimization methods [90], [91].

3.1.2 Realization with saturated magnets

Description of the approach

To advance toward a realistic design of on-chip sources producing asymmetric magnetic fields, we now adjust the simulation parameters accordingly.

We set aside the case of generating a localized magnetic gradient, which is essential for electrically controlling a spin in a single quantum dot [92], and instead focus on producing a field difference **between two quantum dots in a double quantum dot** system. This scenario closely resembles the gradient optimization problem and can be formulated as:

$$Q = B_i^R - B_i^L \tag{3.15}$$

where B_i^L and B_i^R are the components of the magnetic field along direction i at the positions of the right and left quantum dots, respectively. In this simplified model, we treat the quantum dots as

point-like, assuming the electron's probability density is non-zero only at two discrete positions, QD_L and QD_R.

Unlike in the ideal case presented earlier, the internal distribution of magnetic moemnt within a realistic micro-magnet cannot be freely engineered. This is primarily due to two physical constraints:

- **Internal dipolar interactions**, associated with the magnet's demagnetizing energy,
- **Presence of an external magnetic field**, contributing to the Zeeman energy.

The external magnetic field, which is symmetric with respect to the DQD system, is required to define the Zeeman splitting of the spin qubit, offering a means of tuning the qubit frequency through external control. In addition, it can be used to adjust the overall magnetization of the micro-magnet, thereby tuning the strength of the antisymmetric field component it generates.

Because both the internal dipolar energy and the external magnetic field favor magnetization patterns that may diverge from the previously derived ideal configurations, we now shift our focus to the **optimization of the micro-magnet's shape, under the assumption of a uniform magnetization and finite thickness**.

We consider two main cases:

- **In-plane saturated magnetization**, favored by the shape anisotropy inherent to thin-film magnets. This configuration is compatible with in-plane external magnetic fields, making it suitable for integration with standard superconducting microwave resonators.
- **Out-of-plane magnetization**, enabled by materials exhibiting strong perpendicular magnetic anisotropy.

In both cases, uniform magnetization can be stabilized by an appropriately oriented external magnetic field.

In this framework, the optimization task reduces to a binary decision at each point in space: whether or not to include magnetic material at that location. This decision is based on whether the contribution of the corresponding uniformly magnetized volume element increases the objective function Q given its fixed magnetic moment vector $\vec{\mathbf{m}}_j$. The resulting material distribution defines the optimal shape for a uniformly saturated micro-magnet.

Optimized micro-magnet shapes

To optimize the micro-magnet design, we consider a representative double quantum dot (DQD) system composed of two dots separated by 100 nm and positioned 100 nm beneath a magnetic layer of thickness 200 nm. We compute the shapes that maximize the difference of a given magnetic field component - B_x, B_y or B_z -between the two dots, for three cases of uniform saturation magnetization aligned along the x-, y- and z-axes, see Fig. 3.2.

Some of the resulting shapes in Fig. 3.2 can be qualitatively explained by the ideal magnetization distributions discussed earlier. Given the ideal distribution of the magnetic moments $\vec{\mathbf{m}}_{\text{opt}}$ (see Fig.3.1), an approximate optimal shape for a uniformly magnetized magnet can be obtained by selecting the regions of space where $\vec{\mathbf{u}}_x \cdot \vec{\mathbf{m}}_{\text{opt}} > 0$, $\vec{\mathbf{u}}_y \cdot \vec{\mathbf{m}}_{\text{opt}} > 0$ or $\vec{\mathbf{u}}_z \cdot \vec{\mathbf{m}}_{\text{opt}} > 0$, depending on the target field direction.

The corresponding field components obtained for these optimized shapes are listed in Table 3.1.
To characterize the effect of these fields on the DQD system, we define the symmetric and antisymmetric components of each magnetic field component as:

$$B_i^{s,as} = \frac{B_i^R \pm B_i^L}{2} \tag{3.16}$$

To assess the influence of the magnetic field on the energy spectrum-and in particular on the strength of the spin transition's electric dipole-we extract the longitudinal (parallel) and transverse

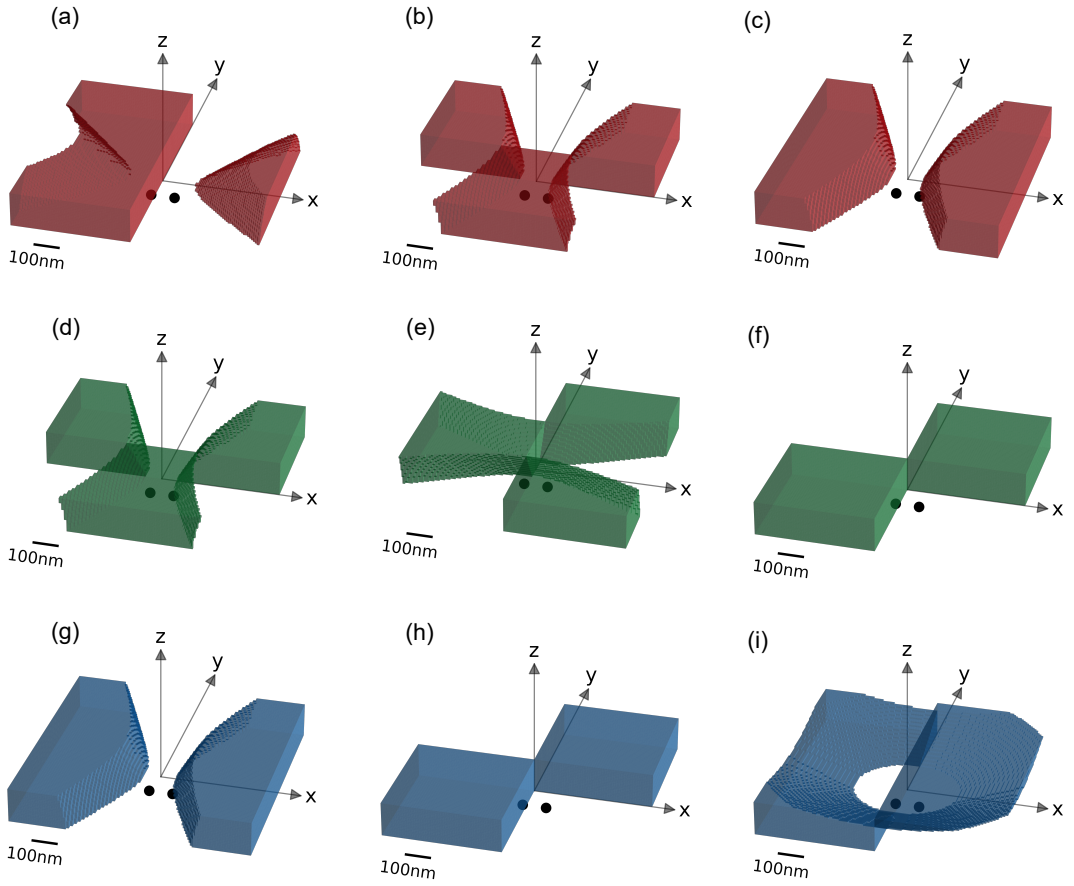

Figure 3.2: **Three-dimensional view of the optimized micromagnet shapes that generate a field difference in a double-quantum-dot system**
(a,d,g) Shapes that maximize the inter-dot field difference B_x
(b,e,h) Shapes that maximize the inter-dot field difference B_y
(c,f,i) Shapes that maximize the inter-dot field difference B_z
(a-c) Uniform magnetization along x
(d-f) Uniform magnetization along y
(g-i) Uniform magnetization along z.
The two black dots in each panel mark the positions of the two quantum dots.

components of the field relative to the DQD axis:

$$\begin{aligned} B_{\parallel}^{s} = B_{x}^{s} = \frac{B_{x}^{R} + B_{x}^{L}}{2} \quad \text{and} \quad B_{\parallel}^{as} = B_{x}^{as} = \frac{B_{i}^{R} - B_{i}^{L}}{2} \\ B_{\perp}^{s} = \sqrt{\left(B_{y}^{s}\right)^{2} + \left(B_{z}^{s}\right)^{2}} \quad \text{and} \quad B_{\perp}^{as} = \sqrt{\left(B_{y}^{as}\right)^{2} + \left(B_{z}^{as}\right)^{2}} \end{aligned} \tag{3.17}$$

The corresponding results are shown in Table 3.2.

Table 3.1: Field components in the DQD system with dot spacing 100nm for the configurations of Fig. 3.2. The magnetic-field amplitudes are expressed in units of $\mu_0 M_s$.

Fig. 3.2 panel	m dir.	Q dir.	B_x^L	B_y^L	B_z^L	B_x^R	B_y^R	B_z^R
					($\mu_0 M_s$)			
(a)	x	x	−0.097	0.000	−0.075	0.022	0.000	−0.081
(b)	x	y	−0.037	−0.035	0.003	−0.037	0.035	−0.003
(c)	x	z	−0.062	0.000	−0.058	−0.062	0.000	0.058
(d)	y	x	−0.035	−0.037	−0.038	0.035	−0.037	−0.038
(e)	y	y	0.000	−0.073	0.000	0.000	−0.001	0.000
(f)	y	z	0.092	−0.037	−0.047	0.092	−0.037	0.047
(g)	z	x	−0.058	0.000	0.016	0.058	0.000	0.016
(h)	z	y	0.003	−0.047	0.074	−0.003	0.047	0.074
(i)	z	z	0.088	0.000	0.016	0.082	0.000	0.132

Table 3.2: Symmetric and anti-symmetric components for the DQD system with dot spacing 100nm for the configurations of Fig. 3.2. The magnetic-field amplitudes are expressed in units of $\mu_0 M_s$.

Fig. 3.2 panel	m dir.	Q dir.	$B_\parallel^s$	$B_\perp^s$	$B_\parallel^{as}$	$B_\perp^{as}$
				($\mu_0 M_s$)		
(a)	x	$\parallel$	−0.037	0.078	0.060	0.003
(b)	x	$\perp_y$	−0.037	0.000	0.000	0.035
(c)	x	$\perp_z$	0.062	0.000	0.000	0.058
(d)	y	$\parallel$	0.000	0.053	0.035	0.000
(e)	y	$\perp_y$	0.000	0.037	0.000	0.036
(f)	y	$\perp_z$	0.092	0.037	0.000	0.047
(g)	z	$\parallel$	0.000	0.016	0.058	0.000
(h)	z	$\perp_y$	0.000	0.074	−0.003	0.047
(i)	z	$\perp_z$	0.085	0.074	−0.003	0.058

It appears that in-plane transverse antisymmetric fields - such as in configurations 3.2 (b), (e), and (h) - are more difficult to realize, as evidenced by their lower values of $B_{\perp}^{as} = B_{y}^{as}$.
Among the designs shown in Fig. 3.2, configurations 3.2(a) and 3.2(i) include features that are difficult to fabricate using standard planar deposition and lithography techniques, as they require elevated structures relative to the reference plane $z = 0$.
In contrast, the remaining configurations are compatible with fabrication from a single, uniformly thick magnetic layer - an important advantage for device integration.

This set of simpler geometries is sufficient to produce asymmetric magnetic field components along any of the three spatial directions x, y or z relative to the DQD axis. Among these, configurations 3.2(c) and 3.2(d) are expected to be easier to implement in practice. This is due to the fact that shape anisotropy can be more easily induced in different regions of the magnetic structure, thereby supporting the intended uniform magnetization direction.

For on-chip micro-magnets producing antisymmetric fields in a DQD system, a practical approach is to apply an external magnetic field along the DQD axis (typically in-plane), and use the micro-magnet to generate a transverse antisymmetric component. Based on these considerations, we focus in the following on the optimal shapes corresponding to uniform magnetization along $+x$, specifically cases 3.2(b) and 3.2(c). Assuming a cobalt micro-magnet with uniform magnetization, we estimate the symmetric and antisymmetric field strengths achievable for two dots spaced by a distance d_{DQD}, as summarized in the Table 3.3.

Table 3.3: Symmetric and anti-symmetric components for the DQD system with dot spacing 100nm shown for two of the configurations of Fig. 3.2. Magnetic-field amplitudes are evaluated assuming a cobalt micromagnet with $M_s = 1400 \times 10^3\,\mathrm{A\,m^{-1}}$.

Fig. 3.2 panel	m dir.	Q dir.	$B_{\parallel}^{s}$	$B_{\perp}^{as}$
			$d_{DQD} = 100$ nm	
(b)	x	$\perp_y$	−66 mT	62 mT
(c)	x	$\perp_z$	109 mT	102 mT

3.2 On-chip-micro-magnet compatible with a spin-qubit architecture

We now examine in greater detail the design of a micro-magnet suitable for integration in a spin qubit architecture hosted in a carbon nanotube.

3.2.1 Optimal geometry of a on-chip micromagnet

A more refined optimization strategy

To ensure practical device compatibility, a constraint is introduced such that the magnetic material is homogeneous along the z-direction. The optimization then reduces to a binary decision at each (x, y) position: whether to include a vertical column of magnetic material spanning the full thickness t of the layer.

We consider a DQD system with linear confinement along the x-axis, representative of suspended carbon nanotube devices. The two quantum dots, located at positions QD_L and QD_R,

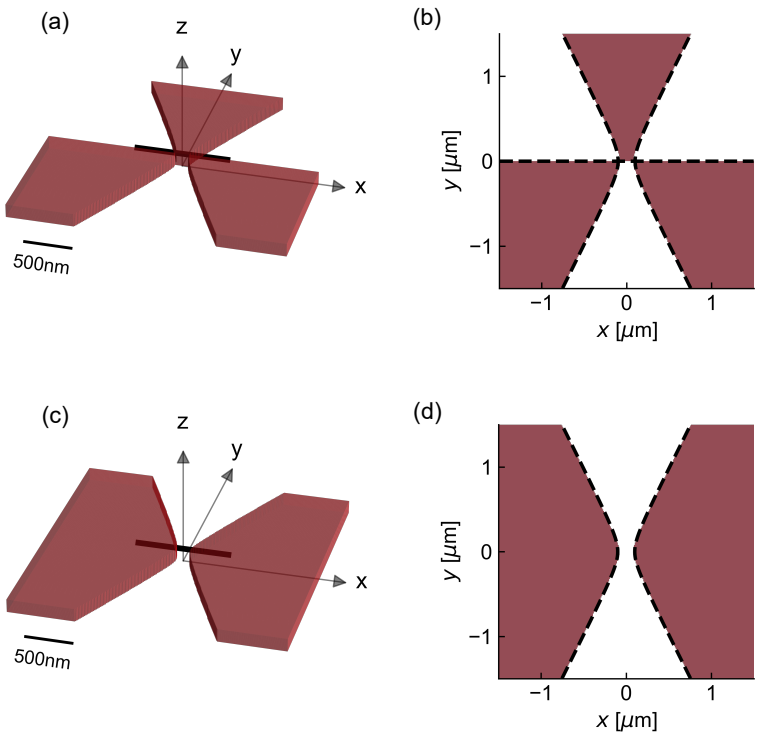

Figure 3.3: **Optimized on-chip micromagnet shapes with uniform magnetization for maximizing B_y and B_z differences between two quantum dots**
Uniform magnetization is set along x. The quantum dots are arranged along a nanowire at positions $QD_{L/R} = \left(\mp d_{\mathrm{DQD}}/2, 0, z_{\mathrm{DQD}}\right)$ with $d_{\mathrm{DQD}} = 100\,\mathrm{nm}$ and $z_{\mathrm{DQD}} = 200\,\mathrm{nm}$. The magnetic layer thickness is fixed at $t = 200\,\mathrm{nm}$.
(a,c) Three-dimensional views of the micromagnet shapes that maximize the inter-dot field differences B_y and B_z respectively. The black line marks the nanowire position.
(b,d) Two-dimensional views of the micromagnet. Dashed lines denote the magnet boundaries defined by Eq. (3.21).

lie in a nanowire suspended at height $z_{\mathrm{DQD}} = \frac{t}{2} + 100\,\mathrm{nm}$, above a magnetic layer extending from $z = -\frac{t}{2}$ to $z = \frac{t}{2}$. The quantity to optimize is:

$$Q = B_i^L - B_i^R \tag{3.18}$$

where B_i^L and B_i^R are the components of the magnetic field in direction i at the positions of the left and right quantum dots, respectively.

The optimized micro-magnet shapes for maximizing the difference in B_y and B_z are shown in Fig. 3.3.

As before, the resulting shapes can be understood in light of the ideal dipolar field distributions, and by analyzing the contribution of individual magnetic dipoles.

Consider an elementary dipole located at position (x, y, z) within the magnetic layer, where $-\frac{t}{2} \leq z \leq \frac{t}{2}$. The left and right quantum dots are positioned at

$$QD_{L/R} = \left(\mp d_{\mathrm{DQD}}/2, 0, z_{\mathrm{DQD}}\right)$$

The magnetic field produced by the elementary dipole at each dot is given by:

$$\begin{aligned} \mathrm{d}\vec{\mathbf{B}}_j^{L/R}\cdot\vec{\mathbf{u}}_y &= \frac{\mu_0 \mathrm{d}\mu}{4\pi r_j^3}\left[3(\vec{\mathbf{e}}_j^{L}\cdot\vec{\mathbf{u}}_y)(\vec{\mathbf{e}}_j^{R}\cdot\vec{\mathbf{m}}_j)-\vec{\mathbf{m}}_j\cdot\vec{\mathbf{u}}_y\right] = \frac{3\mu_0\mathrm{d}\mu}{4\pi}\,\frac{y(x\pm d_{\mathrm{DQD}}/2)}{\left(r_j^{L/R}\right)^5} \\ \mathrm{d}\vec{\mathbf{B}}_j^{L/R}\cdot\vec{\mathbf{u}}_z \frac{\mu_0 \mathrm{d}\mu}{4\pi r_j^3}\left[3(\vec{\mathbf{e}}_j^{L/R}\cdot\vec{\mathbf{u}}_z)(\vec{\mathbf{e}}_j^{L/R}\cdot\vec{\mathbf{m}}_j)-\vec{\mathbf{m}}_j\cdot\vec{\mathbf{u}}_z\right] &= \frac{3\mu_0\mathrm{d}\mu}{4\pi}\,\frac{(z-z_{\mathrm{DQD}})(x\pm d_{\mathrm{DQD}}/2)}{\left(r_j^{L/R}\right)^5} \end{aligned} \tag{3.19}$$

where $r_j^{L/R}=\sqrt{(x\pm d_{\mathrm{DQD}}/2)^2+y^2+\left(z-z_{\mathrm{DQD}}\right)^2}=\sqrt{(x\pm d_{\mathrm{DQD}}/2)^2+y^2+(z')^2}$ and $e_j^{L/R}$ is the unit vector pointing from the dipole to dot L or R.
The dipole contributions to the field difference Q can then be approximated by:

$$\begin{aligned} \mathrm{d}Q_y &= \frac{3\mu_0\mathrm{d}\mu}{4\pi}\left[\frac{y(x+d_{\mathrm{DQD}}/2)}{\left(r_j^L\right)^5}-\frac{y(x-d_{\mathrm{DQD}}/2)}{\left(r_j^R\right)^5}\right] \underset{d_{\mathrm{DQD}}\ll R}{\approx} \frac{3\mu_0\mathrm{d}\mu}{4\pi}\, y\, d_{\mathrm{DQD}}\,\frac{y^2+(z')^2-4x^2}{\left(x^2+y^2+(z')^2\right)^{7/2}} \\ \mathrm{d}Q_z &= \frac{3\mu_0\mathrm{d}\mu}{4\pi}\left[\frac{z'(x+d_{\mathrm{DQD}}/2)}{\left(r_j^L\right)^5}-\frac{z'(x-d_{\mathrm{DQD}}/2)}{\left(r_j^R\right)^5}\right] \underset{d_{\mathrm{DQD}}\ll R}{\approx} \frac{3\mu_0\mathrm{d}\mu}{4\pi}\, z'\, d_{\mathrm{DQD}}\,\frac{y^2+(z')^2-4x^2}{\left(x^2+y^2+(z')^2\right)^{7/2}} \end{aligned} \tag{3.20}$$

here $z'=z-z_{\mathrm{DQD}}$ and $R=\sqrt{x^2+y^2+(z')^2}$.
From these expressions, one can extract the geometric conditions under which the local contribution is positive:

$$\begin{aligned} &\mathrm{d}Q_y>0 \text{ for } |x|\le\frac{1}{2}\sqrt{y^2+(z')^2} \text{ if } y\ge 0 \text{ and } |x|\ge\frac{1}{2}\sqrt{y^2+(z')^2} \text{ if } y\le 0 \\ &\mathrm{d}Q_z>0 \text{ for } |x|\ge\frac{1}{2}\sqrt{y^2+(z')^2} \end{aligned} \tag{3.21}$$

These conditions dictate the spatial regions where magnetic material should be placed to maximize the target field difference, and they correspond closely with the optimized shapes shown in Fig. 3.3(b,d).

A natural question arises: to what extent do simulation parameters such as the magnetic layer thickness, the spatial extent of the magnetic material, the dot spacing, or the dot size influence the achievable magnetic field difference?
In the following, we investigate how these design parameters influence the strength of the magnetic field components generated by the micro-magnet.

Influence of dot spacing and magnet thickness

We first examine the effect of dot spacing while keeping the magnetic layer thickness fixed at 200 nm. The optimized value of the field difference, Q, is computed as a function of the inter-dot spacing, see Fig.3.4(a-c). At small spacings, increasing the distance between the dots leads to a larger antisymmetric field component (Fig. 3.4(b,d)). This occurs because, for a fixed magnet thickness, a comparable magnetic field gradient can extend over a longer distance, increasing the field difference between the two dots. This behavior is consistent with the analytical expression in Eq. (3.20), where dQ scales linearly with the dot spacing d_{DQD} in the small-spacing regime.

More generally, increasing the inter-dot distance enhances the antisymmetric component of the magnetic field while simultaneously reducing the symmetric component. This is advantageous, as it allows the symmetric field to be supplied by an external magnet, while the micro-magnet focuses on generating the antisymmetric component - potentially enabling a higher ratio of antisymmetric to symmetric field at the quantum dot locations. In silicon-based devices,

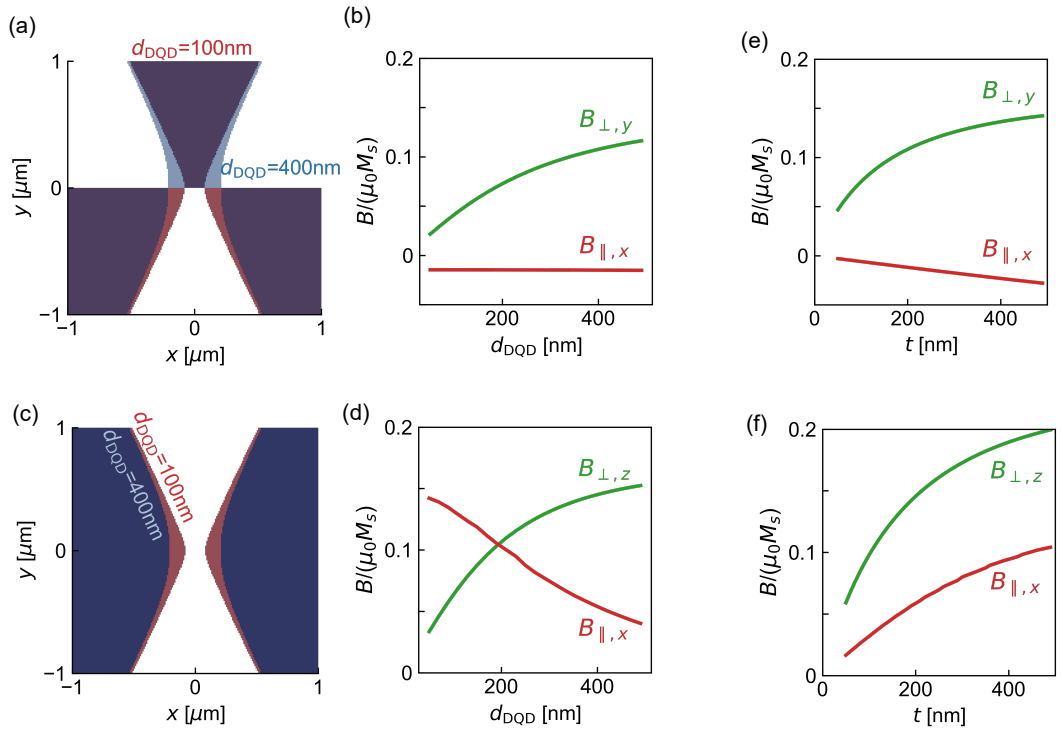

Figure 3.4: **Influence of interdot spacing and magnetic-layer thickness on the magnetic field generated by the magnet**
(a,c) TTwo-dimensional views of the optimized micromagnet geometries that maximize the interdot field differences B_y and B_z respectively respectively, for two values of the interdot spacing d_{DQD}.
(b,d) Amplitudes of the symmetric and antisymmetric field components produced by the micromagnet versus d_{DQD}, with magnetic-layer thickness fixed at $t = 200\,\mathrm{nm}$.
(e,f) Amplitude of the symmetric and anti-symmetric magnetic field component generated versus the magnetic-layer thickness t, for $d_{\mathrm{DQD}} = 400\,\mathrm{nm}$.

the typical dot spacing is around 100 nm, whereas in carbon nanotube-based DQD architectures, spacings of approximately 400 nm can be achieved [93].

Next, we explore the dependence of the optimized field difference Q on the thickness of the magnetic layer, keeping the inter-dot spacing fixed at 400 nm (see Fig. 3.4(e,f)). Increasing the magnetic layer thickness enhances the field difference up to a certain limit. Beyond a thickness of about 500 nm, the improvement begins to saturate. This saturation is again explained by Eq. (3.20): for large vertical distances ($|z| >> 0$), the contribution of an elementary dipole to the field difference vanishes ($\mathrm{d}Q \to 0$). In other words, dipoles located far from the plane of the dots have a negligible effect on the magnetic field components.

In practice, a magnetic layer thickness of around 200 nm is often preferred, as it simplifies nanofabrication and facilitates integration of the DQD system on-chip. In the following, the magnetic layer thickness is therefore fixed at 200 nm.

Finite extension of the dots

We now examine in more detail the impact of the finite spatial extension of the individual dots in the DQD system. The electron probability density in each dot is modeled as a Gaussian, centered at the positions $QD_{L/R}$, with a standard deviation σ. The spatial extent of a dot is thus characterized by its full width at half maximum $l_{dot} = 2.355\sigma$. In this analysis, we consider double

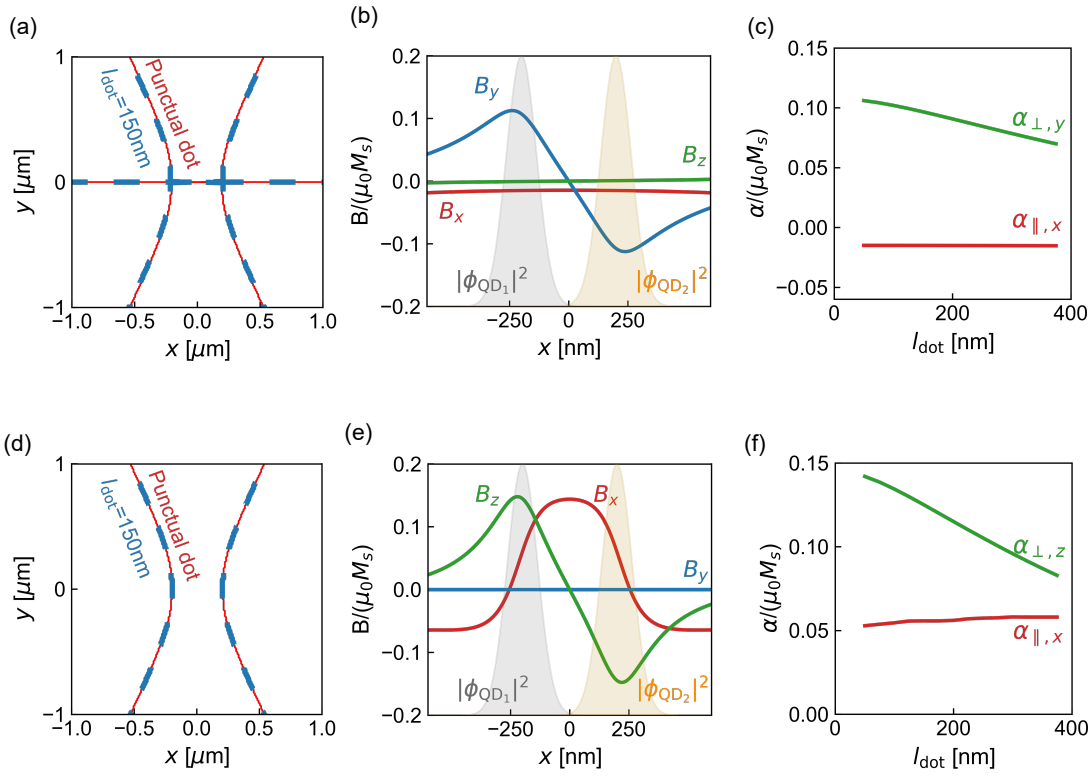

Figure 3.5: **Influence of the finite dot extension on the magnetic field generated by the magnet**
(a,d) Boundaries of the optimized magnet geometry for either point-like dots (red) or finite-size dots with finite extension l_{dot} (blue) with identical dot centers.
(b,e) Magnetic-field profiles B_x, B_y and B_z generated by the magnet along the nanowire, shown together with the electron probability densities in the left/right dots $\left|\phi_{L/R}\right|^2$.
(c,f) Amplitudes of the symmetric ($\alpha_{\parallel,x}$) and anti-symmetric ($\alpha_{\perp,y/z}$) components of the magnetic field generated by the magnet averaged over the dot extension, as functions of l_{dot}. These quantities are defined as $\alpha_{\parallel,x} = \frac{1}{2}\left(\int B_x(x)\left|\phi_L(x)\right|^2 \mathrm{d}x + \int B_x(x)\left|\phi_R(x)\right|^2 \mathrm{d}x\right)$ and the parameter $\alpha_{\perp,y/z} = \frac{1}{2}\left(\int B_{y/z}(x)\left|\phi_L(x)\right|^2 \mathrm{d}x - \int B_{y/z}(x)\left|\phi_R(x)\right|^2 \mathrm{d}x\right)$.

quantum dots located above the magnetic structure. The quantity to optimize becomes:

$$Q = \int B_{y/z}(x)\left|\phi_L(x)\right|^2 \mathrm{d}x - \int B_{y/z}(x)\left|\phi_R(x)\right|^2 \mathrm{d}x \tag{3.22}$$

where $\left|\phi_{L/R}\right|^2$ denotes the electron probability density in the left or right dot.

The optimal micro-magnet shapes for maximizing the difference in B_y and B_z are determined for various values of the dot extension. As illustrated in Fig. 3.5, the differences in the resulting shapes - with and without accounting for finite dot size - are negligible. This indicates that, under typical conditions, the finite spatial extent of the dots can be safely neglected when designing micro-magnets.

The linear profiles of the magnetic field components are determined along the nanowire axis and displayed in Fig.3.5(b,e). The relevant segments of these profiles are those that overlap with the electron density in each dot. Based on this overlap, the optimized quantity Q can be evaluated as a function of the dot size, see Fig.3.5(c,f).

We observe that accounting for the finite size of the quantum dots results in a reduction of the effective antisymmetric magnetic field in the DQD system. This is due to spatial averaging over the extended wavefunctions, which smooths out field variations and lowers the net differential field experienced between the two dots.

Optimizing the micromagnet design for practical integration

An important consideration beyond the optimal shape of a micro-magnet is its physical footprint on the chip. From a practical standpoint, it is valuable to identify which regions of the magnet are critical for generating the target field difference or gradient, and which regions can be removed or simplified without significantly affecting performance.
To this end, Fig. 3.6(a-b) shows the spatial distribution of the local contributions to the optimized parameter Q. The figure confirms that the strongest contributions are highly localized near the positions of the quantum dots. This underscores the critical importance of achieving precise geometric definition through nano-fabrication, especially at the internal edges of the magnet where these high-contribution regions are located.

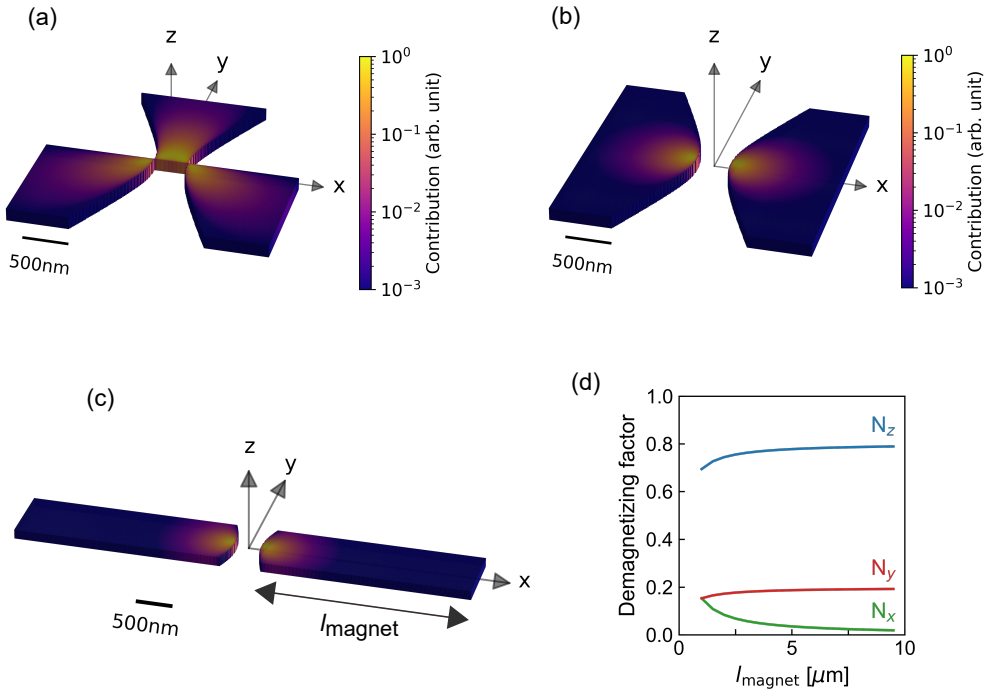

Figure 3.6: **Identifying the magnet regions that most strongly enhance the interdot field differences B_y and B_z**
(a-b) Relative contributions (each normalized to 1 at the maximum) of each part of magnet to the interdot field differences B_y and B_z respectively. respectively. These maps highlight the micromagnet areas that most strongly contribute to the field-difference amplitude across the quantum dots.
(c) Magnet geometry from (b) engineered with shape anisotropy to promote uniform internal magnetization.
(d) Demagnetizing factors N_x, N_y and N_z versus magnet length l_{magnet} computed following [81]. To favor in-plane magnetization along x, N_x should be minimized relative to N_y and N_z. From the plot, this requires $l_{\text{magnet}} > 5\mu$m.

The optimizations presented above assume a uniformly saturated magnetization throughout the micro-magnet volume. In practice, although an external magnetic field is applied to control the magnetization, internal dipolar interactions - associated with the demagnetizing energy - can favor the formation of non-uniform magnetization domains inside the structures. To favor uniform magnetization along the x-axis, it is advantageous to induce a favorable **shape anisotropy**. This need to be achieved without altering the magnet regions that most effectively contribute to Q, as identified in the optimization.

Among the various optimized shapes of saturated micro-magnets, the geometry designed to maximize the field difference along the B_z component allows for the introduction of shape anisotropy without significantly altering the regions of the magnet that contribute most to the field difference, see Fig. 3.6(c) . In contrast, the other optimized geometry would require modifying or removing critical areas of the magnet in order to impose anisotropy, thereby compromising its performance.

To analyze the effect of the induced shape anisotropy, we consider a macrospin model for the magnet and evaluate its **magnetostatic (demagnetizing) energy**, which quantifies the energetic cost associated with different magnetization orientations due to the shape of the magnet. This energy is given by:

$$E_{ms} = \frac{1}{2}\mu_0 V\left[(M_S\cos(\theta))^2 N_x + \left(M_S\sin(\theta)\cos(\varphi)\right)^2 N_y + \left(M_S\sin(\theta)\sin(\varphi)\right)^2 N_z\right] \tag{3.23}$$

where θ and φ are the polar (out of the plane yz) and azimuthal (in the plane yz) angles of the magnetization vector $\vec{\mathbf{M}} = M_s\begin{pmatrix}\cos(\theta)\\ \cos(\varphi)\sin(\theta)\\ \sin(\varphi)\sin(\theta)\end{pmatrix}$. The coefficients N_x, N_y and N_z are the demagnetizing factors, which satisfy the relation $N_x + N_y + N_z = 1$. These factors can be computed for a rectangular prism geometry, following the analytical expressions provided in [81].

In this analysis, the magnet's thickness and width are fixed by the previous optimization results. The length of the magnet, l_{magnet}, is then chosen to ensure that the demagnetizing energy favors alignment of the magnetization along the x-axis. This corresponds to minimizing N_x relative to N_y and N_z, thereby minimizing the energy cost for aligning the magnetization along the desired axis, see Fig. 3.6(d).

3.2.2 Accurate modeling with micro-magnetic simulations

Why performing micromagnetic simulations?

Having optimized the micro-magnet geometry under the assumption of uniform magnetization, we now turn to the question of how much external magnetic field is required to ensure magnetic saturation, taking into account internal demagnetizing effects. In addition, we aim to understand how the stray magnetic field gradients degrade when saturation is not fully achieved. This analysis allows us to estimate the achievable strengths of the symmetric and antisymmetric field components under realistic operating conditions, which are critical for setting the Zeeman splitting and the hybridization energy of the qubit. As discussed in Chapter 1, these two energy scales define both the spin qubit energy spectrum and the strength of its electric dipole.

Micromagnetic simulation methodology

To accurately model the internal magnetic configuration of the micromagnets, we perform micromagnetic simulations using the software Mumax3 [78] and account for exchange interactions, demagnetizing energy, and Zeeman energy.

We simulate a micro-magnet geometry with a width of 1 µm (along y) and a length of 7 µm (along x), which is the largest size compatible with our available computing resources. To eliminate edge effects in the x-direction and approximate an infinitely long structure, we apply periodic boundary conditions along this axis. The magnetic layer has a thickness of 200 nm, and the simulation domain is discretized into a uniform grid with cell size 4 nm × 4 nm × 4 nm.

We consider three common magnetic materials - NiFe, Co, and CoFe - with distinct magnetic parameters, listed in Table 3.4. All parameters used here are taken from the literature.

Table 3.4: Micro-magnetic parameters used in the simulations

	NiFe	Co	CoFe
Exchange stiffness	$13 \times 10^{-12}\,\mathrm{J\,m^{-1}}$ 2	$56 \times 10^{-12}\,\mathrm{J\,m^{-1}}$	$20 \times 10^{-12}\,\mathrm{J\,m^{-1}}$
Saturation magnetization	$800 \times 10^{3}\,\mathrm{A\,m^{-1}}$	$1450 \times 10^{3}\,\mathrm{A\,m^{-1}}$	$2000 \times 10^{3}\,\mathrm{A\,m^{-1}}$
References	[94], [79]	[94], [95]	[94], [96]

Simulations are initialized in a saturated configuration with an external field of 1 T applied along the magnet's long axis, and then gradually decreased in steps of 100 mT. At each step, the system is relaxed to a minimum-energy state.

From the resulting magnetization distribution, we can compute the stray magnetic fields at a height of 100 nm above the surface - consistent with previous analysis.
We then compute the effective symmetric and antisymmetric field components of the magnetic field generated by the magnet, α_s and α_{as}, by spatially averaging the magnetic field over the extent of the two dots, similarly to the idealized case:

$$\begin{aligned} \alpha_s &= \frac{1}{2}\left(\int B_x(x)\left|\phi_L(x)\right|^2 \mathrm{d}x + \int B_x(x)\left|\phi_R(x)\right|^2 \mathrm{d}x\right) \\ \alpha_{as} &= \frac{1}{2}\left(\int B_x(x)\left|\phi_L(x)\right|^2 \mathrm{d}x - \int B_x(x)\left|\phi_R(x)\right|^2 \mathrm{d}x\right) \end{aligned} \tag{3.24}$$

Simulation results and discussion

Figure 3.7 shows two representative equilibrium magnetization distributions. When the applied field is insufficient to fully saturate the magnet, closure domains begin to form-particularly near the ends of the structure-and these decrease the magnetic field generated by the magnet.

The saturation magnetization M_s plays a central role in micromagnetic behavior. While a higher M_s enhances the maximum achievable stray field and gradient, it also increases the demagnetizing energy, making the system more prone to domain formation. As a result, a stronger external magnetic field is required to achieve saturation. This trade-off motivates our choice to simulate three materials with varying

To evaluate the performance of each configuration, we define the figure of merit:

$$\frac{\alpha_{as}}{\alpha_s + \alpha_s^{\mathrm{ext}}} \tag{3.25}$$

where $\alpha_s^{\mathrm{ext}} = B_{\mathrm{ext}}$ is the symmetric contribution from the external field. A larger ratio is desirable, as it corresponds to a stronger hybridization energy - directly related to strength of the electric dipole of the spin transition - for a given symmetric Zeeman field. The objective is therefore to identify the combinations of M_s and B_{ext} values that maximize this ratio under experimentally accessible conditions.

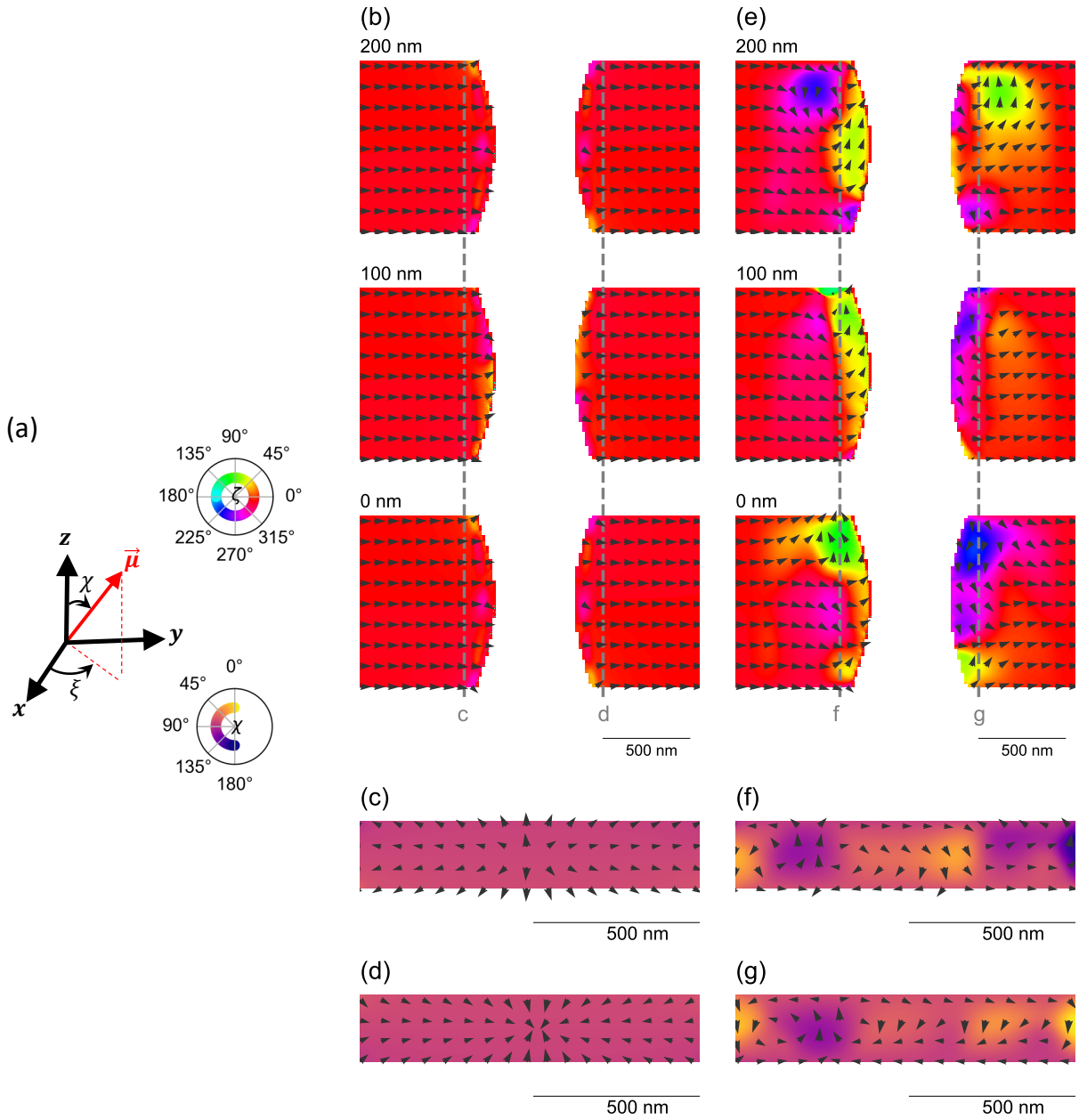

Figure 3.7: **Equilibrium magnetic configuration in an optimized micromagnet engineered to maximize the interdot field difference** B_z
(a) Coordinate definition.
Configurations are obtained with micromagnetic simulations in Mumax3, for CoFe. An external field of 1 T is applied along the magnet's long axis to saturate the sample, then reduced in 0.1 T, steps to determine the equilibrium states at (b-d) 0.5 T and (e-g) 0.1 T.
Color and vector maps of the magnetization $\vec{mu}$.
(b,e) Cuts parallel to the xy plane, plane, showing the in-plane angle ξ at different heights z.
(c,d,f,g) Cuts parallel to the xz plane, showing the out-of-plane angle χ at different positions x along the magnet.

In Fig. 3.8, we show the evolution of the average normalized magnetization μ_x, along with $\epsilon_Z = g_s\mu_B\alpha_s$ and $\epsilon_{\text{hyb}} = g_s\mu_B\alpha_{as}$ as functions of the applied field B_{ext}. Here, ϵ_Z is the Zeeman energy and ϵ_{hyb} is the hybridization energy (introduced in Chapter 1), with g_s the spin g-factor and μ_B the Bohr magneton.
We observe that full saturation is reached at approximately 200 mT for NiFe, 300 mT for Co, and 600 mT for CoFe. Depending on the constraints of a specific qubit architecture (e.g. the value of the external field), an optimal pair (M_s, B_{ext}) can be selected to maximize the effective coupling. In favorable regimes, the antisymmetric field produced by the magnet can reach values comparable to the total symmetric field $\alpha_{as} \sim (\alpha_s + \alpha_s^{\text{ext}})$.

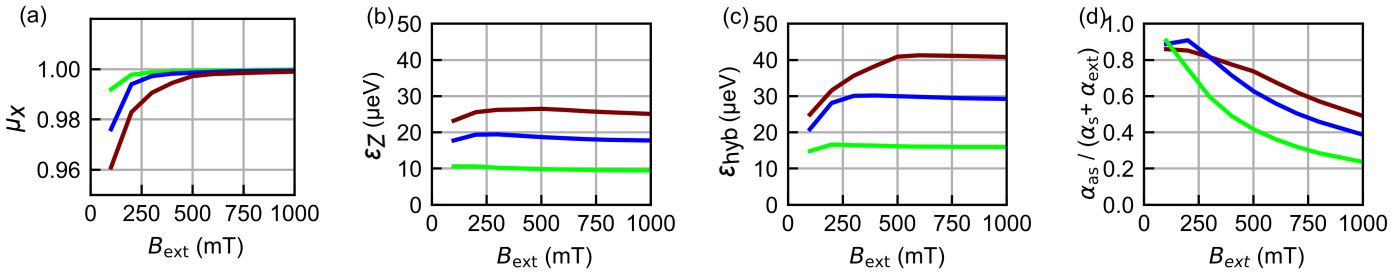

Figure 3.8: **Results of the micro-magnetic simulations for a micromagnet with a shape optimized to maximize the interdot field difference B_z**
(a) Normalized magnetization component μ_x versus external field B_{ext} (applied along the magnet's long axis).
(b) Zeeman energy $\epsilon_Z = g_s\mu_B\alpha_s$ as a function of B_{ext}
(c) Hybridization energy $\epsilon_{\text{hyb}} = g_s\mu_B\alpha_{as}$ as a function of B_{ext}
(d) Ratio of the antisymmetric to the total symmetric field, $\alpha_{as}/(\alpha_s + \alpha_{\text{ext}})$, versus B_{ext}.
The different colors correspond to CoFe (red), Co (blue) and NiFe (green).

Toward experimental validation

While the micromagnetic simulations presented here provide useful insight into the behavior of the magnet under realistic conditions, they rely on idealized material parameters and geometries. In particular, although we have accounted for demagnetizing effects, we have not yet validated the internal magnetization profiles against experimental measurements.

To bridge this gap, and before final integration into a spin qubit device, we carried out both qualitative and quantitative experimental characterizations on the magnetic materials thin film and the fabricated micro-magnets. This will allows us to estimate how closely the experimentally realized figure of merit

$$\frac{\alpha_{as}}{\alpha_s + \alpha_s^{\text{ext}}} \tag{3.26}$$

approaches the values predicted by simulation.

Chapter 4

Magnetic characterization of micro-Magnets for on-chip integration

In this chapter, we investigate the magnetic properties of a micro-fabricated magnet specifically designed to generate an antisymmetric stray field across a double quantum dot system. Such a field configuration enables hybridization between spin and orbital degrees of freedom, allowing for electrical control of spin transitions and coupling to cavity photons-a crucial capability for scalable spin qubit architectures.

Our objective is to fully characterize and predict the magnetic behavior of the magnet both in the saturated and unsaturated regimes. Starting from thin-film-level characterization, we obtain insights into key parameters for modeling the magnetic behavior.

To probe the magnet at the device scale, we explore measurement techniques that offer quantitative magnetic field mapping with sufficient spatial resolution and sensitivity. In particular, we introduce NV center magnetometry as a powerful tool that meets these requirements, enabling us to assess the local magnetic field distribution produced by the magnet.

Finally, we combine experimental data with micromagnetic simulations informed by thin-film parameters to construct a realistic model of the magnet's behavior. This approach enables us to construct a predictive model of the magnet's behavior across both saturated and non-saturated regimes. Crucially, it allows us to accurately predict the stray magnetic field profile, even in the presence of domain formation or partial magnetization-an essential capability for understanding and engineering the spin energy spectrum in quantum dot devices.

4.1 Thin film characterization

4.1.1 Material choice and remanent magnetic configuration of the thin films

Choice of magnetic material

The choice of magnetic material is not straightforward. While selecting a material with a high saturation magnetization M_s can enhance the strength of the stray magnetic field, it also increases the dipolar interaction energy. This promotes the formation of magnetic domains and raises the external magnetic field required to saturate the magnet. As discussed in the previous chapter, an appropriate trade-off must be found between M_s and the achievable external field B_{ext}, depending on the operational constraints of the qubit system.

We consider the Zeeman splitting of the spin transition that defines the qubit to be:

$$\epsilon_Z = g_s \mu_B \alpha_S \text{ with } g_S = 2 \tag{4.1}$$

For optimal coupling of the spin qubit to cavity photons, we aim to match the Zeeman energy to the hybridization energy and the energy related to interdot tunneling:

$$\epsilon_Z \sim \epsilon_{\text{hyb}} \sim t_c \tag{4.2}$$

Here $\epsilon_{\text{hyb}} \sim g_s \mu_B \alpha_{as}$ represents the hybridization energy reflecting the strength of the artificial spin-orbit coupling induced by the antisymmetric magnetic field generated by the magnet.
Since the qubit frequency is primarily determined by the Zeeman energy, achieving a target frequency in the range of 4 GHz – 8 GHz - which is experimentally optimal for electric control - requires :

$$\alpha_s \sim \alpha_{as} \sim 150 - 200 \text{ mT} \tag{4.3}$$

Based on these considerations and our previous study in the last chapter, we focus our study on Cobalt based magnetic materials, which offer high saturation magnetization while still allowing manageable control of domain behavior within the accessible range of external magnetic fields.

The deposition of the materials is done by magnetron sputtering. To eliminate the influence of the substrate on the deposition of the magnetic material, and to ensure good adhesion of the layer, we start by depositing 5 nm of tantalum on the substrate.The magnetic thin film is then deposited and protected against oxidation by a capping layer of 5 nm of Platinium.

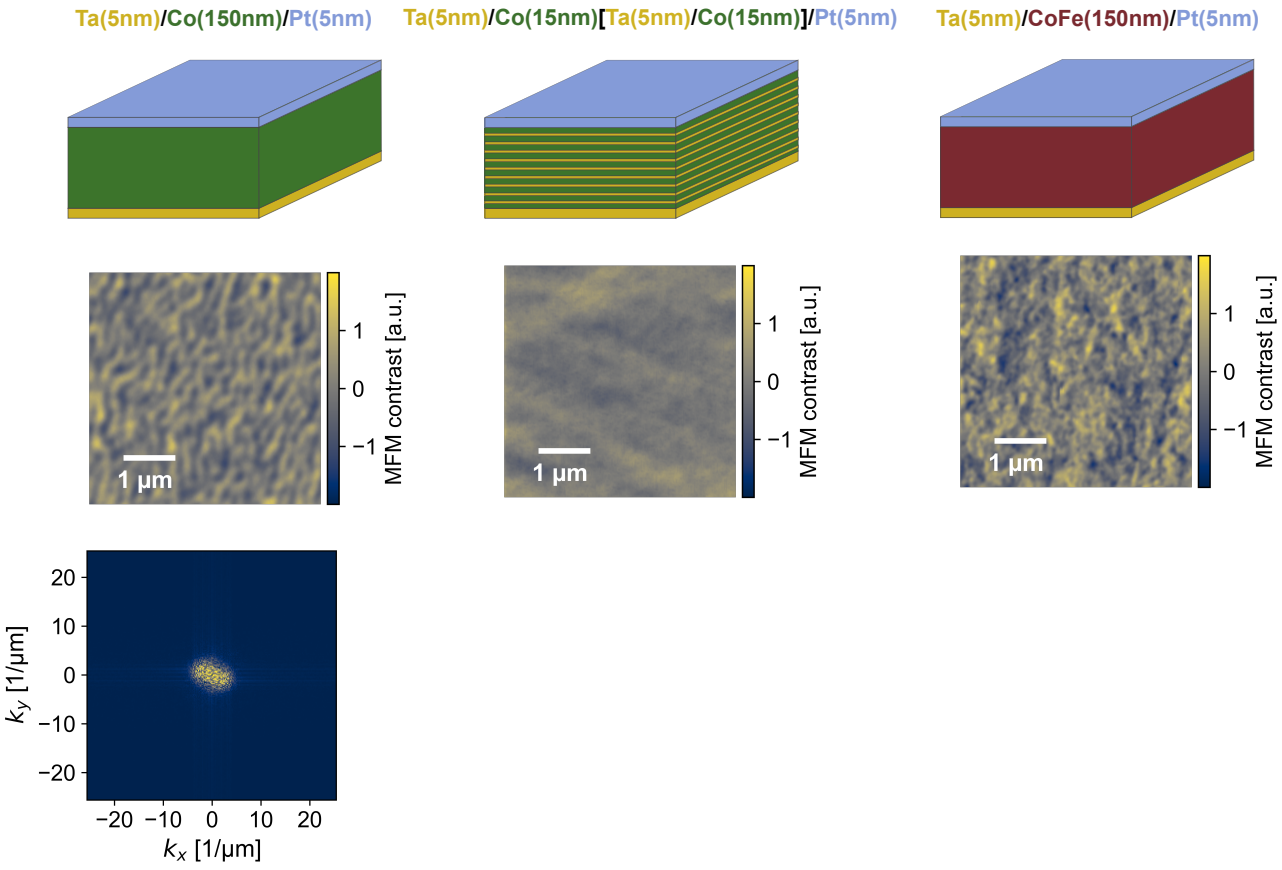

Figure 4.1: **MFM mapping of remanent magnetization of the materials under study**
MFM scans of thin films of Co, Co-Ta multilayers, and CoFe acquired at zero applied field, after initializing the magnetization with a strong in-plane field (≈ 300 mT). The precise layer stacks for each sample are shown in the corresponding schematics.
For the Co layer, we also show the Fourier transform of the MFM image. No clear periodicity is identified in the measurement.

Magnetic Force Microscopy of the remanent magnetization distribution

The magnetic contrast observed in Magnetic Force Microscopy (MFM) directly reflects the underlying magnetic configuration of the thin film. For all samples analyzed, an initial strong in-plane magnetic field is applied to saturate the film, after which the field is reduced to zero. MFM imaging is then performed to investigate the remanent magnetic state. The results are reported Fig. 4.1.

In cobalt thin films, we observe a distinct alternating contrast pattern forming stripe-like domains. These stripes typically arise due to an out-of-plane component of the magnetization, driven by perpendicular magnetic anisotropy (PMA). The system reaches an equilibrium configuration comprising stripe domains- regions with an out of plane magnetization pointing alternately up and down relative to the film plane-which generates the MFM signal.

About weak and strong stripes

Stripe domains are associated with a non-zero out-of-plane magnetization component. Their formation results from a competition among three energy contributions: magnetic anisotropy energy, demagnetizing energy, and exchange energy.

The out-of-plane magnetization component minimizes the anisotropy energy but introduces surface magnetic poles, thereby increasing the demagnetizing energy. To reduce the overall energy, the system forms alternating domains with oppositely directed out-of-plane magnetization. In this configuration, the out-of-plane component varies periodically between positive and negative values across domain boundaries.
Weak stripes correspond to magnetic domains where the magnetization lies predominantly in the film plane, with only a small out-of-plane component. These structures are typically found in materials with moderate perpendicular magnetic anisotropy (PMA), satisfying the condition:

$$K_{\text{perp}} \ll \frac{1}{2}\mu_0 M_s^2 \tag{4.4}$$

Here, M_s^2 is the saturation magnetization and K_{perp} is the uniaxial anisotropy constant, which can stem from crystalline anisotropy, surface or interfacial effects, and magnetoelastic contributions. In **Strong stripe** structures, where the PMA is more pronounced, the magnetization angle with respect to the film plane can vary from a few degrees to 90°.

The stripe periodicity results from a balance between short-range exchange interactions and long-range dipolar (demagnetizing) interactions. Dipolar forces tend to reduce the stripe period, while the exchange interaction acts to smooth variations in the magnetization direction, thereby opposing abrupt reorientations and increasing the stripe period. The resulting stripe periodicity is determined by the balance of these energy contributions and is strongly influenced by the thickness of the magnetic film.
For films with moderate PMA, the formation of weak stripe domains at zero external field can be predicted by the Murayama model [ref], which defines a critical film thickness:

$$t_{\text{crit}} = 2\pi\sqrt{\frac{A_{\text{ex}}}{K_{\text{perp}}}} \tag{4.5}$$

This critical thickness is highly sensitive to deposition conditions, such as pressure, substrate temperature, and crystalline structure, since these factors influence the values of A_{ex} and K_{perp}.

In the literature, weak stripe domains have been reported in epitaxial cobalt films [97]. However, unlike those reports, where the stripes are highly regular and periodic with well-defined ori-

entation, the stripes observed in our sputtered films appear more disordered, making it difficult to identify a clear periodicity (see Fig.4.1). This behavior is most likely a consequence of the granular microstructure of sputtered films, where grains of different orientations break the long-range order seen in epitaxial samples.

The presence of out-of-plane magnetization in Cobalt promotes the formation of domains within the magnet, which can reduce the net stray field generated in the unsaturated regime. One strategy to suppress the formation of stripe domains is to reduce the film thickness, thereby making it energetically unfavorable for magnetization to tilt out of plane.

To further mitigate the stripe formation, we investigated a multilayer structure composed of cobalt and tantalum. The deposited Ta is expected to be amorphous, and its insertion disrupts the crystallographic texture. Consequently, the Co/Ta multilayer is not expected to support strong out-of-plane magnetization components, as confirmed by the MFM measurements Fig. 4.1. The observed contrast is significantly reduced and likely originates from volume magnetic pole density (i.e., non-zero divergence of the magnetization) within the film.

We also examined a thin film of cobalt-iron alloy ($Co_{50}Fe_{50}$), a ferromagnetic material known to exhibit higher saturation magnetization than either pure cobalt or pure iron [71]. Because the demagnetizing energy scales as M_s^2, a higher M_s more strongly penalizes out-of-plane magnetization. In the electrostatic analogy from Chapter 2, any out-of-plane component creates surface magnetic poles; increasing M_s amplifies the resulting stray field, making such configurations energetically less favorable than in materials with lower M_s. In addition, iron's magnetocrystalline anisotropy constant is smaller than cobalt's [71]. Together, these factors suggest that achieving and stabilizing in-plane magnetization should be easier in CoFe than in pure Co.
By the same reasoning, however, the larger M_s in CoFe also promotes the formation of additional closure domains near the magnet ends to reduce surface magnetic poles, which can diminish the generated magnetic field.
MFM measurements on the CoFe films, shown in Fig. 4.1, exhibit a stronger magnetic contrast than in the Co/Ta multilayers and do not display a well-defined domain pattern. This behavior is consistent with a predominantly in-plane magnetization, with more magnetic domains than in the Co/Ta multilayers.

From this initial MFM observation, the thin film that appears to exhibit homogeneous in-plane magnetization, and thus to be the most suitable candidate for our magnet application, is the Co/Ta multilayer. Nevertheless, we proceed with the characterization of all three magnetic materials.

Since the magnetic configuration is governed by parameters that are themselves sensitive to the film's crystallographic structure, the next step of our characterization focuses on X-ray diffraction analysis.

4.1.2 Crystallographic arrangement of the thin film

Principle of X-ray diffraction characterization

X-ray diffraction (XRD) is a powerful analytical technique used primarily to determine the crystalline structure of materials.

XRD relies on the interaction between X-rays and the periodic atomic planes in a crystal. When a beam of X-rays hits a crystalline sample, the rays are scattered by the atoms in the crystal (see Fig.4.2(a)).
For these scattered rays to interfere constructively and to produce detectable diffraction peaks, the incident angle of the X-rays θ must be such that the path difference between X-rays reflected from successive planes equals an integer multiple of the X-ray wavelength λ. This leads to constructive interference, meaning the reflected waves reinforce each other and produce a detectable

peak. The angle θ must therefore match precisely the spacing d between planes. This condition is described by the Bragg's Law:

$$n\lambda = 2d\sin(\theta) \tag{4.6}$$

where n is an integer that denotes the order of reflection.
The typical XRD setup includes an X-ray source- in our case it corresponds to a copper tube generating X-rays ($\lambda_{K_{\alpha_1}} = 1.5406$Å) -, a goniometer - to precisely rotates the sample and detector and a detector to measure the intensity of diffracted X-rays at different angles.
We are performing $\theta - 2\theta$ measurement with θ the angle between the incident X-ray beam and the sample surface and 2θ is the angle between the incident beam and the detector - i.e., the total angle between the incoming and diffracted beam. In a $\theta - 2\theta$ scan: as the angle θ changes, the detector is rotated by 2θ and records the intensity of the diffracted X-rays. The result is a diffraction pattern, a graph of intensity versus angle (2θ), corresponding to specific interplanar spacings (d).
The lattice planes in a crystal are identified by the Miller indices h, k, l : the notation (hkl) refers to a set of lattice planes that intersect the crystal axes in a specific way. The diffraction measurement is sensitive to planes (hkl) that are oriented such that they can satisfy Bragg's Law for the X-ray wavelength used. Therefore, to observe a peak from the lattice planes (hkl) in a $\theta - 2\theta$ experiment, **the planes must be parallel to the sample surface**.
Even if Bragg's Law is satisfied, some (hkl) planes will not diffract because of crystal symmetry and atomic arrangement. This is governed by the **structure factor**, which may cancel out for certain reflections.
From the 1D plot of intensity versus 2θ, phase identification is done by comparing peak positions to databases .

Diffraction measurement results

The magnetic materials under investigation were deposited on a Si/SiO_2 substrat. substrate. Each sample consists of a layered stack comprising a tantalum adhesion layer, the magnetic material of interest, and a platinum capping layer.
The results of the $\theta - 2\theta$ X-ray diffraction scans for the different materials are presented in Figure 4.2. A substrate peak is clearly visible in all patterns at a lattice spacing of $d = 1.3557$ Å consistent with the $(4,0,0)$ lattice plane of diamond-cubic silicon [98]. Additional peaks common to all scans - likely originating from the platinum layers - are also observed but are not the focus of this analysis. Our primary interest lies in the peaks that differ between samples, which are attributed to the respective magnetic materials and highlighted in blue in Fig. 4.2.
To identify these peaks and compare their positions with known crystallographic data, we used the DIFFRAC.EVA software from Bruker.

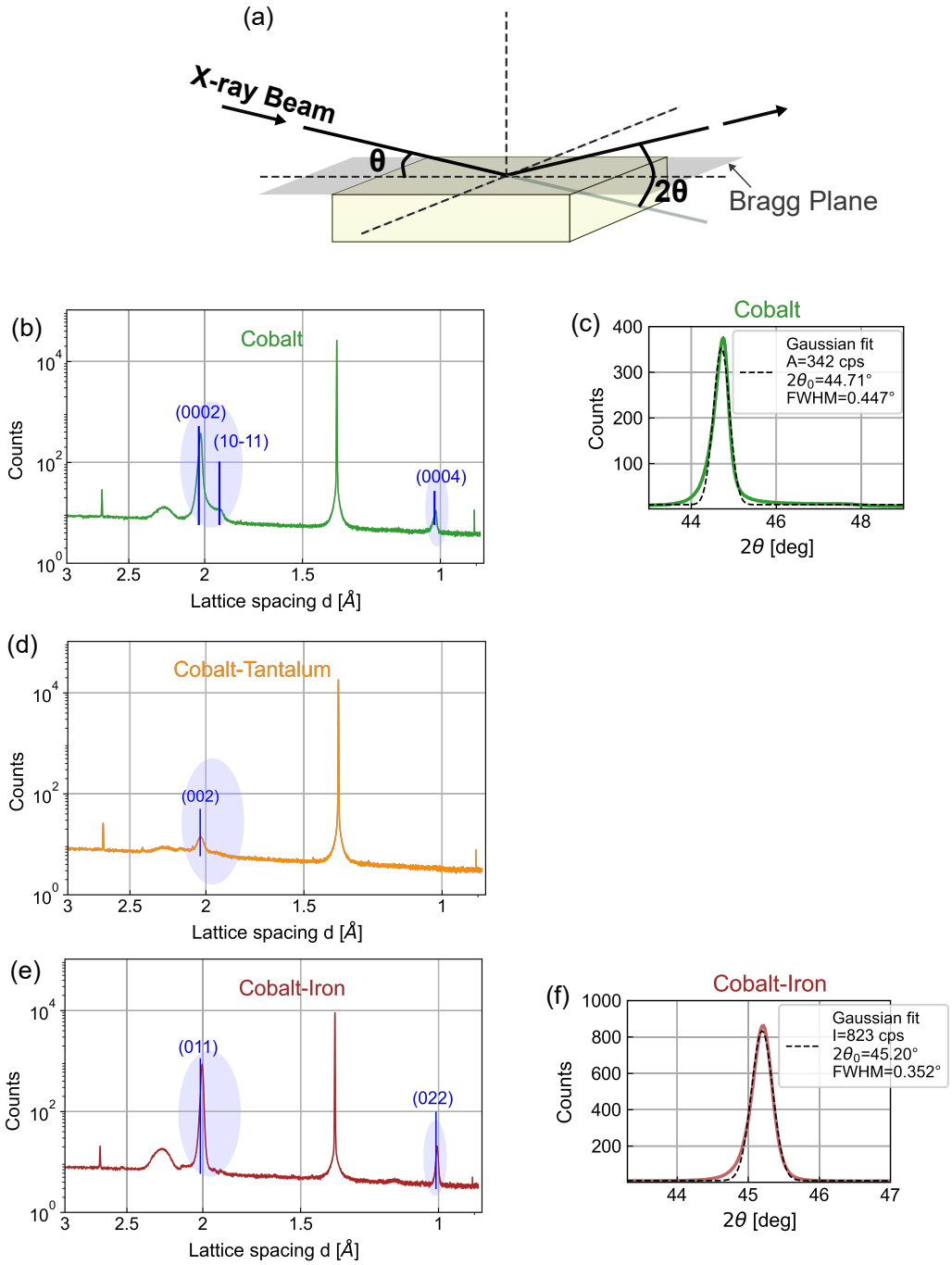

Figure 4.2: **X-ray diffraction (XRD) patterns for the materials under study**
(a) Schematic of the XRD measurement principle.
(b) XRD pattern of the cobalt (Co) thin film. (c) Gaussian fit of the diffraction peak at $d = 2.0227\,\text{Å}$ which corresponds to $2\theta = 44.71°$.
(d) XRD pattern of the cobalt-tantalum (Co-Ta) multilayer film.
(e) XRD pattern of the cobalt-iron (Co-Fe) thin film. (f) Gaussian fit of the diffraction peak at $d = 2.0033\,\text{Å}$ which corresponds to $2\theta = 45.20°$.

Cobalt diffraction pattern

In the case of the cobalt sample, three distinct peaks can be identified in Fig.4.2(b). These correspond to the hexagonal phase of cobalt, specifically the (0002), (0004), and $(01-11)$ planes as detailed in the Table 4.1. From the XRD pattern, the cobalt thin film appears textured rather than polycrystalline, with a clear, identifiable preferred orientation.

Table 4.1: Measured lattice spacings compared with crystallographic values for cubic silicon [98] and hexagonal cobalt [99].

Lattice Plane	Measured lattice spacing	From crystallographic data
Si (400)	$d = 1.3557$ Å	$d = 1.3578$ Å [98]
Co (0002)	$d = 2.0227$ Å	$d = 2.0343$ Å [99]
Co $(10-11)$	$d = 1.9137$ Å	$d = 1.9155$ Å [99]
Co (0004)	$d = 1.0137$ Å	$d = 1.0171$ Å [99]

The crystallite size can be estimated using the Scherrer equation, which relates the broadening of the diffraction peaks to the size of coherently diffracting domains:

$$D = \frac{K\lambda}{\beta\cos(\theta)} \tag{4.7}$$

Here :

- D is the crystallite size,
- K is the shape factor (assumed to be 0.89), it depends on the assumed shape of crystallites,
- λ is the X-ray wavelength, here $\lambda^{Cu}_{K_{\alpha_1}} = 1.5406$Å
- β is the full width at half maximum (FWHM) of the diffraction peak (in radians). The observed FWHM is corrected for instrumental broadening : $\beta = \sqrt{\beta^2_{\text{measured}} - \beta^2_{\text{instrument}}}$.
- θ is the Bragg angle in radians.

It is important to note that this method estimates the size of coherently diffracting domains - referred to as crystallites - which may not correspond directly to the actual grain size. The analysis assumes a uniform crystallite size. With this analysis, we attribute the observed peak broadening primarily to the finite crystallite size, while neglecting additional broadening that may arise from non-uniform lattice strain. For the cobalt film, the estimated crystallite size is approximately 15 nm, the details of the parameters used for this estimate are provided in Fig. 4.2(c).

The identification of a hexagonal lattice is consistent with the magnetic properties observed at remanence. According to the literature, hexagonal cobalt exhibits a uniaxial magnetocrystalline anisotropy along the c-axis, with an anisotropy constant of approximately $K_u \sim 450\,\text{kJ}\,\text{m}^{-3}$ [71]. The presence of Bragg peaks corresponding to the (0002) and (0004) planes suggests that the c-axis is oriented perpendicular to the sample surface. This crystallographic orientation implies that the uniaxial magnetocrystalline anisotropy may be responsible for the perpendicular magnetic anisotropy observed in the sample.

Hexagonal or Cubic Cobalt ?

Although our data supports the presence of a hexagonal cobalt phase, previous studies [100] have reported a cubic phase for thin films of Cobalt.

The observed diffraction peaks at $d = 2.0227$ Å and $d = 1.0137$ Å could be attributed to the (111) and (222) planes of a face-centered cubic (FCC) structure. This would imply a compressive strain reduce the inter-planar spacing of about 1%. However, this interpretation fails to explain the third peak near $d = 1.9137$ Å, which is incompatible with a purely cubic

structure.

Table 4.2: Measured lattice spacings compared with crystallographic values for cubic silicon [98] and cubic cobalt [101].

Lattice Plane	Measured lattice spacing	From crystallographic data
Si (400)	$d = 1.3557$ Å	$d = 1.3578$ Å [98]
Co (111)	$d = 2.0227$ Å	$d = 2.0462$ Å [101]
	$d = 1.9137$ Å	
Co (222)	$d = 1.0137$ Å	$d = 1.0231$ Å [101]

Cobalt-Tantalum multilayer diffraction pattern

In the XRD pattern of the Co-Ta multilayer (Fig.4.2(d)), we observe a general decrease in peak intensity compared to the single cobalt layer. A peak at $d = 2.0340$ Å matches the (002) plane of hexagonal cobalt, suggesting that the hexagonal phase persists and that the compressive strain present in the cobalt-only sample may be relaxed in this configuration.
In multilayer systems, XRD intensity is affected by coherent scattering at the interfaces. Ideally, one would expect to observe satellite peaks arising from the periodicity of the multilayer structure. However, such features are not evident in our measurements-likely due to reduced signal intensity, insufficient structural periodicity, or poorly defined interfaces within the multilayer stack.

Nonetheless, it is important to note that the current diffraction data does not allow us to definitively exclude the possibility that the cobalt layer adopts a cubic crystal structure.

Cobalt-Iron diffraction pattern

In the diffraction pattern of the CoFe sample (Fig.4.2(e)), two main peaks at $d = 2.0033$ Å and $d = 1.0036$ Å correspond well to the (011) and (022) planes of a cubic structure, see detail in Table 4.3. Again, the CoFe film does not appear randomly polycrystalline and it rather shows a clear, identifiable preferred orientation.

Table 4.3: Measured lattice spacings compared with crystallographic values for cubic silicon [98] and cubic cobalt-iron[102].

Lattice Plane	Measured lattice spacing	From crystallographic data
Si (400)	$d = 1.3557$ Å	$d = 1.3578$ Å [98]
CoFe (011)	$d = 2.0033$ Å	$d = 2.0143$ Å [102]
CoFe (022)	$d = 1.0036$ Å	$d = 1.0071$ Å [102]

Using the Scherrer equation, the estimated crystallite size is approximately 20 nm (see Fig. 4.2(f)).

4.1.3 SQUID-VSM measurements analysis

The SQUID-VSM measurements provide insight into the average magnetization behavior of the thin film in response to an applied external magnetic field. These measurements yield a qualitative understanding of the magnetization dynamics and facilitate the identification of the easy and hard axes of magnetization, as predicted by the Stoner-Wohlfarth model. Such analysis can reveal the existence of the presence of magnetic configurations such as weak or strong stripe domains.

These measurements also allow for the determination of key magnetic properties, including the saturation magnetization and the magnetic field needed to reach saturation in a given direction. From this, the magnetic anisotropy constant can be estimated, which is a central parameter influencing the system's magnetization behavior.

In-plane measurement of the magnetization

Figure 4.3(a-c) shows the magnetization behavior measured in the plane of the thin film under an external magnetic field applied along the same direction. All three magnetic materials display a well-defined hysteresis loop in the in-plane magnetization curves. This response aligns with the Stoner-Wohlfarth model and confirms that the easy axis of magnetization lies within the film plane.

Notably, for the cobalt thin film, the coercive field B_c does not coincide with the saturation field B_{sat}. Upon reducing the external field from a saturated state ($|B| \geq B_{\text{sat}}$), the Zeeman energy no longer dominates the total magnetic energy. In the intermediate regime ($B_{\text{sat}} \leq |B| \leq B_c$), the magnetization decreases almost linearly. This behavior suggests the emergence of a magnetic configuration in which the magnetization remains predominantly in-plane but acquires a finite out-of-plane component. The development of stripe-like domains in this regime reflects the system's attempt to minimize its total magnetic energy by balancing the contributions from anisotropy, exchange, and demagnetizing fields.

In contrast, this intermediate regime behavior is not observed in the cobalt-tantalum multilayer and the cobalt-iron film. The magnetization remains aligned with the external field until the magnetization reversal, which is favorable for applications requiring stable in-plane magnetization - such as the magnet design considered in our work.

Comparing remanent magnetization across the three materials in Table 4.4 , the cobalt thin film shows a notably lower value.

To investigate the possibility of in-plane anisotropy in the cobalt and cobalt-iron films, we performed additional magnetization measurements after rotating the samples by 90°, see Fig. 4.3(a) and (c). A small degree of in-plane anisotropy can arise in films deposited by magnetron sputtering, potentially due to shadowing effects such as columnar growth or stray magnetic fields generated by the magnetrons during deposition [103]. In our case, the substrates were continuously rotated during deposition. The hysteresis loops measured after rotation were indistinguishable from the originals, indicating no measurable in-plane anisotropy.

From the saturated magnetization values ($|B| \geq B_c$), and using the known film thickness and surface area, we extracted the saturation magnetization M_s for each material. Interestingly, the Cobalt-Tantalum multilayer exhibits a lower M_s than the pure cobalt thin film, despite having the same nominal magnetic thickness (150 nm). This discrepancy may be attributed to the presence of a magnetic "dead layer"-regions near the interfaces where magnetization is significantly reduced or absent. Such layers, typically few nanometers thick, may result from structural imperfections or interfacial chemical intermixing that disrupt magnetic ordering.

All measurements were also performed at 4 K to assess the temperature dependence of the magnetic properties. This enabled a comparison of magnetization behavior and parameter evolution - such as the magnetization at saturation M_s- between room temperature and low temperature.

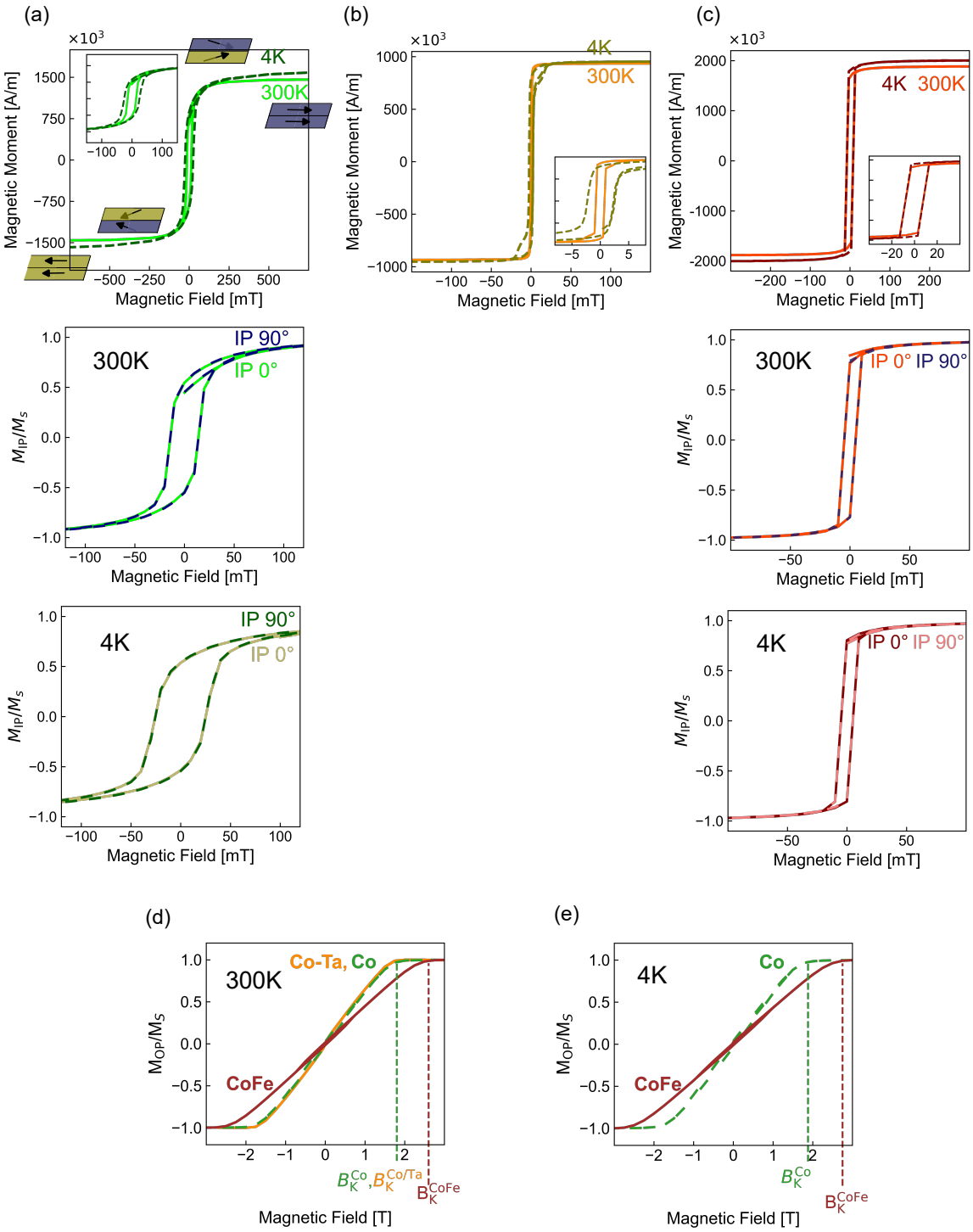

Figure 4.3: **SQUID-VSM measurements on the magnetic thin films.**
(a) In-plane magnetization of the Cobalt film measured at room temperature(300 K) and 4 K. For each temperature, the measurement was repeated after rotating the sample by 90° to probe in-plane anisotropy. For the hysteresis loop, the magnetic-field step size was 5 mT.
(b) In-plane magnetization of the Co/Ta multilayer at RT and 4 K. For the hysteresis loops, the magnetic-field step size was 0.5 mT.
(c) In-plane magnetization of the CoFe film at RT and 4 K; the same 90° rotation protocol as in (a) was used to assess in-plane anisotropy. For the hysteresis loops, the magnetic-field step size was 5 mT.
(d) Out-of-plane magnetization for all three materials at RT.
(e) Same as (d), measured at 4 K.

For all three materials, the saturation magnetization measured at 4 K was higher than that measured at room temperature, as summarized in Table 4.4.

In terms of $M(B)$ curve behavior, likely due to insufficient hysteresis-loop resolution (the magnetic-field step should have been smaller). In contrast, both the cobalt thin film and the cobalt-tantalum multilayer exhibited a noticeable increase in coercive field at 4 K, consistent with reduced thermal agitation at lower temperatures. Thermal fluctuations typically facilitate domain wall motion, and their suppression at low temperature leads to higher coercivity. Lowering the temperature also accentuated a feature only slightly visible at room temperature for the Co/Ta multilayer - with an intermediate linear regime between the hysteresis loop (magnetization switching) and the saturation regime. In particular, we observe at $T = 4\,\mathrm{K}$ a decrease in remanent magnetization at low temperature, see Table 4.4.

Table 4.4: Values of the magnetization at saturation and the magnetization at remanence from the in-plane SQUID-VSM measurement.

Magnetic Material	300 K		4 K	
	M_s [$\mathrm{Am^{-1}}$]	$M(B=0)/M_s$	M_s [$\mathrm{Am^{-1}}$]	$M(B=0)/M_s$
Co	1450×10^3	0.58	1550×10^3	0.56
Co/Ta	930×10^3	0.91	950×10^3	0.82
CoFe	1880×10^3	0.88	2000×10^3	0.90

Out-of-plane measurement of the magnetization

Out-of-plane magnetization measurements were carried out by sweeping the magnetic field perpendicular to the film while measuring the corresponding out-of-plane magnetization component, see Fig.4.3(d-e). The results exhibit behavior consistent with the Stoner-Wohlfarth model. When the applied magnetic field exceeds the effective anisotropy field B_K (as defined in Chapter 2), the Zeeman energy dominates the total magnetic energy, and the magnetization aligns with the external field. As the field is reduced, the out-of-plane component of the magnetization decreases linearly, indicating a gradual reorientation of the magnetic moments into the plane of the film.

The effective anisotropy field B_K is an interesting parameter, as its value depends on the magnetization at saturation and the anisotropy constant. Assuming a uniaxial perpendicular anisotropy and a macrospin approximation (i.e., the film behaves as a uniformly magnetized ellipsoid), B_K is given by:

$$B_K = \mu_0 M_s - \frac{2K_\perp}{M_s} \tag{4.8}$$

The measured values of B_K for the different materials are reported in Table 4.5. B_K is taken as the field at which the measured magnetization reaches 99% of M_s, as shown in Fig. 4.3(c-d)

Table 4.5: Values of the magnetization at saturation and the magnetization at remanence from the out-of-plane SQUID-VSM measurement.

Magnetic Material	300 K		4 K	
	B_K [T]	$\mu_0 M_s$ [T]	B_K [T]	$\mu_0 M_s$ [T]
Co	1.85	1.82	1.94	1.98
Co/Ta	1.8			
CoFe	2.6	2.36	2.75	2.51

The effective anisotropy fields and normalized out-of-plane magnetization curves for the cobalt thin film and the cobalt-tantalum multilayer are similar. This suggests that the intrinsic magnetic

properties- in particular the saturation magnetization M_s -are comparable in both systems. This observation supports the previous hypothesis that dead magnetic layers reduce the overall magnetic response without significantly altering the magnetic properties of the active layer.

Comparing the measured B_K values to $\mu_0 M_s$ should provides insight into the presence and strength of perpendicular anisotropy. In principle, for a material with uniaxial anisotropy aligned along the c-axis (i.e., perpendicular to the film plane), one expects $B_K < \mu_0 M_s$ within the macrospin approximation. However, for the cobalt thin film, we observe $B_K \sim \mu_0 M_s$ which does not clearly indicate the presence of such perpendicular anisotropy based solely on this measurement. Nevertheless, the magnetic configuration observed - particularly the formation of stripe domains - is consistent with the presence of an out-of-plane anisotropy. Therefore, this form of magnetic anisotropy must still be considered in the interpretation of the micromagnetic behavior.

In contrast, for the cobalt-iron multilayer, we find $B_K > \mu_0 M_s$, an unexpected result. This can be explained by considering magneto-crystalline anisotropy in cubic crystals. Although specific data for cubic anisotropy in cobalt-iron alloys is not well documented, it is known that iron exhibits cubic anisotropy, with easy axes along the crystallographic directions (001) and a first-order anisotropy constant $K_1 \sim 48\,\mathrm{kJ\,m^{-3}}$ [71], [104].

The Stoner-Wohlfarth model with cubic anisotropy

We recall that the Stoner-Wohlfarth model assumes a macrospin approximation, treating the thin film as a uniformly magnetized ellipsoid. Within this model, the demagnetizing field energy is given by:

$$E_{ms} = \frac{1}{2}\mu_0 M_s^2 V \cos^2(\theta) \tag{4.9}$$

where θ is the angle between the magnetization vector $\vec{\mathbf{M}}$ and the axis normal to the film surface.
The Zeeman energy can be written as:

$$E_{\text{Zeeman}} = -B_{\text{ext}} M_s \cos(\theta) \tag{4.10}$$

For cubic crystals, the magnetocrystalline anisotropy energy can be expressed as:

$$E_{Kc} = K_1 V\left(\alpha_1^2\alpha_2^2 + \alpha_1^2\alpha_3^2 + \alpha_2^2\alpha_3^2\right) \tag{4.11}$$

Here, K_1 is the first-order anisotropy constant, and α_1, α_2, and α_3 are the direction cosines of the magnetization vector with respect to the crystallographic axes [001], [010], and [100]. X-ray diffraction patterns of the CoFe thin film show Bragg peaks corresponding to the $(0,1,1)$ and $(0,2,2)$ planes, allowing us to infer that the $[0,1,1]$ direction is normal to the film. Under this assumption, the anisotropy energy becomes:

$$E_{Kc} = K_1 V\left(m_{001}^2 m_{010}^2 + m_{010}^2 m_{100}^2 + m_{001}^2 m_{100}^2\right) \tag{4.12}$$

where:

$$\begin{aligned} \text{with} \quad & m_{001} = \sin(\theta)\cos(\varphi), \\ & m_{010} = \frac{1}{\sqrt{2}}\left(\cos(\theta) + \sin(\theta)\sin(\varphi)\right), \\ \text{and} \quad & m_{010} = \frac{1}{\sqrt{2}}\left(\cos(\theta) - \sin(\theta)\sin(\varphi)\right) \end{aligned}$$

Here, φ is the azimuthal angle of the magnetization vector $\vec{M}$.
By numerically minimizing the total magnetic energy - comprising the demagnetizing field energy, Zeeman energy, and magnetocrystalline anisotropy energy - we obtain the equilibrium angles θ and φ that define the magnetization direction. From these, the expected out-of-plane magnetization response $M_\perp(B_\perp)$ can be reconstructed. The results are presented in the figure Fig. 4.4.

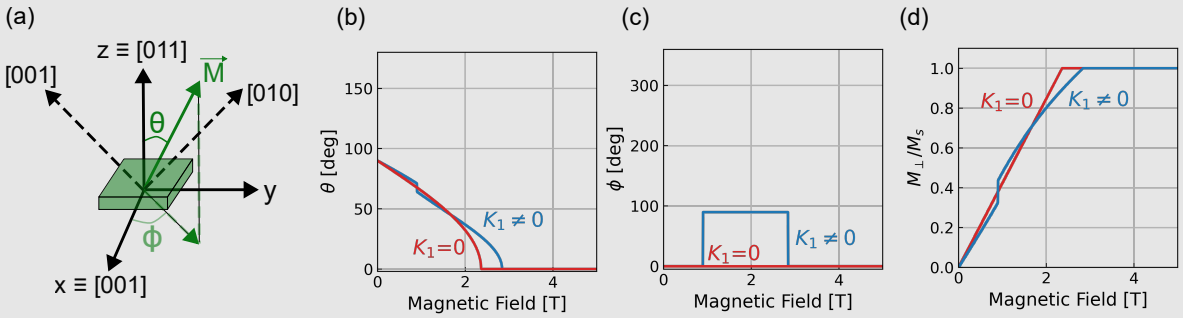

Figure 4.4: **Simulated $M_\perp(B_\perp)$ with cubic anisotropy**.
(a) Schematic of a thin magnetic film with uniform magnetization $\vec{\mathbf{M}}$. crystallographic axes are indicated. The magnetization orientation is parameterized by the polar angle θ and azimuthal angle φ.
(b-c) Evolution of θ and φ under a magnetic field applied perpendicular to the film, $B_\perp$, shown with and without cubic anisotropy.
(d) Resulting out-of-plane magnetization $M_\perp(B_\perp)$ computed with and without cubic anisotropy.

This model shows that $B_K > \mu_0 M_s$ can indeed arise in systems with significant cubic anisotropy, consistent with our experimental observations.

Similar measurements were performed at low temperature for both the cobalt thin film and the cobalt-iron thin film, leading to comparable conclusions.

Although the macrospin model provides useful insights into how system parameters affect the effective anisotropy field B_K, it is not suitable for precise quantitative comparison in this context. The samples are textured, composed of grains with slightly varying crystallographic orientations, which deviated from the uniform magnetization assumption of the model. Therefore, rather than relying solely on the macrospin approximation, we compare the SQUID-VSM experimental data with micromagnetic simulations that take into account the structural and magnetic inhomogeneity of the samples.

4.1.4 Extracting micro-magnetic simulation parameters from the thin-film measurements

The thin-film characterizations presented above provide essential input parameters for constructing micromagnetic models specific to each material system under study - namely, Co, Co/Ta multilayer, and CoFe alloy - which are subsequently used in simulations performed with the Mumax[3] software.

A micromagnetic model at room-temperature

Cobalt film:

For the cobalt thin film, we consider a thickness of approximately 150 nm[1]. The granular nature of the film is modelled using a three-dimensional Voronoi tessellation. The details of this grain-structure modelling with the Voronoi tessellation are given in Appendix A. Within each grain, the magnetocrystalline anisotropy axis is slightly perturbed around the out-of-plane direction and defined as:

$$\vec{\mathbf{u}}_{\text{anis}} = (a_1, a_2, 1) \tag{4.13}$$

where a_1 and a_2 are sampled from a normal distribution $\mathcal{N}(0,1)$. The first-order anisotropy constant is set to $500\,\text{kJ}\,\text{m}^{-3}$, consistent with values reported in the literature [71], [105]. The second-order anisotropy term is neglected. The saturation magnetization is set to $M_s = 1450 \times 10^3\,\text{A}\,\text{m}^{-1}$, based on SQUID-VSM measurements. The exchange stiffness is taken as $30\,\text{pJ}\,\text{m}^{-1}$, in agreement with values reported in the literature [106] [107], and the intergranular exchange is reduced by a factor of 10.

Cobalt-Tantalum multilayer:

Ideally, this system would be modeled as a true multilayer structure, incorporating both reduced interlayer exchange and a granular microstructure within each layer.
However the Mumax[3] software does not currently allow the implementation of a model that simultaneously incorporates a granular structure and a multilayer geometry with reduced exchange coupling between adjacent layers. From MFM measurements, we know that the individual cobalt layers are thin enough to suppress the formation of stripe domains typically stabilized by perpendicular anisotropy. As a result, we model the system as a stack of 10 uniform magnetic layers, each with a thickness of 16 nm (accounting for 15 nm Co and 1 nm Ta). Granular structure and magnetocrystalline anisotropy are not included in this model.
The saturation magnetization is set to $M_s = 930 \times 10^3\,\text{A}\,\text{m}^{-1}$ based on SQUID-VSM data and the total magnetic thickness of 160 nm. The exchange stiffness is again set to $30\,\text{pJ}\,\text{m}^{-1}$, similarly to the cobalt thin film. The interlayer exchange is reduced by an adjustable factor chosen to match the experimental measurements. In practice, a reduction by a factor of 100 between layers provides the best agreement with the experimental data presented in this Chapter.

Cobalt-Iron film:

For the **Cobalt-Iron** thin film, the model used is similar to the one of the Cobalt thin film.
The CoFe thin film is modeled similarly to the Co thin film. The granular structure is implemented using a 3D Voronoi tessellation. The cubic magnetocrystalline anisotropy is considered with easy axes aligned along the crystallographic directions [001], [010], and [100]. Based on XRD data, the crystallographic axis normal to the film surface is identified as $[0,1,1]$. Therefore, the anisotropy directions for each grain are randomly perturbed around these axes:

$$\begin{aligned}
&\theta = \pi \times r \\
&\vec{\mathbf{u}}_{\text{anis},1} = \big(\cos(\theta)(1+0.5a_1), \quad \sin(\theta)(1+0.5a_2), \quad 1\big) \\
&\vec{\mathbf{u}}_{\text{anis},2} = \big(\sin(\theta)(1+0.5a_2), \quad -\cos(\theta)(1+0.5a_1), \quad 0\big) \\
&\vec{\mathbf{u}}_{\text{anis},3} = \vec{\mathbf{u}}_{\text{anis},1} \times \vec{\mathbf{u}}_{\text{anis},2}
\end{aligned} \tag{4.14}$$

where r is a random number uniformly distributed between 0 and 1, and a_1 and a_2 are random variables drawn from a normal distribution $\mathcal{N}(0,1)$, introducing slight grain-to-grain variations

[1] For numerical convenience, the thickness is rounded to the nearest multiple of 4 nm, matching the discretization cell size used in the simulations.

in the anisotropy orientation. The first-order cubic anisotropy constant $K_1 = 450\,\mathrm{kJ/metre^3}$ is adjusted to match the out-of-plane SQUID-VSM measurements and the micromagnetic configuration observed in the MFM measurement. Higher-order terms are neglected. The saturation magnetization is set to $M_s = 1880 \times 10^3\,\mathrm{A\,m^{-1}}$, based on experimental VSM-SQUID data. The exchange stiffness of the CoFe-based films is taken as $A = 20\,\mathrm{pJ\,m^{-1}}$, consistent with reported values for CoFe and CoFeB thin films [108], [109], [110] and within the typical range for magnetic thin films [94]. The intergranular exchange reduced by a factor of 10.
The full Mumax^3 configuration details are provided in the Appendix A. All simulations use a discretized 3D grid with a uniform cell size of $4\,\mathrm{nm} \times 4\,\mathrm{nm} \times 4\,\mathrm{nm}$.

Using the micro-magnetic simulation framework described above, we performed micromagnetic simulations with Mumax^3. These simulations yield equilibrium micromagnetic configurations that can be directly compared with MFM measurements (see Figure 4.5).

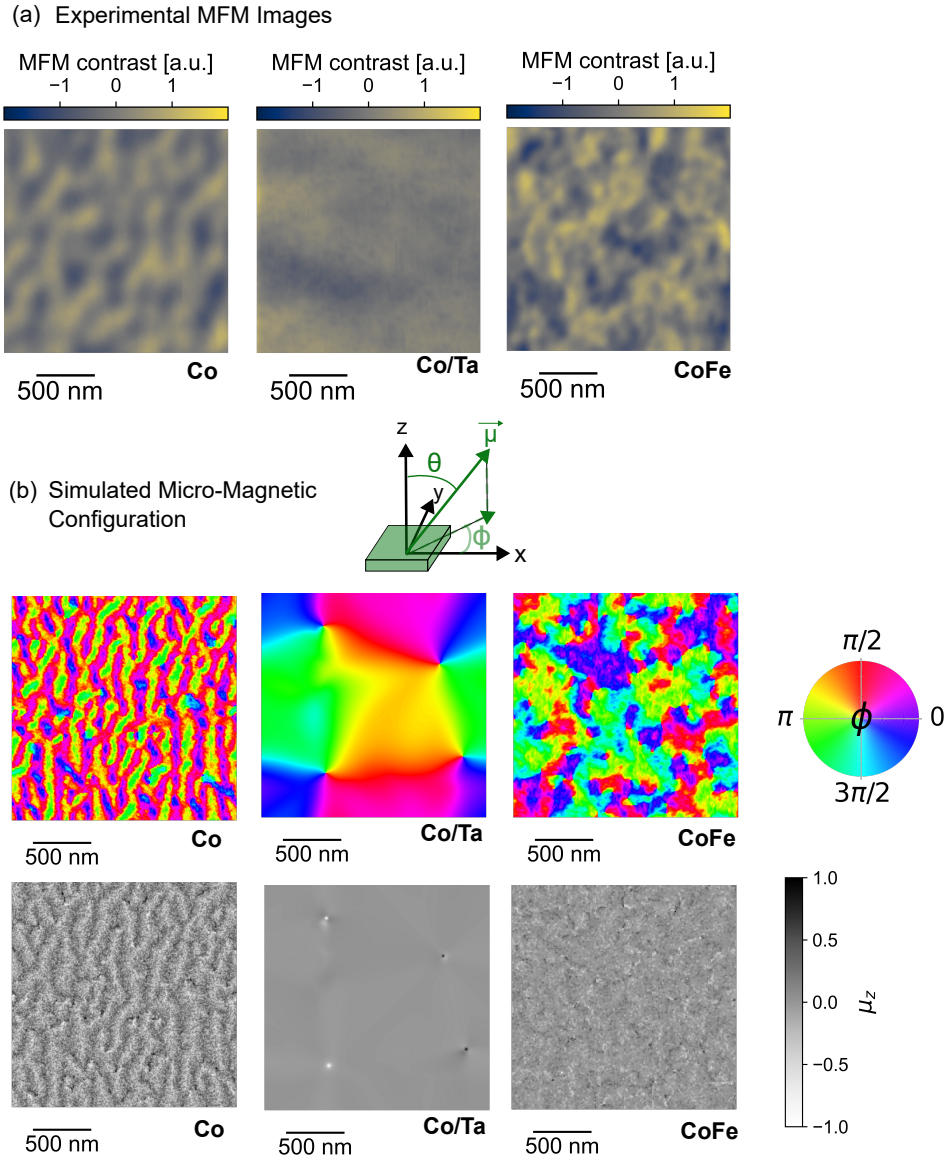

Figure 4.5: **Comparison between the MFM scans and the micromagnetic configurations from MuMax3 simulations at remanence**
(a) MFM scans of the thin films.
(b) Simulated micromagnetic configurations at the top surface of the corresponding films . Top panels: in-plane magnetization orientation, the color bar gives the azimuthal angle of the unit magnetization $\vec{\boldsymbol{\mu}} = \vec{\mathbf{M}}/M_s$. Bottom panels: out-of-plane magnetization component $\mu_Z = M_z/M_s$.

Additionally, they allow simulation of the magnetization response under an applied external magnetic field, enabling direct comparison with SQUID-VSM data, see Fig. 4.6. In particular, we simulated the average out-of-plane magnetization as a function of a magnetic field applied perpendicular to the film plane. The simulated results show good overall agreement with the experimental measurements.

It should be noted that in-plane SQUID-VSM measurements were not simulated. The coercive field in in-plane geometry is strongly influenced by factors that are difficult to capture in micromagnetic simulations, such as dislocations, structural defects affecting domain nucleation, and thermal agitation that facilitates domain wall motion. As such, accurate modeling of the in-plane coercive field remains beyond the scope of this approach.

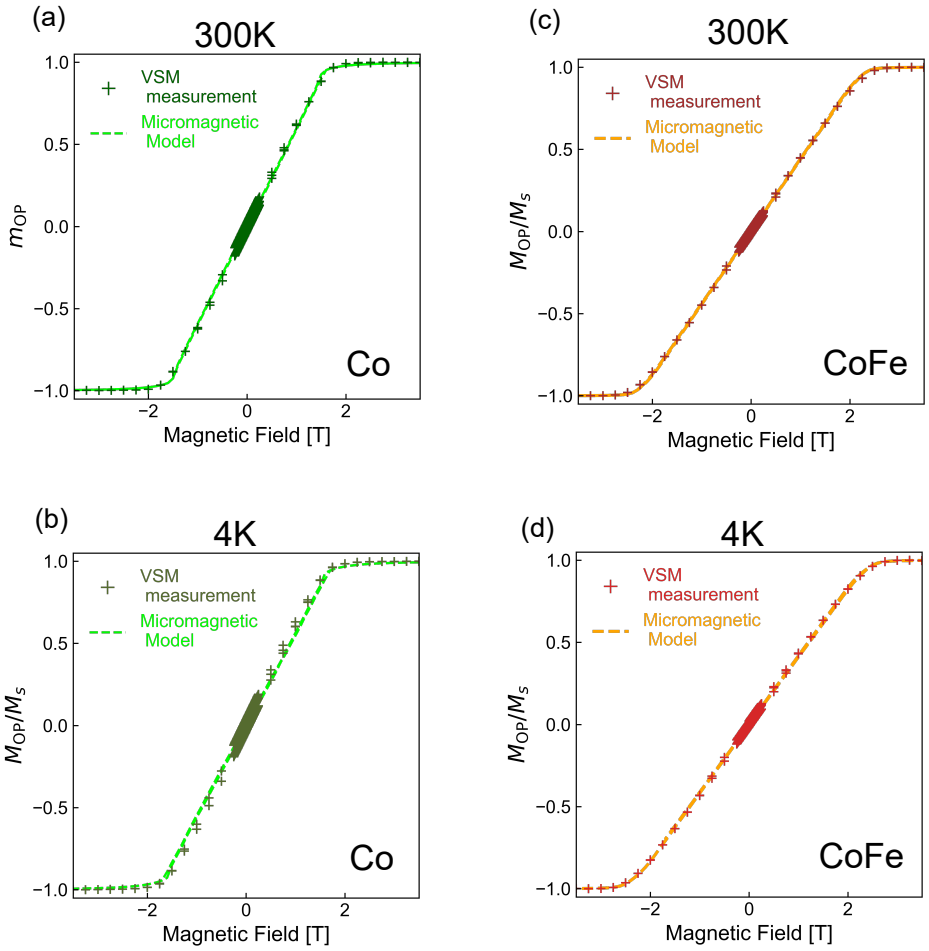

Figure 4.6: **Comparison between out-of-plane magnetization measured by SQUID-VSM and simulated out-of-plane magnetization from micromagnetic simulations**
(a-b) Room-temperature ($T = 300\,\mathrm{K}$) and low-temperature ($T = 4\,\mathrm{K}$) out-of-plane magnetization of the Cobalt thin film, compared with the simulated out-of-plane magnetization for the same film using the parameters detailed in Sec. 4.1.4.
(c-d) Same as (a-b), but for the CoFe thin film.

Adapting the simulation framework at low temperature

Interestingly, the micromagnetic models described above can be adapted to simulate behavior at **low temperature** by modifying the input parameters according to both experimental measurements at ~ 4 K and theoretical expectations. Specifically, the values of key micromagnetic parameters - such as the saturation magnetization and anisotropy constants - are updated to reflect their temperature dependence. The saturation magnetization values measured at low temperature for the three materials under study are presented in Table 4.6.

Table 4.6: Saturation magnetization (M_s) and first-order anisotropy constant (K_1) for the low temperature micro-magnetic simulations for the different materials studied.

Magnetic Material	M_s (*From the SQUID-VSM measurements*)	K_1
Co	$1550 \times 10^3\,\mathrm{A\,m^{-1}}$	$600\,\mathrm{kJ\,m^{-3}}$
Co/Ta	$950 \times 10^3\,\mathrm{A\,m^{-1}}$	
CoFe	$2000 \times 10^3\,\mathrm{A\,m^{-1}}$	$550\,\mathrm{kJ\,m^{-3}}$

For the variation of the anistropy constant with temperature, it is expectedd that magneto-crystalline anisotropy constants increase as temperature decreases [71] . For cobalt thin films, a uniaxial anisotropy constant on the order of $700\,\mathrm{kJ\,m^{-3}}$ is expected at cryogenic temperatures [111]. In our study, to achieve the best agreement with the measured out-of-plane SQUID-VSM magnetization curve, the uniaxial anisotropy constant in the micromagnetic model was set to $600\,\mathrm{kJ\,m^{-3}}$, see Fig. 4.6.
In the case of the CoFe alloy, the cubic magneto-crystalline anisotropy constant K_1 is once again adjusted to reproduce the out-of-plane magnetization behavior measured by SQUID-VSM (see Fig. 4.6).

This approach ensures consistency between the micromagnetic model and the experimental data across temperature regimes.

Toward comparing the model with magnet-scale characterization

While the micromagnetic model has been compared with thin-film-level characterizations, we also aim to validate it at the **magnet scale**. To this end, magnetic force microscopy (MFM) measurements can be performed above the surface of the microfabricated magnets. These measurements offer the advantage of local spatial resolution but provide primarily qualitative insights into the magnetization distribution.
Performing SQUID-VSM measurements at the scale of a single micro-magnet presents several challenges. First, the sensitivity of the instrument is insufficient for detecting signals from an individual micro-magnet. Second, SQUID-VSM provides only the average magnetization over the sample volume, whereas in the case of micro-magnets, the most relevant contribution to the external magnetic field arises from the surface magnetic poles located near the magnet edges.
The central challenge is thus to apply a measurement technique that offers both sufficient sensitivity and spatial resolution at the scale of individual magnets - without perturbing the intrinsic magnetic configuration. This will be the focus of the next section.

4.2 Characterization of individual magnets

Geometry and structure of the micro-magnets

The geometry of the micro-magnet was determined through numerical optimization, as detailed in the previous chapter, with the goal of maximizing the anti-symmetric magnetic field generated by the structure. The design consists of two parallel ractangles facing each other, separated by a fixed distance of 500 nm. Each rectangle has a width of 1 µm.

4.2.1 Fabrication process of the micro-magnets

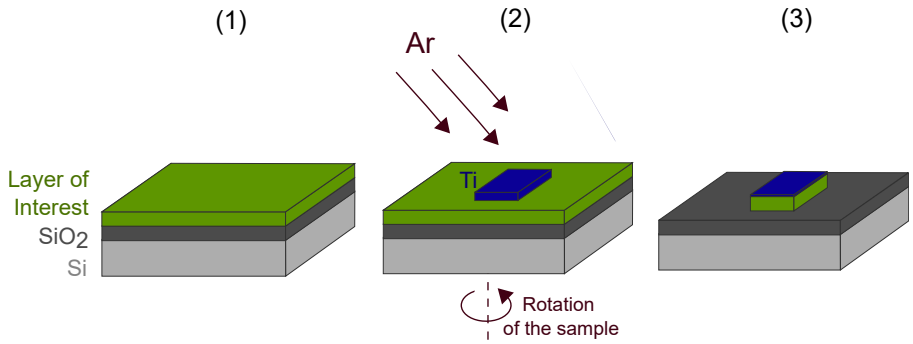

Figure 4.7: **Schematic of the micro-magnet nanofabrication process**
A thin magnetic film is deposited on the substrate. A titanium hard mask is then used for argon ion etching to define the magnet geometry.

The micro-magnets were fabricated using a subtractive patterning approach involving dry etching techniques. A schematic of the nano-fabrication process is presented Fig. 4.7.

The process begins with the deposition of a thin-film magnetic stack onto a Si/SiO_2 substrate. This stack includes a 5 nm Tantalum adhesion layer, followed by the magnetic material of interest, and is capped with a 5 nm Platinum layer to prevent oxidation.

To define the geometry of the micro-magnets, a Titanium hard mask is used. This mask is created through a lift-off process following electron beam lithography. A bilayer positive resist stack consisting of (PMMA/MA)/PMMA is spin-coated on the substrate. After exposure and development, the resist is removed in regions corresponding to the magnet structures. The bilayer resist system creates an undercut profile, which facilitates clean lift-off after metal deposition.
Titanium is then deposited onto the patterned resist, and the remaining resist is lifted off, leaving behind a Titanium mask that precisely defines the desired micro-magnet pattern.

The final fabrication step is the anisotropic dry etching of the magnetic stack using ion beam etching (IBE) with an Argon ion source. The ion beam is accelerated, focused, and neutralized before impinging on the sample surface. When the energy of the ions is sufficient, atoms from the sample are sputtered away. The etching characteristics are highly sensitive to the angle of incidence of the ion beam, which affects both the etch rate and the etching profile. To minimize re-deposition and the formation of ridges on the sidewalls, an optimized angle of 10° is used.

Etch progress is monitored in real-time via mass spectrometry, which detects species sputtered from the surface (see Fig.4.8 and Fig.4.9). This allows precise identification of the transitions between layers-Tantalum, the magnetic layer, and Platinum. To ensure complete removal of magnetic material, especially in the inter-rectangle spacing, the etching process is extended slightly beyond the point at which the Tantalum adhesion layer is fully removed.

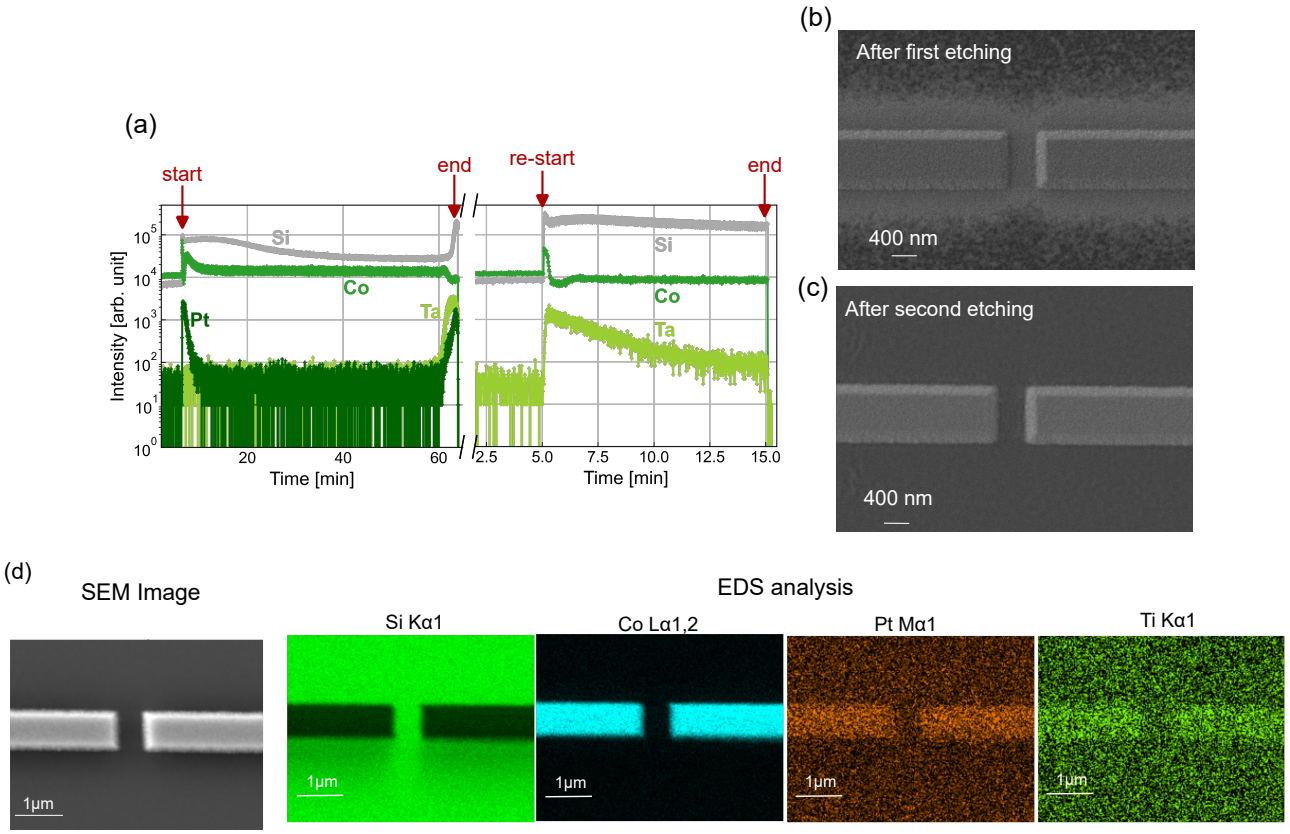

Figure 4.8: **Nanofabrication process of the cobalt magnet**
(a) Real-time monitoring of cobalt etching by mass spectrometry. The signal intensity of a given chemical species increases when that material is being etched, enabling real-time tracking of the etching of the different layers in the stack.
(b-c) SEM images acquired during the etch process. The process was stopped to take image (b) and then resumed and image (c) was recorded after the second etch step.
(d) EDS analysis was used to identify the elements in the stack. The corresponding SEM image of the analyzed area is shown. The color intensity in the EDS maps represents the emission strength of the characteristic X-ray lines (Kα, Lα or Mα) from the detected elements (Si, Co, Pt, Ti).

Titanium is chosen as the hard mask material due to its low etch rate under the IBE conditions used (approximately 0.64 nm min^{-1} [103]), which allows the use of a relatively thin mask-45 nm for Cobalt samples, and 65 nm for Cobalt-Iron and Cobalt-Tantalum samples.

Post-fabrication characterization

Following fabrication, the micro-magnet structures are characterized using scanning electron microscopy (SEM) and energy-dispersive X-ray spectroscopy (EDS) (see Fig.4.8 and Fig.4.9). EDS identifies the elemental composition by detecting X-rays emitted from the sample when bombarded by an electron beam. When inner-shell electrons are ejected, higher-energy electrons fall into the vacancy, emitting X-rays with characteristic energies unique to each element. The EDS detector measures both the energy and intensity of these emissions.
EDS scans can be performed to verify that all magnetic material outside the defined magnet structures has been completely removed, and to confirm that the full stack (Ta / Magnetic Material / Pt) remains intact within the patterned regions. The EDS results for the cobalt magnet are shown in Fig. 4.8.

Additionally, atomic force microscopy (AFM) is used to assess the surface topography and measure film thicknesses (see Fig. 4.10). This provides further confirmation that the fabricated structure matches the intended dimensions.

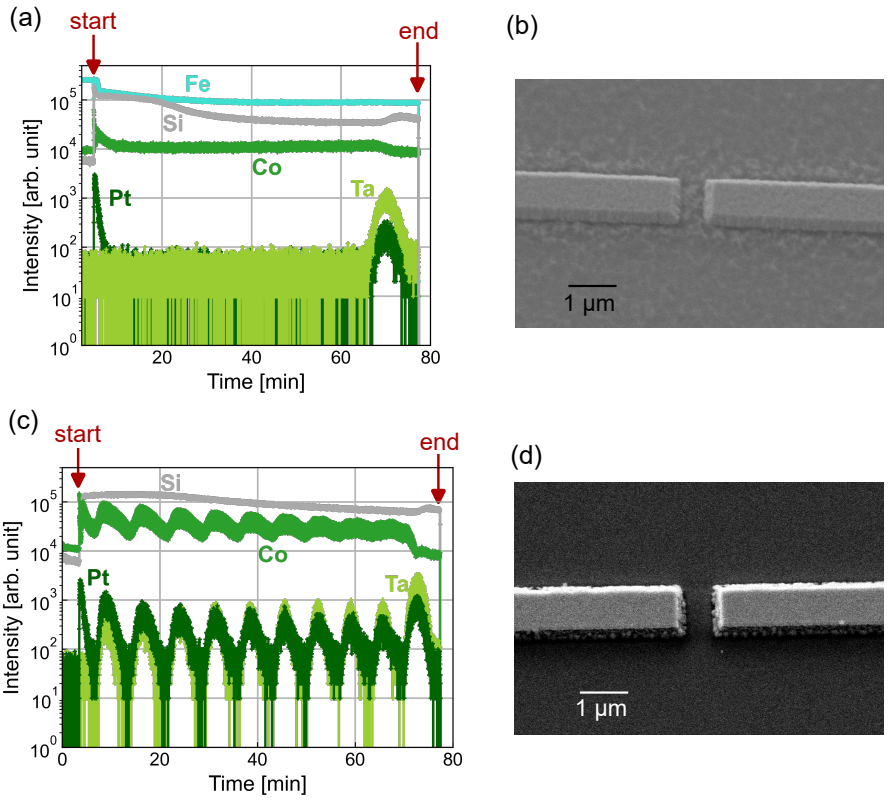

Figure 4.9: **Nanofabrication process of the cobalt-iron and cobalt-tantalum magnets**
(a) Real-time monitoring of cobalt-iron etching by mass spectrometry.
(b) SEM image of the cobalt-iron magnet acquired after the etching process.
(c-d) Same as (a-b), but for the cobalt-tantalum magnet.

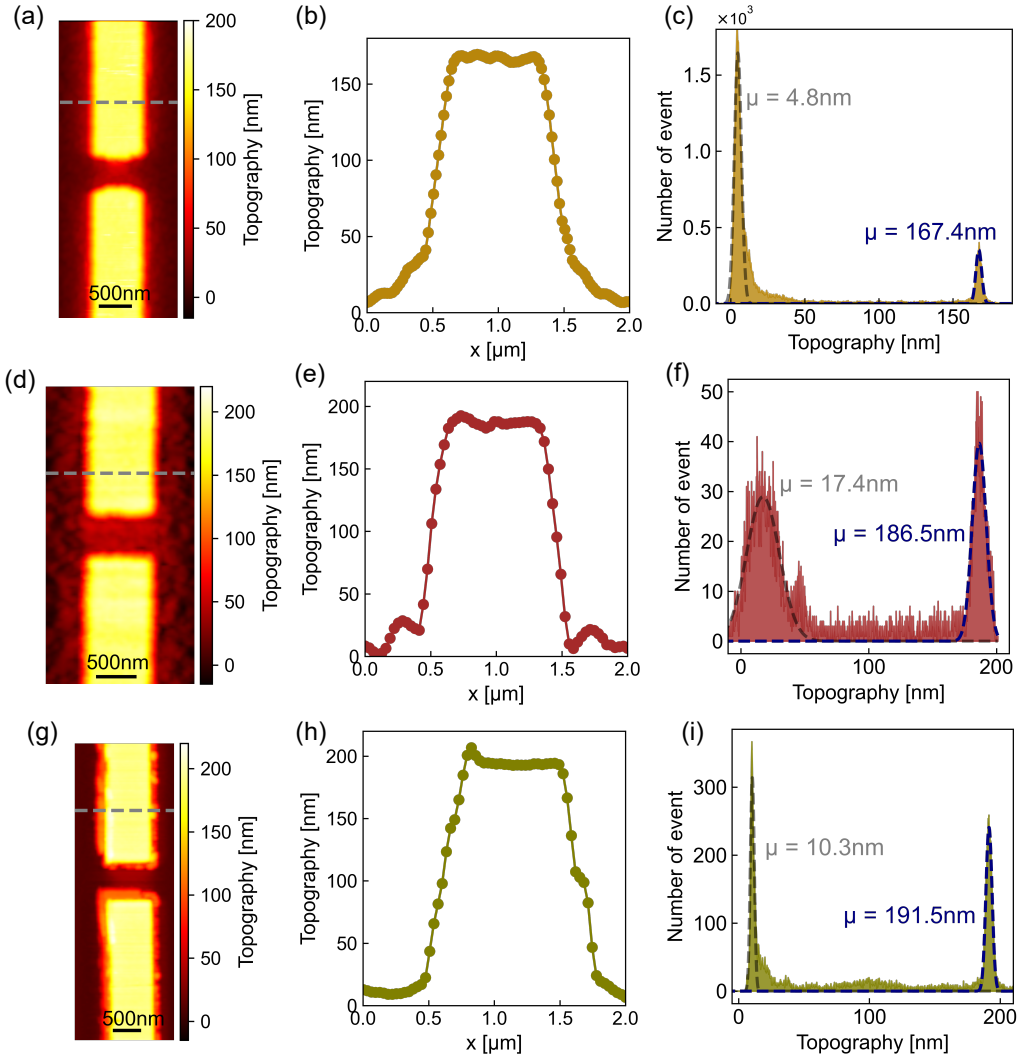

Figure 4.10: **AFM measurements to assess the magnet topography**
(a) AFM topography of the cobalt magnet.
(b) Line profile along the dashed path in (a).
(c) Height analysis of (a); the peak distributions are fitted with Gaussians. The total stack thickness is obtained by subtracting the mean height of the substrate peak from that of the magnet peak. The cobalt magnet total stack (Ta/Co/Pt/Ti residual mask) is 162.6 nm.
(d-f) Same analysis as (a-c) for the cobalt-iron magnet. The measured total stack thickness of the magnet is 169.1 nm.
(g-i) Same analysis as (a-c) for the cobalt-tantalum magnet. The measured total stack thickness of the magnet is 181.2 nm.

4.2.2 Magnetic Force Microscopy: local qualitative mapping of the distribution of the magnetization

Magnetic force microscopy (MFM) is sensitive to local variations of the magnetic field. The resulting two-dimensional scans reveal local inhomogeneities in the magnetic configuration within the micromagnet, arising both from magnetization divergence in the bulk and from magnetic poles at the magnet edges.

MFM measurements can be performed both at remanence (see Fig. 4.11) and under an applied external magnetic field aligned along the length of the magnet (see Fig. 4.12).

Magnetization at remanence

At remanence-i.e., after the magnets have been saturated and the external magnetic field has been reduced to zero-we observe that shape anisotropy alone is insufficient to completely suppress the formation of magnetic domains.
Stripe-like contrasts, indicative of domain structures, remain visible along the length of the magnet composed of pure Cobalt.

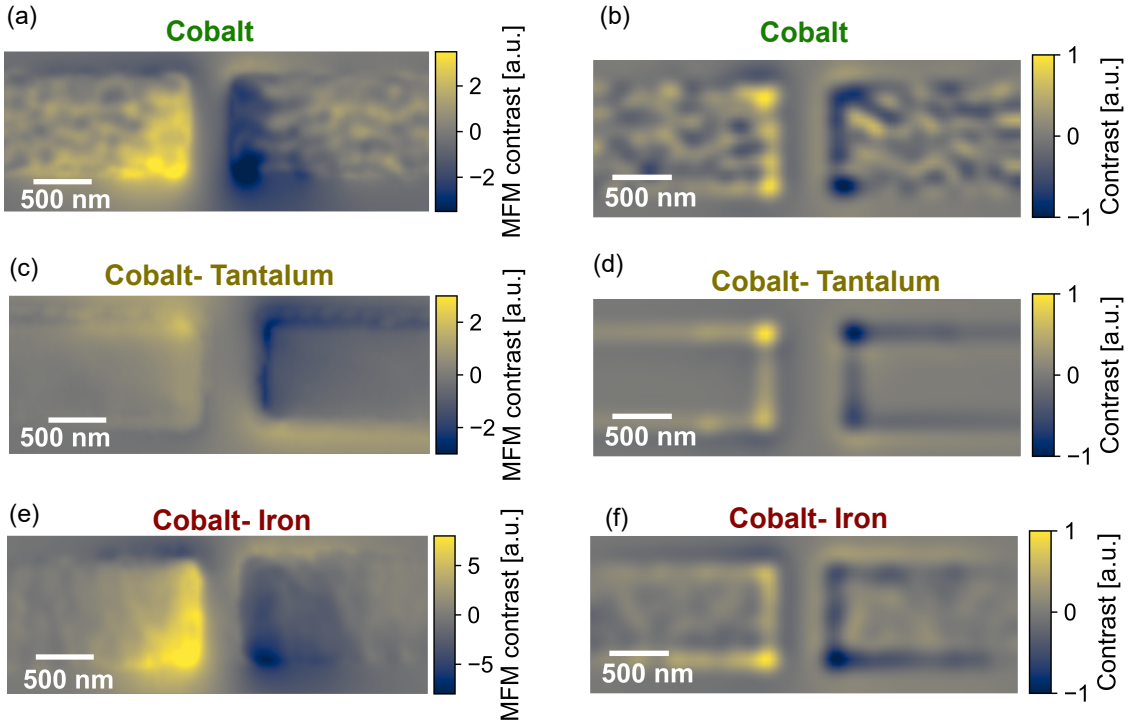

Figure 4.11: **Measured and simulated MFM scans at remanence for different magnet materials**
MFM scans acquired at zero applied field - after first applying a magnetic field of a few hundred millitesla along the long axis of the magnets (along the x-direction).
(a,c,e) Experimental MFM images, (b,d,f) corresponding simulated contrasts.
The simulated MFM contrast is computed from the second derivative (along z) of the stray field. Because the tip's magnetic moment seems not perfectly out-of-plane - particularly evident in Fig. 4.12, despite prior initialization with a magnet - the simulation includes a finite in-plane sensitivity. Accordingly, the reported contrast is $\frac{\partial^2 H_d^y}{\partial z^2} + \frac{\partial^2 H_d^z}{\partial z^2}$ (from Eq. (2.55)), convolved with a Gaussian to account for the finite tip response during imaging.

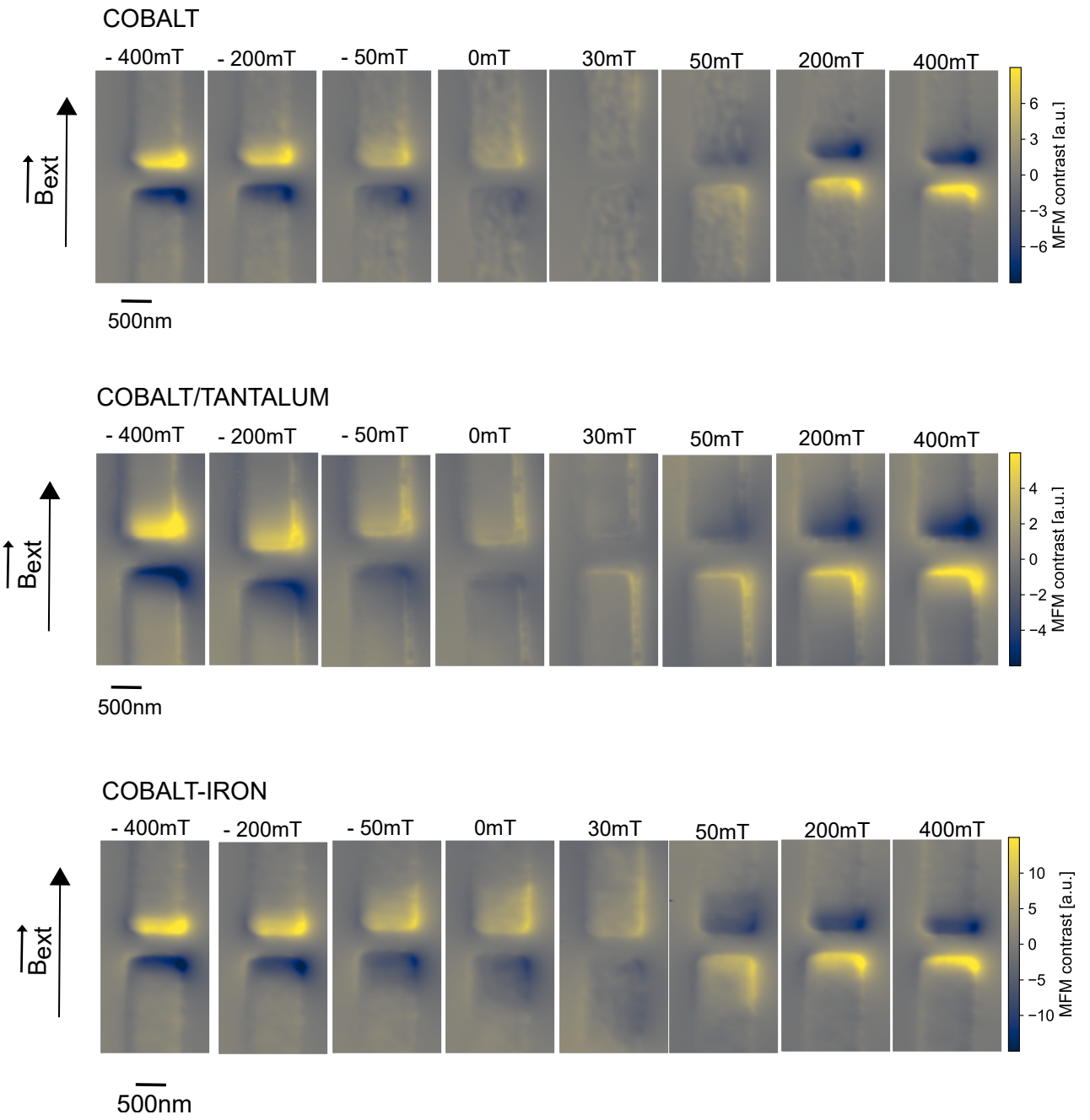

Figure 4.12: **MFM scans under varying external magnetic-field amplitudes**
MFM images acquired while varying the amplitude of an external field applied along the magnet's long axis for the three magnets studied. At high fields, the magnetic contrast appears asymmetric, which could be associated with a finite in-plane component of the MFM tip's magnetic moment (along the in-plane direction transverse to the magnet's long axis).

For the magnet made of Cobalt-Tantalum multilayer, minimal contrast is observed along the magnet, suggesting a nearly homogeneous magnetization along its length. However, some contrast appears at the rectangle ends, which likely originates from surface magnetic poles and potential domain closure structures near the edges.

In contrast, the Cobalt-Iron magnet exhibits stronger magnetic contrast, implying a larger size of closure domains at the magnet's ends. This observation is consistent with the higher saturation magnetization measured for Cobalt-Iron.

To further interpret these results, micromagnetic simulations based on the models developed in the previous section can be used to compute the remanent magnetization distribution. From

this, the stray magnetic field and its spatial derivatives can be calculated, enabling simulation of the expected MFM contrast. These results, shown in Figure 4.11, demonstrate good qualitative agreement between the measured and simulated magnetic configurations.

Magnetization under an external magnetic field

By sweeping an external magnetic field along the long axis of the magnet, we observe the evolution of the magnetic contrast in the MFM images, see Fig. 4.12.This serves two purposes:

- It confirms that the observed contrast originates from magnetic effects.
- It allows identification of key magnetic parameters such as the saturated regime and the coercive field at which magnetization reversal occurs.

Although MFM provides only qualitative data and does not yield absolute field values, it offers valuable insights into the field ranges relevant for device operation.

It is important to note that all MFM measurements were conducted at room temperature. At lower temperatures, slight modifications in the observed magnetic configuration are expected. In particular, a shift in the coercive field is anticipated, as indicated by the results of thin-film magnetic characterizations.

While MFM offers qualitative validation of our micromagnetic model, it does not allow for direct, quantitative measurement of the magnetic field produced by the magnet. For that purpose, we turn to NV center magnetometry.

4.2.3 NV center sensor: local quantitative mapping of the magnet's stray field

In this section, we describe the working principle of NV center magnetometry and how a microscope based on NV centers enables high-precision, local measurements of the magnetic field generated by micro-magnets.

The NV center: a nanoscale magnetic field sensor

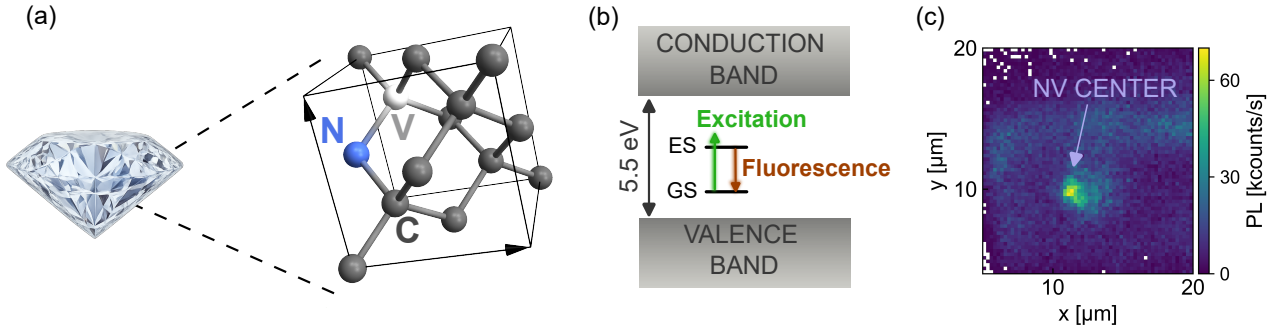

Figure 4.13: **Structure and optical properties of the NV center**.
(a) Schematic NV center crystal structure. The NV center axis is the line connecting the nitrogen atom and the vacancy (b) Diamond is a semiconductor with large bandgap. The schematics shows the ground state and excited state of the NV colored center between which optical transition can be induced. (c) Confocal scan: a green excitation laser ($\lambda = 532\,\text{nm}$) is scanned across the AFM tip, and the corresponding photoluminescence (PL) signal is recorded. The bright spot indicates the location of a single NV center.

Diamond consists of a tetrahedral lattice of carbon atoms giving it exceptional mechanical hardness and thermal conductivity. It is widely used in industrial application (e.g., cutting, grinding, drilling). Diamond is also widely used in fine jewelry due to its rarity and brilliance. It is a wide-bandgap semiconductor ($E_g = 5.5\,\text{eV}$), transparent from the ultraviolet to the far-infrared,

making it a suitable host for optically active defects with energy levels lying within the bandgap [112].

Among these defects, the **nitrogen-vacancy (NV) center** has attracted particular interest due to its spin-dependent optical properties. The NV center consists of a substitutional nitrogen atom replacing a carbon atom and a neighboring vacancy, see Fig. 4.13.

NV centers predominantly exist in two charge states: the neutral state (NV^0) and the negatively charged state (NV^-), the latter formed by the capture of an extra electron from a donor in the lattice. Only the negatively charged NV center exhibits spin dependent optical properties, and it is this charge state - referred to simply as the NV center in the following - that is used for magnetometry.

The NV center can be viewed as an artificial atom, with electronic states lying deep within the diamond bandgap (see Fig. 4.13). It possesses a ground state and an excited state connected by an optical dipole transition with a zero-phonon line (ZPL) at 1.945 eV (corresponding to a wavelength of 637 nm). Excitation is typically performed off-resonance using a green laser at 532 nm.

The electronic configuration of the NV^- center includes six electrons: three from carbon dangling bonds, two from the nitrogen atom, and one additional electron. Of these, two remain unpaired, resulting in a spin-1 system for both the ground and excited states. These spin states are split by spin-spin interaction into three sublevels: $|m_s = 0\rangle$ and $|m_s = \pm 1\rangle$. The quantization axis of the NV center is defined by the line connecting the nitrogen atom and the vacancy. In the absence of an external magnetic field, the $|m_s = \pm 1\rangle$ levels of the ground state are degenerate and separated from the $|m_s = 0\rangle$ state by $D = 2.87\,\text{GHz}$.

Excitation of the NV center from the ground to the excited state results in fluorescence via two possible decay paths (Fig.4.14):

- **Radiative decay**, producing broadband red photoluminescence;
- **Non-radiative decay** via a spin-selective intersystem crossing to a metastable state.

While optical transitions conserve spin ($\Delta m_s = 0$), non-radiative decay through the metastable state is more likely for the $|m_s = \pm 1\rangle$ states. Consequently, these states emit less fluorescence and are referred to as **dark states**, whereas the $|m_s = 0\rangle$ state is a **bright state** due to its higher radiative decay probability. Relaxation from the metastable state predominantly returns the system to $|m_s = 0\rangle$, enabling optical spin polarization under continuous laser excitation.

Optical pumping of the NV center, combined with spin-state-dependent photoluminescence, enables **optically detected magnetic resonance (ODMR)** measurements on a single NV center [113], see Fig.4.14. This is made possible by the high photostability of the NV center, as it exhibits minimal blinking or photobleaching under continuous illumination. In this scheme, the NV center is optically pumped into the $|m_s = 0\rangle$ ground state while a microwave field is applied. When the microwave frequency matches the energy difference between $|m_s = 0\rangle$ and $|m_s = \pm 1\rangle$, spin transitions are induced, increasing non-radiative decay and thereby reducing the observed photoluminescence. By monitoring the fluorescence while sweeping the microwave frequency, dips appear at the **electron spin resonance (ESR)** frequencies, $f_\pm$.

In zero external magnetic field, a single resonance is observed at $f_\pm = D \approx 2.87\,\text{GHz}$, see Fig.4.14. When an external magnetic field is applied along the NV axis, the degeneracy of the $|m_s = \pm 1\rangle$ levels is lifted due to the Zeeman effect, resulting in two distinct resonance frequencies. These frequency shifts are directly proportional to the local magnetic field component along the NV axis, allowing quantitative extraction of the magnetic field at the nanoscale.

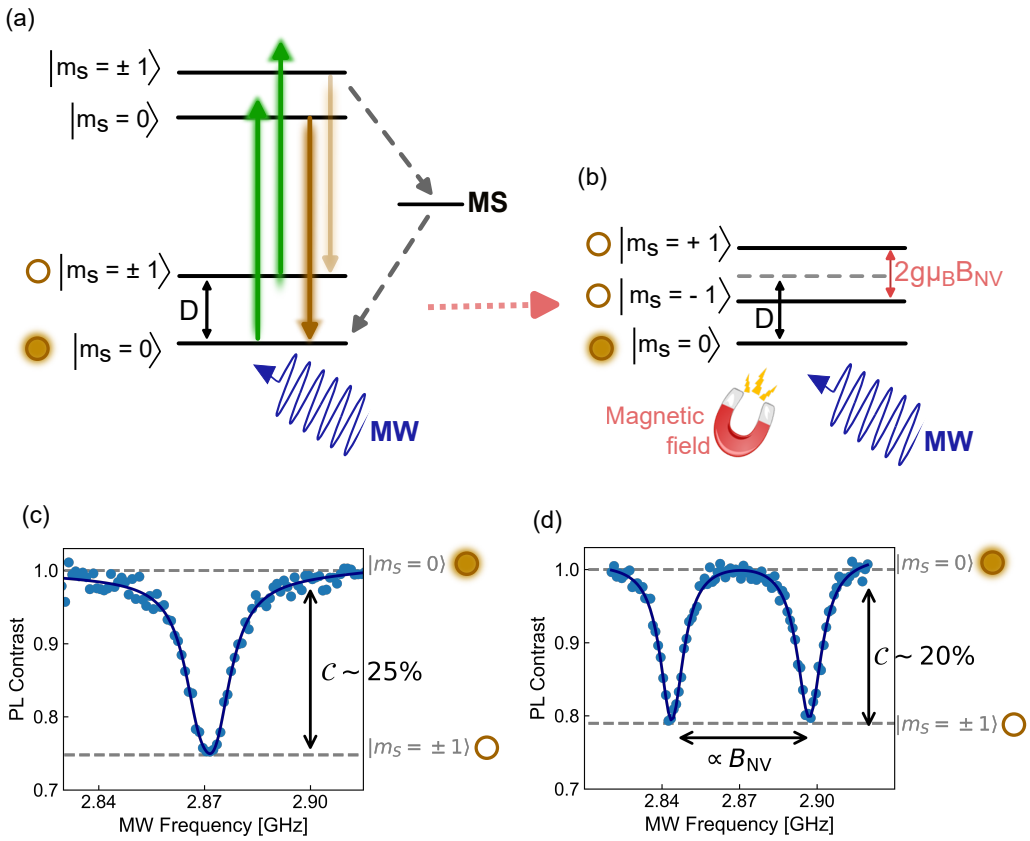

Figure 4.14: **Energy diagram and principle of ODMR**.
(a) Schematic representation of the NV center energy levels. Both the ground and excited states are spin-1 systems. Optical transitions between these states conserve the spin projection m_s along the NV center axis. The green line is the excitations at 532 nm while the orange line is the photoluminescence emitted by the center. A non-radiative, spin-non-conserving decay pathway via a metastable singlet state (MS) also exists.
(b) Splitting of the ground state spin sublevels under the application of an external magnetic field due to the Zeeman effect.
(c) Typical ODMR spectrum measured at zero magnetic field: the photoluminescence is measured as a function of the applied microwave frequency. Strain in the diamond lattice can cause a splitting between the two resonance frequencies, characterized by the parameter E. In this case, the strain-induced splitting is not resolved, as it lies below the full width at half maximum (FWHM) of the resonance dip, estimated at 10 MHz. The linewidth of the NV resonance depends not only on intrinsic properties of the defect but also on experimental parameters such as excitation and microwave power; no specific optimization of these parameters was performed in our measurements. The zero-field splitting parameter D, corresponding to the transition frequency between the $|m_s = 0\rangle$ and $|m_s = \pm 1\rangle$ states in the absence of magnetic field and strain, is measured to be $D = 2.873$ GHz. The photoluminescence contrast is about 25%.
(d) ODMR spectrum acquired under an external magnetic field of $B_{\mathrm{NV}} = 2$ mT aligned with the NV axis. The FWHM of the resonance dip remains 10 MHz, and the photoluminescence contrast is approximately 20%.

NV Center response to an external magnetic field

For magnetic sensing applications, it is essential to understand how the electron spin resonance (ESR) frequencies of the NV center depend on both the magnitude and orientation of an external magnetic field.

Spin Hamiltonian and energy Levels

To describe this behavior, we examine the NV center's ground-state Hamiltonian. Neglecting hyperfine interactions with nearby nuclear spins and nuclear Zeeman terms, the Hamiltonian can be expressed as:

$$H_{\mathrm{NV}} = hD\hat{\mathbf{S}}_z^2 + hE\left(\hat{\mathbf{S}}_x^2 + \hat{\mathbf{S}}_y^2\right) + g\mu_B\,\vec{\mathbf{B}}\cdot\vec{\mathbf{S}} \tag{4.15}$$

Here, h is Planck's constant, μ_B is the Bohr magneton, $g \approx 2$ is the electron spin g-factor, and $\hat{\mathbf{S}}_i$ (for $i \in \{x, y, z\}$) are spin-1 operators acting on the basis states $\{+1, 0, -1\}$:

$$\hat{\mathbf{S}}_x = \frac{1}{\sqrt{2}}\begin{pmatrix} 0 & 1 & 0 \\ 1 & 0 & 1 \\ 0 & 1 & 0 \end{pmatrix} \quad \hat{\mathbf{S}}_y = \frac{1}{\sqrt{2}}\begin{pmatrix} 0 & -i & 0 \\ i & 0 & -i \\ 0 & i & 0 \end{pmatrix} \quad \text{and} \quad \hat{\mathbf{S}}_z = \begin{pmatrix} 1 & 0 & 0 \\ 0 & 0 & 0 \\ 0 & 0 & -1 \end{pmatrix}$$

The zero-field splitting parameters $D \approx 2.87\,\mathrm{GHz}$ and E originate from spin-spin interaction and local lattice strain, respectively. While D defines the energy separation between $|m_s = 0\rangle$ and $|m_s = \pm 1\rangle$, the transverse parameter E causes additional splitting and typically ranges from 100 kHz to 10 MHz, depending on the strain in the diamond matrix.
In the Hamiltonian Eq. (4.15), the NV center axis is assumed to be aligned with the z-axis.

By diagonalizing the Hamiltonian in Eq. (4.15), the ESR transition frequencies $f_\pm$ (with f_+ being the higher and f_+ the lower of the two) can be obtained for any external magnetic field $\vec{\mathbf{B}}$.

Zero magnetic field regime

In the absence of an external magnetic field, the resonant frequencies are given by:

$$f_\pm = D \pm E \tag{4.16}$$

Thus, an ODMR measurement in zero field allows extraction of the zero-field splitting parameters D and E. In nanodiamonds, high internal strain can lead to relatively large values of E, often on the order of 5 MHz.

Magnetic field dependence

When an external magnetic field is present, the Zeeman term in Eq. (4.15) can be decomposed into components parallel and perpendicular to the NV axis:

$$H_{\mathrm{NV}} = hD\hat{\mathbf{S}}_z^2 + hE\left(\hat{\mathbf{S}}_x^2 + \hat{\mathbf{S}}_y^2\right) + \underbrace{g\mu_B B_\parallel \hat{\mathbf{S}}_z}_{H_{Z,\parallel}} + \underbrace{g\mu_B\left(B_x\hat{\mathbf{S}}_x + B_y\hat{\mathbf{S}}_y\right)}_{H_{Z,\perp}} \tag{4.17}$$

When the transverse magnetic field is weak, $B_\perp = \sqrt{B_x^2 + B_y^2} \ll \frac{hD}{g\mu_B}$, the ESR frequencies are given by:

$$f_\pm = D \pm \sqrt{\left(\frac{g\mu_B}{h}B_\parallel\right)^2 + E^2} \tag{4.18}$$

Two distinct regimes can be identified:

- **Low field regime**:
  For $B_\parallel \leq \frac{hE}{g\mu_B}$, the ESR frequencies evolves quadratically with the external magnetic field. If the strain-induced parameter E is too large - i.e. $\frac{hE}{g\mu_B} \gg B_\parallel$ - the NV center becomes insensitive to small magnetic fields. This limitation can be overcome by applying a bias field $B_{\parallel,\mathrm{bias}} \gg \frac{hE}{g\mu_B}$.

- **High field regime**:
  When $B_{\parallel} \gg \frac{hE}{g\mu_B}$, tthe ESR frequencies vary linearly with the field, see Fig.4.15(a-b):

$$f_{\pm} = D \pm \frac{g\mu_B}{h} B_{\parallel} \tag{4.19}$$

When the transverse field becomes significant ($B_{\perp} \geq \frac{hD}{g\mu_B}$), the eigenstates of the system no longer align with the original m_s basis, and m_s ceases to be a good quantum number. In this regime, the ESR frequencies deviate asymmetrically from D, and their dependence on the external magnetic field becomes more complex, see Fig.4.15(c-f).

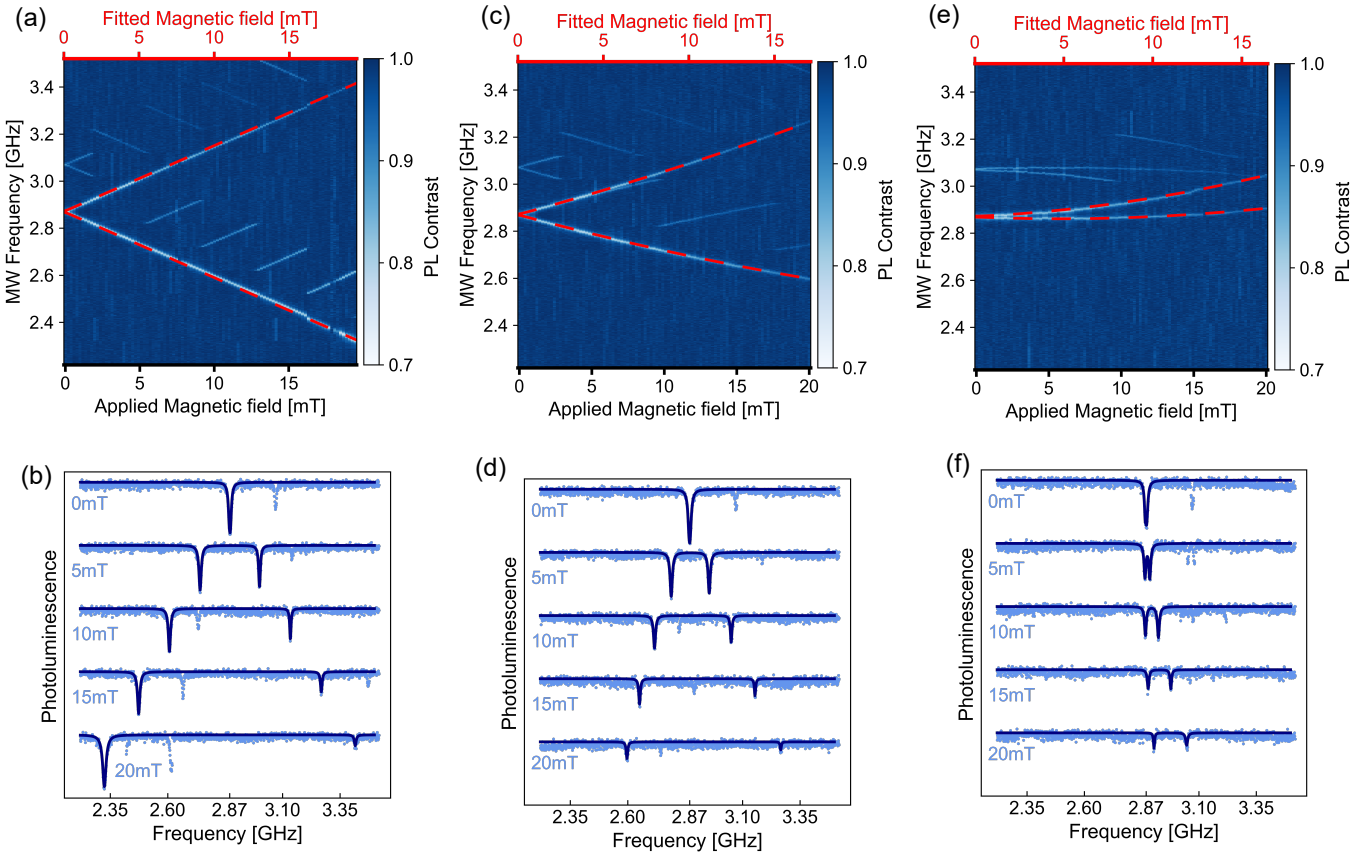

Figure 4.15: **ODMR spectra in different magnetic field regimes**.
(a), (b) Splitting of the ESR frequencies as a function of the magnetic field amplitude applied along the NV center axis. Panel (b) shows the corresponding Lorentzian fit of the ODMR dips.
(c), (d) ODMR spectra and fits for a magnetic field oriented at an angle of 45° with respect to the NV axis.
(e), (f) Same, but for a magnetic field applied perpendicular to the NV axis (90° orientation). In the transverse field configurations, the ESR frequencies become asymmetric with respect to the zero-field splitting parameter D, and the photoluminescence contrast is noticeably reduced due to spin state mixing.
For each orientation, the measured ESR frequencies are compared to those predicted from the NV center Hamiltonian [Eq. (4.15)]. The top red axis labeled “Fitted Magnetic Field” corresponds to the magnetic field amplitude that best reproduces the measured ESR frequencies using the theoretical model. For fields transverse to the NV axis, the magnetic field values (top red) appear lower than the applied ones - likely due to vector magnet miscalibration in transverse directions.
The "mirage" features observed in the ODMR spectra are artifacts caused by harmonics of the Arbitrary Waveform Generator (AWG) sidebands used to generate the microwave tone. The AWG carrier frequency is 100 MHz, resulting in spectral replicas spaced by 200 MHz.

In this case, the magnetic field amplitude B and its angle θ elative to the NV axis can be extracted from the measured ESR frequencies $f_\pm$ using the following expressions [114]:

$$\begin{aligned}\left(g\mu_B B\right)^2 &= \frac{1}{3}\left(f_+^2 + f_-^2 - f_+ f_- - D^2 - 3E^2\right) \\ \cos(2\theta) &= \frac{7D^3 + 2\left(f_- + f_+\right)\left(2\left(f_-^2 + f_+^2\right) - 5f_- f_+ - 9E^2\right) - 3D(f_+^2 + f_-^2 - f_- f_+ + 9E^2)}{9D\left(f_+^2 + f_-^2 - f_- f_+ - D^2 - 3E^2\right)}\end{aligned} \tag{4.20}$$

Hence, by measuring the full ODMR spectrum and knowing the zero-field splitting parameters D and E, it is possible to quantitatively determine both the amplitude and orientation of the magnetic field at the NV site.

Magnetic field imaging with a NV center sensor

Quantitative imaging of the stray magnetic field produced by the micro-magnet can be achieved by acquiring the full ODMR spectrum while scanning the sample beneath the NV sensor. At each spatial point, the two resonance frequencies are extracted, and the local magnetic field amplitude and orientation are computed using Eq. (4.20) - since the magnetic field generated by the magnet has components along all three spatial directions, including significant transverse components relative to the NV axis.

In our study, rather than reconstructing the magnetic field vector directly from the NV measurements, we take an alternative approach: the micromagnetic simulation framework developed in the previous section is used to simulate the expected magnetic field distribution. From this, we compute the corresponding NV center resonance frequencies at each spatial position using the full spin Hamiltonian given in Eq. (4.15). This allows for a direct comparison between the experimentally measured and theoretically predicted resonance frequencies.

In these measurements, the sensitivity of the NV center is not the limiting factor: commercially available diamond scanning tips report energy sensitivities below $\eta \leq 5\mu\text{eV}/\sqrt{\text{Hz}}$ [115]. Instead, the limitation arises from the maximum detectable magnetic field. Near the surface of the magnet, strong transverse magnetic field components induce spin-state mixing, which significantly alters the NV center's spin dynamics under optical illumination. As a result, optical spin polarization becomes inefficient, and the spin-dependent photoluminescence contrast diminishes. In such conditions, the ODMR signal can vanish entirely, rendering the ESR frequencies undetectable. This constitutes a well-known limitation of NV magnetometry. In practice, NV center measurements become increasingly challenging when the transverse magnetic field exceeds $B_\perp \geq 10\,\text{mT}$. To circumvent this, we performed our measurements at a larger distance from the sample surface, maintaining a stand-off height of at least $h \geq 600\,\text{nm}$.

It is worth noting that changes in the NV center's fluorescence properties under strong transverse magnetic fields can also be exploited for qualitative, all-optical magnetic field sensing. Specifically, increased non-radiative decay rates and reduced spin polarization lead to a global drop in photoluminescence, which can serve as an indicator of high transverse field regions. However, in this work, we chose not to pursue this qualitative approach and instead focused exclusively on quantitative magnetic field mapping via ODMR.

4.2.4 Scanning NV-magnetometry

Working principle of the NV Center Microscope

The measurements presented in this work were carried out using the Quantum Scanning Microscope developed by Qzabre. A schematic of the system if presented Fig. 4.16. The system consists of two key components:

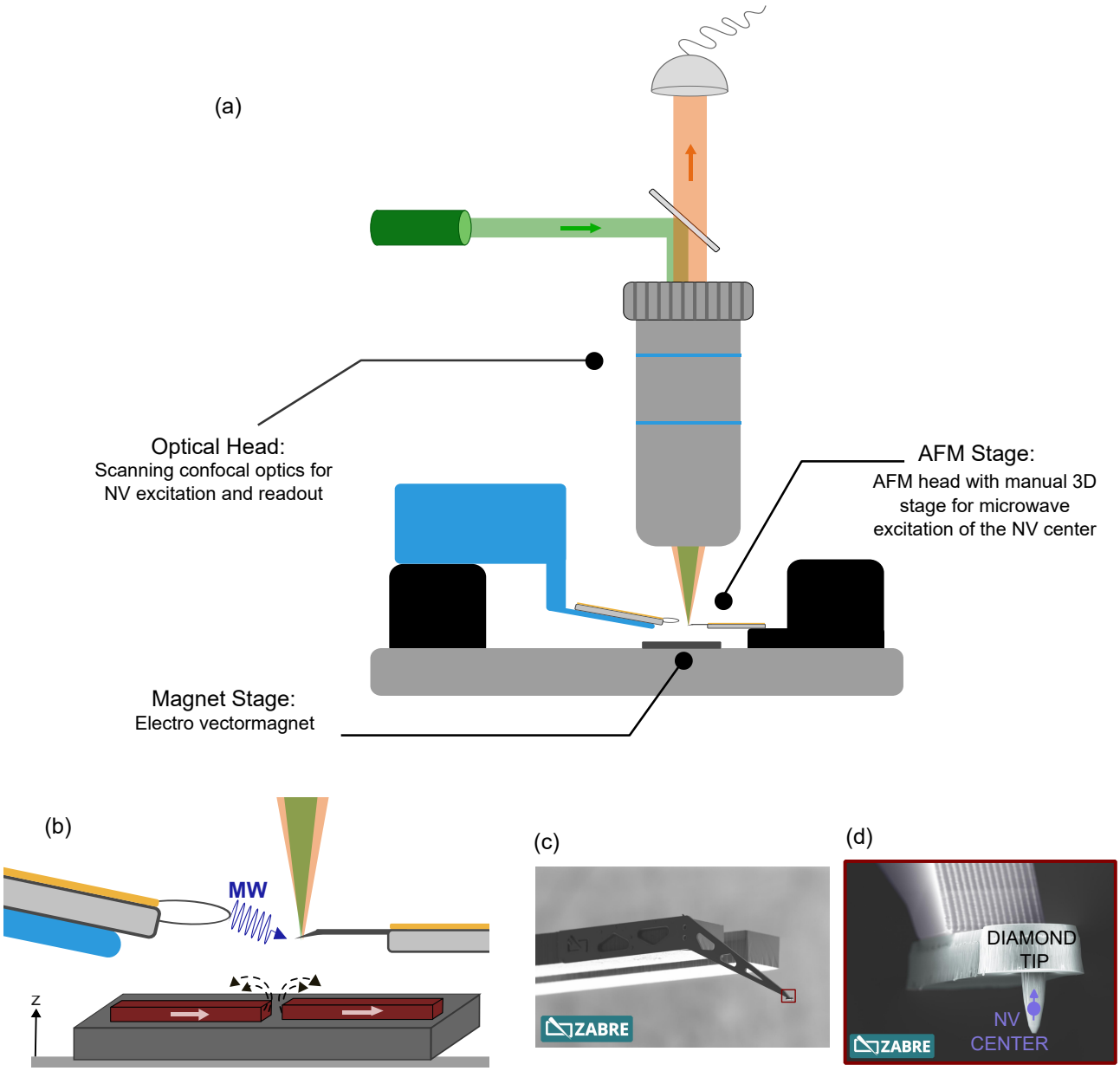

Figure 4.16: **NV-center microscope**
(a) Schematic of the NV-center microscope highlighting the key components.
(b) Enlarged view of panel (a). A microwave antenna placed near the NV center drives its spin transitions. As the NV tip scans across the magnet structure, the transition frequencies-shifted by the local magnetic field-are measured via ODMR.
(c,d) SEM images of the cantilever and the diamond tip hosting a single NV center. Images courtesy of Qzabre.

- An **AFM head and control unit** which enables surface topography acquisition (as detailed in Chapter 2) and is used here primarily to regulate the probe-to-sample distance. Although we do not employ it for topographical imaging in this study, it is essential for maintaining a stable and precise measurement height above the sample surface.
- A **confocal optical microscope**, which focuses a green laser onto the diamond tip containing the NV center. This enables optical spin polarization and allows the collection of NV photoluminescence for spin-state readout.

The NV sensor consists of a single negatively charged NV center located near the apex of a diamond scanning tip - typically within 10 nm of the surface per Qzabre specifications, though in some tips

it can be as far as 80 nm to 90 nm. The diamond tip is mounted on a tuning fork, allowing atomic force feedback for for AFM operation.

Transitions between spin states are driven by applying a microwave field via a nearby antenna. The interaction is mediated by magnetic dipole coupling between the oscillating microwave magnetic field $\vec{\mathbf{B}}_{\mathrm{MW}}(t)$ and the NV center's spin. The corresponding interaction Hamiltonian is:

$$H_{\mathrm{int}} = -\vec{\boldsymbol{\mu}} \cdot \vec{\mathbf{B}}_{\mathrm{MW}}(t) = -g\mu_B \vec{\mathbf{S}} \cdot \vec{\mathbf{B}}_{\mathrm{MW}}(t) = -g\mu_B \left[\hat{\mathbf{S}}_x B_{\mathrm{MW,x}}(t) + \hat{\mathbf{S}}_y B_{\mathrm{MW,y}}(t) + \hat{\mathbf{S}}_z B_{\mathrm{MW,z}}(t)\right] \tag{4.21}$$

Here $\hat{\mathbf{S}}_x$, $\hat{\mathbf{S}}_y$ and $\hat{\mathbf{S}}_z$ denote the spin-1 operators, and the NV axis is taken to be aligned with the z-axis.
To effectively drive transitions between spin states $|m_s = 0\rangle$ and $|m_s = \pm 1\rangle$, the interaction Hamiltonian must include off-diagonal elements. This requires the microwave magnetic field to have components **perpendicular** to the NV axis. Consequently, the orientation and placement of the microwave antenna are critical: the antenna must be positioned such that it generates a magnetic field orthogonal to the NV axis. In our configuration, the NV centers are oriented along the [111] crystallographic direction, which is perpendicular to the sample surface. To achieve efficient coupling and maximize ODMR contrast, the antenna is positioned above the scanning tip. If placed at the same height or below the tip, the field would align with the NV axis, suppressing spin transitions and reducing ODMR contrast.

Additionally, the experimental setup includes a vector electromagnet used to apply a controlled bias magnetic field to the NV center. This field can be tuned in direction and magnitude to lift the degeneracy of the spin states, optimize contrast, or perform magnetic field mapping under specific conditions.

Characterization of the sensor

The orientation of the NV center is fixed during fabrication and specified by the manufacturer. For the characterization of the magnetic samples presented in this work, we employed a scanning tip with the NV axis oriented perpendicular to the sample surface (out-of-plane configuration).
To experimentally confirm the NV center's orientation, we performed two complementary optimization procedures:

- **Common-mode shift minimization**: In this method, an external magnetic field is applied, and both ESR frequencies (i.e., those above and below the zero-field splitting D) are recorded. The direction of the external field is then varied to minimize the average shift of the ESR frequencies from the zero-field value. When this shift is minimized, the magnetic field is align with the NV axis.
- **Contrast maximization** :In this approach, the external magnetic field orientation is adjusted to maximize the photoluminescence contrast observed in the ODMR spectrum. Maximum contrast occurs when the magnetic field is aligned along the NV axis.

Results from these measurements, performed using an out-of-plane NV tip, are shown in Figure 4.17.

In addition to these alignment procedures, we performed ODMR measurements while varying both the amplitude and orientation of the external magnetic field Figure 4.15. By examining the evolution of the ESR frequencies under these conditions, we independently confirmed the NV center orientation based on the spectral response.

Principle of the measurements performed

Scanning NV-magnetometry measurements are performed at a fixed height above the sample surface. Prior to acquisition, the resonance frequency and quality factor of the tuning fork are determined.

Each scan begins with AFM tip engagement at three points around the magnet. During this process, forced oscillations-near the resonance frequency of the tuning fork-are applied at the

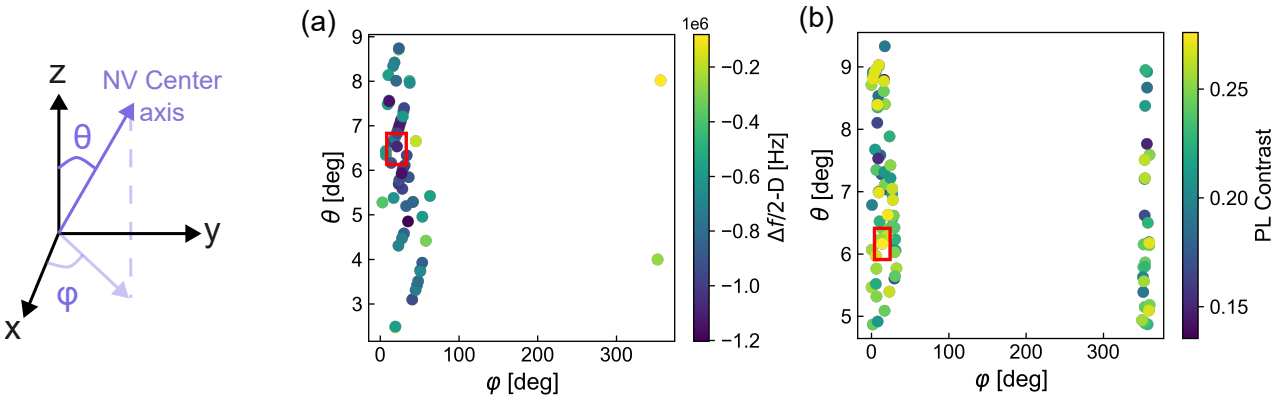

Figure 4.17: **Experimental optimization of the NV orientation** using two methods:
(a) Common-mode ESR shift minimization, yielding optimal angles $\theta_{\text{opt}} = 6.2°$ and $\varphi_{\text{opt}} = 14.0°$
(b) ODMR contrast maximization, yielding optimal angles $\theta_{\text{opt}} = 7.0°$ and $\varphi_{\text{opt}} = 24.1°$
In the common-mode method, the extracted frequency shift can appear negative if the zero-field splitting parameter D is slightly overestimated during analysis. These measurements confirm that the NV axis is oriented perpendicular to the sample surface. Both optimization procedures were developed by Qzabre.

selected drive amplitude. As the tip approaches the surface, interactions with the sample reduce the oscillation amplitude. Engagement is defined when the oscillation amplitude drops to 75% of its free-space value (i.e., in the absence of surface interaction). These three points define the reference plane $h = 0$ allowing correction for any sample tilt.

During scanning, the tip is re-engaged along each vertical scan line, and measurements are taken at a constant height $h = h_{\text{m}}$ above the corrected surface. At each scan point, a full ODMR spectrum is acquired, allowing extraction of the local ESR frequencies. This results in a spatial map of the magnetic field projected along the NV axis.

4.2.5 Measurement and comparison with the micromagnetic model

We aim to characterize the magnetic field generated by three types of micro-magnets: one made of Cobalt, one of a Cobalt-Tantalum multilayer, and one of Cobalt-Iron. Prior to NV scanning, the magnets are coated with a thin sputtered layer of SiO_2. This serves two purposes:

- To prevent the apex NV center from contacting the magnetic sample and accumulating magnetic residues on the tip. We observed that, without this protective layer, the NV centers were frequently damaged.
- To replicate the dielectric capping layer that will be used in the final device, as the magnets will be encapsulated in SiO_2 during chip integration.

For each magnet, the spatial distribution of the two ESR frequencies is measured by scanning above the surface at various heights h_{m}. The measurements performed are presented Figures 4.18 and 4.19.

Before scanning, the magnet is initialized by applying a 300 mT in-plane magnetic field along the magnet long axis. This field is removed for the measurement of the Cobalt magnet but reduced to 5 mT for the Cobalt-Tantalum and Cobalt-Iron samples to shorten the convergence time of the micromagnetic simulations.

Although the experimental conditions differ slightly - since a small bias field is applied for some samples - a comparison of measurement heights among the samples suggests that the CoFe magnet, despite its higher M_s and its tendency to form more magnetic domains, generates stronger stray magnetic fields.

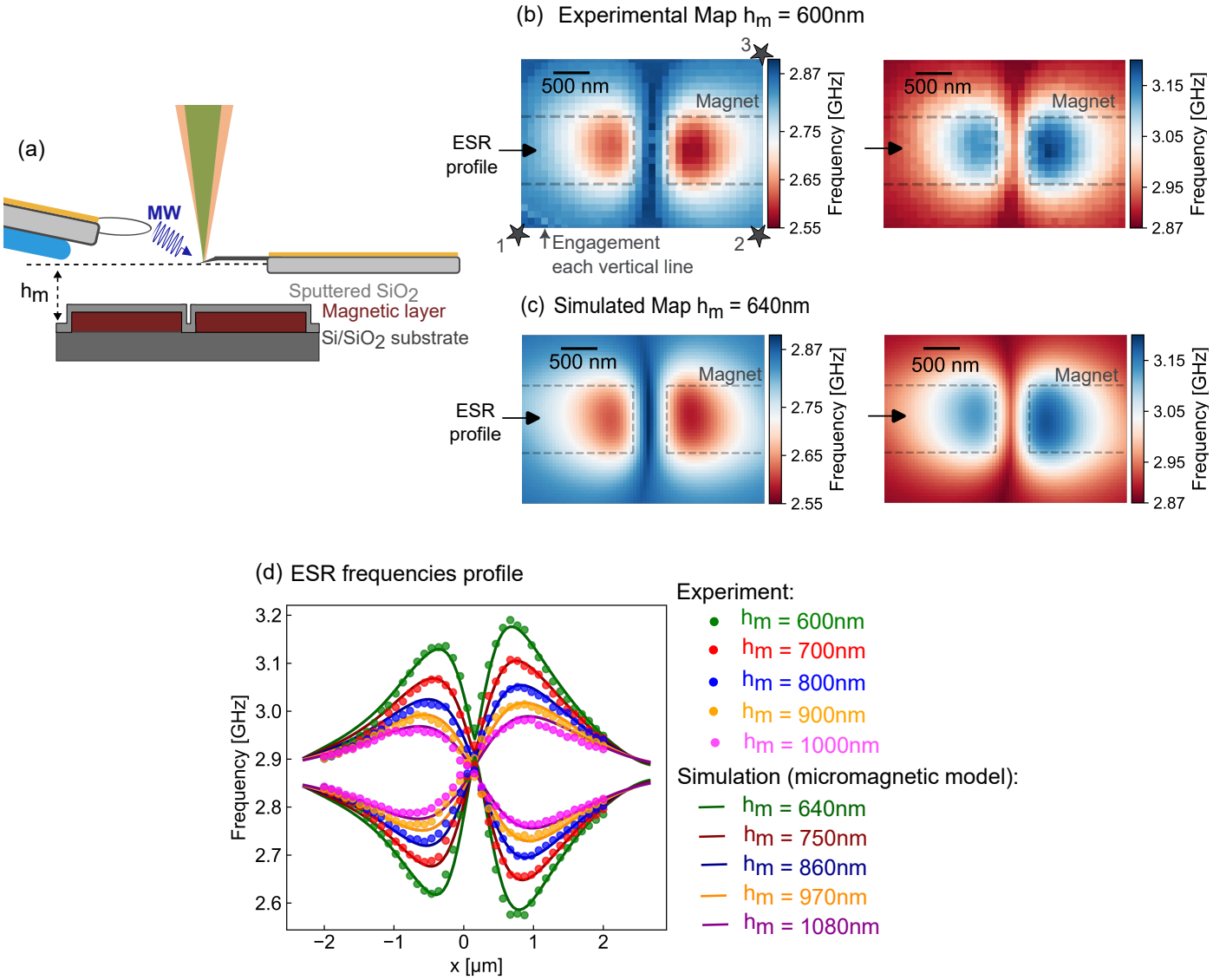

Figure 4.18: **ESR Frequency Landscape of a Nitrogen-Vacancy Center Probed Above a Cobalt Magnet**.
(a) Schematic illustration of the NV-center-based scanning probe and microwave antenna positioned above the magnetic sample. The NV center is located at a height h_m above the surface, which is coated with a sputtered SiO_2 layer.
(b) **Experimental map**: spatial distribution of the ESR frequencies measured with the NV center at a stand-off distances from the magnet $h_m = 600\,nm$.
(c) **Simulated map**: calculated spatial distribution of ESR frequencies using the stray magnetic field of the magnet (obtain from the magnetic configuration simulated with MuMax[3]) and NV spin Hamiltonian.
(d) Comparison between experimentally measured ESR frequencies (circles) and simulated values from the micromagnetic model (lines) along the line indicated by the arrow in panels (b) and (c) at various stand-off distances from the magnet surface.

To compare with experimental results, we use the micromagnetic parameters obtain in the previous section to perform micro-magnetic simulations. The geometry of the simulated magnets matches the shapes observed in SEM and AFM images. Periodic boundary conditions are applied along the rectangle length to approximate the behavior of long rectangles. Using the micromagnetic simulation software MuMax^3, the equilibrium magnetic configuration is computed. From this, the stray magnetic field is computed, and the expected ESR frequencies are calculated by diagonalizing the spin Hamiltonian given in Eq. (4.15).

We find good qualitative and quantitative agreement between the experimental data and the simulations. Small discrepancies in the measurement height can be attributed to three main factors: (1) uncertainty in the NV center's exact position relative to the tip apex; (2) variations introduced during the tip-sample engagement procedure and (3) nonlinearities in the piezoelectrics controlling the position of the cantilever. Despite these sources of error, the deviation between the microscope height setting and the effective simulation height required to match experimental data remains below 10%, though it increases slightly with larger tip-sample distances.

To further validate the simulation parameters, additional comparisons between the micromagnetic model and experimental data varying the cubic anisotropy constant for the CoFe magnet are presented in the Appendix A.

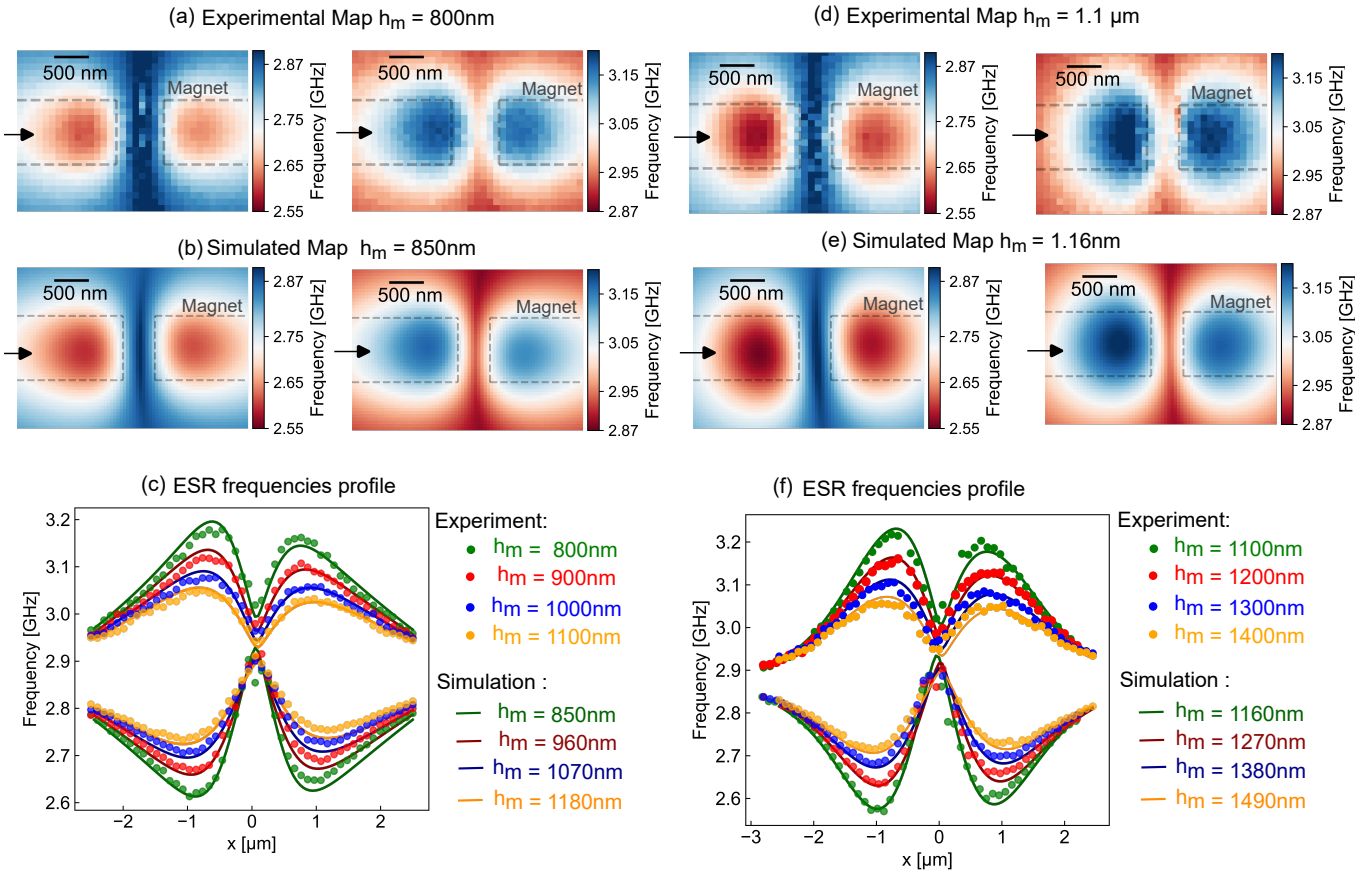

Figure 4.19: **ESR frequency landscape of a nitrogen-vacancy center above Cobalt-Tantalum and Cobalt-Iron magnets**
(a-c) Cobalt-Tantalum magnet. (a) Experimental map of the ESR frequencies recorded with the NV center at a stand-off distance $h_m = 800\,\text{nm}$. (b) Simulated map of the ESR frequencies obtained by combining micromagnet stray-field with the NV spin Hamiltonian. (c) Line cut comparing measured ESR frequencies (circles) and simulated values (lines) along the arrow indicated in (a) and (b), shown for multiple stand-off distances.
(d-f) Cobalt-Iron magnet, same as (a-c) but measured at larger h_m. (d) Experiment, (e) simulation and (f) corresponding line-cut comparison.

Outlook on Other On-Tip Magnetometry Sensors

It is worth highlighting that alternative on-tip magnetometry techniques have been proposed in the literature and could provide complementary, local, and quantitative magnetic characterization to that offered by NV center magnetometry. Below, we briefly review two notable approaches.

SQUID-on-tip magnetometry is one such method. It employs a Superconducting Quantum Interference Device (SQUID) fabricated directly at the apex of an AFM tip, allowing local magnetic imaging through the detection of magnetic flux threading the SQUID loop. Unlike NV centers, which operate as atomic-scale field sensors, SQUID-on-tip measurements integrate the perpendicular magnetic field $B_\perp$ over the loop area to yield the total magnetic flux:

$$\phi = \int B_\perp \mathrm{d}A \tag{4.22}$$

Typical loop diameters range from 100-200 nm.
SQUID-on-tip sensors require cryogenic conditions to maintain superconductivity, which aligns well with our intended application of micro-magnets at low temperatures. Notably, NV scanning magnetometry can also be operated at cryogenic temperatures.
The magnetic flux ϕ threading the SQUID loop is related to the device's critical current, I_c via:

$$I_c = 2I_0\left|\cos\left(\pi\phi/\phi_0\right)\right| \tag{4.23}$$

where ϕ_0 is the magnetic flux quantum. In practice, measurements are typically performed by biasing the SQUID slightly above its critical current and monitoring the voltage across the device. A change in I_c then leads to a measurable change in voltage.

However, due to the periodic nature of the cosine dependence in the expression for I_c there is an inherent ambiguity in determining the absolute flux value - this limits the ability to perform unambiguous flux measurements and requires calibration procedures [116]. To achieve meaningful and interpretable measurements, the SQUID must operate in the linear response regime, where the current response is approximately proportional to the magnetic flux. This requires that the sensed magnetic field remain significantly below one flux quantum, typically at least one order of magnitude smaller. While techniques such as flux-locked loops (FLL) can extend the dynamic range, they are challenging to implement on scanning probes due to the difficulty of integrating miniature feedback coils.
While the sensitivity of this technique is not expected to be a limiting factor for our application [117], [118], the dynamic range-particularly the maximum measurable magnetic field-remains a constraint. This is a similar limitation to that encountered in NV center magnetometry, where strong magnetic fields can compromise spin readout fidelity.

Another approach is **Scanning Hall Probe Microscopy (SHPM)**. In this method, a Hall bar is patterned at the edge of an AFM cantilever to enable spatially resolved magnetic field measurements. At each pixel, the Hall voltage, V_H, generated by the perpendicular component of the magnetic field is measured:

$$V_H = \frac{R_H I}{t} B_\perp = \frac{I}{nqt} B_\perp \tag{4.24}$$

Here, R_H is the Hall coefficient, I the bias current through the Hall bar, t the thickness of the conducting layer, n the carrier density and q the carrier charge magnitude.
Because the Hall cross senses the field over its active area, the measured $B_\perp$ is an area-averaged value over the active region of the Hall cross. Spatial resolution is therefore lim-

ited by the Hall cross dimensions; reducing the cross width improves resolution but also degrades sensitivity and increases noise.
In contrast to SQUID or NV sensors, sensitivity may become a limiting factor in SHPM. To improve performance, low-carrier-density materials can be used. For example, [119] reported a gold-based Hall sensor with a thickness of 30 nm and an active area of $5 \times 5\ \mu m^2$ achieving a sensitivity of 2.9−3.3mV/(AT).Applying a current of 10 mA and measuring a magnetic field $B_\perp = 50\,mT$ would yield a Hall voltage of approximately 1.6 µV, which is within detectable limits [119].
It is also worth noting that the same work presents Hall crosses with significantly smaller active areas down to $50 \times 50\ nm^2$ although their sensitivity was not characterized in detail. While such miniaturization could improve spatial resolution, the impact on sensitivity and noise performance remains an open question and could limit the technique's applicability for weak magnetic field measurements.
This method allows the probing of higher magnetic fields than NV-based approaches, potentially enabling measurements closer to the sample surface. However, placing the Hall cross sufficiently close to the apex of the tip to minimize the sensor-sample distance (h_m) remains a significant technical challenge; typical separations exceed 4 µm. Therefore unlike SQUID-on-tip or NV center probes, the sensitivity of this method may impose practical limits for small-scale field mapping.

4.3 Modeling and predicting magnet performance for spin qubit integration

From micromagnetic simulations informed by thin-film magnetic characterization, we can develop a predictive model of the magnet's behavior across both saturated and non-saturated regimes. NV center scanning magnetometry has allowed us to quantitatively map the stray magnetic field produced by the micromagnets. Leveraging micromagnetic simulations parametrized using parameters obtained from thin-film characterization (see section 4.1.4), we accurately reproduce the measured field profiles with the NV center microscope, validating our simulation workflow. Due to the NV center's operational constraints, these measurements were carried out far above the sample surface and under a very weak (or no) external magnetic field - i.e., in a partially magnetized (unsaturated) regime.

However, we can use the validated simulation framework to compute magnetization and the magnetic field closer to the magnet surface - precisely where the carbon nanotube (CNT) will reside in the final device - while applying a significant external magnetic field.

4.3.1 Performance of the optimized magnet geometry

We begin by analyzing the magnetic field generated by a magnet composed of two opposing rectangles - a geometry previously optimized and characterized in this work.

Figure 4.20 shows the simulated magnetization distribution for the three magnetic materials as the amplitude of an external field applied along the magnet's long axis is varied, using room-temperature magnetic parameters determined Section 4.1.4. The corresponding magnetization curves versus external field are also presented in Fig. 4.20. Using the parameters extracted from thin-film characterization at 4 K (Table 4.6), we repeat the micromagnetic simulations, and the resulting magnetization curves versus external field are likewise shown in Fig. 4.20.

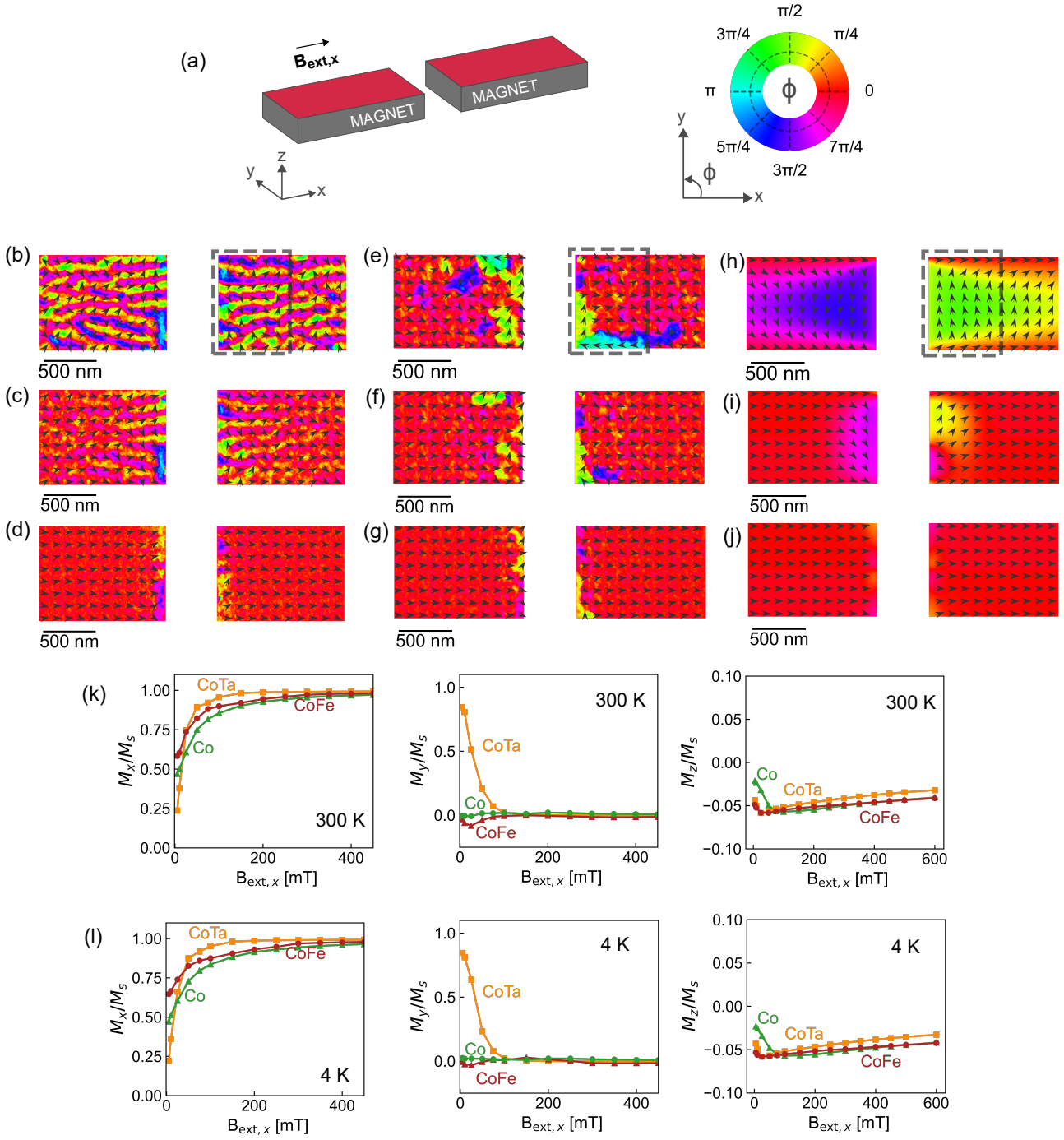

Figure 4.20: **Micromagnetic configurations under varying bias field**
(a) Schematic of the magnet and coordinate axes.
(b-j) In-plane micromagnetic configurations for three materials at increasing external field applied along the long axis of the magnet $B_{\text{ext},x}$. The corlorbar is related to the orientation of the azimutal angle of the magnetization ϕ. (b-d) Cobalt: $B_{\text{ext},x} = 5\,\text{mT}$, $B_{\text{ext},x} = 50\,\text{mT}$ and $B_{\text{ext},x} = 200\,\text{mT}$. (e-g) Cobalt-iron at the same fields. (h-j) Cobalt-tantalum at the same fields. Micromagnetic configurations were computed in MuMax3 employing the room-temperature parameters outlined Section 4.1.4.
(k) Evolution of the normalized magnetization components M_i/M_s (with $i \in \{x, y, z\}$) versus $B_{\text{ext},x}$. Values are spatial averages over the rectangular regions indicated in (b), (e), and (h).
(l) Same as (k), but obtained from micromagnetic simulations using magnetic parameters at 4 K (see Table 4.6).

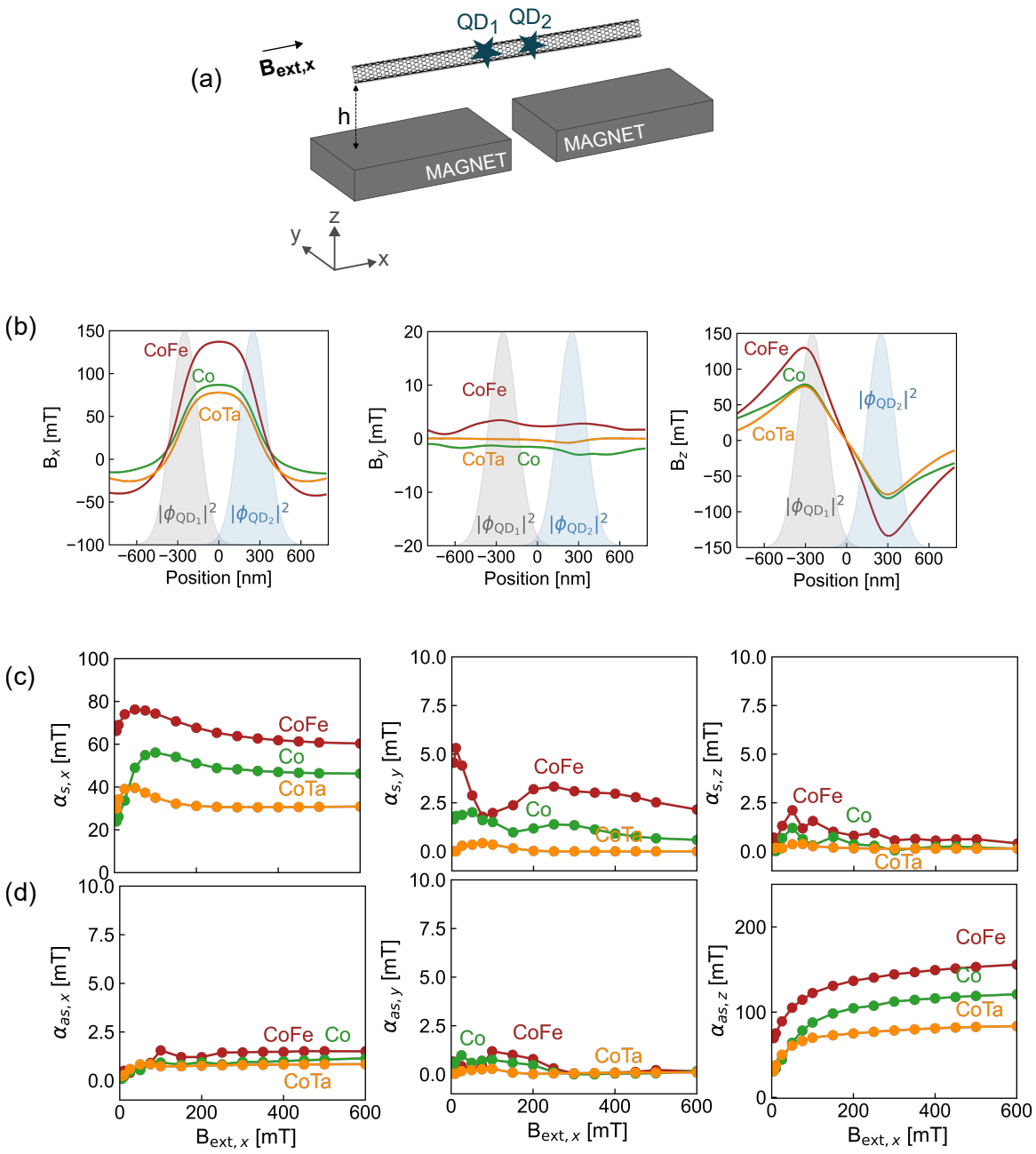

Figure 4.21: **Magnetic field generated by the magnets.**
(a) Schematic of the magnet; the CNT is located at a height h above the magnet surface.
(b) Spatial distributions of B_x, B_y and B_z along the CNT for the three magnets at $h = 150\,\text{nm}$ with an external field $B_{\text{ext},x} = 50\,\text{mT}$. The magnetic field profile was computed from the micro-magnetic simulations using the parameters determined at room-temperature. The electron probability density in each dot is modeled as a Gaussian with a standard deviation of 100 nm.
(c-d) Symmetric and antisymmetric components of B_x, B_y and B_z averaged over the spatial extent of the two dots (defined Eq. (4.25)) versus the external magnetic field $B_{\text{ext},x}$. These components were computed from the magnetic field distribution of (b).

From the micromagnetic configurations, we can compute the magnetic field generated by the magnet along the carbon-nanotube. An example for a carbon-nanotube located at $h = 150\,\text{nm}$ above the magnet surface with $B_{\text{ext},x} = 50\,\text{mT}$ is shown in Fig. 4.21(b). This magnetic field distribution was computed from the micromagnetic simulations with the room-temperature magnetic parameters. Let us note that we choose $h = 150\,\text{nm}$ as it is compatible with realistic CNT spin-qubit device geometries.

From the simulated magnetic field distributions, we extract the symmetric and antisymmetric components of the magnetic field averaged over the two quantum dots:

$$\begin{aligned}\alpha_{s,i} &= \frac{1}{2}\int \mathrm{d}x \left[B_i^{\text{magnet}}(x)\left|\phi^*_{\text{QD}_1}(x)\right|^2 + B_i^{\text{magnet}}(x)\left|\phi^*_{\text{QD}_2}(x)\right|^2\right] \\ \alpha_{as,i} &= \frac{1}{2}\int \mathrm{d}x \left[B_i^{\text{magnet}}(x)\left|\phi^*_{\text{QD}_1}(x)\right|^2 - B_i^{\text{magnet}}(x)\left|\phi^*_{\text{QD}_2}(x)\right|^2\right]\end{aligned} \tag{4.25}$$

with $i \in \{x, y, z\}$ and $\left|\phi^*_{\text{QD}}(x)\right|^2$ is the electron probability density in each dot, modeled as a Gaussian with a standard deviation of 100 nm. The resulting averages are plotted in Figs. 4.21(c-d). In particular, since $\alpha_{s,y}$, $\alpha_{s,z}$, $\alpha_{as,x}$ and $\alpha_{as,y}$ are negligible, we can define:

$$\begin{aligned}&\alpha_s = \alpha_{s,x} \quad \text{and} \quad \alpha_{s,\text{tot}} = \alpha_{s,x} + \frac{1}{2}\int \mathrm{d}x \left[B_{\text{ext},x}\left|\phi^*_{\text{QD}_1}(x)\right|^2 + B_{\text{ext},x}\left|\phi^*_{\text{QD}_2}(x)\right|^2\right] = \alpha_{s,x} + B_{\text{ext},x} \\ &\alpha_{as} = \alpha_{as,z}\end{aligned} \tag{4.26}$$

Using these definitions and the expressions derived in Chapter 1, we can estimated both the Zeeman splitting and the spin-charge hybridization energy for a double quantum dot:

$$\begin{aligned}\epsilon_Z &= g_s \mu_B \alpha_s \\ \epsilon_{\text{hyb}} &= g_s \mu_B \alpha_{as}\end{aligned} \tag{4.27}$$

where $g_s \approx 2$ is the electronic spin g-factor and μ_B is the Bohr magneton.

Finally, we compute the spin transition frequency and the expected spin-photon coupling strength as functions of the external magnetic field amplitude for all three materials, using simulations based on both room-temperature and 4 K parameters (Fig. 4.22). For these estimations, the inter-dot tunneling was set such that $t_c = \epsilon_Z$.

From Fig. 4.22, the expected spin-photon coupling reaches

$$\frac{2|g|}{|\Delta_g|} \approx 0.3 - 0.5 \tag{4.28}$$

with an associated qubit frequency of $f_\sigma \approx 4 - 5\text{GHz}$ for the three magnetic materials under study. This performance is nearly an order of magnitude higher than that obtained with the first magnet geometry presented in Chapter 2.
Comparison between the different magnets indicates that cobalt-iron is the most promising magnet material. Accordingly, we focus on this magnetic material for what follows. Finally, this analysis also suggests that the magnet's performance at room temperature and at 4 K is similar.

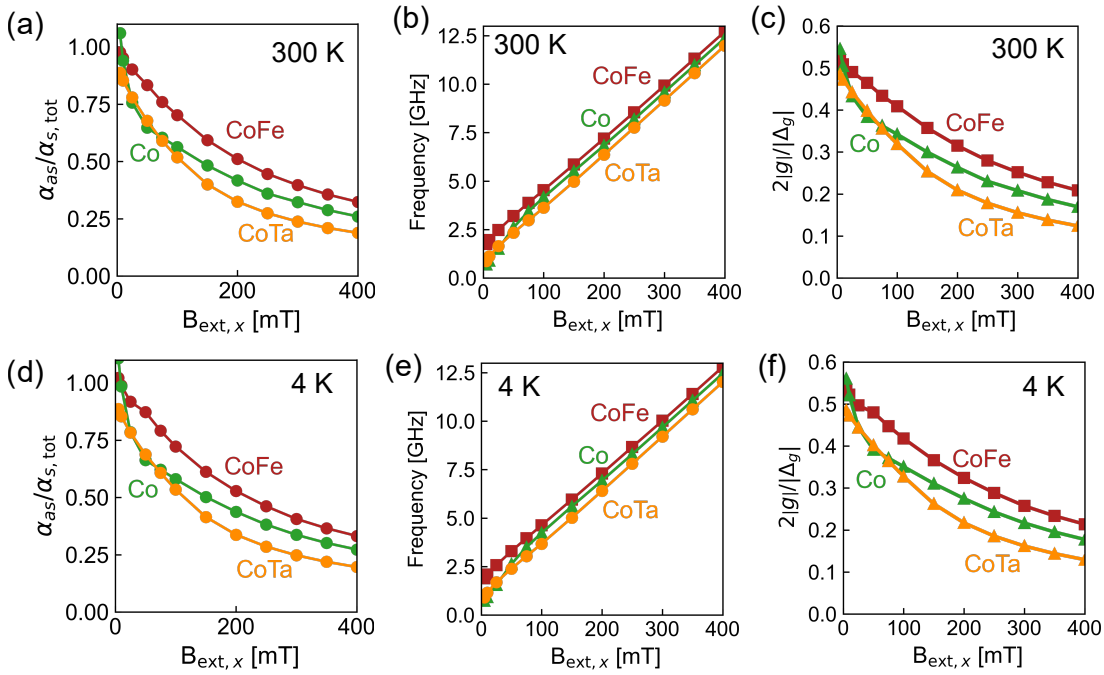

Figure 4.22: **Predicting the spin-qubit frequency and spin-photon coupling**
(a) Ratio between the symmetric and anti-symmetric magnetic fields as a function of the external magnetic field $B_{\text{ext},x}$ for the three materials. These quantities are defined in Eq. (4.26).
(b) Computed spin-qubit frequency, using the values of α_s and α_{as} obtained from micromagnetic simulations for the three materials, plotted as a function of $B_{\text{ext},x}$. The interdot tunneling rate of the double quantum dot was set to $t_c = \epsilon_Z = g_s \mu_B \alpha_s$.
(c) Simulated spin-photon coupling strength, again using the values of α_s and α_{as} from the micromagnetic simulations, as a function of $B_{\text{ext},x}$. The interdot tunneling rate was set to $t_c = \epsilon_Z = g_s \mu_B \alpha_s$.
Panels (a-c) were obtained using micromagnetic simulations parameterized with the magnetic parameters measured at room temperature. Panels (d-f) show the corresponding results using the 4 K magnetic parameters defined in the first section of this chapter.

4.3.2 Adapted magnet geometry for CNT spin qubit integration

For practical integration into a carbon nanotube-based spin qubit architecture, the magnet geometry composed of two opposing rectangles must be modified. In the following, we present the adapted geometry and evaluate its expected performance.

Why do we need to adapt the magnet geometry ?

In semiconductor quantum circuits based on suspended carbon nanotubes, the CNT is transferred to the device at the end of the fabrication process of the chip. This reduces contamination and preserves the nanotube's integrity. The transfer process - based on a "stapling" protocol developed at the ENS Hybrid Quantum Circuits group [120] and C12 Quantum Electronics, and inspired by techniques from the Weizmann Institute [55] - uses a a separate cantilever chip for CNT growth and then transfers the carbon nanotube into the circuit chip.
However, this transfer introduces uncertainty in the final position of the CNT, which motivates a length of $\sim 30\,\mu$m for the gates defining the electrostatic potential below the tube.

Due to this positional uncertainty, the previously optimized two-rectangle magnet geometry must be adapted. To ensure robust magnetic field delivery across the entire potential deposition area, we design a periodic array ("comb") of parallel rectangles, see Fig.4.23(a). This retains the benefits of shape anisotropy - favoring uniform magnetization along the magnet length - while increasing tolerance to CNT placement variability.
The inter-rectangle spacing must be carefully chosen. If too large, the CNT could fall between rectangles and experience a significantly reduced magnetic field. If too small, adjacent rectangles may collapse during fabrication. Using the 20 kV lithography system available in Nancy, we found that spacings below 300 nm were not feasible. However, with the 100 kV lithography system at C12 - along with proximity effect correction - a spacing of 100 nm was successfully achieved.
The results presented here assume an inter-rectangle spacing of 300 nm.

Performance of the adapted "Comb" magnet

The micromagnetic model used for the optimized magnet can be extended to simulate the comb geometry by introducing periodic boundary conditions. In addition to the periodic conditions already implemented to simulate a long rectangle, we add further periodic conditions to mimic the presence of rectangular magnets on both sides. Simulations are performed using the low-temperature magnetic parameters of the CoFe alloy (see Table. 4.6), which provides, from the previous discussion, the strongest performance for enhancing spin-charge hybridization.

The in-plane magnetization distribution in one of the double rectangles forming the magnet as a function of the external biasing field is shown in Fig. 4.23.

As before, from the micro-magnetic configuration we compute the spatial magnetic field distribution and its impact on the spin qubit properties. Figure 4.24 shows the magnetic field components B_x, B_y, and B_z for an external magnetic field $B_{\text{ext},x} = 50\,$mT and for a CNT located at $h = 150\,$nm above the magnet surface. Since the CNT position with respect to the magnet can vary during the nano-assembly process, we present the magnetic field distribution for various CNT positions relative to the magnet.

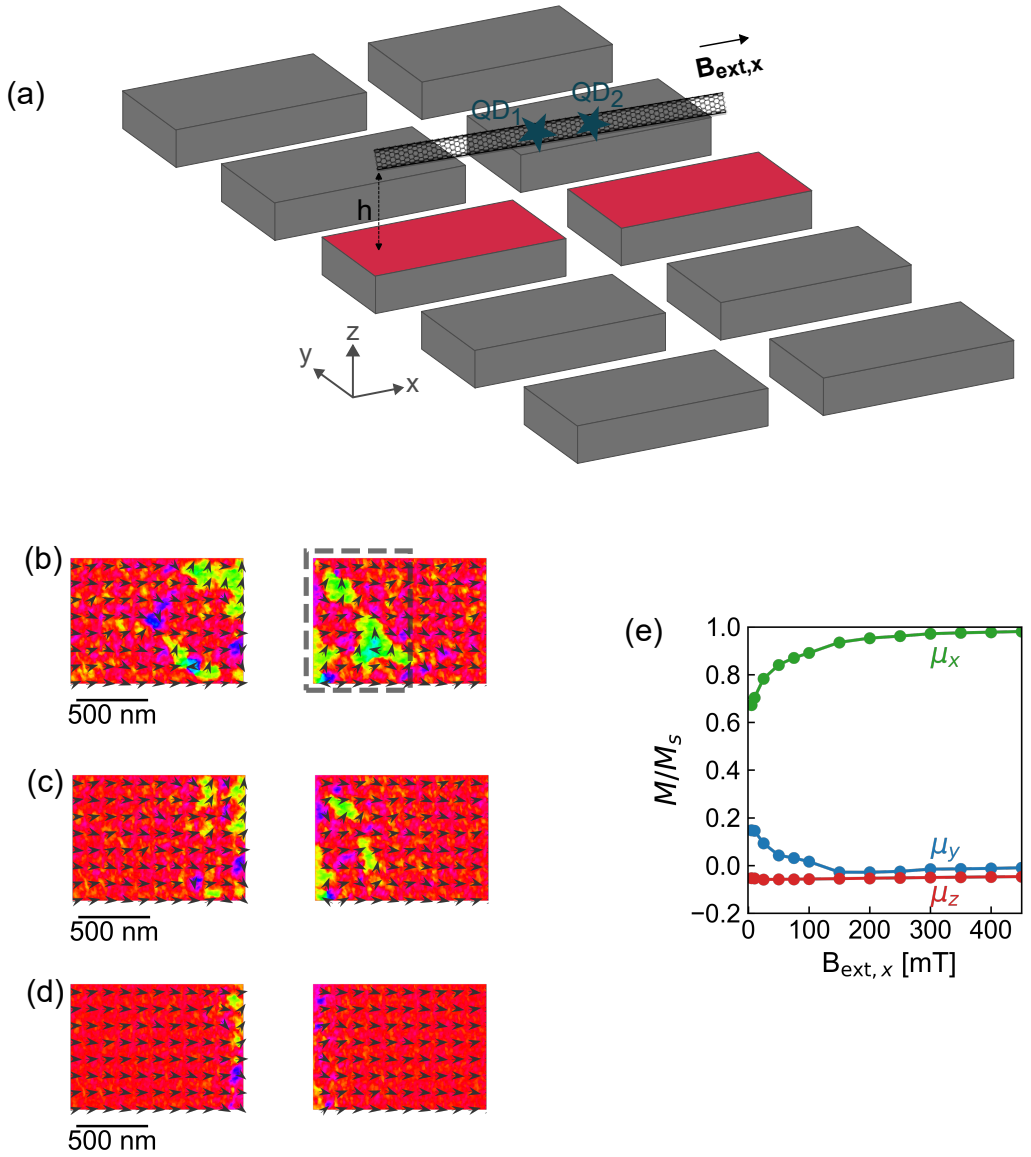

Figure 4.23: **Magnetic configuration in the comb magnet**
(a) Schematic of the magnet showing the periodic repetition of pairs of facing rectangles.
(b-d) Magnetic configuration within one repeating unit of the magnet (two rectangles facing each other). The in-plane magnetization at the magnet surface is shown for external fields (b) $B_{\mathrm{ext},x} = 5\,\mathrm{mT}$, (c) $B_{\mathrm{ext},x} = 50\,\mathrm{mT}$, and (d) $B_{\mathrm{ext},x} = 200\,\mathrm{mT}$. The color bar is identical to Fig. 4.20.
(e) Evolution of the normalized magnetization components $\mu_i = M_i/M_s$ (with $i \in \{x, y, z\}$) versus $B_{\mathrm{ext},x}$. Values are spatial averages over the rectangular regions indicated in (b).

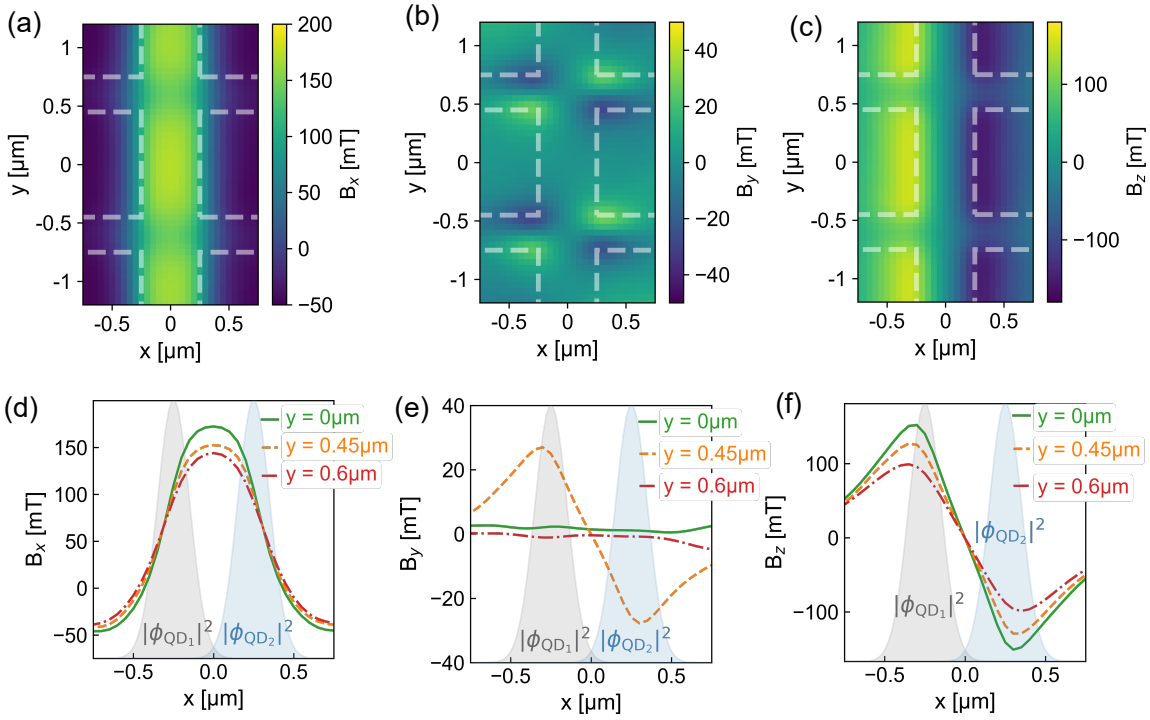

Figure 4.24: **Spatial distribution of the magnetic field generated by the comb magnet**
(a-c) Two-dimensional magnetic field maps of B_x, B_y, and B_z for an external field $B_{\text{ext},x} = 50\,\text{mT}$ and a CNT located at $h = 150\,\text{nm}$ above the magnet surface. The magnet position is indicated by white dashed lines.
(d-f) Magnetic field profiles B_x, B_y, and B_z along the CNT for various CNT positions. The quantum dots are indicated by the electron probability density in each dot, $|\phi_{\text{QD}}|^2$, modeled as a Gaussian with standard deviation $\sigma = 100\,\text{nm}$.

From these results, we extract - for the various CNT positions - the symmetric and antisymmetric magnetic field components relevant for spin qubit operation, see Fig. 4.25(a-f). Contrary to the previous section, here $\alpha_{as,y}$ is not negligible for the different CNT positions. The symmetric and antisymmetric magnetic field components are then defined as:

$$\begin{aligned} \alpha_s &= \alpha_{s,x} \quad \text{and} \quad \alpha_{s,\text{tot}} = \alpha_{s,x} + B_{\text{ext},x} \\ \alpha_{as} &= \sqrt{\alpha_{as,z}^2 + \alpha_{as,y}^2} \end{aligned} \tag{4.29}$$

With these magnetic field components, we estimate the resulting Zeeman and hybridization energies and compute the spin qubit frequency as well as the expected spin-photon coupling strength as functions of the external field amplitude and of the CNT position, see Fig. 4.25(h-i). The interdot tunneling rate is set to $t_c = \epsilon_Z = g_s \mu_B \alpha_s$.
Depending on the CNT position, the qubit frequency may vary by approximately 100 MHz for a given external magnetic field amplitude, see Fig. 4.25(h). Targeting a spin qubit frequency f_σ = 4-5GHz, the resulting spin-photon coupling is:

$$\frac{2|g|}{|\Delta_g|} \approx 0.3 - 0.45 \tag{4.30}$$

The spin-photon coupling obtained here is still one order of magnitude higher than for the previous magnet design described in Chapter 2, for all CNT positions considered. The ratio $\alpha_{as}/\alpha_{s,\text{tot}}$

reaches approximately $0.5-0.75$. Although the regime $\alpha_{as}/\alpha_{s,\mathrm{tot}} \approx 1$ is not achieved in this configuration, the condition $2t_c\epsilon_Z \geq (\epsilon_Z^2+\epsilon_{\mathrm{hyb}}^2)$ is satisfied, which contributes to reduce decoherence due to charge noise.
Let us note, that the regime $\alpha_{as}/\alpha_{s,\mathrm{tot}}$ could be increased by experimentally placing the nanotube closer to the magnet surface (reducing h).

We have so far neglected specific considerations for CNT-based spin qubits. In particular, for carbon nanotubes exhibiting strong spin-orbit coupling (see Chapter 1), the spin-orbit interaction effectively enhances the g-factor longitudinal to the nanotube - thus increasing ϵ_Z - and reduces the g-factor transverse to the nanotube - thus decreasing ϵ_{hyb}. This leads, for the same ratio $\alpha_{as}/\alpha_{s,\mathrm{tot}}$, to a reduced ratio $\epsilon_Z/\epsilon_{\mathrm{hyb}}$ and consequently a reduced spin-photon coupling.
Therefore, as previously mentionned tighter control and understanding of the carbon nanotube properties remain crucial for achieving a scalable architecture. To this end, characterization workflows - Raman spectroscopy, Rayleigh measurements in an optical setup, and electrical tests performed prior to the assembly - are being developed at C12. Such pre-selection techniques could enable improved control over CNT properties.

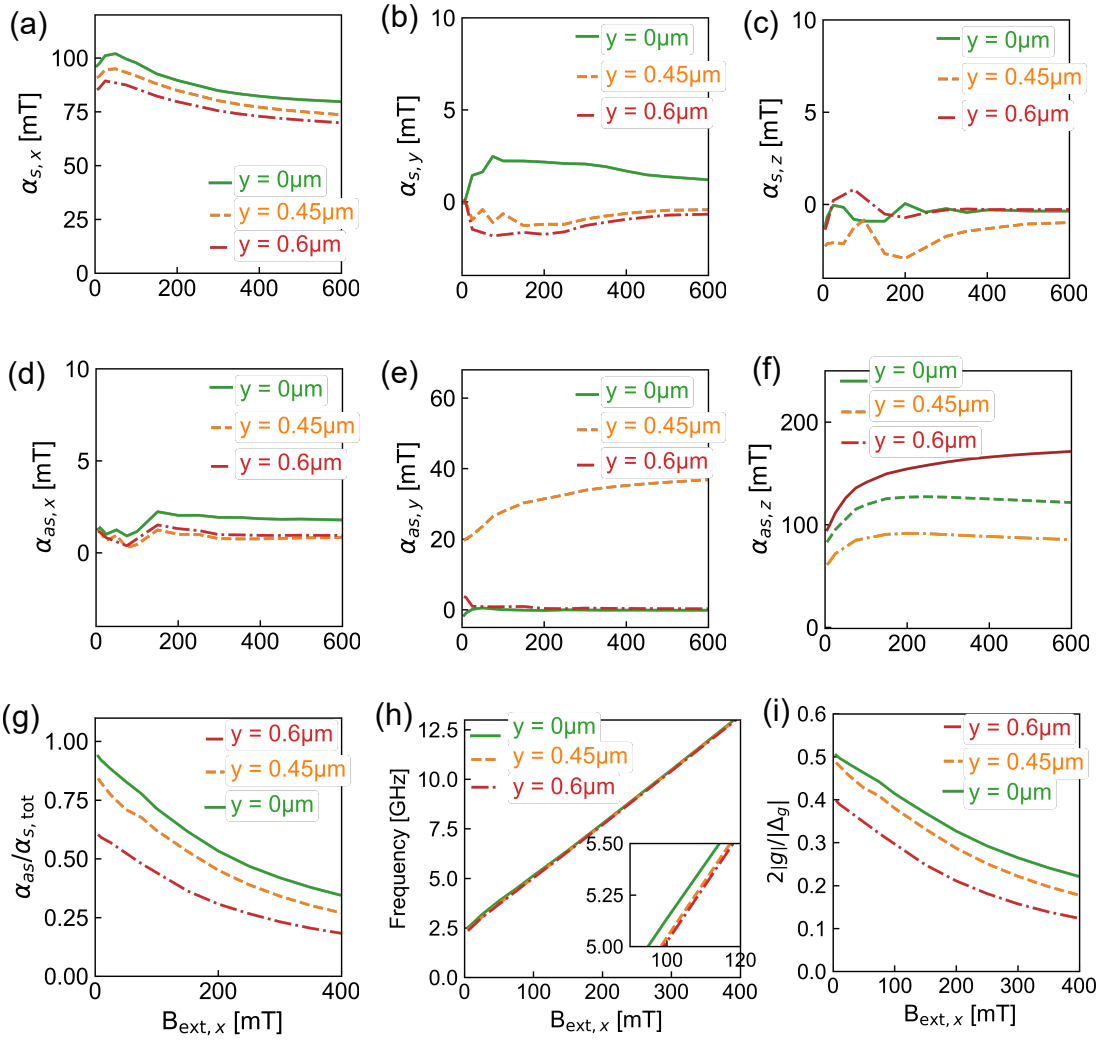

Figure 4.25: **Predicting the spin-qubit frequency and spin-photon coupling for the adapted magnet geometry**
(a-f) Symmetric and antisymmetric components of B_x, B_y, and B_z, averaged over the spatial extent of the two dots (definitions in Eq. (4.25)), versus the external magnetic field $B_{\text{ext},x}$ for various CNT positions.
(g) Ratio between the antisymmetric and symmetric fields, $\alpha_{as}/\alpha_{s,\text{tot}}$, as a function of $B_{\text{ext},x}$ for various CNT positions (see Eq. (4.29)).
(h) Computed spin-qubit frequency using α_s and α_{as} obtained from micromagnetic simulations for various CNT positions, plotted versus $B_{\text{ext},x}$. The interdot tunneling rate is set to $t_c = \epsilon_Z = g_s\mu_B\alpha_s$. The inset shows a zoom around $B_{\text{ext},x} = 100\,\text{mT}$, where the qubit frequency is close to $f_\sigma = 5\,\text{GHz}$.
(i) Simulated spin-photon coupling strength, again using α_s and α_{as} from the micromagnetic simulations, as a function of $B_{\text{ext},x}$ for various CNT positions. The interdot tunneling rate is set to $t_c = \epsilon_Z = g_s\mu_B\alpha_s$.

Chapter 5

A high kinetic inductance and magnetic-field-resilient superconducting circuit for spin-qubit architecture

Coupling a qubit to a superconducting microwave circuit allows to mediate long-range interactions between spatially separated qubits, and also enables fast, high -fidelity read-out. In the realm of superconducting devices - in particular transmon qubits formed by a Josephson junction shunted with a capacitor - dispersive measurement techniques have matured to achieve read-out fidelities as high as 99.9% - that corresponds to average not error of the read-out below 0.1%- in times on the order of 50 ns [121] .

Achieving similarly high performance with semiconductor spin qubits demands pushing into the strong-coupling regime, where:

$$\frac{g^2}{\kappa\Gamma} \gg 1 \tag{5.1}$$

Here, κ and Γ denote the energy decay rates of the cavity and the qubit, respectively, and g is the coupling of the qubit with the photons of the microwave cavity :

$$g \propto d \cdot V_{\text{zpf}} \propto d \cdot \omega_c \sqrt{Z_c} \tag{5.2}$$

Where d is the electric dipole of the spin transition, V_{zpf} is zero-point voltage fluctuation of the cavity that scales with the frequency of the cavity $\omega_c/(2\pi)$ and its characteristic impedance Z_c.

In the previous chapters, our work focused on the design and characterization of on-chip micromagnet producing an anti-symmetric magnetic stray field across a double quantum dot to hybridize the spin and charge degree of freedom, thereby endowing the spin transition with a sizable electric dipole moment.

An alternative and complementary approach to boost g is to increase the voltage fluctuations of the cavity via high-impedance resonators fabricated from materials with large kinetic inductance. In this chapter, we present the design and implementation of a high-impedance microwave circuit - compatible with the presence of a micromagnet - using a magnetic-field-resilient NbN superconductor.

In this chapter, we first outline key theoretical foundations for designing superconducting circuits. We then present simulations -based on established microwave architectures - to clarify the behavior of each circuit element and to guide the choice of dimensions parameters in the circuit. Finally, we report the experimental characterization of NbN superconducting resonators to assess their properties.

5.1 A superconducting circuit with high kinetic inductance superconducting material

5.1.1 High kinetic inductance superconducting material

In a conventional conductor or circuit, the geometric (or magnetic) inductance L_{geom} arises because a flowing current I creates a magnetic flux ϕ and the associated energy

$$E_{\text{mag}} = \frac{1}{2} L_{\text{geom}} I^2 \tag{5.3}$$

is stored in the magnetic field surrounding the conductor. Formally, L_{geom} encapsulates how geometry - length, cross-section, loop configurations - and proximity to nearby conductors influence the amount of magnetic energy stored in the surrounding magnetic field.

Kinetic inductance, by contrast, has no macroscopic field component but instead reflects the carriers' inertia at the microscopic level. When charge carriers of effective mass m^* and density n move at velocity v to carry current through a volume V, they store kinetic energy:

$$E_K = \sum_{\text{carriers}} \frac{1}{2} m^* v^2 = \frac{1}{2}\left(m^*\right) v^2 (nV) = \frac{1}{2} L_K I^2 \tag{5.4}$$

where I is the current and L_K is the kinetic inductance. In essence, the kinetic inductance reflects the energy stored energy by the motion of the carriers.
In a superconductor, the carriers are Cooper pairs of mass $m^* = 2m_e$ and charge $\left|q\right| = 2e$. For a thin strip of length l, width w, and thickness t. Since the current in the strip can be written:

$$I = n\, q\, (t w)\, v \tag{5.5}$$

the kinetic inductance becomes:

$$L_K = \frac{m_e}{2e^2 n} \frac{l}{t w} \tag{5.6}$$

Thus, L_K grows when the carrier density n is reduced or when the aspect ratio $l/(wt)$ - is increased- providing two clear routes to engineer large kinetic inductance.

A fully rigorous derivation proceeds from the complex, frequency-dependent conductivity of a superconductor:

$$\sigma(\omega) = \sigma_1(\omega) - i\sigma_2(\omega) \tag{5.7}$$

as first derived by Mattis and Bardeen within the framework of BCS (Bardeen, Cooper, and Schrieffer) theory. The real part $\sigma_1(\omega)$ is associated to dissipation (irreversible losses) of current. This term vanishes as the temperature T goes to zero, onsistent with the absence of resistance in the superconducting state. In the other hand, the imaginary part $\sigma_2(\omega)$ captures the material's reactive response and thus its ability to store energy. In the low-temperature regime $T \ll T_c$ and for microwave frequencies satisfying $\hbar\omega \ll \Delta_0$ (with Δ_0 is the zero-temperature superconducting energy gap), this term takes the form [122]:

$$\frac{\sigma_2}{\sigma_n} \approx \frac{\pi \Delta_0}{\hbar \omega} \tag{5.8}$$

here σ_n is the DC normal-state conductivity just above the critical temperature T_c of the superconducting material. For thin superconducting films - where the thickness t is small compared to the penetration depth λ of the superconducting material [123] - the surface impedance Z_s of the material can be written as:

$$Z_s = \frac{1}{t\sigma(\omega)} \tag{5.9}$$

so that its imaginary part defines the sheet kinetic inductance:

$$L_K^{\square} = \frac{1}{\omega}\mathrm{Im}\{Z_s\} = \frac{\hbar\rho_n}{\pi\Delta_0 t} = \frac{\hbar R_{\square}}{\pi\Delta_0} \tag{5.10}$$

here $\rho_n = 1/\sigma_n$ is the normal-state resistivity just above T_c and $R_{\square} = \rho_n/t$ is the corresponding sheet resistance. The kinetic inductance of the material then corresponds to:

$$L_K = \frac{l}{w} L_K^{\square} = \frac{l}{tw}\frac{\hbar\rho_n}{\pi\Delta_0} \tag{5.11}$$

Hence, both the intrinsic material parameter $R_{\square}$ and the geometric aspect ratio $l/(wt)$ control the total kinetic inductance. By using high-resistivity films - typically disordered alloys films - and optimizing the aspect ratio $\frac{l}{wt}$ one can enhance the kinetic inductance of the material.

Experimentally, a variety of disordered superconducting alloys exhibit large kinetic inductance per unit length. Notable examples include nanowire mades of TiN [124], NbTiN [125], Granular aluminium [126] or NbN [6].

An alternative approach is to engineer "artificial" inductors such as series Josephson Junctions [127] or SQUID arrays [128]. These platforms allow tunable, high-impedance elements that can exceed the kinetic inductance of homogeneous films.

For our spin-qubit microwave resonator-where both high impedance and resilience to applied magnetic fields are required-we select disordered NbN films. Previous work has demonstrated that NbN-based resonators can achieve both large kinetic inductance and operation in strong magnetic fields, making them an ideal choice for our application [6], [129]. The NbN films are deposited at the Laboratoire PHotonique ELectronique et Ingénierie QuantiqueS (PHELIQS) (Grenoble, France) using the same sputtering protocol described in [130]. Therefore, the resulting material is expected to exhibit the same high kinetic inductance and magnetic-field resilience as reported in those studies.

5.1.2 Superconducting coplanar-waveguide resonators

In this section we review how a high-kinetic-inductance material may be used to realize a high-impedance microwave cavity based on the coplanar-waveguide (CPW) architecture. We begin by introducing the CPW transmission line and its lumped-element description, then show how the kinetic inductance adds to the geometric inductance to raise the line impedance, and finally outline two common CPW resonator configurations.

Coplanar-waveguide transmission line

A CPW consists of a central conductor of width w flanked on either side by gaps of width s that separate it from the ground planes. The electromagnetic mode has its electric field concentrated between the center strip and the grounds. Although a CPW is a distributed network, an infinitesimal segment of length Δx can be modeled by the lumped elements shown in Fig. 5.1, with per-unit-length resistance R_l, inductance L_l, conductance G_l and capacitance C_l [131].

Under sinusoidal steady state, the Telegrapher's equations governing voltage $V(x)$ and current $I(x)$ propagation can be written as :

$$\frac{\mathrm{d}V}{\mathrm{d}x} = -(R_l + i\omega L_l)I(x), \quad \frac{\mathrm{d}I}{\mathrm{d}x} = -(G_l + i\omega C_l)V(x) \tag{5.12}$$

In the lossless limit (setting $R_l = G_l = 0$), the solutions are:

$$V(x) = V_o^+ e^{-ikx} + V_o^- e^{ikx}, \quad I(x) = \frac{V_o^+}{Z_0}e^{-ikx} - \frac{V_o^-}{Z_0}e^{ikx} \tag{5.13}$$

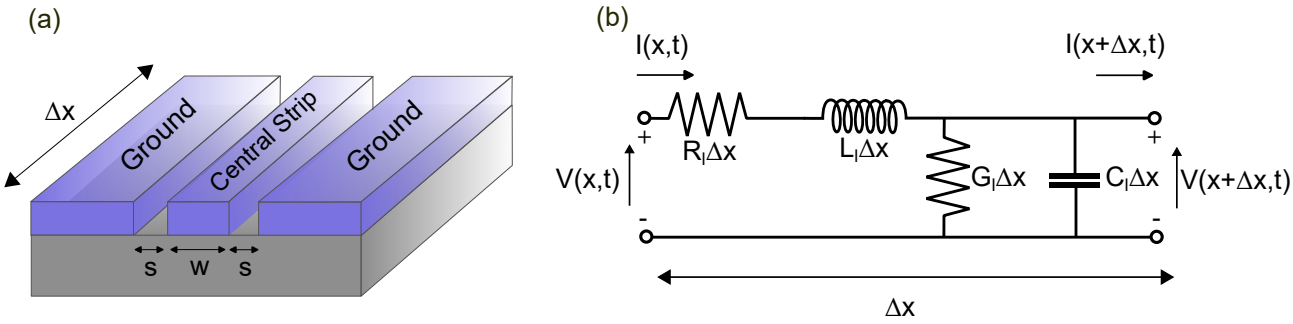

Figure 5.1: **Coplanar waveguide transmission line**
(a) Schematic of a coplanar-waveguide segment.The center conductor has width w and each gap has width s
(b) Lumped-element equivalent for a CPW segment of length Δx

where the characteristic impedance and propagation constant in the line are:

$$Z_0 = \frac{V_0^+}{I_0^+} = -\frac{V_0^-}{I_0^-} = \sqrt{\frac{L_l}{C_l}}, \qquad k = \omega\sqrt{L_l C_l}, \qquad v_p = \frac{\omega}{k} = \frac{1}{\sqrt{L_l C_l}}. \tag{5.14}$$

For a lossless CPW on a uniform dielectric, conformal-mapping methods give expressions for the per-unit-length geometric contribution of the inductance and capacitance [132] :

$$L_l^{\text{geom}} = \frac{\mu_0}{4}\frac{K(k_0')}{K(k_0)} \quad \text{and} \quad C_l^{\text{geom}} = 4\epsilon_0\epsilon_{\text{eff}}\frac{K(k_0)}{K(k_0')} \tag{5.15}$$

where

- μ_0 is the vacuum permeability,
- ϵ_0 is the vacuum permittivity,
- ϵ_{eff} is the CPW's effective dielectric constant, set by the geometry and the permittivities of the substrate layers (in our case a Silicon layer covered by a SiO_2 overlayer). Analytic formulas for in multilayer substrates can likewise be derived via extended conformal-mapping techniques [133].
- K denotes the complete elliptic integral of the first kind with the argument:

$$k_0 = \frac{w}{w+2s} \quad \text{and} \quad k_0' = \sqrt{1-k_0^2} \tag{5.16}$$

here s and w are related to the geometry of the CPW line as decsribed in 5.1.

Adding Kinetic Inductance

In a high-kinetic-inductance film, the total per-unit-length inductance is the sum of the geometric and kinetic parts:

$$L_l = L_l^{\text{geom}} + L_l^K \tag{5.17}$$

For a CPW in the limit $s \gg w$ (approximating the center conductor as a thin wire of width w) the kinetic contribution per unit lenght is:

$$L_l^K \approx \frac{L_K^\square}{w} \tag{5.18}$$

where $L_K^\square$ is the sheet kinetic inductance. Hence, from Equation Eq. (5.14) increasing $L_K^\square$ (via material choice) or reducing w raises the impedance of the line.

CPW resonators

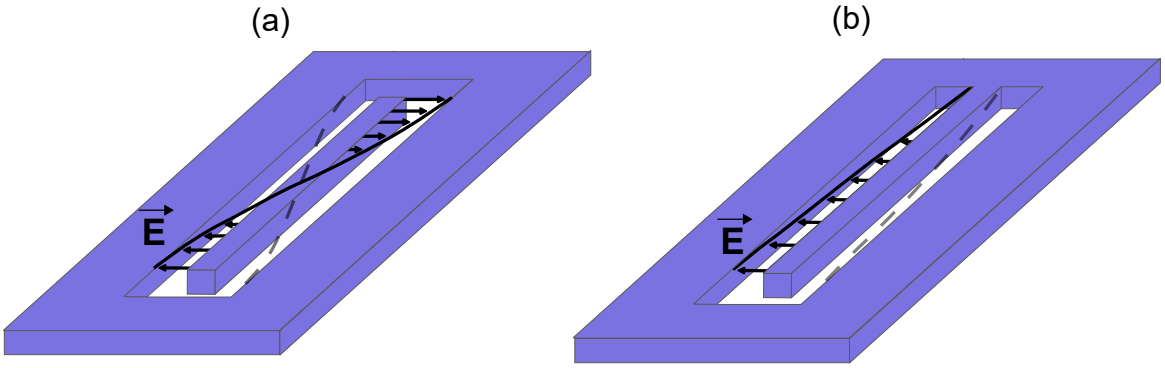

Figure 5.2: **Coplanar waveguide resonators**
(a) Schematic of a half-wavelength CPW resonator, realized as an open-ended section of a CPW transmission line.
(b) Schematic of a quarter-wavelength CPW resonator, realized as a CPW line with one end open and the other end shorted to ground.

By appropriately terminating a finite-length CPW (open- or short-circuited at one or both ends), one realizes standing-wave resonators. Below, we will describe the two resonator geometries that will be employed in our microwave circuit.

Half-wavelenght CPW resonators

A half-wavelength CPW resonator is realized by an open-ended section of transmission line of physical length l, see Fig.5.2(a). In its fundamental mode, the voltage has antinodes at both ends and a node at the center. The condition $l = \lambda/2$ sets the fundamental resonance frequency, so that:

$$f_c = \frac{v_p}{\lambda} = \frac{1}{2l\sqrt{C_l L_l}} \tag{5.19}$$

where v_p is the phase velocity defines Eq. (5.14).

Near resonance, the distributed resonator can be mapped onto a parallel R-L-C circuit whose parameters are [131]:

$$R_{\lambda/2} = \frac{Z_0}{\alpha l} \quad C_{\lambda/2} = \frac{\pi}{2\omega_c Z_0} \quad L_{\lambda/2} = \frac{1}{\omega_c^2 C_{\lambda/2}} \tag{5.20}$$

where Z_0 is the characteristic impedance of the line defined Eq. (5.14) and α its attenuation constant.
Equivalently, one may express $L_{\lambda/2}$ and $C_{\lambda/2}$ directly in terms of the per-unit-length values:

$$L_{\lambda/2} = \frac{2l}{\pi^2} L_l \quad \text{and} \quad C_{\lambda/2} = \frac{l}{2} C_l \tag{5.21}$$

The fundamental resonance frequency then follows from

$$f_c = \frac{\omega_c}{2\pi} = \frac{1}{2\pi\sqrt{C_{\lambda/2} L_{\lambda/2}}} \tag{5.22}$$

and the effective mode impedance is

$$Z_c = \sqrt{\frac{L_{\lambda/2}}{C_{\lambda/2}}} = \frac{2}{\pi}\sqrt{\frac{L_l}{C_l}} = \frac{2}{\pi} Z_0 \tag{5.23}$$

Quarter wavelength CPW resonators

A quarter-wavelength CPW resonator is realized by terminating a transmission line of length l with one end open and the other end shorted to ground, see Fig.5.2(b). In its fundamental mode, the voltage reaches an antinode at the open end and a node at the grounded end. More generally, the resonance condition is:

$$l = (2n-1)\frac{\lambda}{4}, \quad \text{with} \quad n = 1,2,3,..., \tag{5.24}$$

so that the n-th harmonic resonates at:

$$f_n = \frac{v_p}{\lambda} = (2n-1)\frac{1}{4l\sqrt{C_l L_l}} \tag{5.25}$$

with v_p is the phase velocity defines Eq. (5.14).

Near resonance, the structure can be mapped onto a parallel R-L-C circuit with parameters [131]:

$$R_{\lambda/4} = \frac{Z_0}{\alpha l} \quad C_{\lambda/4} = \frac{\pi}{4\omega_c Z_0} \quad L_{\lambda/4} = \frac{1}{\omega_c^2 C_{\lambda/2}} \tag{5.26}$$

Expressed in terms of the distributed line parameters, these become:

$$L_{\lambda/4} = \frac{8l}{\pi^2} L_l \quad \text{and} \quad C_{\lambda/4} = \frac{l}{2} C_l \tag{5.27}$$

Consequently, the fundamental resonance frequency and the effective mode impedance are:

$$f_1 = \frac{\omega_c}{2\pi} = \frac{1}{2\pi\sqrt{C_{\lambda/4} L_{\lambda/4}}} \quad \text{and} \quad Z_c = \sqrt{\frac{L_{\lambda/4}}{C_{\lambda/4}}} = \frac{4}{\pi} Z_0 \tag{5.28}$$

5.1.3 A microwave circuit with high kinetic superconducting material

Our microwave circuit design closely follows previous implementations [134], [49], [135]. In the following we describe the individual circuit elements in detail.

Geometry of the Microwave Cavity

The core of the circuit is a half-lenght CPW resonator fabricated from a high-kinetic-inductance film. By choosing the CPW dimensions-center-conductor width w, the gap s, and total lenght l - we target a fundamental resonance f_c in the 4-8 GHz band. In this mode the voltage has antinodes at both ends of the resonator, which allows two spatially separated spin qubits to be coupled by wiring each qubit to one end of the CPW.
To excite and measure the resonator we capacitively couple it to a 50 Ω CPW feedline. Two coupling geometries are commonly employed:

- **The hanger geometry**:
  The feedline is capacitively coupled to the resonator. An input tone is launched into one end of the feedline and we monitor the transmission S_{21} at the other end. For a tone send off the resonance of cavity, the feedline appears essentially transparent ($|S|_{21} \approx 1$). When the tone is on resonance with the frequency of the cavity, the energy is transferred into the resonator and then reflected back or dissipated producing a notch (dip) in the amplitude of the transmitted parameter along with a phase shift in S_{21}. The transmitted signal can be written as:

  $$S_{21}(\omega) = S_{\mathrm{H}}(\omega) = \frac{2i(\omega-\omega_c)-\kappa_i}{\kappa-2i(\omega-\omega_c)} \tag{5.29}$$

  where $\kappa = \kappa_c + \kappa_i$ is the total decay rate, that combines the external coupling rate into the feedline κ_c and the resonator's intrinsic loss rate κ_i. A derivation of this formula is given on the first chapter of this thesis.

- **The Reflection (One-Port) Geometry**:
  The feedline terminates in the resonator via a coupling capacitance. A tone launched into the feedline is reflected, and we measure the reflexion coefficient S_{11}. For a off-resonance tone, nearly all power reflects ($|S|_{11} \approx 1$). For a tone at resonance with the cavity, the reflected amplitude dips and its phase shifts according to:

$$S_{11}(\omega) = \frac{\kappa_c - \kappa_i + 2i(\omega - \omega_c)}{\kappa - 2i(\omega - \omega_c)} \tag{5.30}$$

  where $\kappa = \kappa_c + \kappa_i$. As with the hanger geometry, fitting the amplitude and phase response around ω_c yields both the external coupling rate to the feedline κ_c and the intrinsic loss rate of the resonator κ_i.

Hanger geometries are ideal for multiplexed readout of several resonators on one feedline, while one-port setups can be simpler when only a single resonator is used.
In both cases the coupling capacitance C_c must be taken into account. The total capacitance becomes $C_{\lambda/2} + C_c$, so that

$$f_c = \frac{1}{2\pi} \frac{1}{\sqrt{(C_{\lambda/2} + C_c)(L_{\lambda/2})}} \tag{5.31}$$

Since $C_{\lambda/2} \gg C_c$ - the resulting frequency shift is only a few MHz and can be neglected for our broad range 4-8 GHz target frequency.

Microwave leakage into DC gates in spin-qubit architectures

In spin-qubit devices, maximally efficient coupling between the spin transition and the cavity field requires an antisymmetric electric field distribution across the double quantum dot (see Chapter 1). To realize this, the CPW resonator is connected to one of the electrodes shaping the electrostatic potential along the carbon nanotube, see the schematic presented Fig. 5.3(a).

However, this configuration introduces two primary channels for unwanted microwave photon leakage:

- **DC bias injection**: the resonator's center conductor must be DC-biased, which can allow RF energy to escape through the bias network.
- **Parasitic gate coupling**: neighboring gate electrodes couple capacitively to the resonator, providing an alternate path for microwave photons to leak away.

Minimizing these leakage channels is critical both for fast, high-fidelity qubit readout and for preserving coherent, high-fidelity cavity-mediated interactions between distant qubits.

To bias the CPW without spoiling its microwave performance, we incorporate a DC-tap filter connected to the resonator similar to that in [134]. This filter consists of a shunt capacitor C_{tap} to ground in series with an inductor L_{tap} . For DC signal, the capacitor is open and the inductor passes the bias voltage into the resonator. For microwave frequencies, C_{tap} provides a low-impedance path to ground, while L_{tap} blocks the RF, preventing leakage back into the bias line.

Moreover, the CPW sections that link one open end of the half-wavelength resonator to the DC-tap filter act themselves as quarter-wavelength resonators in which the shunt capacitor behaves as a RF short to ground [134], see Fig.5.3(c). By engineering this quarter-wavelength resonator to resonate at half the fundamental of the main cavity we create a narrow-band band-pass filter. Only photons within

$$\left[f_1^{\lambda/4} - \frac{\Delta f^{\lambda/4}}{2}, f_1^{\lambda/4} + \frac{\Delta f^{\lambda/4}}{2} \right] \quad \text{where} \quad \Delta f^{\lambda/4} = \frac{\kappa^{\lambda/4}}{2\pi} \tag{5.32}$$

$\kappa^{\lambda/4}$ being the total rate losses of the quarter-wavelength resonator, can leak into the bias network. Positioning spatially the T-junction that connects the DC-tap filter to the half-wavelength mode resonator at a voltage node of this resonator further reduces spurious leakage.

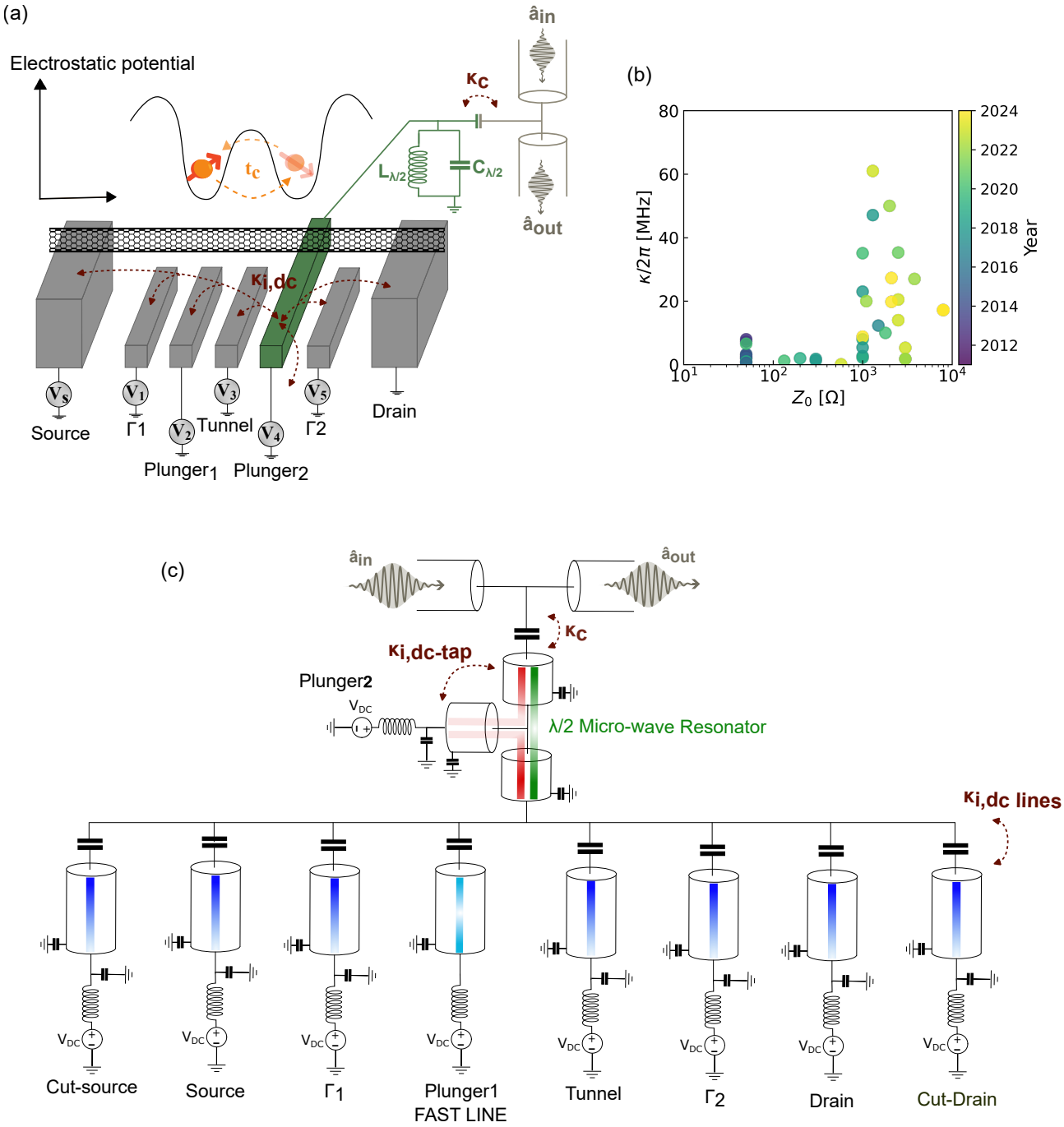

Figure 5.3: **Microwave Challenges in Spin Qubit architectures**
(a) Schematic of the double quantum dot architecture with the microwave circuit. One plunger gate is connected to a half-wavelength CPW resonator, modeled as a parallel $L-C$ circuit capacitively coupled to a hanger feedline. The resonator is also capacitively coupled to the various dc electrodes
(b) Resonator loss rate κ versus characteristic impedance Z_0 of the CPW resonator, extracted from various works : [136],[48],[137],[138], [139], [140], [141], [142], [143], [66] , [3], [144], [145], [146], [147], [148], [149], [150], [151], [152], [153], [86], [64], [49], [154], [155], [156], [157], [158], [159], [4], [160], [161]. The color bar encodes the publication year
(c) Simplified electrical model of the microwave circuit. The half-wavelength mode (green) coexists with two quarter-wavelength modes (red). Quarter-wavelength standing waves are also stabilized on the dc lines (dark blue). A dedicated "fast" line, with a different layout, supports a half-wavelength mode (light blue). Dominant leakage paths for the half-wavelength mode are indicated by dark-red arrows. The resonator is probed in a hanger geometry via capacitive coupling to the feedline.

Similarly, each gate electrode that couples capacitively to the main resonator must be carefully filtered. As the resonator impedance Z_0 increases, losses through these parasitic capacitances increase significantly, directly impacting the resonator's intrinsic decay rate κ_i. Figure 5.3(b) compiles data from the literature showing κ versus Z_0. In practice, higher-impedance resonators tends to exhibit larger loss rates. This underscores the necessity of rigorous RF filtering on all DC lines in high-impedance, spin-qubit circuits.

The DC-line filters introduced later in this chapter mirror the resonator's DC-bias network. Each uses the same LC elements arranged as a quarter-wavelength resonator providing attenuation at the half-wavelength cavity's frequency thereby attenuating leakage into the gate lines. A simplified electrical model of the microwave circuit is presented Fig.5.3(c).

Estimation of the coupling losses

Following the approach of [162], we model the leakage path from the CPW resonator into a line connected to a lossy load Z_g via a small coupling capacitance C. The schematic is shown in Fig.5.4

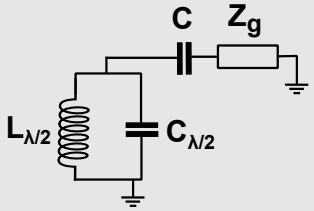

Figure 5.4: The resonator modeled as a parralel $L-C$ circuit is coupled through a capacitor C into a lossy load Z_g

Energy Stored in the Resonator

For the fundamental mode of a $\lambda/2$ resonator, the total stored energy is:

$$E = \left[\frac{1}{2}C_{\lambda/2}V_{\mathrm{RMS}}^2 + \frac{1}{2}L_{\lambda/2}I_{\mathrm{RMS}}^2\right] = \left[\frac{1}{2}C_{\lambda/2}V_{\mathrm{RMS}}^2 + \frac{1}{2}L_{\lambda/2}\frac{V_{\mathrm{RMS}}^2}{Z_c^2}\right] = C_{\lambda/2}V_{\mathrm{RMS}}^2$$

where $Z_c = \sqrt{L_{\lambda/2}/C_{\lambda/2}}$ is the mode impedance.

Power Dissipated into the Lossy Load

The power dissipated into the lossy load Z_g through the capacitance C is

$$P_{\mathrm{diss}}(\omega) = V_{\mathrm{RMS}}^2\,\mathrm{Re}\{Y(\omega)\} = V_{\mathrm{RMS}}^2\frac{(\omega C)^2 Z_g}{1+\left(\omega C Z_g\right)^2}$$

Here $Y(\omega)$ is the equivalent complex admittance of the two elements in series : the coupling capacitance C and the impedance Z_g. In the weak-coupling limit $Z_g(\omega C) \ll 1$, this simplifies to:

$$P_{\mathrm{diss}}(\omega) = V_{\mathrm{RMS}}^2(\omega C)^2 Z_g$$

Coupling-Induced Decay Rate

The $1/e$ energy-decay time $\tau_{1/e}$ due solely to this leakage channel is:

$$\tau_{1/e} = \frac{E}{P_{\mathrm{diss}}(\omega_c)} = \frac{C_{\lambda/2}}{\omega_c^2 C^2 Z_g}$$

so the corresponding coupling-limited decay rate $\kappa_g = 1/\tau_{1/e}$ is:

$$\kappa_g = \frac{\omega_c^2 C^2 Z_g}{C_{\lambda/2}} = \frac{2}{\pi} Z_g Z_0 \omega_c^3 C^2 \tag{5.33}$$

This relationship confirms that as the CPW's impedance rises, so do its losses due to the coupling to the lossy load - underscoring the critical need to implement careful RF filtering on all the DC lines capacitively coupled to the resonator.

5.2 RF circuit design and validation via lumped and electromagnetic modeling

In this section, we describe the various simulations carried out to gain a deeper understanding of the microwave circuit's behavior. This enables us to make informed decisions regarding the dimensions of the circuit components to minimize microwave losses in the main half-wavelength resonator.

5.2.1 Quite Universal Circuit Simulator (QUCS): modeling the circuit with lumped elements

QUCS is an open-source, GUI-based tool for designing and simulating electronic circuits. It allows users to assemble circuits in a schematic editor using lumped elements, and numerically solves the corresponding circuit equations.

Building the schematic

The CPW transmission lines are modeled using their lumped-element equivalents, represented by per-unit-length parameters R_l, L_l, C_l, G_l described earlier. In our case, the lines are assumed lossless, i.e., $R_l = G_l = 0$. The geometric contributions to the per-unit-length inductance and capacitance are calculated using conformal mapping techniques (see equation Eq. (5.15)). The total inductance per unit length includes both geometric and kinetic inductance contributions (see equations Eq. (5.17) and Eq. (5.18)).
In our work, the high-inductance, magnetic-field-resilient NbN films are expected to exhibit a kinetic inductance of approximately $200\,\mathrm{pH\,m^{-2}}$ [6]. For a CPW line with a gap of $s = 2\,\mu\mathrm{m}$ and a track width of $w = 0.8\,\mu\mathrm{m}$, we estimated the per-unit-length inductance and capacitance as $L_l = 248\,\mu\mathrm{H\,m^{-1}}$ and $C_l = 80\,\mathrm{pF\,m^{-1}}$, respectively.

Resonators are modeled as sections of CPW transmission lines whose terminations determine their behavior. For the main resonator, a half-wavelength cavity, both ends are left open. The length of this cavity was chosen as $l_{\lambda/2} = 500\,\mu\mathrm{m}$, corresponding to a resonance frequency of $f_c^{\lambda/2} = 7.12\,\mathrm{GHz}$ calculated via equation Eq. (5.19).
The *LC* filters used to suppress cavity photon leakage into DC lines are modeled using lumped elements and terminated with a lossy load of impedance $\mathrm{Z} = 50\,\Omega$.

To drive and read out the cavity, a hanger-line geometry is employed. The hanger line is modeled as a transmission line with a characteristic impedance of $Z_0 \approx 50\,\Omega$, with ports at both ends of impedance $\mathrm{Z} = 50\,\Omega$ enabling signal injection and scattering parameter simulation.

Nodal Analysis for Scattering Parameter Estimation

QUCS treats all circuit components - including resistors, capacitors, inductors, and $R_l L_l C_l G_l$ transmission line models - as linear elements at each discrete frequency point.

The software constructs a modified nodal analysis (MNA) matrix $\mathbf{Y}(\omega)$ based on Kirchhoff's Current Law (KCL) and Kirchhoff's Voltage Law (KVL). For each node i in the circuit, the relationship between currents and voltages across all nodes j is expressed as:

$$I_i = \sum_j Y_{ij}(\omega) V_j \tag{5.34}$$

For a transmission line of characteristic impedance Z_0, the incident and reflected scattering-wave amplitudes at port i are defined as:

$$a_{\text{in},i} = \frac{V_i^+}{\sqrt{Z_0}}, \quad a_{\text{out},i} = \frac{V_i^-}{\sqrt{Z_0}} \tag{5.35}$$

Thus, the forward and backward traveling powers are $\left|a_{\text{in},i}\right|^2$ and $\left|a_{\text{out},i}\right|^2$, respectively.
Since the voltage and current at the port can be written as:

$$V_i = V_i^+ + V_i^-, \quad I = \frac{V_i^+}{Z_0} - \frac{V_i^-}{Z_0} \tag{5.36}$$

Rewriting these in terms of total voltage and current yields:

$$a_{\text{in},i} = \frac{V_i + Z_0 I_i}{2\sqrt{Z_0}}, \quad a_{\text{out},i} = \frac{V_i - Z_0 I_i}{2\sqrt{Z_0}} \tag{5.37}$$

To determine the transmission parameter between ports 1 and 2, an incident wave is applied at port 1 (with $a_{\text{in},i} = 1$). Solving the linear system $\mathbf{I} = \mathbf{Y}(\omega)\mathbf{V}$ under this excitation yields the voltages and currents throughout the circuit, allowing calculation of the S-parameter:

$$S_{21} = \frac{a_{\text{out},2}}{a_{\text{in},1}} \tag{5.38}$$

By evaluating this transmission coefficient over a frequency sweep, the frequency-dependent complex behavior of the S_{21} parameter is obtained.

In our study, port 1 corresponds to one end of the hanger line coupled to the cavity, while port 2 corresponds to the opposite end. Thus, the frequency-dependent transmission response $S_{21} = S_{\text{H}}$ (defined in equation Eq. (5.29)) can be simulated for any given circuit configuration.

5.2.2 Modelling of the main resonator with DC-bias filtering

In this section, we focus on a circuit consisting of a half-wavelength resonator, to which a DC tap filter is connected at its midpoint. This filter comprises a shunt capacitor to ground in series with an inductor, terminated by a lossy load with impedance $Z = 50\,\Omega$. We investigate how the length $l_{\text{dc-tap}}$ of the T-junction - extending from the center of the resonator to the *LC* filter and modeled as a CPW transmission line - influences the quality factor of the half-wavelength resonator, Fig. 5.5(a-b).
For the *LC* filter, the capacitance and inductance values are chosen to reflect practical on-chip realizations of capacitors and inductors [130].

Using QUCS, we simulate the S_{21} parameter of the circuit shown in Fig. 5.5(b) for various values of $l_{\text{dc-tap}}$. From the frequency dependence of the scattering parameter's amplitude $|S_{21}|$, we can identify resonance dips corresponding to both the main half-wavelength resonator and the quarter-wavelength resonator formed by the DC-tap filter. The resonance frequencies and loss rates of these modes are determined by fitting the complex scattering parameter $S_{21}(\omega)$ according to the method described in [163].

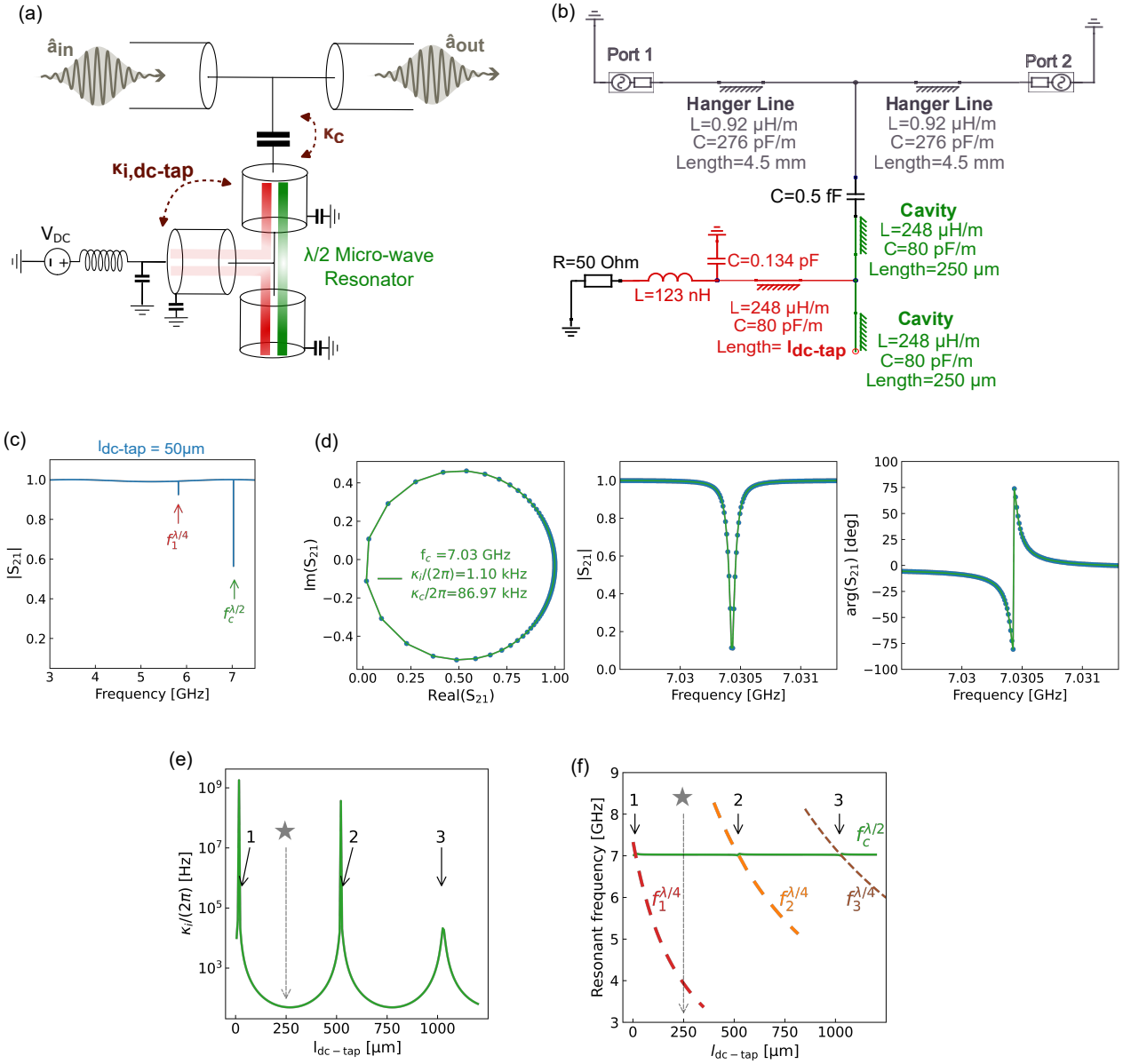

Figure 5.5: **Micro-wave resonator with DC-bias filtering**
(a) Simplified electrical model of a dc-biased half-wavelength resonator. To mitigate losses introduced by the dc bias, a dc-tap filter is connected at the resonator midpoint. The resonator is probed in a hanger geometry via capacitive coupling to the feedline.
(b) Circuit implemented in QUCS to simulate the microwave network in (a). The length of the CPW section between the resonator center and the *LC* filter is variable and denoted $l_{\mathrm{dc-tap}}$.
(c) Simulated magnitude of the transmission parameter $|S_{21}|(f)$ for $l_{\mathrm{dc-tap}} = 50\mu\mathrm{m}$.
(d) Fit of the complex signal $S_{21}(f)$ around the resonance of the half-wavelength resonator for $l_{\mathrm{dc-tap}} = 50\mu\mathrm{m}$. The fit follows the procedure of [163].
(e-f) By repeating the fit for various $l_{\mathrm{dc-tap}}$, the dependence of the $\lambda/2$ mode resonance frequency $f_c^{\lambda/2}$ (f) and the internal loss rate κ_i (e) are obtain as a function of $l_{\mathrm{dc-tap}}$. The quarter-wavelength harmonic frequencies shown in (f) are obtained by fitting the complex signal $S_{21}(f)$ around the resonance of the $\lambda/4$ resonator. The star plotted in the panels (e-f) corresponds to the selected value of $l_{\mathrm{dc-tap}}$ to minimized photon losses from the $\lambda/2$ resonator.

From these simulations, we can reconstruct how the internal losses of the main half-wavelength resonator depend on the length $l_{\mathrm{dc-tap}}$. Interestingly, certain values of $l_{\mathrm{dc-tap}}$ cause an increase in the resonator's loss rate. To understand this effect, we examine how the resonance frequencies of the different circuit modes vary with $l_{\mathrm{dc-tap}}$.

The dependence of the fundamental resonance frequency of the main resonator $f_c^{\lambda/2}$ on $l_{\mathrm{dc-tap}}$ is shown in Figure 5.5. As expected, this frequency remains constant with varying $l_{\mathrm{dc-tap}}$ yielding $f_c^{\lambda/2} \approx 7\,\mathrm{GHz}$. Likewise, we extract the fundamental and harmonic frequencies of the quarter-wavelength resonator $f_n^{\lambda/4}$, where n is an integer indexing the harmonics.
From equations Eq. (5.19) and Eq. (5.25), for half-wavelength and quarter-wavelength resonators with identical per-unit-length inductance and capacitance, we expect:

$$f_n^{\lambda/4} = f_c^{\lambda/2} \quad \text{for} \quad l^{\lambda/4} = \frac{2n-1}{2} l^{\lambda/2} \tag{5.39}$$

Given that:

$$l_{\lambda/4} = \frac{l_{\lambda/2}}{2} + l_{\mathrm{dc-tap}} \tag{5.40}$$

we find that the frequencies of the half-wavelength mode coincide with those of the quarter-wavelength mode when:

$$l_{\mathrm{dc-tap}} \approx n \times l^{\lambda/2} \tag{5.41}$$

It should be noted that in our simulations, this relation is not recovered exactly. This discrepancy is attributed to the coupling capacitance included in the simulated circuit model.

Interestingly, the points where the resonator's loss rate increases correspond to lengths where the frequency of the main cavity matches a mode of the quarter-wavelength resonator. In other words, as previously discussed, the quarter-wavelength resonator acts as a band-pass filter: when $f_c^{\lambda/2} \in \left[f_n^{\lambda/4} - \frac{\Delta f_n^{\lambda/4}}{2}, f_n^{\lambda/4} + \frac{\Delta f_n^{\lambda/4}}{2}\right]$, the resonator's loss rate increases.

To minimize photon leakage from the main half-wavelength cavity, we select $l_{\mathrm{dc-tap}} = \frac{l_{\lambda/2}}{2}$, see Fig. 5.5(e-f). This choice results in the quarter-wavelength resonator frequencies:

$$f_n^{\lambda/4} = \frac{2n-1}{2} f_c^{\lambda/2} \tag{5.42}$$

Purcell Effect Due to Additional Modes

Coupling a qubit to an electromagnetic mode induces radiative decay of the two-level system, known as the Purcell effect.

A recent study [50] focusing on a hole spin qubit embedded in a NbN-based microwave circuit demonstrates radiative decay of the qubit due to the quarter-wavelength mode formed by the DC-tap. The decay rate of the qubit increases when the qubit frequency is tuned to match that of the quarter-wavelength resonator.

This result underscores the importance of controlling both the resonance frequencies and the loss rates of all microwave circuit modes coupled to the spin qubits to minimize additional dissipation channels for the qubit.

5.2.3 Modeling of the main resonator with filtering of capacitively coupled DC gates

The circuit model and simulation approach here closely follow those described in the previous section. In this part, we consider a circuit comprising a half-wavelength resonator that is capacitively coupled to a CPW transmission line of length $l_{\mathrm{dc-line}}$. This line is terminated with a LC-filter

connected to a lossy load with impedance $Z = 50\,\Omega$. This setup models one of the DC lines that can couple parasitically to the resonator, see Fig.5.6(a-b). The *LC* filter used is identical to the one described previously.

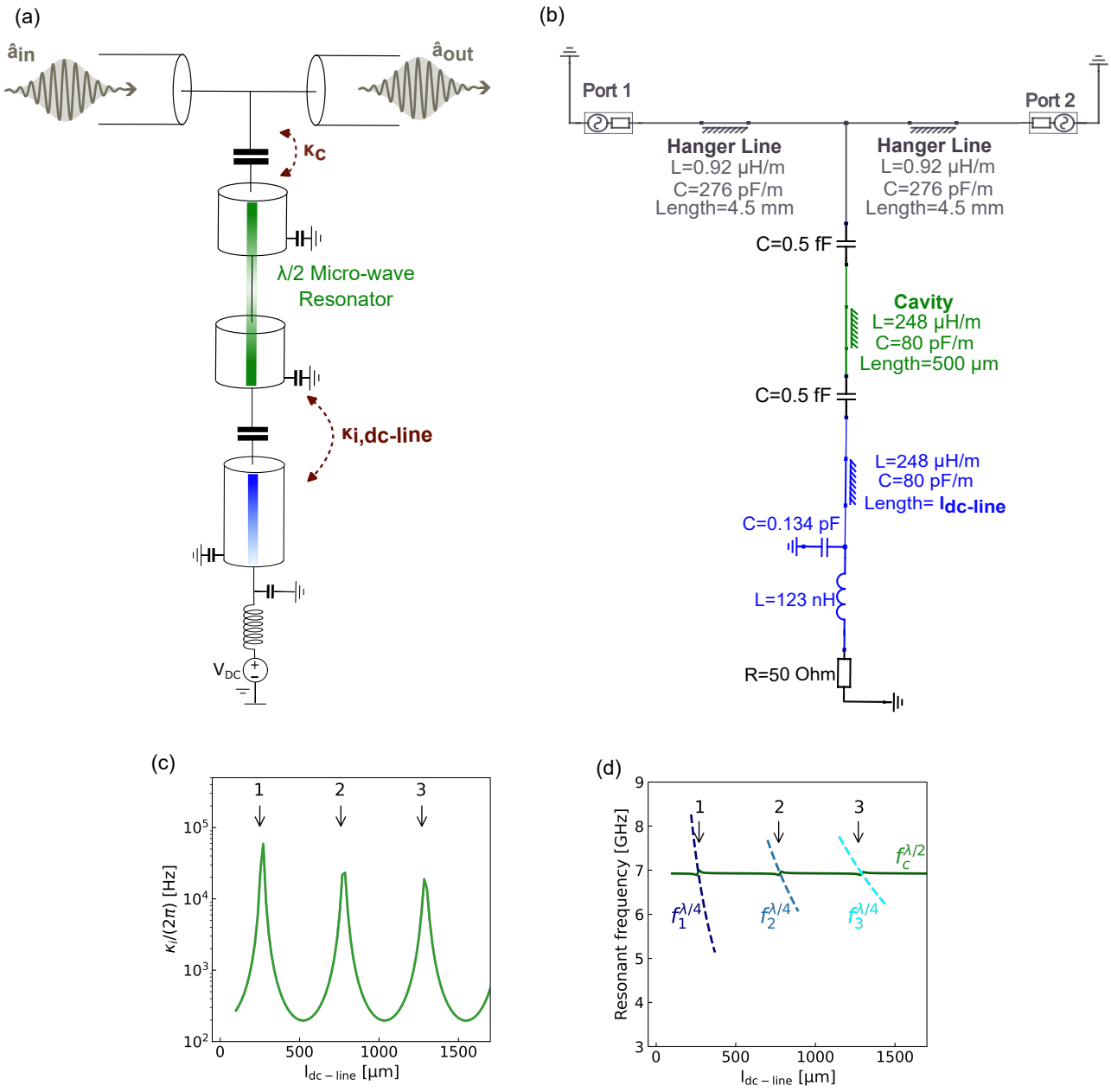

Figure 5.6: **Micro-wave resonator capacitively coupled to a dc-line with filtering**
(a) Simplified electrical model of a half-wavelength resonator capacitively coupled to a dc line. To mitigate losses introduced by this coupling, a dc-tap *LC* filter is connected at the end of the dc line. The resonator is probed in a hanger geometry via capacitive coupling to the feedline.
(b) Circuit implemented in QUCS to simulate the microwave circuit in (a). The length of the CPW section between the coupling capacitor and the *LC* filter is variable and denoted $l_{\mathrm{dc-line}}$.
(c-d) By fitting the complex parameter S_{21} simulated with QUCS around the half-wavelength resonance for various $l_{\mathrm{dc-line}}$, the dependence of the $\lambda/2$ mode resonance frequency $f_c^{\lambda/2}$ (d) and the internal loss rate κ_i (c) are obtain as a function of $l_{\mathrm{dc-line}}$. The quarter-wavelength harmonic frequencies shown in (d) are obtained from separate simulations of the $\lambda/4$ resonator formed by the CPW section between the coupling capacitor and the *LC* filter together with the *LC* filter.

Here, we study how the length $l_{\mathrm{dc-line}}$ influences the loss rate of the half-wavelength resonator. As in the previous section, we simulate the scattering parameter S_{21} to extract both the resonance frequency of the half-wavelength mode and its internal losses. Similar to earlier observations, we find that for certain specific values of $l_{\mathrm{dc-line}}$, the internal losses of the resonator increase noticeably, see Fig.5.6(c).

To investigate this phenomenon, we perform additional simulations where the DC line is directly coupled to the hanger line. This allows us to determine the resonance frequencies of the quarter-wavelength mode that extends from the capacitive coupling point-an effective open end-to the *LC* filter, where the capacitor acts as an RF short to ground. Interestingly, and similarly to the earlier case, we find that increases in the internal loss rate of the resonator correspond to situations where the frequency of the half-wavelength mode coincides with a harmonic of the quarter-wavelength mode, see Fig.5.6(d). This condition is expected when:

$$l_{\mathrm{dc-line}} = l^{\lambda/4} = \frac{2n-1}{2} l^{\lambda/2} \tag{5.43}$$

which aligns well with the results observed in our simulations.
Analogous to DC-bias filtering, filtering of the DC lines functions as a band bandpass filter. It is therefore crucial to select the length $l_{\mathrm{dc-line}}$ such that $f_c^{\lambda/2} \notin \left[f_n^{\lambda/4} - \frac{\Delta f_n^{\lambda/4}}{2}, f_n^{\lambda/4} + \frac{\Delta f_n^{\lambda/4}}{2} \right]$ in order to minimize the resonator's loss rate.

Optimizing the dimensions of CPW DC lines

Reducing the length $l_{\mathrm{dc-line}} = l^{\lambda/4}$ can shift the resonance frequency of the quarter-wavelength mode to higher values, ensuring that $f_0^{\lambda/4} \gg f_c^{\lambda/2}$. This would position the quarter-wave resonances well above the main resonator frequency, thereby effectively suppressing cavity losses.
However, minimizing $l_{\mathrm{dc-line}}$ is practically challenging due to the spatial footprint required for the *LC*-filter. Some works in the literature [134] propose *LC* filter architectures with reduced footprints that could help achieve this goal.
In our case, the minimum feasible length of $l_{\mathrm{dc-line}}$ is limited to approximately 800 µm to accommodate the *LC* filter.
With this length, the expected resonance frequencies of the quarter-wavelength modes are:

$$f_1^{\lambda/4} = 2.2\,\mathrm{GHz}, \quad f_2^{\lambda/4} = 6.6\,\mathrm{GHz} \quad \text{and} \quad f_3^{\lambda/4} = 11.1\,\mathrm{GHz},$$

This situation could be problematic, as some of these resonances lie close to the cavity's operating frequency.

Another strategy is to engineer the dimensions of the CPW line forming the DC line. In our current design, the CPW track and gap widths are identical to those of the main cavity. However, it is possible to alter these dimensions. For instance, by choosing a track width of $w = 4\,\mu\mathrm{m}$ and a gap of $s = 2\,\mu\mathrm{m}$, and setting $l_{\mathrm{dc-line}} = 1000\,\mu\mathrm{m}$ we obtain:

$$f_1^{\lambda/4} = 3.0\,\mathrm{GHz}, \quad f_2^{\lambda/4} = 8.9\,\mathrm{GHz} \quad \text{and} \quad f_3^{\lambda/4} = 14.8\,\mathrm{GHz}$$

This geometry ensures that none of the harmonics of the quarter-wavelength resonator fall within the $4-8$GHz range, which helps avoid additional loss channels for the cavity.

Filtering the Fast Line

Among the five gates used to define the electrostatic potential along the carbon nanotube, one of the plunger gates (as shown in the schematic in Figure 5.3) is connected to the resonator, while

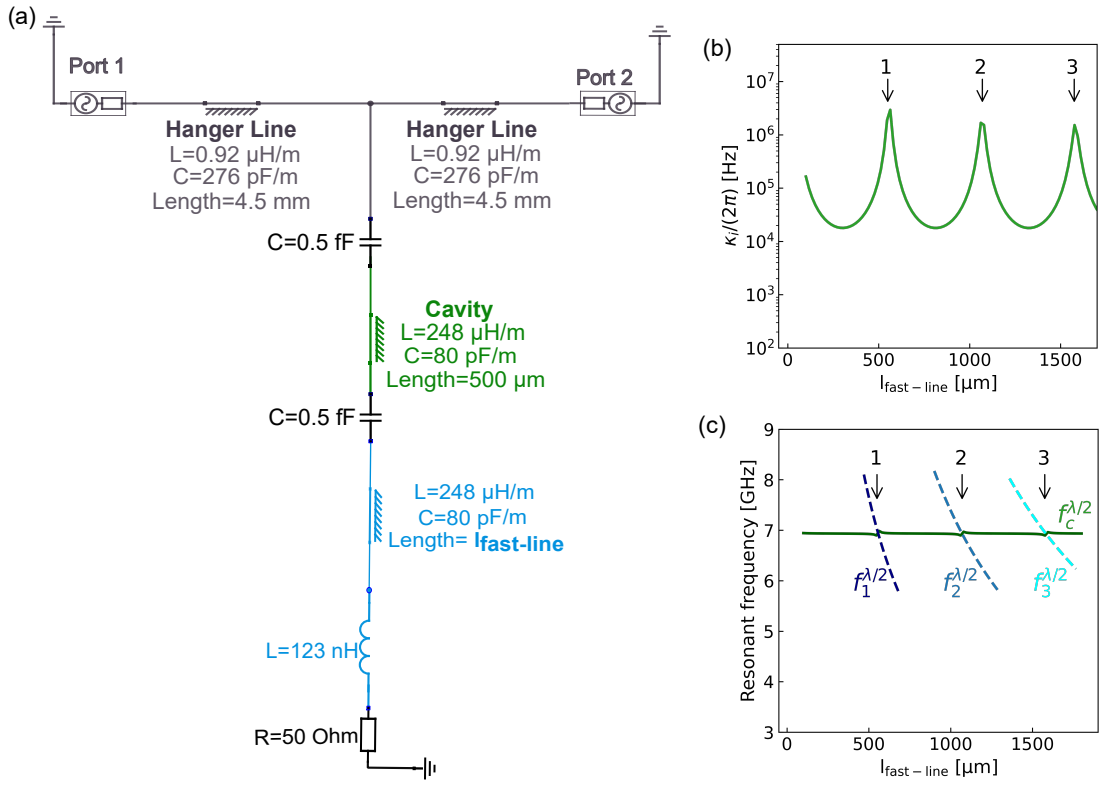

Figure 5.7: **Micro-wave resonator capacitively coupled to a dc-line with adjusted filtering scheme (Fast Line)**
(a) Circuit implemented in QUCS to simulate a microwave circuit composed of a half-wavelength resonator capacitively coupled to a dc line. To mitigate losses introduced by this coupling, an inductance filter is connected at the end of the dc line. The length of the CPW section between the coupling capacitor and the *LC* filter is variable and denoted $l_{\text{fast-line}}$.
(b-c) By fitting the complex parameter S_{21} simulated with QUCS around the half-wavelength resonance for various $l_{\text{fast-line}}$, the dependence of the $\lambda/2$ mode resonance frequency $f_c^{\lambda/2}$ (c) and the internal loss rate κ_i (b) are obtain as a function of $l_{\text{fast-line}}$. The half-wavelength harmonic frequencies shown in (c) are obtained from separate simulations of the $\lambda/2$ resonator formed by the CPW section between the coupling capacitor and the *L* filter together with the *L* filter.

another can be employed to deliver microwave excitations to the qubit. For this reason, a different filtering scheme can be applied to this particular gate, omitting the capacitor from the *LC* filter to avoid excessive attenuation of the microwave signal.

In this context, we model a circuit similar to the one presented previously but replace the *LC* filter with a filter consisting solely of an inductor, see Fig.5.7(a). Since an inductor presents a high impedance at RF frequencies, the mode confined within the CPW line of length $l_{\text{fast-line}}$ located between the open end of the line and the inductor, should behave as a half-wavelength resonator mode.

By performing simulations in QUCS following the same procedure used previously, we investigate how the internal losses of the main half-wavelength resonator vary with the length $l_{\text{fast-line}}$, Fig.5.7(b). We observe increases in the internal losses for the condition :

$$l_{\text{fast-line}} = l_{\lambda/2} \tag{5.44}$$

Once again, the resonance frequency of the half-wavelength mode formed in the DC line can be simulated independently by considering a circuit in which the hanger line is directly coupled to the DC line (thus suppressing the CPW section corresponding to the main cavity). Comparing

the frequency of the main cavity to the resonance frequencies of the modes supported by the DC line, we find that the increase in internal losses occurs for values of $l_{\text{fast-line}}$ where the main cavity frequency coincides with one of the harmonics of the mode in the DC line, see Fig.5.7(c).

Interestingly, we also observe that for this geometry, even under the most favorable conditions, the minimum internal loss rate of the resonator remains two orders of magnitude higher than when employing the *LC* filter. Consequently, using such a purely inductive filter for the fast line - rather than a *LC* filter - remains an open question, since the issue of microwave attenuation might be mitigated by increasing the power of the applied microwave signal.

5.2.4 HFSS eigenmode simulations: electromagnetic modeling of the circuit

HFSS (High Frequency Structure Simulator) is Ansys's industry-standard 3D full-wave electromagnetic solver. It employs the finite-element method to solve Maxwell's equations in complex structures-such as antennas, microwave circuits, waveguides, filters, PCBs, and more-across a broad frequency range. HFSS includes an eigenmode solver that computes the natural resonant frequencies (the eigenvalues) and the corresponding electromagnetic field patterns (the eigenmodes) of a given structure. In this work, we use this solver to simulate the eigenmodes supported by the actual microwave circuit implementations of our design.

The general workflow of the simulation process is as follows:

- **Geometry and material property definition**:
  We construct a 3D model that replicates the geometry of our experimental chip. Accounting for the kinetic inductance of NbN in the material definition is crucial. We incorporate kinetic inductance in two ways.
  For the ground plane and the CPW track of the hanger line, we apply an impedance boundary condition corresponding to a surface impedance. Specifically, we assign a purely imaginary surface impedance of $\omega L_K^{\square} = 8.44\,\Omega \cdot \square^{-1}$, calculated at a frequency of $f = \omega/(2\pi) = 7\,\text{GHz}$.
  Since this impedance boundary is specified at a single frequency, it is insufficient for eigenmode simulations spanning a frequency range. Therefore, for the central track of the CPW lines forming the main half-wavelength resonator - and also for the CPW sections comprising the resonators formed by the DC-tap and DC lines with *LC* filters - we implement kinetic inductance via lumped inductance boundary conditions. This boundary condition introduces a lumped series inductance element between the two edges of the CPW line, such that any current crossing from one side to the other encounters this series inductance. This approach enables the inclusion of a strip inductance given by $L = \frac{l}{w} L_K^{\square}$, where l is the length and w the width of the CPW segment.
- **Definition of** $50\,\Omega$ **Ports**
  In the simulations, $50\,\Omega$ resistive ports can be placed at the two ends of the hanger line and at the end of the DC tap line. This effectively "loads" the resonators with $50\,\Omega$ terminations in the eigenmode problem.
- **Simulation Setup and Convergence**:
  In the eigenmode setup, we specify parameters such as the desired number of modes to solve, the frequency range of interest for resonant modes, and the frequency shift tolerance. This last parameter estimates the error by comparing the resonance frequencies of each mode between successive simulation passes. HFSS automatically refines the mesh if the estimated frequency shift exceeds the specified tolerance. Once convergence is achieved, HFSS provides the resonant frequencies and the quality factors of the modes. Note that the quality factors here account for losses primarily due to the $50\,\Omega$ resistive ports of the model. The solver also returns the electric and magnetic field distributions of the computed modes.

Here, we perform HFSS eigenmode simulations to confirm the presence of the modes that we previously predicted.

5.2.5 Eigenmode simulation outcomes and analysis

Half-wavelength resonator with the DC-tap filter

We begin by simulating a section of the circuit consisting of a 500 µm half-wavelength resonator that is capacitively coupled to a hanger line. The dimensions of the CPW line forming the cavity are shown in Figure 5.8. The DC tap filter - composed of an interdigitated capacitor followed by a narrow strip acting as the inductance - is connected to the midpoint of the cavity, with the length of the CPW section set to $l_{\mathrm{dc-tap}} = 250\,\mu\mathrm{m}$. 50 Ω ports are included at both ends of the hanger line and at the end of the DC tap.

By performing HFSS eigenmode simulations, we determine the eigenmodes of this circuit configuration. Specifically, we identify the resonance frequencies of both the half-wavelength resonator and the quarter-wavelength resonator. The resulting eigenfrequencies and corresponding quality factors are summarized in Table 5.1.

The electric field distributions of these two modes are also visualized in Figure 5.8. From these simulations, we confirm that the two modes predicted through lumped-element simulations are indeed present when performing electromagnetic modeling of the circuit with realistic on-chip structures.

Table 5.1: **Resonance frequencies and quality factors of the modes for different circuit configurations**.
It is noteworthy that the quality factor of the quarter-wavelength mode is generally low. Developing more efficient on-chip realizations of the *LC* filters could help improve this quality factor.

	Quarter-wavelength mode		**Halft-wavelength mode**	
Fig.	Frequency [GHz]	Q	Frequency [GHz]	Q
5.8	3.2	821	7.0	38 000
5.9(b),(c)	3.2	540	7.0	700
5.9(e),(f)	3.0	1 050	6.6	12 700

Importance of ground plane definition

A coplanar waveguide (CPW) consists of a center strip conductor flanked by two ground planes on the **same** metal layer, separated by gaps. In practice, the two ground planes are never perfectly equipotential, allowing unwanted slotline modes to be excited. Coupling to these parasitic modes increases photon losses in the cavity [164].

In our geometry, cuts in the ground plane near the resonator can disturb ground-plane uniformity, potentially leading to slotline modes. Experimental observations in a NbN-based microwave circuit [130], [134] showed that wire bonds connecting metallic ground planes were necessary to reduce photon losses and to measure the cavity's resonance frequency accurately.

Here, we perform the same simulation as before but remove the wire bond placed above the interdigitated capacitor of the *LC* filter, see Fig. 5.9(a-c). We observe that eliminating this wire bond leads to a significant decrease in the quality factor of the half-wavelength mode (see Table 5.1). Furthermore, the electric field distribution of this mode exhibits noticeable asymmetries near the interdigitated capacitor. These observations highlight the importance of wire bonds in maintaining a uniform ground plane. In our circuit design, **we ensure sufficient spacing around the *LC* filter capacitors to accommodate wire bonds**.

Additionally, we performed simulations including the wire bond above the interdigitated capacitor but introducing the ground-plane discontinuity present in the actual chip, see Fig. 5.9(d-f). This discontinuity results from the trenches required for the assembly of a carbon nanotube into the chip. The effect of adding this ground-plane discontinuity on the modes' quality factors is less clear: unlike the previous case, the decrease in the half-wavelength resonator's quality factor is less pronounced, see Table 5.1.

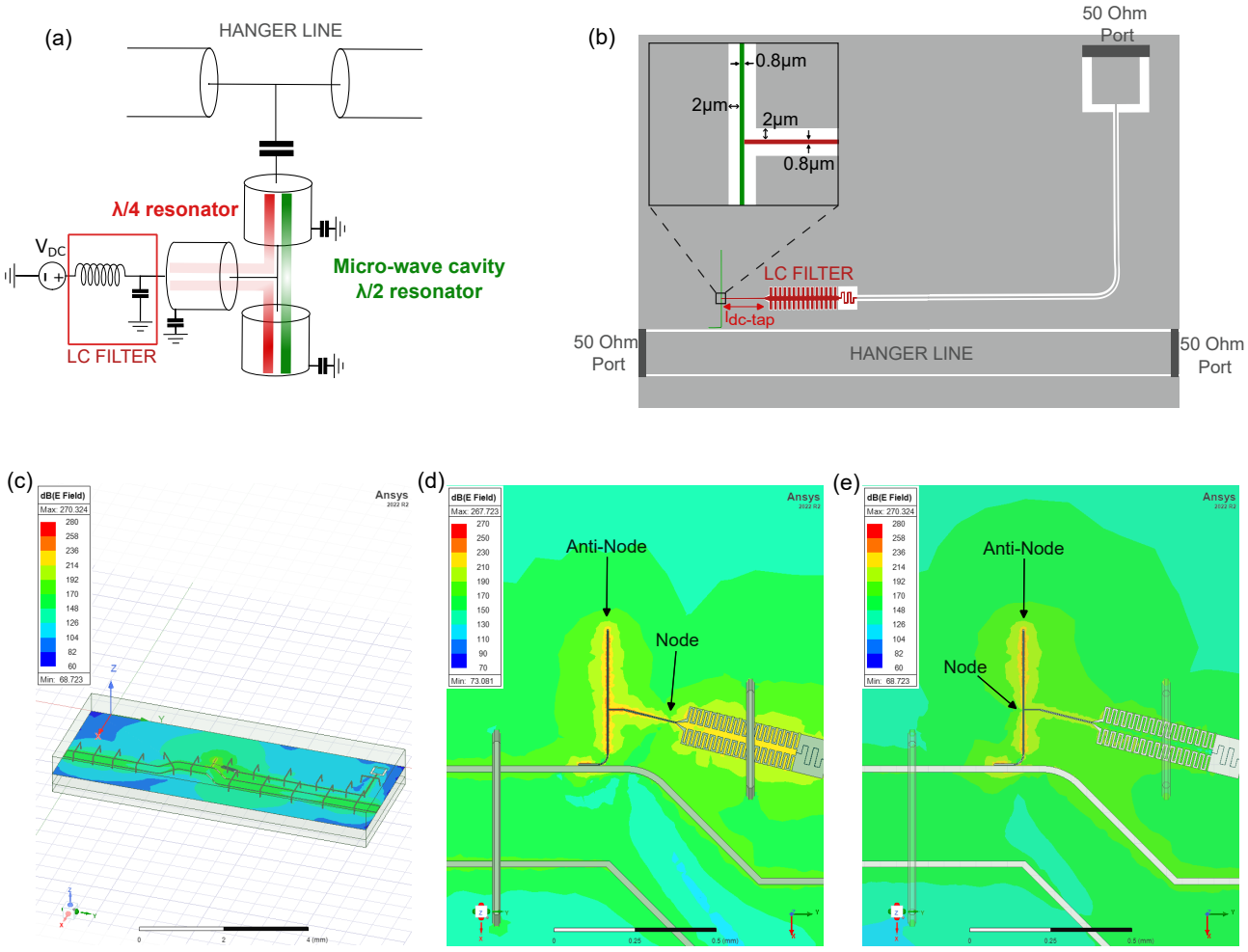

Figure 5.8: **Electromagnetic modeling of the resonator with DC-bias filtering**
(a) Simplified electrical model of a dc-biased half-wavelength resonator.
(b) Geometry simulated with the HFSS eigenmode solver. The *LC* filter consists of an interdigitated capacitor followed by a narrow strip acting as the inductance, similar to [130], [134]. 50 Ω resistive ports are placed at the two ends of the hanger feedline and at the end of the dc-bias line.
(c-e) Electric-field distributions of the chip eigenmodes: (d) quarter-wavelength modes, (e) the half-wavelength mode.

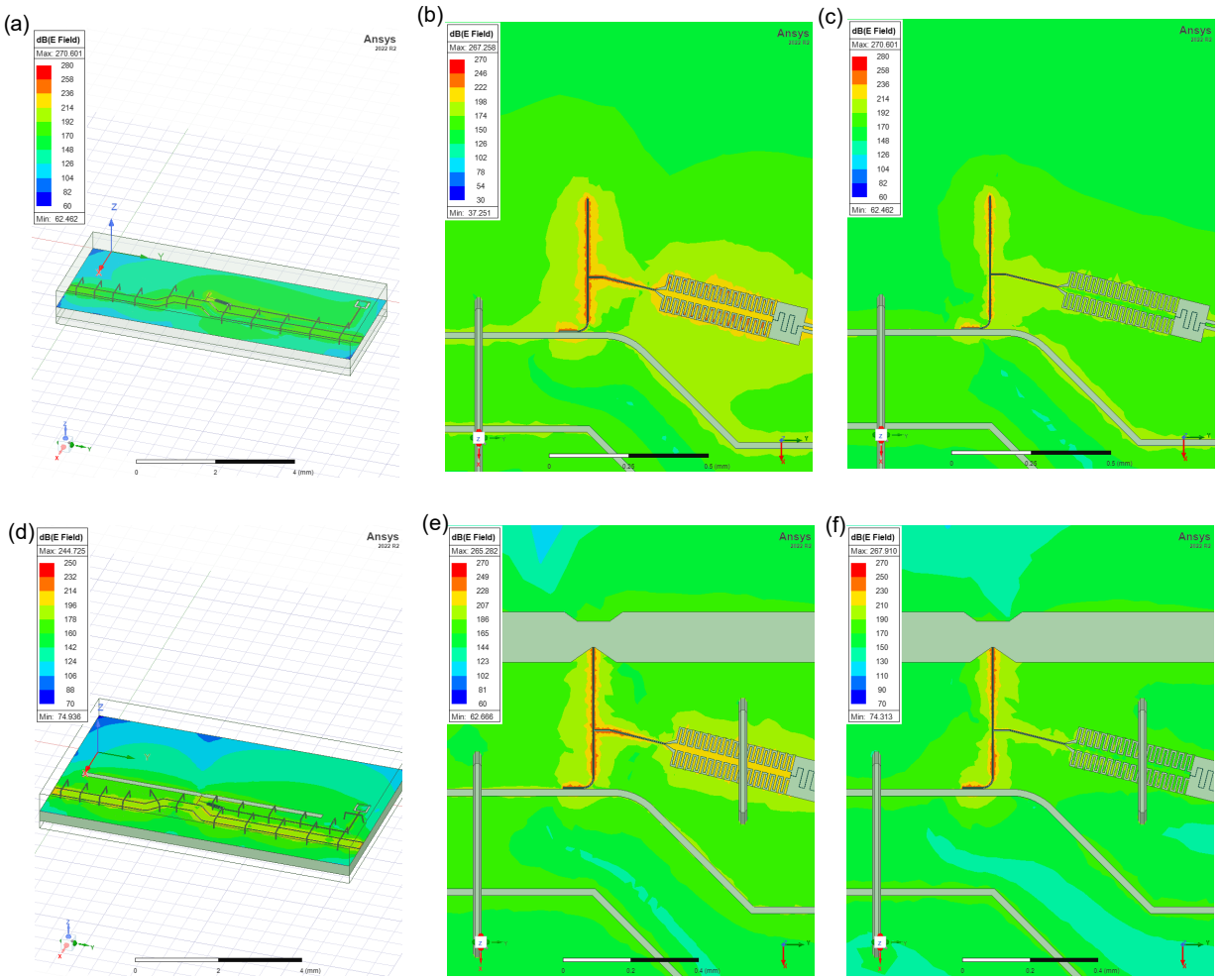

Figure 5.9: **Electromagnetic modeling of a DC-biased resonator: importance of ground-plane definition for the filters**
(a-c) Simulations **without a wirebond bridging the interdigitated capacitor** of the *LC* filter.Panels show electric-field distributions of the chip eigenmodes: (a) simulated layout (b) quarter-wavelength modes, (c) half-wavelength mode.
(d-f) Case with a **ground-plane trench discontinuity**. Panels show electric-field distributions of the chip eigenmodes: (d) simulated layout, (e) quarter-wavelength modes, (f) the half-wavelength mode.

Incorporating DC lines into the circuit simulation

We take into account the DC lines that couple capacitively to the main cavity. The geometry of the main half-wavelength cavity and the DC tap remains unchanged, and we continue to consider a hanger-line configuration. The CPW waveguides forming the DC lines have the same geometry as the main resonator, with a track width of 0.8 µm and a gap of 2 µm. The simulated microwave circuit is shown in Figure 5.10. The dimensions of the the CPW DC-lines used in these simulations were not specifically optimized, as the primary goal was to identify potential resonance frequencies that could exist within the microwave circuit.

For these simulations, we do not include 50 Ω ports, meaning that evaluating the quality factors of the resonant modes is not relevant here. A table summarizing the different resonance frequencies assigned to each mode is presented in Table 5.2.

Table 5.2: **Resonance frequencies of the modes formed in the DC lines**.
The CPW length of the fast line is $l_{\text{fast-line}} = 900\,\mu\text{m}$ corresponding to an expected frequency of 3.9 GHz (from equation Eq. (5.19)). The CPW lengths of the other DC lines are $l_{\text{dc-line}} = 900\,\mu\text{m}$ with expected frequencies $f_1^{\lambda/4} = 1.9\,\text{GHz}$ and $f_2^{\lambda/4} = 5.8\,\text{GHz}$(from equation Eq. (5.25)).
Because the simulated region was quite large, excessive mesh refinement was challenging, and we were only able to achieve a convergence of approximately 5% for these simulations.

DC Line	Frequency [GHz]
Cut-source	$f_2^{\lambda/4} = 4.5$
Source	$f_2^{\lambda/4} = 4.9$
Γ_1	$f_2^{\lambda/4} = 5.0$
Plundger_1 (Fast Line)	$f_1^{\lambda/2} = 3.5$
Tunnel	$f_2^{\lambda/4} = 4.4$
Γ_2	$f_2^{\lambda/4} = 5.3$
Drain	$f_2^{\lambda/4} = 5.0$
Cut-Drain	$f_2^{\lambda/4} = 4.9$

From the electric field distributions presented in Figure 5.10, we confirm the existence of quarter-wavelength modes in the DC lines and a half-wavelength mode in the fast line.

These results align with our previous lumped-element simulations, confirming that the different filters act as resonators functioning as bandpass filters. For the final circuit design, the dimensions - track width, gap, and length - will be carefully optimized to position the resonance frequencies of the modes in the various DC lines appropriately, particularly to avoid resonances within the 4-8 GHz range.

However, in order to determine the optimal geometry for the DC lines it is crucial to calibrate the kinetic inductance of our NbN film. Although the expected value is $200\,\text{pH}.\square^{-1}$, verifying this value is necessary to finalize the design of the microwave circuit.

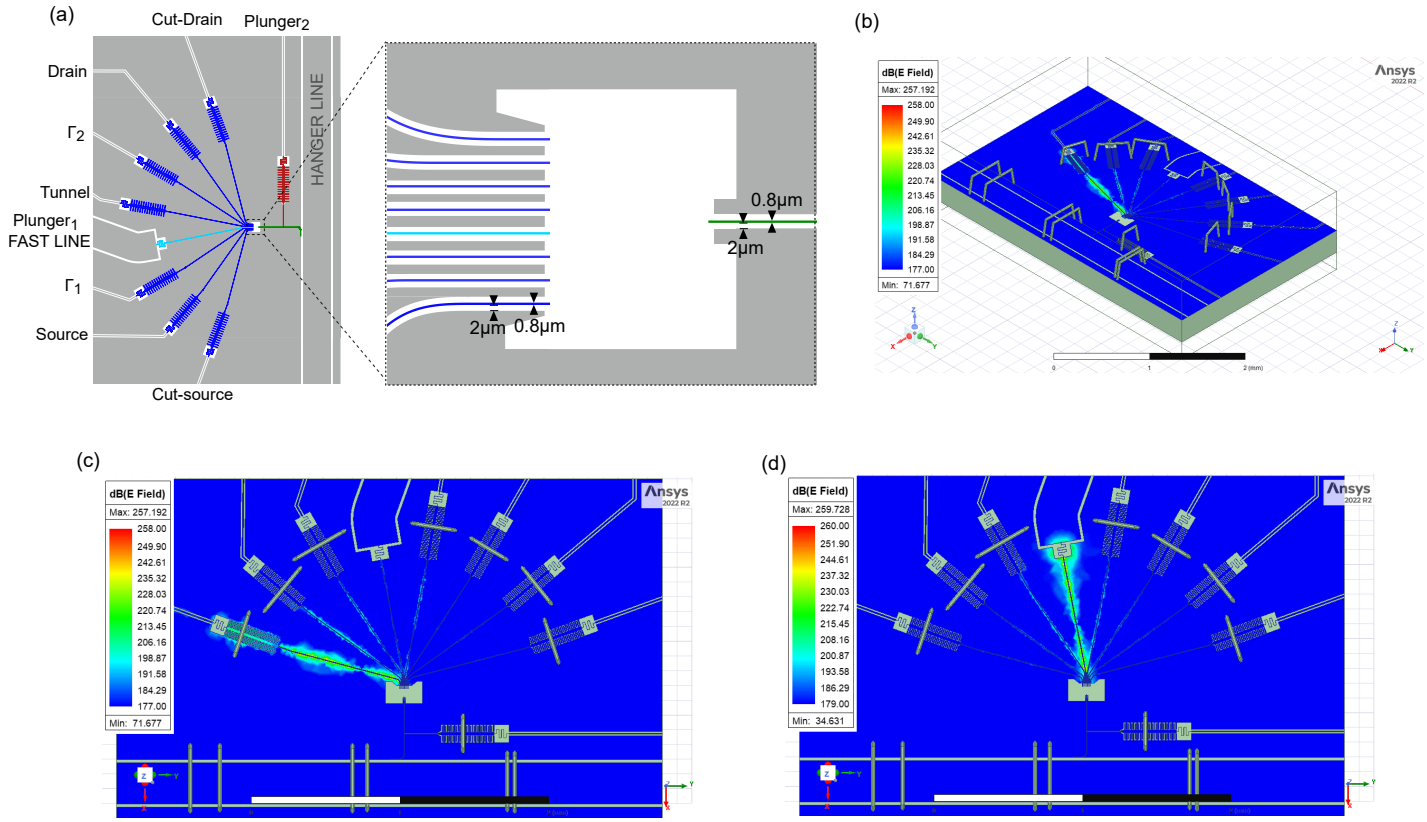

Figure 5.10: **Electromagnetic modeling of the complete microwave circuit**
(a) Geometry simulated with the HFSS eigenmode solver. No resistive ports are included in this simulation. The coplanar waveguides have a track width of $w = 0.8\,\mu$m and a gap width $s = 2\,\mu$m. (b-d) Electric-field distributions of two eigenmodes of the chip. (c) Second harmonic of the quarter-wavelength mode of one of the DC-line (Cut-source). (d) Fundamental half-wavelength mode of the fast line.

5.3 Characterization of NbN superconducting resonators

As previously mentioned, the NbN thin films were deposited at the PHELIQS Laboratory (Grenoble, France). The deposition protocol follows the recipe developed during Cecile Yu's PhD work [130], optimized to achieve a sheet kinetic inductance of approximately $200\,\mathrm{pH}\square^{-1}$.

The deposition is carried out on silicon wafers, 280 µm thick, thermally oxidized to form a 525 nm (±10%) thick SiO_2 layer, supplied by Neyco. On some wafers we further sputter an additional $Si0_2$ layer of thickness ~ 200 nm.

5.3.1 Patterning of structures in the NbN Film

To enable the measurements described in the following sections, resonator structures must be patterned into the NbN films. The fabrication workflow is summarized in Fig. 5.11.

The patterning process began with electron-beam lithography using the positive-tone resist CSAR 62. Pattern transfer was then performed via inductively coupled plasma (ICP) reactive-ion etching using a SF_6/O_2 plasma. In an ICP reactive-ion etcher, an RF coil outside the chamber sustains a high-density plasma, while an independent RF bias on the wafer controls the energy of ions that reach the surface. The process enables fast, chemically driven etch with highly directional ion assistance enabling straight features.

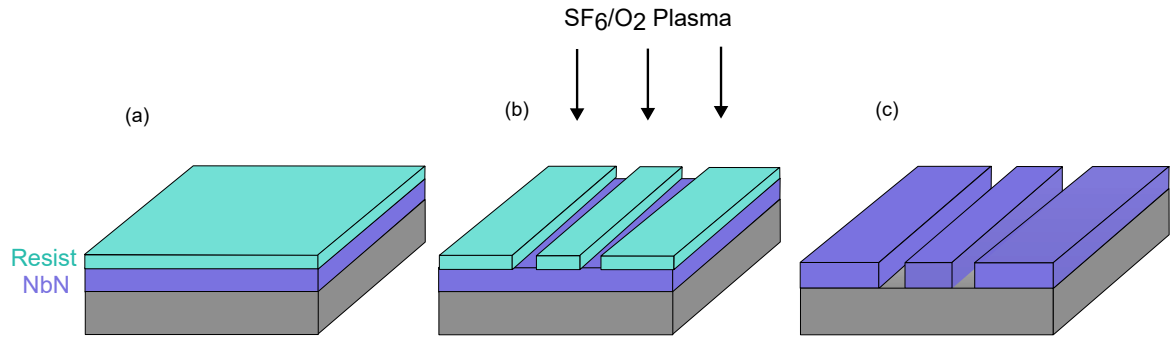

Figure 5.11: **Process flow for patterning NbN structures**
The CPW geometry is transferred into the NbN film by reactive-ion etching in a SF_6/O_2 plasma.

Following etching, the resist was removed using an NMP-based solvent. However, significant resist residues remained. A subsequent low-power argon plasma etch was required to fully eliminate these residues.

5.3.2 Estimation of the kinetic inductance of the NbN film

The kinetic inductance of NbN thin films can be estimated using both DC and RF measurements [6]. In this section, we focus on the extraction of kinetic inductance via RF measurements. Extraction of the kinetic inductance from DC measurment is discussed in the Appendix B. The results presented here were obtained from a chip fabricated from wafer C12-013, which consists of a $Si/SiO_2/SiO_2$ (sputtered) substrate.

To extract the kinetic inductance, we measured the resonance frequencies of the harmonic modes of a coplanar waveguide (CPW) resonator with a low fundamental frequency. The CPW forming the resonator has a track width $w = 3\,\mu m$, a gap $s = 5\,\mu m$, and a total length $l = 7.5\,mm$. The resonator is coupled to a hanger-type feedline. An optical image of the chip used in these measurements is shown in Fig. 5.12.

For these measurements, the sample was cooled to approximately $T \approx 30\,mK$ in a Qinu dilution refrigerator. The measurement setup is illustrated in Fig. 5.12. Due to the bandwidth limitations of the amplifiers, the accessible measurement frequency range was restricted to 4-8, GHz. To characterize the resonator, we measured the transmission coefficient S_{21} of the hanger-coupled feedline as a function of the input frequency, using a Keysight Vector Network Analyzer (VNA) capable of GHz-range measurements. A representative transmission spectrum is shown in Fig. 5.13. By fitting the complex S_{21} response near each resonance, we extracted the resonance frequencies f_n for various harmonic mode. The values of $\omega_n = 2\pi f_n$ are then plotted as a function of $k_n = \pi n/l$, see Fig.5.13(c).

The kinetic inductance is extracted by analyzing the dispersion relation of the resonator:

$$\omega_n = v_p\, k_n \tag{5.45}$$

where v_p is the phase velocity of the microwave signal, defined in Eq. (5.14).
Fitting the dispersion curve ω_n vs. k_n allows us to determine v_p. As v_p depends on the total per-unit-length inductance and capacitance of the resonator, and since the geometric contributions can be calculated using a conformal mapping approach, the kinetic inductance can be inferred.

The geometric components of the per-unit-length capacitance and inductance are estimated from the CPW dimensions as:

$$C_l^{\text{geom}} = 105\,\text{pF}\,\text{m}^{-1} \quad \text{and} \quad L_l^{\text{geom}} = 568\,\text{nH}\,\text{m}^{-1}. \tag{5.46}$$

Using these values, the kinetic inductance per unit length the corresponding sheet kinetic inductance are given by:

$$L_l^K = \frac{1}{v_p^2 C_l^{\text{geom}}} - L_l^{\text{geom}} \quad \text{and} \quad L_K^{\square} = L_l^{\text{geom}} \times w \tag{5.47}$$

Based on the phase velocity extracted from the dispersion curve in Fig. 5.13, we obtain:

$$L_K^{\square} = 775\,\text{pH}.\square^{-1} \tag{5.48}$$

This value significantly exceeds the expected value of approximately $200\,\text{pH}\square^{-1}$.

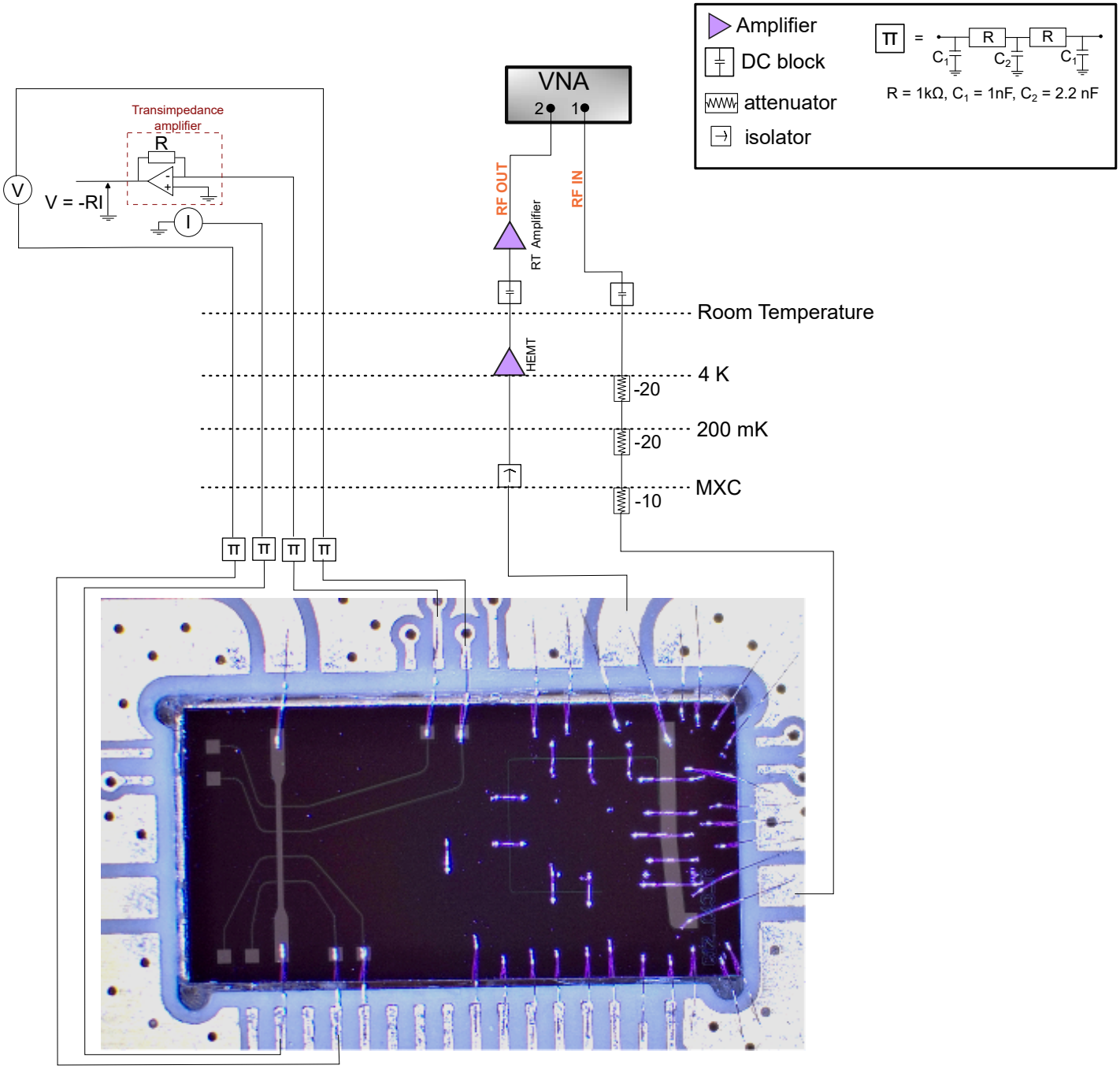

Figure 5.12: **Measurement setup for RF estimation of kinetic inductance**.
Schematic of the cryostat wiring and RF setup, along with an optical image of the chip from wafer C12-013 used for RF estimation of the kinetic inductance (see Fig. 5.13). The chip also features a four-probe structure for DC characterization, discussed in the Appendix B.

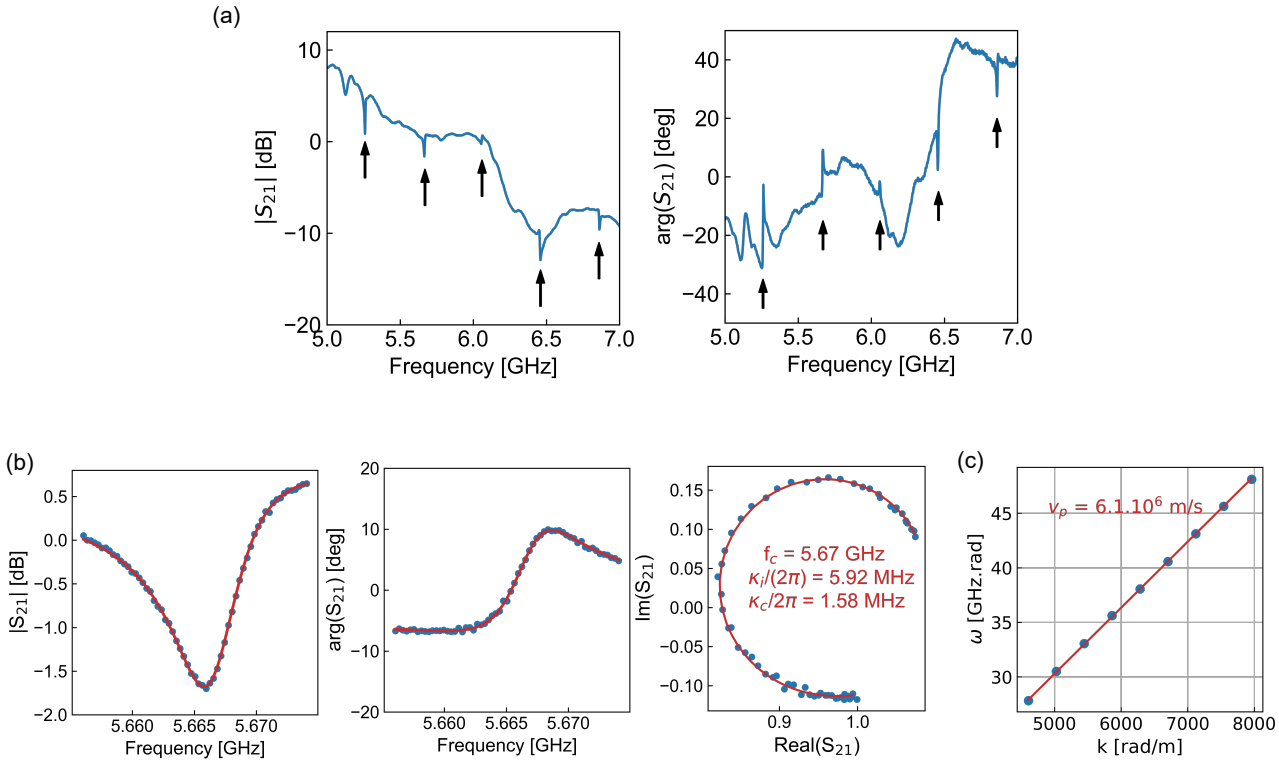

Figure 5.13: **RF estimation of the kinetic inductance**.
(a) Amplitude and phase of the complex transmissions parameter S_{21} . Arrows mark the resonances of harmonic modes of the low-frequency CPW resonator.
(b) Fit of a representative resonance corresponding to one harmonic of the low-frequency CPW resonator.
(c) Harmonic angular frequencies $\omega_n = 2\pi f_n$ plotted versus $k_n = \pi n/l$.

Why is the measured kinetic inductance significantly higher?

The extracted kinetic inductance is nearly four times higher than expected. We attribute this discrepancy to issues during nanofabrication.

As discussed earlier, CSAR resist was used for patterning the resonator. Post-etching, significant resist residues remained despite cleaning with an NMP-based solvent. Complete removal required low-power argon plasma etching. Notably, both wafers processed using CSAR exhibited similarly high kinetic inductance values.

To mitigate this issue, we transitioned to using ZEP520A resist. This alternative resist did not leave visible residues after processing. RF characterization of wafers processed with ZEP520A yielded kinetic inductance values consistent with expectations.
The comparative results for different wafers are summarized in Table 5.3.

Table 5.3: **Comparison of kinetic inductance across wafers.**
Summary of NbN nanofabrication processes and the sheet resistance and the kinetic inductance measured at different step. The value of the sheet resistance refers to the value measured right after the depostion at room temperature. The value of the kinetic inductance was measured after the NbN etching by RF measurements at low temperature. For the three wafers the NbN etching was performed with the same ICP reactive-ion recipe - including an SF_6/O_2 plasma. The cleaning procedure of the resist after the etching is detailed. All wafers underwent the same NbN etching recipe using an SF_6/O2 plasma. For wafer C12-013, due to patterning issues, two separate lithography and etching steps were performed.

Wafer Name	Substrate	$R_\square$ ($\Omega.\square^{-1}$)	NbN etching		$L_K^\square$ ($pH.\square^{-1}$)
			Resist used	Cleaning of the resist	
C12-013	$Si/SiO_2/SiO_2$(sputtered)	640	CSAR	5h in Remover AR600-71 at 75°C 2 min 30 s + 3 × 5 min of Ar Mealing	775
			CSAR	3h in Remover AR600-71 at 75°C	
C12-017	Si/SiO_2	660	CSAR	3h in Remover AR600-71 at 75°C 2 min 30 s + 5 min + 10 min of Ar Mealing	450
C12-025	Si/SiO_2	650	ZEP520A	10 min of Ozone cleaning 1h in Remover AR600-71 at 75°C	246

5.3.3 CPW resonator characterization

In addition to calibrating the kinetic inductance, we also performed a detailed characterization of coplanar waveguide (CPW) resonators, focusing on the evolution of their resonance frequencies and quality factors as functions of both input power and applied magnetic field. All measurements presented in this section were performed using the same Qinu dilution refrigerator and RF setup described previously (see Fig. 5.12).

The CPW resonator under study has a center conductor width of $w = 0.8\,\mu m$, a gap of $s = 2\,\mu m$, and a total length of $l = 600\,\mu m$. The structure is patterned on a chip from wafer C12-017 (see Table 5.3) and is capacitively coupled to a hanger-style feedline. Resonance frequencies are extracted from transmission measurements through the hanger line.

Power dependance

To probe the power dependence, we sweep the input power while continuously monitoring the resonance frequency. By fitting the complex scattering parameter S_{21} at each power level, we extracted the resonance frequency, the internal loss rate κ_i, and the coupling loss rate κ_c as functions of input power. The results are shown in Fig. 5.14.

At high input powers, we observe a shift in the resonance frequency attributed to **Kerr nonlinearities** - a second-order effect in the resonator Hamiltonian that becomes significant at high photon numbers [43][165]. Interestingly, we also observe a decrease in internal losses before the onset of the nonlinear regime.

To understand the observed behavior of internal losses, we review the **main dissipation mechanisms leading to internal losses** in superconducting CPW resonators:

- **Dielectric losses (Two-Level Systems Dynamics)**: A primary source of internal losses in superconducting resonators stems from dielectric losses caused by parasitic two-level systems (TLS). These TLSs are typically associated with structural and chemical defects, such as oxides at the metal-air interface, unterminated dangling bonds and oxides at the substrate-air interface, as well as defects in the bulk material or at the metal-substrate interface. The TLSs couple to the

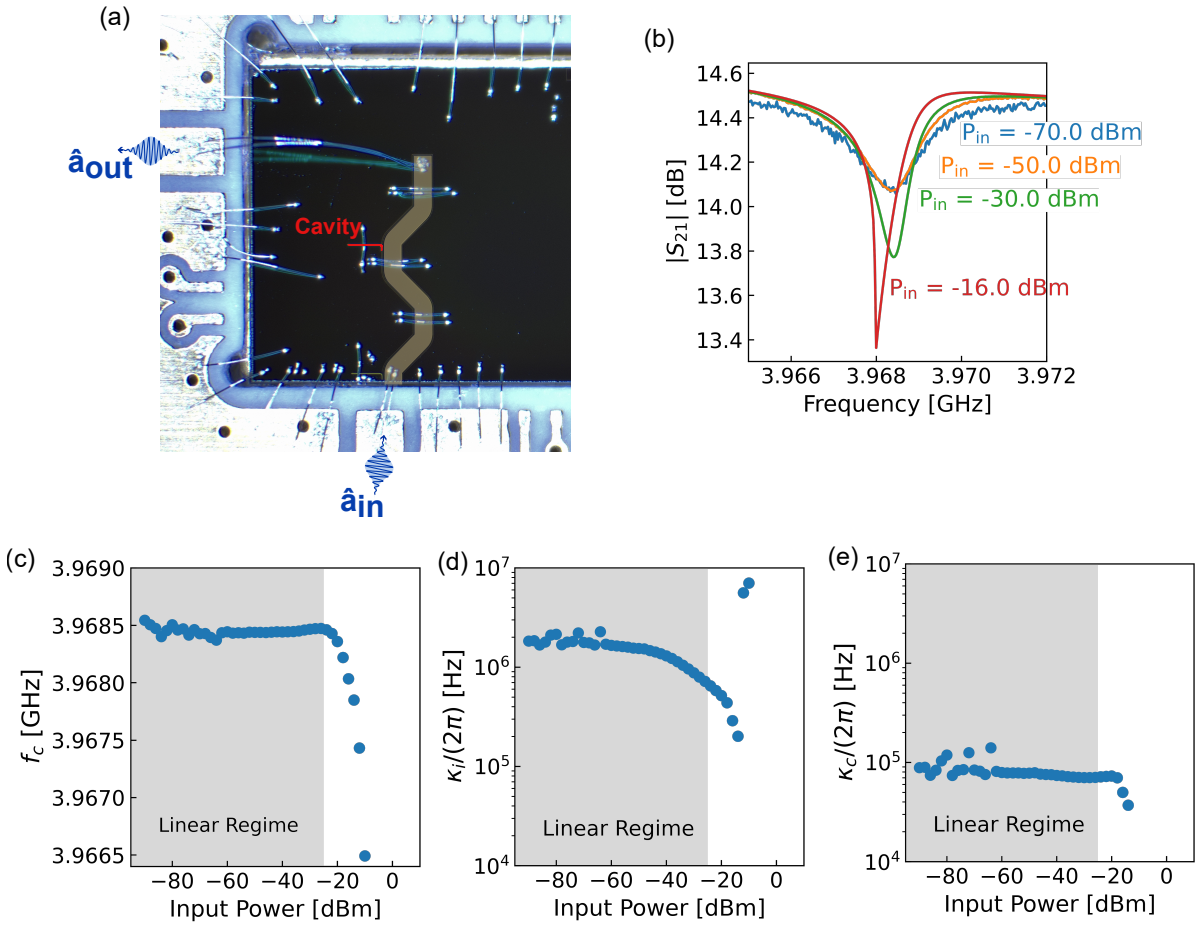

Figure 5.14: **Power dependence of the CPW resonator**.
(a) Optical micrograph of the measured chip from wafer C12-017. The cavity highlighted in red is capacitively coupled to a hanger feedline
(b) Amplitude of the transmission parameter $|S_{21}|$ near the cavity resonance for various input powers.
(c-e) Extracted resonance frequency f_c and decay rates - internal κ_i and coupling κ_c - as functions of input power, obtained by fitting the complex parameter S_{21} at each input power.
The input powers reported correspond to the VNA output power.

electric field of the resonator and can absorb microwave photons, thereby introducing dissipation. At low temperatures and low input powers, the TLSs are unsaturated and absorb energy efficiently, leading to higher internal losses. As the input power increases, the TLSs become saturated, reducing their absorption and resulting in an decrease in the internal loss rate of the resonator. This power-dependent behavior of κ_i is an experimental signature of TLS-induced loss, which we observe clearly in our measurements.
A more comprehensive review of TLS-related loss mechanisms can be found in [166].

- **Magnetic vortices** : When exposed to a magnetic field, superconductors expel the field via screening currents-a phenomenon known as the Meissner effect. However, in type-II superconductors, magnetic fields perpendicular to the thin film can penetrate the material in the form of magnetic vortices.These vortices interact with the oscillating microwave currents through the Lorentz force, resulting in dissipative motion that contributes to internal losses in the resonator. Further details on vortex-induced losses can be found in [167].
- **Quasiparticles** : Quasiparticles-excitations above the superconducting gap-contribute to microwave losses by dissipating energy through resistive channels. Their population can increase

due to stray infrared light, cosmic rays, or elevated temperatures. More detail on the mechanism loss can be found in [168].

The observed reduction in internal loss rate with increasing input power, within the linear regime, is a hallmark signature of TLS-dominated behavior. In our devices, we suspect that residual resist layers-particularly those resulting from the use of CSAR resist during nanofabrication-leave behind amorphous oxides that act as hosts for TLSs. Despite multiple cleaning attempts, we believe that these amorphous residues may persist and constitute the dominant mechanism responsible for internal losses in the resonator.

Reducing Internal Losses in CPW Resonators

On a resonator patterned from wafer C12-025, we observed a marked improvement in internal quality factor, approaching the values reported in [6].
This resonator was patterned on a chip with a slightly modified design, including a cavity connected to a DC-tap, and trenches for carbon nanotube placement. Most importantly, this wafer was processed using ZEP520A resist, which resulted in significantly cleaner surfaces, with no residuals detected post-etching.
The improvement in κ_i, along with the continued power dependence of internal losses, confirms that TLSs remain the limiting factor - but that their density is significantly reduced by improved fabrication protocols.

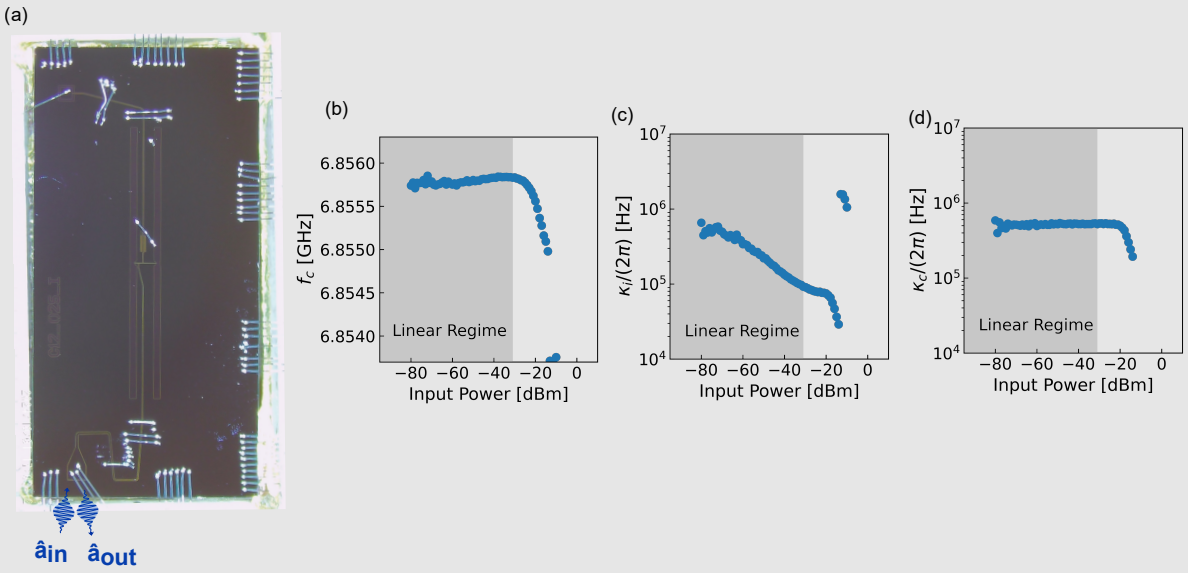

Figure 5.15: **Power dependence of a CPW resonator with an improved nanofabrication recipe**
(a) Optical micrograph of the measured chip. The cavity is characterized in reflection. A dc tap is connected to the resonator and trench ground-plane discontinuities are implemented.
(b-d) Extracted resonance frequency f_c and decay rates - internal κ_i and coupling κ_c - as functions of input power, obtained by fitting the complex parameter S_{11} at each input power. The input powers reported correspond to the VNA output power.

Magnetic field dependence

The response of the CPW resonator to an in-plane magnetic field was investigated by sweeping the amplitude of a static magnetic field while monitoring the resonance frequency and quality factor. The resonator corresponds to the one presented 5.14(a). The results are presented in Fig. 5.16.

For these measurements, we used a uniaxial superconducting magnet (a superconducting solenoid) mounted on the 4 K stage of the Qinu cryostat. As the magnetic field direction is fixed relative to the magnet, its orientation with respect to the thin film is determined by the alignment of the sample with the magnet. This introduces a possibility of angular misalignment, and any out-of-plane magnetic field component can lead to the nucleation of vortices in the superconductor, resulting in additional microwave losses.

To suppress vortex nucleation, the width w of the central conductor in the CPW resonator can be designed such that $w < \lambda$, where λ is the London penetration depth. In the thin-film limit ($t \ll \lambda_L$), this effective penetration depth can be expressed as [169]:

$$\lambda_L = \sqrt{\frac{L_K^{\square} t}{\mu_0}} \tag{5.49}$$

where t is the film thickness, $L_K^{\square}$ is the sheet kinetic inductance, and μ_0 is the permeability of free space. For superconductors with high kinetic inductance, the London penetration depth λ_L is increased, making it easier to satisfy the $w < \lambda_L$ condition and thereby enhance resilience to magnetic fields. For the wafers listed in Table 5.3, the London penetration depths are estimated to be 2.0 µm, 1.6 µm, and 1.2 µm for wafers C12-013, C12-017, and C12-025, respectively. The measurement shown in Fig. 5.16 are performed on a resonator with a center conductor width of $w = 0.8$ µm, thus satisfying the $w < \lambda_L$ condition.

When sweeping the magnetic field from 0 mT to 1 T, we observe no significant shift in the resonance frequency and no measurable increase in the internal loss rate. This confirms that the resonator exhibits magnetic field resilience. As expected from prior work [6], the use of high-kinetic-inductance NbN in narrow-linewidth CPW resonators provides robustness against vortex-induced losses, even under large in-plane magnetic fields.

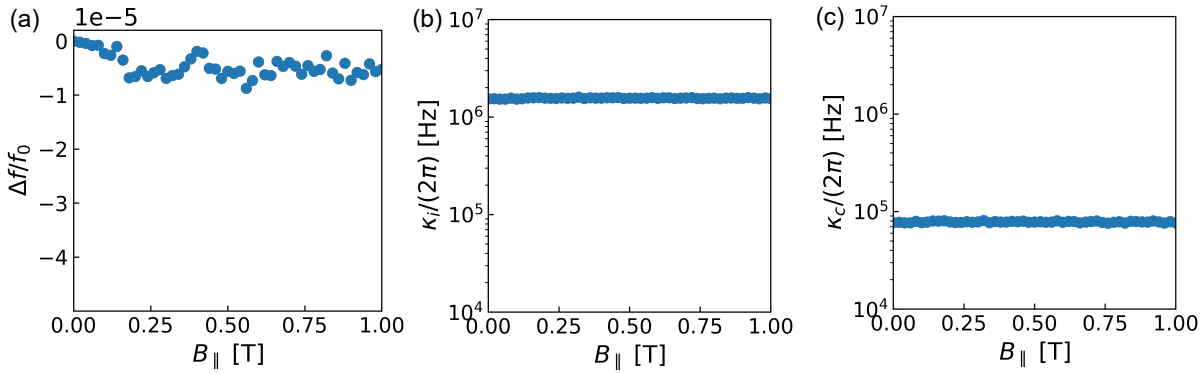

Figure 5.16: **Magnetic field resilience of a CPW resonator.**
(a) Normalized resonance-frequency shift versus in-plane magnetic field $B_\parallel$ (up to 1 T).
(b-c) Decay rate - internal κ_i and coupling κ_c - versus $B_\parallel$. No significant dependence of the cavity's internal losses on $B_\parallel$ is observed. However, the measured κ_i is notably higher than in prior work that reported a modification of the internal loss rate [6].
The resonator center conductor width is $w = 0.8$ µm.
For this measurement, the input power of the microwave tone is set to P_{in} =-50dBm.

5.3.4 Overview of the final microwave architecture

Following the characterization of the NbN film's kinetic inductance, the resonance frequencies of the various modes stabilized within the microwave circuit are tuned by engineering the geometry of CPW lines. The layout of the complete circuit is shown in Fig.5.17. This specific design is optimized for a sheet kinetic inductance of $L_K^{\square} = 775\,\mathrm{pH}\square^{-1}$, corresponding to the value extracted for wafer C12-013. The dimensions of the CPW lines, summarized in Table 5.4, are chosen based on the conclusions drawn from the RF simulations presented earlier in this chapter.

The geometry of the CPW line for the main resonator was chosen to yield a fundamental resonance frequency in the range of 4-8 GHz. The DC-tap line has the same width and gap as the cavity, and its length is set to $l_{\mathrm{dc-tap}} = \frac{l^{\lambda/2}}{2}$, where $l^{\lambda/2}$ is the half-wavelength length of the main resonator. This configuration minimizes photon leakage from the main resonator.

In addition, the CPW lines corresponding to the DC electrodes, which are capacitively coupled to the main resonator, are designed such that the resonance frequencies of their quarter-wavelength modes are well-detuned from the main cavity resonance. As detailed previously, these lines act effectively as band-pass filters. Their lengths are also chosen to allow sufficient spacing between adjacent *LC* filters to accommodate wire-bonds.

Each *LC* filter consists of an on-chip interdigitated capacitor followed by an inductor. The interdigitated capacitor geometry is shown in Fig. 5.17, and the inductor is implemented as a 320 µm long wire with a width of 600 nm. The same *LC* filter design is used across all control lines. For the fast line, a slightly different inductor geometry is employed: a 200 µm long wire with the same width of 600 nm.

Table 5.4: **Geometry of the CPW lines hosting resonant modes in the microwave circuit.** Resonance frequencies were estimated using Eq. (5.19) for half-wavelength resonators and Eq. (5.25) for quarter-wavelength sections. Calculations assume a sheet kinetic inductance of $L_K^{\square} = 755\,\mathrm{pH}\square^{-1}$.

	CPW line geometry			Resonance frequency
	w [µm]	s [µm]	l [µm]	
Main Resonator	2	3	500	$f_c^{\lambda/2} = 5.1\,\mathrm{GHz}$
DC Tap (Plundger$_2$)			250	$f_1^{\lambda/4} = 2.5\,\mathrm{GHz}$, $f_2^{\lambda/4} = 7.6\,\mathrm{GHz}$
Cut-source Source Γ_1 Tunnel$_1$ Γ_2 Drain Cut-Drain	8	1.5	800	$f_1^{\lambda/4} = 2.3\,\mathrm{GHz}$, $f_2^{\lambda/4} = 7.0\,\mathrm{GHz}$
Plundger$_1$ (Fast Line)	8	1.5	500	$f_1^{\lambda/2} = 7.5\,\mathrm{GHz}$

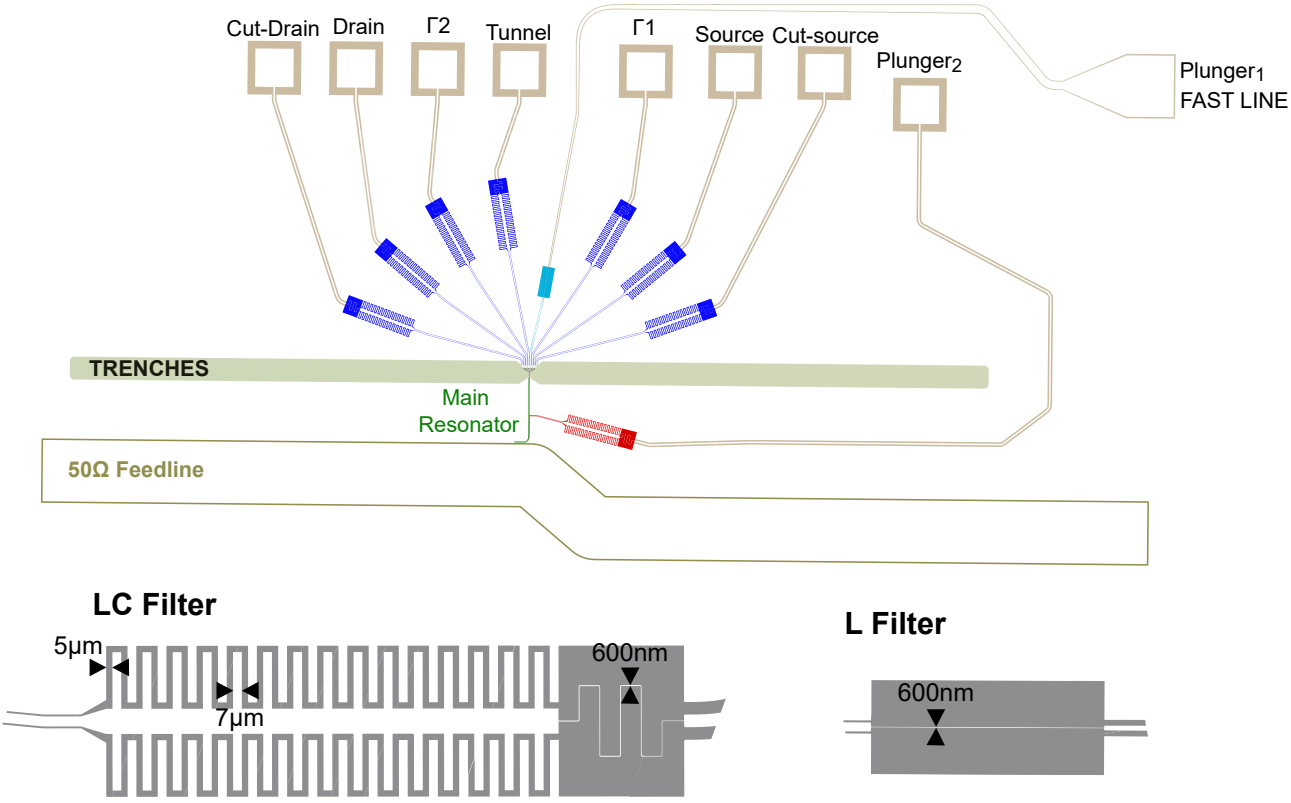

Figure 5.17: **Microwave circuit design.**
Schematic of the complete microwave circuit designed for wafer C12-013. Details of the LC-filter geometry are shown, and the CPW dimensions are listed in Table 5.4.

Chapter 6

Demonstrating the integration of a micro-magnet with a high impedance superconducting resonator in a carbon nanotube device

In the preceding chapters, we presented two complementary strategies to enhance the coupling between a spin qubit and a superconducting resonator. This work contributes to a broader effort aimed at developing a hybrid quantum platform that integrates spin qubits-realized in quantum dots formed within a carbon nanotube-with circuit quantum electrodynamics (cQED) elements. Specifically, we described the design and characterization of a magnetic microstructure enabling precise control over the spin orientation in a carbon nanotube. In parallel, we introduced a high-impedance, magnetic-field-resilient superconducting resonator engineered for on-chip integration.

In this chapter, we demonstrate the complete nanofabrication process developed to co-integrate both the spin control magnet and the superconducting resonator on a single chip. We then characterize the device by calibrating the coupling between an electron confined in a quantum dot and the cavity mode. Finally, we perform excited-state spectroscopy of the electron to assess the functionality of the integrated hybrid quantum architecture.

6.1 Co-integration of a micro-magnet and a superconducting coplanar waveguide resonator in a carbon nanotube device architecture

6.1.1 How to integrate a micro-magnet on-chip ? - Fabrication process

In the integrated device architecture-comprising a carbon nanotube, electrostatic gates for quantum dot definition, and circuit cQED elements for electric control and readout of quantum states-the available chip surface is heavily constrained. Due to this spatial limitation, positioning the micro-magnet close enough to the nanotube to effectively control the spin becomes a significant challenge. To address this, we opt to place the magnet below the gate electrodes, which themselves lie beneath the suspended nanotube, as illustrated in Figure 6.1.
To prevent electrical shorting between the magnet and the electrodes, we introduce an insulating layer between the two. This configuration requires the development of a dedicated nanofabrication process to effectively **bury** the micro-magnet beneath the electrode structure while maintaining compatibility with the rest of the device stack.

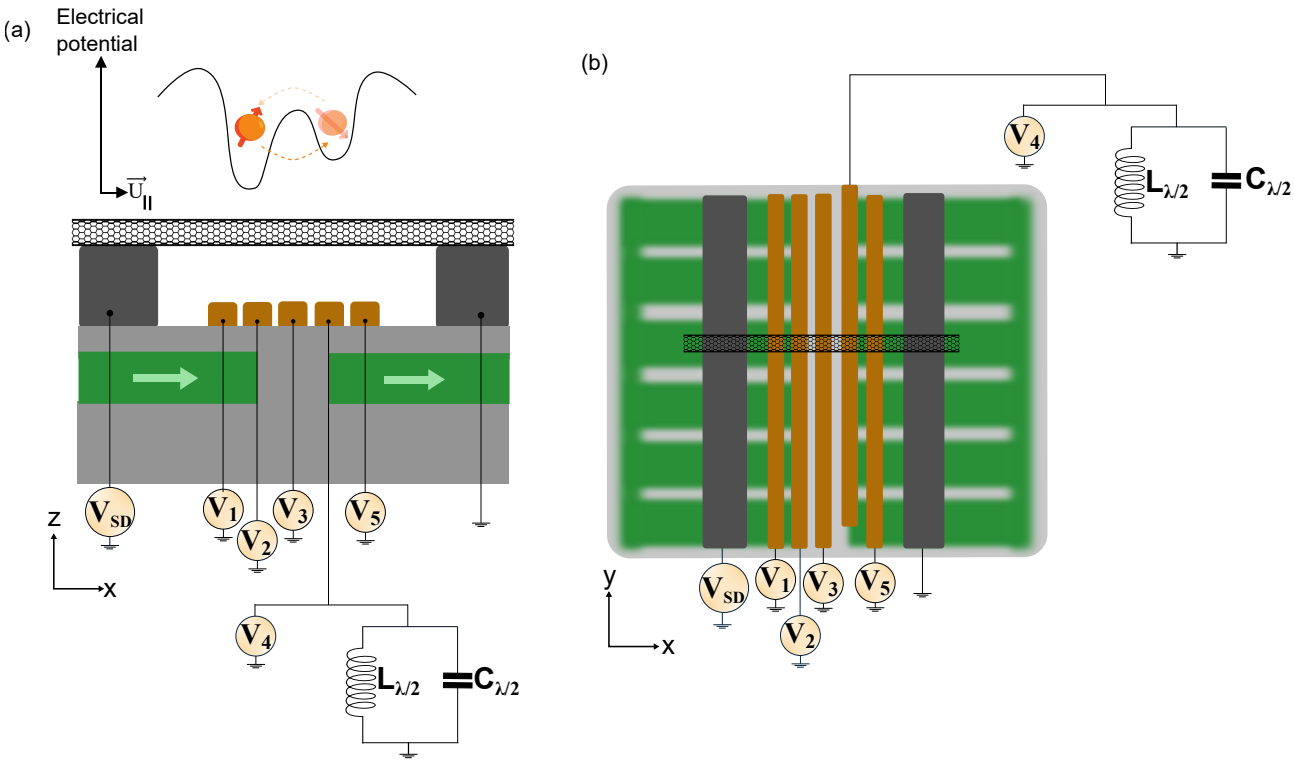

Figure 6.1: **Integration of a micromagnet in a carbon-nanotube quantum-dot architecture** (a) Side and (b) top-view schematics of the envisioned design integrating a micro-magnet into a quantum circuit based on a suspended carbon nanotube. The magnet geometry follows the optimized design presented in Chapter 4.

We have investigated several strategies for the development of a suitable nanofabrication process, which we briefly outline below.

Our initial efforts focused on establishing a fully in-house fabrication process. To this end, we envisioned two possible approaches.

- **Auto-aligned process combining etching and lift-off steps**.

  This approach is summarized in Figure 6.2.
  The process begins with the spin-coating of a positive bilayer resist (PMMA/PMMA-MA) onto a silicon substrate. An electron-beam lithography step is then used to define the magnet pattern in the resist.

  Following lithography, we perform a 200 nm etch of the silicon substrate using a Reactive Ion Etching (RIE) process with an SF_6-O_2 plasma. Like the Inductively Coupled Plasma (ICP) method described in the previous chapter, RIE relies on both chemical reactions - via reactive radicals from the plasma gases-and physical sputtering by ions. However, unlike ICP, RIE features a lower plasma density, resulting in reduced anisotropy control and less precise pattern transfer.

  Without removing the resist, we proceed with the deposition of 200 nm of Cobalt-based magnetic material via sputtering. The lift-off step removes both the resist and the excess magnetic material deposited outside the patterned region, resulting in a magnet structure that is embedded within the silicon surface. This structure can, in principle, be covered with a thin insulating layer before patterning the electrostatic gates on top.

  However, successful gate patterning requires a sufficiently flat surface. Post lift-off SEM images (Figure 6.2) reveal the presence of 'fencing' artifacts at the pattern edges. These are caused by

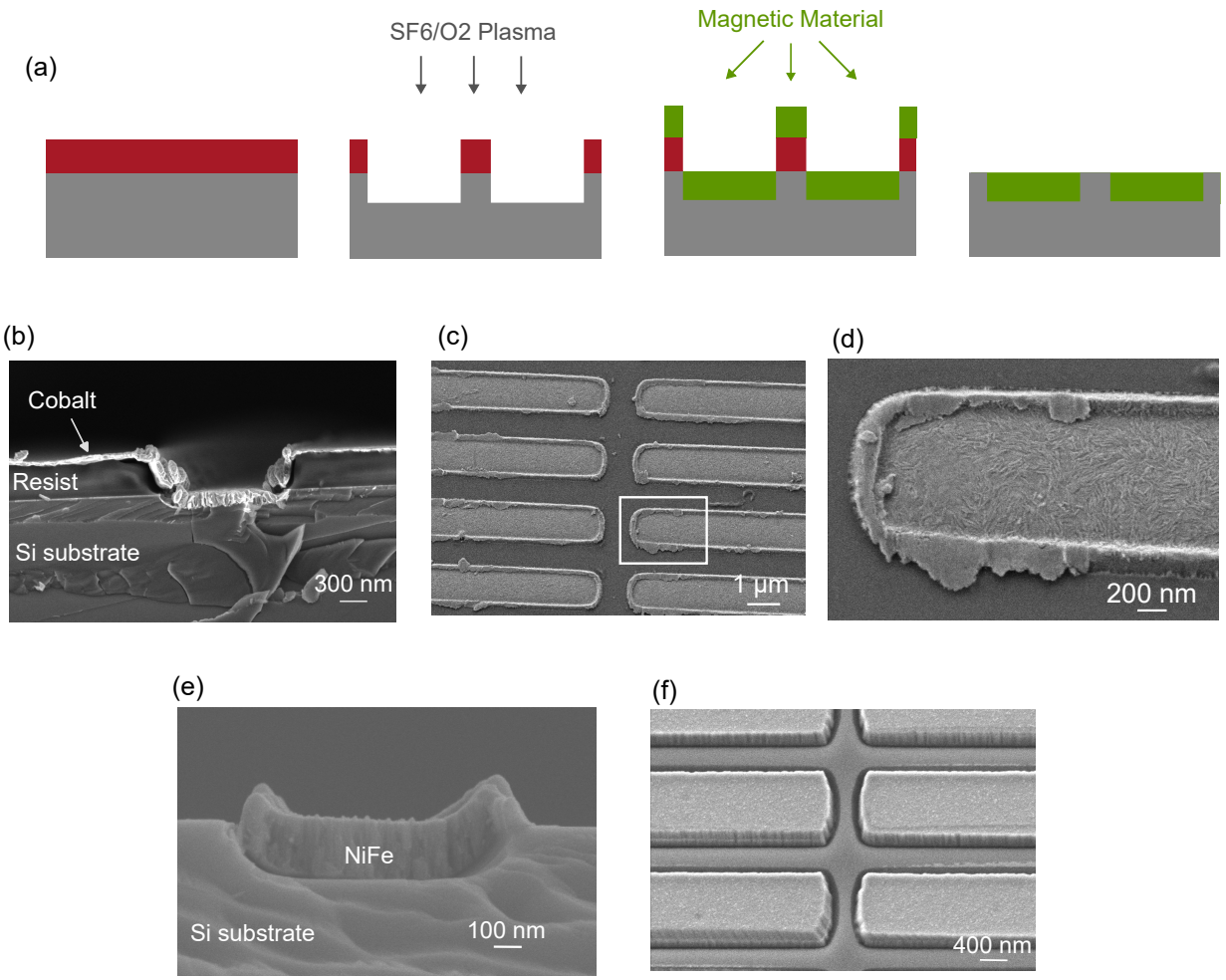

Figure 6.2: **A nanofabrication flow based on self-aligned etch and lift-off.**
(a) Schematic of the self-aligned process. The magnet footprint is patterned in resist; substrate etching and magnetic-film deposition are performed sequentially without removing the resist. A subsequent lift-off then removes material deposited outside the patterned magnet area.
(b) SEM cross-section image acquired after sputter deposition of the magnetic layer and before lift-off. The Si substrate, resist layer, and magnetic film are visible.
(c-d) SEM images of the Co micro-magnet obtained after lift-off.
(e) SEM cross-section image acquired after lift-off for a device in which the magnetic laye (NiFe) was deposited by evaporation.
(f) SEM image of the NiFe micromagnet after lift-off.

the contact between material deposited on the resist and that within the etched region, and are attributed to excessive deposition anisotropy during sputtering.

We also attempted to deposit 200 nm of NiFe via thermal evaporation, as NiFe is the only magnetic material available with this deposition technique. However, in this case, the non-uniformity of the silicon etch profile proved to be a limiting factor: the evaporated NiFe conformed to the underlying surface topography, resulting in poor planarity. This lack of flatness rendered the surface unsuitable for the subsequent fabrication of electrostatic gates.

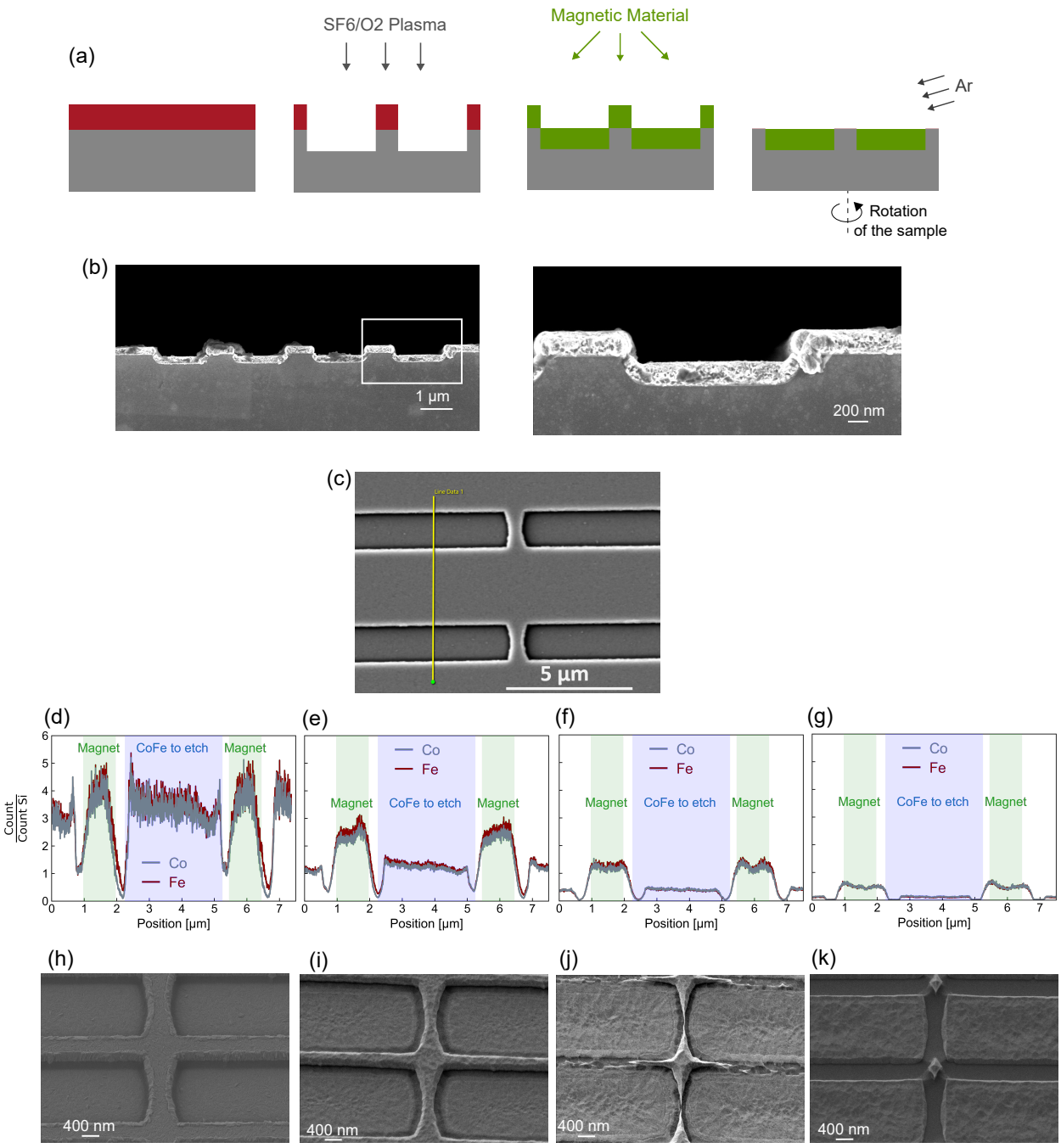

Figure 6.3: **Nanofabrication flow based on grazing-incidence ion-beam etching**
(a) Process schematic. The magnet footprint is patterned in resist, the substrate is etched and the resist is then removed. A magnetic film is then sputtered onto the chip, and a grazing-incidence argon beam etch oriented 80° from the normal incidence of the sample with beam voltage 500 V removes the magnetic material outside the patterned magnet area.
(b) Cross-section SEM image acquired after magnetic-film deposition.
(c) Plan-view SEM of the wires after magnetic deposition. The yellow line marks the section used for the EDS analysis shown in (e-h).
(d-g) EDS line scans collected along the line in (c) at successive stages of the process, with 10 min etch increments. (h-k) Corresponding SEM image of the magnet area, recorded before each etch step.

- **Process based on grazing incidence etching**
  This approach is summarized in Figure 6.3.
  As in the previous method, the process begins with spin-coating a resist layer followed by etch-

ing 200 nm of silicon from the substrate. However, in contrast to the prior approach, we first remove the resist and then deposit 250 nm of cobalt-based magnetic material by sputtering over the entire chip surface. Cross-sectional SEM images (Figure 6.3) confirm that the magnetic layer uniformly covers both the etched patterns and the surrounding areas.

The key idea of this approach is to selectively remove the magnetic material from the surface regions - while preserving the portions embedded within the etched silicon features - using ion beam etching (IBE) at grazing incidence. The IBE is performed with argon ions, and the process is executed in steps.

Etching is carried out at a grazing angle of 80° with respect to the surface normal. After every ten minutes of etching, we acquired SEM images and performed energy-dispersive X-ray spectroscopy (EDS) to monitor the material composition in both the magnet regions (intended to be preserved) and the inter-magnet regions (intended to be cleared). EDS enables a qualitative assessment by detecting the characteristic X-ray emission from cobalt, iron, and silicon under high-energy electron bombardment. By comparing the count rates for each element in both regions, we can qualitatively evaluate the relative thickness of the remaining magnetic layer. These results, shown in Figure 6.3, indicate that the magnetic material is preferentially etched away in the inter-magnet regions.
However, SEM images in Figure 6.3 also reveal that, before the magnetic material in the inter-magnet regions is fully removed, the silicon substrate begins to be etched. Additional analysis (see Appendix D) shows that, at grazing incidence, the etching rate of silicon is more than five times higher than that of cobalt-iron. As a result, before all the unwanted magnetic material is eliminated, significant etching of the silicon occurs, causing the embedded magnet structure to become partially exposed. This undermines the intended buried geometry of the magnet.

Since neither of the two in-house fabrication approaches presented above yielded satisfactory results, we also investigated a third strategy in parallel, illustrated in Figure 6.4.

Process based on Chemical-Mechanical Planarization (CMP)

In this approach, we begin by fabricating the magnet using the process described in Chapter 4 of this thesis, which we briefly recall here. The cobalt-based magnetic material is first deposited by sputtering with an adhesion layer of 5 nm of Tantalum and a capping layer of 5 nm of Platinium. The magnet geometry is then defined using a Titanium hard mask, followed by etching to remove the magnetic material outside the desired pattern.

Once the magnet is patterned, the entire surface is covered by sputtering a 300 nm thick layer of SiO_2. To ensure a flat surface suitable for the subsequent patterning of electrostatic gates, we apply a chemical-mechanical polishing (CMP) process. CMP relies on the combined action of a polishing pad, which applies mechanical pressure, and a slurry containing precipitated amorphous silica, ammonium hydroxide, sodium hydroxide, and water, which provides both chemical and abrasive effects. As no CMP equipment was available in-house, this process was performed at the Laboratoire Interdisciplinaire Carnot Bourgogne in Dijon (France).

SEM observations of the buried magnet after CMP are shown in Figure 6.4. The surface appears sufficiently flat for our application. Cross-sectional SEM images reveal the full material stack, clearly distinguishing the silicon substrate, the native 100 nm oxide layer, the sputtered SiO_2 layer, and the buried magnetic structure.

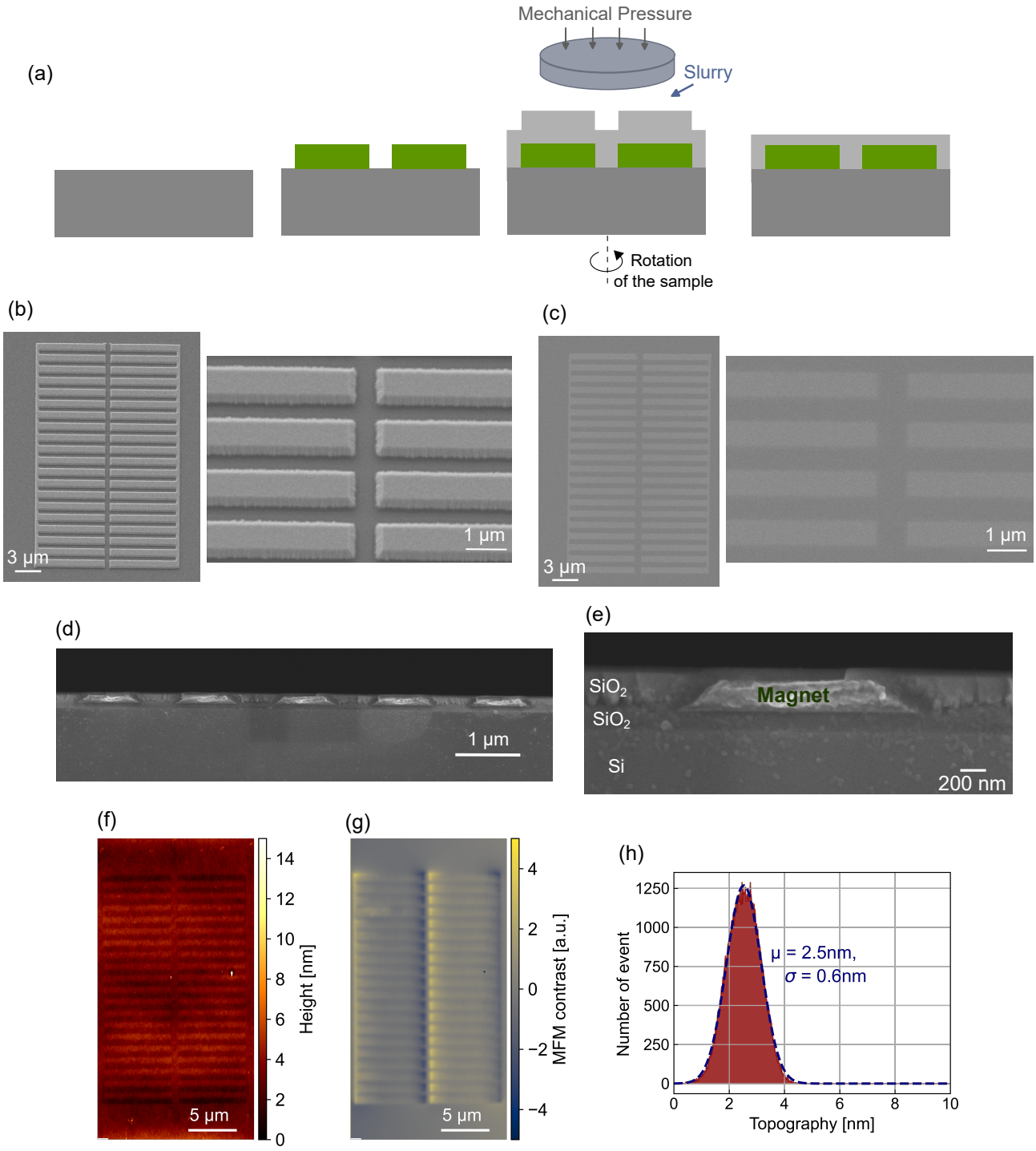

Figure 6.4: **Nanofabrication flow incorporating chemical-mechanical planarization (CMP)**
(a) Process schematic. The micromagnet is defined using a titanium hard mask, after magnetic-film deposition (see process detailed in Chapter 4). The surface is then capped with sputtered SiO_2 and planarized by CMP.
(b) SEM image of the magnet structure before SiO_2 deposition and planarization.
(c) SEM image of the same region after planarization.
(d-e) Cross-section SEM images of magnets after planarization. In (e), the Si/SiO_2 substrate, sputtered SiO_2 and magnetic layer are clearly distinguishable.
(f-g) AFM and MFM maps of the magnet structure after planarization. Magnetic contrast associated with the micromagnet is identifiable.
(h) AFM topography analysis extracted from (f). The height distribution is fit to a Gaussian with mean 2.5 nm and standard deviation 0.6 nm.

Complementary measurements, including atomic force microscopy (AFM) and the corresponding magnetic force microscopy (MFM), are also shown in Figure 6.4. From the AFM data, we evaluate the surface topography, obtaining a standard deviation of 0.6 nm in height. This value-extracted from the distribution peak in the histogram of surface heights-is considered sufficiently low to proceed with further nano-fabrication steps on top of the planarized surface.

Accounting for the $SI0_2$ capping layer for the magnet characterization and cavity design

The nanofabrication process based on the CMP approach includes an additional layer of sputtered SiO_2, deposited not only above the magnet but across the entire chip surface.

To ensure compatibility with magnet performance, we included a similar SiO_2 layer for the NV center characterization described in Chapter 3. Specifically, a SiO_2 capping layer was sputtered on top of the magnet prior to the measurement. This allowed us to verify that the presence of the oxide did not significantly alter the magnetic field properties relevant to the NV measurements.

For the design of the superconducting resonator, we also investigated chips both with and without this additional SiO_2 layer (wafers C12-013 and C12-017, respectively). Immediately after deposition, four-probe measurements indicated no significant difference in the sheet resistance between samples with and without the oxide. However, due to fabrication issues related to resist residues, it remains difficult to draw a definitive conclusion regarding the effect of the SiO_2 layer on the kinetic inductance and quality factor of the resonators measured at low temperature.

6.1.2 Overview of the additional fabrication process steps

After integrating the magnet using the CMP-based approach, we proceed with the nanofabrication of the remaining structures of the chip. Notably, alignment crosses are embedded alongside the magnet to ensure high-precision alignment between subsequent fabrication steps.

The main additional elements to be integrated are:

1. The NbN-based microwave circuit,
2. The five electrodes that control the electrostatic potential beneath the carbon nanotube - the DC gates-, along with four contact electrodes,
3. The trenches, which are necessary for transferring the nanotube from the cantilever chip- where the carbon nanotubes are grown-to the device chip.

NbN microwave circuit fabrication process

The next fabrication step following magnet integration is the deposition of the NbN layer. As previously mentioned, this deposition is carried out at the PHELIQS Laboratory (Grenoble, France), following the process developed in [130]. The microwave circuit is composed of coplanar waveguide (CPW) lines, which are patterned using the NbN etching process described in Chapter 4.

Electrodes nano-fabrication process

It is important to note that the NbN CPW lines - forming both the cavity and the DC bias lines - do not extend all the way to the region where the carbon nanotube is ultimately positioned. Therefore, an additional nano-fabrication step is required to define electrodes. These electrodes consist of narrow metal strips that connect the end of each CPW line to the region where the nanotube is transferred.
The electrodes are patterned using a lift-off process. Their geometry is defined by electron-beam lithography in a bilayer positive resist with an undercut in the resist profile to facilitate clean lift-

off. Metal layers are deposited via electron-beam evaporation. After deposition, the resist - along with the metal deposited on top of it - is removed using a NMP-based solvent.

The DC gates and contact electrodes are fabricated in two separate steps, as they require different metal thicknesses.

- DC gate electrodes, located below the nanotube, consist of a 5 nm titanium adhesion layer followed by 25 nm of palladium.
- Contact electrodes, which make electrical contact with the nanotube, consist of a 10 nm titanium adhesion layer followed by 140 nm of palladium.

SEM images of the electrodes after fabrication are presented 6.5.

Palladium is chosen for the DC gates because it is a noble metal and resists oxidation in air at room temperature. This is critical, as it allows for electrical detection of whether the nanotube has collapsed onto the gates.
For the contact electrodes, palladium is used to promote ohmic contact between the nanotube and the metal. Semiconducting carbon nanotube-metal junctions can typically behave as Schottky barriers [170], which are undesirable for low-bias transport measurements. The height of the barrier depends on the work function mismatch between the nanotube and the metal. Palladium has a work function closely matched to that of carbon nanotubes, which helps minimize the Schottky barrier and facilitates ohmic contact [171].

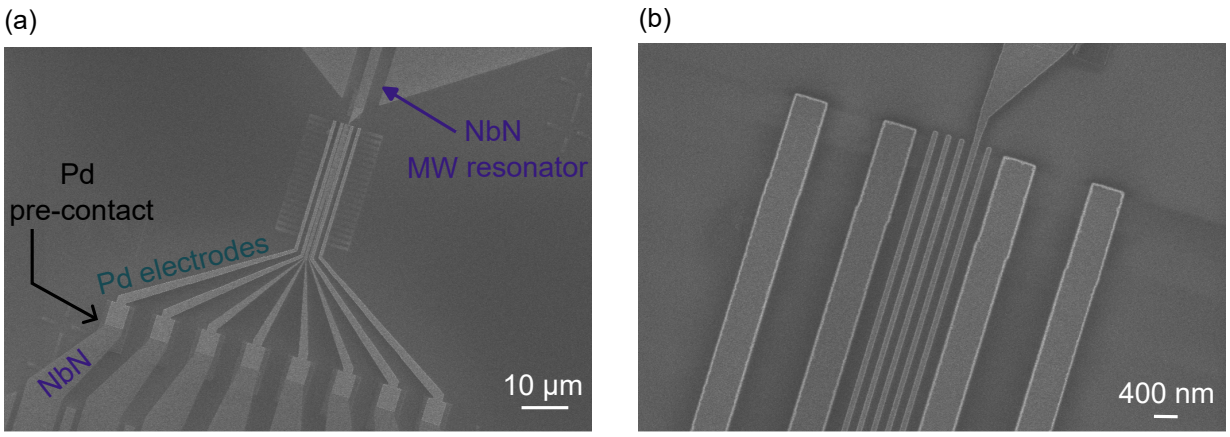

Figure 6.5: **Patterning DC electrodes on top of the buried micromagnet.**
(a-b) SEM images of Pd electrodes patterned above the micromagnet.

Adding pre-contacts between the electrodes and the CPW lines

Following NbN deposition, it is expected that a few nanometers of native oxide may form on the surface [172].

To ensure good electrical contact between the central conductor of the CPW line and the metal electrode, a thin pre-contact pad consisting of Ti(5 nm)/Pd(10 nm) is added at the interface **before** the NbN deposition, as illustrated in the schematic below.

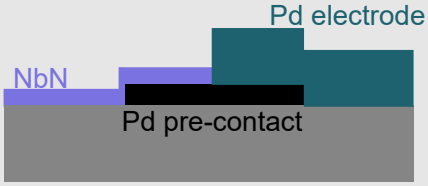

Figure 6.6: Schematic of the pre-contacts implemented at the coplanar waveguide - palladium electrode interface

Palladium is again chosen due to its excellent oxidation resistance in ambient conditions, which helps preserve good conductivity at the interface.

Trenches fabrication process

To enable the transfer of the carbon nanotube from the cantilever chip - on which the nanotubes are grown - to the device chip, the cantilever chip must be brought into close proximity with the device chip surface. To accommodate this, trenches are fabricated on either side of the region where the carbon nanotube will be placed.

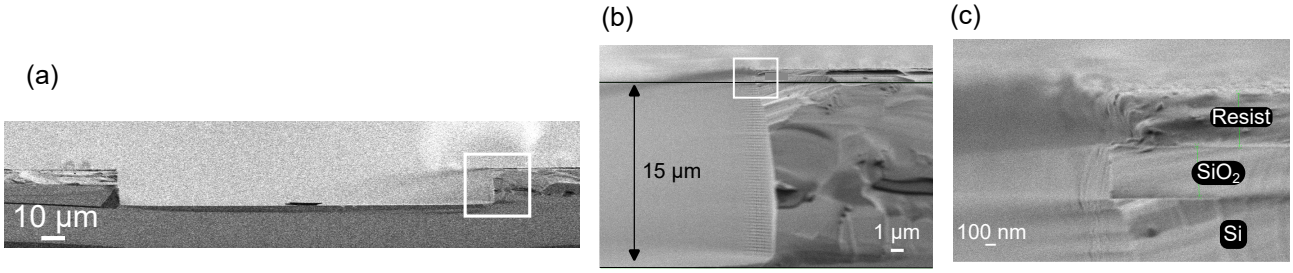

Figure 6.7: **Trench etching on the chip**
(a) Cross-section SEM after the etching process of the trenches used for carbon-nanotube assembly. The etch resist remains on the chip for imaging.
(b) Zoom of (a), from which the trench depth is estimated at ~ 15µm.
(c) Higher-magnification view of (b), where the Si/SiO_2 substrate and the resist layer are distinguishable.
In (b) and (c), scalloped sidewalls characteristic of the Bosch process are distinguishable.

To form the trenches, we etch through a stack consisting of NbN, SiO_2, and underlying silicon. The etching sequence proceeds as follows:

- **NbN** is etched using ICP with a SF_6/O_2 plasma, as described previously.
- **SiO_2** is etched using ICP with a CHF_3/Ar plasma.
- **Silicon** is etched using Deep Reactive Ion Etching (DRIE) with ICP sources, following the **Bosch process**. This technique alternates between isotropic etching (using SF_6) and sidewall passivation (using C_4F_8, which deposits a polymer layer on the sidewalls), enabling the formation of deep, high-aspect-ratio features with near-vertical sidewalls.

The resulting trench depth is approximately 15µm. A cross-sectional SEM image of the etched profile is shown in Figure 6.7.

With this final step, the nanofabrication process of the chip is complete. Optical and SEM images of the fabricated device are presented in Figure 6.8. These observations are complemented by atomic force microscopy (AFM) and magnetic force microscopy (MFM) imaging focused on the electrode region. AFM provides detailed topographical information on the electrode structures, while MFM reveals the magnetic contrast arising from the buried magnet located beneath the electrodes.

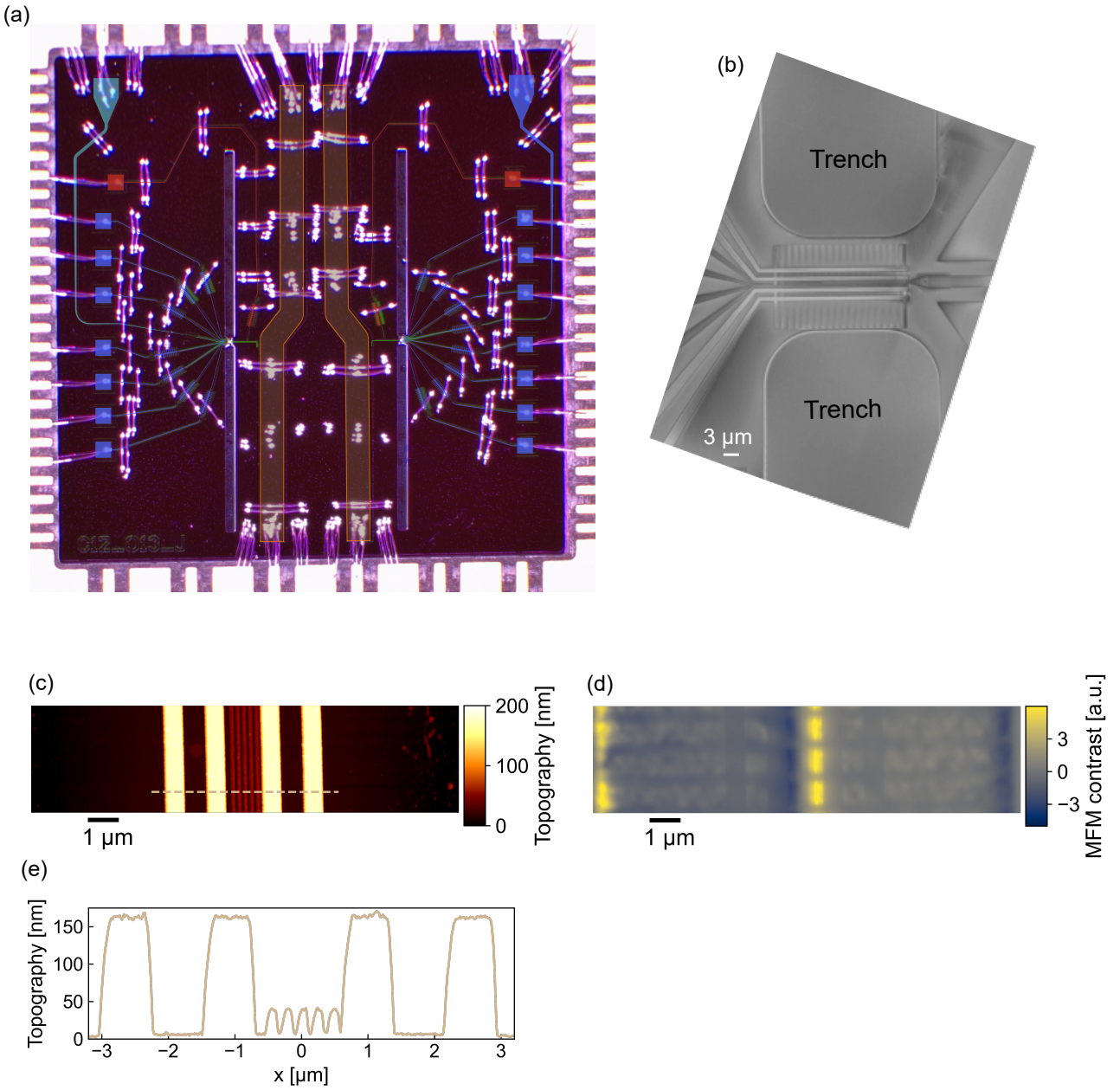

Figure 6.8: **Imaging the final chip.**
(a) Optical image of the chip wire-bonded to the sample-holder PCB (printed circuit board). The chip hosts two devices implementing the microwave circuit described in Chapter 5.
(b) SEM image of the nanotube assembly region. Between the trenches, the buried micromagnet with the electrodes patterned on top is discernible.
(c-d) AFM and MFM images of the micromagnet/DC-electrode area. Magnetic contrast associated with the micromagnet is identifiable.
(e) Line profile from the AFM image in (c) along the red line, showing topography and electrode thicknesses: 30 nm for the DC gate electrodes and 150 nm for the contact electrodes.

6.1.3 Integration of carbon nanotubes into the Chip

Once the chip fabrication is complete, the final component to be integrated is the carbon nanotube.

Carbon nanotubes used for this work were grown by the team CNT-growth team of C12 Quantum Electronics. The growth of the Carbon nanotube in done by Chemical Vapor Deposition, a detail recipe for the nanotube growth can be found in [173].

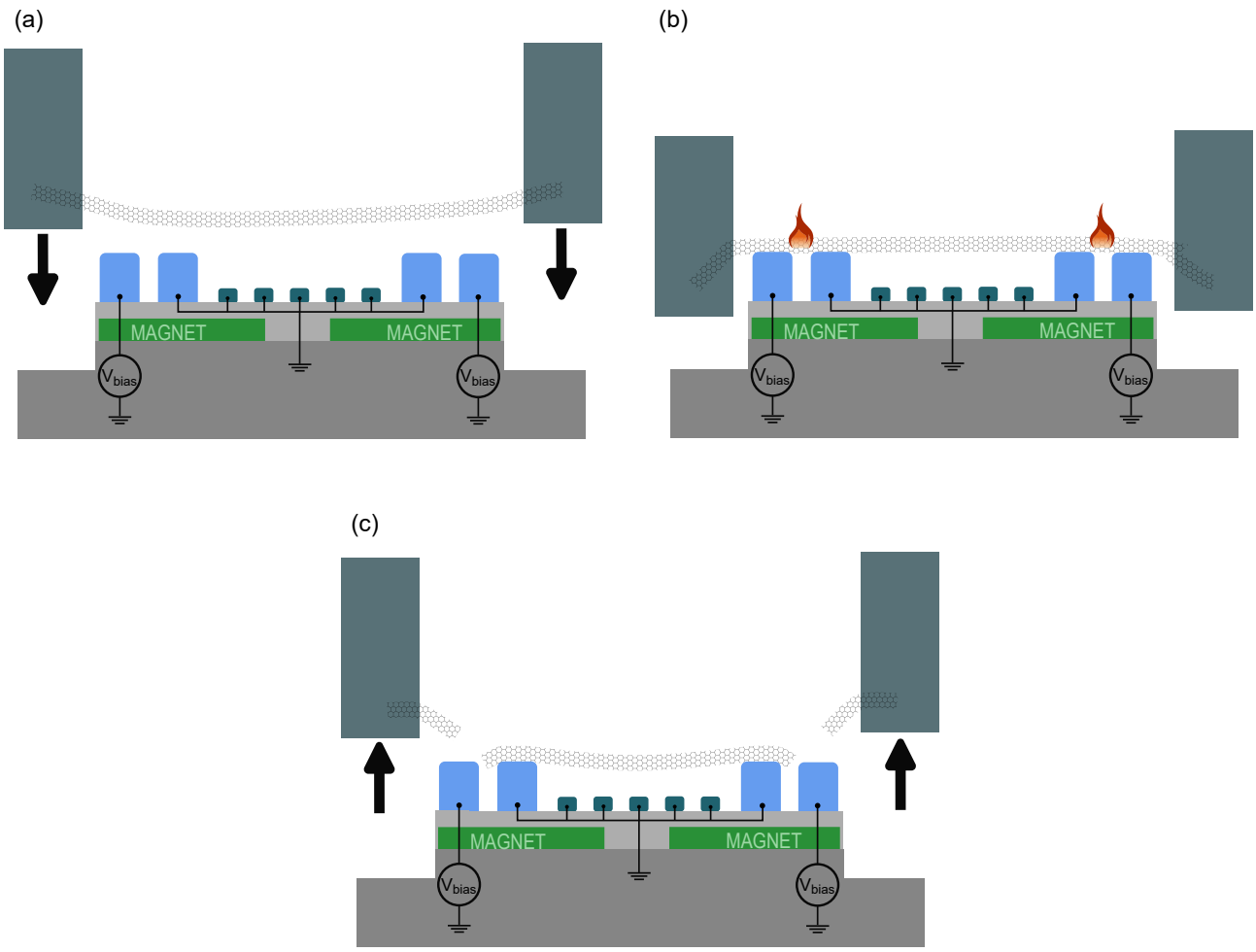

Figure 6.9: **Assembly process of a carbon nanotube on a chip.**
(a) A pair of cantilevers carrying a suitable nanotube is brought into proximity with the device chip while monitoring the current between a contact electrode and its associated cut electrode.
(b) Upon contact of the nanotube with the electrode, a current is detected. The CNT segment bridging the contact and the cut electrode is then cut by Joule heating achieved by ramping up the current through that section.
(c) After the cut, the cantilevers are retracted, leaving the nanotube integrated on the device chip.

The nanotubes are grown on a dedicated substrate known as the cantilever chip, which consists of an array of cantilevers spaced by several tens of micrometers. For a successful transfer, the carbon nanotube must be located at the end of the cantilevers and must bridge a pair of cantilevers.

Characterization of the grown nanotubes on the cantilever chips is carried out by the CNT-Characterization Team at C12. By combining scanning electron microscopy (SEM) with Rayleigh and Raman spectroscopy, they determine both the location and structural properties of the carbon nanotubes - such as whether they are single-wall or multi-wall, and whether they are metallic or semiconducting. This allows for the selection of suitable nanotubes for integration into the device chip.

The nanotube transfer is performed using a dedicated nano-assembler developed by the CNT-Assembly Team at C12. The setup closely resembles the "stapler" system described in [173].

The assembly procedure is conducted under vacuum. The cantilever chip is mounted on a piezoelectric positioning stage with three-axis control. The selected pair of cantilevers containing the desired nanotube is aligned optically with the device chip, and two chips are then brought into

close proximity with high precision.

To enable electrical detection of the carbon nanotube a bias voltage is applied between the contact electrode and its associated cut electrode. When a current is measured between the electrode and the cut-electrode it means that the carbon nanotube has reached the electrode surface.

Before the cantilever chip is removed, the carbon nanotube must be detached from the cantilevers. This is achieved by gradually increasing the bias voltage applied between the Cut-Source and Cut-Drain electrodes, while grounding the corresponding Source and Drain electrodes. When the current between the Cut-Source and Source, and between the Cut-Drain and Drain, reaches a threshold, a sudden drop to zero current is observed. This is interpreted as the nanotube being cut, likely due to Joule heating, as the contact electrodes act as thermal sinks. After this step, the carbon nanotube is connected only to the Source and Drain electrodes of the device chip, suspended above the five gate electrodes, and fully detached from the cantilever chip, which can then be safely withdrawn.

Challenges in cutting the carbon nanotube with a high kinetic inductance circuit

As detailed in the previous chapter, a high kinetic inductance at low temperature is associated with a high sheet resistance of the NbN film at room temperature.

In the design presented in the previous chapter, the four contact lines are primarily implemented using coplanar waveguide (CPW) structures that include an LC filter and terminate at a palladium contact electrode. However, this design leads to a high total resistance for each contact line. Taking into account the resistance of the CPW center conductor, the total resistance of a single contact line fabricated on wafer C12-013 is estimated to be approximately 1.2 MΩ. This estimate is based on a sheet resistance of $R_{\square}$ = 1500 Ω/□ measured at room temperature on wafer C12-013 after completion of the nanofabrication process (see Appendix B for more detail).

This high resistance significantly complicates the cutting procedure. Even when applying bias voltages of up to 20 V between the contact electrode and its associated cut-electrode, the current does not reach the threshold required to cut the nanotube.

As a result, we employed an alternative approach based on **mechanical assembly**. In this method, the carbon nanotube is transferred from the cantilever chip to the device chip by physically bringing the two chips into contact. While effective, this approach is less controlled and often requires multiple attempts to successfully transfer and adhere the nanotube to the device chip.

To overcome this limitation, the design was revised in subsequent wafers. Specifically, for the cut-electrodes, the LC filter was removed, and the width of the CPW center conductor was increased in order to reduce the line resistance. These modifications significantly lowered the total resistance of the cut-lines, enabling successful cutting of the carbon nanotube during the assembly process on the chip.

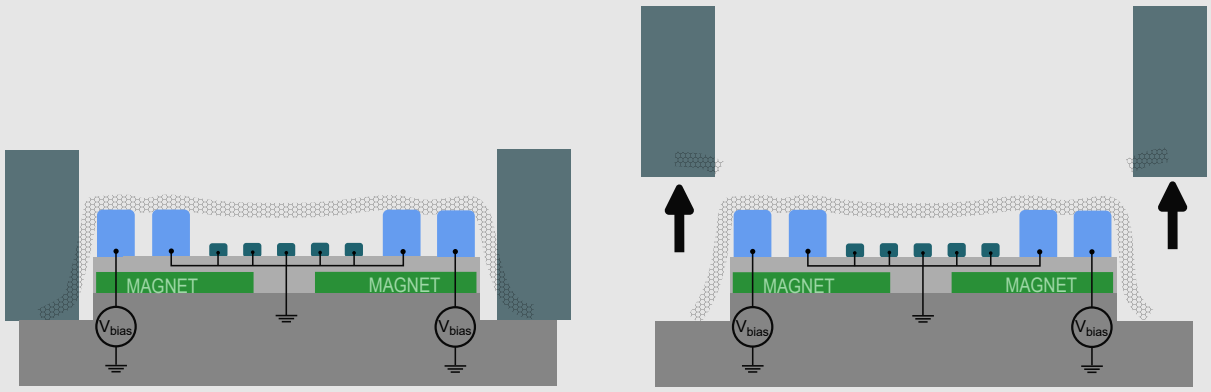

Figure 6.10: **Schematic of the mechanical transfer approach for CNT assembly**
The carbon nanotube is transferred from the cantilever chip to the device chip by bringing the two chips into contact

6.1.4 Initial characterization after chip fabrication and carbon nanotube integration

This section presents the first measurements and characterization of the device following full chip fabrication. For this work, we focused on two chips from wafer C12-013: C12-013-E and C12-013-J. The calibration of the kinetic inductance was discussed in the previous chapter, and the microwave circuit is identical for both chips, corresponding to the design elaborated earlier. An optical image of chip C12-013-J is shown in Figure 6.8. Each chip contains two devices, with each device featuring its own cavity coupled to a separate feedline.

The preliminary measurements presented here were conducted in the Qinu dilution refrigerator at a base temperature of approximately 30 mK. The RF setup used is similar to that described in the previous chapter, and microwave characterization of the resonators was performed using a vector network analyzer (VNA).

The superconducting resonators of chip C12-013-E were first characterized prior to carbon nanotube integration. A broadband transmission measurement of the feedline connected to device 1, spanning 4 GHz to 8 GHz, is shown in Figure 6.11. This measurement was performed in the many-photon regime, with an input power of the VNA of -30 dBm.
Two resonance peaks are visible in the spectrum at 4.17 GHz and 4.21 GHz. These correspond to the two cavities on the chip and appear due to microwave crosstalk between the two devices. The input power is then reduced, and a fit to the resonances allows the extraction of the loss rates for each cavity at low power. However, from this measurement alone, it is not possible to determine which resonance corresponds to which device without further measurements involving coupling to the quantum dot.

Carbon nanotube integration on chip C12-013-E proved to be challenging. For device 1, the assembly was unsuccessful despite multiple attempts. Probe station measurements revealed that the failure originated from faulty wire bonds. Although the wire bonds appeared to adhere properly to both the contact pads on the device chip and the printed circuit board (PCB) of the sample holder, they did not did not establish an electrical connection. The cause of this poor connection is not fully understood but may be attributed to the very thin NbN layer (less than 10 nm) used in the pad region.
For device 2, mechanical assembly was successful, but electrical contact with the source and drain electrodes was poor: large bias voltages were required to observe any current flow between the source and drain.

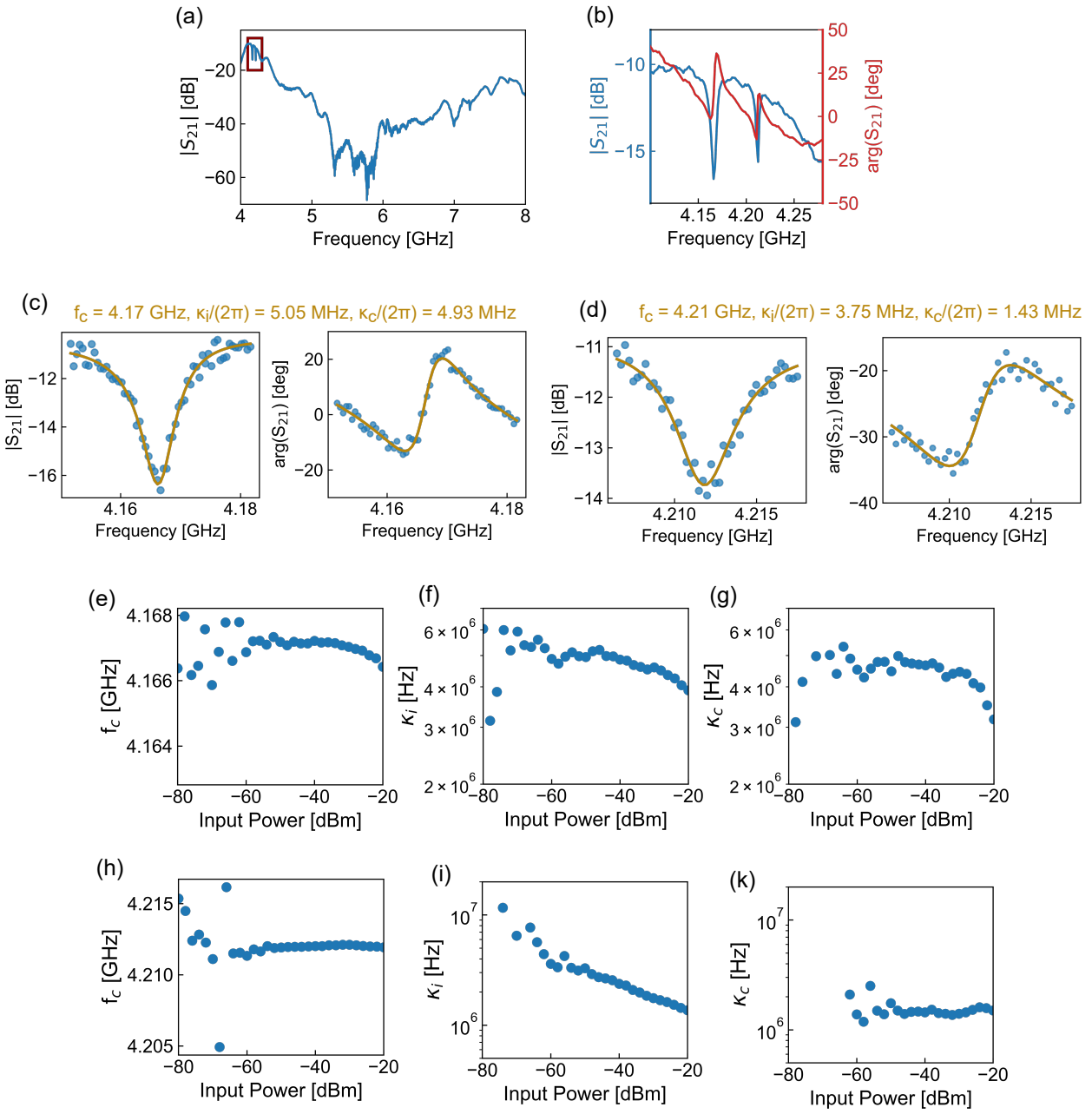

Figure 6.11: **Microwave characterization of chip C12-013-E before carbon-nanotube integration**
(a) Amplitude of the transmission coefficient $|S_{21}|^2$ of the feedline of device 1.
(b) Zoom near 4.2 GHz showing two resonances visible in amplitude and phase. The two resonances arise from crosstalk between the two devices. Similar features appear for device 2.
(c-d) Fits of amplitude and phase for each resonance to extract the resonance frequency f_c, the internal loss rate κ_i and the coupling loss rate. The fit were performed following method of [163]. The input power was set to -60 dBm.
(e-g) Evolution of f_c, κ_i and κ_c with increasing input power on the feedline (corresponding to the output power by the VNA).
(h-k) Same analysis for the second resonance.
For both modes, κ_i decreases with power - consistent with losses related to two-level systems (TLS) - most notably for the 4.21 GHz mode.

Design improvements from first characterization

The initial characterization of the chip C12-013-E has highlighted several areas for potential optimization in future designs.

First, regarding the microwave architecture: a more suitable design would involve coupling both devices to a single transmission line, with the two resonators having different lengths to allow clear frequency distinction.
An alternative approach could involve using a reflection measurement setup instead of the hanger-type transmission line currently employed. However, within our RF setup, the transmission configuration was more practical, as it avoided the need for an RF circulator.

Second, in light of the wire-bonding issues encountered, improvements to the bonding pads are necessary. To prevent poor electrical contact at the wire bonds, an additional metal layer - typically a few hundred nanometers of gold or palladium - can be deposited on the bonding pads of the device chip. This strategy has been implemented in the design of subsequent wafers featuring high-impedance microwave circuits.

Since integrating a carbon nanotube on chip C12-013-E proved to be challenging, we shifted our focus to chip C12-013-J. The mechanical assembly of the carbon nanotube on this chip was successful on the device 1 of this chip. The characterization team at C12 Quantum Electronics identified the integrated nanotube as either a multiwall carbon nanotube or a bundle, exhibiting metallic behavior at room temperature. Preliminary DC measurements showed promising results, some of which were presented in Chapter 1 of this PhD thesis.

However, after assembling the carbon nanotube onto the chip, additional issues arose with the wire bonds connected to the RF lines. Prior to nanotube assembly, these wire bonds provided reliable electrical connections between the device chip and the PCB of the sample holder, enabling successful resonator measurements. After assembly, however, several RF wire bonds were found to have detached from the device chip. The cause of this detachment remains unclear. Re-bonding of the RF lines was required; unfortunately, this process caused the carbon nanotube to collapse onto the tunnel gate, see Fig.6.12.

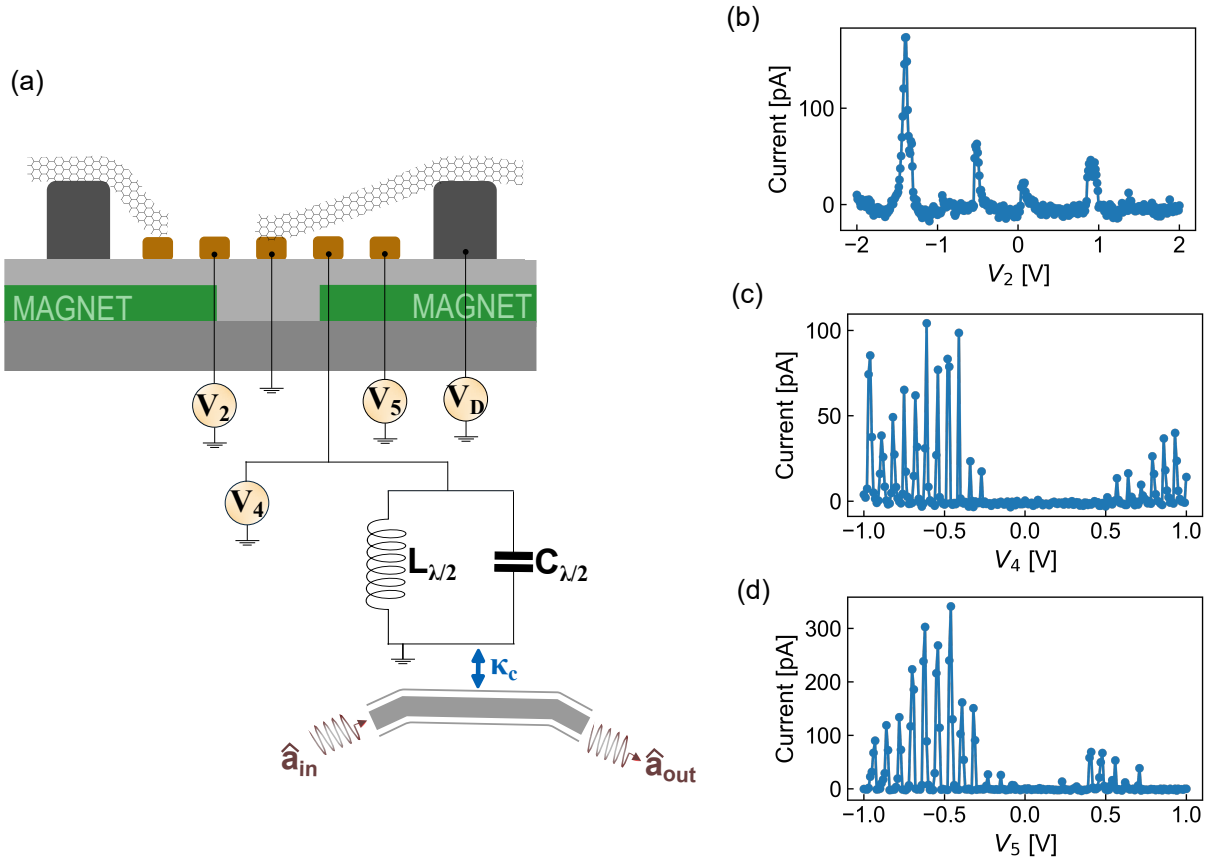

Figure 6.12: **DC characterization of device 1 on chip C12-013-J after carbon-nanotube integration**
(a) Device configuration after nanotube integration. The current through the tube is measured with the drain contact biased and DC gate 3 grounded.
(b-d) Coulomb-peak measurements obtained by sweeping the voltages on gates 2, 4, and 5, respectively. Panel (b) was measured at a bias $V_D = 10\,\text{mV}$, panels (c) and (d) at $V_D = 5\,\text{mV}$.

Following re-bonding, the resonator of device 1 was characterized via spectroscopy by measuring the transmission through its feedline. The results, shown in Figure 6.13, reveal higher loss rates compared to the previous device. This degradation could be attributed to the presence of two spurious modes located near the cavity resonance, although the origin of these modes was not further investigated. Notably, unlike the resonance modes observed on chip C12-013-E (see Fig. 6.11), the loss rates-and in particular the internal loss rate-show no dependence on the input power applied to the resonator drive line.
Furthermore, in contrast to the previous device, only a single cavity mode could be identified in the transmission spectrum of the feedline for device 1.

Although the collapse prevents the formation of a double quantum dot in this device, it remains functional for creating a single quantum dot. This configuration can still be used to calibrate the coupling between an electron confined in the quantum dot and the microwave resonator [174] [175].
Interestingly, the collapse of the nanotube onto the tunnel gate has brought the nanotube closer to the micro-magnet. Since the DC signal from the device is promising, further study of the energy dispersion of both the fundamental and excited states of the single quantum dot could provide insight into how the magnetic field from the micro-magnet influences the excited-state spectrum of the quantum dot.

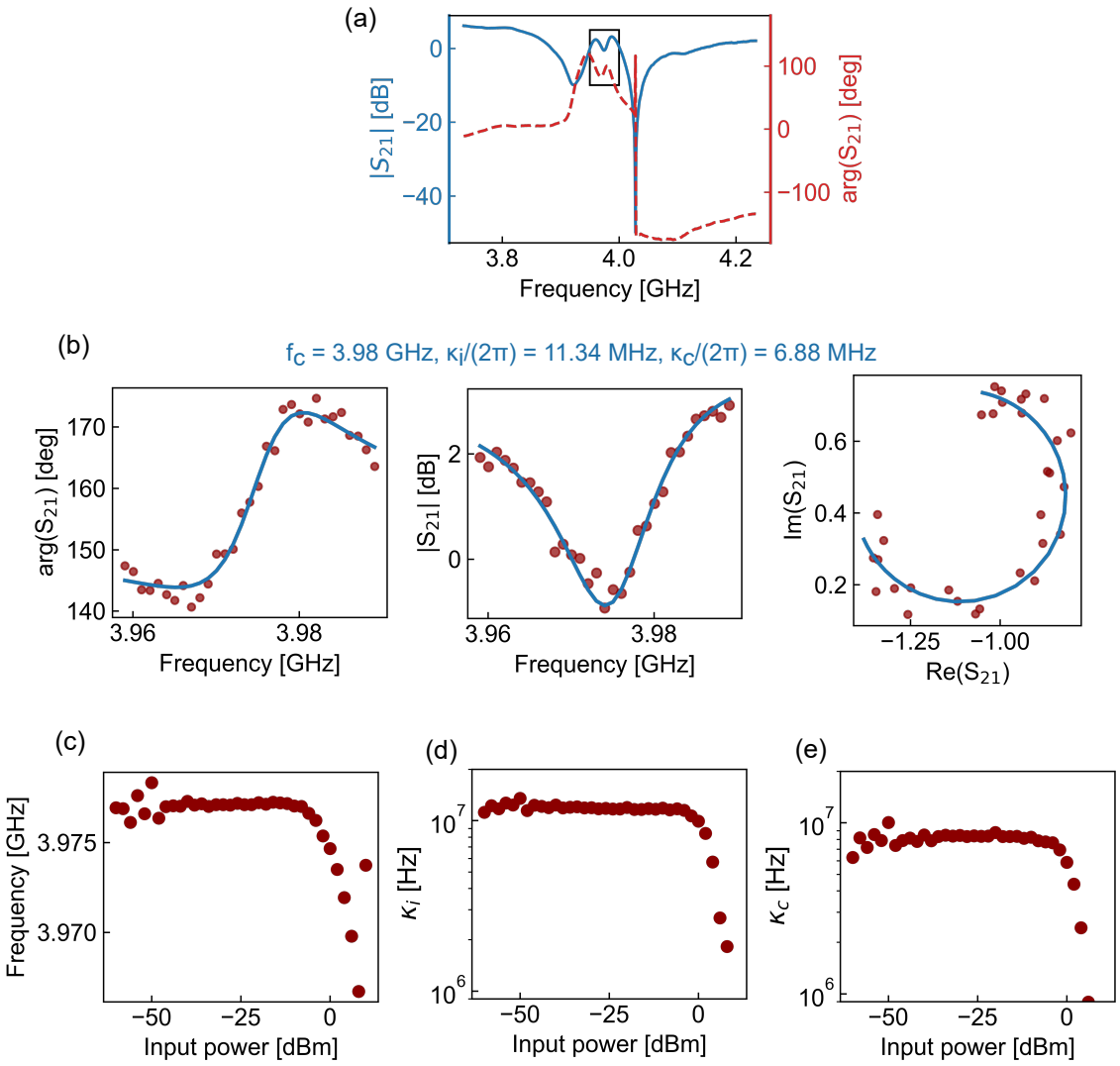

Figure 6.13: **Microwave characterization of device 1 on chip C12-013-J after carbon-nanotube integration**
(a) Amplitude and phase of the feedline transmission parameter S_{21}.The cavity resonance (boxed) is surrounded by two spurious modes.
(b) Fit of the cavity resonance to extract the resonance frequency f_c, the internal loss rate κ_i and the coupling loss rate κ_c following [163]. The input power was set to -56 dBm.
(c-d) Evolution of f_c, κ_i and κ_c with increasing input power on the feedline (equal to the VNA output power). No clear power dependence of κ_i is observed.

6.2 Calibration of the electron-photon coupling

In this section, we present the calibration of the electron-photon coupling using complementary approaches.

6.2.1 Photon-number dependence of the differential conductance in the Coulomb blockade regime

A first method to determine the electron-photon coupling strength in a quantum dot device connected to two reservoirs (source and drain) and operated in the Coulomb blockade regime is to analyze how the conductance of Coulomb peaks depends on the resonator photon number.

Conductance in a double-barrier structure

We consider a quantum dot in the Coulomb blockade regime, operating in the coherent transport limit, i.e. when the tunneling rate from the dot to the leads is much larger than the thermal energy ($\Gamma \gg kT$), so that quantum coherence strongly influences electron transport.
When the electrochemical potentials of the source, drain, and dot are aligned, the conductance through the system is given by [176]:

$$\begin{aligned} G &= \frac{e^2}{h}\frac{\Gamma_D\Gamma_S}{\Gamma_D+\Gamma_S}\int \mathrm{d}\epsilon \frac{\Gamma}{(\epsilon_d-\epsilon)^2+(\Gamma/2)^2}\left(\frac{\partial f}{\partial \epsilon}\right) \\ &= \frac{e^2}{h}\frac{\Gamma_D\Gamma_S}{\Gamma_D+\Gamma_S}\frac{\Gamma}{\left(\epsilon_d-\epsilon_f\right)^2+(\Gamma/2)^2} \end{aligned} \tag{6.1}$$

where

- $\Gamma_{S(D)}$ denotes the tunneling rate between the dot and the source (drain), with $\Gamma = \Gamma_S + \Gamma_D$,
- ϵ_d is the quantum dot energy level,
- f is the Fermi-Dirac distribution of the leads, assumed to be symmetric. At low temperature this can be approximated by $f(\epsilon) = \Theta(\epsilon_f - \epsilon)$, where Θ is the Heaviside step function and ϵ_f the Fermi level of the reservoirs.

We assume non-degenerate dot states. In the presence of degeneracy, the above expression is multiplied by a factor ν, equal to the degeneracy of the level under consideration.

Modulation of the conductance by the photons of the cavity

We now assume $\epsilon_f = 0$. In the adiabatic limit ($\hbar\omega_c \ll \Gamma$), the AC electric field of the resonator modulates the dot's energy level with amplitude $\alpha_{\mathrm{pg}} V_{\mathrm{AC}}$, yielding:

$$G(t) = G(\epsilon_d + e\alpha_{\mathrm{pg}} V_{AC}\cos(\omega_c t)) = \frac{e^2}{h}\frac{\Gamma_D\Gamma_S}{\Gamma_D+\Gamma_S}\frac{\Gamma}{(\epsilon_d + e\alpha_{\mathrm{pg}} V_{AC}\cos(\omega_c t))^2+(\Gamma/2)^2} \tag{6.2}$$

where:

- e is the electron charge,
- α_{pg} is the gate lever-arm that quantifies the sensitivity of the dot level to gate voltage,
- V_{AC} is the amplitude of the AC voltage applied by the resonator modulating the quantum dot energy,
- $\omega_c/(2\pi)$ is the cavity resonance frequency.

The AC voltage from the resonator can be derived from its **LC model**. The resonator is modeled as a parallel $L_{\lambda/2}C_{\lambda/2}$ circuit. In the quantum description [47], the relevant operators are the flux and charge operators, which read:

$$\hat{\mathbf{\Phi}} = \Phi_{\mathrm{zpf}}(\hat{\mathbf{a}}^\dagger + \hat{\mathbf{a}}) \quad \hat{\mathbf{Q}} = i\mathrm{Q}_{\mathrm{zpf}}(\hat{\mathbf{a}}^\dagger - \hat{\mathbf{a}}) \tag{6.3}$$

with $\Phi_{\text{zpf}} = \sqrt{\hbar/(2\omega_c C_{\lambda/2})} = \sqrt{\hbar Z_c/2}$, $Q_{\text{zpf}} = \sqrt{\hbar\omega_c C_{\lambda/2}/2} = \sqrt{\hbar/(2Z_c)}$ and $\hat{\mathbf{a}}, \hat{\mathbf{a}}^\dagger$ the photon annihilation and creation operators. The effective mode impedance is $Z_c = (2/\pi)Z_0$, with Z_0 the characteristic impedance of the coplanar waveguide forming the resonator.

The AC voltage applied by the resonator is given by its root-mean-square (RMS) value.
In the Fock state basis of the cavity, the RMS voltage of the resonator is obtained from the variance of the voltage operator $\hat{\mathbf{V}} = \hat{\mathbf{Q}}/C_{\lambda/2}$:

$$\begin{aligned} V_{\text{RMS}} &= \sqrt{\langle n|(\hat{\mathbf{V}}^2|n\rangle - \langle n|\hat{\mathbf{V}}|n\rangle^2} \\ &= V_{\text{zpf}}\sqrt{1+2n} \end{aligned} \tag{6.4}$$

where n is here the average number of photons in the cavity, and:

$$V_{\text{zpf}} = \frac{Q_{\text{zpf}}}{C_{\lambda/2}} = \hbar\omega_c\sqrt{\frac{Z_c}{2\hbar}} = \hbar\omega_c\sqrt{\frac{2Z_0}{h}}, \quad C_{\lambda/2} = \frac{\pi}{2}\frac{1}{Z_0\omega_c}. \tag{6.5}$$

In the Fock basis, the voltage operator can thus be written as:

$$\hat{\mathbf{V}} = V_{\text{RMS}}\,|n\rangle\langle n| = V_{\text{zpf}}\sqrt{1+2n}\;|n\rangle\langle n| \tag{6.6}$$

When the cavity is driven by a classical source, the intra-cavity field is better described by a coherent state $|\alpha\rangle$ [177]. In this case, the RMS voltage expectation value becomes:

$$V'_{\text{RMS}} = \int \mathrm{d}\alpha^2\, V_{\text{RMS}}\,\langle\alpha|n\rangle\,\langle n|\alpha\rangle = V_{\text{zpf}}\sqrt{1+2n}\,\pi \tag{6.7}$$

and the AC modulation amplitude on the dot is:

$$V_{\text{AC}} = \sqrt{2}\times V'_{\text{RMS}} = \sqrt{2}\,\pi\, V_{\text{zpf}}\sqrt{1+2n} \tag{6.8}$$

Thus, the dot level modulation depends directly on the photon number in the cavity, and the conductance can be expressed as:

$$G(t) = G\Big(\epsilon_d + e\alpha_{\text{pg}}V_{\text{zpf}}\sqrt{1+2n}\,\sqrt{2}\,\pi\cos(\omega_c t)\Big) = G\Big(\epsilon_d + \hbar g\sqrt{1+2n}\,\sqrt{2}\,\pi\cos(\omega_c t)\Big) \tag{6.9}$$

where $\hbar g = e\alpha_{\text{pg}}V_{\text{zpf}}$ [178] defines the electron-photon coupling strength.
For large photon occupation, this simplifies to:

$$G(t) = G(\epsilon_d + e\alpha_{\text{pg}}V_{\text{zpf}}\sqrt{1+2n}\,\sqrt{2}\,\pi\cos(\omega_c t)) \approx G(\epsilon_d + \hbar 2g\sqrt{n}\,\pi\cos(\omega_c t)) \tag{6.10}$$

In the adiabatic limit ($\hbar\omega_c \ll \Gamma$), the dot conductance follows the modulation without delay, and the time-averaged conductance over one period reads:

$$G = \frac{1}{2\pi}\int_0^{2\pi}\mathrm{d}\theta\, G(\epsilon_d + 2\hbar g\sqrt{n}\,\pi\cos(\theta)) = \frac{1}{2\pi}\int_0^{2\pi}\mathrm{d}\theta\,\frac{e^2}{h}\frac{\Gamma_D\Gamma_S}{\Gamma_D+\Gamma_S}\frac{\Gamma}{(\epsilon_d + \hbar g 2\sqrt{n}\,\pi\cos(\theta))^2 + (\Gamma/2)^2} \tag{6.11}$$

Conductance measurements as a function of resonator photon number

The measurements were performed with the sample mounted in a Bluefors dilution refrigerator at a base temperature of ~ 10 mK. The combined RF and DC measurement setup is shown in Fig. 6.14.

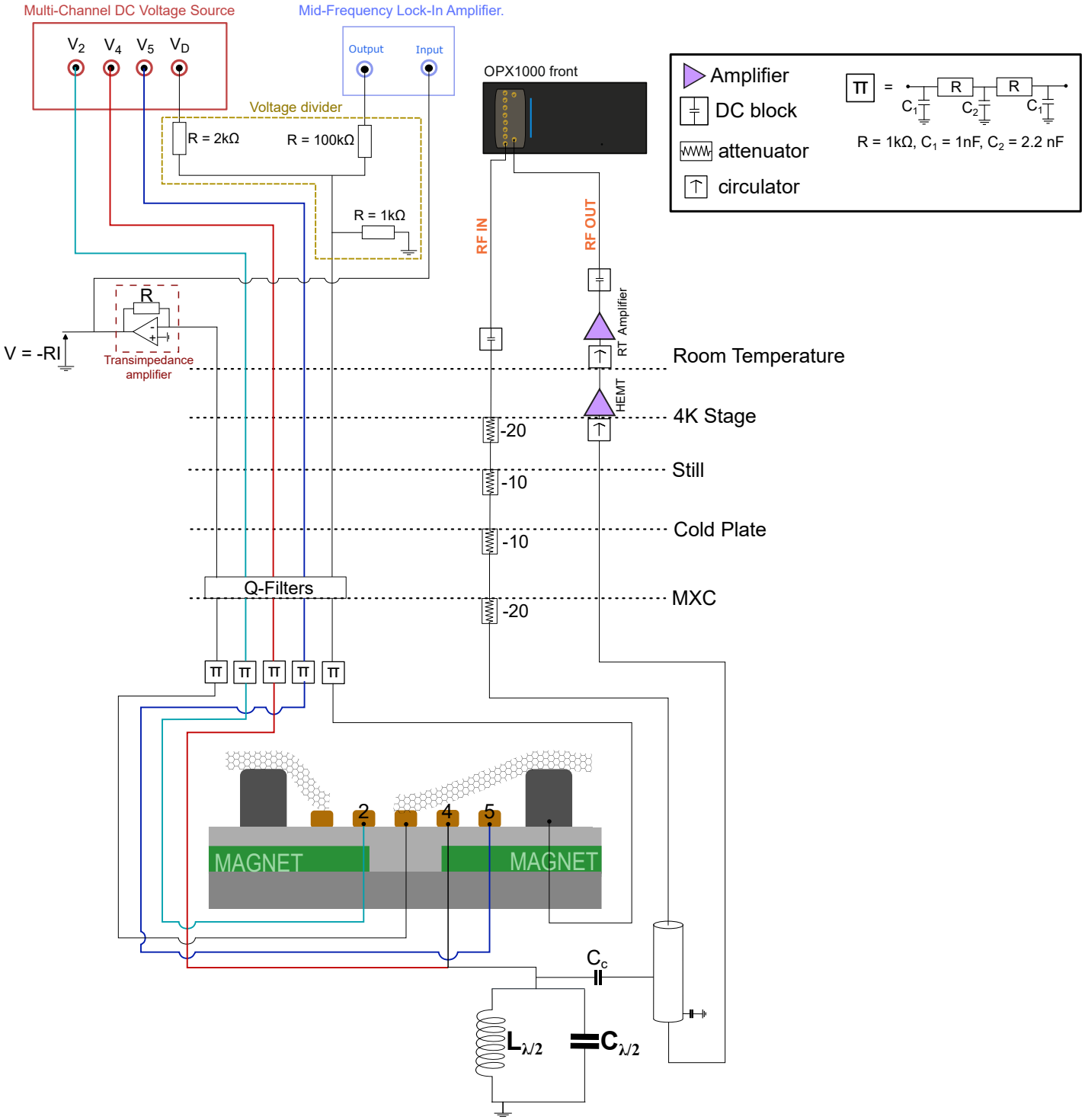

Figure 6.14: **Schematic of the measurement setup**
Differential conductance is measured using a lock-in a lock-in detection scheme. The DC lines are filtered Q-filters, QDevil's compact cryogenic multi-stage low-pass filters, and π-filters, implemented to prevent electrical discharges on the CNT. A Quantum Machines Front-End Module supplies a microwave tone at the cavity frequency to the feedline. The transmitted signal is then amplified and analyzed by the same module.

The experiment focuses on the differential conductance through the carbon nanotube, which is extracted using a standard lock-in detection scheme.

The CNT is biased with a combination of a DC voltage and a small low-frequency AC excitation. To ensure that the AC component remains small compared to both the DC bias and the gate voltage ($V_{\text{bias}}^{\text{AC}} \ll V_{\text{bias}}^{\text{DC}}, V_G$), the signal is attenuated by a voltage divider.

The resulting effective bias can be expressed as:

$$V_{\text{bias}} = \frac{\frac{V_{\text{bias}}^{\text{DC}}}{2\times10^3} + \frac{V_{\text{bias}}^{\text{AC}}}{100\times10^3}}{\frac{1}{10^3} + \frac{1}{2\times10^3} + \frac{1}{100\times10^3}} \approx \frac{\frac{V_{\text{bias}}^{\text{DC}}}{2\times10^3} + \frac{V_{\text{bias}}^{\text{AC}}}{100\times10^3}}{\frac{1}{10^3} + \frac{1}{2\times10^3}} = \frac{V_{\text{bias}}^{\text{DC}}}{3} + \frac{2V_{\text{bias}}^{\text{AC}}}{300} \tag{6.12}$$

The resulting current through the CNT is:

$$\begin{aligned} I(V_G, V_{\text{bias}}) &= I\left(V_G, \frac{V_{\text{bias}}^{\text{DC}}}{3} + \frac{2V_{\text{bias}}^{\text{AC}}}{300}\cos(\omega_{\text{AC}}t)\right) \\ &\approx I\left(V_G, \frac{V_{\text{bias}}^{\text{DC}}}{3}\right) + \frac{2V_{\text{bias}}^{\text{AC}}}{300}\cos(\omega_{\text{AC}}t)\left.\frac{\partial I}{\partial V_{\text{bias}}}\right|_{V_G, V_{\text{bias}}^{\text{DC}}/3} \\ &\approx I\left(V_G, \frac{V_{\text{bias}}^{\text{DC}}}{3}\right) + \frac{2V_{\text{bias}}^{\text{AC}}}{300}G\left(V_G, V_{\text{bias}}^{\text{DC}}/3\right)\cos(\omega_{\text{AC}}t) \end{aligned} \tag{6.13}$$

where G is the differential conductance.

Since the lock-in demodulation isolates the response at ω_{AC}, the measured signal corresponds to the term:

$$I_{\text{LI}} = \frac{2V_{\text{bias}}^{\text{AC}}}{300}G\left(V_G, V_{\text{bias}}^{\text{DC}}/3\right). \tag{6.14}$$

In the Coulomb blockade regime, at resonance ($\epsilon_d = \epsilon_f$) and assuming symmetric coupling ($\Gamma_S = \Gamma_D = \Gamma/2$), the conductance can reach the quantum limit $G_0 = e^2/h \approx 39\,\mu\text{S}$ [see Eq. (6.1)]. With an applied AC excitation of $V_D^{\text{AC}} = 6\,\text{mV}$ before the voltage divider, the effective AC bias on the CNT is about $40\,\mu\text{V}$. The corresponding maximum current is:

$$I_{\text{LI}}^{\max} = \frac{2V_{\text{bias}}^{\text{AC}}}{300}G_0 \approx 1.5\,\text{nA}. \tag{6.15}$$

In practice, the current of a small CNT in the Coulomb blockade regime is often significantly lower due to reduced transmission. To improve signal visibility, we use a transimpedance amplifier (see Fig. 6.15), which converts current to voltage with gain $-R$, where R is the feedback resistor.

Differential conductance as a function of gate bias (applied to DC gate 2, 4, or 5) is shown for device 1 of chip C12-013-J in Fig. 6.15. The resulting charge stability diagram is consistent with earlier reports on multiwall carbon nanotubes or tightly bound double-wall CNT bundles, which often host several quantum dots with distinct characteristics [52] [51]. In our measurements, the charge stability diagram reveals at least two quantum dots, Fig. 6.15(d-f).

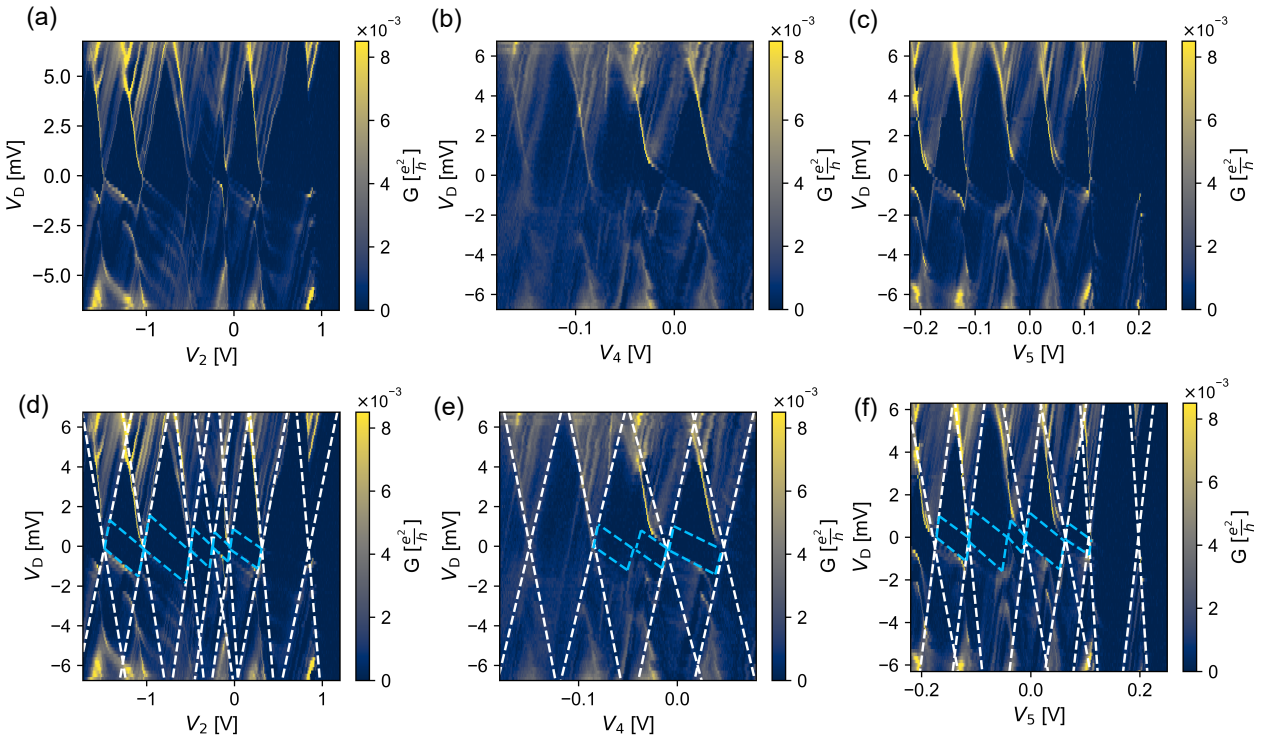

Figure 6.15: **Quantum-dot charge-stability diagrams**.
(a-c) Color-scale maps of the differential conductance versus drain bias V_D and plunger-gate voltage V_i with $i \in \{2,4,5\}$.
(d-f) Same data as (a-c), overlaid with schematic charge-stability diagrams of parallel dots inferred from the measurements. From the diamond structure, the gates' lever arms $\alpha_{pg,i}$ - which convert gate-voltage changes into shifts of the dot electrochemical potential (see Chapter 1) - are estimated. Especially, in (d), for the dot outlined by the white dashed diagram, $\alpha_{pg,2} \approx 0.015$ and for the dot outlined in blue $\alpha_{pg,2} \approx 0.002$. In (e), for the dot outlined by the white dashed diagram $\alpha_{pg,4} = 0.12$.

To calibrate the electron-photon coupling, we focus on the zero-bias Coulomb peak obtained by sweeping the potential on gate 2.

Simultaneously with the low-frequency measurement of the differential conductance, a microwave tone is sent to the feedline coupled to the CPW resonator, allowing us to vary and control the resonator's mean photon population.

The mean photon number in the resonator can be derived from the Master equations introduced in Chapter 1. The time evolution of the photon annihilation operator is given by:

$$\partial_t \hat{\mathbf{a}} = -i\omega_c \hat{\mathbf{a}} - \frac{\kappa}{2}\hat{\mathbf{a}} + \sqrt{\kappa_c}\hat{\mathbf{a}}_{\text{in}} \tag{6.16}$$

where $\hat{\mathbf{a}}$ is the photon annihilation operator of the resonator mode, and $\hat{\mathbf{a}}_{\text{in}}$ is the incoming field operator. In the steady-state regime ($\partial_t \hat{\mathbf{a}} = 0$), the intracavity field operator is given by:

$$\hat{\mathbf{a}} = 2\frac{\sqrt{\kappa_c}}{\kappa}\hat{\mathbf{a}}_{\text{in}} \tag{6.17}$$

with the corresponding creation operator:

$$\hat{\mathbf{a}}^\dagger = 2\frac{\sqrt{\kappa_c}}{\kappa}\hat{\mathbf{a}}^\dagger_{\text{in}} \tag{6.18}$$

The mean photon number inside the resonator is then:

$$n = \left\langle \hat{\mathbf{a}}^\dagger \hat{\mathbf{a}} \right\rangle = 4\frac{\kappa_c}{\kappa^2} \left\langle \hat{\mathbf{a}}_{\text{in}}^\dagger \hat{\mathbf{a}}_{\text{in}} \right\rangle = 4\frac{\kappa_c}{\kappa^2}, \frac{P_{\text{in}} A_{\text{att}}}{\hbar\omega_c}, \tag{6.19}$$

where $P_{\text{in}} A_{\text{att}}$ is the effective input power at the feedline. This quantity corresponds to the output power of the microwave source multiplied by the total attenuation A_{att} of the RF line, including all attenuators and cable losses. A detailed characterization of the attenuation chain is given in the Appendix C. For our setup, the total attenuation is estimated to be 68 ± 1 dB.
By measuring the transmitted signal through the feedline coupled to the resonator, we perform spectroscopy and extract the external (κ_c) and internal (κ_i) loss rates, together with the resonance frequency f_c of the resonator, as shown in Fig. 6.16. These parameters are used to estimate the photon number.
The average photon number in the resonator is tuned directly by adjusting the input power of the microwave tone.

The Coulomb peaks at zero bias are measured as a function of the input power applied to the feedline at the frequency of the resonator, which directly sets the number of photons in the resonator. The resulting differential conductance as a function of photon number is shown in Fig.6.16. At zero photon number, the Coulomb peak can be fitted using Eq. (6.1) in order to extract the total tunneling rate Γ and a fitting parameter A, yielding

$$G = \frac{e^2}{h} A \frac{1}{(\epsilon_d - \epsilon_f)^2 + (\Gamma/2)^2}. \tag{6.20}$$

For one of the Coulomb peaks shown in Fig.6.16, no peak is observed at zero photon number. In this case, the values of Γ and A obtained from the fit of the other Coulomb peak are used. With these parameters fixed, the conductance measured at finite photon number can then be fitted using Eq. (6.11). The fit was performed on the two-dimensional cuts shown in Figs. 6.16(e)-(g). From this analysis, the extracted electron-photon coupling strength is:

$$\frac{\mathbf{g}}{\mathbf{2\pi}} = (\mathbf{300 \pm 40})\,\mathbf{MHz} \tag{6.21}$$

In this analysis, the uncertainty on the photon number stems from the uncertainty in the attenuation of the lines.

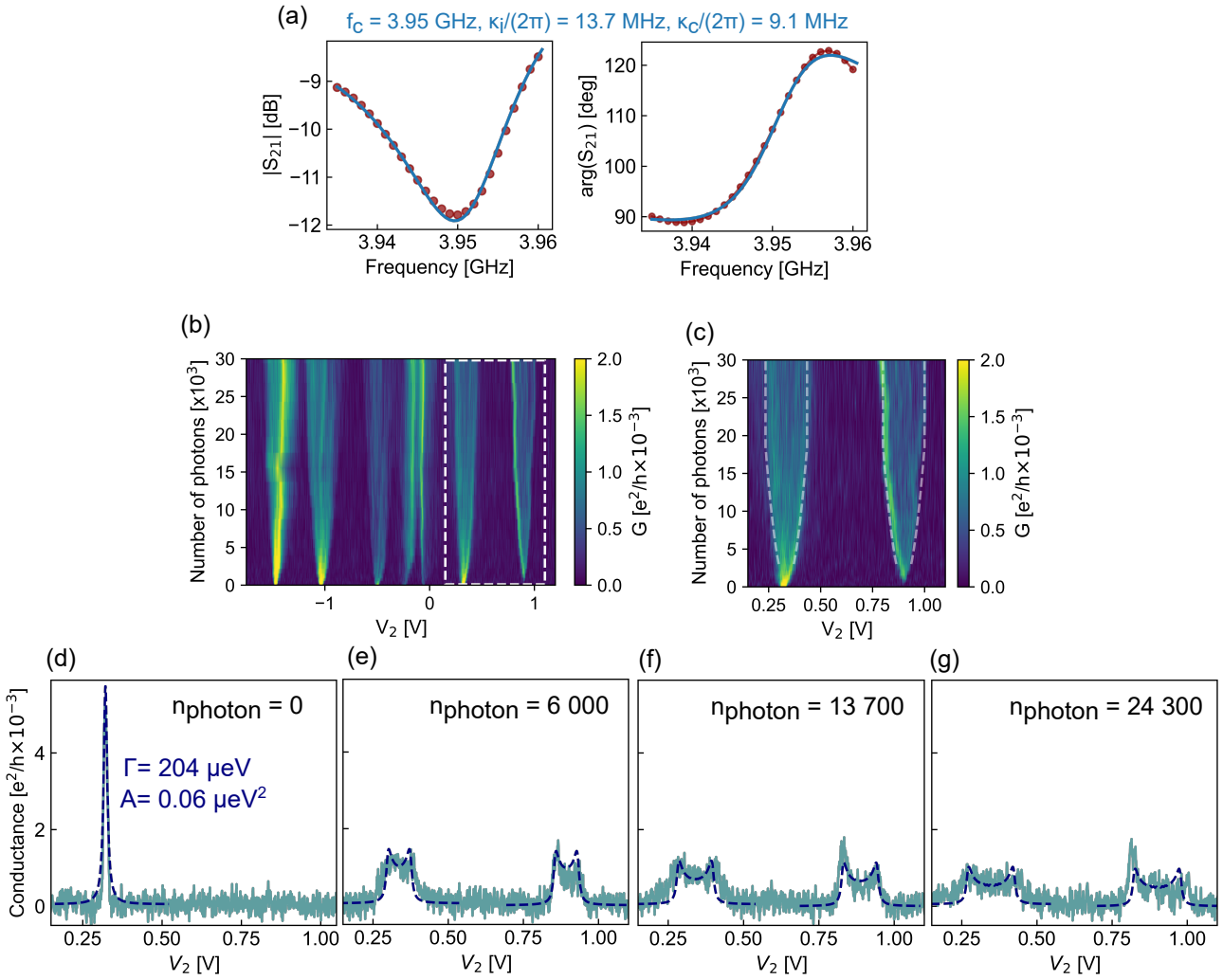

Figure 6.16: **Power dependence of the Coulomb peak for calibrating the electron-photon coupling**

(a) Extraction of the cavity resonance frequency f_c and loss rates (κ_i, κ_c) of the resonator. The input power was set to -16 dBm. These parameters are used to run the experiment and estimate the electron-photon coupling.

(b) Power dependence of the Coulomb peak while sweeping gate-2 voltage at zero bias.

(c) Zoom of (b) highlighting the two Coulomb peaks used to estimate the electron-photon coupling. The dashed lines mark the envelop of the conductance peak predicted by the theoretical expression $G(\epsilon_d, n)$ in Eq. (6.11),

(d-g) Conductance peaks plotted as the mean photon number in the resonator is increased. In (d), the data are overlaid with the zero-photon fit using Eq. (6.20). In (e-g), the data are overlaid with Eq. (6.11), using the amplitude A and tunneling rate Γ determined from the fit in (d).

For the coupling calibration, the lever arm of plunger gate 2 is $\alpha_{pg,2} = 0.015$, estimated from the charge stability diagram in Fig. 6.15.

6.2.2 Dispersive shift of the resonator frequency induced by the quantum dot

When a quantum-dot orbital aligns with the Fermi level of a lead (i.e., the dot is resonant with a reservoir), electrons can tunnel back and forth between the dot and the lead, forming an electric dipole. This dipole couples to the cavity electric field and produces a dispersive shift of the resonator frequency.

Semi-classical linear response of the resonator

The electron-photon coupling mechanism for this circuit was introduced in Chapter 1. Retaining the dominant terms of Eq. (1.42), the interaction Hamiltonian can be written:

$$\mathrm{H}_{e-ph} = \hat{\mathbf{h}}_{\mathrm{int}}(\hat{\mathbf{a}}^\dagger + \hat{\mathbf{a}}) = \sum_j \hbar g_j \hat{\mathbf{c}}_j^\dagger \hat{\mathbf{c}}_j \, (\hat{\mathbf{a}}^\dagger + \hat{\mathbf{a}}) \tag{6.22}$$

with coupling coefficients:

$$g_j = -e \int \mathrm{d}r^3 \left|\psi_j\right|^2(\vec{\mathbf{r}}) V_\perp(\vec{\mathbf{r}}) \tag{6.23}$$

where $j \equiv (o,i)$ labels orbital o of circuit element i, ψ_j is the corresponding electronic wavefunction, and $V_\perp$ is the cavity-induced scalar pseudo-potential.

The photon dynamics in the cricuit follow the quantum Langevin equation including the dot backaction:

$$\partial_t \hat{\mathbf{a}} = -i\omega_c \hat{\mathbf{a}} - \frac{\kappa}{2}\hat{\mathbf{a}} + \sqrt{\kappa_c}\hat{\mathbf{a}}_{in} - \frac{i}{\hbar}\hat{\mathbf{h}}_{\mathrm{int}} \tag{6.24}$$

with total decay rate $\kappa = \kappa_i + \kappa_c$ (internal loss κ_i and external coupling κ_c), and input/output mode operators $\hat{\mathbf{a}}_{\mathrm{in}}$ and $\hat{\mathbf{a}}_{\mathrm{out}}$ related (for a hanger-type coupling) by:

$$\hat{\mathbf{a}}_{\mathrm{in}} + \hat{\mathbf{a}}_{\mathrm{out}} = \frac{\sqrt{\kappa_c}}{2}\hat{\mathbf{a}} \tag{6.25}$$

Near resonance and for a large number of photons in the cavity, we use a mean-field ansatz:

$$\hat{\mathbf{a}} \to \langle\hat{\mathbf{a}}\rangle \equiv \bar{a} e^{-i\omega t} \qquad \hat{\mathbf{a}}_{\mathrm{in(out)},j} \to \langle\hat{\mathbf{a}}_{\mathrm{in(out)},j}\rangle \equiv \bar{a}_{\mathrm{in(out)},j} e^{-i\omega t} \tag{6.26}$$

To asses the photon dynamics in the circuit, we need to derive the electronic response. For this device, a minimal model retains only the modulation of the quantum-dot orbital. Within this approximation, the interaction reduces to:

$$\mathrm{H}_{e-ph} = \hbar g \hat{\mathbf{n}} \, (\hat{\mathbf{a}}^\dagger + \hat{\mathbf{a}}) \tag{6.27}$$

If the cavity-induced modulation of the dot chemical potential-written as $\delta\epsilon_d(\omega) = g\bar{a}(\omega)$ - is small compared with the relevant electronic energy scales (charging energy E_C and the tunneling rate to the leads Γ), the charge occupation in the orbital of the quantum dot $\langle\hat{\mathbf{n}}\rangle$ responds linearly to the excitation:

$$\begin{aligned} \langle\hat{\mathbf{n}}(t)\rangle &= \frac{1}{\hbar}\int \mathrm{d}t' \, \chi(t-t')\delta\epsilon(t) \\ \langle\hat{\mathbf{n}}(\omega)\rangle &= \frac{1}{\hbar}\,\chi(\omega)\delta\epsilon_d(\omega) \end{aligned} \tag{6.28}$$

where $\chi(\omega)$ is the quantum-dot charge susceptibility.
Solving Eq. (6.24) in the frequency domain then gives:

$$\bar{a} = \frac{\sqrt{\kappa_c}\bar{a}_{\mathrm{in}}}{-i(\omega-\omega_c) + \kappa/2 + ig^2\chi(\omega)} \tag{6.29}$$

In the adiabatic limit - where the dot's charge dynamics are much faster than the AC drive - the mean electron number follows the chemical-potential modulation instantaneously:

$$\langle \hat{\mathbf{n}} \rangle (t) = \frac{\partial n}{\partial \epsilon_d} \delta\epsilon_d(t) \tag{6.30}$$

and the charge susceptibility of the quantum dot can then be expressed as :

$$\chi = \hbar \frac{\partial n}{\partial \epsilon_d} \tag{6.31}$$

In the coherent regime - when $\Gamma \gg k_B T$ - the quantum state in the dot exhibits coherence with the reservoir states. In this regime, the mean number of photon in the orbital of the dot is given by [179]:

$$n(\epsilon) = \frac{1}{2} + \frac{1}{\pi} \arctan\left(\frac{\epsilon_f - \epsilon_d}{\Gamma/2}\right) \tag{6.32}$$

where ϵ_f is the reservoir Fermi energy and $\Gamma = \Gamma_S + \Gamma_D$ is the total tunnel broadening of the level. The static charge susceptibility of the quantum dot is then given by:

$$\chi = -\frac{\hbar}{\pi} \frac{\Gamma/2}{(\epsilon_d - \epsilon_f)^2 + (\Gamma/2)^2} \tag{6.33}$$

For a cavity coupled to a hanger-type transmission line, the complex scattering coefficient can be written as:

$$S_{\mathrm{H}} = \frac{\bar{a}_{out}}{\bar{a}_{in}} = \frac{-\kappa_i/2 + i(\omega - \omega_c) - i g^2 \chi(\omega)}{\kappa/2 - i(\omega - \omega_c) + i g^2 \chi(\omega)} = \frac{-\kappa_i/2 + i\left[\omega - \left(\omega_c + g^2\chi\right)\right]}{\kappa/2 - i\left[\omega - \left(\omega_c + g^2\chi(\omega)\right)\right]} \tag{6.34}$$

where the dispersive cavity shift of the resonance frequency induced by the nano-circuit is:

$$\Delta\omega_c = g^2 \chi \tag{6.35}$$

Monitoring the transmitted signal at $\omega \approx \omega_c$, the phase of S_{H} acquires a shift:

$$\Delta\phi = -\frac{2\kappa_c}{\kappa_i \kappa} \Delta\omega_c = -\frac{2\kappa_c}{\kappa_i \kappa} \Delta g^2 \chi = \frac{2\kappa_c}{\kappa_i \kappa} g^2 \frac{\hbar}{\pi} \frac{\Gamma/2}{(\epsilon_d - \epsilon_f)^2 + (\Gamma/2)^2} \underset{\epsilon_d = \epsilon_f}{=} \frac{4}{\pi} \frac{\kappa_c}{\kappa_i \kappa} g^2 \frac{\hbar}{\Gamma} \tag{6.36}$$

Measurement of the resonator phase response across the charge-stability diagram

Using the setup of Fig.6.14, we sweep V_g and V_D as for a charge-stability measurement and simultaneously monitor the phase of the transmission through the hanger line coupled to the resonator, with a fixed probe tone at frequency f_c. The resulting phase maps are presented in Fig.6.17.

Phase contrasts, consistent with a dot orbital resonant with the source gate (corresponding to gate 3 see schematic Fig.6.12), are visible on the charge stability diagrams acquired with gate 2 and gate 5. Notably, these features seems to occur in regions where the second dot is weak or not clearly resolved in the DC map of Fig. 6.15.

Focusing on the zero-bias phase feature obtained with gate 2, we estimate the electron-photon coupling using Eq. (6.36). The total tunneling rate Γ and the on-resonance phase shift $\Delta\phi_{\max}$ (at $\epsilon_d = \epsilon_f$) are extracted by fitting the phase trace in Fig.6.17 to Eq. (6.36).

We find that the fitted Γ is approximately a factor of two smaller than the value obtained from the differential-conductance calibration in Fig. 6.16. This is consistent with the phase response being primarily sensitive to tunneling into the source lead (single-lead susceptibility), whereas the conductance depends on both couplings ($\Gamma = \Gamma_S + \Gamma_D$).

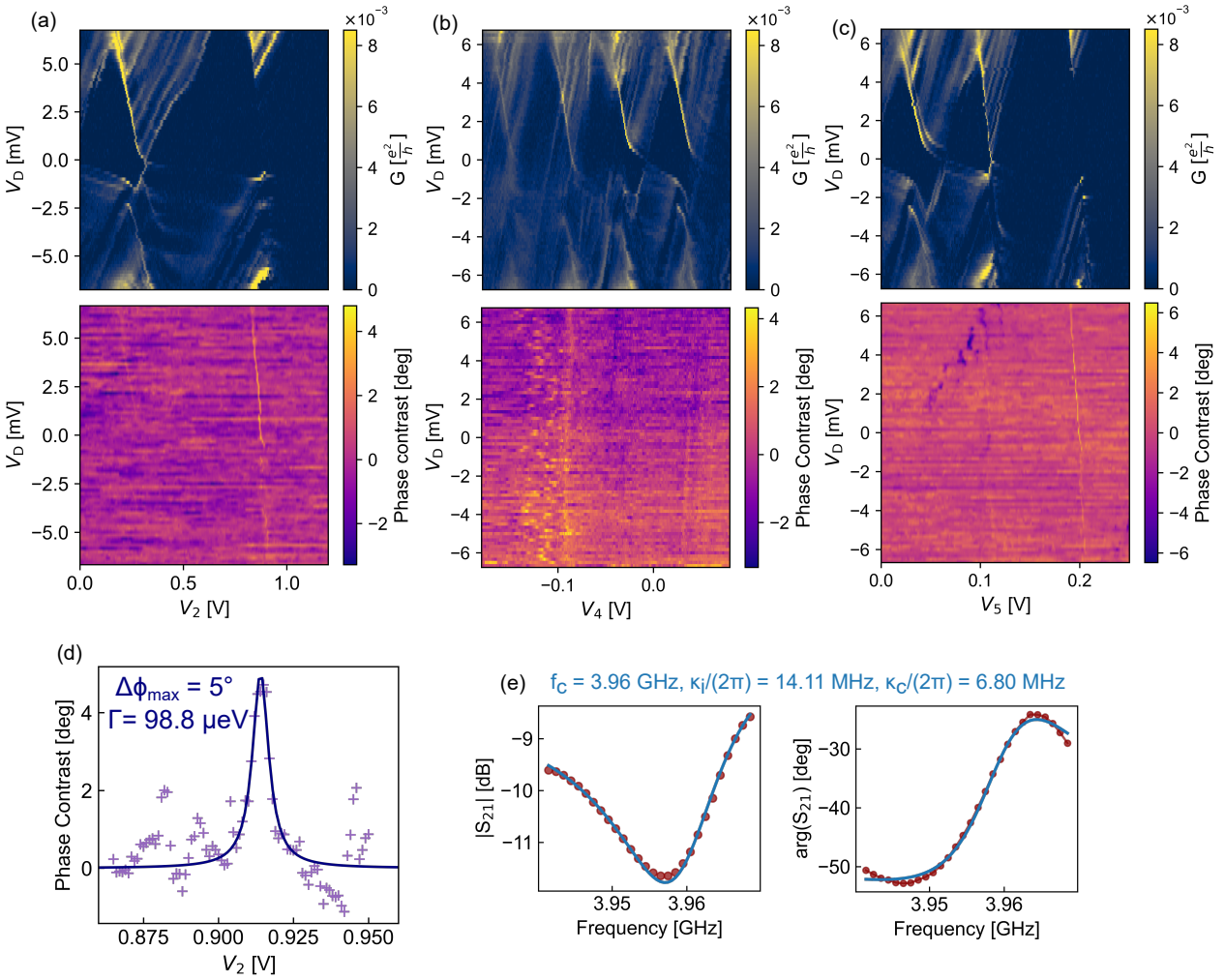

Figure 6.17: **Electron-photon coupling calibration from the cavity response**
(a-c) Differential-conductance and cavity phase maps in the V_g-V_D plane for plunger gates 2, 4, and 5. The phase of microwave tone transmitted through the feedline coupled to the resonator is monitored at the cavity frequency f_c.
(d) Phase shift at zero drain bias ($V_D = 0\,\text{mV}$) from panel (a). A Lorentzian fit yields the tunneling rate Γ and the maximum phase contrast $\Delta\phi_{\text{max}}$ used to estimate the electron-photon coupling. The lever arm for gate 2 is fixed to $\alpha_{pg,2} = 0.015$, as extracted from the charge stability diagram in Fig. 6.15.
(e) Extraction of the cavity resonance f_c and loss rates (κ_i, κ_c) used in the coupling estimate.

The cavity loss rates and resonance frequency were remeasured by transmission spectroscopy through the hanger line coupled to the resonator (see Fig.6.17). This additional calibration was necessary because, relative to the data of Fig.6.16, a magnetic field had been applied to the sample and the cryostat had been warmed up.

Using the fitted values of $\Delta\phi_{\text{max}}$, Γ, κ_i, and κ_c, the electron-photon coupling follows from:

$$g = \sqrt{\Delta\phi_{\mathbf{max}} \frac{\pi}{4} \frac{\Gamma}{\hbar} \frac{\kappa_i \kappa}{\kappa_c}} \tag{6.37}$$

yielding:

$$\frac{\mathbf{g}}{\mathbf{2\pi}} = \mathbf{260\,MHz} \tag{6.38}$$

6.2.3 Discussion on the cavity-quantum dot coupling

The two calibration methods yield consistent values for the electron-photon coupling, $g/2\pi \approx$ 260-340 MHz.
Let us note that for the two analyses above, we assumed that the cavity field modulates only the quantum dot's electrochemical potential. However, the cavity field could also modulate the source and drain electrochemical potentials. In that situation - discussed in [179] - coupling to the reservoirs reduces the effective electron-photon coupling strength extracted from the measurement. In the fully symmetric limit, where all electrodes are modulated equally, the cavity exhibits no dispersive response, and the Coulomb peak becomes independent of the photon number in the cavity.

The experimentally determined coupling strength can be benchmarked against a simple theoretical estimate. The maximal coupling of a single dot orbital to the cavity field is [178]:

$$g = \frac{e\alpha_{\mathrm{pg},4} V_{\mathrm{zpf}}}{\hbar} = \frac{e\alpha_{\mathrm{pg},4}}{\hbar}\hbar\omega_c\sqrt{\frac{2Z_0}{h}} \tag{6.39}$$

where V_{zpf} is the cavity voltage zero-point fluctuation and Z_0 the characteristic impedance of the CPW line forming the resonator.

The impedance is estimated using the calibrated kinetic inductance (see previous chapter). For a half-wavelength CPW with center-conductor width $w = 2\,\mu$m and gap $s = 3\,\mu$m, the resulting characteristic impedance Z_0 is estimated to be $Z_0 \approx 2\,\mathrm{k}\Omega$. The lever-arm of the gate 4 $\alpha_{\mathrm{pg},4}$ is estimated from the charge stability diagram Figure 6.15 to be $\alpha_{\mathrm{pg},4} \sim 0.12$.

Using these parameters, we estimate:

$$g \sim 2\pi \times 190\,\mathrm{MHz} \tag{6.40}$$

This value is lower than the one obtained experimentally.Two factors may account for the difference: (i) the characteristic impedance Z_0 could be higher than the design estimate due to increased kinetic inductance introduced by the pre-assembly cleaning (in particular the argon etch) performed to facilitate the carbon nanotube integration; and (ii) the gate - 4 lever arm used here was extracted for a dot formed by gate 4, whereas the calibrated coupling pertains to a dot stabilized with gate 2, for which the effective lever arm of gate 4 may differ slightly.

Despite this slight discrepancy with the simple estimate, the calibrated coupling strength in our device is approximately two to three times larger than values reported for carbon-nanotube quantum dots coupled to Nb $\lambda/2$ resonators with characteristic impedance $Z_0 \approx 50\,\Omega$ [175].

From the calibrated electron-photon coupling, we can estimate the expected coupling in a double-quantum-dot (DQD) architecture.
For a charge-dipole transition, the light-matter coupling is given by (see Eq. (1.48)):

$$g_{\mathrm{DQD}} = \frac{\Delta g}{2} = \frac{g_R - g_L}{2}. \tag{6.41}$$

Here, g_L and g_R denote the coupling coefficients between the cavity electric field and the single dot orbital localized in the left and right quantum dots, respectively.
In the case of a spatially asymmetric resonator electric-field profile that predominantly overlaps with one of the quantum dots ($g_L \to 0$ or $g_R \to 0$), the charge-photon coupling can be related to the single-dot coupling strength as:

$$\left|g_{\mathrm{DQD}}\right| = \frac{|g|}{2} = \frac{1}{2}\frac{e\alpha_{\mathrm{pg}} V_{\mathrm{zpf}}}{\hbar} \tag{6.42}$$

Using our measured range $g/(2\pi) \approx 260 - 340\text{MHz}$, this gives:

$$\frac{|g_{\text{DQD}}|}{2\pi} \approx 130 - 170\text{MHz} \tag{6.43}$$

If one allows for device-to-device variations (e.g., lever arms and impedance), a broader range may be observed.

6.3 Spectroscopic study of excited states under magnetic-field variation

From the charge-stability diagram in Fig. 6.15, well-defined conductance peaks appear at positive bias, corresponding to transport through excited states of the quantum dot. Tracking the energy dispersion of these states while sweeping an external magnetic field can provide access to intrinsic properties of carbon nanotubes [180] and also reveal the influence of the local magnetic field in the dot's environment [181].

6.3.1 Protocol for magnetic-field spectroscopy of excited states in a carbon-nanotube quantum dot

The DC setup for these measurements is the same as that used to calibrate the electron-photon coupling (see Fig. 6.14). All measurements were performed in the same dilution refrigerator with a base temperature of approximately 10 mK.

Excited states are most clearly identified in charge-stability diagrams acquired with plunger gate 2. Accordingly, we focus on the quantum dot defined by tuning this gate. In addition, forming the dot with gate 2 likely places it closer to the on-chip magnet - given the collapsed nanotube - enhancing the effective magnetic field generated by the magnet experienced by the dot.

Our analysis focuses on two bias triangles visible in the stability diagram (Fig. 6.18). When a source-drain bias is applied, a finite bias window opens; if an excited state falls within this energy window, transport through the (N, n) state - an N-electron configuration with ground state $n = 0$ and excited states indexed by $n \geq 1$ - is allowed, yielding a peak in the differential conductance, as shown in Fig. 6.18.

An external magnetic field can be applied using a one-dimensional magnet mounted to the cryostat. This field can shift the energy levels of the quantum dot. We track these shifts by sweeping the voltage on plunger gate 2, which linearly tunes the dot's electrochemical potentials:

$$\Delta\mu_{\text{N}}^{(n)} = -e\alpha_{pg,2}\,\Delta V_2$$

here $\alpha_{pg,2}$ is the lever arm of gate 2, determined from the charge-stability diagram in Fig. 6.15.

By measuring the differential conductance while varying both the magnetic field and the plunger-gate voltage, we obtain a spectroscopic map of the magnetic-field dispersion of the quantum dot's excited states.

Here, we assume that the lever arm of the plunger gate $\alpha_{pg,2}$ is determined solely by the device geometry and capacitances and therefore remains constant as a function of magnetic field. This assumption is supported by the linear magnetic-field dependence of the energy levels observed in the spectra shown in Fig. 6.19 and Fig. 6.22, and the absence of any measurable change in the bias-spectroscopy slopes.

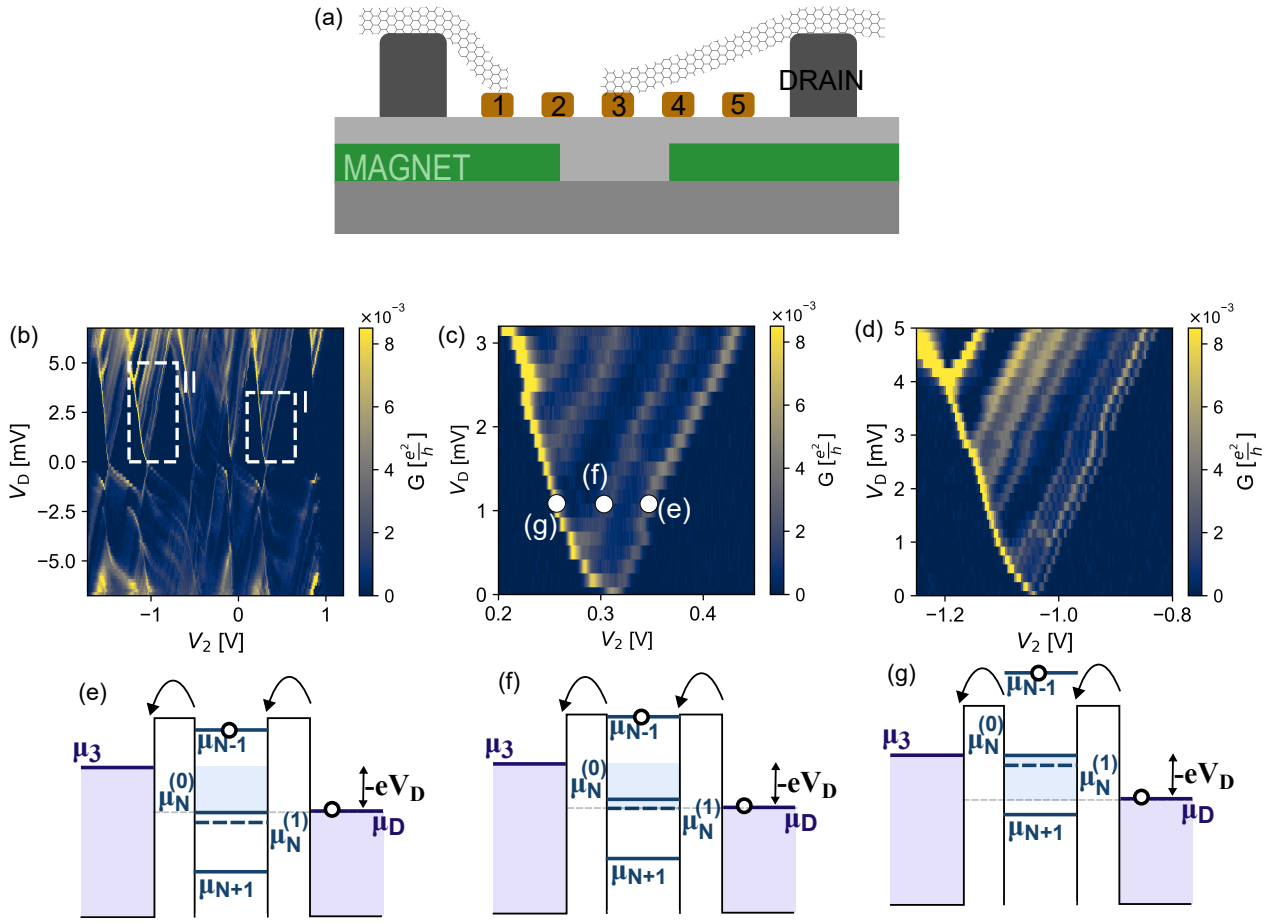

Figure 6.18: **Signatures of transport through excited states in the charge-stability diagram**
(a) Device schematic with the collapsed carbon nanotube and DC electrodes. The micromagnet is buried beneath the DC electrodes.
(b) Charge-stability diagram while sweeping gate-2 voltage. Two triangles, labeled I and II, exhibit positive-bias signatures of transport via excited states.
(c) Zoom on triangle I at positive bias. The resolved lines correspond to excited-state transport by hole carriers, as sketched in (e-g).
(d) Zoom on triangle II at positive bias, again revealing lines due to transport through excited states.

Furthermore, the amplitude of the conductance peaks remains essentially constant over the investigated magnetic-field range, except at points where two orbital levels become degenerate, resulting in enhanced conductance due to peak overlap. This behavior indicates that the magnetic field does not induce significant changes in the tunnel couplings to the leads [182], and therefore does not measurably reshape the electron wave function in a way that affects the transport signatures through the quantum dot. Consequently, no magnetic-field-induced variation of the experimentally extracted lever arm is expected.

Alternatively, spectroscopy of the quantum-dot states could be performed by fixing the dot electrochemical potential through a constant gate voltage V_2, while sweeping the drain electrochemical potential via the drain bias V_D. This approach would allow the spectroscopy to be carried out without the need to account for lever arms in the system, since the drain electrochemical potential is directly given by $\mu_D = -eV_D$.

6.3.2 Excited-state spectroscopy in triangle I

Figure 6.19 presents the magnetic-field dispersion of the excited states of the quantum dot identified by the Triangle I in Fig. 6.18.
In what follows, we analyze the first four resolvable energy levels visible in the measurement.

In a quantum dot, the confinement potential quantizes the energy levels into discrete orbitals, with successive orbital modes separated by the orbital level spacing Δ_{orb}.
Each orbital mode can be occupied by carriers with distinct internal quantum numbers. In a carbon-nanotube quantum dot, a mode is fourfold degenerate (spin $\uparrow$ / $\downarrow$ and valley K/K'). As discussed in Chapter 1, spin-orbit coupling, intervalley scattering, and an applied magnetic field can lift this fourfold degeneracy.
On top of the single-particle spectrum, transport of charge carriers also involves an additional energy cost when adding an electron in the quantum dot, given by the charging energy E_c.

To interpret the observed dispersions, we model the single-particle spectrum within a single orbital mode using the Hamiltonian introduced in Chapter 1 of this thesis. Assuming no electron-hole mixing - i.e., $E_G^0 \gg \mu_B g_{\text{orb}} B_\parallel, \Delta_{SO}^1$ (where Δ_{SO}^1 denotes the orbital-like contribution to the spin-orbit coupling defined in Chapter 1 and $B_\parallel$ is the amplitude of the magnetic field applied along the carbon nanotube) - the Hamiltonian reads [53]:

$$\text{H}_{\text{CNT}} = E_0 \hat{\gamma}_0 \hat{\sigma}_0 + \left(g_{\text{orb}} \hat{\gamma}_z \hat{\sigma}_0 + \frac{1}{2} g_s \hat{\gamma}_0 \hat{\sigma}_z \right) \mu_B B_\parallel + \frac{1}{2} g_s \mu_B B_\perp \hat{\gamma}_0 \hat{\sigma}_x + \frac{\Delta_{SO}}{2} \hat{\gamma}_z \hat{\sigma}_z + \frac{\Delta_{KK'}}{2} \hat{\gamma}_x \hat{\sigma}_0 \tag{6.44}$$

where the Hamiltonian is written considering hole-like carriers and the single-particle energy - in the absence of spin-orbit coupling, inter-valley scattering and magnetic field - is given by:

$$E_0 = -\sqrt{\left(E_G^0\right)^2/4 + E_{\text{conf}}^2} \tag{6.45}$$

Here, E_G^0 is the band gap of the nanotube, and $E_{\text{conf}} \approx n\Delta_{\text{orb}}$ is the longitudinal confinement energy associated with orbital mode index n.
The operators $\hat{\gamma}_i$ and $\hat{\sigma}_i$ ($i \in \{0, x, y, z\}$) are Pauli matrices acting in the valley and spin subspaces, respectively. We set the spin g-factor to $g_s = 2$, while g_{orb} denotes the orbital g-factor. The field components $B_\parallel$ and $B_\perp$ are defined along and transverse to the nanotube axis.

The spectrum is obtained by numerically diagonalizing Eq. (6.44) to find eigenenergies E_n and eigenvectors ϕ_n.

Given the position of the external magnet in the cryostat, we expect the applied field to be approximately aligned with the nanotube axis.
However, assuming perfect alignment - i.e. $B_\parallel = B_{\text{ext}}$ and $B_\perp = 0$ - does not reproduce the experimental dispersions.
We therefore allow for a slight misalignment between the field and the nanotube. Two factors can contribute:

- the tube's on-chip orientation, which varies from device to device,
- the sample holder's orientation in the cryostat with respect to the external field.

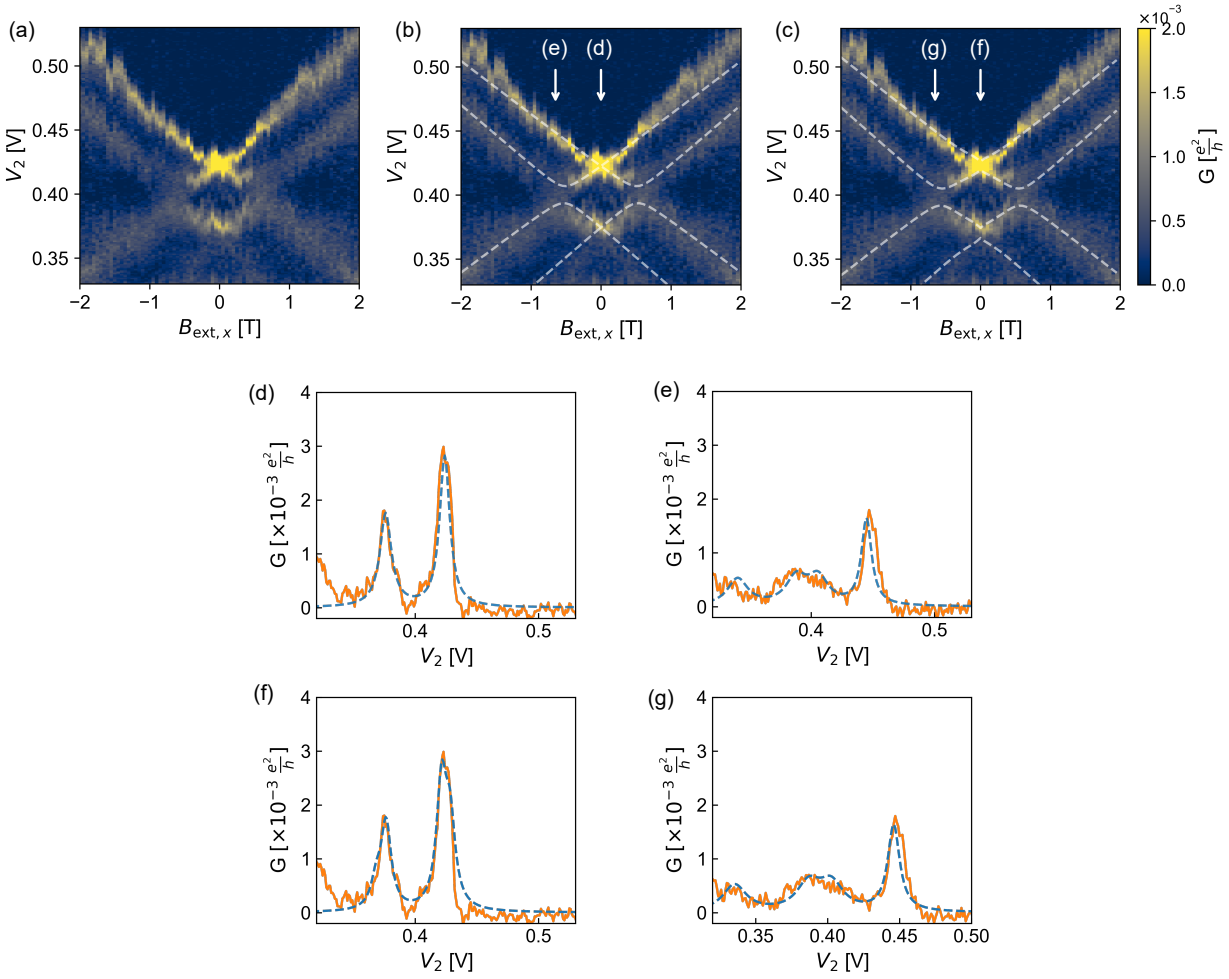

Figure 6.19: **Excited-state spectroscopy in Triangle I**
(a) Magnetic-field dispersion of the first four excited states identified in triangle I. Measurement conditions: a DC bias of 2 mV is applied to the drain (the gate 3 is grounded). The field is swept from −2 T to 2 T in 50 mT steps.
(b) Same data overlaid with the theoretical model, **micro-magnet field neglected**. Dashed lines are eigenenergies from diagonalizing the Hamiltonian in Eq. (6.44).
(c) As in (b), but **including the magnetic field generated by the micromagnet** (see Fig. 6.21).
(d-e) Line cuts at $B_{\text{ext},x} = 0$ mT and $B_{\text{ext},x} = -650$ mT from (c) (see the white arrows), comparing experiment and theory.
(f-g) Line cuts at $B_{\text{ext},x} = 0$ mT and $B_{\text{ext},x} = -650$ mT from (d) (see the white arrows), comparing experiment and theory.
In (d-g), conductance peaks associated with transport through excited states are modeled using Eq. (6.20): level energies come from diagonalizing Eq. (6.44), and the dot-lead tunneling rate is fixed to best match the data with $\Gamma \sim 150 - 300\mu$eV . The lever arm of gate 2, estimated from Fig. 6.15, is $\alpha_{pg,2} = 0.015$.

Accounting for this, we take the external magnetic field to be applied along the x-axis :

$$\vec{\mathbf{B}}_{\text{ext}} = \big(B_{\text{ext}},\quad 0,\quad 0\big)$$

and we define the unit vector along the carbon nanotube axis as:

$$\vec{\mathbf{u}}_{\text{CNT}} = \big(\cos(\theta)\cos(\varphi),\quad \sin(\theta)\cos(\varphi),\quad \sin(\varphi)\big)$$

The components of the magnetic field parallel and transverse to the caron nanotube are then:

$$\begin{aligned} B_{\parallel} &= \vec{\mathbf{B}}_{\text{ext}} \cdot \vec{\mathbf{u}}_{\text{CNT}} = B_{\text{ext}}\cos(\theta)\cos(\varphi) \\ B_{\perp} &= \sqrt{B_{\text{ext}}^2 - B_{\parallel}^2} = \sqrt{\big(B_{\text{ext}}\sin(\theta)\cos(\varphi)\big)^2 + \big(B_{\text{ext}}\sin(\varphi)\big)^2} \end{aligned} \tag{6.46}$$

here θ and φ parametrize the misalignment between the external magnetic field and the carbon nanotube.

Based on the collapsed-tube geometry (Fig. 6.20), we estimate $\varphi \sim 7°$, which can be neglected such that we set $\varphi = 0°$.
The remaining angle θ is adjusted to best fit the data; for our measurements, $\theta = 35°$ seems to satisfactorily reproduce the observed excited-state dispersions (see Fig. 6.19). The parameters g_{orb}, $\Delta_{KK'}$, and Δ_{SO} are then chosen to achieve quantitative agreement with the experiment. The values of these parameters are given in the Table 6.1.

Including the magnetic field generated by the micromagnet

Up to this point, we fit the experimental dispersions using the simulated dot spectrum while neglecting the stray field from the on-chip micromagnet.

We now include the micromagnet field obtained from micromagnetic simulations (using the software Mumax3), using the magnetic parameters for a CoFe magnet at 4 K determined in Chapter 4 (see Sec. 4.1.4 and Table 4.6).
The micromagnet geometry is the periodic arrangement of two opposing bars described earlier in this manuscript (see Fig. 6.20). The simulations account for this periodicity by employing periodic boundary conditions, as described in the Chapter 4.
The micro-magnetic configurations in the magnet are computed varying the amplitude of the external magnetic field. In these simulations, we neglect any misalignment between the externally applied field B_{ext} and the micromagnet's longitudinal axis (the x-axis in Fig. 6.20).

In our device stack (schematic in Fig. 6.20), the carbon nanotube lies approximately 100 nm above the magnet surface. The nanotube's position relative to the magnet is determined from post-measurement SEM images (Fig. 6.20).

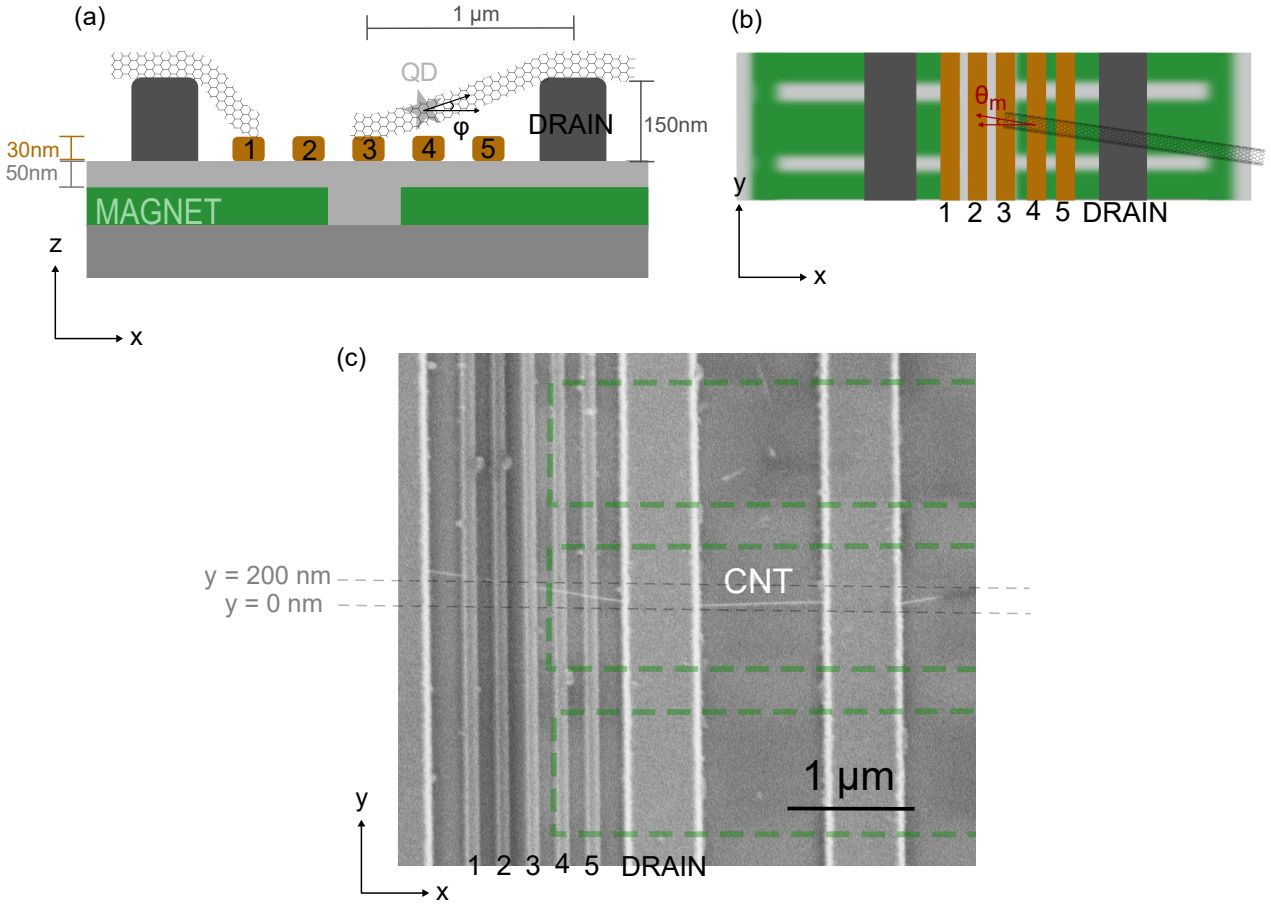

Figure 6.20: **Carbon nanotube placement with respect to the magnet**
(a-b) Schematics (side and top views) of the nanotube's position relative to the magnet. The misalignment of the carbon nanotube with the micro-magnet is parametrized by the angle θ_m.
(c) SEM image acquired after measurements, displaying the nanotube and gates. The dashed green rectangle highlights the magnet position identified from SEM-contrast analysis.

From the micromagnetic configuration and the device geometry (nanotube position and height), we compute the micromagnet's stray field along the nanotube: the resulting profile is shown in Fig. 6.21.
The total magnetic field experienced by the dot can then be expressed as :

$$\begin{aligned} B_{\parallel} &= B_{\text{ext}}\cos(\theta) + \alpha_{\text{magnet},x}\cos(\theta_m) \\ B_{\perp} &= \sqrt{\left(B_{\text{ext}}\sin(\theta) + \alpha_{\text{magnet},x}\sin(\theta_m)\right)^2 + \alpha^2_{\text{magnet},z}} \end{aligned} \tag{6.47}$$

where θ is the misalignment of the external field with respect to the nanotube axis, and θ_m is the misalignment between the nanotube and the micromagnet's longitudinal axis, estimated from SEM to be $\sim 15°$ (see Fig. 6.20). The coefficients:

$$\alpha_{\text{magnet},i} = \int \mathrm{d}x\, B_{\text{magnet},i}(x)\, \left|\psi(x)\right|^2 \tag{6.48}$$

are spatial averages of the simulated micromagnet field components $B_{\text{magnet},i}(x)$ weighted by the probability density $|\psi(x)|^2$ of the confined carrier, taken as a Gaussian with FWHM 150 nm.The FWHM is set to 150 nm to account for the dot's spatial extent. Since $\alpha_{\text{magnet},y} \ll \alpha_{\text{magnet},z}$, we decide to neglect the y-component. The value of the parameters $\alpha_{\text{magnet},i}$ as a function of the external magnetic field are given Fig. 6.21.

Using the total field of Eq. (6.47), we simulate the dot spectrum (Fig. 6.19). The carbon-nanotube parameters are unchanged (see Table 6.1), so no additional fitting parameters are introduced. The agreement with the experimental data is qualitatively good (Fig. 6.19(d-g)). Including the field generated by the micro-magnet seems to improve the match relative to a model without it, but the improvement is not yet decisive due to limited energy resolution. Accordingly, we also analyze a second Coulomb triangle.

Table 6.1: Values of the orbital g-factor g_{orb}, the inter-valley scattering $\Delta_{KK'}$, and the spin-orbit coupling Δ_{SO} used for the theoretical models. For Dot 2 of Coulomb Triangle II, the spin-orbit coupling and inter-valley scattering are sufficiently small to be unresolved in our measurements.

	Coulomb Triangle I	**Coulomb Triangle II**	
		Dot 1	Dot 2
g_s	2	2	2
g_{orb}	14.5	9.5	8.5
Δ_{SO} [µeV]	760	600	$\Delta^0_{SO} \sim 0$ $\Delta^1_{SO} \sim 0$
$\Delta_{KK'}$ [µeV]	200	80	~ 0

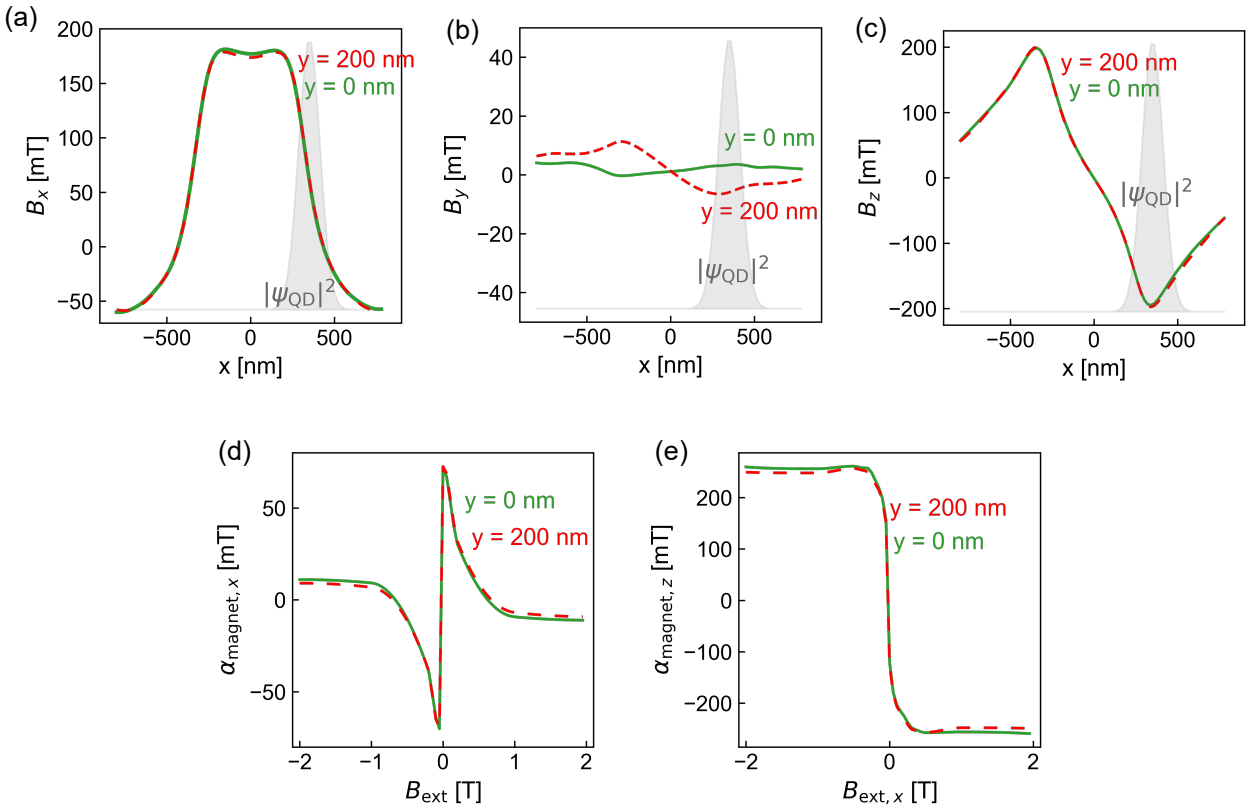

Figure 6.21: **Magnetic field generated by the micromagnet along the carbon nanotube**
(a-c) Spatial profiles of B_x, B_y, B_z from micromagnetic simulations for different CNT positions (see Fig. 6.20). The nanotube is assumed to lie 100 nm above the micromagnet, with an external field $B_{ext,x} = 50\,\text{mT}$. The magnetic field profiles are computed from the micro-magnetic simulation obtained with Mumax3 simulations. The quantum-dot location is indicated by the electron probability density $|\psi_{DQ}|^2$, modeled as a Gaussian with FWHM 150 nm.
(d-e) Dot-averaged fields, computed by spatial averaging as in Eq. (6.48), plotted versus the amplitude of the external magnetic field $B_{ext,x}$ for the different CNT positions.
We see that differences between possible CNT positions are negligible.

6.3.3 Excited-state spectroscopy in triangle II

Figure 6.22 shows the magnetic-field dispersion of the excited states extracted from Coulomb Triangle II identified in Fig. 6.18.

Compared with Triangle I, several additional energy levels are resolved. To interpret this richer spectrum, we first examine the charge-stability diagram in Fig. 6.15. As noted earlier, at least two quantum dots with different properties can be identified in the charge stability diagram. Independent pre-assembly characterization by the C12 Quantum Electronics team indicates that the device hosts a multiwall carbon nanotube. We therefore can attribute these two dots to distinct shells of the nanotube.

To account for the data in Fig. 6.22, we thus model two quantum dots with potentially different parameters, and compare the resulting spectra with the measurement.

Energy spectrum of the first dot

We first consider the dot whose parameters are expected to be closest to those extracted from Coulomb Triangle I. Several energy levels in the spectrum of Fig. 6.22 can indeed be identified with levels of a dot sharing similar characteristics to the one analyzed previously.

As in the previous section, we initially compute the spectrum without the micromagnet stray field, using the Hamiltonian of Eq. (6.44). The orientation of the external field relative to the nanotube is kept identical to before, so that the field components follow Eq. (6.46) with $\theta = 30°$ and $\phi = 0°$. The value of the orbital g-factor, inter-valley scattering and spin-orbit coupling used are given Table 6.1.

The resulting spectrum is shown in Fig. 6.22. We denote the eigenenergies by E_n^{QD1} and the corresponding eigenvectors by $\phi_{\mathrm{QD}_1,n}$. Notably, inspection of the charge-stability diagram in Fig. 6.15 indicates that the system moves from Triangle I to Triangle II by adding four charges (one shell), which is consistent with the multiplicity and ordering of the levels discussed here (see Fig. 6.22(d)).

Energy spectrum of the second dot

Three of the levels resolved in the spectroscopy are attributed to a second dot. Based on their magnetic-field dispersions, we model this dot using a Hamiltonian appropriate for a nearly metallic nanotube, which is written as [53]:

$$\mathrm{H_{CNT}} = E_0^{\mathrm{m}}\hat{\gamma}_0\hat{\sigma}_0 + \frac{1}{2}g_s\mu_B B_\parallel \hat{\gamma}_0\hat{\sigma}_z + \frac{1}{2}g_s\mu_B B_\perp \hat{\gamma}_0\hat{\sigma}_x + \Delta_{SO}^0\hat{\gamma}_z\hat{\sigma}_z + \frac{\Delta_{KK'}}{2}\hat{\gamma}_z\hat{\sigma}_0 \tag{6.49}$$

with:

$$E_0^{\mathrm{m}} = -\sqrt{\left(\frac{E_G^0}{2} + \gamma\sigma\Delta_{SO}^1 + \gamma\mu_B g_{\mathrm{orb}} B_\parallel\right)^2 + E_{\mathrm{conf}}^2} \tag{6.50}$$

Here $\gamma = \pm 1$ labels the valley degree of freedom, and $\sigma = \pm 1$ the spin projection along z. Δ_{SO}^0 denotes the Zeeman-like spin-orbit coupling, whileΔ_{SO}^1 denotes the orbital-like spin-orbit coupling introduced in Chapter 1.

The magnetic-field dispersions of the second dot's energy levels, obtained by diagonalizing Hamiltonian Eq. (6.49) is shown in Fig. 6.22(d).
We denote E_n^{QD2} the eigenenergies computed and $\phi_{QD_2,n}$ the associated eigenvector.
To align the simulated spectrum with the measurements, we extract the lever arm of the plunger gate 2 from the charge-stability diagram, considering the second dot (the blue lines in the charge stability diagram of Figure 6.15). The resulting estimate is $\alpha_{pg,2} = 0.002$.

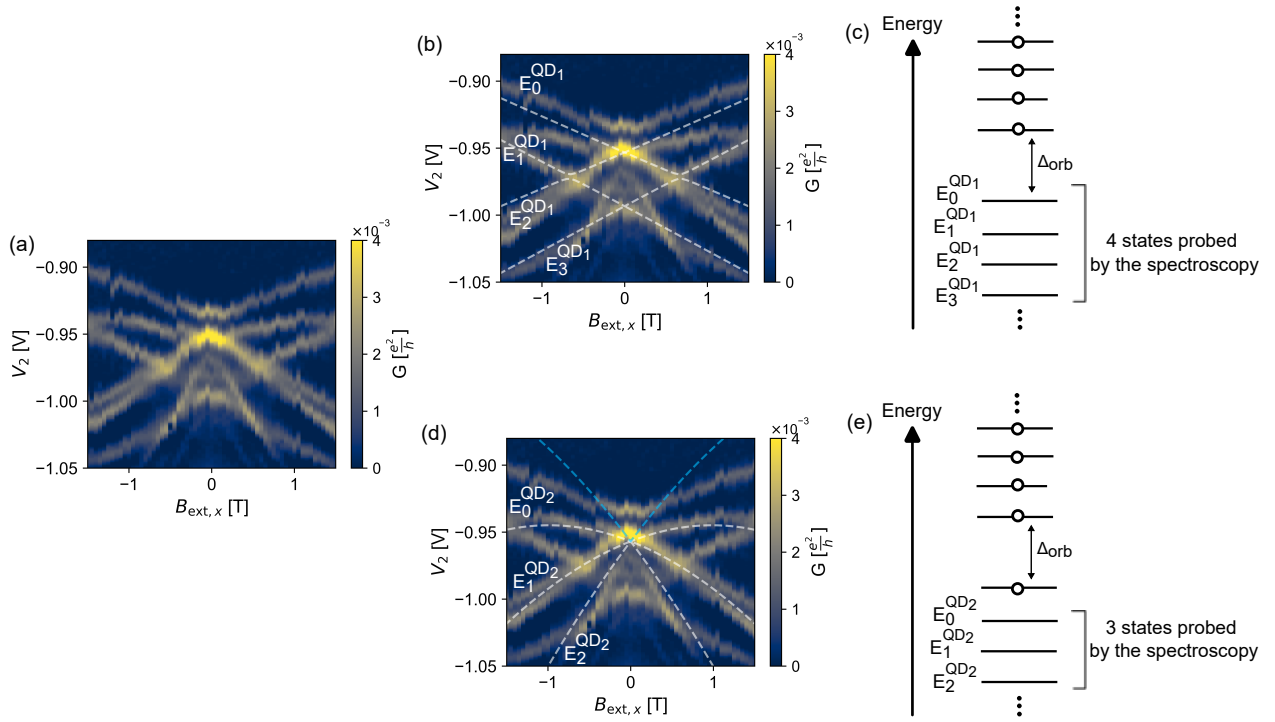

Figure 6.22: **Excited-state spectroscopy in Triangle II**
(a) Magnetic-field dispersion of the excited states identified in triangle II. Measurement conditions: a DC bias 3 mV is applied to the drain (gate 3 grounded). The field is swept from −2 T to 2 T in 50 mT steps.
(b) Same data as in (a) overlaid with the theoretical model for the first dot, **micromagnet field neglected**. Dashed lines are eigenenergies from diagonalizing Eq. (6.44). The lever arm of gate 2, estimated from Fig. 6.15 used for the overlaid , is $\alpha_{pg,2} = 0.015$.
(c) Schematic energy level with hole charge carriers for the first dot: the four levels of one orbital shell appear to be probed.
(d) Same data as in (a), overlaid with the theoretical model for the second dot, **micromagnet field neglected**. Dashed lines are eigenenergies from Eq. (6.49). The lever arm of gate 2, estimated from Fig. 6.15 used for the overlaid is $\alpha_{pg,2} = 0.002$.
(e) Schematic energy level with hole charge carriers for the second dot: three of the four levels of an orbital shell appear to be probed. In transport, the occupied-state level (dashed blue in panel (d)) is separated from the other three by the charging energy E_c.

The orbital g-factor, intervalley scattering, and spin-orbit coupling used to best reproduce our simulations are listed in Table 6.1. Unlike the case of a carbon nanotube with a sufficiently large band gap to avoid electron-hole mixing - described by Eq. (6.44) - where the CNT energy band-gap E_G^0 and the confinement energy E_{conf} do not affect the magnetic-field dispersion of the dot levels, in a nearly metallic tube both E_G^0 and E_{conf} do modify the dispersion [58]. We therefore adjust these parameters to match the experiment, finding $E_G^0 = 0.9\,\text{meV}$ and $E_{\text{conf}} = 3.5\,\text{meV}$.
For comparison, prior work on nearly metallic tubes reported energy band-gap of $E_G^0 = 2\,\text{meV}$ and confinement energy of $E_{\text{conf}} = 1\,\text{meV}$ [58].

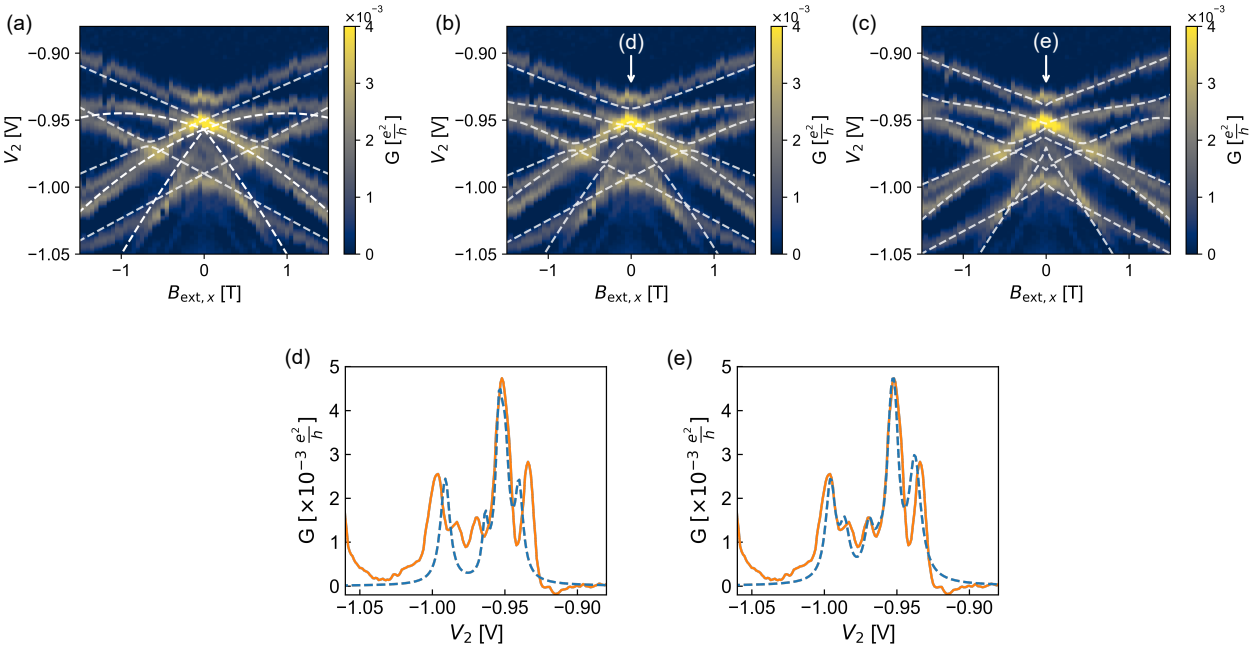

Figure 6.23: **A theoretical model to understand the excited state spectroscopy of the Triangle II**
(a) Same experimental data as in Fig. 6.22 (a) overlaid with the theoretical model for the first dot and second, without taking into account coupling between the states of the two quantum dots nor the magnetic field generated by the magnet.
(b) Same as in (a) taking into account coupling between some states of the two dots given by Eq. (6.51), but not the magnetic field generated by the micro-magnet.
(c) Same than in (a) taking into account coupling between some states of the dots given by Eq. (6.51) and the magnetic field generated by the micro-magnet.
(d) Line cuts from (b) at $B_{\text{ext},x} = 0\,\text{mT}$ comparing experiment and theory.
(e) Line cuts from (c) at $B_{\text{ext},x} = 0\,\text{mT}$ comparing experiment and theory.
In (d-e), conductance peaks associated with transport through excited states are modeled using Eq. (6.20): level energies come from diagonalizing Eq. (6.44) and Eq. (6.49), and the dot-lead tunneling rate is fixed to best match the data.

Overall, the measured spectrum is consistent with the superposition of levels generated by Eq. (6.44) and Eq. (6.49), as presented Fig.6.23. To capture anti-crossings between the energy levels of the two dot, we introduce some coupling between the different states of the two dots [51][52]:

$$H_{\text{coupl}} = \sum_{n,m} \hbar g_{nm} \left[\phi_{QD_1,n} \phi^{\dagger}_{QD_2,m} + \phi^{\dagger}_{QD_1,n} \phi_{QD_2,m} \right] \tag{6.51}$$

with coupling amplitudes g_{nm} adjusted to best reproduce the experimental dispersions.

We find $g_{0,m} = 100\,\mu\text{eV}$ - corresponding to a coupling between $\phi_{QD_1,0}$ and the three states of the quantum dot 2, $\phi_{QD_2,m}$ with $m \in \{0,1,2\}$ - and $g_{1,0} = 100\,\mu\text{eV}$ - corresponding to a coupling between $\phi_{QD_1,1}$ and $\phi_{QD_2,0}$. All other coupling constants are set to zero, as they seem sufficiently small to be neglected.
The eigenenergies computed with this coupling are overlaid in Fig. 6.22.

Including the magnetic field generated by the micromagnet

As in the previous section, we now include the contribution of the on-chip micromagnet. The stray field is taken from the micromagnetic simulations, with the only change that the dot positions are allowed to shift slightly relative to the Triangle I case (see Fig. 6.24). This is plausible because increasing the plunger-gate 2 voltage modifies the longitudinal confinement potential, which can reposition the dot along the nanotube.

The effective micromagnet field experienced by the dot, $\alpha_{\text{magnet},i}$ with $i \in \{x, y, z\}$, is plotted in Fig. 6.24. The total field used to compute the spectrum is given by Eq. (6.47).

The spectrum obtained taking into account the magnetic field generated by the micromagnet included is shown in Fig. 6.23. Note that, as before, the parameters used to reproduce the magnetic-field dispersion of the energy levels are identical whether or not the micromagnet's field is included.
Quantitatively, the micromagnet's effect is most evident at zero externally applied field ($B_{\text{ext}} = 0$), where it can lift the fourfold degeneracy of each orbital mode and produces level splittings that cannot be explained by intrinsic spin-orbit coupling and inter-valley scattering alone.
A direct comparison between experiment and the theoretical model at $B_{\text{ext}} = 0$ is provided in Fig. 6.23(d-e). Incorporating the micromagnet stray field yields markedly better agreement with the measured zero-field splittings.

This supports the conclusion that the integrated micromagnet can indeed tailor the magnetic-field profile along the nanotube and thereby shapes the spin/valley spectrum of the quantum dot. Thanks to the micromagnetic characterization performed in this thesis, we have a detailed understanding of the field generated by the magnet, which lays the foundation for advanced spin-qubit experiments.

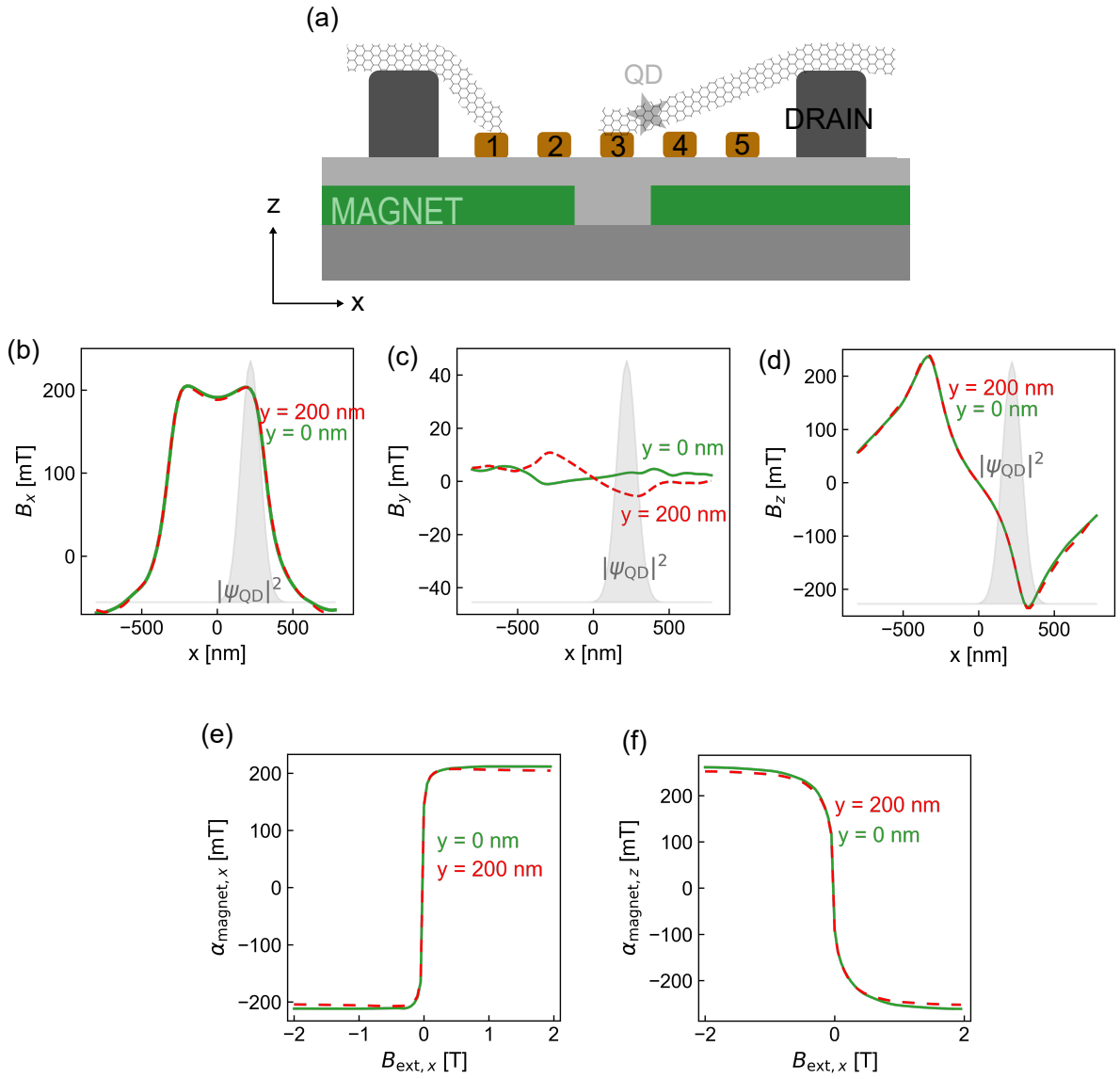

Figure 6.24: **Magnetic field generated by the micromagnet for the quantum-dot configuration corresponding to Triangle II**
(a) Schematic showing the quantum-dot position. Relative to Fig. 6.21, the dot is believed to have shifted slightly.
(b-c) Spatial profiles of B_x, B_y, B_z computed from micromagnetic simulations for different carbon-nanotube positions. The nanotube is assumed to lie 80 nm above the micromagnet, with an external field $B_{\mathrm{ext},x} = 50\,\mathrm{mT}$. The dot location is indicated by the electron probability density $|\psi_{\mathrm{DQ}}|^2$, modeled as a Gaussian with FWHM 150 nm.
(d-e) Dot-averaged magnetic fields, computed by spatial averaging as in Eq. (6.48), plotted versus the external magnetic field $B_{\mathrm{ext},x}$ for the different carbon nanotube positions.
Differences between plausible CNT positions are, once again, negligible.

Conclusion and perspectives

This thesis develops, characterizes, and implements an on-chip micromagnet to enhance the coupling of a carbon-nanotube spin qubit with the photons of a microwave resonator, enabling a spin-qubit architecture based on carbon-nanotube quantum dots within a circuit-QED framework. The circuit-QED platform is built from a high-kinetic-inductance superconductor, which further strengthens the coupling between the carbon-nanotube spin qubit and the microwave photons.

Chapter 1 shows that the magnetic-field profile along the nanotube directly sets the qubit spectrum and its coupling to resonator photons. Balancing the advantages of strong spin-charge hybridization against decoherence indicates a favorable operating regime near:

$$\mu_B g_s \alpha_s \sim \mu_B g_s \alpha_{as} \sim t_c$$

with α_s and α_{as} are the symmetric and antisymmetric field components across the double quantum dot, respectively, and t_c is the interdot tunneling energy. This estimate neglects nanotube spin-orbit coupling; when spin-orbit effects are appreciable, larger antisymmetric-field amplitudes and smaller symmetric-field amplitudes are required.

Chapter 2 introduces a first, easily integrable micromagnet geometry. Magnetic characterization shows that this design does not reach the target regime: $\alpha_{as}/\alpha_s \leq 0.1$, and for $t_c \sim \mu_B g_s \alpha_s$ the expected spin-photon coupling is $g < 0.06 \frac{\Delta_g}{2}$. Although the term $\frac{\Delta_g}{2}$ - set by the cavity voltage fluctuations and the photonic pseudo-potential profile across the double dot - can be boosted (e.g., by engineering an antisymmetric pseudo-potential and using a high-impedance resonator), these results motivate a new magnet design to reach the ideal regime and increase g.

Chapter 3 therefore focuses on magnet geometry. Numerical simulations explore several layouts and magnetic configurations to maximize on-chip gradients. Despite the simple underlying ideas, the methodology offers a practical recipe for designing field gradients with patterned magnets. A specific geometry and internal magnetization configuration are selected, accounting for chip-level constraints and external-field requirements. Initial micromagnetic simulations use material parameters from the literature.

Chapter 4 refines these simulations to faithfully capture the magnetic properties of thin-film materials available for fabrication. We present magnetic characterization of candidate films and direct measurements -through NV center microscopy - of the magnetic fields produced by the optimized magnet geometry for different material stacks. These measurements agree with micromagnetic predictions based on the thin-film characterizations, validating the simulations as reliable predictors of the field profile along the nanotube. In particular, a cobalt-iron micromagnet can realize $\alpha_{as}/\alpha_s \geq 0.5$ with $\alpha_{as}/\alpha_s \approx 0.75$ for a qubit frequency of 4 GHz . For $t_c \sim \mu_B g_s \alpha_s$, this implies $g \sim 0.3-0.5 \frac{\Delta_g}{2}$ about an order of magnitude larger than with the initial design. The magnet geometry - and the accompanying magnetic characterizations - developed for a carbon-nanotube spin-qubit architecture are readily transferable and useful for Si-based spin-qubit platforms.

The full device - comprising a carbon-nanotube quantum-dot circuit, a micromagnet, and a high-kinetic-inductance circuit-QED platform - is integrated into a modular chip.

Chapter 5 presents the design of the circuit-QED architecture, building on existing implementations. Electromagnetic and circuit-level simulations are used to clarify how each circuit element operates and to inform the choice of their dimensions.
A nanofabrication process that buries the magnet in the substrate beneath the DC electrodes yields complete devices in which the magnet does not measurably perturb electrostatic control along the nanotube, as confirmed by transport through single- and double-dot circuits. From a single-dot device we extract an electron-photon coupling $g_{\mathrm{QD}} \sim 2\pi \times 260\,\mathrm{MHz}$ indicating a reachable spin-photon coupling of $g \sim 0.3-0.45\,\frac{g_{\mathrm{QD}}}{2} \sim 2\pi \times 40-50\mathrm{MHz}$. This value is of the same order as the spin-photon coupling reported for two qubits undergoing cavity-mediated iSWAP oscillations between distant spins ($g \sim 2\pi \times 21-32\mathrm{MHz}$ reported in [5]) and about an order of magnitude larger than the coupling reported for carbon-nanotube quantum states coupled to cavity photons [7].
Excited-state spectroscopy in a quantum-dot circuit, presented in Chapter 6, show promising results that seems to indicate that the micromagnet can indeed tailor the magnetic-field profile along the carbon nanotube.

Looking forward, several improvements are within reach.

Assembly of nanotubes onto high-impedance resonators proved to be challenging in this PhD work. Reducing the resistance of the contact electrode line - approaches already implemented at C12 Quantum Electronics - ease nano-assembly process.

For scalable circuit-QED, lowering the cavity decay rate is essential. This could come from cleaner nanofabrication recipes and better on-chip filtering. In particular, compact filters, as the ones proposed in [134], with well-defined ground planes can reduce loss through DC lines. Flip-chip architectures may also help enforce ground connectivity or physically separate DC and microwave circuitry to limit cross-coupling.

On the magnet side, stronger fields can still be achieved by bringing the magnet closer to the nanotube. Optimizing the burying process and the oxide between the magnet and DC electrodes - e.g., using ALD-grown Al_2O_3 to allow thinner dielectrics without shorts - would help. Knowing the detailed field profile along the nanotube opens the path to purely electrical tuning of individual qubit frequencies - crucial for multi-qubit operation on a shared resonator - by adjusting dot position and length to modulate α_s and α_{as}.

Finally, tighter control and understanding of the carbon nanotube properties remain important. To this end, characterization workflows - Raman spectroscopy, Rayleigh measurements in an optical setup, and electrical tests performed directly on the cantilever chips used for nanotube growth-are being developed at C12. Together, these characterizations could identify and preselect nanotubes with optimal properties for integration into spin-qubit devices. Encapsulation is another promising route: recent hBN-encapsulated nanotubes [68] exhibit clean four-fold degeneracy in shell filling, consistent with suppressed spin-orbit coupling and intervalley scattering, suggesting a path to more reproducible qubits.

As these improvements come together, coherent control of a spin qubit and cavity-mediated coupling between distant spin qubits in carbon nanotubes move from prospect to practice.

Appendix A : Micro-magnetic simulations

Mumax3 code presentation

In this Appendix, we present a representative Mumax3 script used for the simulations reported in this PhD. The other micromagnetic scripts follow the same structure, with only the geometry definition and magnetic parameters adapted as needed.

The example models a micromagnet formed by two rectangular elements facing each other, but can be adapted to simulate a comb geometry. Material parameters correspond to a Co-Fe alloy, using the values determined at 4 K. The polycrystalline grain structure is generated with `ext_make_3dgrains`. For each grain, the magnetocrystalline anisotropy orientation is randomized as described in Chapter 4.

The magnetization is initialized randomly. The system is then relaxed to equilibrium under an external magnetic field B_{ext} applied along the long axis of the micromagnet, and the resulting configuration is saved.

The code is given here :

```
// ============================================================================
// Geometry presets

// All distances are in meters; magnetization in A/m; exchange in J/m.
// The mesh and PBC settings below define two alternative device layouts.
// Choose one block (simple magnet or comb) and comment out the other.
// ============================================================================

// Simple magnet geometry: two rectangular bars facing each other


SetGridsize(3750, 224, 38)
SetCellsize(4e-9, 4e-9, 4e-9)
OutputFormat = OVF1_TEXT
OutputFormat = OVF2_TEXT
SetPBC(1, 0, 0)


// Comb geometry: multiple rectangles facing each other

// SetGridsize(3750, 299, 38)
// SetCellsize(4e-9, 4e-9, 4e-9)
// OutputFormat = OVF1_TEXT
// OutputFormat = OVF2_TEXT
// SetPBC(1,1,0)

// ============================================================================
// Material parameters
```

```
// ========================================================================


Msat = 2000e3
Aex = 20e-12

// ========================================================================
// Geometric decomposition for grain generation
// ------------------------------------------------------------------------
// The device is decomposed into longitudinal slices.
// This lets ext_make3dgrains operate on smaller volumes to accelerate the
// Voronoi-like grain tessellation, while preserving the overall device shape.
// The full geometry is the union of all these cuboids.
// Dimensions: (Lx, Ly, Lz) and then translated to the desired position.
// ========================================================================

// Left half (negative x)
q := cuboid(500e-9, 900e-9, 188e-9).transl(-7250e-9, 0e-9, 0e-9)
a := cuboid(1000e-9, 900e-9, 188e-9).transl(-6500e-9, 0e-9, 0e-9)
b := cuboid(1000e-9, 900e-9, 188e-9).transl(-5500e-9, 0e-9, 0e-9)
c := cuboid(1000e-9, 900e-9, 188e-9).transl(-4500e-9, 0e-9, 0e-9)
d := cuboid(1000e-9, 900e-9, 188e-9).transl(-3500e-9, 0e-9, 0e-9)
e := cuboid(1000e-9, 900e-9, 188e-9).transl(-2500e-9, 0e-9, 0e-9)
f := cuboid(1000e-9, 900e-9, 188e-9).transl(-1500e-9, 0e-9, 0e-9)
g := cuboid(750e-9, 900e-9, 188e-9).transl(-625e-9, 0e-9, 0e-9)

// Right half (positive x)
w := cuboid(500e-9, 900e-9, 188e-9).transl(7250e-9, 0e-9, 0e-9)
h := cuboid(1000e-9, 900e-9, 188e-9).transl(6500e-9, 0e-9, 0e-9)
i := cuboid(1000e-9, 900e-9, 188e-9).transl(5500e-9, 0e-9, 0e-9)
o := cuboid(1000e-9, 900e-9, 188e-9).transl(4500e-9, 0e-9, 0e-9)
k := cuboid(1000e-9, 900e-9, 188e-9).transl(3500e-9, 0e-9, 0e-9)
l := cuboid(1000e-9, 900e-9, 188e-9).transl(2500e-9, 0e-9, 0e-9)
p := cuboid(1000e-9, 900e-9, 188e-9).transl(1500e-9, 0e-9, 0e-9)
n := cuboid(750e-9, 900e-9, 188e-9).transl(625e-9, 0e-9, 0e-9)

// Union of all slices defines the full magnet
setgeom(b.add(c).add(d).add(e).add(f).add(g).add(i).add(o).add(k).add(l).add(p).add(
n).add(a).add(h).add(q).add(w))

saveas(geom, "geom")


// ========================================================================
// Polycrystalline grain generation
// ------------------------------------------------------------------------
// ext_make3dgrains(grainSize, orientationMode, maxRegion, mask, seed)
// - grainSize: target mean grain diameter [m]
// - orientationMode: 0 = random in-plane axis with fixed out-of-plane bias,
//                    (behavior refined below via explicit anisotropy)
// - maxRegion: maximum number of regions available in this simulation
// - mask: geometric volume to tessellate
// - seed: random number seed (repeatable microstructure if the same seed is reused)
```

```
// ========================================================================


grainSize := 15e-9 //Mean grain size
randomSeed := 1234
maxRegion := 256

ext_make3dgrains(grainSize, 0, maxRegion, a, randomSeed)
ext_make3dgrains(grainSize, 0, maxRegion, b, randomSeed)
ext_make3dgrains(grainSize, 0, maxRegion, c, randomSeed)
ext_make3dgrains(grainSize, 0, maxRegion, d, randomSeed)
ext_make3dgrains(grainSize, 0, maxRegion, e, randomSeed)
ext_make3dgrains(grainSize, 0, maxRegion, f, randomSeed)
ext_make3dgrains(grainSize, 0, maxRegion, g, randomSeed)
ext_make3dgrains(grainSize, 0, maxRegion, h, randomSeed)
ext_make3dgrains(grainSize, 0, maxRegion, i, randomSeed)
ext_make3dgrains(grainSize, 0, maxRegion, o, randomSeed)
ext_make3dgrains(grainSize, 0, maxRegion, k, randomSeed)
ext_make3dgrains(grainSize, 0, maxRegion, l, randomSeed)
ext_make3dgrains(grainSize, 0, maxRegion, p, randomSeed)
ext_make3dgrains(grainSize, 0, maxRegion, n, randomSeed)
ext_make3dgrains(grainSize, 0, maxRegion, q, randomSeed)
ext_make3dgrains(grainSize, 0, maxRegion, w, randomSeed)

// Define the magnetic parameters per grain :

for i := 0; i < maxRegion; i++ {
        K1 :=550e3
        theta := pi*rand()
        axis1 := vector(cos(theta)*(1+0.5*RandNorm()),sin(theta)*(1+0.5*RandNorm()),
        1)
        helper := vector(0, 0, 1)
        axis2 := axis1.cross(helper)
        AnisC1.SetRegion(i,axis1)
        AnisC2.SetRegion(i,axis2)
        Kc1.SetRegion(i, K1)

}


// Inter-grain exchange reduction by a factor 10
for i:=0; i<maxRegion; i++{          for j:=i+1; j<maxRegion; j++{
                ext_ScaleExchange(i, j, 0.1)
        }
}

save(AnisC1)
save(AnisC2)

// ========================================================================
// Initialization, field, and relaxation
// ========================================================================
```

```
m = RandomMag()

B_ext = vector(Bext, 0, 0)        // External field along x
relax()
saveas(m, "m_Bext")

// The magnetization configuration for an external magnetic field B_ext is saved.
```

Computing the magnetic field from the micro-magnetic configuration

The dipolar field can be computed from the micromagnetic configuration obtained from Mumax3 simulations. For each discretization cell (i), the dipolar field is evaluated from its magnetic dipole moment :

$$\vec{\mathbf{m}}_i = M_s dr^3 \vec{\boldsymbol{\mu}}_i$$

here M_s is the saturation magnetization, dr^3 is the cell volume and $\vec{\boldsymbol{\mu}}_i$ is the normalized magnetization vector.

The dipolar magnetic field at an observation point $\vec{\mathbf{r}}$ generated by a magnetic moment $\vec{\mathbf{m}}_i$ located at $\vec{\mathbf{r}}_\mathbf{i}$ is:

$$\vec{\mathbf{B}}_i(\vec{\mathbf{r}}) = \frac{\mu_0}{4\pi}\frac{3\vec{\mathbf{e}}_i\left(\vec{\mathbf{e}}_i\cdot\vec{\mathbf{m}}_i\right)-\vec{\mathbf{m}}_i}{R_i^3}, \qquad \text{with} \qquad \vec{\mathbf{R}}_i = \vec{\mathbf{r}}-\vec{\mathbf{r}}_i,\ \ R_i = \|\vec{\mathbf{R}}_i\|,\ \ \vec{\mathbf{e}}_i = \frac{\vec{\mathbf{R}}_i}{R_i}$$

The total field generated by the magnet at $\vec{\mathbf{r}}$ is then obtained by summing the dipolar contributions of all cells. Repeating the evaluation for a set of observation points yields the magnetic field throughout the region of interest.

Discussion on the grain structure of the materials

From the X-ray diffraction measurements presented in Chapter 4, the characteristic length of the crystallites (i.e. the size of the coherently diffracting domains) was determined.

In order to represent the grain structure of the Cobalt and Cobalt-Iron thin films in the micromagnetic simulations, we generate grains as regions using the built-in three-dimensional Voronoi tessellation. Material parameters are then allowed to vary from one region to another, in particular the anisotropy direction and the exchange coupling at the grain boundaries.

As described in Chapter 4, the grain orientation distributions imposed in the micro-magnetic model are chosen to reproduce the orientation distributions obtained from the XRD measurements: the mean orientation is aligned with the measured texture.
There is, however, no unique or strictly “correct” one-to-one correspondence between the crystallite size estimated from XRD and the grain size defined in the micro-magnetic simulations. In this work, we therefore chose the Mumax^3 grain size to be approximately of the same order as the relevant physical microstructural length scale.

In the following, we present micro-magnetic simulations for the Cobalt films in which the mean grain size imposed by the Voronoi tessellation is varied.
The micromagnetic simulations are performed for three mean grain sizes: 7 nm, 10 nm and 15 nm. The resulting configurations are shown in Figure 6.25. From the comparison of these micromagnetic configurations, we observe that for a grain size of 7 nm, a stripe-like domain pattern is obtained, in agreement with the MFM measurements. As the grain size is increased, this stripe-like configuration progressively disappears.

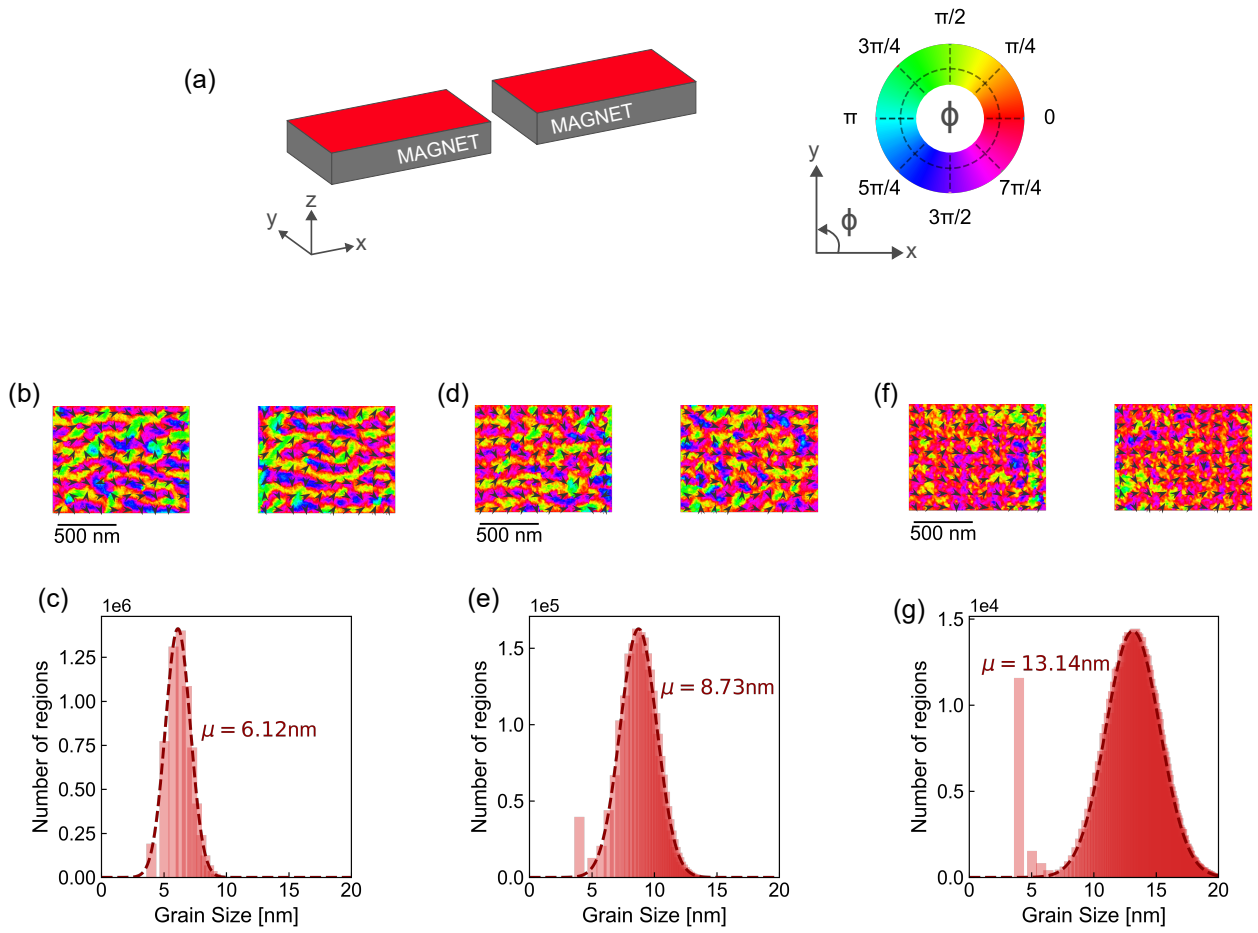

Figure 6.25: **Magnetization distributions in a Cobalt magnet for three mean grain sizes.**
(a) Schematic of the magnet and color scale used in the plots shown in this figure.
(b) In-plane (x-y plane) magnetization at the surface of the magnet, computed with zero applied field. The color scale represents the in-plane angle ϕ of the magnetization. Only the region close to the magnet edge is shown; the full simulation domain is 7 µm long with periodic boundary conditions to emulate a long magnet.
(c) Histogram of grain size versus number of regions obtained using the built-in three-dimensional Voronoi tessellation with a mean grain size of 7 nm. The resulting distribution is fitted with a Gaussian function with mean value $\mu = 6.12\,\text{nm}$ and standard deviation $\sigma = 1.00\,\text{nm}$.
(d-e) Same as (b-c), but using a Voronoi tessellation with a mean grain size of 10 nm. The grain-size distribution is fitted with a Gaussian function with mean value $\mu = 8.73\,\text{nm}$ and standard deviation $\sigma = 1.46\,\text{nm}$.
(f-g) Same as (b-c), but using a Voronoi tessellation with a mean grain size of 15 nm. The grain-size distribution is fitted with a Gaussian function with mean value $\mu = 13.14\,\text{nm}$ and standard deviation $\sigma = 2.16\,\text{nm}$.

To obtain a quantitative comparison with the measurements presented in Chapter 4 of this thesis, the stray magnetic field generated by the simulated magnetization is computed at a height above the surface corresponding to the NV center-surface distance used in the microscopy experiments. The resulting magnetic field distributions are shown in Figure 6.25.

The NV resonance frequencies are then obtained from the NV spin Hamiltonian (see Eq. Eq. (4.15)), using the computed magnetic field distribution, similarly to what is presented in Chapter 4. The results are reported in Fig. 6.30.

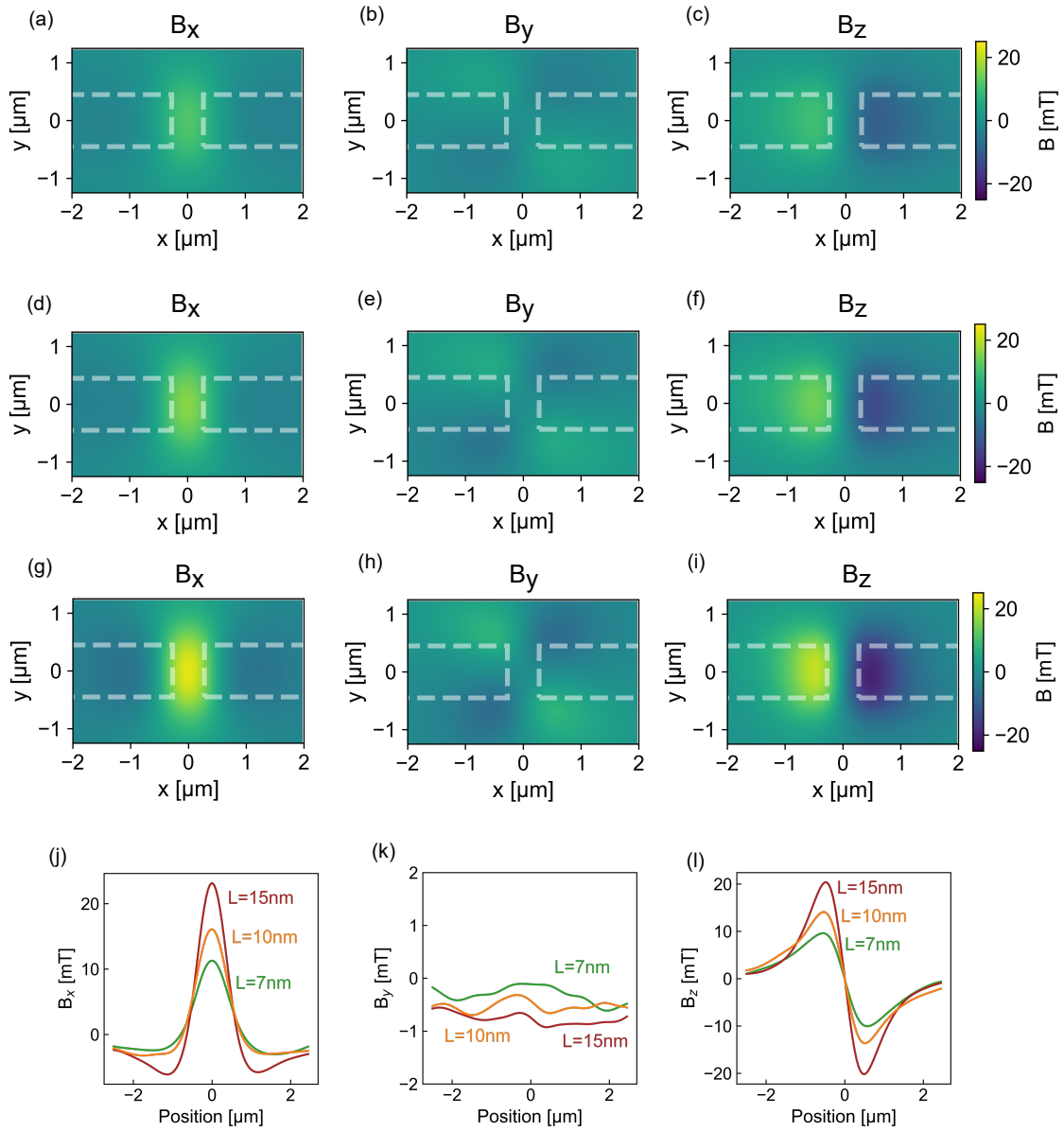

Figure 6.26: **Comparison of the magnetic field generated by the magnet for three mean grain sizes.**
(a-c) Two-dimensional maps of the magnetic-field components B_x, B_y, and B_z computed at a height $h = 640\,\text{nm}$ above the surface, from micromagnetic simulations with a mean grain size of 7 nm. The dashed white line indicates the magnet position.
(d-f) Same as (a-c), but for a mean grain size of 10 nm.
(g-i) Same as (a-c), but for a mean grain size of 15 nm.
(j-l) Line-cut profiles of B_x, B_y, and B_z at $y = 0\,\mu\text{m}$, extracted from panels (a-i), for micromagnetic simulations with mean grain sizes of 7 nm (green), 10 nm (orange), and 15 nm (red).

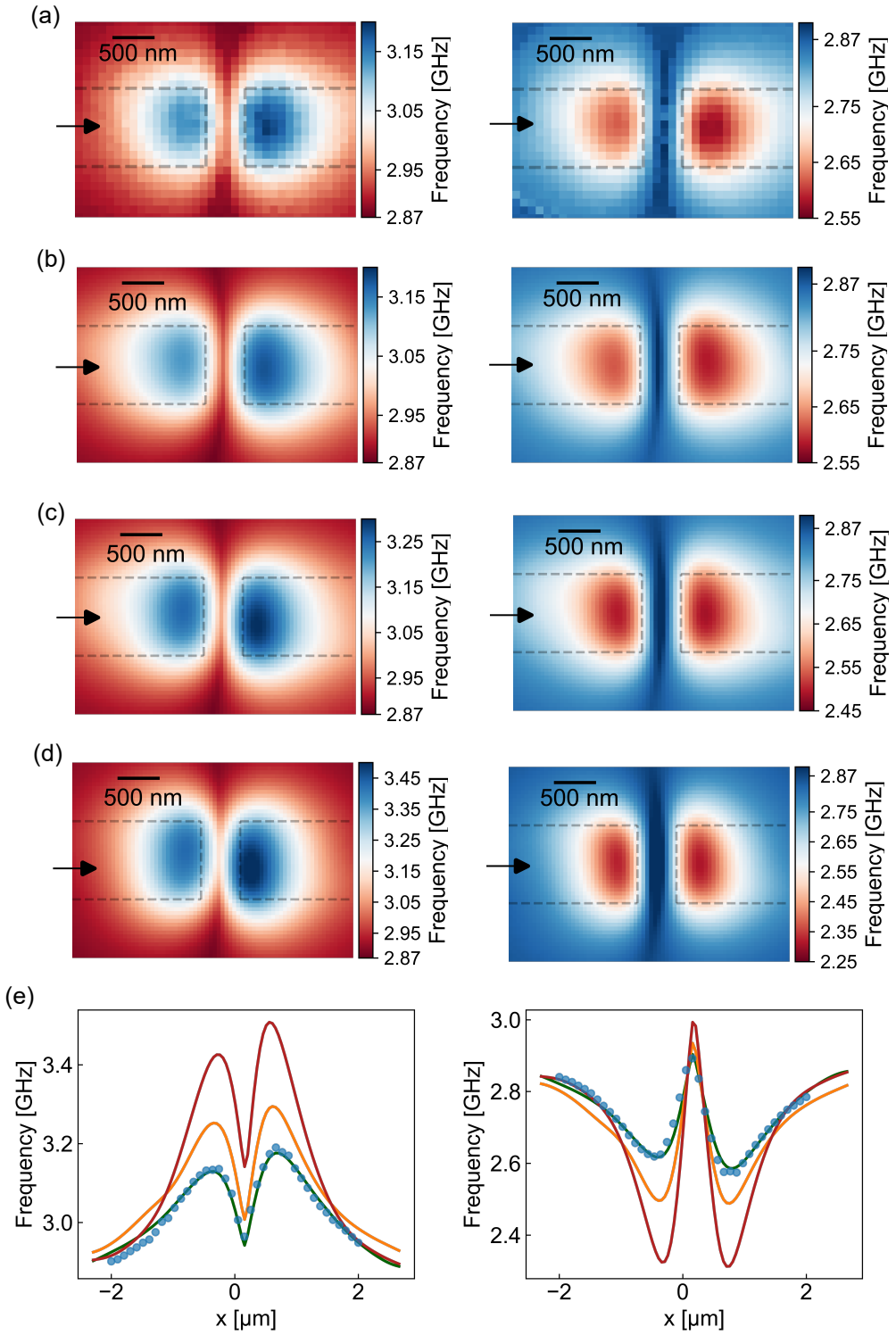

Figure 6.27: **ESR frequencies of an NV center above a Co magnet**
(a) Experimental map of the NV ESR frequencies measured at a stand-off distance $h_m = 600\,\text{nm}$.
(b) Simulated ESR map obtained by combining the micromagnet stray field with the NV spin Hamiltonian. Micromagnetic parameters use mean grain size of 7 nm.
(c) Same as (b), but using mean grain size of 10 nm.
(d)Same as (b), but using mean grain size of 15 nm. (e) Line cut comparing the measured ESR frequencies (orange circles) with simulations for mean grain size 7 nm (green), 10 nm (orange) and 15 nm (red). The cut follows the arrow indicated in (a)-(d)

By comparing the measured NV center ESR frequencies with the simulated NV center ESR frequencies obtained from the micromagnetic simulations for the three mean grain sizes, we find that the simulated ESR frequency profile corresponding to a mean grain size of 7 nm is in good agreement with the experiment. In contrast, the simulated ESR frequency profiles for mean grain sizes of 10 nm and 15 nm do not reproduce the measured ESR frequencies: in these cases, the magnetic field generated by the simulated magnetization is overestimated.

Both the qualitative and quantitative comparison of the micromagnetic simulations with the experimental results from the MFM and NV center microscopy measurements indicate that, in order to correctly model the Cobalt thin film, a mean grain size of 7 nm for the Voronoi tessellation is the most suitable choice. Let us emphasize that the thin-film micromagnetic simulations presented in Chapter 4, which successfully reproduce the thin-film characterization (MFM and SQUID-VSM), were also performed using this mean grain size.

Similarly, for the Cobalt-Iron thin film, the grain size used in the Voronoi tessellation for the micromagnetic simulations was set to 15 nm, as this value provided good agreement with both the thin-film and magnet-scale measurements.

Discussion on the cubic anisotropy constant in CoFe

We compare micromagnetic simulations of a magnet consisting of two opposing rectangles for two values of the cubic anisotropy constant K_1: (i) $K_1 = 450\,\mathrm{kJ\,m^{-3}}$, adjusted to reproduce the out-of-plane SQUID-VSM data and the thin film magnetization distribution observed by MFM in Chapter 6 (see Section4.1.4), and (ii) $K_1 = 50\,\mathrm{kJ\,m^{-3}}$, corresponding to the value expected for cubic Iron [71]. The crystallographic orientations are fixed from X-ray diffraction measurements (see Chapter 4 for details).

Figure 6.28 shows the simulated micromagnetic configurations under an external field applied along the magnet, $B_{\mathrm{ext},x} = 5\,\mathrm{mT}$. Notably, reducing K_1 leads to more pronounced domain closure at the magnet ends.

From this configuration we can compute the magnetic field generated by the magnet at a height that corresponds to the height at which the NV center measurements are performed. The magnetic field distribution along the line cut presented Fig. 4.19(f) are shown Fig. 6.29.

From these configurations, we compute the magnetic field produced by the magnet at a height matching the NV measurement stand-off. The resulting spatial distribution is shown in Fig. 6.29.

The corresponding NV resonance frequencies are then obtained from the NV spin Hamiltonian (see Eq. (4.15)), similarly to what is presented in Chapter 4. The results are reported in Fig. 6.30.

With $K_1 = 450\,\mathrm{kJ\,m^{-3}}$ - the value determined from thin-film characterization - the simulated NV center ESR frequencies profile agrees with the measurements. In contrast, using $K_1 = 50\,\mathrm{kJ\,m^{-3}}$, the value expected for Fe, yields simulated ESR profiles that does not match the experiment.

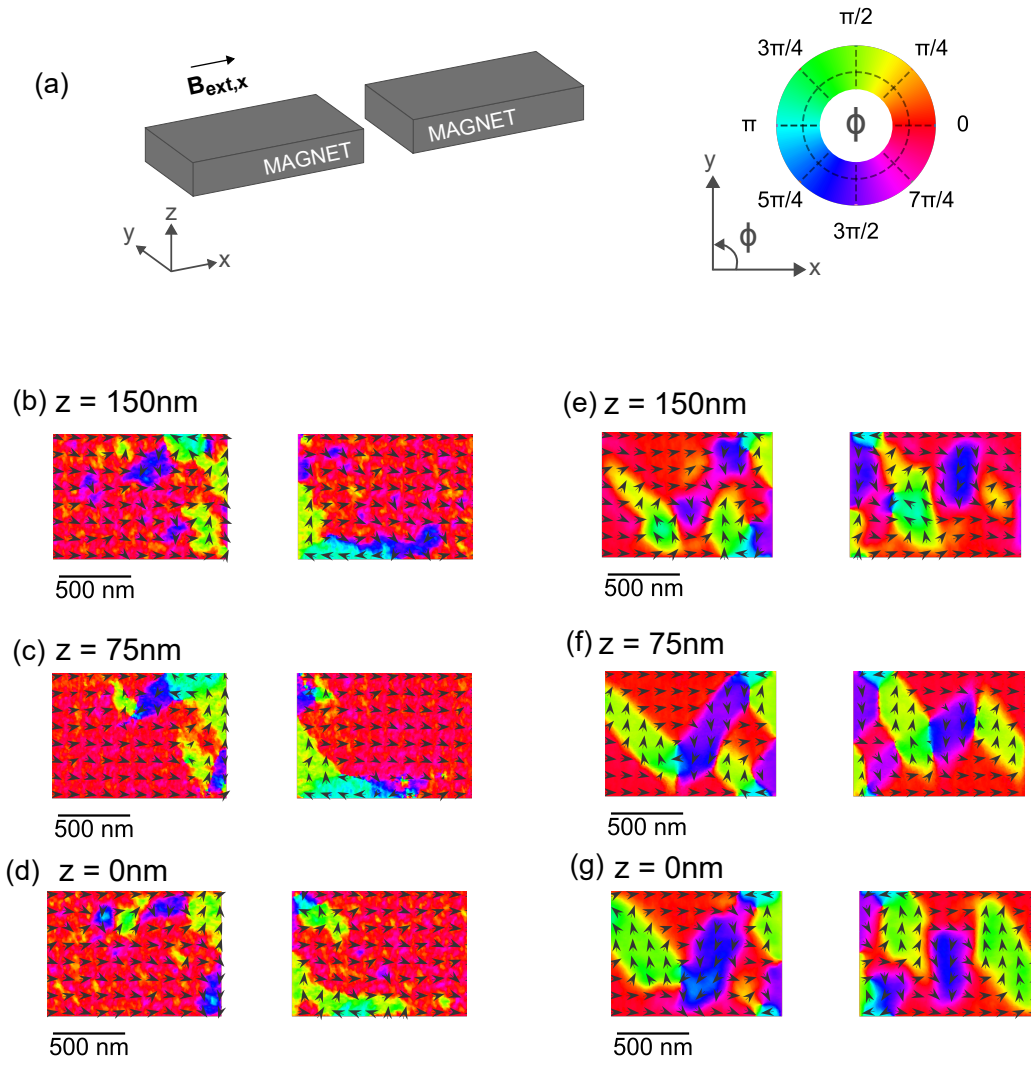

Figure 6.28: **Magnetization distributions for two cubic anisotropy constants**
(a) Schematic of the magnet.
(b-g) In-plane (xy-plane) magnetization at selected thicknesses (heights), computed with an external field $B_{\mathrm{ext},x} = 5\,\mathrm{mT}$. Colors indicate the in-plane angle ϕ of the magnetization. Only the edge region is shown; the full simulation used a 7 µm length with periodic boundary conditions to emulate a long magnet.
(b-d) Magnetization distribution considering $K_1 = 450\,\mathrm{kJ\,m^{-3}}$.
(e-g) Magnetization distribution considering $K_1 = 50\,\mathrm{kJ\,m^{-3}}$.

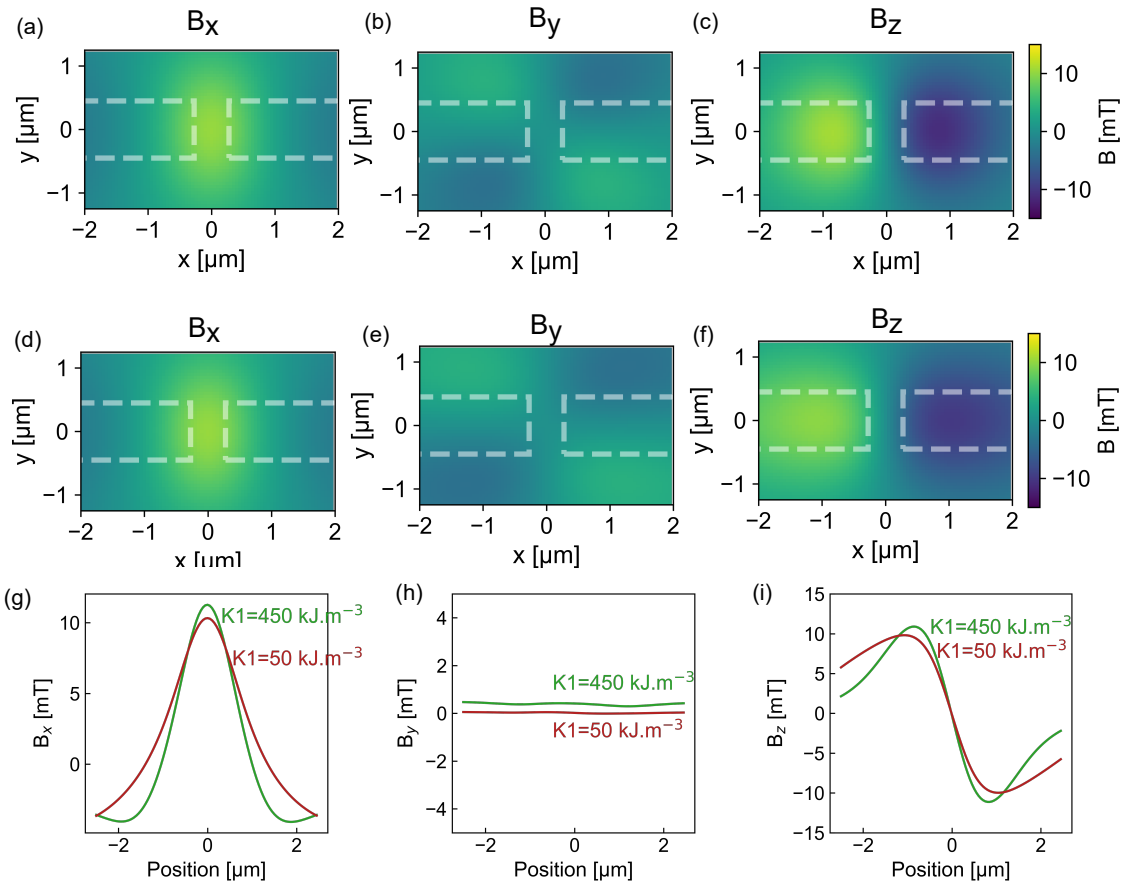

Figure 6.29: **Comparison of the magnetic field generated by the magnet for two different cubic anisotropy constants**
(a-c) Two-dimensional maps of the magnetic-field components B_x, B_y, and B_z computed at a height $h = 1160\,\mathrm{nm}$ above the surface, from micromagnetic simulations with $K_1 = 450\,\mathrm{kJ\,m^{-3}}$. The dashed white line indicates the magnet position.
(d-f) Same as (a-c), but for $K_1 = 50\,\mathrm{kJ\,m^{-3}}$.
(g-i) Line-cut profiles of B_x, B_y, and B_z at $y = 0\,\mu\mathrm{m}$ extracted from panels (a-f) computed from micromagnetic simulations with $K_1 = 450\,\mathrm{kJ\,m^{-3}}$ (green) and $K_1 = 50\,\mathrm{kJ\,m^{-3}}$ (red).

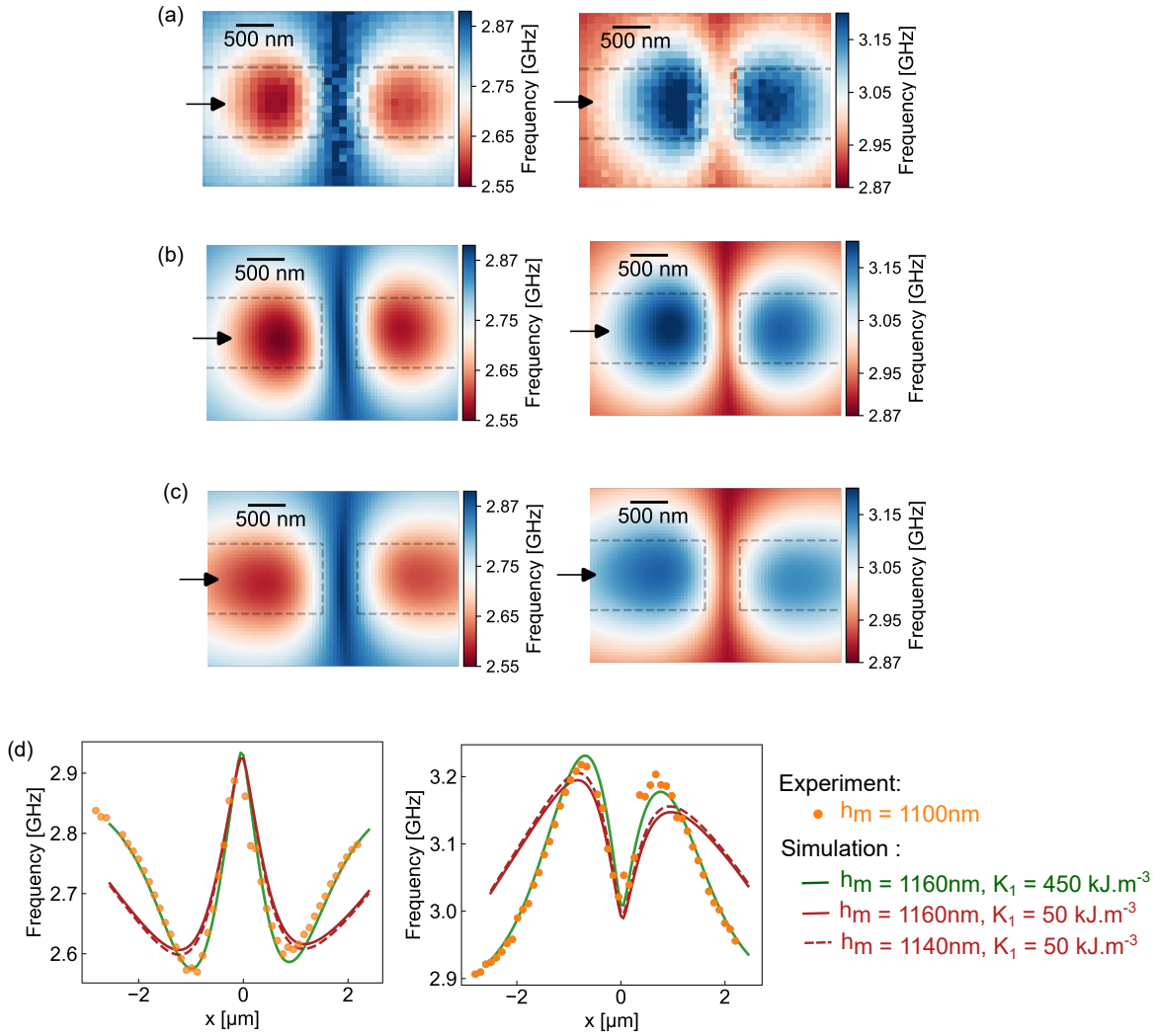

Figure 6.30: **ESR frequencies of an NV center above a CoFe magnet**
(a) Experimental map of the NV ESR frequencies measured at a stand-off distance $h_m = 1100\,\mathrm{nm}$.
(b) Simulated ESR map obtained by combining the micromagnet stray field with the NV spin Hamiltonian. Micromagnetic parameters use $K_1 = 450\,\mathrm{kJ\,m^{-3}}$.
(c) Same as (b), but using $K_1 = 50\,\mathrm{kJ\,m^{-3}}$.
(d) Line cut comparing the measured ESR frequencies (orange circles) with simulations for $K_1 = 450\,\mathrm{kJ\,m^{-3}}$ (green) and $K_1 = 50\,\mathrm{kJ\,m^{-3}}$ (red). The cut follows the arrow indicated in (a)-(c)

Appendix B : Additional characterization of NbN thin film

Estimation of the kinetic inductance from DC measurements

We determine the sheet kinetic inductance from a four-probe DC measurement of the NbN film. The resistance R of a segment of length l and width w of NbN is monitored while the sample is cooled down. From the resulting $R(T)$ curve we extract the sheet resistance just above the superconducting transition and the critical temperature of the superconducting material (defined here as the midpoint of the resistive transition).
The sheet kinetic inductance is then given by:

$$L_K^{\square} = \frac{\hbar R_{\square}}{\pi \Delta_0}$$

with $R_{\square} = R\frac{w}{l}$ and $\Delta_0 = 1.76\, k_B T_c$

To perform the measurement the sample is mounted into a Qinu dilution refrigerator. This allows to cooldown the sample from room-temperature to about 30 mK.

The result of the measurement is presented Fig. 6.31. We extract a sheet resistance before the superconducting transition of $R_{\square} \approx 2557\Omega.\square^{-1}$ and a critical temperature of $T_c \approx 3.7\,\mathrm{K}$ (the associated uncertainty with this value is discussed below)

The kinetic inductance of the film is then estimated to be:

$$L_K^{\square} \approx 954\ \mathrm{pH}.\square^{-1} \tag{6.52}$$

This result is higher than the value obtained from the RF estimation of the kinetic inductance presented in the Chapter 5 of the thesis. We believe this discrepancy can be attributed to uncertainty of the evaluation of the critical temperature. In the following we will detail why the measured critical temperature might be wrong.

This value exceeds the RF-extracted kinetic inductance reported in Chapter 5. We attribute the discrepancy primarily to the uncertainty on T_c. The following discusses both the uncertainties in our estimate and the reasons why the measured transition temperature may not equal the intrinsic

Uncertainty on the critical temperature

One uncertainty comes from thermalization during the cooldown. Indeed, for this measurement we where using a Qinu fridge and the measurement was performed during the cooldown procedure. The temperature sweep of the cryostat during the cooldown process (from 10 K to below 1 K) was estimated to be about $2.4\,\mathrm{K\,min^{-1}}$. This fast temperature sweep lead us to believe that we could have an uncertainty of the measured critical temperature - but hard to evaluate.

In addition to this consideration, self-heating of the NbN wire must be assessed. A conservative bias condition under which self-heating can be neglected is

$$eV \leq k_B T \tag{6.53}$$

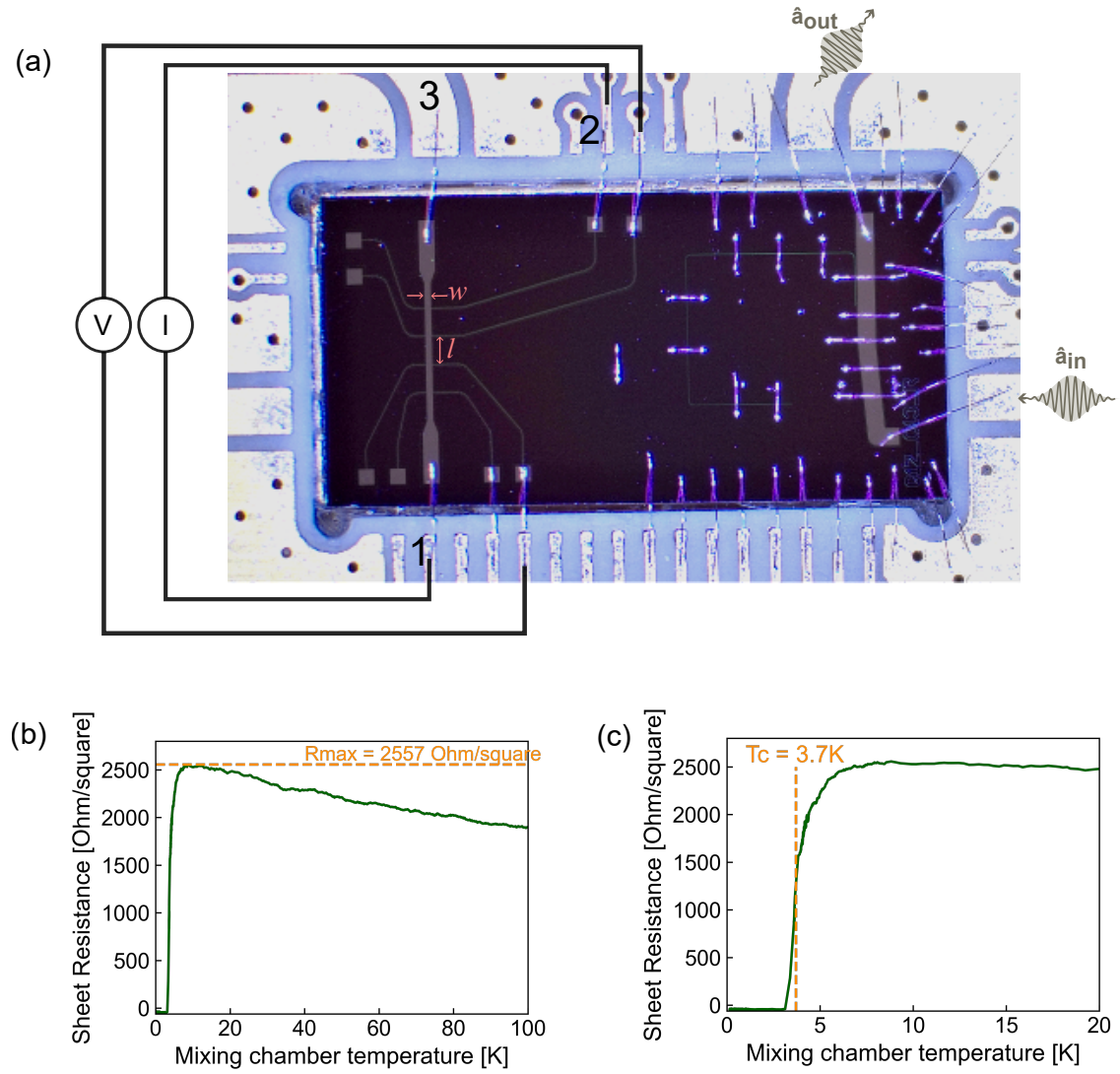

Figure 6.31: **DC estimation of the kinetic inductance**
(a) Optical image of the chip used to calibrate the kinetic inductance with a four-probe resistivity structure. A bias current of 10 nA flows from port 1 to port 2. The voltage is measured across a section of length $l = 450\,\mu$m and width $w = 100\,\mu$m.
(b-c) Sheet resistance of the NbN wire as a function of temperature.

where e is the elementary charge, V is the potential difference across the NbN wire (such that $E = eV$ corresponds to the energy an electron gains in crossing the potential drop V), T the temperature of the sample and k_B the Boltzmann constant. When Eq. (6.53) holds, the electronic temperature is expected to track the bath temperature closely, and bias-induced overheating can be neglected.
Considering a temperature of $T = 4\,$K, the voltage across the NbN wire should be $V = \frac{k_B T}{e} = 0.3\,$mV, so that the maximum current is :

$$I_{\max} = \frac{k_B T}{R\, e} \tag{6.54}$$

In our measurements the current was fixed to $I_{\text{applied}} = 10\,$nA (lower currents led to an excessive noise floor). From Eq. (6.54), this satisfies the no-overheating condition only if $R \lesssim V_T / I_{\text{applied}} \approx 34.5\,$kΩ. For larger R (see Fig. 6.31), we have $I_{\text{applied}} > I_{\max}$, and the electron temperature in the wire can exceed the bath temperature, potentially biasing the extracted transition temperature.

From the device layout, the bias current traverses a long NbN segment (from pad 1 to pad 2 in Fig. 6.31) whose resistance exceeds 34.5 kΩ. In this regime, $I_{\max} = \frac{k_B T}{e R} < I_{\text{applied}}$, so self-heating

cannot be neglected. Consequently, the extracted transition temperature may not reflect the intrinsic T_c.

Appendix C : Calibration of the RF setup for photon number estimation

To determine the photon number in the cavity, we calibrate the total RF attenuation of the measurement chain - from the Front-End Module to the sample - shown in Fig. 6.14.
We proceed in three steps: (i) estimation of the attenuation from the Front-End Module to the sample, (ii) estimation of the amplification from the sample back to the Front-End Module and (iii) comparison of the inferred attenuation with a transmission line measurement.

Input attenuation of the RF setup

Here, we calibrate the attenuation in the RF chain from the microwave tone generator output to the sample. To estimate the total input attenuation, we itemize the contribution of each element in the setup and sum their losses.

- Between the microwave generator and the cryostat, the RF path includes two 10 ft SMA-SMA coaxial cables (Mini-Circuits CBL-10-FT-SMSM+). At 4 GHz, each cable has an insertion loss of 2.2 dB, giving a total cable attenuation of 4.4 dB. The insertion loss of the DC block (typically 0.1-0.5 decibel at a few GHz) is neglected.
- Inside the cryostat, from room temperature to the 4 K stage, the RF connections use SCuNi semi-rigid coax (SN086, 0.86 mm, SCuNi-CuNi).
  Manufacturer data list attenuations of 3.0 dB m^{-1} at 1 GHz and 9.5 dB m^{-1} at 10 GHz at Room Temperature, and 1.5 dB m^{-1} at 1 GHz and 4.6 dB m^{-1} at 10 GHz at 4 K.
  For a cable length of 490 mm [183], interpolating between 1 and 10 GHz and averaging over the temperature gradient gives a resulting loss at 4 GHz is estimated to be 1.8 dB
- Inside the cryostat, from the 4 K stage to the mixing chamber, RF connections use the same SCuNi semi-rigid coax (SN086, 0.86 mm, SCuNi-CuNi). Using the 4 K attenuation specifications, the loss at 4 GHz for a cable length of 560 mm [183] is estimated to be 1.4 dB.
- Cryogenic attenuators: the fixed attenuators installed along the input line sum to −60 dB

From these contributions, **the total attenuation is set to 68 ± 1 dB**. The ±1dB accounts for uncertainties in the above estimates as well as possible additional losses from the PCB and wirebonds.

Output Gain of the RF setup

Using the same methodology, we calibrate the attenuation from the sample holder output to the input port of the microwave front-end module.

- From mixing chamber to the 4 K the RF connection are made of NbTi cables (NT086 0.86mm NbTi superconducting coaxial line). Niobium-titanium has a critical temperature $T_c = 9.2$ K [184], so this line is superconducting. We thus treat the cable attenuation as negligible.

- 4 K stage low-noise amplification : a cryogenic HEMT amplifier (LNF-LNC4-8F-LG) provides 26 dB of gain. It is preceded by an isolator with an insertion loss of ≈ 0.5 dB.
- From the 4 K stage to room temperature, the RF connections use SCuNi-CuNi semi-rigid coax (SN219, 2.19 mm). Manufacturer data:
  At room temperature : 1.2 dB m^{-1} at 1 GHz and 3.8 dB m^{-1} at 10 GHz,
  At 4 K : 0.6 dB m^{-1} at 1 GHz, 1.8 dB m^{-1} at 10 GHz.
  For a cable length of 490 mm and operation near 4 GHz, the estimated insertion loss is 0.7 dB
- A first SMA-SMA coaxial cable (Mini-Circuits CBL-0.5M-SMSM+) - with attenuation 0.4 dB - connects the cryostat output to an isolator (insertion loss ≈ 0.5 dB), followed by a room-temperature amplifier providing 40 dB of gain. Two additional SMA-SMA coaxial cables (Mini-Circuits CBL-2M-SMSM+), each with 2.1 dB attenuation, connect the amplifier output to the microwave front-end module.

The overall attenuation (or gain) is obtained by summing gains and losses along the RF path (taking gains as positive and attenuations as negative). For this chain,**the net gain is estimated to be 60 dB**.

Comparison with the measurement

Summing the gains and losses along the RF chain implies that the transmission parameter S_{21} of a transmission line - measured for example with a VNA - should have a magnitude close to $|S_{21}| \approx -8$ dB. To verify this, we use the hanger line coupled to the cavity and evaluate the transmission away from the cavity resonance. The measured S_{21} of the hanger line is shown in Fig. 6.32 : its amplitude agrees with the calibration.

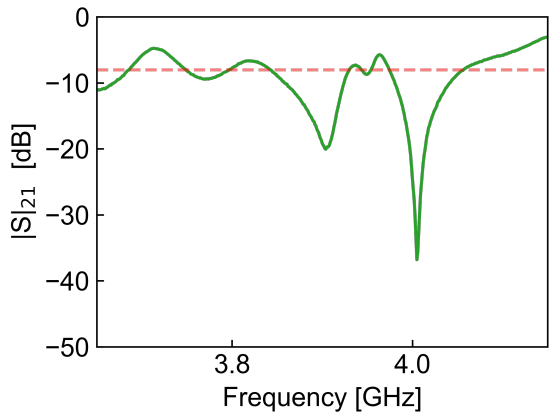

Figure 6.32: Magnitude of the transmission parameter S_{21} through the hanger line coupled to the cavity. The dashed line indicates the calibrated expectation of −8 dB.

Appendix D : Etching rate calibration for Silicum and Cobalt-Iron

We report the etch-rate calibration for cobalt-iron (CoFe) and silicon as a function of the ion-beam incidence angle relative to the sample surface normal.

To determine the etch rate, we first pattern a wire structure on the thin film by optical lithography and retain the resist as an etch mask. The film is then etched by argon ion beam etching (IBE), varying both the acceleration voltage and the incidence angle with respect to the surface normal. After etching, the resist is stripped so that the masked regions remain unetched. The removed thickness is then measured to extract the etch rate (thickness removed per unit time). The results are shown in Fig. 6.33.

As noted in Chapter 6, at an incidence angle of 80° relative to the surface normal, the silicon etch rate is approximately 6.5 times higher than that of cobalt-iron.

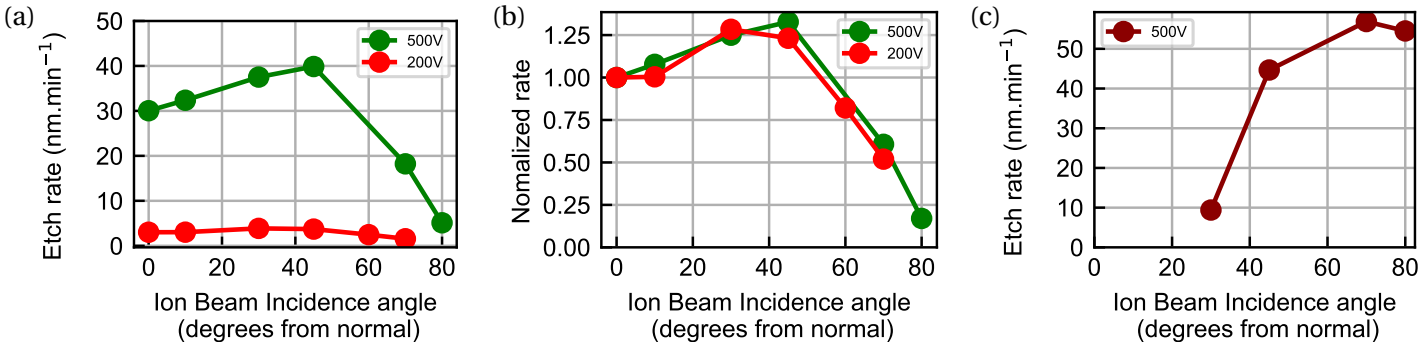

Figure 6.33: **Etch-rate calibration for CoFe and Si**
(a) CoFe etch rate versus ion-beam incidence angle (relative to the surface normal) for acceleration voltages of 500 V (green) and 200 V (red).
(b) Normalized CoFe etch rate showing similar angular dependence for both acceleration voltages.
(c) Si etch rate versus ion-beam incidence angle for an acceleration voltage of 500 V.

References

[1] D. Loss and D. P. DiVincenzo, "Quantum computation with quantum dots," *Physical Review A*, vol. 57, pp. 120–126, 1998. DOI: 10.1103/PhysRevA.57.120.

[2] L. M. K. Vandersypen, H. Bluhm, J. S. Clarke, *et al.*, "Interfacing spin qubits in quantum dots and donors—hot, dense, and coherent," *npj Quantum Information*, vol. 3, p. 34, 2017. DOI: 10.1038/s41534-017-0038-y.

[3] N. Samkharadze, G. Zheng, N. Kalhor, *et al.*, "Strong spin-photon coupling in silicon," *Science*, vol. 359, no. 6380, pp. 1123–1127, 2018. DOI: 10.1126/science.aar4054.

[4] X. Mi, M. Benito, S. Putz, *et al.*, "A coherent spin–photon interface in silicon," *Nature*, vol. 555, no. 7698, pp. 599–603, 2018. DOI: 10.1038/nature25769.

[5] J. Dijkema, X. Xue, P. Harvey-Collard, *et al.*, "Cavity-mediated iswap oscillations between distant spins," *Nature Physics*, vol. 21, pp. 168–174, 2025. DOI: 10.1038/s41567-024-02694-8.

[6] C. X. Yu, S. Zihlmann, G. Troncoso Fernández-Bada, *et al.*, "Magnetic field resilient high kinetic inductance superconducting niobium nitride coplanar waveguide resonators," *Applied Physics Letters*, vol. 118, no. 5, p. 054 001, 2021. DOI: 10.1063/5.0039945.

[7] B. Neukelmance, B. Hue, Q. Schaeverbeke, *et al.*, "Microsecond-lived quantum states in a carbon-based circuit driven by cavity photons," *Nature Communications*, vol. 16, p. 5636, Jul. 2025. DOI: 10.1038/s41467-025-60952-6. [Online]. Available: https://www.nature.com/articles/s41467-025-60952-6.

[8] W. Gerlach and O. Stern, "Der experimentelle Nachweis der Richtungsquantelung im Magnetfeld," *Zeitschrift für Physik*, vol. 9, pp. 349–352, 1922. DOI: 10.1007/BF01326983.

[9] G. E. Uhlenbeck and S. Goudsmit, "Spinning electrons and the structure of spectra," *Nature*, vol. 117, no. 2938, pp. 264–265, 1926. DOI: 10.1038/117264a0.

[10] P. A. M. Dirac, "The quantum theory of the electron," *Proceedings of the Royal Society A*, vol. 117, no. 778, pp. 610–624, 1928. DOI: 10.1098/rspa.1928.0023.

[11] W. Pauli, "Zur Quantenmechanik des magnetischen Elektrons," *Zeitschrift für Physik*, vol. 43, pp. 601–623, 1927. DOI: 10.1007/BF01397326.

[12] W. Heisenberg, "Zur Theorie des Ferromagnetismus," *Zeitschrift für Physik*, vol. 49, pp. 619–636, 1928. DOI: 10.1007/BF01328601.

[13] P. W. Anderson, "Antiferromagnetism. theory of superexchange interaction," *Physical Review*, vol. 79, pp. 350–356, 1950. DOI: 10.1103/PhysRev.79.350.

[14] M. N. Baibich, J. M. Broto, A. Fert, *et al.*, "Giant magnetoresistance of (001)fe/(001)cr magnetic superlattices," *Physical Review Letters*, vol. 61, pp. 2472–2475, 1988. DOI: 10.1103/PhysRevLett.61.2472.

[15] J. S. Moodera, L. R. Kinder, T. M. Wong, and R. Meservey, "Large magnetoresistance at room temperature in ferromagnetic thin film tunnel junctions," *Physical Review Letters*, vol. 74, pp. 3273–3276, 1995. DOI: 10.1103/PhysRevLett.74.3273.

[16] P. Bruno, "Tight-binding approach to the orbital magnetic moment and magnetocrystalline anisotropy of transition-metal monolayers," *Physical Review B*, vol. 39, pp. 865–868, 1989. DOI: 10.1103/PhysRevB.39.865.

[17] I. Dzyaloshinsky, "A thermodynamic theory of "weak" ferromagnetism of antiferromagnetics," *Journal of Physics and Chemistry of Solids*, vol. 4, pp. 241–255, 1958. DOI: 10.1016/0022-3697(58)90076-3.

[18] T. Moriya, "Anisotropic superexchange interaction and weak ferromagnetism," *Physical Review*, vol. 120, pp. 91–98, 1960. DOI: 10.1103/PhysRev.120.91.

[19] S. Mühlbauer *et al.*, "Skyrmion lattice in a chiral magnet," *Science*, vol. 323, pp. 915–919, 2009. DOI: 10.1126/science.1166767.

[20] X. Z. Yu *et al.*, "Real-space observation of a two-dimensional skyrmion crystal," *Nature*, vol. 465, pp. 901–904, 2010. DOI: 10.1038/nature09124.

[21] C. L. Kane and E. J. Mele, "
$mathbbZ_2$ topological order and the quantum spin hall effect," *Physical Review Letters*, vol. 95, p. 146 802, 2005. DOI: 10.1103/PhysRevLett.95.146802.

[22] B. A. Bernevig, T. L. Hughes, and S.-C. Zhang, "Quantum spin hall effect and topological phase transition in hgte quantum wells," *Science*, vol. 314, pp. 1757–1761, 2006. DOI: 10.1126/science.1133734.

[23] A. V. Chumak, V. I. Vasyuchka, A. A. Serga, and B. Hillebrands, "Magnon spintronics," *Nature Physics*, vol. 11, pp. 453–461, 2015. DOI: 10.1038/nphys3347.

[24] J. R. Maze *et al.*, "Nanoscale magnetic sensing with an individual electronic spin in diamond," *Nature*, vol. 455, pp. 644–647, 2008. DOI: 10.1038/nature07279.

[25] G. Balasubramanian *et al.*, "Nanoscale imaging magnetometry with diamond spins under ambient conditions," *Nature*, vol. 455, pp. 648–651, 2008. DOI: 10.1038/nature07278.

[26] L. Rondin *et al.*, "Magnetometry with nitrogen-vacancy defects in diamond," *Reports on Progress in Physics*, vol. 77, p. 056 503, 2014. DOI: 10.1088/0034-4885/77/5/056503.

[27] G. Kucsko *et al.*, "Nanometre-scale thermometry in a living cell," *Nature*, vol. 500, pp. 54–58, 2013. DOI: 10.1038/nature12373.

[28] F. Dolde *et al.*, "Electric-field sensing using single diamond spins," *Nature Physics*, vol. 7, pp. 459–463, 2011. DOI: 10.1038/nphys1969.

[29] M. W. Doherty, N. B. Manson, P. Delaney, F. Jelezko, J. Wrachtrup, and L. C. L. Hollenberg, "The nitrogen-vacancy colour centre in diamond," *Physics Reports*, vol. 528, pp. 1–45, 2013. DOI: 10.1016/j.physrep.2013.02.001.

[30] L. Robledo *et al.*, "High-fidelity projective read-out of a solid-state spin quantum register," *Nature*, vol. 477, pp. 574–578, 2011. DOI: 10.1038/nature10401.

[31] R. Hanson, L. P. Kouwenhoven, J. R. Petta, S. Tarucha, and L. M. K. Vandersypen, "Spins in few-electron quantum dots," *Reviews of Modern Physics*, vol. 79, pp. 1217–1265, 2007. DOI: 10.1103/RevModPhys.79.1217.

[32] G. Burkard, T. D. Ladd, A. Pan, J. M. Nichol, and J. R. Petta, "Semiconductor spin qubits," *Reviews of Modern Physics*, vol. 95, no. 2, p. 025 003, 2023. DOI: 10.1103/RevModPhys.95.025003. [Online]. Available: https://journals.aps.org/rmp/abstract/10.1103/RevModPhys.95.025003.

[33] A. Morello, J. J. Pla, P. Bertet, and D. N. Jamieson, "Donor spins in silicon for quantum technologies," *Advanced Quantum Technologies*, vol. 3, no. 3, p. 2 000 005, 2020. DOI: 10.1002/qute.202000005.

[34] McKinsey & Company, *How quantum computing could change the world*, Article, Jun. 2022. [Online]. Available: https://www.mckinsey.com/featured-insights/themes/how-quantum-computing-could-change-the-world (visited on 09/13/2025).

[35] D. P. DiVincenzo, "The physical implementation of quantum computation," *Fortschritte der Physik*, vol. 48, no. 9-11, pp. 771–783, 2000. DOI: 10.1002/1521-3978(200009)48:9/11<771::AID-PROP771>3.0.CO;2-E.

[36] J. R. Petta, A. C. Johnson, J. M. Taylor, *et al.*, "Coherent manipulation of coupled electron spins in semiconductor quantum dots," *Science*, vol. 309, no. 5744, pp. 2180–2184, 2005. DOI: 10.1126/science.1116955.

[37] A. M. Tyryshkin, S. Tojo, J. J. L. Morton, *et al.*, "Electron spin coherence exceeding seconds in high-purity silicon," *Nature Materials*, vol. 11, no. 2, pp. 143–147, 2012. DOI: 10.1038/nmat3182.

[38] Y.-H. Wu, L. C. Camenzind, P. Bütler, *et al.*, *Simultaneous high-fidelity single-qubit gates in a spin qubit array*, Primitive $\pi/2$ gate fidelities >99.99%, some ≈99.999%; ~99.9% maintained during fully parallel 5-qubit operation, 2025. arXiv: 2507.11918 [quant-ph].

[39] S. G. J. Philips, M. T. Mądzik, S. V. Amitonov, *et al.*, "Universal control of a six-qubit quantum processor in silicon," *Nature*, vol. 609, pp. 919–924, 2022. DOI: 10.1038/s41586-022-05117-x.

[40] M. De Smet, Y. Matsumoto, A.-M. J. Zwerver, *et al.*, "High-fidelity single-spin shuttling in silicon," *Nature Nanotechnology*, vol. 20, pp. 866–872, 2025. DOI: 10.1038/s41565-025-01920-5.

[41] M. Künne, A. Willmes, M. Oberländer, *et al.*, "The spinbus architecture for scaling spin qubits with electron shuttling," *Nature Communications*, vol. 15, p. 4977, 2024. DOI: 10.1038/s41467-024-49182-4.

[42] R. Xue, I. Seidler, T. Struck, and et al., "Si/sige qubus for single electron information-processing devices with memory and micron-scale connectivity function," *Nature Communications*, vol. 15, p. 2579, 2024. DOI: 10.1038/s41467-024-46519-x.

[43] A. Blais, R.-S. Huang, A. Wallraff, S. M. Girvin, and R. J. Schoelkopf, "Cavity quantum electrodynamics for superconducting electrical circuits: An architecture for quantum computation," *Physical Review A*, vol. 69, p. 062 320, 2004. DOI: 10.1103/PhysRevA.69.062320.

[44] A. Wallraff, D. I. Schuster, A. Blais, *et al.*, "Strong coupling of a single photon to a superconducting qubit using circuit quantum electrodynamics," *Nature*, vol. 431, pp. 162–167, 2004. DOI: 10.1038/nature02851.

[45] J. Majer, J. M. Chow, J. M. Gambetta, *et al.*, "Coupling superconducting qubits via a cavity bus," *Nature*, vol. 449, pp. 443–447, 2007.

[46] P. Krantz, M. Kjaergaard, F. Yan, T. P. Orlando, S. Gustavsson, and W. D. Oliver, "A quantum engineer's guide to superconducting qubits," *Applied Physics Reviews*, vol. 6, p. 021 318, 2019. DOI: 10.1063/1.5089550.

[47] A. Blais, A. L. Grimsmo, S. M. Girvin, and A. Wallraff, "Circuit quantum electrodynamics," *Reviews of Modern Physics*, vol. 93, p. 025 005, 2021. DOI: 10.1103/RevModPhys.93.025005.

[48] T. Frey, P. J. Leek, M. Beck, *et al.*, "Dipole coupling of a double quantum dot to a microwave resonator," *Physical Review Letters*, vol. 108, p. 046 807, 2012. DOI: 10.1103/PhysRevLett.108.046807.

[49] C. X. Yu, S. Zihlmann, J. C. Abadillo-Uriel, *et al.*, "Strong coupling between a photon and a hole spin in silicon," *Nature Nanotechnology*, vol. 18, pp. 741–746, 2023. DOI: 10.1038/s41565-023-01332-3.

[50] L. Noirot, C. X. Yu, J. C. Abadillo-Uriel, *et al.*, *Coherence of a hole spin flopping-mode qubit in a circuit quantum electrodynamics environment*, 2025. arXiv: 2503.10788 [cond-mat.mes-hall]. [Online]. Available: https://arxiv.org/abs/2503.10788.

[51] G. Abulizi, A. Baumgartner, and C. Schönenberger, "Full characterization of a carbon nanotube parallel double quantum dot," *physica status solidi (b)*, vol. 253, no. 12, pp. 2428–2432, 2016. DOI: 10.1002/pssb.201600293.

[52] K. Goß, M. Leijnse, S. Smerat, M. R. Wegewijs, C. M. Schneider, and C. Meyer, "Parallel carbon nanotube quantum dots and their interactions," *Physical Review B*, vol. 87, p. 035 424, 2013. DOI: 10.1103/PhysRevB.87.035424.

[53] E. A. Laird, F. Kuemmeth, G. A. Steele, *et al.*, "Quantum transport in carbon nanotubes," *Reviews of Modern Physics*, vol. 87, pp. 703–764, 2015.

[54] J. Cao, Q. Wang, D. Wang, and H. Dai, "Suspended carbon nanotube quantum wires with two gates," *Nature Materials*, vol. 4, pp. 745–749, 2005. DOI: 10.1038/nmat1485.

[55] J. Waissman, M. Honig, S. Pecker, A. Benyamini, A. Hamo, and S. Ilani, "Realization of pristine and locally tunable one-dimensional electron systems in carbon nanotubes," *Nature Nanotechnology*, vol. 8, no. 7, pp. 569–574, 2013. DOI: 10.1038/nnano.2013.143.

[56] G. Kiršanskas, J. Paaske, and K. Flensberg, "Cotunneling renormalization in carbon nanotube quantum dots," *Physical Review B*, vol. 86, p. 075 452, Aug. 2012. DOI: 10.1103/PhysRevB.86.075452.

[57] T. S. Jespersen, K. Grove-Rasmussen, J. Paaske, *et al.*, "Gate-dependent spin–orbit coupling in multielectron carbon nanotubes," *Nature Physics*, vol. 7, no. 4, pp. 348–353, 2011. DOI: 10.1038/nphys1880.

[58] G. A. Steele, F. Pei, E. A. Laird, J. M. Jol, H. B. Meerwaldt, and L. P. Kouwenhoven, "Large spin–orbit coupling in carbon nanotubes," *Nature Communications*, vol. 4, p. 1573, 2013. DOI: 10.1038/ncomms2584. [Online]. Available: https://www.nature.com/articles/ncomms2584.

[59] A. Secchi and M. Rontani, "Intervalley scattering induced by coulomb interaction and disorder in carbon-nanotube quantum dots," *Physical Review B*, vol. 88, no. 12, p. 125 403, 2013. DOI: 10.1103/PhysRevB.88.125403.

[60] H. O. H. Churchill, F. Kuemmeth, J. W. Harlow, *et al.*, "Relaxation and dephasing in a two-electron ^{13}c nanotube double quantum dot," *Physical Review Letters*, vol. 102, no. 16, p. 166 802, Apr. 2009. DOI: 10.1103/PhysRevLett.102.166802.

[61] T. Hayashi, T. Fujisawa, H. D. Cheong, Y. H. Jeong, and Y. Hirayama, "Coherent manipulation of electronic states in a double quantum dot," *Physical Review Letters*, vol. 91, p. 226 804, 2003. DOI: 10.1103/PhysRevLett.91.226804.

[62] Z. Shi, C. B. Simmons, J. R. Prance, *et al.*, "Fast hybridization control of a silicon charge qubit," *Physical Review Letters*, vol. 108, p. 140 503, 2013. DOI: 10.1103/PhysRevLett.108.140503.

[63] T. Petersen, A. K. Hüttel, G. A. Steele, *et al.*, "Signatures of charge coherence in a carbon nanotube double quantum dot," *Physical Review Letters*, vol. 114, p. 247 003, 2015. DOI: 10.1103/PhysRevLett.114.247003.

[64] P. Scarlino, J. H. Ungerer, D. J. van Woerkom, *et al.*, "In situ tuning of the electric-dipole strength of a double-dot charge qubit: Charge-noise protection and ultrastrong coupling," *Physical Review X*, vol. 12, no. 3, p. 031 004, 2022. DOI: 10.1103/PhysRevX.12.031004. [Online]. Available: https://link.aps.org/doi/10.1103/PhysRevX.12.031004.

[65] A. Cottet, M.-C. Dartiailh, M. M. Desjardins, *et al.*, "Cavity qed with hybrid nanocircuits: From atomic-like physics to condensed matter phenomena," *Journal of Physics: Condensed Matter*, vol. 29, no. 43, p. 433 002, 2017. DOI: 10.1088/1361-648X/aa7b4d.

[66] X. Mi, J. V. Cady, D. M. Zajac, P. W. Deelman, and J. R. Petta, "Strong coupling of a single electron in silicon to a microwave photon," *Science*, vol. 355, no. 6321, pp. 156–158, 2017. DOI: 10.1126/science.aal2469.

[67] B. D'Anjou and G. Burkard, "Optimal dispersive readout of a spin qubit with a microwave resonator," *Physical Review B*, vol. 100, no. 24, p. 245 427, Dec. 2019. DOI: 10.1103/PhysRevB.100.245427. [Online]. Available: https://link.aps.org/doi/10.1103/PhysRevB.100.245427.

[68] S. Annabi, E. Arrighi, A. Peugeot, *et al.*, "Josephson junctions based on ultraclean carbon nanotubes," *Physical Review Applied*, vol. 22, no. 6, p. 064 035, Dec. 2024. DOI: 10.1103/PhysRevApplied.22.064035. [Online]. Available: https://link.aps.org/doi/10.1103/PhysRevApplied.22.064035.

[69] J. M. Fink, M. Göppl, M. Baur, *et al.*, "Climbing the jaynes–cummings ladder and observing its $\sqrt{n}$ nonlinearity in a cavity qed system," *Nature*, vol. 454, no. 7202, pp. 315–318, 2008. DOI: 10.1038/nature07112.

[70] D. J. van Woerkom, P. Scarlino, J. H. Ungerer, *et al.*, "Microwave photon-mediated interactions between semiconductor qubits," *Physical Review X*, vol. 8, no. 4, p. 041 018, 2018. DOI: 10.1103/PhysRevX.8.041018.

[71] B. D. Cullity and C. D. Graham, *Introduction to Magnetic Materials*, 2nd ed. Hoboken, NJ: Wiley–IEEE Press, 2009. DOI: 10.1002/9780470386323.

[72] D. Jordán *et al.*, "Detection of magnetic moment in thin films with a home-made vibrating sample magnetometer," *Journal of Magnetism and Magnetic Materials*, vol. 456, pp. 56–61, Jun. 2018. DOI: 10.1016/j.jmmm.2018.01.088.

[73] J. Ben Youssef, N. Vukadinovic, D. Billet, and M. Labrune, "Thickness-dependent magnetic excitations in permalloy films with nonuniform magnetization," *Physical Review B*, vol. 69, no. 17, p. 174 402, May 2004. DOI: 10.1103/PhysRevB.69.174402.

[74] J. Wei *et al.*, "Understanding stripe domains in permalloy films via the angular dependence of permeability spectra," *Journal of Magnetism and Magnetic Materials*, vol. 432, pp. 245–249, Jun. 2017. DOI: 10.1016/j.jmmm.2016.12.147.

[75] M. Hehn, "Élaboration et étude des propriétés structurales et magnétiques de couches et réseaux de plots submicroniques à base de cobalt," Thèse de doctorat, Institut de Physique et Chimie des Matériaux de Strasbourg (IPCMS); directeur: K. Ounadjela, Ph.D. dissertation, Université Louis Pasteur (Strasbourg I), Strasbourg, France, 1997.

[76] Y. Martin, C. C. Williams, and H. K. Wickramasinghe, "Atomic force microscope–force mapping and profiling on a sub 100-å scale," *Journal of Applied Physics*, vol. 61, no. 10, pp. 4723–4729, May 1987. DOI: 10.1063/1.338807.

[77] S. N. Magonov, V. Elings, and M.-H. Whangbo, "Phase imaging and stiffness in tapping-mode atomic force microscopy," *Surface Science*, vol. 375, no. 2, pp. L385–L391, Apr. 1997. DOI: 10.1016/S0039-6028(96)01591-9.

[78] A. Vansteenkiste, J. Leliaert, M. Dvornik, M. Helsen, F. Garcia-Sanchez, and B. Van Waeyenberge, "The design and verification of mumax3," *AIP Advances*, vol. 4, no. 10, p. 107 133, 2014. DOI: 10.1063/1.4899186.

[79] N. Sorensen, R. Camley, and Z. Celinski, "Exchange stiffness as a function of composition in $cu_x(ni_{0.80}fe_{0.20})_{1-x}$ alloys," *Journal of Magnetism and Magnetic Materials*, vol. 477, pp. 344–348, 2019. DOI: 10.1016/j.jmmm.2019.01.099. [Online]. Available: https://doi.org/10.1016/j.jmmm.2019.01.099.

[80] S. Choi, K.-S. Lee, K. Y. Guslienko, and S.-K. Kim, "Strong radiation of spin waves by core reversal of a magnetic vortex and their wave behaviors in magnetic nanowire waveguides," *Physical Review Letters*, vol. 98, no. 8, p. 087 205, 2007. DOI: 10.1103/PhysRevLett.98.087205.

[81] A. Aharoni, "Demagnetizing factors for rectangular ferromagnetic prisms," *Journal of Applied Physics*, vol. 83, no. 6, pp. 3432–3434, 1998. DOI: 10.1063/1.367113.

[82] Y. Tokura, W. G. van der Wiel, T. Obata, and S. Tarucha, "Coherent single electron spin control in a slanting zeeman field," *Physical Review Letters*, vol. 96, p. 047 202, 2006. DOI: 10.1103/PhysRevLett.96.047202.

[83] M. Pioro-Ladrière, T. Obata, Y. Tokura, *et al.*, "Electrically driven single-electron spin resonance in a slanting zeeman field," *Nature Physics*, vol. 4, pp. 776–779, 2008. DOI: 10.1038/nphys1053.

[84] T. Obata, M. Pioro-Ladrière, Y. Tokura, *et al.*, "Coherent manipulation of individual electron spin in a double quantum dot integrated with a micromagnet," *Physical Review B*, vol. 81, p. 085 317, 2010. DOI: 10.1103/PhysRevB.81.085317.

[85] K. Takeda, J. Kamioka, T. Otsuka, *et al.*, "A fault-tolerant addressable spin qubit in a natural silicon quantum dot," *Science Advances*, vol. 2, no. 8, e1600694, 2016. DOI: 10.1126/sciadv.1600694.

[86] P. Harvey-Collard, J. Dijkema, G. Zheng, A. Sammak, G. Scappucci, and L. M. K. Vandersypen, "Coherent spin–spin coupling mediated by virtual microwave photons," *Physical Review X*, vol. 12, no. 2, p. 021 026, 2022. DOI: 10.1103/PhysRevX.12.021026.

[87] F. Forster, M. Mühlbacher, D. Schuh, W. Wegscheider, and S. Ludwig, "Electric-dipole-induced spin resonance in a lateral double quantum dot incorporating two single-domain nanomagnets," *Physical Review B*, vol. 91, no. 19, p. 195 417, 2015. DOI: 10.1103/PhysRevB.91.195417.

[88] R. P. G. McNeil, R. J. Schneble, M. Kataoka, *et al.*, "Localized magnetic fields in arbitrary directions using patterned nanomagnets," *Nano Letters*, vol. 10, no. 4, pp. 1549–1553, 2010. DOI: 10.1021/nl9039359.

[89] W. Legrand, S. Lopes, Q. Schaeverbeke, F. Montaigne, and M. M. Desjardins, "Optimal design of nanomagnets for on-chip field gradients," *Physical Review Applied*, vol. 20, no. 4, p. 044 062, 2023. DOI: 10.1103/PhysRevApplied.20.044062. [Online]. Available: https://doi.org/10.1103/PhysRevApplied.20.044062.

[90] S. Turcotte, S. Boutin, J. Camirand Lemyre, I. Garate, and M. Pioro-Ladrière, "Optimized micromagnet geometries for majorana zero modes in low g-factor materials," *Physical Review B*, vol. 102, no. 12, p. 125 425, 2020. DOI: 10.1103/PhysRevB.102.125425. arXiv: 1904.06275. [Online]. Available: https://link.aps.org/doi/10.1103/PhysRevB.102.125425.

[91] C. Abert, C. Huber, F. Bruckner, C. Vogler, G. Wautischer, and D. Suess, "A fast finite-difference algorithm for topology optimization of permanent magnets," *Journal of Applied Physics*, vol. 122, no. 11, p. 113 904, 2017. DOI: 10.1063/1.4998532. arXiv: 1707.09898. [Online]. Available: https://doi.org/10.1063/1.4998532.

[92] E. Kawakami, P. Scarlino, D. R. Ward, *et al.*, "Electrical control of a long-lived spin qubit in a si/sige quantum dot," *Nature Nanotechnology*, vol. 9, pp. 666–670, 2014. DOI: 10.1038/nnano.2014.153.

[93] T. Cubaynes, M. R. Delbecq, M. C. Dartiailh, *et al.*, "Highly coherent spin states in carbon nanotubes coupled to cavity photons," *npj Quantum Information*, vol. 5, p. 47, 2019. DOI: 10.1038/s41534-019-0169-4. arXiv: 1903.05229. [Online]. Available: https://www.nature.com/articles/s41534-019-0169-4.

[94] T. Thomson, "Magnetic properties of metallic thin films," in *Metallic Films for Electronic, Optical and Magnetic Applications: Structure, Processing and Properties*, K. Barmak and K. Coffey, Eds., Cambridge, UK: Woodhead Publishing, 2014, ch. 10, pp. 454–546. DOI: 10.1533/9780857096296.2.454.

[95] M. D. Kuz'min, K. P. Skokov, L. V. B. Diop, I. A. Radulov, and O. Gutfleisch, "Exchange stiffness of ferromagnets," *The European Physical Journal Plus*, vol. 135, p. 354, 2020. DOI: 10.1140/epjp/s13360-020-00294-y. [Online]. Available: https://doi.org/10.1140/epjp/s13360-020-00294-y.

[96] H. S. Jung, W. D. Doyle, and S. Matsunuma, "Influence of underlayers on the soft properties of high magnetization feco films," *Journal of Applied Physics*, vol. 93, no. 10, pp. 6462–6464, May 2003. DOI: 10.1063/1.1557653. [Online]. Available: https://pubs.aip.org/aip/jap/article/93/10/6462/472467.

[97] M. Hehn, S. Padovani, K. Ounadjela, and J.-P. Bucher, "Nanoscale magnetic domain structures in epitaxial cobalt films," *Physical Review B*, vol. 54, p. 3428, 1996. DOI: 10.1103/PhysRevB.54.3428.

[98] C. O. Database, *Silicon (diamond–cubic), cod entry 2104737*, Crystal data: Fd-3m, a = 5.43096(6) Å. Available from the Crystallography Open Database: https://www.crystallography.net/cod/2104737.html, 2020.

[99] *Cobalt (co), hexagonal close-packed (hcp), p6_3/mmc (space group 194)*, https://crystallography.net/cod/9008492.html, Crystallography Open Database (COD) entry 9008492. Licensed under CC0 1.0., 2025. (visited on 09/20/2025).

[100] J. E. Fisher, "Structure and magnetic anisotropy of f.c.c. cobalt films between 150° and 870 °k," *Thin Solid Films*, vol. 5, no. 1, pp. 53–60, 1970. DOI: 10.1016/0040-6090(70)90051-9.

[101] Crystallography Open Database, *Cobalt, fcc ($fm\bar{3}m$), a = 3.544 å*, https://www.crystallography.net/cod/9012949.html, COD entry 9012949, 2023.

[102] Crystallography Open Database, *Feco alloy, b2 (cscl-type), $pm\bar{3}m$, $a \approx 2.86$ å*, https://www.crystallography.net/cod/9004229.html, COD entry 9004229, 2023.

[103] K. A. Oukaci, "Periodic magnetic domains for channeled spin wave propagation," French title: Structures en domaines magnétiques périodiques pour la propagation guidée d'ondes de spin, PhD thesis, Université de Lorraine, Nancy, France, Oct. 2021. [Online]. Available: https://theses.fr/257432078.

[104] J. C. D. Graham and B. L. Averbach, "Magnetocrystalline anisotropy constants of iron at room temperature," *Physical Review*, vol. 112, no. 4, pp. 1117–1122, 1958, $K_1(300\,\mathrm{K}) \approx 4.8 \times 10^4\,\mathrm{J\,m^{-3}}$ (converted from $4.8 \times 10^5\,\mathrm{erg\,cm^{-3}}$). DOI: 10.1103/PhysRev.112.1117. [Online]. Available: https://link.aps.org/doi/10.1103/PhysRev.112.1117.

[105] R. M. Bozorth, *Ferromagnetism*. New York: Van Nostrand, 1951, Classic data compilation; tabulates Co anisotropy constants near room temperature. [Online]. Available: https://www.wiley.com/en-us/Ferromagnetism-p-9780780310322.

[106] B. Zimmermann, G. Bihlmayer, M. Böttcher, *et al.*, "Comparison of first-principles methods to extract magnetic parameters in ultrathin films: Co/pt(111)," *Physical Review B*, vol. 99, p. 214 426, 2019. DOI: 10.1103/PhysRevB.99.214426.

[107] S. Michea, J. Briones, J. L. Palma, *et al.*, "Forc and micromagnetism approach to the domain structure of cobalt antidot arrays," *Journal of Physics D: Applied Physics*, vol. 47, p. 335 001, 2014. DOI: 10.1088/0022-3727/47/33/335001.

[108] T. Devolder, J.-V. Kim, L. E. Nistor, R. C. Sousa, B. Rodmacq, and B. Dieny, "Exchange stiffness in ultrathin perpendicularly magnetized cofeb layers determined using the spectroscopy of electrically excited spin waves," *Journal of Applied Physics*, vol. 120, no. 18, p. 183 902, 2016. DOI: 10.1063/1.4967826.

[109] A. Mouhoub, F. Millo, C. Chappert, *et al.*, "Exchange energies in cofeb/ru/cofeb synthetic antiferromagnets," *Physical Review Materials*, vol. 7, p. 044 404, 2023. DOI: 10.1103/PhysRevMaterials.7.044404.

[110] S. A. Bunyaev, B. Budinska, R. Sachser, *et al.*, "Engineered magnetization and exchange stiffness in direct-write co–fe nanoelements," *Applied Physics Letters*, vol. 118, no. 2, p. 022 408, 2021. DOI: 10.1063/5.0036361.

[111] Y. Barnier, R. Pauthenet, and G. Rimet, "Thermomagnetic study of a hexagonal cobalt single crystal," *Cobalt (English Edition)*, vol. 15, pp. 1–7, 1962, Centre d'Information du Cobalt, Brussels.

[112] A. M. Zaitsev, *Optical Properties of Diamond: A Data Handbook*. Springer, 2000.

[113] A. Gruber, A. Dräbenstedt, C. Tietz, L. Fleury, J. Wrachtrup, and C. von Borczyskowski, "Scanning confocal optical microscopy and magnetic resonance on single defect centers in diamond," *Science*, vol. 276, no. 5321, pp. 2012–2014, 1997. DOI: 10.1126/science.276.5321.2012.

[114] G. Balasubramanian, I. Y. Chan, R. Kolesov, *et al.*, "Nanoscale imaging magnetometry with diamond spins under ambient conditions," *Nature*, vol. 455, no. 7213, pp. 648–651, 2008. DOI: 10.1038/nature07278.

[115] QZabre AG. "Quantum scanning tips." (2025), [Online]. Available: https://www.qzabre.com/QST.

[116] E. Marchiori, L. Ceccarelli, N. Rossi, *et al.*, "Magnetic imaging of superconducting qubit devices with scanning squid-on-tip," *Applied Physics Letters*, vol. 121, no. 5, p. 052 601, 2022. DOI: 10.1063/5.0103597. [Online]. Available: https://poggiolab.unibas.ch/full/QubitImage.pdf.

[117] S. Chatraphorn, E. F. Fleet, F. C. Wellstood, L. A. Knauss, and T. M. Eiles, "Scanning squid microscopy of integrated circuits," *Applied Physics Letters*, vol. 76, pp. 2304–2306, 2000.

[118] L. A. Knauss, A. B. Cawthorne, N. Lettsome, *et al.*, "Scanning squid microscopy for current imaging," *Microelectronics Reliability*, vol. 41, pp. 1211–1229, 2001.

[119] M. Gerken, A. Solignac, D. Momeni Pakdehi, *et al.*, "Traceably calibrated scanning hall probe microscopy at room temperature," *Journal of Sensors and Sensor Systems*, vol. 9, pp. 391–399, 2020, Published: 13 Nov 2020. DOI: 10.5194/jsss-9-391-2020. [Online]. Available: https://jsss.copernicus.org/articles/9/391/2020/.

[120] T. Cubaynes, L. C. Contamin, M. C. Dartiailh, *et al.*, "Nanoassembly technique of carbon nanotubes for hybrid circuit-qed," *Applied Physics Letters*, vol. 117, no. 11, p. 114 001, Sep. 2020. DOI: 10.1063/5.0021838.

[121] P. A. Spring, L. Milanovic, Y. Sunada, *et al.*, "Fast multiplexed superconducting-qubit readout with intrinsic purcell filtering using a multiconductor transmission line," *PRX Quantum*, vol. 6, p. 020 345, 2025. DOI: 10.1103/PRXQuantum.6.020345.

[122] M. Tinkham, *Introduction to Superconductivity*, 2nd ed. Mineola, NY: Dover Publications, 2004, Unabridged republication of the 1996 McGraw–Hill edition.

[123] A. S. Kher, "Superconducting nonlinear kinetic inductance devices," CaltechTHESIS:06042018-004220017, Ph.D. dissertation, California Institute of Technology, Pasadena, CA, 2017. [Online]. Available: https://ui.adsabs.harvard.edu/abs/2017PhDT.....472K/abstract.

[124] H. G. Leduc, B. Bumble, P. K. Day, *et al.*, "Titanium nitride films for ultrasensitive microresonator detectors," *Applied Physics Letters*, vol. 97, no. 10, p. 102 509, 2010. DOI: 10.1063/1.3480420.

[125] N. Samkharadze, A. Bruno, P. Scarlino, *et al.*, "High-kinetic-inductance superconducting nanowire resonators for circuit qed in a magnetic field," *Physical Review Applied*, vol. 5, p. 044 004, 2016. DOI: 10.1103/PhysRevApplied.5.044004.

[126] L. Grünhaupt, M. Spiecker, D. Gusenkova, *et al.*, "Granular aluminium as a superconducting material for high-impedance quantum circuits," *Nature Materials*, vol. 18, no. 8, pp. 816–819, 2019. DOI: 10.1038/s41563-019-0350-3.

[127] N. A. Masluk, I. M. Pop, A. Kamal, Z. K. Minev, and M. H. Devoret, "Microwave characterization of josephson junction arrays: Implementing a low loss superinductance," *Physical Review Letters*, vol. 109, no. 13, p. 137 002, 2012. DOI: 10.1103/PhysRevLett.109.137002.

[128] R. Kaufman, C. Liu, K. Cicak, *et al.*, "Simple, high saturation power, quantum-limited, rf squid array-based josephson parametric amplifiers," *arXiv preprint arXiv:2402.19435*, 2024. DOI: 10.48550/arXiv.2402.19435. arXiv: 2402.19435 [quant-ph]. [Online]. Available: https://arxiv.org/abs/2402.19435.

[129] C. Roy, S. Frasca, and P. Scarlino, "Study of magnetic field resilient high impedance high-kinetic inductance superconducting resonators," *arXiv preprint arXiv:2503.13321*, 2025. DOI: 10.48550/arXiv.2503.13321. arXiv: 2503.13321 [quant-ph]. [Online]. Available: https://arxiv.org/abs/2503.13321.

[130] C. X. Yu, "Hybrid circuit quantum electrodynamics with a hole spin in silicon," Thesis defense on 15 Sep 2022; Laboratory: CEA-IRIG/PHELIQS, Ph.D. dissertation, Université Grenoble Alpes, Grenoble, France, Sep. 2022. [Online]. Available: https://theses.fr/2022GRALY053.

[131] D. M. Pozar, *Microwave Engineering*, 5th ed. Hoboken, NJ: Wiley, 2021.

[132] M. Göppl, A. Fragner, M. Baur, *et al.*, "Coplanar waveguide resonators for circuit quantum electrodynamics," *Journal of Applied Physics*, vol. 104, no. 11, p. 113 904, 2008. DOI: 10.1063/1.3010859.

[133] S. Gevorgian, L. J. P. Linnér, and E. L. Kollberg, "Cad models for shielded multilayered cpw," *IEEE Transactions on Microwave Theory and Techniques*, vol. 43, no. 4, pp. 772–779, Apr. 1995. DOI: 10.1109/22.375223.

[134] P. Harvey-Collard, G. Zheng, J. Dijkema, *et al.*, "On-chip microwave filters for high-impedance resonators with gate-defined quantum dots," *Physical Review Applied*, vol. 14, no. 3, p. 034 025, Sep. 2020. DOI: 10.1103/PhysRevApplied.14.034025. [Online]. Available: https://link.aps.org/doi/10.1103/PhysRevApplied.14.034025.

[135] X. Zhang, Z. Zhu, N. P. Ong, and J. R. Petta, "High-impedance superconducting resonators and on-chip filters for circuit quantum electrodynamics with semiconductor quantum dots," *Physical Review Applied*, vol. 21, p. 014 019, 2024. DOI: 10.1103/PhysRevApplied.21.014019.

[136] T. Frey, P. J. Leek, M. Beck, K. Ensslin, A. Wallraff, and T. Ihn, "Characterization of a microwave frequency resonator via a nearby quantum dot," *Applied Physics Letters*, vol. 98, no. 26, p. 262 105, 2011. DOI: 10.1063/1.3604784.

[137] K. D. Petersson, L. W. McFaul, M. D. Schroer, *et al.*, "Circuit quantum electrodynamics with a spin qubit," *Nature*, vol. 490, no. 7420, pp. 380–383, 2012. DOI: 10.1038/nature11559.

[138] H. Toida, T. Nakajima, and S. Komiyama, "Vacuum rabi splitting in a semiconductor circuit qed system," *Physical Review Letters*, vol. 110, no. 6, p. 066 802, 2013. DOI: 10.1103/PhysRevLett.110.066802.

[139] J. Basset, D.-D. Jarausch, A. Stockklauser, *et al.*, "Single-electron double quantum dot dipole-coupled to a single photonic mode," *Physical Review B*, vol. 88, no. 12, p. 125 312, 2013. DOI: 10.1103/PhysRevB.88.125312.

[140] J. J. Viennot, M. R. Delbecq, M. C. Dartiailh, A. Cottet, and T. Kontos, "Out-of-equilibrium charge dynamics in a hybrid circuit quantum electrodynamics architecture," *Physical Review B*, vol. 89, no. 16, p. 165 404, 2014. DOI: 10.1103/PhysRevB.89.165404.

[141] Y.-Y. Liu, J. Stehlik, C. Eichler, M. J. Gullans, J. M. Taylor, and J. R. Petta, "Photon emission from a cavity-coupled double quantum dot," *Physical Review Letters*, vol. 113, no. 3, p. 036 801, 2014. DOI: 10.1103/PhysRevLett.113.036801.

[142] A. Stockklauser, V. F. Maisi, J. Basset, *et al.*, "Microwave emission from hybridized states in a semiconductor charge qubit," *Physical Review Letters*, vol. 115, no. 4, p. 046 802, 2015. DOI: 10.1103/PhysRevLett.115.046802.

[143] G.-W. Deng, D. Wei, J. R. Johansson, *et al.*, "Charge number dependence of the dephasing rates of a graphene double quantum dot in a circuit qed architecture," *Physical Review Letters*, vol. 115, no. 12, p. 126 804, 2015. DOI: 10.1103/PhysRevLett.115.126804.

[144] A. J. Landig, J. V. Koski, P. Scarlino, *et al.*, "Coherent spin–photon coupling using a resonant exchange qubit," *Nature*, vol. 560, no. 7717, pp. 179–184, 2018. DOI: 10.1038/s41586-018-0365-y.

[145] L. E. Bruhat, T. Cubaynes, J. J. Viennot, *et al.*, "Circuit qed with a quantum-dot charge qubit dressed by cooper pairs," *Physical Review B*, vol. 98, no. 15, p. 155 313, 2018. DOI: 10.1103/PhysRevB.98.155313.

[146] D. J. van Woerkom, P. Scarlino, J. H. Ungerer, *et al.*, "Microwave photon-mediated interactions between semiconductor qubits," *Physical Review X*, vol. 8, no. 4, p. 041 018, 2018. DOI: 10.1103/PhysRevX.8.041018.

[147] P. Scarlino, D. J. van Woerkom, A. J. Landig, *et al.*, "Coherent microwave-photon-mediated coupling between a semiconductor and a superconducting qubit," *Nature Communications*, vol. 10, p. 3011, 2019. DOI: 10.1038/s41467-019-10798-6.

[148] P. Scarlino, D. J. van Woerkom, A. Stockklauser, *et al.*, "Coherent microwave-photon-mediated coupling between a semiconductor and a superconducting qubit," *Nature Communications*, vol. 10, p. 3011, 2019. DOI: 10.1038/s41467-019-10798-6.

[149] G. Zheng, N. Samkharadze, N. Kalhor, *et al.*, "Rapid gate-based spin read-out in silicon using a high-impedance resonator," *Nature Nanotechnology*, vol. 14, no. 8, pp. 742–746, 2019. DOI: 10.1038/s41565-019-0498-0.

[150] F. Borjans, X. Croot, X. Mi, M. J. Gullans, and J. R. Petta, "Resonant microwave-mediated interactions between distant electron spins," *Nature*, vol. 577, no. 7789, pp. 195–198, 2020. DOI: 10.1038/s41586-019-1867-y.

[151] G. Xu, H. Watzinger, A. V. Kuhlmann, *et al.*, "Coherent hole-spin qubit in a ge/si core–shell nanowire," *Nature*, vol. 583, no. 7816, pp. 470–474, 2020. DOI: 10.1038/s41586-020-2441-1.

[152] B. Wang, T. Lin, H. Li, *et al.*, "Correlated spectrum of distant semiconductor qubits coupled by microwave photons," *Science Bulletin*, vol. 66, no. 4, pp. 332–338, 2021. DOI: 10.1016/j.scib.2020.10.005.

[153] M.-B. Chen, S.-L. Jiang, N. Wang, *et al.*, "Microwave-resonator-detected excited-state spectroscopy of a double quantum dot," *Physical Review Applied*, vol. 15, no. 4, p. 044 045, 2021. DOI: 10.1103/PhysRevApplied.15.044045.

[154] Y. Kang, Z.-H. Li, Z.-Z. Kong, *et al.*, "Coupling of hole double quantum dot in planar germanium to a microwave cavity," *arXiv*, 2023. eprint: 2310.08145. [Online]. Available: https://arxiv.org/abs/2310.08145.

[155] F. De Palma, F. Oppliger, W. Jang, *et al.*, *Strong hole-photon coupling in planar Ge: Probing the charge degree and Wigner molecule states*, Version v2 (2024-12-04); published as Nat. Commun. 15, 10177 (2024), 2023. DOI: 10.48550/arXiv.2310.20661. arXiv: 2310.20661 [quant-ph].

[156] J. Corrigan, M. A. Lemonde, M. R. Delbecq, *et al.*, "XGe_x double quantum dot and an off-chip tin resonator," *Physical Review Applied*, vol. 20, no. 6, p. 064 005, 2023. DOI: 10.1103/PhysRevApplied.20.064005.

[157] M. J. Ruckriegel, O. El-Arab, S. Bosco, *et al.*, "Electric dipole coupling of a bilayer graphene quantum dot to a high-impedance superconducting resonator," *Nano Letters*, vol. 24, no. 6, ePub ahead of print, 2024. DOI: 10.1021/acs.nanolett.4c01791.

[158] J. H. Ungerer, P. Scarlino, A. J. Landig, *et al.*, "Strong coupling between a microwave photon and a hole spin in silicon," *Nature Communications*, vol. 15, p. XXXX, 2024, article number to verify. DOI: 10.1038/s41467-024-45235-w.

[159] M. Janík, K. Roux, C. B. Espinosa, *et al.*, "Strong charge-photon coupling in planar germanium enabled by granular aluminium superinductors," *arXiv*, 2024. eprint: 2407.03079. [Online]. Available: https://arxiv.org/abs/2407.03079.

[160] J. J. Viennot, M. C. Dartiailh, A. Cottet, and T. Kontos, "Coherent coupling of a single spin to microwave cavity photons," *Science*, vol. 349, no. 6246, pp. 408–411, Jul. 2015. DOI: 10.1126/science.aaa3786.

[161] C. G. L. Bøttcher, S. P. Harvey, S. Fallahi, *et al.*, "Parametric longitudinal coupling between a high-impedance superconducting resonator and a semiconductor quantum dot singlet-triplet spin qubit," *Nature Communications*, vol. 13, p. 4773, Aug. 2022. DOI: 10.1038/s41467-022-32236-w.

[162] B. A. Mazin, "Microwave kinetic inductance detectors," Advisor: Jonas Zmuidzinas, Ph.D. dissertation, California Institute of Technology, Pasadena, CA, May 2004. [Online]. Available: https://web.physics.ucsb.edu/~bmazin/Papers/2004/Mazin/Caltech%20Thesis%202004%20Mazin.pdf.

[163] S. Probst, F. B. Song, P. A. Bushev, A. V. Ustinov, and M. Weides, "Efficient and robust analysis of complex scattering data under noise in microwave resonators," *Review of Scientific Instruments*, vol. 86, no. 2, p. 024 706, 2015. DOI: 10.1063/1.4907935. [Online]. Available: https://doi.org/10.1063/1.4907935.

[164] G. E. Ponchak, J. Papapolymerou, and M. M. Tentzeris, "Excitation of coupled slotline mode in finite-ground cpw with unequal ground-plane widths," *IEEE Transactions on Microwave Theory and Techniques*, vol. 53, no. 2, pp. 713–719, 2005. DOI: 10.1109/TMTT.2004.840594.

[165] G. Kirchmair, B. Vlastakis, Z. Leghtas, *et al.*, "Observation of quantum state collapse and revival due to the single-photon kerr effect," *Nature*, vol. 495, no. 7440, pp. 205–209, 2013. DOI: 10.1038/nature11902.

[166] W. Woods, G. Calusine, A. Melville, *et al.*, "Determining interface dielectric losses in superconducting coplanar-waveguide resonators," *Physical Review Applied*, vol. 12, no. 1, p. 014 012, 2019. DOI: 10.1103/PhysRevApplied.12.014012.

[167] A. A. Abrikosov, "The magnetic properties of superconducting alloys," *Journal of Physics and Chemistry of Solids*, vol. 2, no. 3, pp. 199–208, 1957.

[168] C. Wang, Y. Y. Gao, I. M. Pop, *et al.*, "Measurement and control of quasiparticle dynamics in a superconducting qubit," *Nature Communications*, vol. 5, p. 5836, 2014. DOI: 10.1038/ncomms6836.

[169] A. Kamlapure, M. Mondal, M. Chand, *et al.*, "Measurement of magnetic penetration depth and superconducting energy gap in very thin epitaxial nbn films," *Applied Physics Letters*, vol. 96, no. 7, p. 072 509, Feb. 2010. DOI: 10.1063/1.3314308.

[170] J.-C. Charlier, X. Blase, and S. Roche, "Electronic and transport properties of nanotubes," *Reviews of Modern Physics*, vol. 79, no. 2, pp. 677–732, 2007. DOI: 10.1103/RevModPhys.79.677. [Online]. Available: https://link.aps.org/doi/10.1103/RevModPhys.79.677.

[171] Z. Chen, J. Appenzeller, J. Knoch, Y.-M. Lin, and P. Avouris, "The role of metal–nanotube contact in the performance of carbon nanotube field-effect transistors," *Nano Letters*, vol. 5, no. 7, pp. 1497–1502, 2005. DOI: 10.1021/nl0508624. [Online]. Available: https://doi.org/10.1021/nl0508624.

[172] A. V. Lubenchenko, A. B. Pavolotsky, S. Krause, *et al.*, "Native oxide on ultra-thin nbn films," in *30th International Symposium on Space THz Technology (ISSTT 2019), Gothenburg, Sweden, April 15-17, 2019*, Paper 2019095098, 4 pages, 2019, —. [Online]. Available: https://www.nrao.edu/meetings/isstt/papers/2019/2019095098.pdf.

[173] B. Neukelmance, "Spin-photon interface and quantum gates for spins in carbon nanotube," Laboratoire de Physique de l'ENS (LPENS), supervisor: Takis Kontos, Ph.D. dissertation, Sorbonne Université (EDPIF), Paris, France, Mar. 2024. [Online]. Available: https://theses.hal.science/tel-04719374v1.

[174] M. R. Delbecq, L. E. Bruhat, J. J. Viennot, S. Datta, A. Cottet, and T. Kontos, "Photon-mediated interaction between distant quantum dot circuits," *Nature Communications*, vol. 4, p. 1400, 2013. DOI: 10.1038/ncomms2407.

[175] M. M. Desjardins, J. J. Viennot, M. C. Dartiailh, *et al.*, "Observation of the frozen charge of a kondo resonance," *Nature*, vol. 545, no. 7652, pp. 71–74, May 2017. DOI: 10.1038/nature21704.

[176] T. Ihn, *Semiconductor Nanostructures: Quantum States and Electronic Transport*. Oxford: Oxford University Press, 2009.

[177] J.-M. Raimond, *Atoms and photons (m2), École normale supérieure – PSL*, Paris, Master 2 lecture on light–matter interaction, 2024. [Online]. Available: https://www.phys.ens.fr/en/cours/atoms-and-photons (visited on 09/24/2025).

[178] F. Beaudoin, D. Lachance-Quirion, W. A. Coish, and M. Pioro-Ladrière, "Coupling a single electron spin to a microwave resonator: Controlling transverse and longitudinal couplings," 2016. arXiv: 1606.04736 [cond-mat.mes-hall]. [Online]. Available: https://arxiv.org/abs/1606.04736.

[179] M. Desjardins, "Explorer des circuits quantiques avec une architecture cqed : Application à des mesures de compressibilité," French, Thèse de doctorat, PSL Research University Paris (École normale supérieure), Paris, France, Dec. 2016. [Online]. Available: https://theses.fr/2016PSLEE044.

[180] F. Kuemmeth, S. Ilani, D. C. Ralph, and P. L. McEuen, "Coupling of spin and orbital motion of electrons in carbon nanotubes," *Nature*, vol. 452, no. 7186, pp. 448–452, Mar. 2008. DOI: 10.1038/nature06822.

[181] L. C. Contamin, T. Cubaynes, W. Legrand, *et al.*, "Inhomogeneous magnetic fields interacting with spinful states in a double quantum dot: Evidence for a staggered spin-orbit interaction," *Physical Review B*, vol. 107, p. 085 152, 2023. DOI: 10.1103/PhysRevB.107.085152. arXiv: 2104.12181 [cond-mat.mes-hall]. [Online]. Available: https://link.aps.org/doi/10.1103/PhysRevB.107.085152.

[182] M. Marganska, D. R. Schmid, A. Dirnaichner, *et al.*, "Shaping electron wave functions in a carbon nanotube with a parallel magnetic field," *Physical Review Letters*, vol. 122, no. 8, p. 086 802, 2019. DOI: 10.1103/PhysRevLett.122.086802.

[183] S. Krinner, S. Storz, P. Kurpiers, *et al.*, "Engineering cryogenic setups for 100-qubit scale superconducting circuit systems," *EPJ Quantum Technology*, vol. 6, no. 1, p. 2, 2019. DOI: 10.1140/epjqt/s40507-019-0072-0. [Online]. Available: https://epjquantumtechnology.springeropen.com/articles/10.1140/epjqt/s40507-019-0072-0.

[184] D. Patel, S.-H. Kim, W. Qiu, *et al.*, "Niobium–titanium (nb–ti) superconducting joints for persistent-mode operation," *Scientific Reports*, vol. 9, no. 1, p. 14 287, 2019. DOI: 10.1038/s41598-019-50549-7. [Online]. Available: https://www.nature.com/articles/s41598-019-50549-7.